Tunable Lasers HANDBOOK

EDITED BY

F. J. Duarte

OPTICS AND PHOTONICS

Tunable Lasers HANDBOOK

OPTICS AND PHOTONICS

(formerly Quantum Electronics)

SERIES EDITORS

PAUL F. LIAO

Bell Communications Research, Inc.

Red Bank, New Jersey

PAUL L. KELLEY

Lincoln Laboratory

Massachusetts Institute of Technology

Lexington, Massachusetts

IVAN P. KAMINOW

AT&T Bell Laboratories

Holmdel, New Jersey

A complete list of titles in this series appears at the end of this volume.

Tunable Lasers HANDBOOK

Edited by

F. J. Duarte

Eastman Kodak Company

Rochester, New York

ACADEMIC PRESS

San Diego New York Boston

London Sydney Tokyo Toronto

This book is printed on acid-free paper. ♾

Copyright © 1995 by ACADEMIC PRESS, INC.

All Rights Reserved.
No part of this publication may be reproduced or transmitted in any form or by any means, electronic or mechanical, including photocopy, recording, or any information storage and retrieval system, without permission in writing from the publisher.

Academic Press, Inc.
A Division of Harcourt Brace & Company
525 B Street, Suite 1900, San Diego, California 92101-4495

United Kingdom Edition published by
Academic Press Limited
24-28 Oval Road, London NW1 7DX

Library of Congress Cataloging-in-Publication Data

Duarte, F. J. (Frank J.)
Tunable lasers handbook / F. J. Duarte.
p. cm. — (Optics and photonics series)
Includes index.
ISBN 0-12-222695-X
1. Tunable lasers. I. Title. II. Series.
TA1706.D83 1995
621.36'6—dc20 95-8165
CIP

PRINTED IN THE UNITED STATES OF AMERICA
95 96 97 98 99 00 EB 9 8 7 6 5 4 3 2 1

Contents

Contributors xi
Preface xiii

1 Introduction

F. J. Duarte

1. Introduction 1
2. Tunable Laser Complementarity 4
3. Goal of This Book 5
   References 6

2 Narrow-Linewidth Laser Oscillators and Intracavity Dispersion

F. J. Duarte

1. Introduction 9
2. Dispersive Oscillator Configurations 10

3. Physical Dimensions 15
4. Generalized Interference Equation 16
5. Dispersion Linewidth Equation 17
6. Beam Divergence 19
7. Intracavity Dispersion 19
8. Intracavity Multiple-Prism Dispersion and Pulse Compression 23
9. Transmission Efficiency of Multiple-Prism Arrays 24
10. Wavelength Tuning 26
Appendix: Dispersion of Multiple-Prism Arrays and 4×4 Transfer Matrices 29
References 31

3 Tunable Excimer Lasers

R. C. Sze

D. G. Harris

1. Introduction 33
2. Excimer Active Media 35
3. Tuning of Discharge and Electron Beam Pumped Excimer Lasers 41
4. Discharge Excimer Lasers 53
References 59

4 CO_2 Isotope Lasers and Their Applications in Tunable Laser Spectroscopy

Charles Freed

1. Introduction 63
2. Vibrational Energy-Level Structive of the CO_2 Molecule 65
3. Rotational Energy-Level Substructure of the CO_2 Molecule 69
4. Processes Governing the Excitation of Regular Band Laser Transitions in CO_2 71
5. Additional Characteristics of Regular Band CO_2 Lasers Transitions 74
6. Lineshape Functions and Broadening Due to Gas Pressure and Doppler Shift in CO_2 Gas 76
7. Spectral Purity and Short-Term Stability 79

8. Long-Term Line-Center Stabilization of CO_2 Lasers 82
9. Absolute Frequencies of Regular Band Lasing Transitions in Nine CO_2 Isotopic Species 95
10. Pressure Shifts in Line-Center-Stabilized CO_2 Lasers 137
11. Small-Signal Gain and Saturation Intensity of Regular Band Lasing Transitions in Sealed-off CO_2 Isotope Lasers 144
12. Laser Design 149
13. Spanning the Frequency Range between Line-Center Stabilized CO_2 Laser Transitions 154
14. Spectroscopic Use of CO_2 Lasers outside Their Fundamental 8.9- to 12.4-μm Wavelength Range 159
References 161

5 Dye Lasers

F. J. Duarte

1. Introduction 167
2. Laser-Pumped Pulsed Dye Lasers 172
3. Flashlamp-Pumped Dye Lasers 179
4. cw Laser-Pumped Dye Lasers 184
5. Femtosecond-Pulsed Dye Lasers 191
6. Solid-State Dye Lasers 195
Appendix of Laser Dyes 200
References 215

6 Transition Metal Solid-State Lasers

Norman P. Barnes

1. Introduction 219
2. Transition Metal and Lanthanide Series Lasers 225
3. Physics of Transition Metal Lasers 232
4. $Cr:Al_2O_3$ 246
5. $Cr:BeAl_2O_4$ 251
6. $Ti:Al_2O_3$ 258
7. $Cr:LiCaAlF_6$ and $Cr:LiSrAlF_6$ 263
8. Cr:GSGG, Cr:YSAG, and Cr:GSAG 270
9. $Co:MgF_2$, $Ni:MgF_2$, and $V:MgF_2$ 275
10. Wavelength Control Methods 281
References 288

7 Optical Parametric Oscillators

Norman P. Barnes

1. Introduction 293
2. Parametric Interactions 297
3. Parametric Oscillation 301
4. Spectral Bandwidth and Acceptance Angles 306
5. Birefringence Effects 314
6. Average Power Limitations 317
7. Nonlinear Crystals 321
8. Phase-Matching Calculations 328
9. Performance 334
10. Tuning 343
References 345

8 Tunable External-Cavity Semiconductor Lasers

Paul Zorabedian

1. Introduction 349
2. Semiconductor Optical Gain Media 352
3. Classes of External-Cavity Lasers 368
4. First-Order Properties 370
5. Feedback Model 375
6. External-Cavity Design 377
7. Cavity Components 383
8. Survey of External-Cavity Laser Designs 398
9. Mode Selectivity of Grating Cavities 407
10. Phase-Continuous Tuning 409
11. Characterization Methods for External-Cavity Lasers 412
12. Measurement of Facet and External-Cavity Reflectances 412
13. Multimode Suppression 417
14. Multiple-Wavelength Operation 420
15. Wavelength Stabilization 421
16. Advanced Modeling Topics 422
17. Construction and Packaging 427
18. Applications 430
References 435

9 Tunable Free-Electron Lasers

Stephen Vincent Benson

1. Introduction 443
2. Methods of Wavelength Tuning 450
3. Broadly Tunable Optical Cavities 456
4. Wiggler Considerations 459
5. Tunable Laser Facilities and Their Characteristics 460
6. Summary 468
References 468

Index 471

Contributors

Numbers in parentheses indicate the pages on which the authors' contributions begin.

Norman P. Barnes (219, 293), NASA Langley Research Center, Hampton, Virginia 23681

Stephen Vincent Benson (443), Accelerator Division, Continuous Electron Beam Accelerator Facility, Newport News, Virginia 23606

F. J. Duarte (1, 9, 167), Eastman Kodak Company, Rochester, New York 14650

Charles Freed (63), Lincoln Laboratory and the Department of Electrical Engineering and Computer Science, Massachusetts Institute of Technology, Lexington, Massachusetts 02173

D. G. Harris (33), Rockwell International, Canoga Park, California 91309

R. C. Sze (33), Los Alamos National Laboratory, Los Alamos, New Mexico 87545

Paul Zorabedian (349), Photonic Technology Department, Hewlett-Packard Laboratories, Palo Alto, California 94303

Preface

Light and color are concepts that have always invoked thoughts of joy and wonder. Perhaps the essence of light is well captured in the realm of poetry where light has been identified as a "changing entity of which we can never be satiated" (Gabriela Mistral, 1889–1957).

This book is about changing light; it is about light sources that emit the colors of the rainbow and beyond. Indeed, the central theme of this book is changing light of high spectral purity or, as a physicist would say, tunable coherent radiation.

Tunable lasers ar unique physical systems that enjoy an abundance of applications ranging from physics to medicine. Given this utilitarian aspect, the sense of wonder in tunable lasers extends beyond beauty.

Tunable Lasers Handbook provides a broad and integrated coverage of the field, including dispersive tunable laser oscillators, tunable excimer lasers, tunable CO_2 lasers, dye lasers, tunable solid-state lasers, optical parametric oscillators, tunable semiconductor lasers, and free electron lasers. In this regard, the set of coherent sources considered here spans the electromagnetic spectrum from the near ultraviolet to the far infrared. Further features are the inclusion of both discretely and broadly tunable lasers, pulsed and continuous wave lasers, and gain media in the gaseous, liquid, and solid state.

Although the basic mission of this work is to offer an expeditious survey of the physics, technology, and performance of tunable lasers, some authors have ventured beyond the format of a handbook and have provided comprehensive reviews.

This project was initiated in 1990. Completion in late 1994 has allowed the inclusion of several recent developments in the areas of solid-state dye lasers, optical parametric oscillators, and external cavity tunable semiconductor lasers. The editor is particularly grateful to all contributing authors for their hard work and faith in the vision of this project.

F. J. Duarte
Rochester, NY
January 1995

1 Introduction

F. J. Duarte
Eastman Kodak Company
Rochester, New York

1. INTRODUCTION

Tunable sources of coherent radiation are suitable for a wide range of applications in science, technology, and industry. For instance, the first broadly tunable laser source, the dye laser, is used for a plethora of applications in many diverse fields [1] including physics [2–4], spectroscopy [5,6], isotope separation [6–8], photochemistry [9], material diagnostics [9], remote sensing [9–11], and medicine [12]. In addition to issues of physics, it is this utilitarian aspect of tunable lasers that motivates much of the interest in the field.

In recent years, new sources of tunable coherent radiation have become available that have either extended spectral coverage or yielded appealing emission characteristics. Notable among these sources are optical parametric oscillators and tunable semiconductor lasers.

This field has several natural subdivisions. For instance, although most sources of tunable coherent radiation are lasers, some sources such as the optical parametric oscillator (OPO) do not involve population inversion. An additional classification can be established between broadly tunable sources of coherent radiation, including broadly tunable lasers, and discretely tunable lasers, and/or line-tunable lasers. A subsequent form of classification can be the physical state of the different gain media such as gaseous, liquid, and solid state. Further

Tunable Lasers Handbook
Copyright © 1995 by Academic Press, Inc. All rights of reproduction in any form reserved.

avenues of differentiation can include the required method of excitation and the mode of emission, that is, pulsed or continuous wave (cw). Moreover, sources of tunable coherent radiation can be further differentiated by the spectral region of emission and energetic and/or power characteristics. Also, in the case of pulsed emission, pulse duration, and pulse repetition frequency (prf) are important.

The spectral coverage available from pulsed broadly tunable sources of coherent radiation is listed in Table 1. The spectral coverage available from cw broadly tunable lasers is given in Table 2 and emission wavelengths available

TABLE 1 Wavelength Coverage Available from Pulsed Broadly Tunable Sources of Coherent Radiation

Source	Wavelength range
Dye lasers	320–1200 nm[a] [13]
$Ti^{3+}:Al_2O_3$ laser	660–986 nm [14]
$Cr^{3+}:BeAl_2O_4$ laser	701–818 nm [15]
OPO	
BBO	0.41–2.7 μm [16]
Free-electron lasers (FELs)	2 μm–1 mm[b] [17]

[a]Wavelength range covered with the use of various dyes.
[b]Combined wavelength range from several free-electron lasers.

TABLE 2 Wavelength Coverage Available from cw Broadly Tunable Lasers

Laser source	Wavelength range
Dye lasers	320–1000 nm[a] [18]
$Ti^{3+}:Al_2O_3$ laser	710–870 nm[b] [19]
Semiconductor lasers[c]	
InGaAsP/InP	55 nm at 1500 nm [20]
InGaAsP/InP	1255–1335 nm [21]
GaAlAs	815–825 nm [22]
GaAlAs	20 nm at 780 nm [23]

[a]Wavelength range covered with the use of various dyes.
[b]Wavelength range of single-longitudinal-mode emission. Tuning range limited by coatings of mirrors [19]. Commercial designs offer extended tuning ranges beyond 1000 nm.
[c]Wavelength tuning achieved using external cavity designs.

from discretely tunable lasers are listed in Table 3 of Chapter 5. The information provided in these tables indicates that broadly tunable sources of coherent radiation span the electromagnetic spectrum from ~300 nm to ~1 mm. Excimer lasers offer limited tunability in regions further into the ultraviolet around 193 and 248 nm. The tuning ranges quoted for ArF and KrF lasers are ~17,000 GHz and ~10,500 GHz [24], respectively. An exception among excimer lasers is the XeF laser with its C→A transition, which has demonstrated broadly tunable emission in the 466- to 512-nm range [25]. In Table 3 of Chapter 5 bandwidth and tuning range information is included for a variety of discretely tunable lasers including excimer, N_2, HgBr, and Cu lasers. Wavelength information on line-tunable cw lasers such as Ar^+ and the Kr^+ lasers is included in Table 11 of Chapter 5. Energetic and power characteristics of some tunable sources of coherent radiation are listed in Table 3 of this chapter. Although the title of this book refers specifically to *tunable lasers,* sources that do not involve population inversion in their generation of coherent radiation are included. This approach is justified because the issue under consideration is the generation of tunable coherent radiation, which is precisely what OPOs perform.

In the area of ultrashort-pulse generation, dye lasers have demonstrated 17 fs using intracavity pulse compression [36] and 6 fs using further extra

TABLE 3 Energy and Power Characteristics from Broadly Tunable Sources of Coherent Radiation

Source	Pulse regime		cw regime
	Energy[a]	Power[a]	Power[a]
Dye lasers	400 J[b] [26]	2.5 kW at 13.2 kHz[c] [27]	43 W[d] [28]
Ti^{3+}:Al_2O_3 laser	6.5 J[b,e] [29]	5.5 W at 6.5 kHz[c] [30] 220 W at 110 Hz[b] [31]	43 W[d,f] [32]
Cr^{3+}:$BeAl_2O_4$ laser	>100 J[b] [33]		6.5 W[g] [34]
OPOs			
BBO	>100 mJ [16]		
$LiNbO_3$			10 mW [35]
FELs	~ GW levels in short pulses [17]		

[a]These values may represent the best published performance in this category.
[b]Under flashlamp excitation.
[c]Under copper-vapor–laser (CVL) excitation.
[d]Under Ar^+ laser excitation.
[e]Uses laser dye transfer in the excitation.
[f]Liquid-nitrogen cooled.
[g]Under Hg-lamp excitation.

cavity compression [37]. Utilizing intracavity negative dispersion techniques, $Ti^{3+}:Al_2O_3$ lasers have yielded 11 fs [38]. Also, 62 fs have been reported in OPOs using extracavity compression [39]. Emission from FELs is intrinsically in the short-pulse regime with pulses as short as 250 fs [17].

2. TUNABLE LASER COMPLEMENTARITY

From the data given previously it could be stated that tunable sources of coherent radiation span the electromagnetic spectrum continuously from the near ultraviolet to the far infrared. However, this claim of broad coverage is sustained from a global and integrated perspective of the field. Further, a perspective of complementarity is encouraged by nature, given that different sources of tunable coherent radiation offer different optimized modes of operation and emission.

In this context, under ideal conditions, *the application itself should determine the use of a particular laser* [40,41]. This perspective should ensure the continuation of the utilitarian function traditional of the early tunable lasers that ensured their success and pervasiveness.

To determine an appropriate laser for a given application, the logic of selection should identify the simplest and most efficient means to yield the required energy, or average power, in a specified spectral region. In practice, the issue may be complicated by considerations of cost and availability. In this regard, selection of a particular pulsed laser should include consideration of the following parameters:

1. Spectral region
2. Pulse energy
3. Average power (or prf)
4. Cost (capital and operational)
5. Environment.

More subtle issues that are also a function of design include the following:

6. Emission linewidth
7. Wavelength and linewidth stability
8. Pulse length (femtoseconds, nanoseconds, or microseconds)
9. Physical and optical ruggedness
10. Amplified spontaneous emission (ASE) level.

A basic illustration of complementarity is the use of different types of lasers to provide tunable coherent radiation at different spectral regions. For instance. FELs can be recommended for applications in need of far-infrared emission, whereas dye lasers are suitable for applications requiring high average powers in the visible.

A more specific example of the complementarity approach can be given in reference to isotope separation. In this regard, the necessary spectroscopic information including isotopic shifts, absorption linewidths, and hyperfine structure can be studied using narrow-linewidth tunable cw lasers. On the other hand, for successful large-scale laser isotope separation high-average-power pulsed tunable lasers are necessary [6,27]. A further example is the detection and treatment of surface defects in optical surfaces being used in the transmission mode for imaging applications. The detection and assessment of the surface defects is accomplished using interferometry that applies tunable narrow-linewidth cw lasers. Surface treatment requires the use of pulsed lasers operating in the high prf regime.

Recently, complementarity in tunable lasers has been taken a step further with the integration of systems that utilize complementary technologies to achieve a given performance. An example is the use of a semiconductor–laser oscillator and a dye–laser amplifier [42]. Also, the event of high-performance solid-state dye–laser oscillators [43] has brought the opportunity to integrate these oscillators into OPO systems [44].

3. GOAL OF THIS BOOK

The goal of this book is to provide an expeditious guide to tunable sources of coherent radiation and their performance. Issues of physics and technology are also considered when judged appropriate. In this book, this judgment has been made by each individual contributor. Although the basic function of a handbook is to tabulate relevant physical and performance data, many works under that classification go beyond this basic format. In this book, several chapters go beyond the classical concept of a handbook and provide a detailed discussion of the data presented.

From a practical perspective, the intended function of this book is to offer scientists and engineers the means to gain an appreciation for the elements and performance of tunable lasers and ultimately to assist the reader to determine the merit of a particular laser relative to a given application.

3.1 Book Organization

The book is divided into nine chapters including this introduction. A chapter on narrow-linewidth oscillators is introduced prior to the main collection of chapters given the broad applicability of the subject matter. The main body of the book is basically organized into two groups of chapters categorized as discretely tunable lasers and broadly tunable lasers. Discretely tunable lasers are considered first because that also satisfies the more technocratic division of the

subject matter in terms of physical state, that is, gas, liquid, and solid-state lasers consecutively. Here, note that because dye lasers have been demonstrated to lase in the three states of matter, their positioning between gas and solid state is quite appropriate. Free-electron lasers are listed at the end of the broadly tunable coherent sources given their uniqueness as physical systems.

Chapter 2 treats narrow-linewidth oscillators and intracavity dispersion. The subject matter in this chapter is applicable to both discretely and broadly tunable lasers in the gaseous, liquid, or solid state. Chapter 3 addresses tunable excimer lasers including ArF, KrF, XeCl, and XeF. Chapter 4 is dedicated to tunable CO_2 lasers oscillating in the cw regime. These two chapters deal with discretely tunable lasers in the gaseous phase.

Broadly tunable sources and lasers are considered in Chapters 5 to 9. Chapter 5 deals with dye lasers and Chapter 6 with transition metal solid-state lasers. The latter chapter includes material on $Ti^{3+}:Al_2O_3$ and $Cr^{3+}:BeAl_2O_4$ lasers. Chapter 7 considers the principles of operation and a variety of crystals used in optical parametric oscillators. The subject of tunable semiconductor lasers is treated in Chapter 8 with emphasis on external cavity and wavelength tuning techniques. Chapter 9 provides an up-to-date survey of free-electron lasers.

For historical information and basic references on the various types of tunable lasers, the reader should refer to the literature cited in the chapters. The reader should also be aware that the degree of emphasis on a particular laser class follows the judgment of each contributing author. In this regard, for example, high-pressure pulsed CO_2 lasers are only marginally considered and the reader should refer to the cited literature for further details. A further topic that is related to the subject of interest, but not a central objective of this volume, is frequency shifting via nonlinear optics techniques such as Raman shifting.

REFERENCES

1. F. J. Duarte and D. R. Foster, in *Encyclopedia of Applied Physics* (G. L. Trigg, Ed.), Vol. 8, pp. 331–352, VCH, New York (1994).
2. V. S. Letokhov, in *Dye Lasers: 25 Years* (M. Stuke, Ed.), pp. 153–168, Springer-Verlag, Berlin (1992).
3. J. F. Roch, G. Roger, P. Grangier, J. M. Courty, and S. Reynaud, *Appl. Phys. B* **55,** 291 (1992).
4. M. Weitz, A. Huber, F. Schmidt-Kaler, D. Leibfried, and T. W. Hänsch, *Phys. Rev. Lett.* **72,** 328 (1994).
5. R. J. Hall and A. C. Eckbreth, in *Laser Applications* (J. F. Ready and R. K. Erf, Eds.), Vol. 5, pp. 213–309, Academic, New York (1984).
6. J. A. Paisner and R. W. Solarz, in *Laser Spectroscopy and Its Applications* (L. J. Radziemski, R. W. Solarz, and J. A. Paisner, Eds.), pp. 175–260, Marcel Dekker, New York (1987).
7. F. J. Duarte, H. R. Aldag, R. W. Conrad, P. N. Everett, J. A. Paisner, T. G. Pavlopoulos, and C. R. Tallman, in *Proc. Int. Conf. Lasers '88* (R. C. Sze and F. J. Duarte, Eds.), pp. 773–790, STS Press, McLean, VA (1989).
8. M. A. Akerman, in *Dye Laser Principles* (F. J. Duarte and L. W. Hillman, Eds.), pp. 413–418, Academic, New York (1990).

9. D. Klick, in *Dye Laser Principles* (F. J. Duarte and L. W. Hillman, Eds.), pp. 345–412, Academic, New York (1990).
10. W. B. Grant, *Opt. Eng.* **30,** 40 (1991).
11. E. V. Browell, *Opt. Photon. News* **2**(10), 8 (1991).
12. L. Goldman, in *Dye Laser Principles* (F. J. Duarte and L. W. Hillman, Eds.), pp. 419–432, Academic, New York (1990).
13. F. J. Duarte and L. W. Hillman, in *Dye Laser Principles* (F. J. Duarte and L. W. Hillman, Eds.), pp. 1–15, Academic, New York (1990).
14. P. F. Moulton, *J. Opt. Soc. Am. B* **3,** 125 (1986).
15. J. C. Walling, O. G. Peterson, H. P. Jenssen, R. C. Morris, and E. W. O'Dell, *IEEE J. Quantum Electron.* **QE-16,** 1302 (1980).
16. A. Fix, T. Schröder, R. Wallenstein, J. G. Haub, M. J. Johnson, and B. J. Orr, *J. Opt. Soc. Am. B* **10,** 1744 (1993).
17. S. Benson, private communication, 1994.
18. L. Hollberg, in *Dye Laser Principles* (F. J. Duarte and L. W. Hillman, Eds.), pp. 185–238, Academic, New York (1990).
19. C. S. Adams and A. I. Ferguson, *Opt. Commun.* **79,** 219 (1990).
20. R. Wyatt and W. J. Devlin, *Electron. Lett.* **19,** 110 (1983).
21. P. Zorabedian, *J. Lightwave Technol.* **10,** 330 (1992).
22. M. W. Fleming and A. Mooradian, *IEEE J. Quantum Electron.* **QE-17,** 44 (1981).
23. K. C. Harvey and G. J. Myatt, *Opt. Lett.* **16,** 910 (1991).
24. T. R. Loree, K. B. Butterfield, and D. L. Barker, *Appl. Phys. Lett.* **32,** 171 (1978).
25. T. Hofmann and F. K. Tittel, *IEEE J. Quantum Electron.* **29,** 970 (1993).
26. F. N. Baltakov, B. A. Barikhin, and L. V. Sukhanov, *JETP Lett.* **19,** 174 (1974).
27. I. L. Bass, R. E. Bonanno, R. P. Hackel, and P. R. Hammond, *Appl. Opt.* **33,** 6993 (1992).
28. H. J. Baving, H. Muuss, and W. Skolaut, *Appl. Phys. B* **29,** 19 (1982).
29. A. J. W. Brown and C. H. Fisher, *IEEE J. Quantum Electron.* **29,** 2513 (1993).
30. M. R. H. Knowles and C. E. Webb, *Opt. Lett.* **18,** 607 (1993).
31. A. Hoffstadt, *Opt. Lett.* **19,** 1523 (1994).
32. G. Ebert, I. Bass, R. Hackel, S. Jenkins, K. Kanz, and J. Paisner, in *Conf. Lasers and Electro-Optics,* Vol. 11 of OSA Technical Digest Series, pp. 390–393, Optical Society of America, Washington, DC (1991).
33. J. C. Walling, in *Tech. Digest Int. Conf. Lasers '90,* paper MH.3, Society for Optical and Quantum Electronics, San Diego, CA (1990).
34. J. C. Walling, O. G. Peterson, and R. C. Morris, *IEEE J. Quantum Electron.* **QE-16,** 120 (1980).
35. D. C. Gerstenberger and R. W. Wallace, *J. Opt. Soc. Am. B* **10,** 1681 (1993).
36. A. Finch, G. Chen, W. Sleat, and W. Sibbett, *J. Mod. Opt.* **35,** 345 (1988).
37. R. L. Fork, C. H. Brito-Cruz, P. C. Becker, and C. V. Shank, *Opt. Lett.* **12,** 483 (1987).
38. M. T. Asaki, C. P. Huang, D. Garvey, J. Zhou, H. C. Kapteyn, and M. M. Murnane, *Opt. Lett.* **18,** 977 (1993).
39. Q. Fu, G. Mak, and H. M. van Driel, *Opt. Lett.* **17,** 1006 (1992).
40. F. J. Duarte, *Laser Focus World* **27**(5), 25 (1991).
41. F. J. Duarte, *Lasers Optron.* **10**(5), 8 (1991).
42. A. M. Farkas and J. G. Eden, *IEEE J. Quantum Electron.* **29,** 2923 (1993).
43. F. J. Duarte, *Appl. Opt.* **33,** 3857 (1994).
44. B. J. Orr, private communication, 1994.

2 Narrow-Linewidth Laser Oscillators and Intracavity Dispersion

F. J. Duarte
Eastman Kodak Company
Rochester, New York

1. INTRODUCTION

Efficient tunable narrow-linewidth emission is intimately related to intracavity dispersive configurations. Intracavity dispersive assemblies integrated by multiple-prism arrays and gratings form an essential part of narrow-linewidth pulsed oscillators. However, their importance and significant contribution extend beyond the pulsed regime and into the continuous-wave (cw) mode of oscillation. Further, these dispersive oscillator configurations have been shown to be successful and are widely applied to lasers in the gaseous, liquid, and solid states. Hence, the description and discussion of tunable dispersive oscillators provided here is generalized. In this regard, the active media is referred to as the *gain media* in a generic sense.

Here, a succinct survey of narrow-linewidth oscillator configurations and their respective performances is provided. In addition, elements of intracavity dispersion theory and relevant propagation ray matrices are included.

Tunable Lasers Handbook
Copyright © 1995 by Academic Press, Inc. All rights of reproduction in any form reserved.

2. DISPERSIVE OSCILLATOR CONFIGURATIONS

Dispersive oscillators can be divided into two major classes [1]: Class I oscillators use a narrow and intrinsic TEM_{00} intracavity beam, and Class II oscillators use intracavity beam expansion. Examples of Class I oscillators are grating-mirror resonators, which incorporate intracavity etalons, and pure grazing-incidence grating cavities (Fig. 1). Class II oscillators employ intracavity beam expansion to magnify the original narrow TEM_{00} beam waist in order to illuminate the grating completely (Fig. 2). Intracavity beam expansion can be accomplished using multiple-prism beam expanders and two-dimensional transmission or reflection telescopes, such as Galilean and Cassegrain telescopes, respectively [1,2]. In Fig. 2, two alternative Class II oscillators are illustrated: multiple-prism Littrow (MPL) grating oscillators (Figs. 2a,b) and hybrid multiple-prism grazing-incidence (HMPGI) grating oscillators (Fig. 2c). Table 1 lists reported performance characteristics for Class I and II dispersive oscillators for gain media in the gaseous, liquid, and solid states.

Class I oscillators using intracavity etalons can yield excellent narrow-linewidth performance [8]. The main concerns are the use of intracavity etalons with coatings that may be susceptible to damage by high intracavity energy fluxes. Also, broadband tuning can demand a fine degree of control on the various intracavity elements. The pure grazing-incidence cavity offers very narrow-linewidth emission, compactness, and excellent broadband synchronous tuning capabilities. The main disadvantage of grazing-incidence cavities deployed in a closed-cavity configuration (as shown in Fig. 1b), is their relatively lower efficiency. Higher efficiencies can be obtained in an open-cavity configuration,

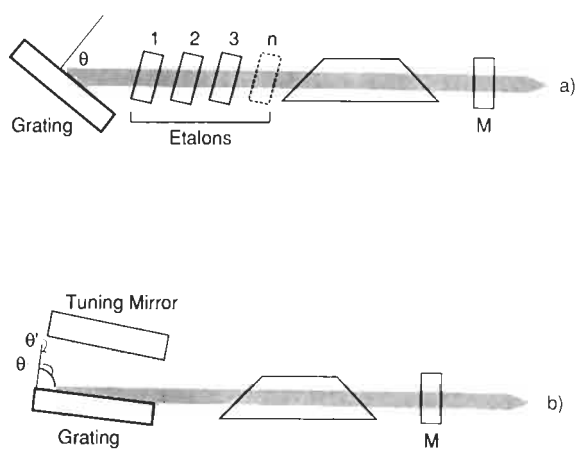

FIGURE 1 Class I oscillators. (a) Grating-mirror resonator incorporating intracavity etalons. (b) Grazing-incidence cavity.

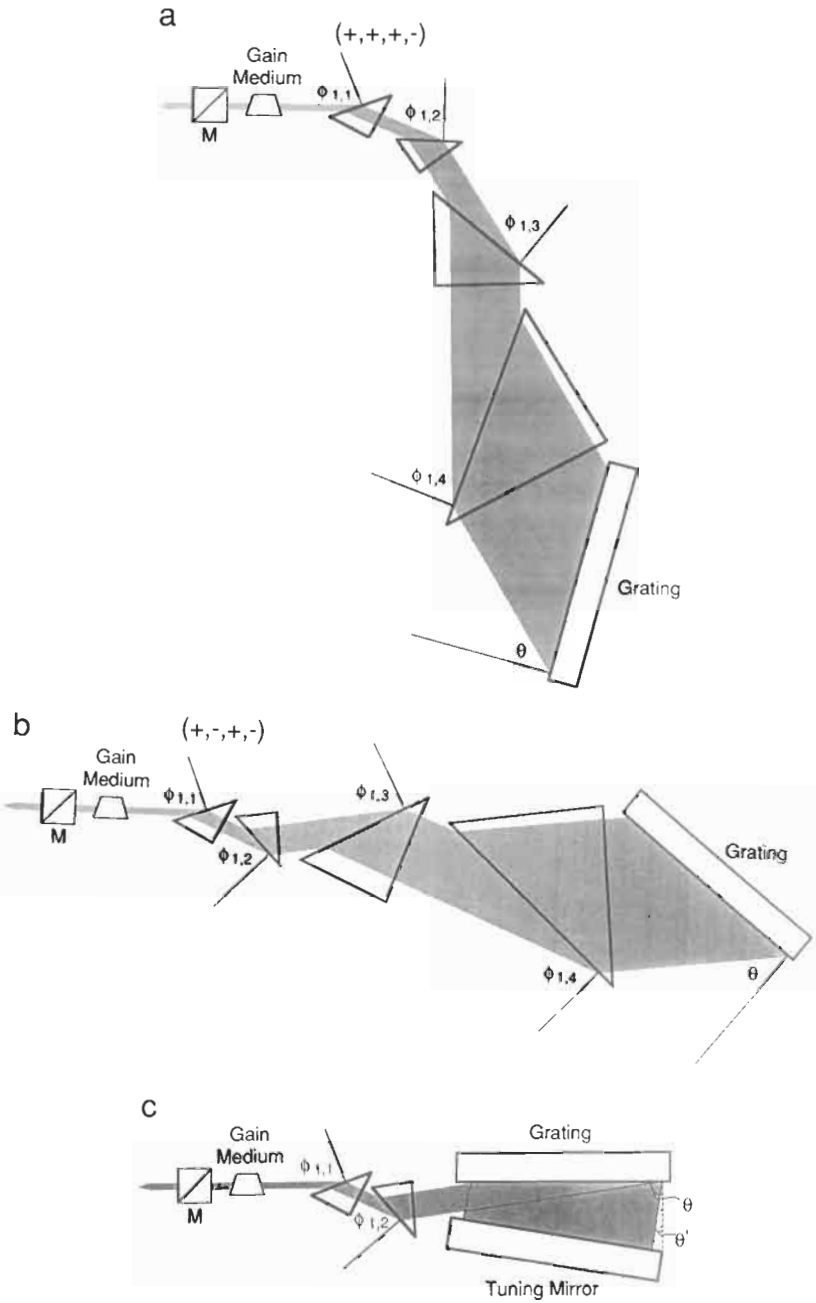

FIGURE 2 Class II oscillators. (a) An MPL oscillator using a multiple-prism beam expander in a (+,+,+,–) configuration. (b) An MPL oscillator using a multiple-prism beam expander in a (+,–,+,–) configuration. (c) An HMPGI oscillator. These oscillators incorporate a polarizer output coupler rather than a conventional mirror (this is an optional feature).

where the output is coupled via the reflection losses of the grating, at a cost of higher amplified spontaneous emission (ASE) levels [2,18,24]. In addition to the information given in Table 1, this class of oscillator design has also been applied to *optical parametric oscillators* [32] (see Chapter 6).

Class II oscillators incorporating multiple-prism beam expanders are, in general, more efficient than pure grazing-incidence designs but they are also more complex. In Fig. 2, MPL oscillators using multiple-prism beam expanders deployed in (+,+,+,–) and (+,–,+,–) configurations are illustrated. In a (+,+,+,–) configuration, the first three prisms are deployed in an additive configuration with the fourth prism deployed in a compensating mode to neutralize the cumulative dispersion of the first three prisms. In a (+,–,+,–) configuration, two pairs of compensating prisms are utilized [1,2]. These configurations are used to yield zero dispersion at a wavelength of design thus reducing beam deviations due to $(\partial n/\partial T)$ factors and leaving the tuning characteristics of the oscillator dependent on the grating. Extensive details on multiple-prism design have been given by Duarte [1] and relevant mathematical formulas are given in a later section on intracavity dispersion. The main design constraint is to provide the necessary beam expansion to achieve total illumination of the grating at a *maximum* transmission efficiency and a *minimum* intracavity length.

The intrinsic intracavity dispersion of a grazing-incidence grating design is higher than the dispersion achieved by an MPL grating configuration. A configuration that provides higher intracavity dispersion than MPL designs and higher conversion efficiency than pure grazing-incidence cavities is the HMPGI grating cavity mentioned earlier [20,24] (Fig. 2c). In HMPGI oscillators the grating is deployed in a near grazing-incidence configuration that is far more efficient than a pure grazing-incidence configuration [24] (see Section 9). Further, because the required intracavity beam expansion is far less than that typical of MPL oscillators, efficient and compact multiple-prism expanders can be readily designed to provide the necessary intracavity preexpansion. Today, HMPGI oscillators are widely used in research and commercial tunable laser systems.

Improved oscillator designs use a polarizer output coupler rather than a traditional mirror as the output coupler [23,33] (see Fig. 2). The output-coupler polarizer is made of a Glan–Thompson polarizer with an antireflection-coated inner surface and an outer surface that is coated for partial reflection. Dispersive oscillators incorporating multiple-prism grating assemblies yield strongly *p*-polarized narrow-linewidth emission [1,2,20]. In this context, the function of the output-coupler polarizer is to suppress single-pass unpolarized ASE in high-gain lasers. Thus, the use of a polarizer output coupler in dispersive dye laser oscillators has yielded extremely low levels of ASE in the 10^{-7} to 10^{-9} range [22,23]. The Glan–Thompson polarizer output coupler is illustrated in Fig. 3.

TABLE 1 Performance Characteristics of Dispersive Oscillators

Gain medium	Excitation source	Cavity configuration	λ (nm)	Tuning range	Δν	E_0	% E_{ff}[a]	Reference
Gas								
ArF	Electron discharge	MPL	193	~6000 GHz	10 GHz	150 μJ		[3]
KrF		GI	248	2437 GHz	≤9 GHz	15 μJ		[4]
XeCl		GI	308	~120 GHz	~31 GHz	50 mJ		[5]
XeCl		GI	308		~1.5 GHz	~1 mJ		[6]
XeCl		GI	308		~1 GHz	4 mJ		[7]
XeCl		3 etalons	308		≤150 MHz	2–5 μJ		[8]
XeCl		MPL[b]	308		3.3 GHz			[9]
XeCl		HMPGI[b]	308		1.8 GHz			[9]
CO_2		GI	10,591		117 MHz	140 mJ		[10]
CO_2		GI	10,591	2.6 GHz	400–700 MHz	230 mJ		[11]
CO_2		MPL	10,591		≤140 MHz	200 mJ		[12]
CO_2		HMPGI	10,591		107 MHz	85 mJ		[12]
Liquid (dye)								
Rhodamine 590	N_2 laser	Telescopic	600		2.5 GHz		20	[13]
		Telescopic[c]			300 MHz		2–4	[13]
	Nd:YAG laser[d]	GI	600		2.5 GHz		~4	[14]
Coumarin 153	N_2 laser	GI	524	519–575 nm	420 MHz		~6	[15]
Rhodamine 590	Nd:YAG laser[d]	GI	600		300 MHz		2	[16]
	Nd:YAG laser[d]	GI			150 MHz		3	[17]
Coumarin 500	N_2 laser	MPL	510	490–530 nm	1.61 GHz		14	[18]

(*continues*)

TABLE 1 (*continued*)

Gain medium	Excitation source	Cavity configuration	λ (nm)	Tuning range	Δν	E_0	% E_{II}[a]	Reference
Rhodamine 590	Cu laser	MPL[c]	572		60 MHz		5	[19]
	Cu laser	MPL	575	565–605 nm	1.4 GHz		5	[20]
	Flashlamp	MPL	580		138–375 MHz	3–10 mJ		[21–23]
Coumarin 500	N_2 laser	HMPGI	510	490–530 nm	1.15 GHz		7	[24]
Rhodamine 590	Cu laser	HMPGI	575	565–603 nm	400–650 MHz		4	[20]
	Flashlamp	HMPGI	580		138–375 MHz	3–10 mJ		[21–23]
Solid State								
Rhodamine 590	Laser	MPL	575	563–610 nm	1.12 GHz		9	[25]
in MPMMA		HMPGI	575	565–603 nm	1.2 GHz[e]		4	[25]
$Cr:BeAl_2O_4$	Flashlamp	MPL[b]	760		~690 MHz			[26]
		HMPGI[b]	760		~315 MHz			[26]
$Ti:Al_2O_3$	Nd:YAG laser[d]	GI		746–918 nm	~1.5 GHz	2 mJ	5	[27]
		GI		720–915 nm	≤500 MHz	1–3 mJ	~5	[28]
Semiconductor								
GaAlAs		GI	780	20 nm @ 780 nm	10 kHz			[29]
InGaAsP/InP		MPL		1255–1335 nm	100 kHz			[30]
Index-guided diode		HMPGI[b]	670		1.2 GHz[f]			[31]

[a]Measured in laser-pumped systems.
[b]Calculated values.
[c]Incorporates intracavity etalon.
[d]Frequency doubled.
[e]Also delivers single-longitudinal-mode emission at Δν ≤ 500 MHz.
[f]Dispersive linewidth.

3. PHYSICAL DIMENSIONS

An important initial condition necessary to achieve narrow-linewidth tunable emission is to attain a single-transverse-mode laser beam profile. This is determined by the beam waist at the gain region and the cavity length. For example, a laser-pumped dye laser, with the excitation laser focused to illuminate a gain volume 10 mm in length and 0.2 mm in diameter, would need a cavity length of ~7 cm (at λ ~580 nm) to obtain a near TEM_{00} beam profile. Dimensions of the gain region in laser-excited dye lasers are typically ~10 mm in length with a cross-sectional diameter in the 0.2- to 0.3-mm range. These dimensions tend to yield divergences near the diffraction limit in the 1- to 2-mrad range, at λ ~580 nm. Flashlamp-pumped dye laser oscillators use gain regions of 10 to 40 cm in length with cross-sectional diameters of ~1 mm or less. For gas lasers, active lengths can vary from 20 to more than 50 cm with cross-sectional diameters of ~1 mm. Semiconductor lasers, on the other hand, offer rather small dimensions with active lengths in the submillimeter range and with cross-sectional dimensions in the micrometer regime.

Diffraction gratings are commercially available in the following varieties: 1200, 2400, 3000, 3600, and 4300 l/mm. Usually the grating length is 5 cm but gratings up to 15 cm long have been used [21–23].

The generalized theory and design of multiple-prism beam expanders have been described in detail by Duarte [1,2,34–36]. The basic elements of this theory are presented in Section 7. In essence, an intracavity multiple-prism beam expander for a HMPGI oscillator incorporating four prisms to yield a beam magnification factor of $M \approx 30$ and a transmission factor of 0.76 can be designed to

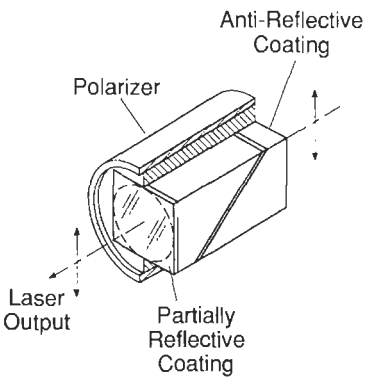

FIGURE 3 The Glan-Thompson polarizer output coupler with its inner surface antireflection coated and its partially reflective outer surface. In the dispersive oscillators described here, the polarizer output coupler is deployed with its polarization axis parallel to the plane of propagation (that is, rotated by $\pi/2$ relative to this figure).

use less than 5 cm of intracavity space to illuminate a 5-cm-long grating [1]. Certainly, further intracavity space is necessary for a multiple-prism beam expander designed to provide $M \approx 100$ in a MPL oscillator.

4. GENERALIZED INTERFERENCE EQUATION

Consider a generalized transmission grating illuminated by a dispersionless multiple-prism beam expander as illustrated in Fig. 4. Using the notation of Dirac the probability amplitude for the propagation of electromagnetic radiation from the beam expander (s) to a total reflector (x) via a grating of N slits is given by

$$\langle x|s\rangle = \sum_{j=1}^{N} \langle x|j\rangle\langle j|s\rangle. \tag{1}$$

Using $\langle x|j\rangle = \Psi\ (r_{j,x})\ e^{-i\phi_j}$ and $\langle j|s\rangle = \Psi\ (r_{s,j})\ e^{-i\theta_j}$, where $\Psi\ (r_{j,x})$ and $\Psi\ (r_{s,j})$ are appropriate diffraction functions, we can write [1,38]

$$\left|\langle x|s\rangle\right|^2 = \sum_{j=1}^{N} \Psi(r_j)^2 + 2\sum_{j=1}^{N} \Psi(r_j)\left[\sum_{m=j+1}^{N} \Psi(r_m)\cos(\Omega_m - \Omega_j)\right], \tag{2}$$

where $\Psi\ (r_j) = \Psi\ (r_{j,x})\ \Psi\ (r_{s,j})$ and $\Omega_j = (\theta_j + \phi_j)$.

This generalized equation enables the prediction of interference and/or diffraction intensity patterns produced by the interaction of electromagnetic radiation with N-slit gratings of any geometry and/or dimensions. An important application of Eq. (2) is the prediction of the transverse-mode structure produced by an intracavity slit [37]. In this case the intracavity slit is represented by an array of a large number of small individual slits [37]. For instance, in Fig. 5 the transverse-mode structures corresponding to Fresnel numbers of 0.86 and 0.25, at $\lambda =$ 580 nm, are illustrated.

The interference term of Eq. (2) can be used, in conjunction with the geometry related to the path differences $|L_m - L_{m-1}|$, to establish the expression $\Delta\lambda \approx \Delta\theta(\partial\theta/\partial\lambda)^{-1}$.

For a two-dimensional slit array the equation for the probability amplitude becomes

$$\langle x|s\rangle = \sum_{z=1}^{N}\sum_{y=1}^{N} \langle x|j_{zy}\rangle\langle j_{zy}|s\rangle. \tag{3}$$

Using $\langle x|j_{zy}\rangle = \Psi\left(r_{j_{zy},x}\right)e^{-i\phi_{zy}}$ and $\langle j_{zy}|s\rangle = \Psi\left(r_{s,j_{zy}}\right)e^{-i\theta_{zy}}$, the two-dimensional probability can be written as

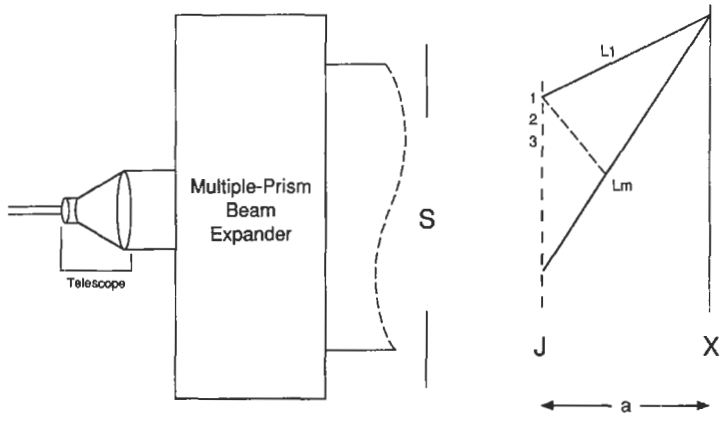

FIGURE 4 Multiple-prism grating assembly. The expanded beam(s) illuminates a transmission grating (j) and interference occurs at x. (Reprinted with permission from Duarte [37] and Elsevier Science.)

$$\left|\langle x|s\rangle\right|^2=\sum_{z=1}^{N}\sum_{y=1}^{N}\Psi\left(r_{j_{zy}}\right)\sum_{\alpha=1}^{N}\sum_{\beta=1}^{N}\Psi\left(r_{j_{\alpha\beta}}\right)e^{i(\Omega_{\alpha\beta}-\Omega_{zy})}, \tag{4}$$

where $\Psi\left(r_{j_{zy}}\right)=\Psi\left(r_{j_{zy}\cdot x}\right)\Psi\left(r_{s,j_{zy}}\right)$ and $\Omega_{zy}=\left(\theta_{zy}+\phi_{zy}\right)$.

For one dimension we can write $\Psi\left(r_{j_{zy}}\right)=\Psi\left(r_j\right)$ and $\Psi\left(r_{j_{\alpha\beta}}\right)=\Psi\left(r_m\right)$ and Eq. 4 reduces to

$$\left|\langle x|s\rangle\right|^2=\sum_{j=1}^{N}\Psi(r_j)\sum_{m=1}^{N}\Psi(r_m)\,e^{i(\Omega_m-\Omega_j)}. \tag{5}$$

Expanding Eq. (5) and rearranging the exponential terms lead to eq. (2).

5. DISPERSION LINEWIDTH EQUATION

The dispersive linewidth in a pulsed high-gain laser is determined by the expression

$$\Delta\lambda\approx\Delta\theta(\partial\theta/\partial\lambda)^{-1}, \tag{6}$$

where $\Delta\theta$ is the beam divergence and $(\partial\theta/\partial\lambda)$ is the intracavity dispersion. This simple equation indicates that in order to achieve narrow-linewidth emission, $\Delta\theta$

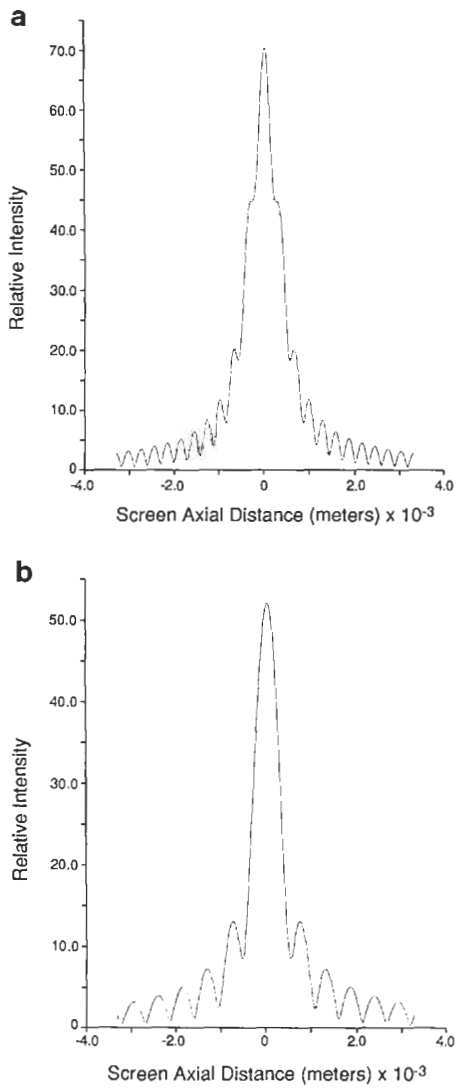

FIGURE 5 Transverse-mode structures for Fresnel numbers of (a) 0.86 and (b) 0.25, at $\lambda = 580$ nm. (Reprinted with permission from Duarte [37] and Elsevier Science.)

should be minimized and $(\partial\theta/\partial\lambda)$ should be maximized. Certainly, the main two functions of the intracavity optics is to yield near-diffraction-limited beams and very high dispersion with maximum transmission efficiency.

Equation (6) can be considered as a purely mathematical statement (see Chapter 6, for example), although physicists working in areas of classical optics

have used geometrical optics arguments in its derivation [39–42]. In addition, recent work [1,38] indicates that the origin of Eq. (3) can be related to intracavity interference as described using Dirac's notation [43].

6. BEAM DIVERGENCE

An expression for beam divergence including all the intracavity components except the active region is given by [1,44]

$$\Delta\theta = \frac{w}{L_r}\left[1 + \left(\frac{L_r}{B}\right)^2 + \left(\frac{L_r A}{B}\right)^2\right]^{1/2}, \tag{7}$$

where w is the beam waist, $L_R = \pi w^2/\lambda$ is the Rayleigh length, and A and B are the corresponding propagation matrix elements. For propagation in free space $A = 1$ and $B = d$ so that $\Delta\theta \approx \lambda\sqrt{3}/\pi w$ for $d = L_r$, $\Delta\theta \approx \lambda\sqrt{2}/\pi w(L_r/d)$ for $d << L_r$, and $\Delta\theta \approx \lambda/\pi w$ for $d >> L_r$.

Appropriate ABCD matrices are given in Table 2. Matrices listed include those for gratings, mirrors, etalons, and multiple-prism beam expanders. The matrices for the multiple-prism beam expanders are general and enable a round-trip analysis.

Alternative 4×4 ray transfer matrices that include dispersion and other optical parameters are discussed in [1,47,48]. The relation between the dispersion of multiple-prism arrays and 4×4 ray transfer matrices is discussed in the Appendix.

7. INTRACAVITY DISPERSION

The return-pass intracavity dispersion for a multiple-prism grating assembly (see Fig. 2) is given by

$$\left(\frac{\partial\theta}{\partial\lambda}\right)_C = M\left(\frac{\partial\theta}{\partial\lambda}\right)_G + \left(\frac{\partial\Phi}{\partial\lambda}\right)_P, \tag{8}$$

where the grating dispersion is given by [14]

$$\left(\frac{\partial\theta}{\partial\lambda}\right)_G = \frac{2\left(\sin\theta + \sin\theta'\right)}{\lambda\cos\theta} \tag{9}$$

for a grating deployed in a grazing-incidence configuration and

TABLE 2 ABCD Propagation Matrices

Optical element/system	ABCD propagation matrix	Reference
Distance L in free space	$\begin{bmatrix} 1 & L \\ 0 & 1 \end{bmatrix}$	[45]
Flat grating	$\begin{bmatrix} \cos\theta'/\cos\theta & 0 \\ 0 & \cos\theta/\cos\theta' \end{bmatrix}$ θ = angle of incidence θ' = angle of diffraction	[46]
Flat mirror or grating in Littrow configuration ($\theta = \theta'$)	$\begin{bmatrix} 1 & 0 \\ 0 & 1 \end{bmatrix}$	[1]
Slab of material with refractive index n and parallel surfaces	$\begin{bmatrix} 1 & (l_e/n)(\cos\phi_e/\cos\psi_e)^2 \\ 0 & 1 \end{bmatrix}$ ϕ_e = angle of incidence ψ_e = angle of refraction l_e = optical path length	[1]
Etalon	$\begin{bmatrix} 1 & l_e/n \\ 0 & 1 \end{bmatrix}$	[1]
Thin convex (positive) lens	$\begin{bmatrix} 1 & 0 \\ -1/f & 1 \end{bmatrix}$ f = focal length	[45]
Thin concave (negative) lens	$\begin{bmatrix} 1 & 0 \\ 1/\lvert f \rvert & 1 \end{bmatrix}$	[45]
Galilean telescope	$\begin{bmatrix} f_2/\lvert f_1 \rvert & f_2-\lvert f_1 \rvert \\ 0 & \lvert f_1 \rvert/f_2 \end{bmatrix}$	[45]
Newtonian telescope	$\begin{bmatrix} -f_2/f_1 & f_2+f_1 \\ 0 & -f_1/f_2 \end{bmatrix}$	[45]
Multiple-prism beam expander	$\begin{bmatrix} M_1M_2 & B \\ 0 & (M_1M_2)^{-1} \end{bmatrix}$ $B = M_1M_2 \sum_{m=1}^{r-1} L_m \left(\prod_{j=1}^{m} k_{1,j} \prod_{j=1}^{m} k_{2,j} \right)^{-2}$ $+ (M_1/M_2) \sum_{m=1}^{r} (l_m/n_m) \left(\prod_{j=1}^{m} k_{1,j} \right)^{-2} \left(\prod_{j=m}^{r} k_{2,j} \right)^{2}$ L_m = distance separating the prisms l_m = optical path length of each individual prism $M_1, M_2, k_{1,j}, k_{2,j}$ are defined in the text	[1,47]
Multiple prism beam expander (return pass)	$\begin{bmatrix} (M_1M_2)^{-1} & B \\ 0 & M_1M_2 \end{bmatrix}$	[1,44]

$$\left(\frac{\partial\theta}{\partial\lambda}\right)_G = \frac{2\tan\theta}{\lambda} \tag{10}$$

for a grating in Littrow configuration [13].

The generalized double-pass dispersion for any prismatic array composed of r prisms (Fig. 6) is given by [1,2,34–36]

$$\left(\frac{\partial\Phi}{\partial\lambda}\right)_P = 2M_1M_2\sum_{m=1}^{r}(\pm 1)\mathcal{H}_{1,m}\left(\prod_{j=m}^{r}k_{1,j}\prod_{j=m}^{r}k_{2,j}\right)^{-1}\frac{\partial n_m}{\partial\lambda}$$
$$+2\sum_{m=1}^{r}(\pm 1)\mathcal{H}_{2,m}\left(\prod_{j=1}^{m}k_{1,j}\prod_{j=1}^{m}k_{2,j}\right)\frac{\partial n_m}{\partial\lambda}\ , \tag{11}$$

where

$$M_1 = \prod_{j=1}^{r}k_{1,j} \tag{12a}$$

and

$$M_2 = \prod_{j=1}^{r}k_{2,j}\ . \tag{12b}$$

Here, $k_{1,j} = \cos\Psi_{1,j}/\cos\phi_{1,j}$ and $k_{2,j} = \cos\phi_{2,j}/\cos\psi_{2,j}$ are the individual beam expansion coefficients corresponding to the incidence and exit face of the prism, respectively. Also $\mathcal{H}_{1,m} = \tan\phi_{1,m}/n_m$, $\mathcal{H}_{2,m} = \tan\phi_{2,m}/n_m$, and $(\partial n_m/\partial\lambda)$ is characteristic of the prism material. To estimate the single-pass dispersion $(\partial\phi_{2,r}/\partial\lambda)$ of the multiple-prism beam expander, the return-pass dispersion given in Eq. (11) should be multiplied by $(2M_1M_2)^{-1}$ to obtain the expression [36]

$$\left(\frac{\partial\phi_{2,r}}{\partial\lambda}\right) = \sum_{m=1}^{r}(\pm 1)\mathcal{H}_{1,m}\left(\prod_{j=m}^{r}k_{1,j}\prod_{j=m}^{r}k_{2,j}\right)^{-1}\frac{\partial n_m}{\partial\lambda}$$
$$+\left(\prod_{j=1}^{r}k_{1,j}\prod_{j=1}^{r}k_{2,j}\right)^{-1}\sum_{m=1}^{r}(\pm 1)\mathcal{H}_{2,m}\left(\prod_{j=1}^{m}k_{1,j}\prod_{j=1}^{m}k_{2,j}\right)\frac{\partial n_m}{\partial\lambda}\ . \tag{13}$$

For multiple-prism assemblies composed of right-angle prisms (as shown in Fig. 2) designed for orthogonal beam exit, Eq. (11) reduces to [2]

$$\left(\frac{\partial\Phi}{\partial\lambda}\right)_P = 2M_1\sum_{m=1}^{r}(\pm 1)\mathcal{H}_{1,m}\left(\prod_{j=m}^{r}k_{1,j}\right)^{-1}\frac{\partial n_m}{\partial\lambda}. \tag{14}$$

Further, if the prisms in the preceding expander are manufactured of the same material and deployed so that the angle of incidence is the Brewster's angle, then Eq. (14) reduces to

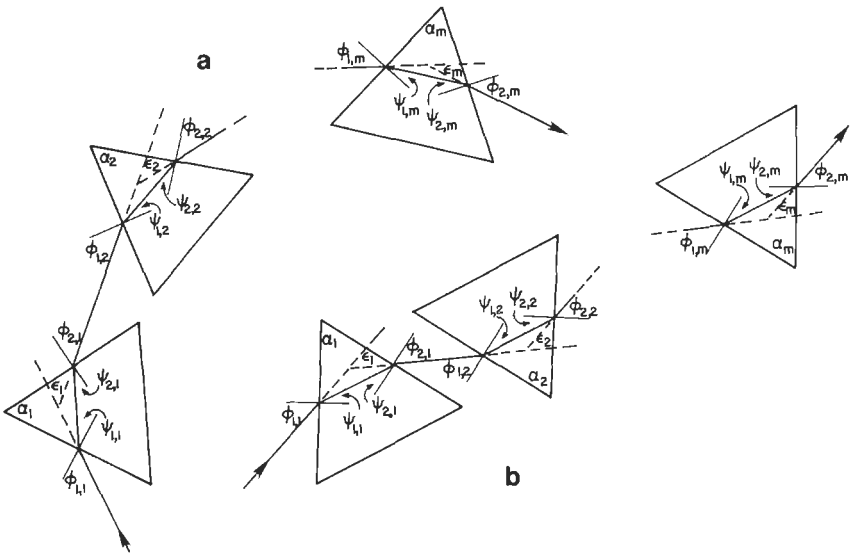

FIGURE 6 Generalized multiple-prism array in (a) additive configuration and (b) compensating configuration. (Reproduced with permission from Duarte [2].)

$$\left(\frac{\partial \Phi}{\partial \lambda}\right)_P = 2 \sum_{m=1}^{r} (\pm 1) n^{m-1} \frac{\partial n}{\partial \lambda}. \tag{15}$$

A multipass analysis performed by Duarte and Piper [49] indicates that the multiple-return-pass dispersion of the multiple-prism grating assembly is given by

$$\left(\frac{\partial \theta}{\partial \lambda}\right)_R = RM \left(\frac{\partial \theta}{\partial \lambda}\right)_G + R\left(\frac{\partial \Phi}{\partial \lambda}\right)_P, \tag{16}$$

where $M = M_1 M_2$. Thus, the dispersive linewidth following an R number of return passes is given by

$$\Delta\lambda \approx \Delta\theta \left[RM\left(\frac{\partial \theta}{\partial \lambda}\right)_G + R\left(\frac{\partial \Phi}{\partial \lambda}\right)_P \right]^{-1}. \tag{17}$$

For copper-vapor laser-pumped dispersive dye laser oscillators, the value of R can be ≤ 4 [49]. Although it is well known that multipasses do reduce the measured laser linewidth [1,2,21,50], the exact mechanism by which this process occurs is not yet completely understood. This is due to the fact that the

dynamics of the active medium influences the outcome in conjunction with intracavity dispersion.

8. INTRACAVITY MULTIPLE-PRISM DISPERSION AND PULSE COMPRESSION

In femtosecond lasers the gain and saturable absorber media introduce group velocity dispersion (GVD) that leads to pulse broadening. The deployment of intracavity prisms allows for the compensation of GVD via the introduction of negative GVD [51]. This occurs because GVD is a function of the second derivative ($d^2P/d\lambda^2$) of the optical path length through the prismatic sequence. In turn, ($d^2P/d\lambda^2$) is a function of the angular dispersion of the multiple-prism array and its derivative and can be made negative by adjusting the inter-prism distance [52]. In general, these parameters can be expressed as [1,2,53,54]

$$\frac{\partial \phi_{2,m}}{\partial n_m} = \mathcal{H}_{2,m} \pm \left(k_{1,m} k_{2,m}\right)^{-1} \left[\mathcal{H}_{1,m} \pm \frac{\partial \phi_{2,(m-1)}}{\partial n_m}\right], \tag{18}$$

$$\begin{aligned}\frac{\partial^2 \phi_{2,m}}{\partial n_m^2} &= \mathcal{H}_{2,m}\left(\frac{\partial \phi_{2,m}}{\partial n_m}\right)^2 n_m + \frac{1}{k_{2,m}}\left(\frac{\partial \psi_{1,m}}{\partial n_m} + \frac{\partial \psi_{2,m}}{\partial n_m}\right) \\ &+ \mathcal{H}_{1,m}\frac{\chi_{1,m}}{k_{2,m}}\left(\frac{\partial \phi_{1,m}}{\partial n_m}\right) n_m + \frac{1}{k_{1,m} k_{2,m}}\left(\frac{\partial^2 \phi_{2,(m-1)}}{\partial n_m^2}\right) \\ &+ \left[\mathcal{H}_{1,m} \pm \frac{\partial \phi_{2,(m-1)}}{\partial n_m}\right]\left(\frac{\chi_{1,m}}{k_{1,m} k_{2,m}}\frac{\partial \psi_{1,m}}{\partial n_m} - \frac{\chi_{1,m}}{k_{2,m}}\frac{\partial \phi_{1,m}}{\partial n_m} n_m - \frac{\mathcal{H}_{2,m}}{k_{1,m}}\frac{\partial \psi_{2,m}}{\partial n_m}\right),\end{aligned} \tag{19}$$

where $\chi_{1,m} = \tan \psi_{1,m}$. These equations are general and enable the design of any multiple-prism array for pulse compression. In this regard, the equations can be applied to one, two, four, six prisms or more [51,52,55–57] (Fig. 7). Further, the equations can be utilized to provide a numerical description of intracavity dispersion in generalized prismatic arrays as a function of angular and/or beam deviations [54]. The use of these multiple-prism arrays in femtosecond dye laser cavities is discussed in Chapter 5.

For the special case of a single prism deployed at Brewster's angle of incidence, the equations reduce to the case discussed by Fork *et al.* [52]:

$$\frac{\partial \phi_{2,1}}{\partial n} = 2\,, \tag{20}$$

$$\frac{\partial^2 \phi_{2,1}}{\partial n^2} = \left(4n - \frac{2}{n^3}\right). \tag{21}$$

Data on the refractive index as a function of wavelength can be obtained in [58]. Also, Diels [59] lists $\partial n/\partial\lambda$ and $\partial^2 n/\partial\lambda^2$ for several optical materials of interest.

9. TRANSMISSION EFFICIENCY OF MULTIPLE-PRISM ARRAYS

The cumulative reflection losses at the incidence surface of the mth prism in a multiple-prism array are given by [1,22]

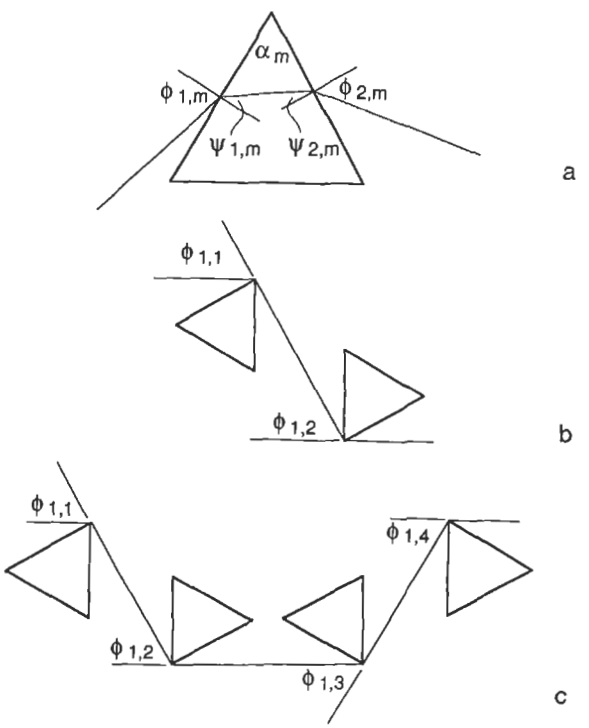

FIGURE 7 Prismatic configurations utilized in pulse compression. (a) Single prism. (b) Two-prism compensating arrangement. (c) Four-prism array composed of two double-prism compensating arrangements. (d) Collinear array integrated by two N-prism compensating configurations. (e) and (f) Two arrays each composed of generalized N-prism-additive configurations. The groups compensate relative to each other.

$$L_{1,m} = L_{2,(m-1)} + \left[1 - L_{2,(m-1)}\right] R_{1,m}, \tag{22}$$

and the losses at the exit surface are

$$L_{2,m} = L_{1,m} + \left(1 - L_{1,m}\right) R_{2,m}. \tag{23}$$

Here $R_{1,m}$ and $R_{2,m}$ are the well-known Fresnel equations for either s- or p-polarization [40].

The efficiency of diffraction gratings depends on parameters such as wavelength, angle of incidence, and polarization. As discussed by Duarte and Piper

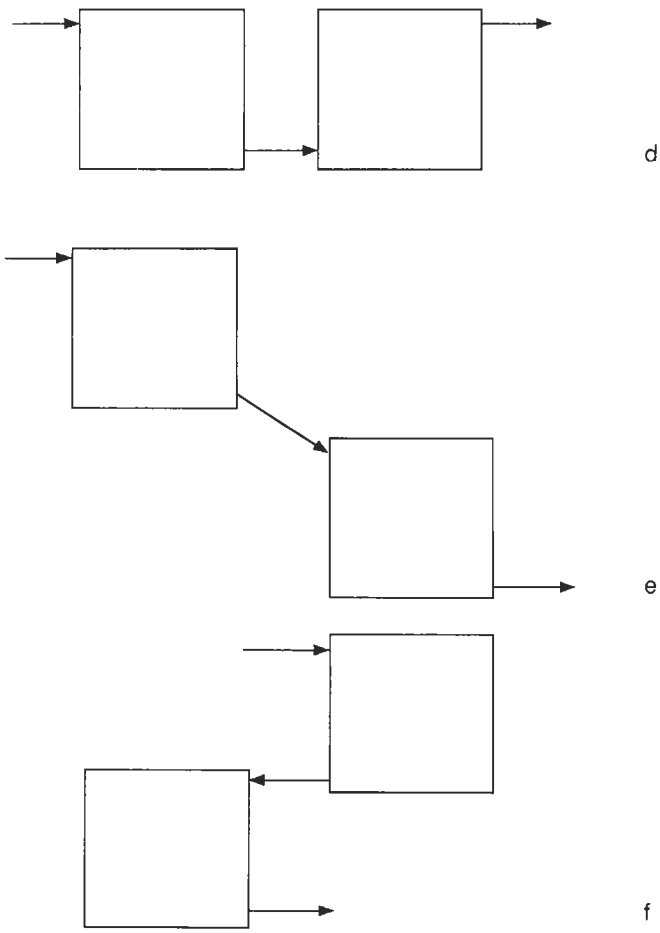

FIGURE 7 *(continued)*

[24], the total efficiency of a typical holographic grating at $\lambda = 632.8$ nm can be ~45% at $\theta = 60°$, ~23% at $\theta = 86°$, and ~7% at $\theta = 89°$. At the given wavelength, most of the contribution to the measured efficiency is from *p*-polarized radiation (defined as being parallel to the propagation plane of the cavity [58]). Holographic gratings blazed for grazing-incidence operation can yield better efficienciens at higher angles of incidence [60]. However, it should be noted that the use of prismatic preexpansion [24] enables the use of the gratings at reduced angles of incidence and hence in a more efficient configuration. Detailed information on grating efficiency as a function of wavelength and other parameters is provided by manufacturers. A detailed discussion of grating efficiency using the electromagnetic theory of gratings is provided by Maystre [61].

10. WAVELENGTH TUNING

Gratings, prisms, and etalons are widely used as tuning elements in dispersive cavities. In simple cavities where the only dispersive element is a grating in a Littrow configuration, or in resonators incorporating a dispersionless beam expander and a grating in a Littrow configuration, the wavelength is given by the simple equation

$$m\lambda = 2a \sin \theta , \tag{24}$$

where m is the diffraction order, a is the groove spacing, and θ is the angle of incidence (and diffraction) on the grating (see Fig. 2a). Thus, simple angular rotation induces a change in λ. For a pure grazing-incidence cavity, or an HMPGI oscillator incorporating a dispersionless multiple-prism expander, the basic grating equation applies:

$$m\lambda = a\left(\sin \theta + \sin \theta'\right) , \tag{25}$$

where θ is the angle of incidence and θ' is the angle of diffraction (see Fig. 2c). Tuning here is accomplished by rotating the tuning mirror in front of the grating.

Wavelength tuning by rotation of the grating, in narrow-linewidth dispersive oscillators, imposes stringent constraints on the angular resolution of the grating kinematic mount. For instance, an MPL oscillator can experience a frequency shift of $\delta\nu \approx 250$ MHz due to an angular rotation of only $\delta\theta \approx 10^{-6}$ rad (see, for example, [1]). This frequency sensitivity requires the use of kinematic mounts with <0.1 sec of arc resolution. Further, frequency stability requirements demand the design of thermally stable resonators and hence the use of materials such as superinvar [23].

A topic of considerable interest in grating tuned cavities is long-range wavelength tuning. One approach utilized in cavities incorporating gratings in a Littrow configuration, intracavity beam expansion, and an intracavity etalon, is to synchronize the motion of the grating and the etalon. Using this technique, several authors have demonstrated extended frequency scanning ranges up to several tens of inverse centimeters [62–64].

An elegant approach to long-range wavelength scanning in single-longitudinal-mode oscillators is the use of synchronous scanning methods. This involves simultaneous adjustment of the cavity length and the feedback angle of the tuning element. This is necessary to suppress mode hopping. The approach introduced by Liu and Littman [65] and Littman [17] for grazing-incidence cavities is to rotate the tuning mirror about an axis defined *approximately* by the intersection of the surface planes (perpendicular to the propagation plane) of the output coupler mirror, the tuning mirror, and the grating. The word *approximately* was used because the gain region makes the physical length of the cavity slightly different from the optical length of the cavity. As discussed by Littman [17,66] the optical length of the gain region alters slightly the optimum position of the pivot. McNicholl and Metcalf [67] provide a scalar diffraction analysis for Littrow and grazing-incidence cavities. For the case of the Littrow cavity, in the absence of intracavity beam expansion, these authors have determined that the optimum position for the rotational axis of the grating is defined by the intersection of the surface plane of the optical origin of the cavity (which is close and parallel to the surface plane of the output coupler) and the surface plane of the Littrow grating. Although Littman [17] reports scanning ranges of up to 15 cm^{-1}, in a grazing-incidence configuration, McNicholl and Metcalf [67] predict considerable extensions in the tuning range.

For a cavity where the dispersion is provided by a chain of prisms in an additive configuration, tuning is performed by rotating a mirror at the exit of the prismatic assembly [68] since the exit angle at the mth prism varies according to [2]

$$\phi_{2,m} = \arcsin\left(n(\lambda)\sin\left\{\alpha_m - \arcsin\left[\frac{\sin\phi_{1,m}}{n(\lambda)}\right]\right\}\right), \tag{26}$$

where $\phi_{1,m}$ is related geometrically to the exit angle of the previous prism $\phi_{2,(m-1)}$, and α_m is the apex angle of the mth prism. The sign in this equation is reversed if $\alpha_m < \psi_{1,m}$ [2]. For an array of r identical prisms deployed in an additive configuration and with identical angles of incidence, the cumulative angular spread at the end prism can be significant since the overall single-pass dispersion is [2]

$$\frac{\partial \phi_{2,r}}{\partial \lambda} = \sum_{m=1}^{r} \frac{\partial \phi_{2,m}}{\partial \lambda} = r \frac{\partial \phi_{2,1}}{\partial \lambda} \tag{27}$$

given that $\partial\phi_{2,1}/\partial\lambda = \partial\phi_{2,2}/\partial\lambda = \ldots = \partial\phi_{2,m}/\partial\lambda$.

The transmission maxima for an etalon is given by [50]

$$m_e \lambda = 2nd_e \cos \theta'_e \ , \tag{28}$$

where m_e is an integer, d_e the space between the reflective surfaces, and θ'_e is the refraction angle. The angular dispersion for an etalon is given by [2]

$$\frac{\partial \theta_e}{\partial \lambda} = \left(\frac{\sin \theta'_e}{\cos \theta_e} \right) \frac{\partial n}{\partial \lambda} + n \left(\frac{\cos \theta'_e}{\cos \theta_e} \right) \frac{\partial \theta'_e}{\partial \lambda} \ , \tag{29}$$

where

$$\frac{\partial \theta'_e}{\partial \lambda} = \left(\tan \theta_e \right)^{-1} \left[\left(\frac{1}{n} \right) \partial n / \partial \lambda - \left(\frac{1}{\lambda} \right) \right] . \tag{30}$$

In addition to the ray matrix given in Table 2, further parameters of interest for intracavity etalons include the free spectral range (FSR)

$$\begin{aligned} \text{FSR} &= \lambda^2 / \left(2nd_e \right) \text{ in wavelength units (m)} \\ &= c / \left(2nd_e \right) \text{ in frequency units (Hz)} \\ &= 1 / \left(2nd_e \right) \text{ in wave numbers (m}^{-1}\text{)} . \end{aligned} \tag{31}$$

Also, the effective finesse is given by [41]

$$\mathcal{F}^{-2} = \mathcal{F}_R^{-2} + \mathcal{F}_F^{-2} + \mathcal{F}_A^{-2} \ , \tag{32}$$

where $\mathcal{F}_R$, $\mathcal{F}_F$, and $\mathcal{F}_A$ represent the reflective, flatness, and aperture finesses, respectively. The reflective finesse is a function of the reflectivity of the surfaces [40]

$$\mathcal{F}_R = \frac{\pi \sqrt{R}}{1 - R} \ , \tag{33}$$

and the minimum resolvable bandwidth provided by the etalon is given by the ratio FSR/$\mathcal{F}$.

Further information on wavelength tuning can be found in Chapter 6, including details on birefringent filters.

APPENDIX: DISPERSION OF MULTIPLE-PRISM ARRAYS AND 4 X 4 TRANSFER MATRICES

The description of optical systems using ray transfer matrices of the 3×3, 4×4, and 6×6 format has been discussed by several authors [45,69,70]. In the 4×4 notation the matrix can have the following form [48]:

$$\begin{bmatrix} A & B & 0 & E \\ C & D & 0 & F \\ G & H & 1 & I \\ 0 & 0 & 0 & 1 \end{bmatrix} , \tag{34}$$

where the ABCD terms have their usual meaning (given in Table 2) and the F term can be related to dispersion [71]. For a flat mirror the matrix becomes

$$\begin{bmatrix} 1 & 0 & 0 & 0 \\ 0 & 1 & 0 & 0 \\ 0 & 0 & 1 & 0 \\ 0 & 0 & 0 & 1 \end{bmatrix} , \tag{35}$$

and for a thin convex lens the ABCD terms have their usual meaning (given in Table 2) and $E = F = G = H = I = 0$ [48].

For a single m'th prism the values of the ABCD terms are as given in Table 2, namely,

$$A_m = k_{1,m} k_{2,m} , \tag{36}$$

$$B_m = \left(k_{2,m} / k_{1,m}\right)\left(l_m / n_m\right) , \tag{37}$$

$$C_m = 0 , \tag{38}$$

$$D_m = \left(k_{1,m} k_{2,m}\right)^{-1} . \tag{39}$$

The remaining terms are given by [48] and can be written in the following form [47]:

$$E_m = B_m \mathcal{H}_{1,m} \frac{\partial n_m}{\partial f} , \tag{40}$$

$$F_m = \left[\mathcal{H}_{1,m} \left(k_{1,m} k_{2,m} \right)^{-1} + \mathcal{H}_{2,m} \right] \frac{\partial n_m}{\partial f} , \tag{41}$$

$$G_m = F_m A_m \left(\lambda_0 \right)^{-1} , \tag{42}$$

$$H_m = B_m \mathcal{H}_{2,m} \left(\lambda_0 \right)^{-1} \frac{\partial n_m}{\partial f} , \tag{43}$$

$$I_m = H_m \mathcal{H}_{1,m} \frac{\partial n_m}{\partial f} - \left(\frac{l_m}{\upsilon^2} \right) \left(\frac{\partial \nu}{\partial f} \right) . \tag{44}$$

Notice that $\mathcal{H}_{1,m} = (\tan \phi_{1,m}/n_m)$, $\mathcal{H}_{2,m} = (\tan \phi_{2,m}/n_m)$ and that Eq. (41) can be easily obtained from the generalized single-pass dispersion equation [Eq. (13)] and by using the identity

$$\partial \phi_{2,1}/\partial \lambda = \left(\partial \phi_{2,1}/\partial f \right) \left(\partial f/\partial \lambda \right) . \tag{45}$$

For a generalized multiple-prism array [47]

$$A_r = M_1 M_2 , \tag{46}$$

$$B_r = M_1 M_2 \sum_{m=1}^{r-1} L_m \left(\prod_{j=1}^{m} k_{1,j} \prod_{j=1}^{m} k_{2,j} \right)^{-2}$$

$$+ \left(M_1/M_2 \right) \sum_{m=1}^{r} \left(l_m/n_m \right) \left(\prod_{j=1}^{m} k_{1,j} \right)^{-2} \left(\prod_{j=m}^{r} k_{2,j} \right)^{2} , \tag{47}$$

$$C_r = 0 , \tag{48}$$

$$D_r = \left(M_1 M_2 \right)^{-1} , \tag{49}$$

$$F_r = \left(\frac{\partial \phi_{2,r}}{\partial \lambda} \right) \left(\frac{\partial \lambda}{\partial f} \right) , \tag{50}$$

$$G_r = \sum_{m=1}^{r} F_m \left(\prod_{j=1}^{m} k_{1,j} \prod_{j=1}^{m} k_{2,j} \right) \left(\lambda_0 \right)^{-1} , \tag{51}$$

where $(\partial\phi_{2,r}/\partial\lambda)$ is given by Eq. (13). The generalized E_r, H_r, and I_r are rather extensive and hence are not included in the text.

In this Appendix the relation between ABCD matrices and 4×4 matrices has been outlined. Further we have shown how to relate the generalized multiple-prism dispersion [34] to the notation of 4×4 ray transfer matrices.

REFERENCES

1. F. J. Duarte, in *High Power Dye Lasers* (F. J. Duarte, Ed.), pp. 7–43, Springer-Verlag, Berlin (1991).
2. F. J. Duarte, in *Dye Laser Principles* (F. J. Duarte and L. W. Hillman, Eds.), pp. 133–183, Academic, New York (1990).
3. K. Ludewigt, W. Pfingsten, C. Mohlmann, and B. Wellegehausen, *Opt. Lett.* **12,** 39 (1987).
4. R. G. Caro, M. C. Gower, and C. E. Webb, *J. Phys. D: Appl. Phys.* **15,** 767 (1982).
5. R. Buffa, P. Burlamacchi, R. Salimbeni, and M. Matera, *J. Phys. D: Appl. Phys.* **16,** L125 (1983).
6. R. C. Sze, N. A. Kurnit, D. E. Watkins, and I. J. Bigio, in *Proc. Int. Conf. Lasers '85* (C. P. Wang, Ed.), pp. 133–144, STS Press, McLean, VA (1986).
7. M. Sugii, M. Ando, and K. Sasaki, *IEEE J. Quantum Electron.* **QE-23,** 1458 (1987).
8. T. J. Pacala, I. S. McDermid, and J. B. Laudenslager, *Appl. Phys. Lett.* **45,** 507 (1984).
9. F. J. Duarte, in *Proc. Int. Conf. Lasers '90* (D. G. Harris and J. Herbelin, Eds.), pp. 277–279, STS Press, McLean, VA (1991).
10. F. J. Duarte in *Proc. Int. Conf. Lasers '84* (K. M. Corcoran, D. M. Sullivan, and W. C. Stwalley, Eds.), pp. 397–403, STS Press, McLean, VA (1985).
11. A. N. Bobrovskii, A. V. Branitskii, M. V. Zurin, A. V. Kozhevnikov, V. A. Mishchenko, and G. D. Mylnikov, *Sov. J. Quantum Electron.* **17,** 1157 (1987).
12. F. J. Duarte, *Appl. Opt.* **24,** 1244 (1985)
13. T. W. Hänsch, *Appl. Opt.* **11,** 895 (1972).
14. M. G. Littman and H. J. Metcalf, *Appl. Opt.* **17,** 2224 (1978).
15. S. Saikan, *Appl. Phys.* **17,** 41 (1978).
16. M. G. Littman, *Opt. Lett.* **3,** 138 (1978).
17. M. G. Littman, *Appl. Opt.* **23,** 4465 (1984).
18. F. J. Duarte and J. A. Piper, *Opt. Commun.* **35,** 100 (1980).
19. A. F. Bernhardt and P. Rasmussen, *Appl. Phys. B* **26,** 141 (1981).
20. F. J. Duarte and J. A. Piper, *Appl. Opt.* **23,** 1391 (1984).
21. F. J. Duarte and R. W. Conrad, *Appl. Opt.* **26,** 2567 (1987).
22. F. J. Duarte, J. J. Ehrlich, W. E. Davenport, and T. S. Taylor, *Appl. Opt.* **29,** 3176 (1990).
23. F. J. Duarte, W. E. Davenport, J. J. Ehrlich, and T. S. Taylor, *Opt. Commun.* **84,** 310 (1991).
24. F. J. Duarte and J. A. Piper, *Appl. Opt.* **20,** 2113 (1981).
25. F. J. Duarte, *Appl. Opt.* **33,** 3857 (1994).
26. F. J. Duarte and R. W. Conrad, in *Proc. Int. Conf. Lasers '89* (D. G. Harris and T. M. Shay, Eds.), pp. 552–554, STS Press, McLean, VA (1990).
27. K. W. Kangas, D. D. Lowenthal, and C. H. Muller, *Opt. Lett.* **14,** 21 (1989).
28. C. E. Hamilton, K. W. Kangas, C. H. Muller, D. D. Lowenthal, and T. D. Raymond, in *Solid State Lasers* (G. Dube, Ed.), Vol. 1223, pp. 208–220, SPIE, Bellingham, WA (1990).
29. K. C. Harvey and C. J. Myatt, *Opt. Lett.* **16,** 910 (1991).
30. P. Zorabedian, *J. Lightwave Technol.* **10,** 330 (1992).
31. F. J. Duarte, *Laser Focus World* **29**(2), 103 (1993).

32. W. R. Bosenberg and D. R. Guyer, *J. Opt. Soc. Am. B* **10,** 1716 (1993).
33. F. J. Duarte, U.S. Patent 5,181,222 (Jan. 19, 1993).
34. F. J. Duarte and J. A. Piper, *Opt. Commun.* **43,** 303 (1982).
35. F. J. Duarte, *Opt. Commun.* **53,** 259 (1985).
36. F. J. Duarte, *Opt. Commun.* **71,** 1 (1989).
37. F. J. Duarte, *Opt. Commun.* **103,** 8 (1993).
38. F. J. Duarte, *Appl. Opt.* **31,** 6979 (1992).
39. J. K. Robertson, *Introduction to Optics: Geometrical and Physical,* Van Nostrand, New York (1955).
40. M. Born and E. Wolf, *Principles of Optics,* 5th ed., Pergamon, New York (1975).
41. J. Meaburn, *Detection and Spectrometry of Faint Light,* Reidel, Boston (1976).
42. R. Kingslake, *Optical System Design,* Academic, New York (1983).
43. P. A. M. Dirac, *The Principles of Quantum Mechanics,* 4th ed., Oxford, London (1978).
44. F. J. Duarte, *Opt. Quantum Electron.* **21,** 47 (1989).
45. A. E. Siegman, *Lasers,* University Science Books, Mill Valley, CA (1986).
46. A. E. Siegman, *J. Opt. Soc. Am. A* **2,** 1793 (1985).
47. F. J. Duarte, *Opt. Quantum Electron.* **24,** 49 (1992).
48. A. G. Kostenbauder, *IEEE J. Quantum Electron.* **26,** 1148 (1990).
49. F. J. Duarte and J. A. Piper, *Opt. Acta* **31,** 331 (1984).
50. F. P. Schäfer, in *Dye Lasers* (F. P. Schäfer, Ed.), pp. 1–89, Springer-Verlag, Berlin (1990).
51. W. Dietel, J. J. Fontaine, and J.-C. Diels, *Opt. Lett.* **8,** 4 (1983).
52. R. L. Fork, O. E. Martinez, and J. P. Gordon, *Opt. Lett.* **9,** 150 (1984).
53. F. J. Duarte, *Opt. Quantum Electron.* **19,** 223 (1987).
54. F. J. Duarte, *Opt. Quantum Electron.* **22,** 467 (1990).
55. J. C. Diels, W. Dietel, J. J. Fontaine, W. Rudolph, and B. Wilhelmi, *J. Opt. Soc. Am. B* **2,** 680 (1985).
56. J. D. Kafka and T. Baer, *Opt. Lett.* **12,** 401 (1987).
57. L. Y. Pang, J. G. Fujimoto, and E. S. Kintzer, *Opt. Lett.* **17,** 1599 (1992).
58. W. G. Driscoll and W. Vaughan, *Handbook of Optics,* McGraw-Hill, New York (1978).
59. J.-C. Diels, in *Dye Laser Principles* (F. J. Duarte and L. W. Hillman, Eds.), pp. 41–132, Academic, New York (1990).
60. I. T. McKinnie, A. J. Berry, and T. A. King, *J. Mod. Opt.* **38,** 1691 (1991).
61. D. Maystre, in *Electromagnetic Theory of Gratings* (R. Petit, Ed.), pp. 63–100, Springer-Verlag, Berlin (1980).
62. T. Suzuki, H. Kato, Y. Taira, Y. Adachi, N. Konishi, and T. Kasuya, *Appl. Phys.* **24,** 331 (1981).
63. T. D. Raymond, S. T. Walsh, and J. W. Keto, *Appl. Opt.* **23,** 2062 (1984).
64. M. R. Olcay, J. A. Pasqual, J. A. Lisboa, and R. E. Francke, *Appl. Opt.* **24,** 3146 (1985).
65. K. Liu and M. G. Littman, *Opt. Lett.* **6,** 117 (1981).
66. M. G. Littman and J. Montgomery, *Laser Focus* **24**(2), 70 (1988).
67. P. McNicholl and H. J. Metcalf, *Appl. Opt.* **24,** 2757 (1985).
68. F. C. Strome and J. P. Webb, *Appl. Opt.* **10,** 1348 (1971).
69. W. Brouwer, *Matrix Methods in Optical Instrument Design,* W. A. Benjamin, New York (1964).
70. H. Wollnik, *Optics of Charged Particles,* Academic, New York (1987).
71. O. E. Martinez, *IEEE J. Quantum Electron.* **24,** 2530 (1988).

3 Tunable Excimer Lasers

R. C. Sze
Los Alamos National Laboratory
Los Alamos, New Mexico

D. G. Harris
Rockwell International
Canoga Park, California

1. INTRODUCTION

Excimer lasers are pulsed gas lasers that intrinsically offer efficient and powerful broadband emission at several spectral regions throughout the ultraviolet. The spectral widths are typically 2 nm. An exception to this categorization is the XeF laser with its broadly tunable C→A transition (approximately 50 nm) in the visible. The broad tunability results from the steeply repulsive A state.

Excimer lasers have two primary formation channels for the excited state: (1) recombination of positive rare gas ions with halide ions and (2) reactions of excited rare gas atoms with halogen compounds [1].

The primary laser excitation techniques are high-energy electron beams, electron beam sustained discharge, preionized avalanche discharges, neutron pumping from reactors, and microwave excitation. The most useful of these have been the pulsed electron beam and preionized avalanche discharge techniques.

The primary loss mechanism for a high-energy electron beam (0.1 to 5 MeV) through a high-pressure gas is the creation of ion/electron pairs. Some simple relationships may be used to relate the ion creation rate to the ionic reaction channel for the formation of the upper laser state.

The details of electron beam devices have been reviewed by several authors (see Ref. [1] for example) so only a brief description is given here. The electrons

Tunable Lasers Handbook
Copyright © 1995 by Academic Press, Inc. All rights of reproduction in any form reserved.

originate by field emission from a cathode (frequently carbon felt), which has been negatively pulsed with respect to the anode, generally maintained at ground. The vacuum diode (generally operating at 10^{-5} to 10^{-7} Torr) is separated from the high-pressure laser gases by a thin foil. The emitted electrons pass through the foil, though losing some energy, and enter the lasing media, creating ions. Although large and expensive, these devices are easily scaled to meter dimensions and allow long-pulse (1 μsec or greater) pumping. They are therefore generally used as amplifiers rather than oscillators.

Preionized avalanche discharges have been utilized to produce a uniform plasma. The low-energy electrons in the plasma acquire sufficient energy to excite the rare gas atoms to a metastable state, thus allowing the reaction kinetics to proceed along the neutral reaction channel. The relative ease and low cost of this approach has led to the rapid development of high-average-power lasers. Discharge excimer lasers are discussed in Section 4.

Table 1 lists some of the best known excimer lasers with their respective electronic transitions and approximate emission bandwidth and/or tuning ranges.

In addition to tunability, an important characteristic in pulsed gas lasers, including excimer lasers, is narrow-linewidth emission. Some of the early work on tunable narrow-linewidth excimer lasers was reported by Loree *et al.* [3] who utilized isosceles prisms to provide intracavity dispersion and wavelength tuning in excimer lasers. These authors report linewidths of 0.1 to 0.2 nm and 0.05 nm for KrF and ArF lasers, respectively [3]. Additional and alternative methods to yield narrow-linewidth emission include the use of intracavity etalons [9] and grazing-incidence (GI) configurations [4]. During this period, *circa* 1984, multiple-prism

TABLE 1 Excimer Laser Transitions[a]

Laser	Transition	λ (nm)	~ Bandwidth	Reference
ArF	B → X	193	17000 GHz[b]	[3]
KrF	B → X	248	10500 GHz[b]	[3]
			2583 GHz	[4]
XeCl	B → X	308	374 GHz	[5]
			204 GHz	[6]
		308.2	397 GHz	[5]
			223 GHz	[6]
XeF	B → X	351	187 GHz[c]	[7]
		353	330 GHz[c]	[7]
	C → A		466–514 nm[b,c]	[8]

[a]Adapted from Duarte [2].
[b]Tuning range.
[c]Electron beam excitation.

TABLE 2 Narrow-Linewidth Gas Laser Oscillators[a]

Laser	Cavity	λ (nm)	Δν	E_0	Reference
ArF	MPL	193	10 GHz	150 μJ	[13]
KrF	GI	248	≤9 GHz	15 μJ	[4]
XeCl	GI[b]	308	~31 GHz	50 mJ	[14]
XeCl	GI[c]	308	~1.5 GHz	~1 mJ	[15]
XeCl	GI	308	~1 GHz	4 mJ	[16]
XeCl	3 etalons	308	≤150 MHz	2–5 μJ	[17]
XeF	MGI[d]	351	~40 MHz	~0.1 μJ	[18]
CO_2	GI[b]	10,591	117 MHz	140 mJ	[19]
CO_2	GI[b]	10,591	400–700 MHz	230 mJ	[20]
CO_2	MPL	10.591	≤140 MHz	200 mJ	[11]
CO_2	HMPGI[e]	10.591	107 MHz	85 mJ	[11]

[a]From Duarte [12].
[b]Open-cavity configuration.
[c]Incorporates Michelson interferometer.
[d]Multipass grating interferometer.
[e]Hybrid multiple-prism grazing-incidence cavity.

grating configurations were also introduced to pulsed gas lasers [10,11]. In this regard, note that multiple-prism Littrow (MPL) grating configurations were subsequently incorporated in commercially available gas lasers. Table 2 provides a useful summary of different types of cavities available for narrow-linewidth gas laser oscillators, including excimer lasers, with their respective emission performance.

The performance of some oscillator/amplifier and master oscillator/forced oscillator excimer laser systems is summarized in Table 3.

Applications for tunable narrow-linewidth excimer lasers include spectroscopy, selective photoionization processes, laser radar, and lidar.

In this chapter first we survey the basic spectroscopic characteristics of excimer laser emission, and then follow up with a review of tuning methods for discharge and electron beam pumped excimer lasers. For a historical perspective on excimer lasers the reader should consult [1].

2. EXCIMER ACTIVE MEDIA

Excimers are an important active media for lasers operating in the ultraviolet and vacuum ultraviolet (VUV) spectral regions.

Although a comprehensive understanding of excimers can involve quite a complex modeling of kinetic reactions and absorbing species, these molecules do share some common features. Consequently, a few simple models and concepts

TABLE 3 Oscillator/Amplifier and Master Oscillator/Forced Oscillator Excimer Lasers

Laser medium	Oscillator configuration	Secondary stage	Linewidth	Output energy (mJ)	Reference
KrF	GI	Amplifier	1 GHz	50	[21]
XeCl	Double etalon	Amplifier	599 MHz	310	[22]
XeCl	GI	Amplifier[a]	4.5 GHz		[23]
XeCl	MPL	Amplifier	15 GHz	300	[24]
XeF (C→A)	Dye laser	Amplifier	6 GHz	450–750	[8]
KrF	3 etalons	Forced oscillator	3 GHz	400	[25]
ArF	Prism expander grating	Forced oscillator	9 GHz	100	[26]
KrF			6 GHz	200	[26]
XeCl			9 GHz	120	[26]

[a]Regenerative.

can be used to explain their spectroscopic features with regard to frequency narrowing and tunability of the lasing spectrum.

Excimers are a class of molecules in which an electronically excited molecular state is formed by one atom in an electronically excited state associating with a second atom in its ground state. The molecular ground state is unbound or only weakly bound (by van der Waals forces). Consequently, a population inversion is automatically established when the excited state is formed. A photon is emitted and the resulting ground state molecule dissociates, along the lower potential curve, in a time comparable to one vibrational period ($\sim 10^{-12}$ sec) (Fig. 1). The practical advantage of such a system is that one photon can be extracted from each excited molecule produced, rather than the situation in conventional laser media in which only enough photons can be extracted to equalize the populations in the upper and lower levels. The emission from the bound repulsive transition is typically a broad continuum resulting from the lack of vibrational structure and the steepness of the unbound ground state. Emissions from excimers with a weakly bound ground state, most notably XeCl and XeF, show a more conventional vibrational and rotational structure.

Using laser rate equations and semiclassical theory, one can go quite far with elementary derivations toward describing the behavior of excimers. Indeed calculations of the gain coefficient, saturation intensity, stimulated emission cross sections and even modeling of the ground state can be quite easily accomplished [27, 27a]. Care must be taken not to rely completely on these models, because these parameters can vary quite differently depending on the experimental conditions. For instance, the saturation parameter may vary by a factor of 2 or more depending on

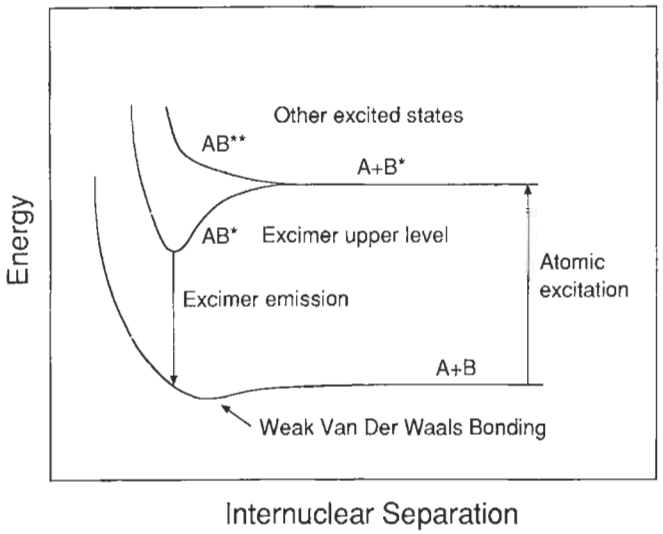

FIGURE 1 Energy level diagram for excimer lasers showing relevant electronic states.

the pumping rate and the plasma conditions. Predicting the lasing spectra, or even fluorescence, can involve more than 100 kinetic reactions and loss processes.

The most developed of this class of molecules as laser media are the rare gas halides, which show strong lasing on the B→X transitions of ArF (193 nm), KrF (248 nm), XeCl (308 nm), and XeF (351 and 353 nm). The C→A transition of XeF (490 nm) has also emerged as a potential high-power tunable laser source in the visible spectrum.

The rare gas excimers are important sources of VUV radiation: Ar_2 (126 nm), Kr_2 (146 nm), and Xe_2 (172 nm). The requirement that the pump source be a relativistic electron beam has limited their availability and development.

2.1 Rare Gas Halide Excimers

The most developed of the excimer lasers are the rare gas halides, which have shown high single pulse energy, high average power, and high efficiency. The most important of these are ArF, KrF, XeCl, and XeF. The former two, with an unbound ground state, exhibit continuous homogeneously broadened spectra. The latter two excimers, with weakly bound ground states, exhibit the highly structured spectra of overlapping rovibrational transitions.

2.1.1 ArF (193 nm)

The ArF spectrum is a continuum similar to that of KrF. The B→X emission is a $^2\Sigma$–$^2\Sigma$ transition. The reaction kinetics are also similar to KrF. However,

there are features in the spectrum due to the absorption of molecular oxygen (Schumann–Runge band) within the resonator cavity. Interest in line narrowing and tuning of ArF has grown as applications for shorter wavelength sources developed in the area of microfabrication. Ochi *et al.* [28] has built an oscillator with a 1.6-pm linewidth at 350 Hz with 7.4 mJ per pulse.

2.1.2 KrF (248 nm)

Much research has been done on KrF lasers because of their use as high-power lasers for laser fusion research as well as their use in the microelectronics industry. The KrF spectrum is a broad continuum (Fig. 2), which is considered to be homogeneously broadened owing to its repulsive ground state. Narrow absorption lines have been observed that are attributed to the excited states of rare gas ions. Spectral tuning has been observed over a continuous range of 355 cm^{-1}.

2.1.3 XeF (BÆX)

The structure of the XeF molecule is significantly different from that of the other rare gas halides and consequently its spectral properties also differ. The X state is bound by 1065 cm^{-1} and therefore has vibrational levels. Additionally, the C state lies about 700 cm^{-1} below the B state. The spectra of the B→X transition show emissions at 353 and 351 nm [30–33]. Early investigators also noted that as the temperature was increased, the lasing efficiency of the B→X transition improved significantly [35,36] (Fig. 3). Several explanations exist to explain this improved efficiency: (1) increased vibrational relaxation of the B state, (2) increased dissociation of the X state, and (3) decreased narrowband absorption at 351 nm. The complexity of the molecular structure implies that energy is not

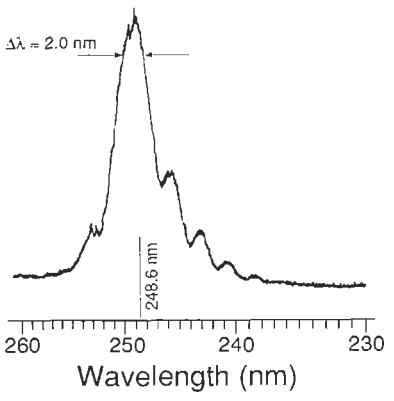

FIGURE 2 Fluorescent spectrum from the $B^2\Sigma_{1/2}$–$X^2\Sigma_{1/2}$ transition in KrF (from Brau and Ewing [29]).

transferred rapidly between the states and therefore the spectrum is not homogeneously broadened.

The 353-nm band emission comes primarily from the XeF (B, $v' = 0$) → XeF (X, $v'' = 3$) transition, whereas the 351-nm band is composed of radiation from the XeF (B, $v' = 1$) → XeF (X, $v'' = 4$) and XeF (B, $v' = 0$) → XeF (X, $v'' = 2$) transitions. Each vibrational transition has four rotational branches: Pe, Re, Pf, and Rf where *e* and *f* represent spin "up" and spin "down" for the transitions. Both bands have considerable structure, which is attributed to overlapping rovibronic transitions. As the temperature is increased, the spectra and efficiency of the 353-nm

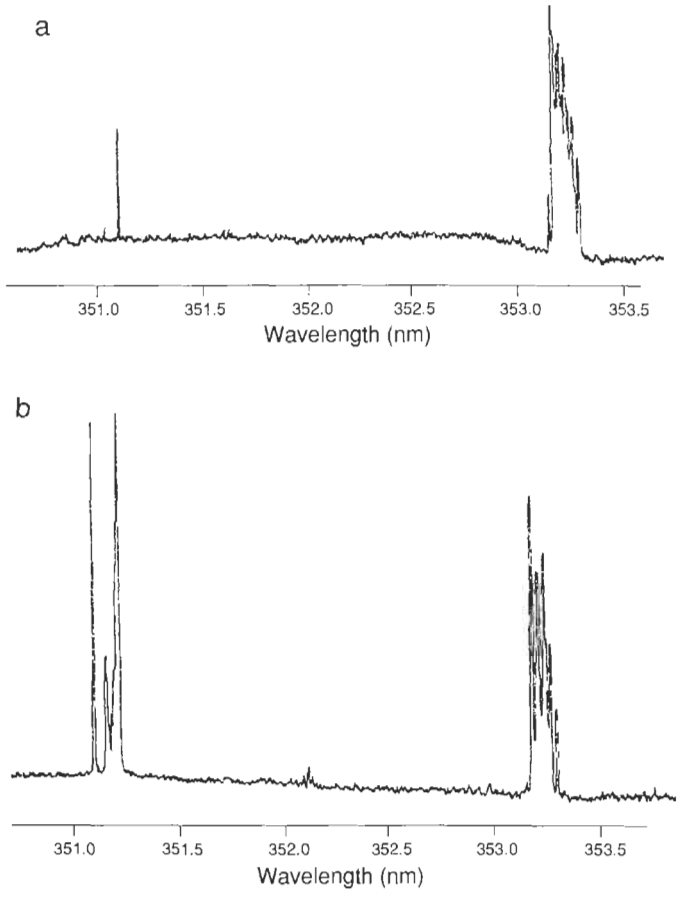

FIGURE 3 Free running lasers spectrum of XeF (B→X transition) at (a) 300°K and (b) 450°K. Inhomogeneous characteristics are evident (from Harris *et al.* [34]).

band remain virtually unchanged, whereas the 351-nm band shows marked changes in both.

The energy stored in XeF resides in a multitude of rotational states, which must be collisionally coupled on time scales that are short compared to the stimulated emission rate in order to achieve narrowband lasing. The appearance of clusters of rotational lines lasing relatively independently suggests that the rotational relaxation rates in the B and/or X states may be too slow to allow narrowband lasing. Indeed, it is difficult to achieve efficient injection locking when the small signal gain is much greater than the threshold gain [37,38].

2.1.4 XeF (C→A)

The XeF molecule also emits a broad continuum between 470 and 500 nm from the C→A transition ($^2\Pi$–$^2\Pi$). The A state is repulsive, without a potential well, so the emission is a true continuum, allowing narrowband lasing as well as continuous tuning across the emission spectrum. The excitation sources have been both short-pulse and long-pulse electron beams. Under short-pulse excitation (10 MW/cm^3 for 10 ns) the media has optical absorption during the electron beam deposition time and then gain (3%/cm) in the plasma afterglow. Narrowband tuning as well as injection seeding has been used to tune across the gain profile [39–43]. The media show gain throughout the energy deposition pulse under low-power long-pulse electron beam excitation (250 kW/cm^3 for 700 ns). However strong lasing is reached only after 300 ns [44].

2.1.5 XeCl (308 nm)

The C state of XeCl molecule lies approximately 230 cm^{-1} below the B state. Additionally, the ground state is bound by 255 cm^{-1}, lasing in the B→X bands occurs predominantly on the 0–1 band but also weakly on the 0–2 and 0–3 bands [45]. Although XeCl lasers have been made to operate narrow band, attempts to injection seed amplifiers have shown a strong wavelength dependence [46], which has been attributed to saturation of the lower vibrational levels [47]. Owing to the long gas lifetime and ability to use inexpensive nonquartz optics, XeCl has been the preferred excimer to test line-narrowing techniques and novel resonators.

2.1.6 Other Rare Gas Halide Excimers

Lasing has been observed in several other rare gas halides, and although these systems have not been developed to the extent of those already discussed they do offer potentially tunable radiation. Excimer emission has been observed at 175.0 nm in ArCl [27], 222 nm in KrCl [48,49], and 281.8 nm in XeBr [50], which are believed to be excimers with repulsive ground states. A short operating lifetime for XeBr has not yet been thoroughly addressed [51]. There has been renewed interest in KrCl because it offers potentially higher efficiency than XeCl [52.53]. The pulse lengths have been extended to 185 ns, but nothing has been pursued in the area of spectral control [54,55].

2.2 Rare Gas Excimer Lasers

The $1\Sigma_u^+ - 1\Sigma_g^+$ transitions in the noble gases (Ar_2, Kr_2, Xe_2) provide VUV laser radiation. They all exhibit continuum emission. The low stimulated emission cross sections and short lifetimes of the upper states require high pump rates, which necessitates an electron beam generator as a pumping source. The expense and cumbersome nature of such systems have unfortunately limited their availability to relatively few laboratories. Despite the dearth of low-loss and damage-resistant optical materials in the VUV, there has been considerable progress in line narrowing and tunability of these three laser media. The performance of these lasers is listed in Table 4.

3. TUNING OF DISCHARGE AND ELECTRON BEAM PUMPED EXCIMER LASERS

The avalanche discharge excimer laser is the most common format that is readily available to the researcher. These devices are relatively compact and occupy a fraction of the space of an optical table. In terms of frequency tunability, they can potentially access the full bandwidth of the excimer laser transitions, which, as we have seen in the previous sections, vary from molecule to molecule. For a typical homogeneously broadened single broadband transition the full-width half-maximum bandwidth is of the order of 200 cm^{-1}.

Typically a narrowband tunable oscillator is developed that is then amplified in single-pass, multiple-pass, or regenerative amplifier configurations to obtain high powers (Fig. 4). Often the amplifier may be an electron beam pumped or electron beam sustained discharge laser. These lasers are generally low-gain, large-volume devices with temporal gain times of a factor of 10 to 20 longer than the commercially available avalanche discharge lasers.

TABLE 4 Performance of Rare Gas Excimer Lasers[a]

Laser	Wavelength (nm)	Linewidth (nm)	Tuning elements	Output power (MW)	Reference
Ar_2^*	124.5–127.5	0.3	Prism	2	[57]
	123.2–127.4	0.6	Grating	0.001	[58]
	126			16	[59]
Kr_2^*	145.7	0.8			[60]
Xe_2^*	170–175	0.13	Prism	0.7	[61]

[a]Adapted from Hooker and Webb [56].

NARROWBAND TUNED OSCILLATOR AND SINGLE PASS AMPLIFIER

NARROWBAND TUNED OSCILLATOR WITH REGENERATIVE AMPLIFIER

FIGURE 4 Generalized oscillator–amplifier configurations. Amplifier stages incorporating unstable resonator optics can also be known as forced oscillators.

The temporal characteristics of the oscillator must meet a number of requirements in terms of obtainable linewidths and in terms of compatibility with the temporal characteristics of the amplifier. The narrowness of the linewidth using a dispersive element, such as a grating or multiple-prism arrangement, is typically improved by an order of magnitude or more over single-pass linewidths when many round-trips are available in the oscillator [62]. Thus, the gain time in the oscillator is an important factor in the achievable linewidth of an excimer laser system. The gain time of the oscillator must also be compatible with the gain time of the amplifier system. It is, however, possible to have oscillator gain times that are shorter than the amplifier system and still extract energy from the amplifier for the full gain time of the amplifier.

In single-pass and multiple-pass configurations, this can be done by beam-splitting the oscillator pulse and restacking the pulses with appropriate time delays so that the total pulse length matches the total gain time of the amplifier. In a regenerative amplifier configuration, a short-pulse oscillator can control the total gain time of the amplifier if the reflected field of the amplified oscillator pulse from the first pass is sufficient to control the frequency output of the second pass and so forth. Generally, the degradation of the narrow frequency field is such that the technique is not effective when factors of 10 in gain times between the oscillator and amplifier are involved. The success of the latter method is generally based on the conservatism of the regenerative amplifier design. In general, care should be taken to ensure the magnification is large enough so that the amplifier is incapable of going into oscillation without the injected oscillator pulse. Remember that the wavelength purity of the amplified pulse cannot be better than the ratio of the injected oscillator intensity over the amplified spontaneous emission (ASE) in the amplifier radiated into the solid angle of the oscillator beam. It

is simplest to have the injected oscillator pulse length equal to or larger than the amplifier gain time.

In the next subsections we briefly discuss the general techniques that are used to obtain narrow-linewidth tunable systems, including a discussion of the gain in the narrowness of the oscillator linewidths as a function of the number of cavity round-trips. The operation of unstable resonators is also discussed so that the limitations of an injection seeded regenerative amplifier can be understood. A brief discussion of avalanche discharge techniques is then given to instill a feel for the type of devices that are generally available. This includes typically short-pulse devices (25 ns) as well as techniques that allow stable discharges resulting in laser pulse lengths of hundreds of nanoseconds. A short review of electron beam and electron beam sustained discharges will be given as well.

3.1 Tuning and Line-Narrowing Methods

The passive spectral width for a Brewster prism, Littrow prism, and beam expander chain such as that shown in Fig. 5 is discussed in detail in Chapter 2.

For the case of Brewster prisms, the generalized equation given by Duarte and Piper [63] reduces to

$$\frac{d\phi_{2,1}}{dn} = 2 \,. \tag{1}$$

For a multiple-prism assembly, or sequence, composed of r prisms the overall single-pass dispersion is given by [12]

$$\frac{d\phi_{2,r}}{d\lambda} = r\frac{d\phi_{2,1}}{d\lambda} \,. \tag{2}$$

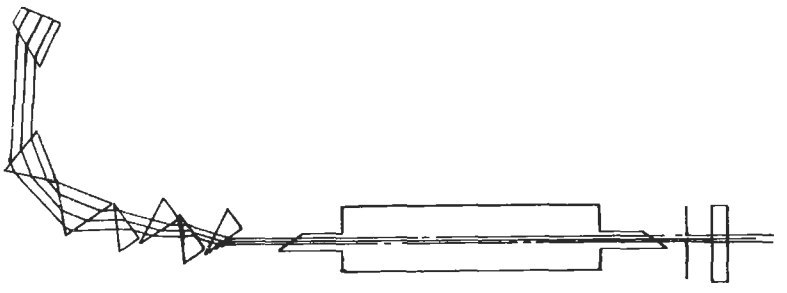

FIGURE 5 Dispersive oscillator incorporating a multiple-prism assembly (from Sze *et al.* [15]).

The exact double-pass multiple-prism dispersion for any geometry can be estimated using Duarte's equations [12]. Note that the double-pass dispersion can also be calculated by multiplying the single-pass dispersion by $2M$, where M is the overall beam expansion factor [12]. For the case of incidence at the Brewster angle, the individual beam expansion at the mth right-angle prism ($k_{1,m}$) can be written

$$k_{1,m} = n,$$

where n is the refractive index. Also, for an angle of incidence ($\phi_{1,m}$) equal to the Brewster angle we have $\tan \phi_{1,m} = n$. Under these conditions, for a prism sequence of r prisms, the overall beam expansion becomes $M = n^r$. Sze *et al.* [15] write an expression for the dispersive (passive) linewidth of the form

$$\Delta\lambda = \Delta\theta\left(2NM\frac{d\phi_{2,r}}{d\lambda}\right)^{-1}, \tag{3}$$

where N is the number of round trips (R in Chapter 2). In this equation the initial beam divergence is expressed as the ratio of the cavity aperture (a) and the cavity length (l). Under the preceding interpretation where the spectral linewidth is estimated through a convergence of the beam divergence, the narrowing of the linewidth cannot proceed indefinitely but must stop as $\Delta\theta$ reaches the diffraction limit [15]

$$\left(\frac{a}{l}\right)\frac{1}{2N} \rightarrow \frac{1.22\lambda}{a}. \tag{4}$$

Hence, the linewidth expression has the form

$$\Delta\lambda = \left(\frac{1.22\lambda}{a}\right)\left(M\frac{d\phi_{2,r}}{d\lambda}\right)^{-1}. \tag{5}$$

Figure 6a shows the situation for a number of initial geometric beam divergence's versus the number of round-trips as calculated using Eq. (3) with the straight line given as the diffraction limit. The corrected curves are given in Fig. 6(b). Therefore, in many situations where the cavity length is long and the aperture is made very small, the diffraction limit can be reached in one or two round-trips, implying that there is therefore no need to go to long-pulse lasers. In fact, however, what was observed in flashlamp-pumped dye lasers [62] and what is observed in long-pulse excimer lasers [64] is that when a large number of cavity round-trip times are available the linewidth is generally one-tenth that calculated by Eq. (5). It was argued in [64] that a frequency-selective aperture transfer function needs to be incorporated into the general formula in Eq. (3).

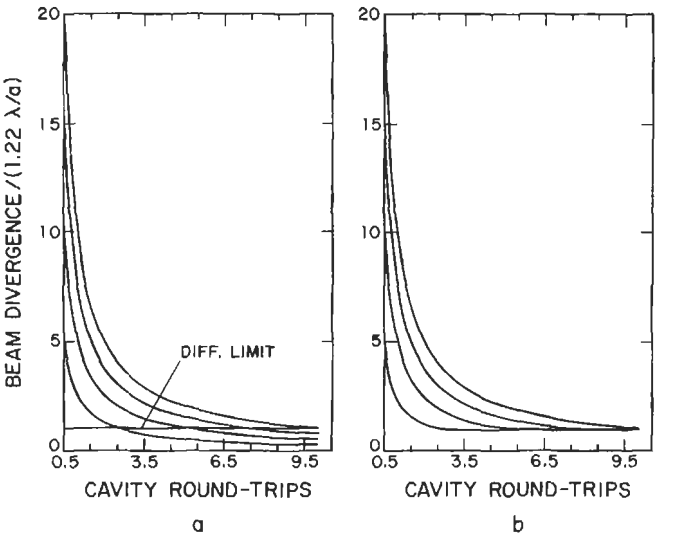

FIGURE 6 (a) Beam divergence as a function of cavity roundtrips (N). (b) Curves in part (a) corrected to go to the diffraction limit (from Sze *et al.* [15]).

Figure 7 shows the schematic of a grating giving the incidence angle and the diffracted angle. The order of the diffracted beam m and its angle is dependent on the distance between groove separations d and the wavelength of light and is given by

$$\sin\theta + \sin\theta' = m\lambda/d \quad . \tag{6}$$

In the simplest form, the grating can be set up in two configurations as given in Fig. 8. Figure 8a shows the Littrow configuration. The diffracted light usually in first order of the grating ($m = 1$) is reflected back in the direction of the incident beam ($\theta = \theta'$). The angular dispersion is

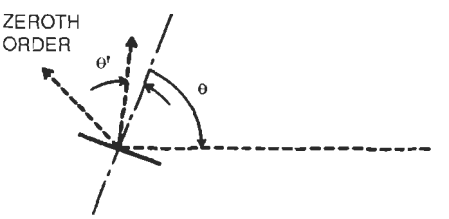

FIGURE 7 Diffraction grating diagram showing incidence (θ) and diffraction (θ') angles.

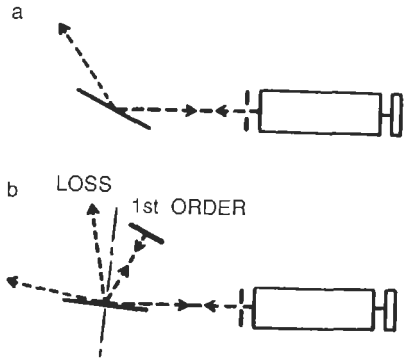

FIGURE 8 (a) Littrow configuration. (b) Grazing-incidence configuration (from Sze *et al.* [15]).

$$d\theta/d\lambda = m/\left(d \cos \theta\right) , \tag{7}$$

and the passive spectral linewidth, in analogy with Eq. (3), is given by

$$\Delta\lambda = \left(a/l\right)\left(1/2N\right)\left(d/m\right) \cos \theta , \tag{8}$$

where (a/l) is the initial geometric beam divergence and N is the number of round-trips. The problem with this configuration is that usually for small aperture devices only a very small part of the grating is used, and the dispersion is relatively small. This can be corrected by the use of beam expanders so that the small aperture is expanded to fill the whole of the grating [12]. By going to the grazing-incidence configuration shown in Fig. 8(b), one can choose the angle of incidence to be near 90° so as to fill the grating and make cos θ very small, this configuration reduces the linewidth in Eq. (8) by an additional factor of 2 because the grating is used twice. The price one pays for this is that at near grazing incidence the power diffracted into the first order is often quite small, with most of the power appearing as a loss in the zero order [12]. Since the grating is used twice in first order, the reflected energy is generally quite weak. In situations where the feedback is sufficient to control the lasing, the oscillation bandwidth can be extremely narrow. Calculated linewidths for multiple-prism grating XeCl laser oscillators are given in Chapter 2.

The linewidth can be further reduced by the addition of resonant elements to the cavity. In Fig. 9(a) we show a grazing incidence configuration that incorporates a Michelson interferometer in place of the other cavity mirror. This sinusoidally modulates the gain with a period given by the difference in length between the two arms. As an example, Sze *et al.* [15] obtained in XeCl 1/10th of a wave number linewidth using a 3600 groove/mm grating at grazing incidence in first order with

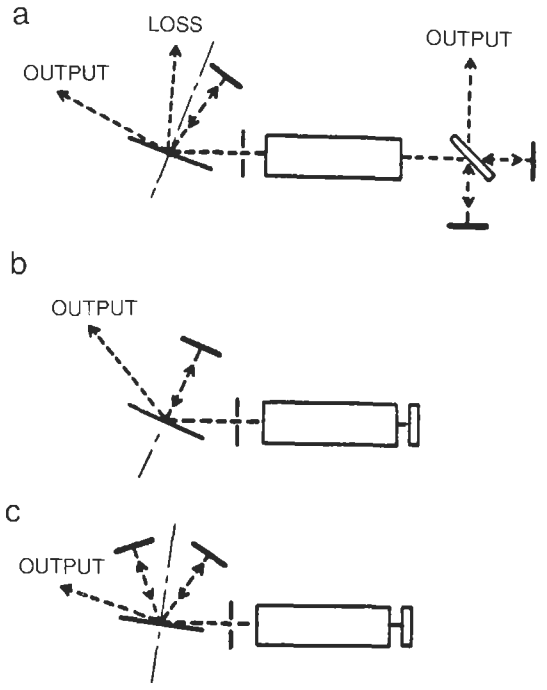

FIGURE 9 Grazing-incidence oscillator configurations incorporating (a) a Michelson interferometer, (b) a multipass grating interferometer, and (c) a Fox–Smith interferometer (from Sze *et al.* [15]).

a long-pulse excimer discharge laser. Incorporation of a Michelson interferometer arm narrowed the linewidth further to 1/50th of a wave number. This configuration can be altered to a high-Q Fox–Smith cavity [65] by turning the beamsplitter by 90° and making it a high reflector. In principle, this can give a large reduction in linewidth but the mirror spacing must be kept very small because the resonance condition is for the sum of the path lengths for the two arms.

Figure 9b tunes the grating angle so that the first order is normal to the grating. This configuration [18] allows the first order to be reflected back to the incident beam with its zero order reflected straight back on itself and therefore setting up a cavity with additional resonance conditions. Armandillo *et al.* [18] report obtaining single-longitudinal-mode lasing in XeF using this technique. This was, however, done at very low gains. We had a great deal of trouble using this technique in systems with reasonable gain. The difficulty arises from the fact that when the first order of the grating is tuned normal to the grating, the second order is in the Littrow condition. Thus, the second order often controls the oscillator, making the first-order resonant technique useless.

Figure 9c attempts to improve the grazing incidence of Fig. 9(b) by reflecting back the loss from zeroth order of the first-order diffracted signal. Again the

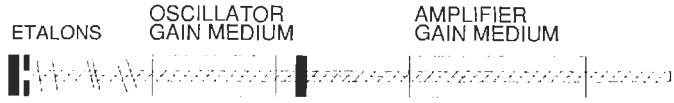

ETALONS NARROWED OSCILLATOR AND SINGLE PASS AMPLIFIER

FIGURE 10 Oscillator incorporating a multiple-etalon arrangement.

extra cavity resonance allows for a Fox–Smith type cavity. In reality, however, it is extremely difficult to make this cavity short enough to have a mode spacing greater than the approximately one wave number needed to select a single mode from the grating-narrowed laser.

Figure 10 shows intracavity narrowing using a series of etalons. Because an etalon is a device with multimode transmissions separated by $c/2nL$ frequency spacing where c is the velocity of light, n the index of refraction, and L the mirror separation, a number of etalons (generally three) is required for lasing in only one frequency region of the total gain bandwidth of the transition. Although narrow-linewidth operation is fairly simple, tuning of this narrowband laser is complicated because all three etalons must be synchronized and tuned together so that they provide a smooth frequency movement of the output laser frequency. Etalons are generally of two types. They are either angle tuned or pressure tuned (see [12], for example).

3.2 Multipass Line Narrowing

A description of line narrowing as a function of the number of cavity round-trips is given by Sze *et al.* [15] and Sze [64]. These authors consider two cases. In Case a the intensity distribution at a frequency λ is displaced a certain distance, $\delta(\lambda-\lambda_0)$, away from the optical axis with each round-trip, but the distribution retains its shape. Thus, after N round-trips the field intensity at λ is displaced by $N\delta(\lambda-\lambda_0)$. Case b discusses a more realistic situation where the shape of the wave function is recovered every round-trip with its attendant transverse offset due to the dispersive elements in the cavity. A schematic of both cases is given in Fig. 11.

For both cases the effect of uniform and Gaussian intensity distributions were numerically considered [15,64]. The normalized linewidth for Cases a and b, assuming uniform illumination, is given as a function of N in Fig. 12. The normalized linewidth as a function of N is given in Fig. 13 for Case a assuming uniform and Gaussian intensity distributions. In Fig. 14 the normalized linewidth as a function of N is given for Cases a and b assuming a Gaussian intensity distribution. Under Gaussian illumination, these authors [15,64] believe that Case b is a more accurate representation of line narrowing as a function of N in a dis-

persive cavity. A more complete analysis would require a Fox and Li [66] type calculation of different gain conditions to obtain a full picture of line narrowing versus the number of round-trips in the cavity.

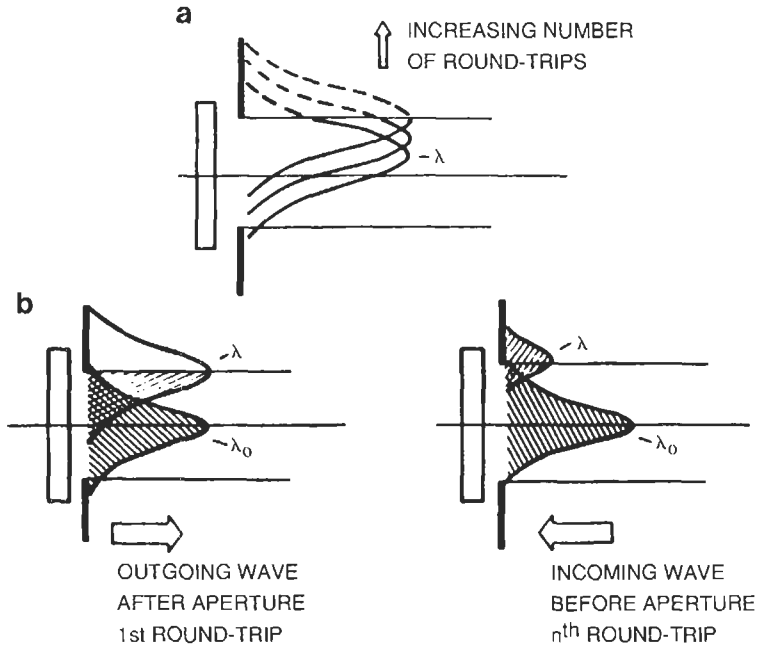

FIGURE 11 Schematics of (a) Case a and (b) Case b (from Sze *et al.* [15]).

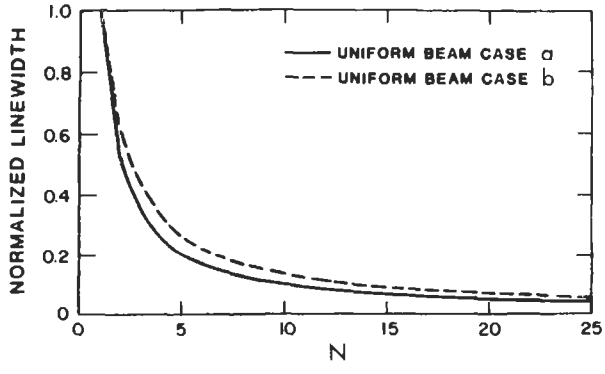

FIGURE 12 Normalized linewidth as a function of round-cavity trips for (a) Case a and (b) Case b under uniform illumination conditions (from Sze *et al.* [15]).

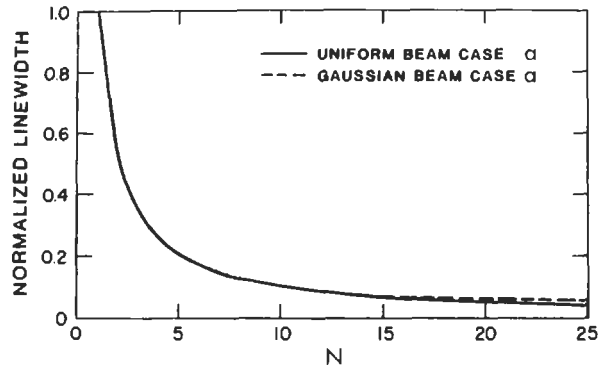

FIGURE 13 Normalized linewidth as a function of round-cavity trips for Case a under (a) uniform and (b) Gaussian intensity distributions (from Sze *et al.* [15]).

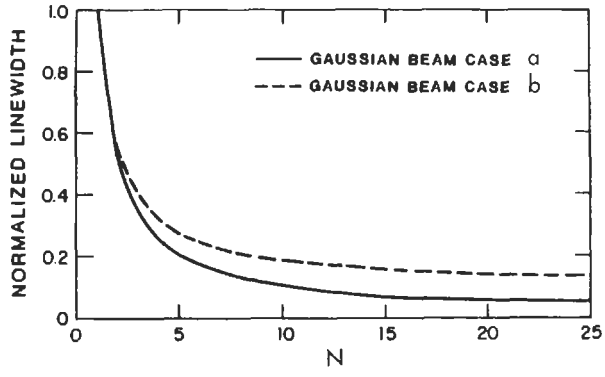

FIGURE 14 Normalized linewidth as a function of N assuming a Gaussian intensity distribution for (a) Case a and (b) Case b (from Sze *et al.* [15]).

3.3 Unstable Resonator Configurations

The use of unstable resonators in high-gain, short-pulse systems is discussed by Isaev *et al.* [67] and by Zemskov *et al.* [68]. Their conclusions are summarized by Caro *et al.* [4]. To understand the formation of diffraction-limited beams in excimer laser systems, one needs to consider how the diffraction-limited mode is developed in unstable resonators. Although the power extracted from the gain medium is accomplished by the expanding beam in the unstable resonator, the diffraction-limited seed is developed from ASE by the oppositely propagating converging beam. The time required for the converging beam to reach the diffraction limit must be short compared to the gain time of

the medium or very little energy will remain to be extracted with good beam divergence. Because the higher the magnification of the unstable resonator the faster the convergence toward a diffraction-limited mode, high-gain, short-pulse systems favor high-magnification unstable optics.

The second criterion deals with the suppression of threshold lasing by keeping the system small-signal gain below a critical value so that the diffraction-limited mode can develop first. Again, the higher the magnification, the harder it is for threshold lasing to commence and the higher the permissible system gain. In lasers where super fluorescence can develop in one pass or in systems where the magnification is small and threshold lasing develops rapidly, it will be virtually impossible to generate diffraction-limited beams.

For a confocal positive-branch unstable resonator as shown in Fig. 15, the time t necessary for the diffraction-limited mode to develop in a resonator system of magnification M is given by

$$t = \left(2L/c\right)\left(1 + lnM_0/lnM\right) , \tag{9}$$

and the critical gain g_{cr}, which the laser system must stay under to avoid threshold lasing, is given by

$$g_{cr} = \left(lnM/L_a\right)\left\{A/\left[2ln\left(MM_0\right)\right] + 1\right\} , \tag{10}$$

where M_0 is a diffraction limit magnification parameter given by

$$M_0 = 2D/1.22\lambda R_2 \ . \tag{11}$$

In Eqs. (9), (10), and (11), D is the large dimension of the discharge area, λ is the wavelength of the laser transition, L is the cavity separation, L_a is the gain length, and A is the gain length product (usually between 20 to 30 for excimer laser systems) for which superradiance becomes observable. The unstable resonator equations are

$$R_1 + R_2 = 2L \tag{12}$$

and

$$M = -R_2/R_1 \ , \tag{13}$$

where R_1 and R_2 are the radii of curvature of the two mirrors with R_2 the less curved of the two mirrors and R_1 having a negative value as indicated in Fig. 15.

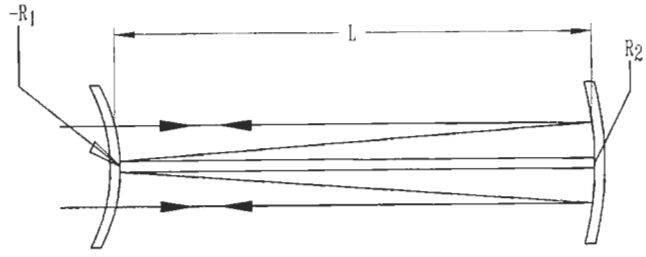

FIGURE 15 Confocal positive-branch unstable resonator.

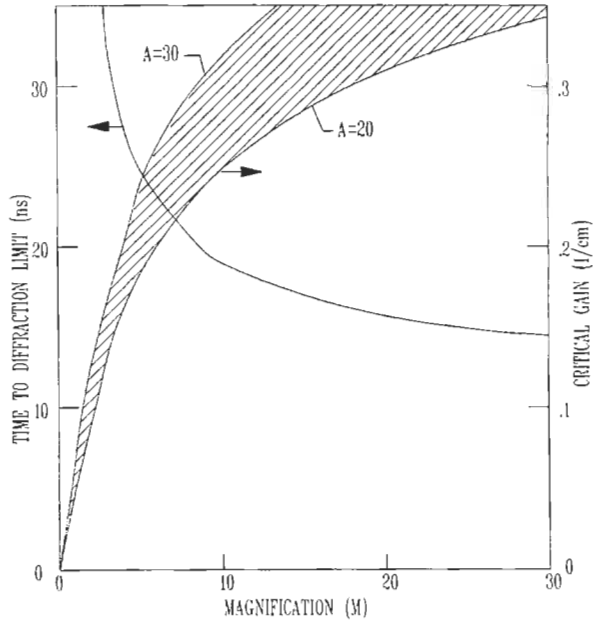

FIGURE 16 Time to reach diffraction limit and gain as a function of magnification.

Consider, for example, a plot of t and g_{cr} for a cavity design where the gain length is $L_a = 20$ cm and, due to mechanical or other constraints, the cavity separation is $L = 76$ cm. We calculate g_{cr} for cases where $A = 20$ and 30. All of the excimer laser transitions should have the A parameter lying within this range. Figure 16 shows that at a magnification of 20 we can have small-signal gains as high as 0.3 cm^{-1}. In short-pulse discharge excimer laser systems, the measured small-signal gain lies between 0.2 to 0.3 cm^{-1}. We see that the problem here lies in the time required to reach the diffraction limit. With the cavity separation at

76 cm it takes greater than 15 ns for the diffraction-limited mode to develop—even at magnifications as high as 20 to 30. Thus, for a typical discharge excimer laser gain time of 15 to 25 ns, very little time is left to extract diffraction-limited energy in the unstable resonator.

The temporal development of the lasing beam quality in unstable cavities has been studied in copper vapor lasers and is shown to be continuously improving until it reaches the diffraction limit. Even if the cavity separation is halved in the preceding example to $L_a = 38$ cm, Eq. (9) shows it still takes some 8.6 ns for the diffraction-limited mode to form. In the case of injection locking of the unstable resonator as a regenerative amplifier, the primary concern is to pick the magnification so that the gain is below the critical gain value so that the unstable cavity cannot go into spontaneous oscillation. This criterion, however, is different for different excimer gases and for different pulse lengths of the injection oscillator seed source. For a system such as XeCl where there are five broad lines lasing into different lower states and where all the transitions cannot be treated as a homogeneously broadened source, the injection source tuned to a frequency in one of the transitions only lowers the gain at other frequencies within that transition. The other transitions still retain their small-signal gain. Therefore, high magnification is required to keep those transitions from oscillating.

4. DISCHARGE EXCIMER LASERS

The development of dependable, long-lived excimer laser systems requires one to address among other questions that of pulse power, gas cleanup, and gas flow. We proceed now with a discussion of pulse power techniques that have been used to obtain lasing of the rare gas halide lasers in avalanche discharges.

Improved pulse power techniques are the most important key to the development of reliable commercial laser systems because the possibilities of manipulating pulse lengths, the elimination of streamer arc formation, and the reduction or elimination of high-current, fast-pulse-power circuits affect other issues of component lifetimes, gas lifetimes, etc.

The engineering of pulse power in commercial lasers today is fundamentally governed by the limited stable discharge times of the electronegative rare gas halide gas mixtures in avalanche discharges. The stable discharge time for a UV preionized laser system is dependent on gas pressure and electrode gap separation. Typically, for a 3-atm, 3-cm gap laser, this time is of the order of 30 to 40 ns. Thus, the problem becomes one of depositing almost all stored energy within this time. Energy deposited subsequently goes into streamer arcs, which do not provide lasing, and greatly shortens the gas lifetime.

The first application of this technique is by Burnham and Djeu [69] when they separated the timing of the UV preionization surface discharge to the main discharge in a very fast L-C inversion circuit used by Tachisto, Inc., for their

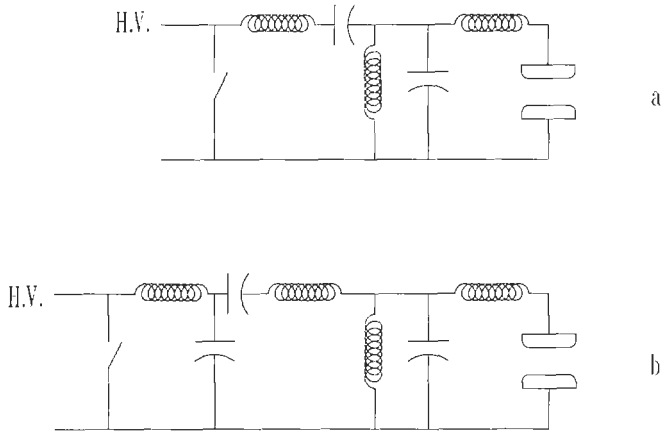

FIGURE 17 Conventional charging circuits.

CO_2 lasers. The physical characteristics of this device were studied by Sze and co-workers [70,71]. Commercial systems today generally transfer the stored energy to a series of peaking capacitors that physically lie very close to the discharge head to minimize inductance. Thus, the energy stored in the peaking capacitors can be deposited very quickly into the discharge. Figure 17 shows typical commercial circuits used today for the pulse power where there is a simple storage capacitor and an L-C inversion storage system. The inductance to ground is a large inductance to allow dc charging of the capacitors and the inductances in the loop are a result of the physical constraints of the discharge head and components.

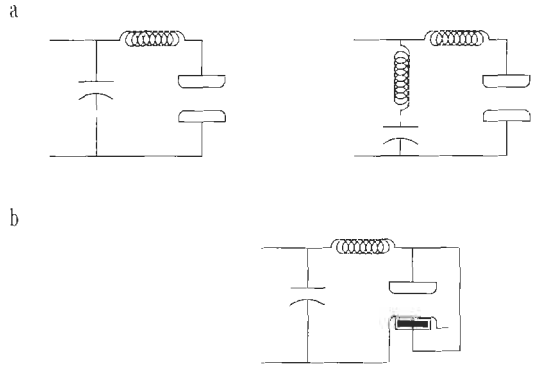

FIGURE 18 Preionization circuits. (a) VUV arc preionization. (b) Corona preionization.

As just mentioned, Burnham and Djeu separated the preionization from the main discharge. This originally required separate capacitors and switches for the two circuits and also imposed timing considerations between the discharges. Present-day commercial systems have very cleverly combined the two by forcing the peaking capacitors to be charged through small gaps via an arc that provides for the preionization. The diagrams in Fig. 18(a) show one of a row of such a peaking capacitor array. An alternate, efficient technique [Fig. 18(b)] is that of corona preionization using the voltage rise time of the system to induce a voltage on the surface of a dielectric by generating displacement currents in the dielectric. Commercial lasers using the preceding techniques usually provide laser energies as high as 1 J/pulse with an operating pulse width between 20 to 30 ns.

A major advance in discharge laser technology is attributed to Lin and Levatter [72,73]. They studied the details of streamer formation and postulated that there is a region in discharge parameter space where long stable discharges are possible. This is accomplished by very uniform preionization and very fast voltage rise times. They developed a laser with X-ray preionization and a series rail-gap switch to accomplish the very fast voltage rise time. Such a system, shown in Fig. 19, indeed showed greatly improved laser performance. However, the stringent requirements make commercialization of the technique difficult.

Attempts to satisfy the Lin–Levatter criteria led to the study of magnetic pulse compression techniques to transform a slow rising pulse to a very fast one. The technique has the added benefit of substantially lowering the current and the rate of current rise through the switch. This will greatly improve the switch lifetime. However, due to the hysteresis loss in the magnetic material, oil cooling is generally necessary and results in substantial complications for a commercial system. Lambda Physik has incorporated the technique into some of their product lines for the purpose of preserving switch lifetime. Figure 20 gives a schematic of the pulse power setup. Due to the development of hollow anode thyratrons by English Electric Valve, Ltd., which allow 50% inverse current transients through the switch, switch lifetime considerations are no longer as severe a problem as previously the case. The use of pulse compression to shorten greatly the voltage rise time was first successfully implemented by Laudenslager

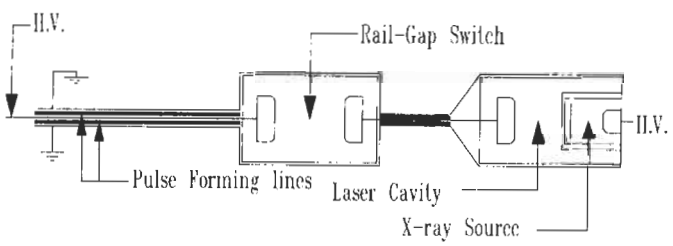

FIGURE 19 Circuit for very fast voltage rise time incorporating a series rail-gap switch.

and Pacala [74]. This involves careful implementation of a racetrack magnetic core of met–glass materials.

Refer to Fig. 20; the compression factor is determined by the rise time of the original storage loop compared to the saturated inductor part of the circuit loop. Thus, it is a comparison between the L-C time constants of the two parts of the circuit. This is given as

$$Compression = \left(L_1/C\right)^{1/2}/\left[L_{2(SAT.)}/C'\right]^{1/2}, \tag{14}$$

where $C = C_1{*}C_2/(C_1 + C_2)$ and $C' = C_2{*}C_3/(C_2 + C_3)$. For multiple stages, imposing the resonance transfer condition so that $C_1 = C_2 = C_3 = \ldots = Cn$ and using the formula for inductance,

$$L_{n(SAT.)} = \mu_{n(SAT.)} N_n A_n^2/volume_n \ , \tag{15}$$

where the stacking factor has been neglected and where A is the core area and volume is the core volume. One obtains, when using the same material for all stages, the compression at each stage as

$$\begin{aligned} Compression\ at\ each\ stage &= \left[L_{n-1(SAT.)}/L_{n(SAT.)}\right]^{1/2} \\ &= \left(A_{n-1}^2\, volume_n/A_n^2 volume_{n-1}\right)^{1/2} . \end{aligned} \tag{16}$$

We can see that one can try to design high compression per stage by minimizing the core area and maximizing magnetic path length or one can design multiple stages but make sure that saturation of each stage occurs at the time of maximum voltage to result in complete transfer of energy into each stage.

If we look at the efficiencies associated with the avalanche discharge system, one obvious problem is the transfer efficiency of the stored energy to the active discharge. The essential problem is that the system requires a much higher voltage for breakdown than after breakdown when the energy is transferred into

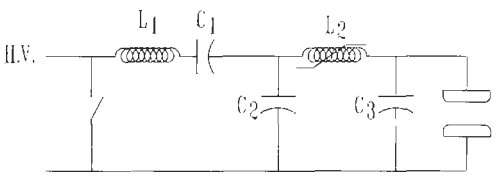

FIGURE 20 Circuit for magnetic pulse compression.

the gas. This is a problem of going from infinite impedance to a value that is some fraction of an ohm. Maximum transfer efficiency occurs when the impedance of the pulse power matches that of the discharge, and the charging voltage of the storage system is equivalent to the operating voltage of the steady-state discharge. In actuality, the discharge operates at a steady-state voltage independent of the current within a certain operating range. Thus, a particular pulse impedance will then define the current density of the discharge.

The decision to construct a particular pulse power impedance is a decision about how hard we want to pump the discharge volume and it is based on whether we wish to obtain the best efficiency by pumping at only 5 to 15 J/l atm or in obtaining a higher energy by pumping harder (typically 30 J/l atm) but sacrificing some inherent efficiency. Long *et al.* [75] solved this problem with the implementation of a high-impedance prepulse. Figure 21 shows a more recent implementation of this idea where a saturating inductor is being used as a high-impedance isolator for a low-impedance storage circuit. Here the prepulse must have sufficient energy to saturate the inductor to allow deposition of the stored energy. Now the storage circuit can be charged to the much lower operating voltage of the discharge and the prepulse circuit is charged to the much higher voltage for breakdown. The latter can be very fast since it has very little energy content, thus, also satisfying the Lin–Levatter fast voltage rise time criterion. Analysis of pulse compression and prepulse magnetic isolation circuits is discussed in some detail in an article by Vannini *et al.* [76].

The type of laser that uses a very fast prepulse generates an extremely stable discharge and, thus, is capable of long-pulse operation. Another technique that allows for long-pulse laser oscillation is that of inductive stabilization. As discussed in the early sections of this chapter, long pulses increase the number of round-trips in the oscillator and greatly enhance the narrow linewidths of the laser with frequency tuning elements. A long laser pulse also allows injection seeding of an amplifier because timing considerations between oscillator and amplifiers are no longer a problem. This technique uses a segmented electrode structure with each discharge segment stabilized by an inductance and was shown capable of sustaining long lasing pulses (90 ns FWHM) in excimer gas mixture [77,78] of XeCl, XeF, and KrF. Presently, FWHM pulse lengths have been extended to 250 ns in XeCl and 180 ns in KrF using this technique [79,80].

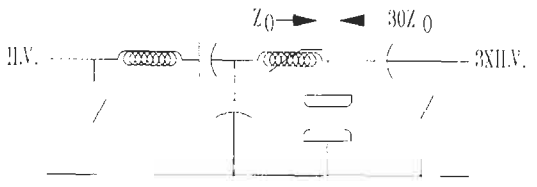

FIGURE 21 Circuit used to yield a high-impedance prepulse.

Additional benefits noted in these studies were order of magnitude increased pulse repetition frequency [81] for a given gas flow and improved pulse-to-pulse energy variations [82] when compared with unstabilized electrodes. One of the most important aspects of this technology is that it allows for very simple pulse power circuits that tend to result in compactness in design and cost effectiveness in construction. Recently Franceschini *et al.* [83] have shown that some of the stability of the inductively stabilized circuit is really due to the small peaking capacitor, which allows for high-frequency modulation of the current. They have obtained long lasing pulses in XeCl using the same circuit but eliminating the inductive stabilization electrode. However, we believe it is still necessary to have such an electrode in order to obtain long lasing pulses in the more unstable gas mixtures of the fluorine-based excimer molecules.

The general circuit configuration is shown in the schematic in Fig. 22. The energy stored in capacitor *Cs* is deposited into the discharge gap when the switch *S* is closed. Because the preionization is through a corona discharge achieved via the *dV/dt* of the rising voltage pulse, preionization only exists before the breakdown of the discharge. Because the main part of the circuit that deposits power to the discharge volume is slow, a peaking capacitor array *Cp* is needed to provide an initial current in the discharge after gas breakdown. The value of the peaking capacitor is only 1/10th to 1/20th the value of the storage capacitance and the energy

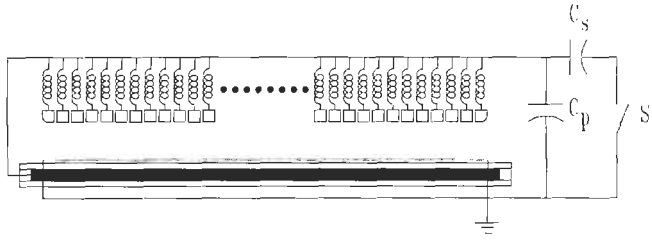

FIGURE 22 Circuit utilized in the excitation of inductively stabilized excimer lasers.

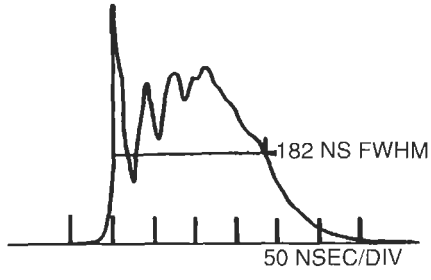

FIGURE 23 Output pulse of XeCl lasing using inductive stabilization.

stored in the peaking capacitors represents a very small part of the energy deposited into the gas. However, even this small capacitance is enough to result in a modulation of the power deposition, as shown in the output waveform given in Fig. 23. Experiments show that for stable discharges in the hundreds of nanosecond timescales an inductance value that gives an impedance corresponding to a 5% change in voltage across the inductor compared to the voltage drop across the discharge gap is sufficient to suppress arcing.

REFERENCES

1. C. K. Rhodes (Ed.), *Excimer Lasers,* Springer-Verlag, Berlin (1979).
2. F. J. Duarte, in *Dye Laser Principles* (F. J. Duarte, Ed.), pp. 239–285, Academic, New York (1990).
3. T. R. Loree, K. B. Butterfield, and D. L. Barker, *Appl. Phys. Lett.* **32,** 171 (1978).
4. R. G. Caro, M. C. Gower, and C. E. Webb, *J. Phys. D: Appl. Phys.* **15,** 767 (1982).
5. V. L. Lyutskanov, K. G. Khristov, and I. V. Tomov, *Sov. J. Quantum Electron.* **10,** 1456 (1980).
6. T. J. McKee, *Can. J. Phys.* **63,** 214 (1985).
7. T. T. Yang, D. H. Burde, G. A. Merry, D. G. Harris, L. A. Pugh, J. H. Tillotson, C. E. Turner, and D. A. Copeland, *Appl. Opt.* **27,** 49 (1988).
8. T. Hofmann and F. K. Tittel, *IEEE J. Quantum Electron.* **29,** 970 (1993).
9. J. Goldhar and J. R. Murray, *Opt. Lett.* **1,** 199 (1977).
10. F. J. Duarte, *Appl. Opt.* **24,** 34 (1985).
11. F. J. Duarte, *Appl. Opt.* **24,** 1244 (1985).
12. F. J. Duarte, in *Dye Laser Principles* (F. J. Duarte, Ed.), pp. 133–183, Academic, New York (1990).
13. K. Ludewigt, W. Pfingsten, C. Mohlmann, and B. Wellegehausen, *Opt. Lett.* **12,** 39 (1987).
14. R. Buffa, P. Burlamacchi, R. Salimbeni, and M. Matera, *J. Phys. D: Appl. Phys.* **16,** L125 (1983).
15. R. C. Sze, N. A. Kurnit, D. E. Watkins, and I. J. Bigio, in *Proc. Int. Conf. Lasers '85* (C. P. Wang, Ed.), pp. 133–144, STS, McLean, VA (1986).
16. M. Sugii, M. Ando, and K. Sasaki, *IEEE J. Quantum Electron.* **QE-23,** 1458 (1987).
17. T. J. Pacala, I. S. McDermid, and J. B. Laudenslager, *Appl. Phys. Lett.* **45,** 507 (1984).
18. E. Armandillo, P. V. M. Lopatriello, and G. Giuliani, *Opt. Lett.* **8,** 327 (1984).
19. F. J. Duarte, in *Proc. Int. Conf. Lasers '84* (K. M. Corcoran, D. M. Sullivan, and W. C. Stwalley, Eds.), pp. 397–403, STS, McLean, VA (1985).
20. A. N. Bobrovskii, A. V. Branitskii, M. V. Zurin, A. V. Kozhevnikov, V. A. Mishchenko, and G. D. Mylnikov, *Sov. J. Quantum Electron.* **17,** 1157 (1987).
21. R. C. Sze, A. McCown, and N. A. Kurnit, in *Proc. Society of Photo-Optical Instrumentation Engineers,* in *High-Power Gas and Solid-State Lasers, Proc. SPIE* **2206,** 122–129. SPIE, Bellingham, WA (1994).
22. H. Rieger, *IEEE J. Quantum Electron.* **25,** 913 (1989).
23. E. Armandillo, *Opt. Commun.* **49,** 198 (1984).
24. M. Bashkansky and J. Reintjes, *Opt. Commun.* **83,** 103 (1991).
25. R. Fedosejevs, I. V. Tomov, D. C. D. McKen, M. Arnfield, C. Domier, and A. A. Offenberger, *J. Appl. Phys.* **54,** 5629 (1983).
26. B. Ruckle, P. Lokai, U. Brinkmann, D. Basting, and W. Muckenheim, *Opt. Laser Technol.* **19,** 153 (1987).
27. M. J. Shaw, *Prog. Quantum Electron.* **6,** 3 (1979).

27a. E. C. Harvey and M. J. Shaw, *Laser and Particle Beams* **9,** 659–673 (1991).

28. H. Ochi, T. Nishisaka, K. Sajiki, Y. Itakura, R. Noudomi, M. Kakimoto, in *Conf. Lasers and Electro-Optics 1992*, OSA Technical Digest Series, Vol. 12, pp. 86–87, Optical Society of America, Washington, DC (1992).
29. C. A. Brau and J. J. Ewing, *J. Chem. Phys.* **63,** 4640 (1975).
30. J. Tellinghuisen, P. C. Tellinghuisen, G. C. Tisone, J. M. Hoffman, and A. K. Hays, *J. Chem. Phys.* **68,** 5177 (1978).
31. P. C. Tellinghuisen, J. Tellinghuisen, J. A. Coxon, J. E. Velazco, and A. K. Hays, *J. Chem. Phys.* **68,** 5187 (1978).
32. P. C. Tellinghuisen and J. Tellinghuisen, *Appl. Phys. Lett.* **43,** 893 (1983).
33. J. Tellinghuisen, G. C. Tisone, J. M. Hoffman, and A. K. Hays, *J. Chem. Phys.* **64,** 4797 (1976).
34. D. G. Harris, T. T. Yang, D. H. Burde, G. A. Merry, L. A. Pugh, J. H. Tillotson, C. E. Turner, and D. A. Copeland, in *Proc. Int. Conf. Lasers '87* (F. J. Duarte, Ed.), pp. 111–125, STS, McLean, VA (1988).
35. H. J. Hsia, J. A. Mangano, J. H. Jacob, and M. Rokni, *Appl. Phys. Lett.* **34,** 208 (1979).
36. R. W. Tuxworth, M. Lawton, and M. J. Shaw, *J. Phys. D: Appl. Phys.* **13,** 135 (1980).
37. J. B. West, H. Komine, and E. A. Stappaerts, *J. Appl. Phys.* **52,** 5388 (1981).
38. I. J. Bigio and M. Slatkine, *IEEE J. Quantum Electron.* **QE-19,** 1426 (1983).
39. N. Hamada, R. Sauerbrey, W. L. Wilson, F. K. Tittel, and W. Nighan, *IEEE J. Quantum Electron.* **QE-24,** 1571 (1988).
40. G. J. Hirst, C. B. Dane, W. L. Wilson, R. Sauerbrey, F. K. Tittel, and W. L. Nighan, *Appl. Phys. Lett.* **54,** 1851 (1988).
41. W. L. Nighan and M. C. Fowler, *IEEE J. Quantum Electron.* **QE-25,** 791 (1989).
42. T. Hofmann, T. E. Sharp, C. B. Dane, P. J. Wisoff, W. L. Wilson, F. K. Tittel, and G. Szako, *IEEE J. Quantum Electron.* **QE-28,** 1366 (1992).
43. C. B. Dane, S. Yamaguchi, Th. Hofmann, R. Sauerbrey, W. L. Wilson, and F. K. Tittel, *Appl. Phys. Lett.* **56,** 2604 (1990).
44. A. Mandl and L. N. Litzenberger, *Appl. Phys. Lett.* **53,** 1690 (1988).
45. J. Tellinghuisen, J. M. Hoffman, G. G. Tisone, and A. K. Hays, *J. Chem. Phys.* **64,** 2484 (1976).
46. O. L. Bourne and A. J. Alcock, *Appl. Phys. Lett.* **43,** 777 (1983).
47. M. Ohwa and M. J. Kushner, in *Conf. Lasers and Electro-Optics 1989*, OSA Technical Digest Series, Vol. 11, p. 270, Optical Society of America, Washington, DC (1989).
48. J. R. Murray and H. T. Powell, *Appl. Phys. Lett.* **29,** 252 (1976).
49. J. G. Eden and S. K. Searles, *Appl. Phys. Lett.* **29,** 350 (1976).
50. S. K. Searles and G. A. Hart, *Appl. Phys. Lett.* **27,** 243 (1975).
51. G. Balog, R. K. Sander, and E. Seegmiller, *Appl. Phys. Lett.* **35,** 727 (1979).
52. A. N. Panchenko, V. F. Tarasenko, and E. V. Bukatyi, *Sov. J. Quantum Electron.* **19,** 1547 (1989).
53. V. E. Peet, E. V. Slivinskii, and A. B. Treshchalov, *Sov. J. Quantum Electron.* **20,** 372 (1990).
54. J. M. Hueber, B. L. Fontaine, N. Bernard, B. M. Forstier, M. L. Sentis, and Ph. C. Delaporte, *Appl. Phys. Lett.* **61,** 2269 (1992).
55. N. Bernard, J. M. Hueber, B. L. Fontaine, Ph. C. Delaporte, M. Sentis, and M. Ngo Kobhio, in *Conf. Lasers and Electro-Optics 1993*, Vol. 11, p. 422, Optical Society of America, Washington, DC (1993).
56. S. M. Hooker and C. E. Webb, *Prog. Quant. Electr.* **18,** 227–274 (1994).
57. Y. Uehara, W. Sasaki, S. Kasai, S. Saito, E. Fujiwara, Y. Kato, C. Yamanaka, M. Yamanaka, K. Tsuchida, and J. Fujita, *Opt. Lett.* **10,** 487 (1985).
58. W. G. Wrobel, H. Rohr, and K. H. Stever, *Appl. Phys. Lett.* **36,** 113 (1980).
59. K. Kurosawa, Y. Takigawa, W. Sasaki, M. Okuda, E. Fujiwara, K. Yoshida, and Y. Kato, *IEEE J. Quantum Electron.* **QE-27,** 71 (1991).
60. P. Hoff, J. Swingle, and C. Rhodes, *Appl. Phys. Lett.* **23,** 245 (1973).
61. M. H. R. Hutchinson, *Appl. Opt.* **19,** 3883 (1980).
62. F. Schäfer, in *Dye Lasers* (F. P. Schäfer, Ed.), pp. 1–89, Springer-Verlag, Berlin (1990).
63. F. J. Duarte and J. A. Piper, *Opt. Commun.* **43,** 303 (1982).

64. R. C. Sze, in *Conf. Lasers and Electro-Optics 1984,* p. 203, Optical Society of America, Washington, DC (1984).
65. P. W. Smith, *Proc. IEEE* **60,** 422 (1972).
66. A. G. Fox and T. Li, *Bell Syst. Tech. J.* **40,** 453 (1961).
67. A. A. Isaev, M. A. Kazaryan, G. G. Petrash, and S. G. Rautian, *Sov. J. Quantum Electron.* **4,** 761 (1974).
68. K. I. Zemskov, A. A. Isaew, M. A. Kazaryan, G. G. Petrash, and S. G. Rautian, *Sov. J. Quantum Electron.* **4,** 474 (1974).
69. R. Burnham and N. Djeu, *Appl. Phys. Lett.* **29,** 707 (1976).
70. R. C. Sze and T. R. Loree, *IEEE J. Quantum Electron.* **QE-14,** 944 (1978).
71. R. C. Sze, *IEEE J. Quantum Electron.* **QE-15,** 1338 (1979).
72. S. Lin and J. I. Levatter, *Appl. Phys. Lett.* **34,** 505 (1979).
73. J. I. Levatter and S. Lin, *J. Appl. Phys.* **51,** 210 (1980).
74. J. B. Laudenslager and T. J. Pacala, NASA Technical Brief NPO-14556 (1980).
75. W. H. Long, M. J. Plummer, and E. A. Stappaerts, *Appl. Phys. Lett.* **43,** 735 (1983).
76. M. Vannini, R. C. Sze, and F. Hommeau, in *Proc. Int. Conf. Lasers '87* (F. J. Duarte, Ed.), pp. 103–110, STS, McLean, VA (1988).
77. R. C. Sze, *J. Appl. Phys.* **54,** 1224 (1983).
78. R. C. Sze, in *Proc. Society of Photo-Optical Instrumentation Engineers,* in *Metal Vapor Laser Technology and Applications, Proc. SPIE* **1041,** 176–185, SPIE, Bellingham, WA (1989).
79. R. C. Sze, in *Proc. Int. Conf. Lasers '89,* (D. G. Harris and T. M. Shay, eds.), pp. 76–79, STS, McLean, VA (1990).
80. Stablelase, Incorporated, Santa Fe, New Mexico, private communications.
81. R. C. Sze, in *Proc. 5th Int. Symp. Gas Flow and Chemical Lasers,* Inst. Phys. Conf. Series, pp. 227–232, Adam Hilger Ltd., Bristol, England (1985).
82. M. Sentis, R. C. Sze, F. Hommeau, B. Forestier, B. Fontaine, in *Am. Inst. Physics Conf. Proc.,* Vol. 172, pp. 59–61, AIP, New York (1988).
83. M. A. Franceschini, R. Pini, R. Salimbeni, and M. Vannini, *Appl. Phys. B* **54,** 259 (1992).

4 CO_2 Isotope Lasers and Their Applications in Tunable Laser Spectroscopy*

Charles Freed

Lincoln Laboratory and the Department of Electrical Engineering and Computer Science Massachusetts Institute of Technology Lexington, Massachusetts

1. INTRODUCTION

CO_2 molecular-gas lasers were invented by C. K. N. Patel in 1964 [1,2], about four years after the first practical demonstration of a laser by Maiman [3]. Patel's search for more efficient lasers led him to the first experiments utilizing vibrational-rotational transitions of gas molecules, starting with CO_2. Indeed, it would be difficult to overemphasize the significance of Patel's many sided contributions to laser physics in general and to the development of CO_2 lasers in particular. Within about a year after the invention, Patel and his coworkers determined the most salient aspects of CO_2 laser physics and processes that opened the floodgate toward the development of truly high efficiency, high-power laser systems [4].

The history, astonishing versatility, and multiplicity of applications of the CO_2 laser system are most appropriately summarized in Patel's seminal paper entitled "Carbon Dioxide Laser, Journey from Milliwatts to Megawatts," which marked the 25th anniversary of the discovery of laser action on the vibrational-rotational transitions of a molecule [5]. By that time in 1989, Patel found more than 10,000 papers on the science, technology, and applications of CO_2 or other molecular vibrational-rotational transition lasers, in addition to several books on

*Dedicated to Ruth and Louis D. Smullin.

Tunable Lasers Handbook
Copyright © 1995 by Academic Press, Inc. All rights of reproduction in any form reserved.

those subjects. Insofar as CO_2 laser applications are concerned, Patel grouped them into ten categories listed [5] as follows:

1. Science
   High-resolution spectroscopy
   Saturation spectroscopy
   Two-photon spectroscopy
   Nonlinear optics
   Raman scattering and Raman lasers
2. Pollution detection
3. Industrial applications (materials fabrication)
   Vaporizing: cutting, drilling, material removal, etching, scribing, trimming, etc.
   Melting: welding, cladding, alloying, etc.
   Submelting: annealing, hardening, and other phase changes
4. Communications
5. Pumps for tunable lasers and for X-ray, IR, and far-IR lasers
6. Laser-induced fusion
7. Isotope separation
8. Medicine and surgery
9. Metrology, remote sensing, and radar
10. Military

The CO_2 lasers that were developed for these applications range in size from a few cubic centimeters that can easily be held in one hand, to many cubic meters that weigh several tons and occupy an entire building. The lasing time durations may range from less than 10^{-12} sec to cw, with peak and average power levels greatly exceeding a terawatt and megawatt, respectively. The laser excitation schemes used in the past include conventional dc or rf discharges, high-energy electron beams, X rays, gas dynamic, and nuclear pumping. The pressures at which CO_2 laser gas mixtures were operated range from less than 1 Torr to nearly 100 atm.

Within the scope of a single book chapter the amount of material that can be discussed must be severely limited. Accordingly, only those aspects of CO_2 laser physics and engineering will be covered here that are most appropriate for a book on tunable lasers.

We should mention at this time that very little emphasis will be given to continuously tunable CO_2 lasers, because such lasers are generally very complex, expensive, and difficult to build and maintain. Continuously tunable CO_2 lasers operate at very high pressures (8 to 15 atm typical), and must have very complex optical cavities in order to provide continuous tunability. Almost invariably they have short output pulses ($<10^{-7}$ sec) leading to poor spectral purity. Although high-pressure continuously tunable CO_2 lasers have been built in the past [6–15] and are certainly feasible to construct, to the best of my knowledge such lasers are not commercially available at the present time.

Relatively low-power (1 to 25 W), easy-to-construct CO_2 lasers that are also commercially readily available do, however, play an important role in tunable laser spectroscopy because of the following characteristics. CO_2 isotope lasers can oscillate in a very large number of vibrational-rotational transitions. These lasing transitions have inherently high spectral purity and may be line-center stabilized with a long-term stability comparable to commercial cesium atomic clocks. Approximately 1500 of the CO_2 lasing transition frequencies have been determined thus far, and many more may be measured if necessary. The accuracies of the published frequencies are within a few kilohertz relative to the primary Cesium frequency standard. Thus CO_2 isotope lasers can be very conveniently used as secondary frequency standards in the 8.9- to 12.4-μm wavelength region. One can also utilize difference frequencies [16] and harmonics [17] of CO_2 lasing transitions to synthesize precisely known reference lines well beyond the 8.9- to 12.4-μm range. Because of the large number of lasing transitions measured to date, the average spacing between adjacent lines is only about 3 to 6 GHz, which may well be within the tuning range of moderate-pressure (waveguide) CO_2 lasers, optical frequency shifters, and lead-salt tunable diode lasers.

The intention of this chapter is to give an overview of only those aspects of CO_2 laser physics and engineering that most intimately relate to tunable laser spectroscopy. For all other areas of CO_2 laser physics, engineering, and applications, the reader is referred to the vast array of publications that appeared (and continue to appear) in textbooks [18,19], books and book chapters [20–22], SPIE proceedings [23–28], numerous other scientific publications [29,30], and conference proceedings, just to name a few.

We should emphasize, however, that many of the most important aspects of CO_2 laser physics described in the beginning of this chapter are excerpted from the seminal papers of C. K. N. Patel [1,2,4,5]. On the other hand, virtually all of the experimental results and calculations presented in the latter part of the chapter originate from years of painstaking research performed at MIT's Lincoln Laboratory, the Time and Frequency Division of the National Institute of Standards and Technology [NIST previously called the National Bureau of Standards (NBS)] in Boulder, Colorado, and the National Research Council (NRC) in Ottawa, Canada. Those individuals whose collaboration I had the privilege to receive over the years are acknowledged at the end of this chapter.

2. VIBRATIONAL ENERGY-LEVEL STRUCTURE OF THE CO_2 MOLECULE

The CO_2 molecule is linear and symmetric in configuration and has three degrees of vibrational freedom as illustrated in Fig. 1. In the symmetric stretch mode, denoted by ν_1, the atoms of the molecule vibrate along the internuclear axis in a symmetric manner. In the bending mode, denoted by ν_2, the atoms also vibrate symmetrically but in planes perpendicular to the internuclear axis. In the

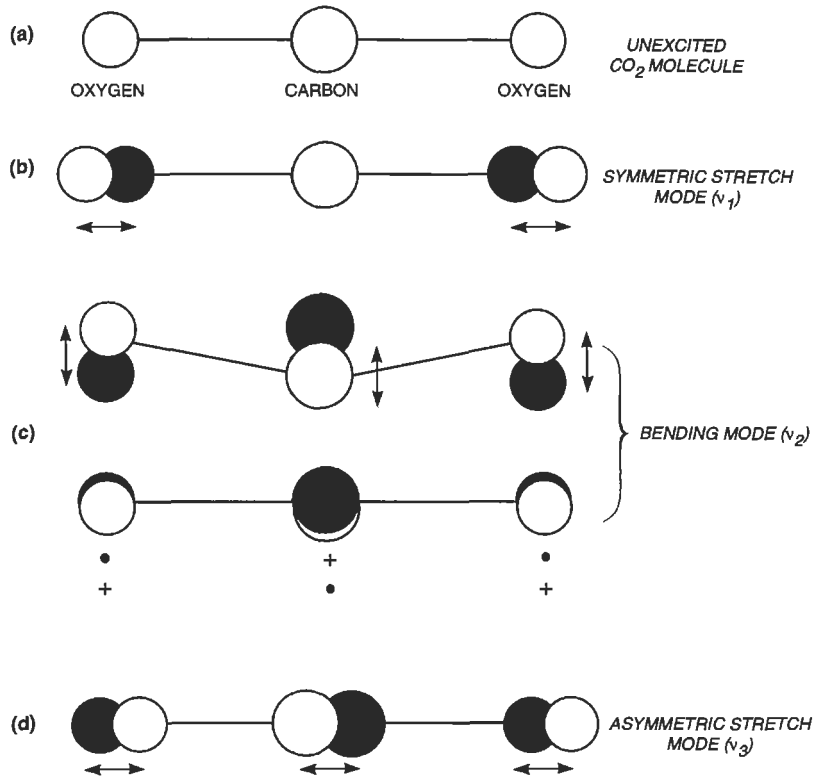

FIGURE 1 The three normal modes of vibration of a linear symmetric CO_2 molecule. (a) Unexcited CO_2. (b) Symmetric stretch mode. (c) Bending mode (doubly degenerate). (d) Asymmetric stretch mode. (After C. K. N. Patel.)

asymmetric stretch mode, denoted by ν_3, the atoms vibrate asymmetrically along the internuclear axis. In the ν_1 mode, the carbon atom remains stationary during the vibrational motion, whereas in the ν_2 and ν_3 modes it is the distance between the oxygen atoms that remains the same. Note the degeneracy in the ν_2 mode since the atoms can vibrate in two mutually perpendicular planes of excitation. This double degeneracy is indicated [31] by l, where $l_i = \upsilon_i, \upsilon_i - 2, \upsilon_i - 4, \ldots, 1$ or 0, depending on whether υ_i is odd or even, where υ_i denotes the number of vibrational quanta in the ν_i vibrational mode. The rules of quantum mechanics require that the energies of all the vibrational modes be quantized and different. The excited CO_2 molecule can have any linear combination of the three individual modes of vibration ν_1, ν_2, and ν_3. Therefore, the vibrational state of the CO_2 molecule must be described by the corresponding three quantum numbers υ_1, υ_2^l υ_3. Thus a particular vibrational energy level will be denoted by $(\upsilon_1\ \upsilon_2^l\ \upsilon_3)$, and the total vibrational energy of the CO_2 molecule is given by

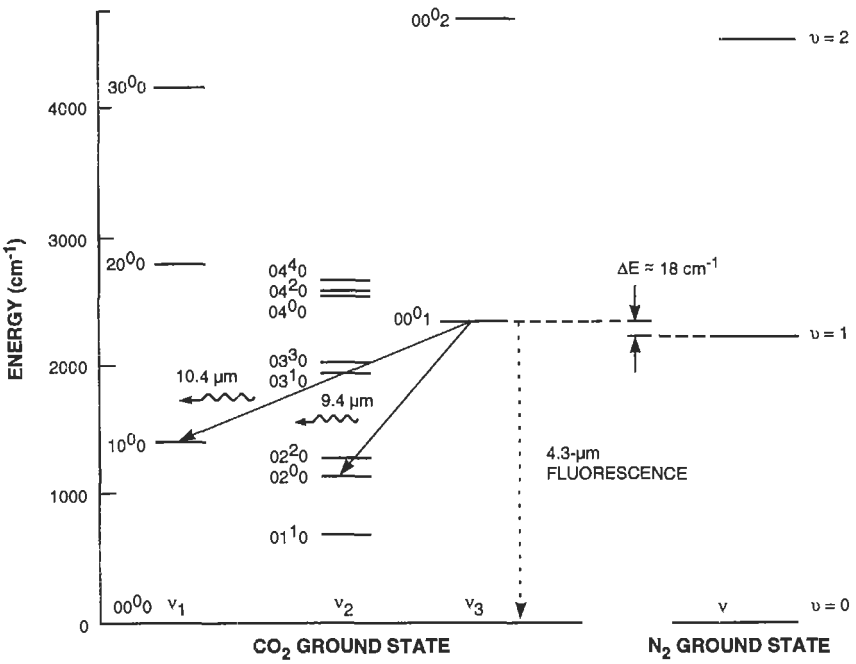

FIGURE 2 Some of the low-lying vibrational levels of CO_2 and N_2. (After C. K. N. Patel.)

$$E_\upsilon = hc\left[\nu_1\left(\upsilon_1 + \frac{1}{2}\right) + \nu_2\left(\upsilon_2 + \frac{1}{2}\right) + \nu_3\left(\upsilon_3 + \frac{1}{2}\right)\right], \tag{1}$$

where ν_1, ν_2, and ν_3 are the frequencies (in inverse centimeters) of the symmetric stretch, bending, and asymmetric stretch modes; the υ_i are the integers 0, 1, 2, 3, ... , and h and c denote Planck's constant and the velocity of light, respectively.

A simplified energy-level diagram of some of the low-lying vibrational states of the ν_1, ν_2, and ν_3 modes of the CO_2 molecule is shown in Fig. 2. The lowest vibrational states of the N_2 molecule are also shown on the right side of Fig. 2, because they play very important roles in the selective excitation of the CO_2 molecules to the upper laser levels. Because N_2 is a diatomic molecule it has only one degree of vibrational freedom; hence one vibrational quantum number (υ) completely describes its vibrational energy levels. Note that the rotational substructures of each of the vibrational levels are not shown in Fig. 2. The rotational levels are spaced much closer than the vibrational states and are discussed in the next section of this chapter. Figure 2 clearly indicates that the various vibrational levels, with different quanta in the ν_1, ν_2, and ν_3 modes of CO_2 and the ν mode of N_2, form almost equally spaced ladders.

The most readily obtainable and widely utilized lasing transitions in CO_2 lasers are the so-called regular band transitions. These occur between the (00^01) upper laser level and the (10^00) and (02^00) lower laser levels as indicated by the solid-line arrows interconnecting those levels in Fig. 2. The (10^00) and (02^00) levels have nearly the same energy in spite of belonging to different vibrational modes, and are "accidentally degenerate" [31]. As was first recognized by Fermi [32] in the case of CO_2, such "Fermi resonance" leads to a perturbation of the energy levels. Thus for CO_2 one of the two previously mentioned energy levels is shifted up and the other down so that the separation of the two levels is much greater than expected, and a mixing of the eigenfunctions of the two states occurs. Thus the correct regular band transition assignments are denoted by $[00^01—(10^00, 02^00)_I]$ for the 10.4-μm band and by $[00^01—(10^00, 02^00)_{II}]$ for the 9.4-μm band, respectively. This follows Amat's notation [33] in which the components of a Fermi multiplet are labeled with Roman subscripts in order of decreasing energy. It has been determined [33–35] relatively recently that the $[10^00, 02^00]_I$ level is to be identified with the unperturbed (02^00) level in $^{12}C^{16}O_2$, $^{12}C^{18}O_2$, and $^{13}C^{18}O_2$, and with the unperturbed (10^00) level in $^{13}C^{16}O_2$. Note that this identification is the reverse of the traditional notation for $^{12}C^{16}O_2$ in many older publications (including the pioneering ones by Patel). Fermi resonances similar to the one observed for the (10^00) and (02^00) vibrational levels also exist between certain higher levels and will be similarly designated in other lasing transitions of the CO_2 system in later portions of this chapter.

Two additional aspects of the CO_2 laser system should be emphasized in the energy-level diagram of Fig. 2. The first of these relates to the 4.3-μm fluorescence, indicated by a dotted arrow, that emanates from the (00^01) upper laser level of the regular band into the (00^00) ground state due to spontaneous emission. This spontaneous emission at 4.3 μm plays a most important role in the long-term line-center stabilization of the lasing transitions that constitute a salient portion of this chapter.

Finally, attention is drawn to the very small energy difference ($\Delta E \approx 18\,\text{cm}^{-1}$) that exists between the (00^01) upper laser level of $^{12}C^{16}O_2$ and the ($\upsilon = 1$) level of $^{14}N_2$. Nitrogen molecules can be very efficiently excited from the ($\upsilon = 0$) level to the ($\upsilon = 1$) level by electron impact in a low-pressure discharge. Because the energy of excitation of the N_2 ($\upsilon = 1$) molecule nearly equals the energy of excitation of the CO_2 (00^01) molecule, an efficient transfer of vibrational energy takes place from N_2 to CO_2 in collisions between N_2 ($\upsilon = 1$) molecules and CO_2 (00^00) molecules. In such a collision, the nitrogen molecule returns from the ($\upsilon = 1$) level to its ground state by losing one quantum of its vibrational energy, thereby exciting the carbon dioxide molecule from its ground state to the (00^01) level. The CO_2 can then radiatively decay to either the $[10^00, 02^00]_I$ or $[10^00, 02^00]_{II}$ levels, and emit infrared light at 10.4 or 9.4 μm, respectively, during this process [1,2,4,5].

In an analogous fashion, consideration should be given to the energy-level differences that exist between the (00^01) upper levels of rare isotopes of CO_2 and the $(\upsilon = 1)$ levels of rare isotopic N_2 in order to optimize lasing efficiency (e.g., $^{13}C^{16}O_2$ and $^{15}N_2$).

3. ROTATIONAL ENERGY-LEVEL SUBSTRUCTURE OF THE CO_2 MOLECULE

In the CO_2 laser system eigenstates of the molecule are characterized by the rotational quantum number J in addition to the vibrational quantum numbers υ_1, υ_2, and υ_3. Lasing transitions actually occur between rotational levels that belong to two different vibrational modes, as illustrated in Fig. 3, which shows the detailed vibrational-rotational energy-level structure of the CO_2 molecule that is characteristic of the laser transitions in the (00^01)—$[10^00, 02^00]_{I,II}$ regular bands. Laser oscillations occur between two rotational levels belonging to the two different vibrational modes. The center of the band corresponds to the spacing between the vibrational levels in the absence of any rotational energy ($J = 0$). The rotational energies of a given vibrational state, ν_i, relative to the $J = 0$ level are [31,36–38]

$$E_{\upsilon,J} = hc\left\{B_\upsilon J(J+1) - D_\upsilon\left[J(J+1)\right]^2 + H_\upsilon\left[J(J+1)\right]^3 + L_\upsilon\left[J(J+1)\right]^4 \ldots\right\}, \quad (2)$$

where B_υ is the rotational constant of the i'th vibrational state, and D_υ, H_υ, L_υ, etc., are spectroscopic constants of the molecule, which are very small compared to B_υ.

Quantum-mechanical selection rules allow only those transitions between vibrational-rotational levels of the regular band for which the change in the rotational quantum number J corresponds to $\Delta J = \pm 1$. Transitions from (J) to $(J+1)$ are called $P(J)$ lines, whereas those from (J) to $(J-1)$ are named $R(J)$ lines. According to spectroscopic custom, the rotational part of the transitions is designated by the rotational quantum number J that is characterizing the lower level of a lasing transition. This form of designation is illustrated in Fig. 3, which explicitly shows the $P(20)$ and $R(20)$ lasing transitions of the P and R branches in the (00^01)—$[10^00, 02^00]_I$ and (00^01)—$[10^00, 02^00]_{II}$ regular bands centered about the 10.4- and 9.4-μm wavelengths, respectively. Frequently, abbreviated forms of laser line designations, such as I-$P(20)$, $P_I(20)$ or $10P(20)$ are also used. In view of the more recently discovered hot bands, sequence bands, and sequence hot bands (which are described in a later section of this chapter), abbreviated forms of line designations should only be used when no ambiguities exist about the vibrational band affiliations. As indicated in Fig. 3, the spacings between rotational levels gradually increase toward the higher

rotational quantum numbers J, even though adjacent levels seem almost equally spaced in each of the vibrational modes. Correspondingly, the frequency differences between adjacent lines in the P and R branches of the regular band $^{12}C^{16}O_2$ laser transitions will vary from less than 1 cm^{-1} (~30 GHz) for high J number R lines to somewhat more than 2 cm^{-1} (~60 GHz) for high J number P lines.

Further restrictions on allowed CO_2 lasing transitions are imposed by the nuclear spin properties of the various oxygen isotopes. The spins in both ^{16}O and ^{18}O are zero, and symmetry considerations therefore preclude the existence of the antisymmetric odd transitions in the regular bands of $^{12}C^{16}O_2$, $^{13}C^{16}O_2$, $^{14}C^{16}O_2$, $^{12}C^{18}O_2$, $^{13}C^{18}O_2$, and $^{14}C^{18}O_2$. However, in the mixed CO_2 isotopes where the two oxygen atoms are dissimilar isotopes, or when the nuclear spin is finite (e.g., ^{17}O), all rotational lasing transitions are allowed. We should emphasize, however, that different selection rules may apply for the other bands, such as sequence and hot bands for example, that also can provide oscillating transitions in the CO_2 laser system.

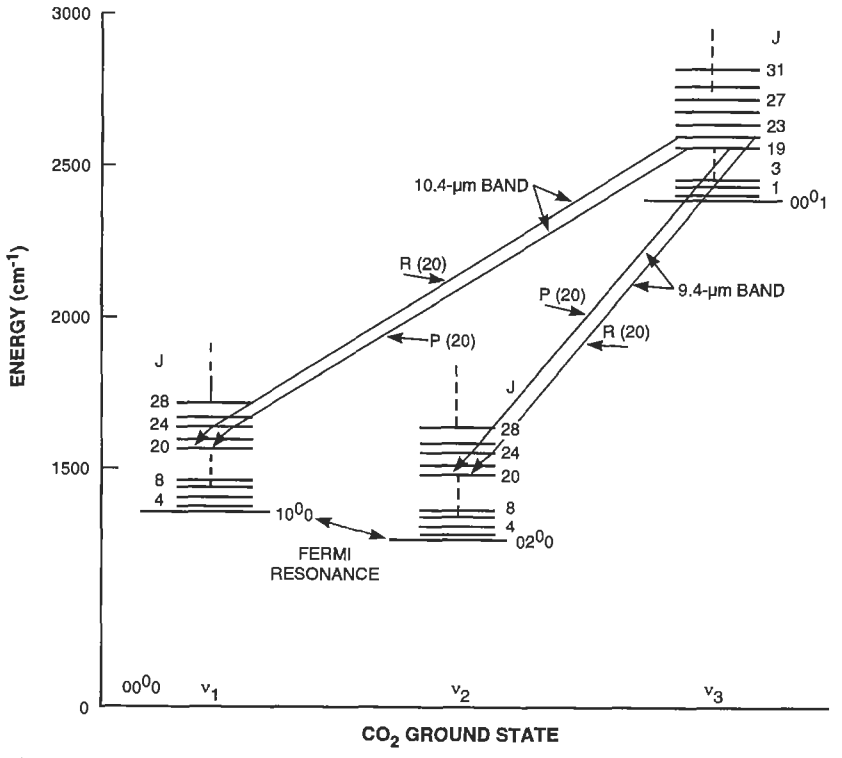

FIGURE 3 Detailed vibrational-rotational energy level diagram for the (00^01)—$[10^00, 02^00]_{I,II}$ regular band laser transitions. (After C. K. N. Patel.)

4. PROCESSES GOVERNING THE EXCITATION OF REGULAR BAND LASER TRANSITIONS IN CO_2

The most basic configuration of a CO_2 laser consists of an amplifying gain section within an optical cavity. In its simplest form the optical cavity consists of two mirrors; however, a diffraction grating is often substituted for one of the mirrors in order to provide frequency dispersion and easily controllable line selectivity among the many lasing transitions that could otherwise oscillate. The gain medium is a gas discharge, which uses a (typical) mixture of CO_2, N_2, He, Xe, and a small amount of H_2 or H_2O vapor in the sealed-off CO_2 isotope lasers that are most useful in laser spectroscopy. The dominant processes that govern the regular band CO_2 laser transitions are depicted in Fig. 4. Gain will occur due to either complete or partial inversion of the vibrational population densities of the (00^01) upper laser level over the (10^00) or (02^00) lower laser levels [1,2,4,5].

Up to 50% of all N_2 molecules may become vibrationally excited in the gas discharge and transfer most of their vibrational energy to the CO_2 molecules by exciting the vibrational levels of the ν_3 mode, primarily the (00^01) level of $^{12}C^{16}O_2$, which is only about $\Delta E \approx 18$ cm^{-1} higher than the $(\upsilon = 1)$ level of $^{14}N_2$. This 18-cm^{-1} energy difference is much smaller than the average kinetic energy

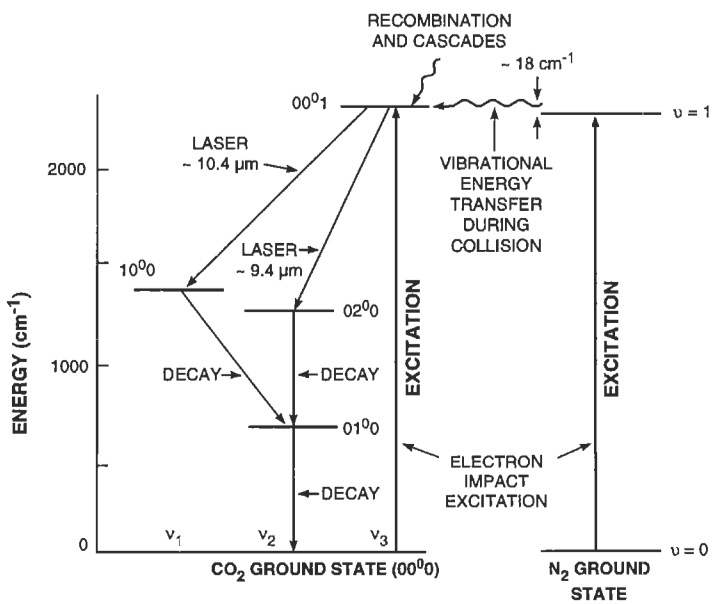

FIGURE 4 The vibrational energy levels most relevant to the regular band CO_2 laser transitions. (After C. K. N. Patel.)

so that during these near-resonant collisions the excited N_2 molecules can readily transfer their vibrational energy to the CO_2 molecules and excite the vibrational levels of the ν_3 mode in CO_2.

Excitation of CO_2 molecules to the upper laser levels may also occur by means of electron impact excitation from the ground state, from recombinations, or from cascades from levels above the (00^01) upper laser level. We already mentioned in Section 2 and also illustrated in Fig. 2 that the levels in the ν_3 mode form an almost equally spaced ladder so that during a collision an excited CO_2 $(00^0\upsilon_3)$ molecule can lose one quantum of ν_3 vibrational energy and become a CO_2 $(00^0\upsilon_3-1)$ molecule, while the CO_2 (00^00) molecule in the ground state gains that quantum of energy and becomes an excited CO_2 (00^01) molecule in the upper laser level [1,2,4,5]. As Patel was the first to point out, this type of process is resonant in the sense that there is a redistribution of the energy of the excited molecule without any loss of the total internal energy by its conversion into kinetic, or thermal, energy [1,2,4,5]. Similarly, resonant redistribution of energy can also occur in the vibrational ladder of the excited N_2 molecules. Thus the excitation of the CO_2 molecules to the required upper laser level may be very efficiently accomplished by electron impact in the gas discharge of a CO_2 laser. Note that CO plays a role similar to N_2 in the gas discharge. CO may be present in the gas discharge as a result of dissociation of CO_2, or it may be initially added to the laser gas fill in order to reduce the deleterious buildup of O_2 that also occurs due to dissociation of CO_2 in the laser gas discharge.

During laser operation the excited CO_2 molecules in the (00^01) upper laser level will go to the $[10^00, 02^00]_I$ and $[10^00, 02^00]_{II}$ lower laser levels while emitting photons in the lasing transitions belonging to the 10.4- and 9.4-μm regular bands of CO_2, respectively. The molecules in the lower laser levels are then deexcited through collisions with other molecules. The possibility of resonant vibrational energy transfer again plays an important role in vacating the $[00^01, 02^00]_{I,II}$ lower laser levels, because molecules in these levels have nearly twice the energy required to excite a CO_2 molecule in the (00^00) ground state to the (01^00) vibrational level. Thus a collision involving a molecule in one of the $[10^00, 02^00]$ lower laser levels with a molecule in the (00^00) ground state will efficiently redistribute the vibrational energy between the two molecules by exciting both of them to the CO_2 (01^00) level. Because of the resonant nature of this collision, the vibrational deexcitation of the lower laser level can be also very efficient.

Finally, however, the CO_2 molecules in the (01^00) level still must be deexcited to the (00^00) ground state before they can be reutilized in the laser gas mixture. This deexcitation of CO_2 molecules in the (01^00) level is governed by collisions with other CO_2, or other gas particles, or the walls of the laser tube. Because of the nonresonant nature of this vibrational energy conversion into kinetic energy, the deexcitation of the CO_2 molecules in the (01^00) level can be relatively slow and cause a "bottleneck" in the overall cycle of excitation and

deexcitation processes in CO_2 lasers [1,2,4,5]. By 1965, however, Patel *et al.* had demonstrated that the addition of He to the CO_2–N_2 gas fill can be very effective in the deexcitation of the (01^00) level [39] and it became clear that "the CO_2 laser was," in Patel's words, "a quintessential collision laser in which all the excitation and de-excitation mechanisms depended crucially on collisions."

The addition of He into the CO_2 laser gas mixture is also very effective in the cooling of the discharge gas because the thermal conductivity of He is significantly higher than that of CO_2 or N_2. The resulting increase of heat transfer to the cooled wall of the discharge tube enables laser operation at higher excitation current, which leads to greater power output. Helium typically constitutes at least 50% of a CO_2 laser's gas fill.

During the initial three years of CO_2 laser development, all lasers utilizing He–N_2–CO_2 gas mixtures had to be open, continuous-flow systems, in order to replenish the CO_2 that rapidly dissociated in the gas discharge.

Sealed-off CO_2 laser operation was first reported in 1967 by Witteman [40] in Holland and by Carbone [41] at MIT Lincoln Laboratory. Witteman used platinum electrodes and the admixture of a small amount (~0.15 Torr) of H_2O vapor or H_2 as catalysts, whereas Carbone utilized oxidized Ni cathodes. Both of them reported sealed-off operating lifetimes exceeding 1000 hours.

Shortly thereafter, significant reductions in the CO_2 dissociation rate and simultaneous enhancement of the efficiency and/or power output of sealed-off CO_2 lasers by Xe gas additive was reported by Paanannen [42] at Raytheon Research Laboratory and by Clark and Wada [43] at Hughes Research Laboratory. Wieder and McCurdy [44] were the first to obtain laser operation with a rare CO_2 isotope in 1966.

The addition of Xe has a significant influence on the gas discharge. Xenon changes the electron energy distribution by increasing the number of electrons with lower energy and decreasing the number of those with higher energy. This change in electron energy distribution has a favorable effect on the vibrational excitation of CO_2 and N_2 and also reduces the dissociation rate of CO_2. Also, the ionization potential of Xe is several electron-volts less than that of the other gas constituents. The low ionization potential facilitates the production of electrons for maintaining the discharge with a lower longitudinal electric field while maintaining the same excitation current through the discharge. This, in turn, leads to either an increase in laser efficiency or an increase in output power or a combination of both.

During the last 10 to 15 years the steadily increasing interest in the use of very long-life sealed-off CO_2 lasers for remote and satellite-borne applications and in large systems [45] using rare (and expensive) CO_2 isotopes of limited availability, greatly spurred the research and development of both homogeneous and heterogeneous catalysts to be used in long-life CO_2 lasers. Valuable additional information may be found in the proceedings of several topical conferences that were held on this subject during the last decade [45–47].

5. ADDITIONAL CHARACTERISTICS OF REGULAR BAND CO_2 LASER TRANSITIONS

We can define the molecular quantum efficiency of an emitted laser photon in the regular band as

$$\eta_{mol} = \frac{E\left(00^01\right) - E\left[10^00, 02^00,\right]_{I \text{ or } II}}{E\left(00^01\right)} . \tag{3}$$

It becomes clear from Eq. (3) and the energy-level diagram of Fig. 4 that theoretical quantum efficiencies of about 45 and 40% are possible for the 9.4- and 10.4-μm laser transitions, respectively, in the regular band of CO_2. The "wallplug" efficiencies of CO_2 lasers is lower, of course, as a result of inevitable losses during excitation. However, actual efficiencies as high as 30% have been achieved due to the remarkably efficient collisional excitation and deexcitation processes, as summarized in the previous section of this chapter.

Another, spectroscopically highly useful characteristic of cw CO_2 lasers is the fact that the entire output power corresponding to the total inversion between two vibrational levels may be extracted in a single $P(J)$ or $R(J)$ transition. An explanation of this characteristic may be found from examination of the vibrational-rotational lifetimes of the excited molecules in the various energy levels.

The vibrational level radiative lifetime τ_{vib} of an excited molecule in the (00^01) upper laser level is ~3 sec. Its actual lifetime is determined by collisions with other molecules and, therefore, is pressure dependent. At typical operating pressures characteristic to relatively small cw CO_2 lasers the vibrational-level lifetime, including radiative and collisional relaxation, is about $\tau_{vib} \sim 10^{-3}$ sec. The energy spacing between the relevant vibrational levels is much greater than the kinetic energy of the molecules, which is about 0.025 eV at room temperature. Thus the vibrational thermalization rate is very small, about 10^3 sec^{-1}. The spacings of the rotational levels, on the other hand are smaller than the kinetic energy of the molecules and the rotational lifetime is only about 10^{-7} sec. Thus a molecule can experience a very large number of thermalizing rotational collisions during its lifetime in a given vibrational level. This results in a Boltzmann distribution of the molecules among the various rotational levels of a vibrational state. Figure 5 illustrates the Boltzmann distribution of population densities, N_J, as a function of the rotational quantum number J for two rotational temperatures, $T_{rot} = 400$ K (solid lines) and 1000 K (dashed line), respectively.

The existence of a Boltzmann distribution requires that a change of population density in one rotational level be accompanied by appropriate changes in the population densities of all other rotational levels of the vibrational state in order to maintain the Boltzmann distribution. Hence, once a laser transition starts oscillating and begins to deplete the population of the affected rotational level in

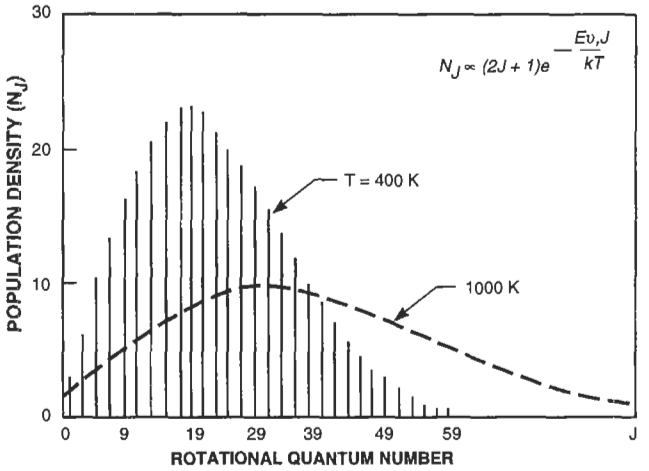

FIGURE 5 Boltzmann distribution of population densities as a function of the rotational quantum number J, for T_{rot} = 400 and 1000 K, respectively. (After C. K. N. Patel.)

the (00^01) upper laser level, the requirement to maintain the Boltzmann distribution will result in a transfer of excited molecules from all other rotational levels into the rotational level that directly contributes to the lasing transition. This cross-relaxation among all the rotational levels in the inverted population of the (00^01) upper vibrational level results in very strong competition among the possible laser transitions, and once a transition (usually the one with the highest gain) starts oscillating it will draw on all available inverted population in the upper laser level so that other transitions will not have sufficient gain to oscillate. This phenomenon also explains the high saturation intensity of CO_2 lasers, and the fact that the entire available power may be extracted in a single regular band transition of a well-designed cw CO_2 laser.

The gain itself varies approximately in accordance with the Boltzmann distribution of the upper laser level population, as given by

$$N_{00^01}(J) \propto (2J+1)\exp\left(-\frac{E_{00^01,J}}{k_rT_{rot}}\right) . \tag{4}$$

The theoretical derivation and experimental verification of the gain in regular band CO_2 laser transitions was first accomplished by Patel [1,2,4,5]. By computer matching the theory to experimental data, Patel found [1,2] a good match at a rotational temperature T_{rot} of about 400 K. By differentiating Eq. (4) and setting $d\,N_{00^01}(J)/dJ = 0$, we get

$$J_{max} \approx \left(\frac{kT_{rot}}{2hcB}\right)^{1/2} - \frac{1}{2} , \tag{5}$$

where B is the principal rotational constant given in Eq. (2). At $t_{rot} = 400$ K, $J_{max} = 19$. This is the primary explanation of why the (00^01)—$[10^00, 02^00]_I$ $P(20)$ transition dominates in a $^{12}C^{16}O_2$ laser. It also explains that in a long CO_2 laser with a simple two-mirror cavity only the I-$P(20)$ transition will oscillate. As an example, a CO_2 laser with an optical cavity mirror spacing of $L = 3$ m, will have longitudinal cavity modes [18,19] spaced every $c/2L = (3 \times 10^8)/6 = 50$ MHz apart. This mode spacing is less (as explained in the next section) than even the Doppler-broadened gain profile of about 60 MHz, so that there always will be a cavity mode under the gain profile no matter how far a cavity mirror is tuned. Hence, a frequency-dispersive optical cavity element, such as a diffraction grating for instance, should always be used when low-gain transitions are to be obtained.

6. LINESHAPE FUNCTIONS AND BROADENING DUE TO GAS PRESSURE AND DOPPLER SHIFT IN CO_2 GAS

The phenomena of laser emission and saturable absorption are both the result of an electromagnetic wave interacting with an atomic or molecular medium. This interaction occurs over a finite frequency bandwidth.

Spontaneous emission occurs without the inducement of a radiation field because there is a finite probability that an atom (molecule in the case of CO_2) in level 2 of a system of energy levels E_i will spontaneously undergo a transition to level 1, emitting in the process a photon of energy $h\nu = E_2 - E_1$. It can be shown [18,19] from basic quantum-mechanical considerations and verified experimentally that both the emission and the absorption of radiation are described by the same lineshape function $g(\nu)$ that gives the distribution of emitted (or absorbed) intensity as a function of frequency ν. The lineshape function is usually normalized so that

$$\int_{-\infty}^{+\infty} g(\nu)\, d\nu = 1 \,. \tag{6}$$

One of the possible causes for the frequency spread of spontaneous emission is the finite lifetime τ_i of the emitting level. In the case of atomic or molecular transitions between an upper level (u) and a lower level (l), the coherent interaction of an atom or molecule in either level (u or l) with the electromagnetic field can be interrupted by the finite lifetime of the level (τ_u or τ_l) or by an elastic collision, which erases any phase memory (τ_{cu} or τ_{cl}). In this case, a normalized lineshape function with a Lorentzian profile is obtained:

$$g(\nu) = \frac{\Delta\nu_L}{2\pi\left[(\nu - \nu_0)^2 + (\Delta\nu_L / 2)^2\right]} \,, \tag{7}$$

where $\Delta\nu_L$ denotes the separation between the two frequencies at which the Lorentzian is down to half of its peak value, usually referred to as the FWHM (full width at half-maximum) linewidth,

$$\Delta\nu_L = 1/\pi\left(\tau_u^{-1} + \tau_l^{-1} + \tau_{cu}^{-1} + \tau_{cl}^{-1}\right) . \tag{8}$$

The type of broadening described by Eq. (7) is called *homogeneous broadening* because it describes the response of any of the atoms or molecules, which are thus indistinguishable from each other.

As mentioned before, homogeneous broadening is often due to the finite interaction lifetime of the emitting or absorbing atoms or molecules. In the CO_2 system the dominant source of homogeneous broadening is gas pressure. At sufficiently high densities, the collisions between the molecules become frequent enough to dominate the broadening mechanism by shortening the lifetime termination and phase interruption processes.

The pressure-broadening coefficient in pure CO_2 is approximately 7.5 MHz/Torr [48]. Thus, the absorption linewidth in a gas reference cell (to be used for long-term frequency stabilization of CO_2 lasers) filled with 40 mTorr (typical pressure) of pure CO_2 is approximately 200 kHz due to self-broadening.

In CO_2 lasers the usual gas fills also include He, N_2, CO, and Xe. The broadening coefficients due to these four collision partners are approximately 5.4, 7.4, 6.5, and 6.7 MHz/Torr [20,49,50], respectively. Because most CO_2 lasers contain helium-rich gas mixtures, 6 MHz/Torr (4.6 GHz/atm) is a reasonably good assumption for the pressure-broadening coefficient for typical CO_2 laser mixtures. In high-pressure CO_2 lasers, the continuous-tuning range of output frequency is determined by the homogeneous pressure broadening of the gain profile since the responses of the excited molecules are indistinguishable from each other.

During the discussion of the rotational energy level substructure in Sec. 3 of this chapter, we stated that the frequency spacings between adjacent lasing transitions of the regular band $^{12}C^{16}O_2$ lines vary from about 30 GHz to somewhat more than 60 GHz. Hence, assuming about 4.6 GHz/atm pressure broadening of the gain profile, an overall pressure of about 15 atm is required to obtain continuous tunability with a CO_2 laser using a single isotope of CO_2. By using several isotopic species of CO_2, continuous tunability can be achieved, of course, at a lower laser gas fill pressure. Indeed such designs have been proposed and experimented with in the past [51–54]. However, the construction of a reliably operating and useful, continuously tunable multiple isotope CO_2 laser that is still above atmospheric pressure is far from trivial, and (to the best of my knowledge) is not commercially available.

There are also physical situations in which the individual atoms or molecules are distinguishable, each having a slightly different transition frequency ν.

The spectral distribution of the spontaneous emission observed in such situations is due to the spread in the individual transition frequencies, and the resulting broadening is called *inhomogeneous* [18,19].

In the CO_2 system, inhomogeneous broadening occurs when the transition frequency ν of the gaseous CO_2 is Doppler-shifted due to the finite thermal velocity of the molecules according to:

$$\nu = \nu_0 + \frac{v_x}{c}\,\nu_0 \ , \tag{9}$$

where ν_0 is the frequency of the stationary molecule and v_x is the component of the velocity (vector) along the direction connecting the observer with the moving molecule. The Maxwellian velocity distribution function of a gas with atomic mass M at equilibrium at temperature T is given by

$$f\left(v_x, v_y, v_z\right) = \left[\frac{M}{\left(2\pi kT\right)}\right]^{3/2} \exp\left[-\frac{M}{\left(2kT\right)}\left(v_x^2 + v_y^2 + v_z^2\right)\right], \tag{10}$$

where k is the Boltzmann constant and $f(v_x, v_y, v_z)\, dv_x\, dv_y\, dv_z$ corresponds to the fraction of all the molecules whose x, y, and z components of velocity are contained in the velocity intervals v_x to $v_x + dv_x$, v_y to $v_y + dv_y$, and v_z to $v_z + dv_z$, respectively. One can show that this physical situation will give rise to the so-called normalized Doppler-broadened lineshape:

$$g(\nu)_D = \frac{c}{\nu_0}\left(\frac{M}{2\pi kT}\right)^{1/2} \exp\left[-\left(\frac{M}{2kT}\right)\left(\frac{c}{\nu_0}\right)^2\left(\nu - \nu_0\right)^2\right] . \tag{11}$$

The functional dependence of the line profile in Eq. (11) is referred to as Gaussian, with a FWHM Doppler linewidth given by:

$$\Delta\nu_D = 2\nu_0\left(\frac{2kT}{Mc^2}\,ln\,2\right)^{1/2} . \tag{12}$$

Equation (11) can be written in terms of $\Delta\nu_D$ as:

$$g(\nu)_D = \frac{2\left(ln\,2\right)^{1/2}}{\pi^{1/2}\Delta\nu_D} \exp\left[4\left(ln\,2\right)\left(\nu - \nu_0\right)^2/\Delta\nu_D^2\right] . \tag{13}$$

For the most commonly used (00^01)—$[10^00, 02^00]_I$ band $^{12}C^{16}O_2$ $P(20)$ transition (at a 10.6-μm wavelength) the Doppler linewidths calculated for $T = 300$ and 400 K result in $\Delta\nu_D = 53$ and 61 MHz, respectively. Thus, the frequency-tuning

range of CO_2 lasers becomes increasingly dominated by the Doppler-limited linewidth for laser gas fill pressures much below 10 Torr.

As a corollary, one can also deduce that gas lasers are generally tunable over a frequency range that is at least as wide as the Doppler-broadened lineshape. Since the invention of the laser, various techniques have been sought to defeat the limits imposed by Doppler broadening so that the inherently great spectral purity of lasers may be more fully utilized (e.g., in high-resolution spectroscopy). The various techniques of Doppler-free spectroscopy utilize the laser's inherently high intensity, spectral purity, and low divergence to produce some nonlinear effect that can discriminate against Doppler broadening. Saturation spectroscopy, two-photon spectroscopy, and laser-induced line-narrowing are the best known methods developed so far for overcoming Doppler broadening. The line-center stabilization of CO_2 lasers to be discussed in Sec. 8 of this chapter is based on the nonlinear saturation resonance that can be observed in low-pressure room-temperature CO_2 gas when the cell containing it is subjected to a strong standing-wave field of CO_2 laser radiation. However, prior to a more thorough discussion of the standing-wave saturation resonance [48], it is appropriate to briefly review the spectral purity and short-term stability of CO_2 lasers [55,56].

7. SPECTRAL PURITY AND SHORT-TERM STABILITY

The output waveform of a stable, single-frequency CO_2 laser far above the threshold of oscillation may be approximated by an almost perfect sine wave with nearly constant amplitude and frequency. For a laser operating in an ideal environment, the spectral purity is measured by a linewidth that is determined by frequency fluctuations caused by a random walk of the oscillation phase under the influence of spontaneous emission (quantum) noise. In their fundamental 1958 paper, Schawlow and Townes predicted [57] that the quantum-phase-noise-limited line profile will be a Lorentzian with a full width between the half-power points (FWHM), which may be approximated by:

$$\Delta\nu_{FWHM} \sim \frac{a\pi h\nu_0}{P_0}\left(\frac{\nu_0}{Q_c}\right)^2, \tag{14}$$

where a, h, ν_0, P_0, and Q_c denote the population inversion parameter, Planck's constant, the center frequency, power output, and "cold" cavity Q of the laser, respectively. In a well-designed small CO_2 laser the "cold" cavity Q is given by:

$$Q_c \sim \frac{2\pi L\nu_0}{ct_r}, \tag{15}$$

where L, c, and t_r denote the cavity length, velocity of light, and mirror transmission, respectively (diffraction losses are usually negligible compared to output

coupling loss). In a small CO_2 laser with $L = 50$ cm and $t_r = 5\%$, Q_c is of the order of 10^7; thus for a typical power output of 1 to 10 W (which is easily obtainable with a small TEM_{00q} mode CO_2 laser) the quantum-phase-noise-limited linewidth is less than 10^{-6} Hz. Note that 10^{-6} Hz represents less than 1 part in 10^{19} of the output frequency ($\nu_0 \sim 3 \times 10^{13}$ Hz) of a CO_2 laser. This inherent spectral purity of CO_2 lasers can be explained as follows: The linewidth $\Delta\nu$ is inversely proportional to the product of P_0 and Q_c^2, and the combination of high P_0 and high Q_c can be simultaneously achieved with relative ease even in a small CO_2 laser oscillator. Oscillators in the radio-frequency (rf) and microwave domain have either high P_0 or high Q_c but not both together in a single device.

Laser stabilities are most frequently measured in the laboratory from the results of heterodyne experiments with two lasers. Laser stabilities can be determined by either frequency-domain (Fourier spectrum) or time-domain (Allan variance) analysis of the beat-note spectra of the laser pairs. To establish the spectral purity we can heterodyne two CO_2 lasers of equal high quality so that the resulting beat-note spectrum can be apportioned equally to each laser. Two problems arise, however, in trying to measure the Schawlow–Townes linewidth of high-quality CO_2 lasers. The first of these problems is instrumental: The stability of the available instrumentation itself generally cannot reliably measure spectral purities of 10^{-6} Hz or better.

The origin of the second problem is that for well-designed CO_2 lasers [56] the so-called technical noise sources dominate over the quantum-phase-noise-limited Schawlow–Townes linewidth [57]. Examples of technical noise sources are acoustic and seismic vibrations, and power-supply ripple and noise. These sources can cause frequency instabilities by perturbing the effective cavity resonance via the sum of fractional changes in the refractive index n and the optical-cavity length L:

$$\Delta\nu = \nu\left(\frac{\Delta n}{n} + \frac{\Delta L}{L}\right) . \tag{16}$$

As an example, a change of only 10^{-3} Å (about 1/1000 of the diameter of a hydrogen atom) in a 50-cm-long CO_2 laser cavity will cause a frequency shift of approximately 6 Hz. A 6-Hz variation in the approximately 3×10^{13} Hz frequency of a CO_2 laser corresponds to a fractional instability of 2×10^{-13}.

Figure 6 shows the real-time power spectrum of the beat signal between two free-running lasers that were designed and built at Lincoln Laboratory [56]. The spectral width of Fig. 6 implies a frequency stability at least as good as 2×10^{-13}. The discrete modulation sidebands in the figure were primarily due to ac-power-line frequency harmonics, cooling fan noise, and slow frequency drift; however, each spectral line was generally within the 10-Hz resolution bandwidth of the spectrum analyzer. The measurement of the spectral width was limited to a 10-Hz resolution by the 0.1-sec observation time that was set by the instrumentation, not by the laser stability itself.

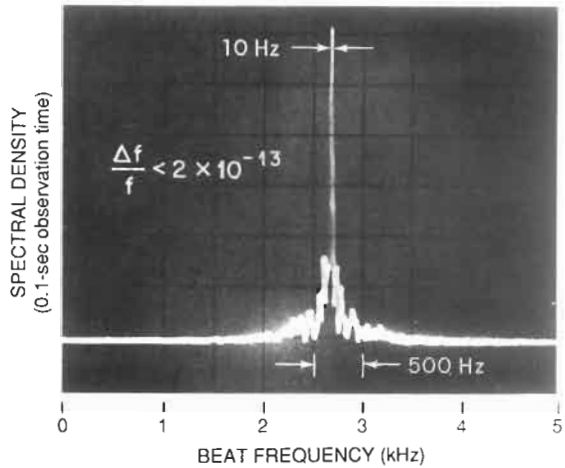

FIGURE 6 Real-time power spectrum of the beat signal between two free-running CO_2 lasers. The horizontal scale of the figure is 500 Hz/division, which indicates that the optical frequencies of the two lasers producing the beat note were offset by less than 3 kHz. The 10-Hz width of the line shown is limited by instrumentation; the linewidth of the beat note falls within this limit.

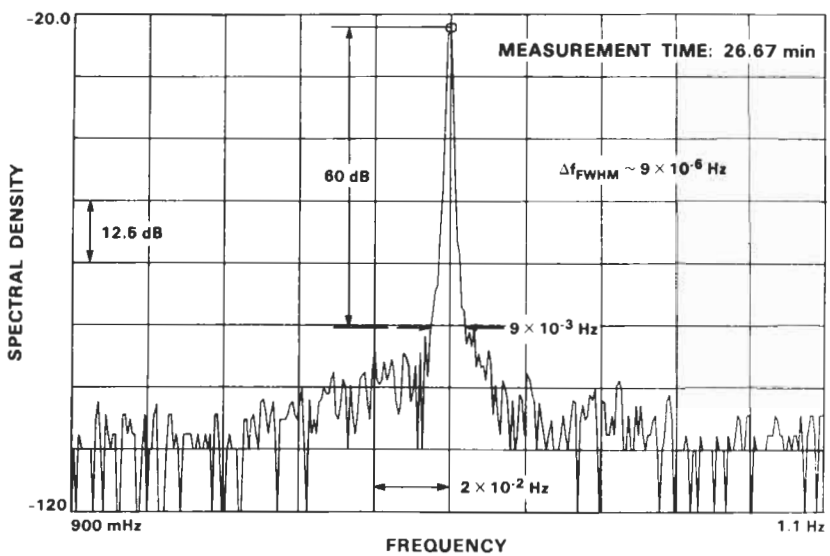

FIGURE 7 Spectral purity of beat note between two CO_2 lasers that were phase-locked to each other with a frequency offset of 10 MHz. The FWHM spectral width of the beat note was about 9×10^{-6} Hz during the 26.67-min measurement time.

Figure 7 shows the real-time power spectrum of the beat note of two ultra-stable CO_2 lasers that were phase-locked with a fixed 10-MHz frequency offset between the two lasers and with the unity-gain bandwidth of the servoamplifier

set to about 1.2 kHz [56]. Note that the horizontal scale in the figure is only 2×10^{-2} Hz/division and the vertical scale is logarithmic, with 12.5 dB/division. Using the results from Fig. 7 and the equation for a Lorentzian lineshape, we calculate the FWHM spectral width of the beat note to be about 9×10^{-6} Hz.

It took 26.67 min of measurement time to obtain just a single scan with the frequency resolution of Fig. 7. Because tracking even by a very good servosystem would still be limited by quantum phase noise, the narrow linewidth in Fig. 7 is an indirect but clear confirmation of the high spectral purity of CO_2 lasers, as predicted by the Schawlow–Townes formula.

The (so far at least) unsurpassed spectral purity and short-term stabilities measured in the frequency domain and illustrated in Figs. 6 and 7 were also confirmed by analyzing the signal returns from orbiting satellites that were obtained by a long-range CO_2 radar at the Firepond facility of MIT Lincoln Laboratory [56,58–62]. Additional confirmation was also obtained at MIT Lincoln Laboratory from extensive time-domain frequency stability measurements on pairs of ultrastable CO_2 lasers under free-running and phase-locked conditions, and both in acoustically quiet and in noisy environments [63].

8. LONG-TERM LINE-CENTER STABILIZATION OF CO_2 LASERS

CO_2 lasers can possess exceptionally high spectral purity and short-term frequency stability. Long-term stability, however, is generally lacking because all lasers are more or less tunable over a frequency band that is determined by the detailed physics of the gain-profile characteristics of each particular laser system. In a typical low-pressure (~15-Torr) CO_2 laser, the width of the gain profile is about 90 MHz, and is dominated by the ~61-MHz Doppler broadening as previously described in Sec. 6.

The first effective means of overcoming Doppler broadening was predicted in the "Theory of an Optical Maser," which Lamb developed and published [64] in 1964 as an "atonement for his own sin of not believing that optical Masers can be realized" [65] (the word "laser" was coined later). Lamb described and predicted in his purely theoretical paper a standing-wave saturation effect that produces a narrow resonant change in the level population of a Doppler-broadened transition interacting with a standing-wave laser field as the laser frequency is tuned across the center frequency of the transition. This change is superimposed on a broad background population change, which, for a constant amplitude laser field, closely follows the Gaussian Doppler line profile as the laser frequency is tuned within the Doppler linewidth. This standing-wave saturation resonance results from the nonlinearity of the interaction of the standing-wave field in the laser cavity with molecules (or atoms) having velocities resonant with the Doppler-shifted frequency of the field as experienced by the molecules (or atoms). When the laser is tuned to the center frequency of a particular transition

($\nu = \nu_0$), a narrowband resonant dip appears in the intensity of the laser output power, because the traveling-wave components constituting the standing-wave field interact with the same group of molecules (or atoms), namely, those that have zero velocity in the direction of the laser's optical axis ($k \bullet v = 0$). This dip in the laser's output power was first verified by Szöke and Javan in the output of a He–Ne laser at 1.15 μm [66], and was appropriately named "Lamb-dip" since Lamb predicted its occurrence.

An even more useful variant of the standing-wave saturation resonance was first demonstrated by Lee and Skolnick [67] who inserted a low-pressure absorber gas cell, which had a resonantly interacting absorption line, within the standing-wave field of the laser's optical cavity. In this case the narrow resonant change appeared as a "pip" increase in the laser's output power and was named "inverted Lamb-dip."

To a very good first approximation, the line shapes and FWHM widths of the Lamb-dips and the inverted Lamb-dips are determined by collision broadening and thus have Lorentzian profiles. In actual practice the absorber gas reference cells can be effectively used with much lower pressure gas fills than the typical mixture pressures required to operate gas lasers. Thus both in principle and in practice the long-term frequency stabilization techniques utilizing the inverted Lamb-dip can provide much better frequency discriminators than those using the Lamb-dip.

One of the best known early examples of inverted Lamb-dip stabilization is the methane–(CH_4) stabilized He–Ne laser oscillating at 3.39 μm. This absorber–laser combination was first suggested and demonstrated by Shimoda in 1968 [68] and was also extensively studied and utilized by Barger and Hall [69].

In the case of the CO_2 laser system the initial attempts to use CO_2 itself as a reference via either the Lamb-dip or the inverted Lamb-dip techniques were not very successful. Lamb-dip was only obtained with very low-pressure laser gas fills and was prone to severe asymmetrical distortions due to competition from adjacent transitions [70]. The inverted Lamb-dip stabilization method on the other hand required very long (~1.7-m) CO_2 absorption cells heated to several hundred (400°C) degrees above room temperature [71]. The poor results were due to the fact that the lower state rotational-vibrational levels of the CO_2 laser transitions do not belong to the ground state, and therefore the absorption coefficient of low-pressure room-temperature CO_2 at 10 μm is very small. The small absorption coefficient in turn made it difficult to observe and utilize directly the inverted Lamb-dip resonance in the full-power output of the CO_2 laser. These difficulties were overcome at Lincoln Laboratory in 1970, when, at the suggestion of Javan, we (Freed and Javan) first demonstrated [48] that excellent long-term frequency stability and reproducibility of CO_2 lasers can be readily obtained (and greatly improved on if necessary) by the frequency stabilization of the lasers to the standing-wave saturation resonance observed in the 4.3-μm upper-state-to-ground-state fluorescence of CO_2, as graphically illustrated in Fig. 8.

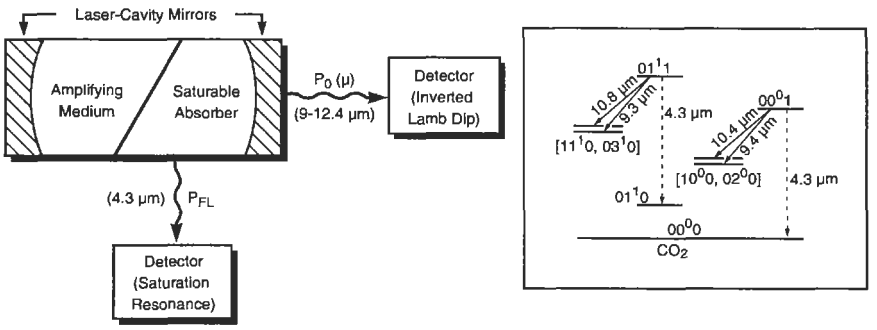

FIGURE 8 Graphic illustration of the saturation resonance observed in CO_2 fluorescence at 4.3 μm. Resonant interaction occurs for $\nu = \nu_o$ (when $k \bullet v = 0$). The figure shows an internal absorption cell within the laser cavity. External cells can also be used. (Reprinted with permission from SooHoo *et al.* [76]. © 1985 IEEE.)

In the initial experiments, a short gas cell with a total absorption path of about 3 cm was placed inside the cavity of each stable CO_2 laser [72] with a Brewster angle window separating the cell from the laser gain tube. Pure CO_2 gas at various low pressures was introduced inside the sample cell. A sapphire window at the side of the sample cell allowed the observation of the 4.3-μm spontaneous emission signal with a liquid-nitrogen-cooled InSb detector. The detector element was about 1.5 cm from the path of the laser beam in the sample cell. To reduce the broadband noise caused by background radiation, the detector placement was chosen to be at the center of curvature of a gold-coated spherical mirror, which was internal to the gas absorption cell. The photograph of the laser with which the standing-wave saturation resonance was first observed via the fluorescence signal at 4.3 μm is shown in Fig. 9. More than two orders of magnitude improvements in signal-to-noise ratios (SNRs) were subsequently achieved with improved design low-pressure CO_2 stabilization cells external to the lasers [73]. One example of such improved design is schematically shown in Figure 10.

In the improved design, the low-pressure gas cell, the LN_2-cooled radiation collector, and the infrared (IR) detector are all integral parts of one evacuated housing assembly. This arrangement minimizes signal absorption by windows and eliminates all other sources of absorption. Because of the vacuum enclosure, diffusion of other gases into the low-pressure gas reference cell is almost completely eliminated; therefore, the time period available for continuous use of the reference gas cell is greatly increased and considerably less time has to be wasted on repumping and refilling procedures. One LN_2 fill can last at least several days.

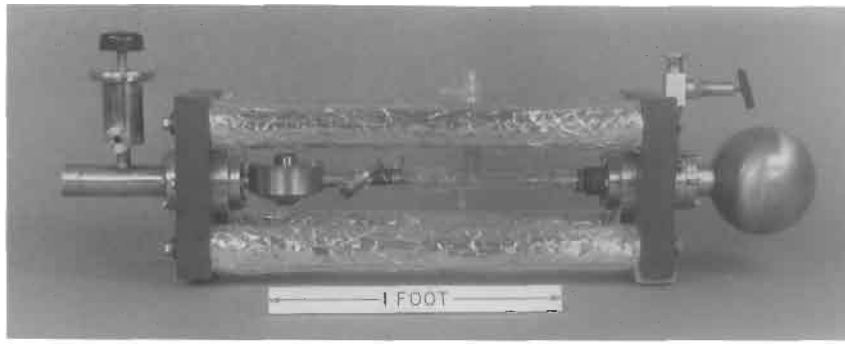

FIGURE 9 Two-mirror stable laser with short intracavity cell. This laser was used for the first demonstration of the standing-wave saturation resonance observed via the 4.3-μm fluorescence signal.

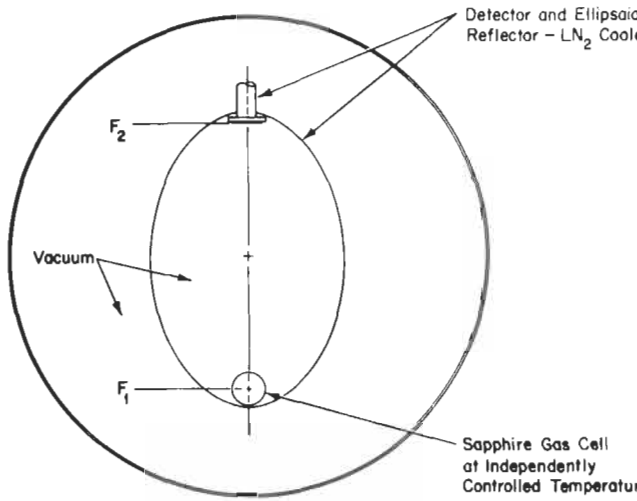

FIGURE 10 Schematic illustration of improved external CO_2 reference gas stabilization cell.

With the improved cells, significantly larger signal collection efficiency was achieved simultaneously with a great reduction of noise due to background radiation, which is the primary limit for high-quality InSb photovoltaic detectors. We have evaluated and tested several large-area InSb detectors and determined that the LN_2-cooled background greatly diminished $1/f$ noise in addition to the expected reduction in white noise due to the lower temperature background radiation.

Figure 11 shows a typical recorder tracing of the observed 4.3-μm intensity change as the laser frequency is tuned across the 10.59-μm $P(20)$ line profile

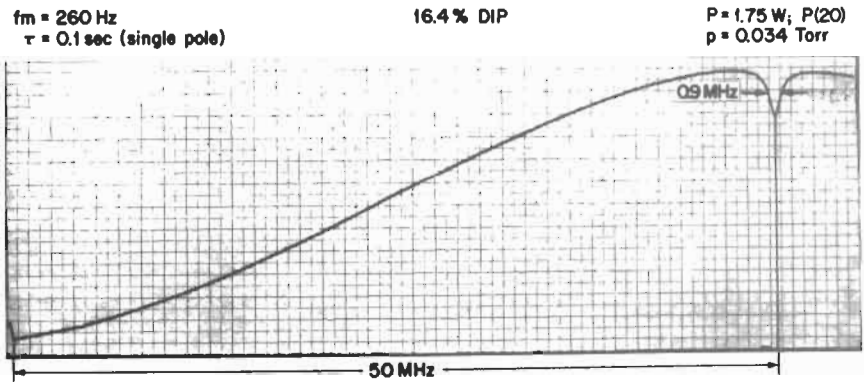

FIGURE 11 Lamb-dip-like appearance of the resonant change in the 4.3-μm fluorescence. The magnitude of the dip is 16.4% of the 4.3-μm fluorescence signal. The pressure in the reference cell was 0.034 Torr and the laser power into the cell was 1.75 W in the I-$P(20)$ transition. A frequency dither rate of 260 Hz was applied to the piezoelectric mirror tuner.

with a 0.034-Torr pressure of $^{12}C^{16}O_2$ absorber gas. The standing-wave saturation resonance appears in the form of a narrow resonant 16.4% "dip" in the 4.3-μm signal intensity, which emanates from all the collisionally coupled rotational levels in the entire $(00^01)\rightarrow(000)$ band. The broad background curve is due to the laser power variation as the frequency is swept within its oscillation bandwidth. Because collision broadening in the CO_2 absorber is about 7.5 MHz/Torr FWHM [72], in the limit of very low gas cell pressure the linewidth is determined primarily by power broadening and by the molecular transit time across the diameter of the incident beam. The potentially great improvements in SNR, in reduced power and transit-time broadening, and in short-term laser stability were the motivating factors that led to the choice of stabilizing cells external to the laser's optical cavity. The one disadvantage inherent with the use of external stabilizing cells is that appropriate precautions must be taken to avoid optical feedback into the lasers to be stabilized.

For frequency reference and long-term stabilization, it is convenient to obtain the derivative of the 4.3-μm emission signal as a function of frequency. This 4.3-μm signal derivative may be readily obtained by a small dithering of the laser frequency as we slowly tune across the resonance in the vicinity of the absorption-line center frequency. With the use of standard phase-sensitive detection techniques we can then obtain the 4.3-μm derivative signal to be used as a frequency discriminator. Figure 12 shows such a 4.3-μm derivative signal as a function of laser tuning near the center frequency of the 10.59-μm $P(20)$ transition. The derivative signal in Fig. 12 was obtained by applying a ±200-kHz frequency modulation to the laser at a 260-Hz rate. A 1.75-W portion of the laser's output was directed into a small external stabilization cell that was filled with

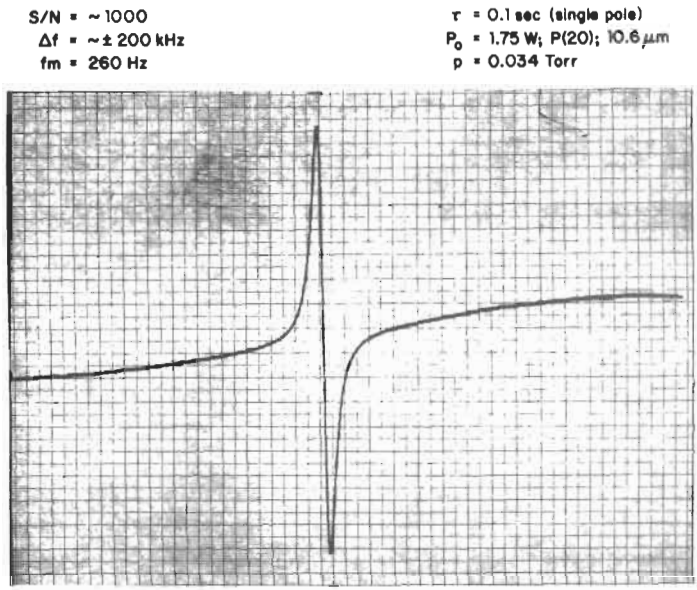

FIGURE 12 Derivative signal at 4.3 μm in the vicinity of the standing-wave saturation resonance shown in Fig. 11. SNR ~ 1000, $\Delta f \sim \pm 200$ kHz, and $t = 0.1$ sec (single pole).

pure CO_2 to a pressure of 0.034 Torr at room temperature. It is a straightforward procedure to line-center-stabilize a CO_2 laser through the use of the 4.3-μm derivative signal as a frequency discriminant, in conjunction with a phase-sensitive detector. Any deviation from the center frequency of the lasing transition yields a positive or negative output voltage from the phase-sensitive detector. This voltage is then utilized as a feedback signal in a servoloop to obtain the long-term frequency stabilization of the laser output.

Figure 13 shows a block diagram of a two-channel heterodyne calibration system. In the system, two small, low-pressure, room-temperature CO_2-gas reference cells external to the lasers were used to line-center-stabilize two grating-controlled stable lasers. The two-channel heterodyne system was used extensively for the measurement and calibration of CO_2-isotope laser transitions [36,37].

Figure 14 shows the spectrum-analyzer display of a typical beat-note of the system shown in Fig. 13. Note that the SNR is greater than 50 dB at the 24.4 GHz beat frequency of the two laser transitions with the use of varactor photodiode detection developed at MIT Lincoln Laboratory [74,75].

Figure 15 illustrates the time-domain frequency stability that we have routinely achieved with the two-channel heterodyne calibration system by using the

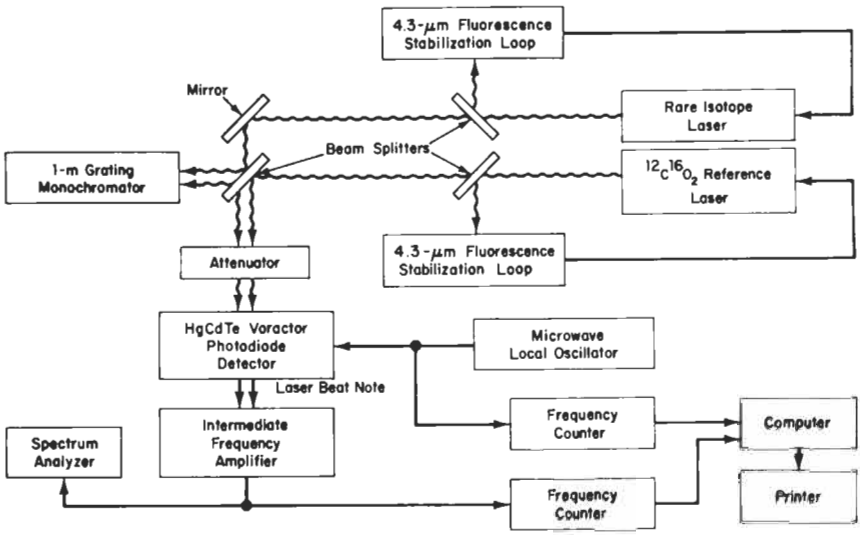

FIGURE 13 Block diagram of the two-channel line-center-stabilized CO_2-isotope calibration system. In the figure, wavy and solid lines denote optical and electrical paths, respectively. (Reprinted with permission from Freed [75]. © 1982 IEEE.)

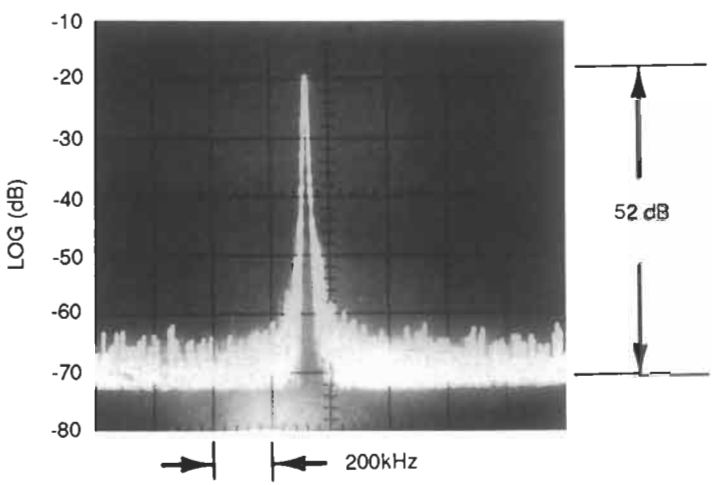

FIGURE 14 The 24.4104191-GHz beat note of a $^{16}O^{12}C^{18}O$ laser I-P(12) transition and a $^{12}C^{16}O_2$ laser I-P(6) transition. The power levels into the photodiode were 0.48 mW for the $^{16}O^{12}C^{18}O$ laser and 0.42 mW for the $^{12}C^{16}O_2$ laser. The second harmonic of the microwave local oscillator was generated in the varactor photodiode. The intermediate-frequency noise bandwidth of the spectrum analyzer was set to 10 kHz.

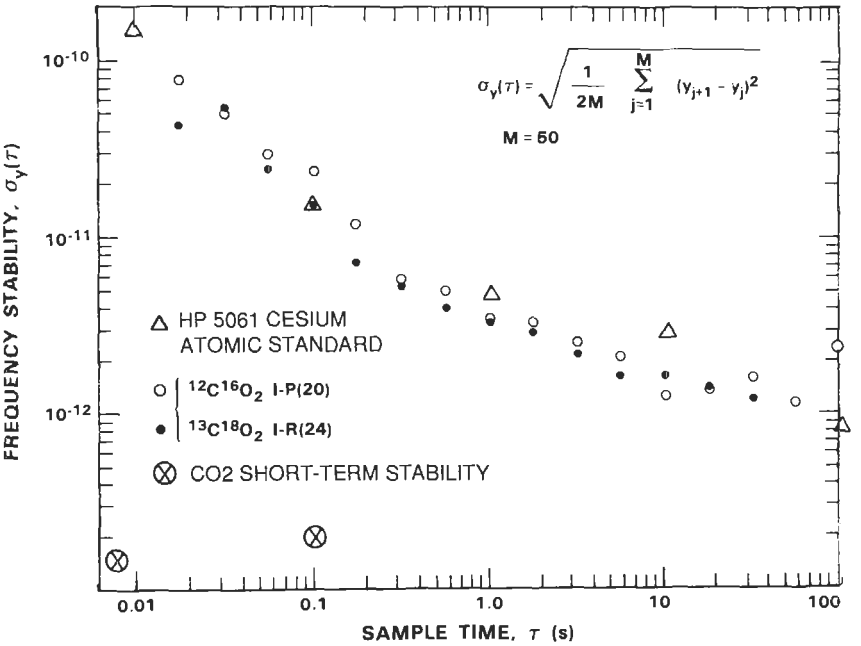

FIGURE 15 Time-domain frequency stability of the 2.6978648-GHz beat note of the $^{13}C^{18}O_2$ laser *I-R*(24) transition and the $^{12}C^{16}O_2$ reference laser I-*P*(20) transition in the two-channel heterodyne calibration system (Fig. 13) with the 4.3-μm fluorescence stabilization technique. For the sake of comparison, the stabilities of a cesium clock and short-term stabilities of individual CO_2 lasers are also shown. Note that the frequency stabilities of the CO_2 and the cesium-stabilized systems shown are about the same and that the CO_2 radar has achieved short-term stabilities of at least two to three orders of magnitude better than those of microwave systems. (Reprinted with permission from SooHoo *et al.* [76]. © 1984 IEEE.)

4.3-μm fluorescence stabilization technique [56,76,77]. The solid and hollow circles represent two separate measurement sequences of the Allan variance of the frequency stability

$$\sigma_y(\tau) = \sqrt{\frac{1}{2M}\sum_{j=1}^{M}\left(y_{j+1}-y_j\right)^2} \quad . \tag{17}$$

Each measurement consisted of $M = 50$ consecutive samples for a sample time duration (observation time) of τ seconds. Figure 15 shows that we have achieved $\sigma_y(\tau) < 2\times10^{-12}$ for $\tau \sim 10$ sec. Thus a frequency measurement precision of about 50 Hz may be readily achieved within a few minutes.

The triangular symbols in Fig. 15 represent the frequency stability of a Hewlett-Packard (HP) model 5061B cesium atomic frequency standard, as specified in the HP catalog. Clearly, the frequency stabilities of the CO_2 and the cesium-stabilized systems shown in Fig. 15 are about the same.

The two cross-circles in the lower left corner of Fig. 15 denote the upper bound of the short-term frequency stabilities, as measured in the laboratory (Fig. 6) and determined from CO_2 radar returns at the Lincoln Laboratory Firepond Facility [56,58]. Note that the CO_2 radar has achieved short-term stabilities of at least two to three orders of magnitude better than those of microwave systems.

Figure 16 shows the frequency reproducibility of the two-channel line-center-stabilized CO_2 heterodyne calibration system. The figure contains a so-called drift run that was taken over a period of 8.5 hours beginning at 1:00 P.M. [56,76,77]. The frequency-stability measurement apparatus was fully automatic; it continued to take, compute, and record the beat-frequency data of the two line-center stabilized CO_2 isotope lasers even at night, when no one was present in the laboratory. Approximately every 100 sec the system printed out a data point that represented the deviation from the 2.6976648-GHz beat frequency, which was

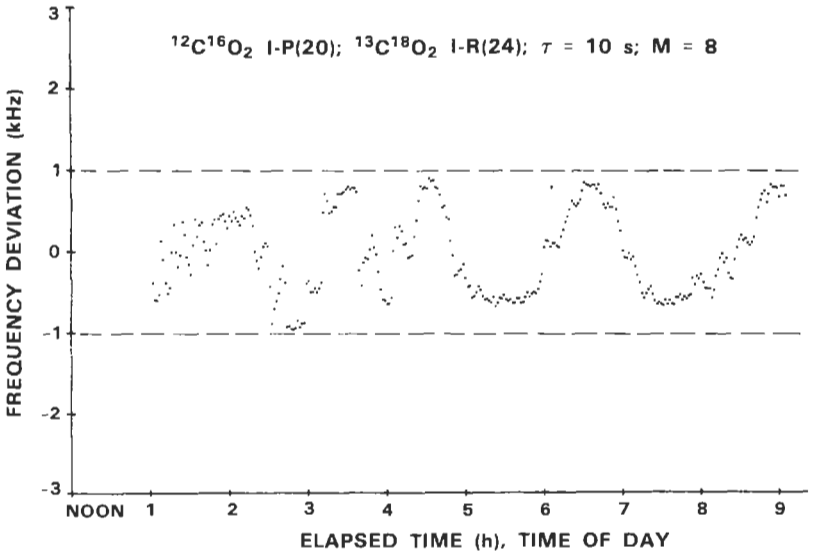

FIGURE 16 Slow drifts in the 2.6978648-GHz beat frequency due to small frequency-offsetting zero-voltage variations of the electronics. The frequency deviations were caused by ambient temperature variations. The beat note was derived from the $^{13}C^{18}O_2$ I-R(24) and the $^{12}C^{16}O_2$ I-P(20) laser transitions. An observation time of τ = 10 sec and a sample size of M = 8 were used for each data point. (Reprinted with permission from SooHoo *et al.* [76]. © 1985 IEEE.)

averaged over 8.5 hours. The system used a measurement time of $\tau = 10$ sec and $M = 8$ samples for each data point, yielding a measurement accuracy much better than the approximately ±1-kHz peak-frequency deviation observable in Fig. 16.

The frequency drift was most likely caused by small voltage-offset errors in the phase-sensitive detector-driven servoamplifier outputs that controlled the piezoelectrically tunable laser mirrors. Because 500 V was required to tune the laser one longitudinal mode spacing of 100 MHz, an output voltage error of ±2.5 mV in each channel was sufficient to cause the peak-frequency deviation of ±1 kHz that was observed in Fig. 16. By monitoring the piezoelectric drive voltage with the input to the lock-in amplifier terminated with a 50-Ω load (instead of connected to the InSb 4.3-μm fluorescence detector), we determined that slow output-offset voltage drifts were the most probable cause of the ±1-kHz frequency drifts observed in Fig. 16. It is important to note that no special precautions were taken to protect either the lasers or the associated electronic circuitry from temperature fluctuations in the laboratory. The temperature fluctuations were substantial—plus or minus several degrees centigrade. Significant improvements are possible with more up-to-date electronics and a temperature-controlled environment.

Perhaps the greatest advantage of the 4.3-μm fluorescence stabilization method is that it automatically provides a nearly perfect coincidence between the lasing medium's gain profile and the line center of the saturable absorber, because they both utilize the same molecule, CO_2. Thus every P and R transition of the (00^01)—$[10^00, 02^00]_{I,II}$ regular bands and the (01^11)—$[01^00, 03^10]_{I,II}$ hot bands [78–81] may be line-center-locked with the same stabilization cell and gas fill. Furthermore, as illustrated in Fig. 8, the saturation resonance is detected separately at the 4.3-μm fluorescence band and not as a fractional change in the much higher power laser radiation at 8.9 to 12.4 μm. At 4.3 μm, InSb photovoltaic detectors that can provide very high background-limited sensitivity are available.

However, it is absolutely imperative to realize that cryogenically cooled InSb photovoltaic elements are extremely sensitive detectors of radiation far beyond the 4.3-μm CO_2 fluorescence band. Thus, cryogenically cooled IR bandpass filters and field-of-view (FOV) shields, which both spectrally and spatially match the detector to the CO_2 gas volume emitting the 4.3-μm fluorescence radiation, should be used. If this is not done, the detected radiation emanating from other sources (ambient light, thermal radiation from laboratory personnel and equipment, even electromagnetic emission from motors, transformers, and transmitters) may completely swamp the desired 4.3-μm fluorescence signal. This procedure is a very familiar and standard technique utilized in virtually every sensitive IR detection apparatus; surprisingly, however, it was only belatedly realized in several very highly competent research laboratories, because the most commonly used and least expensive general-purpose IR detectors are bought in a sealed-off dewar and may not be easily retrofitted with a cryogenically cooled bandpass filter and FOV shield.

Additional precautionary measures should be taken in using the saturated fluorescence signal. The Einstein coefficient for the upper lasing level (00^01) is about 200 to 300 sec^{-1} and, therefore, the modulation frequency must be slow enough so that the molecules in the upper level have enough time to fluoresce down to the ground state; here radiation trapping [82,83] of the 4.3-μm spontaneous emission (because CO_2 is a ground-state absorber) will show up as a variation of the relative phase between the reference modulation and the fluorescence signal as the pressure is varied. The phase lag between the reference signal and the molecular response would increase as the pressure increases because there are more molecules to trap the 4.3-μm radiation and, therefore, hinder the response. This phase lag will increase with increasing modulation frequency, since the molecules will have less time to respond; thus, caution must be taken when selecting the modulation frequency. A large phase lag will reduce the output voltage (feedback signal) of the phase-sensitive detector; however, it will not cause a shift in the instrumental zero [76].

In addition to optimizing the frequency at which to modulate the laser, the amplitude of the modulation (the frequency excursion due to the dithering) was also considered in the experiments at Lincoln Laboratory [76]. The modulation amplitude must be large enough such that the fluorescence signal is detectable, but the amplitude must be kept reasonably small to avoid all unnecessary parasitic amplitude modulation and nonlinearities in the piezoelectric response, in order to avoid distorting the 4.3-μm Lorentzian. The maximum derivative signal is obtained if the peak-to-peak frequency excursion equals 0.7 FWHM of the Lorentzian. But such a large excursion should be avoided in order to minimize the likelihood of introducing asymmetries in the derivative signal. A compromise modulation amplitude based on obtaining sufficient SNR for most J lines was used. This modulation amplitude corresponded to a frequency deviation of approximately 300 kHz peak-to-peak on a Lorentzian with an FWHM of about 1 MHz. Experimental results indicated that the modulation frequency should be kept well below 500 Hz. At such low frequencies, InSb photovoltaic detectors may have very high $1/f$ noise unless operated at effectively zero dc bias voltage. This may be best accomplished by a low-noise current mode preamplifier that is matched to the dynamic impedance of the detector and is adjusted as close as possible to zero dc bias across the detector (preferably less than 0.001 V).

There are other advantages of the 4.3-μm fluorescence stabilization; because the fluorescence lifetime is long compared to the reorientating collision time at the pressures typically employed in the measurements, the angular distribution of the spontaneous emission is nearly isotropic. This reduces distortions of the lineshape due to laser beam imperfections. Furthermore, only a relatively short (3- to 6-cm) fluorescing region is monitored, and the CO_2 absorption coefficient is quite small ($\sim 10^{-6}$ cm^{-1}-$Torr^{-1}$); this eliminates laser beam focusing effects due to the spatial variation of the refractive index of the absorbing medium produced by the Gaussian laser beam profiles [84,85]. Indeed, we have found no

significant change in the beat frequency after interchanging the two stabilizing cells, which had very different internal geometries and volumes, and (within the frequency resolution of our system) no measurable effects due to imperfect and/or slightly truncated TEM_{00q} beam profiles.

We have used external stabilizing cells with 2-cm clear apertures at the beam entrance window. Inside the cell, the laser beam was turned back on itself (in order to provide a standing wave) by means of a flat, totally reflecting mirror. Slight misalignment of the return beam was used as a dispersion-independent means of avoiding optical feedback. External stabilizing cells were used, instead of an internal absorption cell within the laser cavity, in order to facilitate the optimization of SNR in the 4.3-μm detection optics, independent of laser design constraints. External cells were also easily portable and usable with any available laser. The FWHM of the saturation resonance dip ranged from 700 kHz to 1 or 2 MHz as the pressure was varied from 10 to about 200 to 300 mTorr within the relatively small (2-cm clear aperture) stabilizing cells employed in our experiments. By using a 6.3-cm-diameter cell, 164-kHz FWHM saturation resonance dips were reported by Kelly [86]. Because the FWHM of the CO_2 saturation resonance due to pressure is about 7.5 kHz/mTorr, much of the linewidth broadening is due to other causes such as power and transit-time broadening, second-order Doppler shift, and recoil effects. More detailed discussions of these causes can be found in [76,112], and in the literature on primary frequency standards but any further consideration of these effects is well beyond the scope of this chapter.

The saturated 4.3-μm fluorescence frequency stabilization method has been recently extended to sequence band CO_2 lasers by Chou *et al.* [87,88]. The sequence band transitions in CO_2 are designated as $(00^0\upsilon)$—$[10^0(\upsilon-1), 02^0(\upsilon-1)]_{I,II}$, where $\upsilon > 1$ ($\upsilon = 1$ defines the regular bands discussed in this and previous sections of this chapter). Sequence band lasers were intensively studied by Reid and Siemsen at the NRC in Ottawa beginning in 1976 [89,90]. Figure 17 shows the simplified vibrational energy-level diagram of the CO_2 and N_2 molecules, with solid-line arrows showing the various cw lasing bands observed so far. The dotted-line arrows show the 4.3-μm fluorescence bands that were utilized for line-center stabilization of the great multitude of individual lasing transitions.

Figure 17 clearly shows that for the (00^02)—$[10^01, 02^01]_{I,II}$ first sequence band transitions the lower laser levels are approximately 2300 cm^{-1} above those of the regular band transitions and therefore the population densities of the first sequence band laser levels are about four orders of magnitude less than in the corresponding regular band laser levels. Chou *et al.* overcame this problem by using a heated longitudinal CO_2 absorption cell (L-cell) in which the 4.3-μm fluorescence was monitored through a 4.3-μm bandpass filter in the direction of the laser beam [87,88]. Due to the increased CO_2 temperature, photon trapping [82,83,87] was reduced, and by increasing the fluorescence collecting length they increased the intensity of sequence band fluorescence so that a good enough SNR was obtained at relatively low cell temperatures.

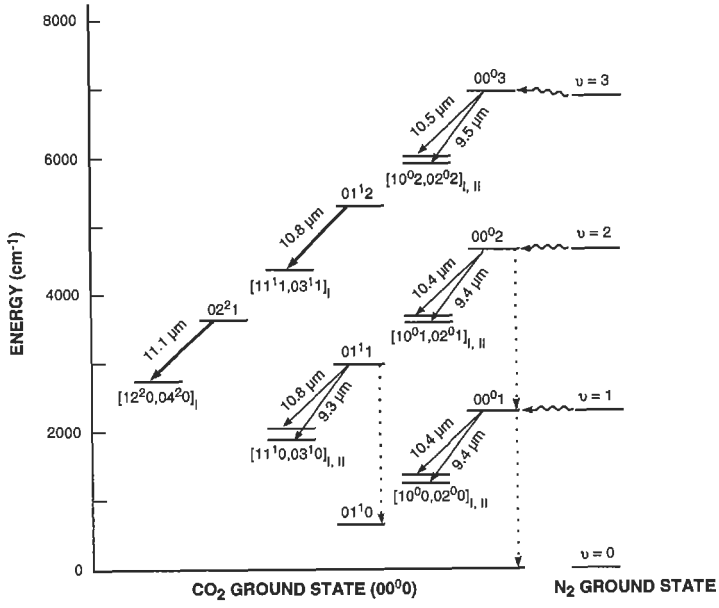

FIGURE 17 Simplified vibrational energy-level diagram of the CO_2 and N_2 molecules. The lasing bands are shown by solid-line arrows. The extra heavy arrows indicate lasing bands that were only recently observed [80,81]. The dotted-line arrows show the 4.3-μm fluorescence bands that were used for line-center-frequency stabilization of the corresponding lasing transitions. (Reprinted with permission from Evenson *et al.* [80]. © 1994 IEEE.)

Although first demonstrated with CO_2 lasers, the frequency stabilization technique utilizing the standing-wave saturation resonances via the intensity changes observed in the spontaneous fluorescence (side) emission can be (and has been) used with other laser systems as well (e.g., N_2O) [86]. This method of frequency stabilization is particularly advantageous whenever the absorbing transition belongs to a hot band with a weak absorption coefficient (such as CO_2 and N_2O). Of course, saturable absorbers other than CO_2 (e.g., SF_6, OsO_4) can and have been used with CO_2 lasers, but their use will not be discussed here; the utilization of such absorbers requires the finding of fortuitous near coincidences between each individual lasing transition and a suitable absorption feature in the saturable absorber gas to be used. Indeed, just the preceding considerations prompted the search for an alternate method of frequency stabilization that could utilize the lasing molecules themselves as saturable absorbers. It was this search for an alternate method of line-center stabilizing of the vast multitude of potentially available lasing transitions in CO_2 lasers that finally led Javan and Freed to the invention [91] and first demonstration [48] of the standing-wave saturation resonances in the 4.3-μm spontaneous emission band of

CO_2 and also the utilization of these narrow Doppler-free resonances for line-center stabilization of all available regular and hot band CO_2 lasing transitions. Since its first demonstration in 1970, this method of line-center stabilization has attained worldwide use and became known as the *Freed–Javan technique*.

9. ABSOLUTE FREQUENCIES OF REGULAR BAND LASING TRANSITIONS IN NINE CO_2 ISOTOPIC SPECIES

Through the use of optical heterodyne techniques [36,37,56,92–98], beat frequencies between laser transitions of individually line-center-stabilized CO_2-isotope lasers in pairs can be generated and accurately measured. Measurements of the difference frequencies are then used to calculate the band centers, rotational constants, and transition frequencies by fitting the measured data to the standard formula for the term values [31,36–38,93] as given here:

$$T(\upsilon,J) = G_\upsilon + B_\upsilon J(J+1) - D_\upsilon\left[J(J+1)\right]^2 + H_\upsilon\left[J(J+1)\right]^3 + L_\upsilon\left[J(J+1)\right]^4 + \ldots \tag{18}$$

The first systematic measurement and really accurate determination of the absolute frequencies and vibrational-rotational constants of the regular band $^{12}C^{16}O_2$ laser transitions was accomplished by Petersen *et al.* of the NBS in 1973 [93,95]. In these initial measurements Petersen *et al.* used 30 adjacent pairs of $^{12}C^{16}O_2$ laser lines in the 10.4-μm regular band and 26 adjacent pairs in the 9.4-μm regular band. The lasing transitions were generated by two grating-controlled $^{12}C^{16}O_2$ lasers, which were line-center-stabilized using the standing-wave saturation resonances observed in the 4.3-μm fluorescence band, and the 32-to 63-GHz beat frequencies were detected and measured using LHe temperature Josephson junctions. These measurements, together with the absolute frequencies of the 10.18-μm I-*R*(30) and 9.33-μm II-R(10) $^{12}C^{16}O_2$ transitions as determined relative to the primary cesium frequency standard at the NBS in Boulder, Colorado, by Evenson *et al.* in 1973 [94], reduced the uncertainties in existing vibrational-rotational constants [92] 20 to 30 times and the additional rotational constant H_υ was determined for the first time with a statistically significant accuracy.

Concurrent with the ongoing work with $^{12}C^{16}O_2$ lasers at the NBS, we at MIT Lincoln Laboratory concentrated our effort on measuring the rare CO_2 isotopic species using LN_2-cooled HgCdTe varactor photodiodes [74,75] and the two-channel line-center-stabilized CO_2-isotope calibration system illustrated in Fig. 13 and described in Sec. 8. In the initial phase of the MIT Lincoln Laboratory work, the band centers, rotational constants, absolute frequencies, and vacuum wave

numbers for $^{12}C^{16}O_2$, $^{13}C^{16}O_2$, $^{12}C^{18}O_2$, $^{13}C^{18}O_2$, $^{12}C^{16}O^{18}O$, $^{14}C^{16}O_2$, and $^{14}C^{18}O_2$ were simultaneously computed from 590 beat frequency measurements between pairs of adjacent (00^01)—$[10^00, 02^00]_{I,II}$ band CO_2 laser transitions. The input data included the 56 beat frequencies measured between adjacent $^{12}C^{16}O_2$ rotational lines by Petersen *et al.* [93], and the absolute frequencies of the 10.18-μm I-*R*(30) and 9.33-μm II-*R*(10) $^{12}C^{16}O_2$ transitions determined by Evenson *et al.* [94] relative to the primary cesium standard. These initial results for the seven CO_2 isotopic species listed were published by Freed *et al.* in 1980 [36].

In 1983 Petersen *et al.* published [99] improved vibrational-rotational constants and absolute frequency tables for the regular bands of $^{12}C^{16}O_2$. These new results obtained at the NBS in Boulder, Colorado, were based on new beat frequency measurements, including high-*J* and across-the-band center measurements, and yielded about a factor of 10 better frequency tables. In addition, some specific $^{13}C^{16}O_2$ lines were also measured with reduced uncertainties. The new results of Petersen *et al.* [99] yielded a more precise determination of the absolute frequency (relative to the primary cesium standard) of the $^{12}C^{16}O_2$ I-*R*(30) line, with an absolute uncertainty of 3.1 kHz. This uncertainty of 3.1 kHz became the principal limit for the uncertainties in the frequency tables for the absolute frequencies of regular band lasing transitions in nine CO_2 isotopic species, published by Bradley *et al.* in 1986 [37]. The data and results published in this paper represented the final phase and outcome of the isotopic CO_2 laser frequency-calibration work that had begun at MIT Lincoln Laboratory more than a decade earlier. This final CO_2 isotope frequency calibration work represented significant improvement over previous results for the following reasons:

1. We have included in our database the most recent measurements on $^{12}C^{16}O_2$ regular band transitions that Petersen *et al.* published [99]; their more precise measurement of the I-*R*(30) line absolute frequency, and the beat frequencies of their widely spaced lines [99] was included in our database as shown in Table 1.
2. We have extended our previous measurements, particularly of $^{13}C^{16}O_2$ to higher *J* values, and have made the first measurements of $^{12}C^{17}O_2$ and $^{13}C^{16}O^{18}O$.
3. We have improved our instrumentation and measurement techniques, and thus have been able to measure pressure shifts in CO_2 laser lines with a more sophisticated two-channel line-center-stabilized calibration system (which is described in the next section).
4. We have recognized deficiencies in our earlier weighting of measurements, and have become familiar with the use of resistant statistical procedures for minimizing the effects of "outliers."

As a result of the preceding changes, the number of beat frequency measurements has increased to 915, the number of isotopic species has increased to nine, and the precision of predicted frequencies has increased by an order of magnitude.

TABLE 1 Absolute Frequency and Four-Frequency Beat Measurements of Petersen *et al.* [99][a]

ABSOLUTE FREQUENCY OF $^{16}O\,^{12}C\,^{16}O$ LINE PETERSEN ET AL. II

	MEASURED FREQUENCY	NOMINAL STD.DEV.	CALCULATED FREQUENCY	MEASURED - CALCULATED
626 R I(30)	29442483.3197	3.1D-03	29442483.3197	0.0000

FOUR-FREQUENCY BEATS PETERSEN ET AL. II

	MEASURED FREQUENCIES	NOMINAL STD.DEV.	CALCULATED FREQUENCIES	MEASURED - CALCULATED	RELATIVE DEVIATION
2*626 R I(12) - 626 R II(10) - 636 P I(50)	22941.9100	2.5D-03	22941.9093	0.0007	0.27
2*626 P I(34) - 636 P II(28) - 636 P I(50)	15433.4420	2.5D-03	15433.4428	-0.0008	-0.33

[a]Reprinted with permission from Bradley *et al.* [37]. © 1986 IEEE.

Figure 18 graphically illustrates the frequency and wavelength domain of the nine CO_2 isotopic species that have been measured to date. The $^{14}C^{16}O_2$ extends the wavelength range to well beyond 12 μm; $^{12}C^{18}O_2$ transitions can reach below 9 μm. We have fitted the data obtained from the 915 beat frequency measurements and the ones shown in Table 1 to the polynomial formula for term values described in Eq. (18). The molecular constants derived from the fit, the frequencies, wave numbers (using c = 299 792 458 m/s), and standard deviations predicted are shown in Tables 2 through 10 for the regular bands of the isotopic species of CO_2 that we measured (out of 18 possible isotopic combinations). We have printed the molecular constants with more figures than their standard deviations warrant so that those who wish to use the constants to generate frequencies will find agreement with our predicted frequencies. We may also remark that some linear combinations of molecular constants [e.g., $B(001)$–$B(I)$] are better determined than any of the constants individually. With each constant is printed an ordinal number; these numbers are used to designate the rows and columns of

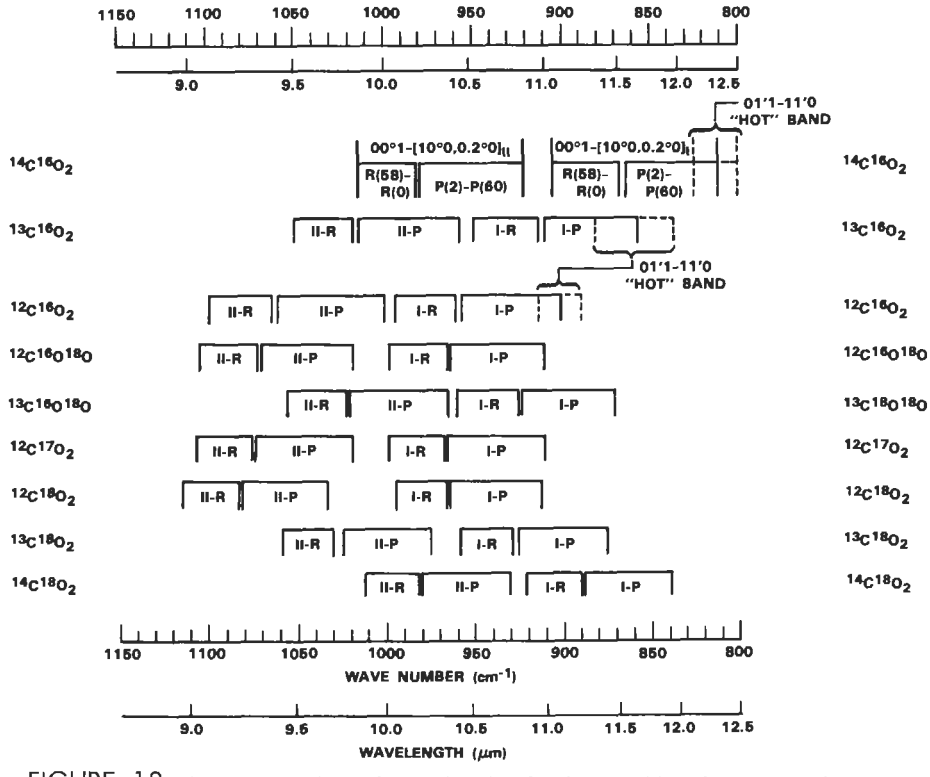

FIGURE 18 Frequency and wavelength domain of lasing transitions in nine CO_2 isotopes. (Reprinted with permission from Freed [56].)

the variance-covariance matrix, the lower triangle of which is shown in Table XII of the original paper [37], but is not reproduced here.

The horizontal lines drawn in the frequency tables denote the highest and lowest J lines within which beat frequency measurements were used in the data for computer fitting. As always, the frequency values outside the measured regions should be used with the greatest caution, and the computed standard deviations for such lines should be considered as only a rough guide.

The original paper [37] also contains the 915 beat frequency measurements and their nominal standard deviations that constituted the input to our computations. These data, which are designated as Files 1 through 50 in Table II of [37], will be useful to those who wish to derive better molecular constants and more accurate frequency determinations as additional beat frequency measurements and more precise intercomparisons of CO_2 lasing transitions with the primary frequency standard (cesium at the present) become available.

The frequencies predicted in Tables 2 through 10 show, for the most accurate lines, standard deviations that are an order of magnitude smaller than those in [36] and are principally limited by the uncertainty in the single absolute frequency measurement. We believe that these standard deviations are reasonable estimates of the uncertainties of their respective frequencies, and that our molecular constants and predicted frequencies are the best currently available for the CO_2 isotopic species, and are as good as any that can be extracted from the available data. In our opinion, they are suitable (with appropriate care about sequence and hot bands [78–81, 89,90,100–103]) for use as secondary standards at the indicated level of precision. Higher precision (by perhaps two orders of magnitude) in the CO_2 comparisons could be attained by application of techniques developed in [76], which are summarized in the next section, but for more precise absolute frequencies, this would need to be accompanied by a similarly precise comparison with the cesium standard.

During the preparation of the manuscript for this chapter I became aware of some very recent work on CO_2 laser line calibration that was carried out at the Time and Frequency Division of NIST in Boulder, Colorado. I am grateful to Dr. K. M. Evenson for providing me with a very recent reprint [80] and three additional manuscripts prior to their publication [38,81,88]. The outcome of this new work will result in improved molecular constants and frequencies for the CO_2 laser and will be very briefly summarized next.

In May 1994, Evenson *et al.* reported [80] the first observation of laser transitions in the (00^11)—$[11^10, 03^10]_{II}$ 9-μm hot band of $^{12}C^{16}O_2$. This band is identified by an extra heavy solid arrow in the vibrational energy level diagram of Fig. 17, which was reproduced from [80]. These transitions, together with the (00^11)—$[11^10, 03^10]_I$ lower frequency hot band transitions that were previously measured by Whitford *et al.* [78] and by Petersen *et al.* [79] were incorporated into a new database by Maki *et al.* [38]. Altogether they included 84 hot band transitions and also 12 higher J value regular band $^{12}C^{16}O_2$ transitions that were not measured by Bradley *et al.* [37]. From the database provided in Bradley *et al.*

TABLE 2 Molecular Constants and Frequencies Calculated for 626[a]

$^{16}O\ ^{12}C\ ^{16}O$

NUMBER	SYMBOL		CONSTANTS (MHZ)	STD.DEV. (MHZ)
1	V(001-I)	=	2.880 881 382 455 D+07	3.6D-03
2	V(001-II)	=	3.188 996 017 636 D+07	3.7D-03
3	B(001)	=	1.160 620 695 034 D+04	2.3D-05
4	B(I)	=	1.169 756 942 611 D+04	2.5D-05
5	B(II)	=	1.170 636 464 791 D+04	2.4D-05
6	D(001)	=	3.988 109 863 D-03	3.2D-08
7	D(I)	=	3.445 940 508 D-03	3.3D-08
8	D(II)	=	4.711 559 114 D-03	3.3D-08
9	H(001)	=	0.481 534 D-09	1.9D-11
10	H(I)	=	5.625 110 D-09	1.8D-11
11	H(II)	=	7.066 300 D-09	1.8D-11
12	L(001)	=	-0.96 936 D-14	3.5D-15
13	L(I)	=	1.06 816 D-14	3.3D-15
14	L(II)	=	-4.31 765 D-14	3.2D-15

BAND I

LINE	FREQUENCY (MHZ)	STD.DEV. (MHZ)	VAC.WAVE NO. (CM-1)
P(60)	2707 7607.5077	0.0246	903.2117 6484
P(58)	2714 6404.4578	0.0154	905.5065 8408
P(56)	2721 4396.1809	0.0097	907.7745 4384
P(54)	2728 1588.8741	0.0064	910.0158 5084
P(52)	2734 7988.4259	0.0049	912.2307 0148
P(50)	2741 3600.4235	0.0043	914.4192 8214
P(48)	2747 8430.1601	0.0040	916.5817 6938
P(46)	2754 2482.6413	0.0038	918.7183 3017
P(44)	2760 5762.5914	0.0037	920.8291 2210
P(42)	2766 8274.4599	0.0036	922.9142 9359
P(40)	2773 0022.4271	0.0036	924.9739 8407
P(38)	2779 1010.4094	0.0036	927.0083 2419
P(36)	2785 1242.0651	0.0035	929.0174 3596
P(34)	2791 0720.7986	0.0035	931.0014 3295
P(32)	2796 9449.7656	0.0035	932.9604 2043
P(30)	2802 7431.8776	0.0035	934.8944 9550
P(28)	2808 4669.8055	0.0035	936.8037 4726
P(26)	2814 1165.9839	0.0035	938.6882 5692

(continues)

TABLE 2 *(continued)*

BAND I *(continued)*

LINE	FREQUENCY (MHZ)	STD.DEV. (MHZ)	VAC.WAVE NO. (CM-1)
P(24)	2819 6922.6147	0.0036	940.5480 9793
P(22)	2825 1941.6703	0.0036	942.3833 3608
P(20)	2830 6224.8967	0.0036	944.1940 2961
P(18)	2835 9773.8165	0.0036	945.9802 2931
P(16)	2841 2589.7314	0.0035	947.7419 7860
P(14)	2846 4673.7246	0.0035	949.4793 1361
P(12)	2851 6026.6628	0.0035	951.1922 6324
P(10)	2856 6649.1983	0.0035	952.8808 4927
P(8)	2861 6541.7701	0.0035	954.5450 8632
P(6)	2866 5704.6061	0.0036	956.1849 8202
P(4)	2871 4137.7235	0.0036	957.8005 3691
P(2)	2876 1840.9300	0.0036	959.3917 4460
V(0)	2880 8813.8246	0.0036	960.9585 9171
R(0)	2883 2026.2225	0.0036	961.7328 7396
R(2)	2887 7902.4412	0.0036	963.2631 3990
R(4)	2892 3046.4336	0.0036	964.7689 8140
R(6)	2896 7457.0695	0.0035	966.2503 6076
R(8)	2901 1133.0097	0.0035	967.7072 3331
R(10)	2905 4072.7058	0.0035	969.1395 4739
R(12)	2909 6274.3988	0.0034	970.5472 4435
R(14)	2913 7736.1185	0.0034	971.9302 5845
R(16)	2917 8455.6817	0.0033	973.2885 1688
R(18)	2921 8430.6909	0.0033	974.6219 3965
R(20)	2925 7658.5324	0.0032	975.9304 3960
R(22)	2929 6136.3740	0.0032	977.2139 2224
R(24)	2933 3861.1629	0.0032	978.4722 8575
R(26)	2937 0829.6231	0.0031	979.7054 2084
R(28)	2940 7038.2525	0.0031	980.9132 1071
R(30)	2944 2483.3197	0.0031	982.0955 3089
R(32)	2947 7160.8609	0.0031	983.2522 4916
R(34)	2951 1066.6762	0.0031	984.3832 2542
R(36)	2954 4196.3256	0.0032	985.4883 1157
R(38)	2957 6545.1250	0.0033	986.5673 5137
R(40)	2960 8108.1417	0.0033	987.6201 8028
R(42)	2963 8880.1900	0.0034	988.6466 2533
R(44)	2966 8855.8259	0.0035	989.6465 0491
R(46)	2969 8029.3420	0.0035	990.6196 2866
R(48)	2972 6394.7621	0.0036	991.5657 9723
R(50)	2975 3945.8353	0.0045	992.4848 0211
R(52)	2978 0676.0297	0.0070	993.3764 2542
R(54)	2980 6578.5263	0.0117	994.2404 3971
R(56)	2983 1646.2123	0.0193	995.0766 0771
R(58)	2985 5871.6737	0.0307	995.8846 8212

BAND II

P(60)	3014 3456.0742	0.0172	1005.4774 6515
P(58)	3021 2223.6949	0.0110	1007.7713 0607
P(56)	3028 0322.1201	0.0072	1010.0428 2503
P(54)	3034 7743.7465	0.0051	1012.2917 6841
P(52)	3041 4481.1364	0.0042	1014.5178 8812
P(50)	3048 0527.0251	0.0039	1016.7209 4183

(continues)

TABLE 2 *(continued)*

BAND II *(continued)*

LINE	FREQUENCY (MHZ)	STD.DEV. (MHZ)	VAC.WAVE NO. (CM-1)
P(48)	3054 5874.3277	0.0038	1018.9006 9322
P(46)	3061 0516.1462	0.0039	1021.0569 1219
P(44)	3067 4445.7759	0.0039	1023.1893 7509
P(42)	3073 7656.7119	0.0039	1025.2978 6496
P(40)	3080 0142.6555	0.0039	1027.3821 7169
P(38)	3086 1897.5199	0.0038	1029.4420 9223
P(36)	3092 2915.4360	0.0038	1031.4774 3083
P(34)	3098 3190.7583	0.0038	1033.4879 9917
P(32)	3104 2718.0700	0.0038	1035.4736 1655
P(30)	3110 1492.1877	0.0037	1037.4341 1009
P(28)	3115 9508.1671	0.0037	1039.3693 1486
P(26)	3121 6761.3064	0.0037	1041.2790 7402
P(24)	3127 3247.1518	0.0038	1043.1632 3901
P(22)	3132 8961.5006	0.0038	1045.0216 6964
P(20)	3138 3900.4054	0.0038	1046.8542 3425
P(18)	3143 8060.1774	0.0037	1048.6608 0978
P(16)	3149 1437.3897	0.0037	1050.4412 8194
P(14)	3154 4028.8804	0.0037	1052.1955 4524
P(12)	3159 5831.7547	0.0037	1053.9235 0313
P(10)	3164 6843.3878	0.0037	1055.6250 6805
P(8)	3169 7061.4264	0.0037	1057.3001 6151
P(6)	3174 6483.7910	0.0037	1058.9487 1415
P(4)	3179 5108.6771	0.0037	1060.5706 6576
P(2)	3184 2934.5560	0.0037	1062.1659 6536
V(0)	3188 9960.1764	0.0037	1063.7345 7121
R(0)	3191 3172.5743	0.0037	1064.5088 5347
R(2)	3195 8996.0672	0.0036	1066.0373 6066
R(4)	3200 4017.3872	0.0036	1067.5391 1025
R(6)	3204 8236.2544	0.0036	1069.0140 9289
R(8)	3209 1652.6660	0.0036	1070.4623 0849
R(10)	3213 4266.8953	0.0036	1071.8837 6618
R(12)	3217 6079.4907	0.0036	1073.2784 8423
R(14)	3221 7091.2743	0.0037	1074.6464 9008
R(16)	3225 7303.3400	0.0037	1075.9878 2021
R(18)	3229 6717.0518	0.0037	1077.3025 2013
R(20)	3233 5334.0411	0.0038	1078.5906 4423
R(22)	3237 3156.2043	0.0039	1079.8522 5580
R(24)	3241 0185.7000	0.0039	1081.0874 2682
R(26)	3244 6424.9456	0.0039	1082.2962 3794
R(28)	3248 1876.6140	0.0040	1083.4787 7831
R(30)	3251 6543.6298	0.0040	1084.6351 4549
R(32)	3255 0429.1653	0.0039	1085.7654 4528
R(34)	3258 3536.6360	0.0039	1086.8697 9163
R(36)	3261 5869.6965	0.0039	1087.9483 0644
R(38)	3264 7432.2354	0.0038	1089.0011 1941
R(40)	3267 8228.3702	0.0038	1090.0283 6790
R(42)	3270 8262.4421	0.0038	1091.0301 9670
R(44)	3273 7539.0104	0.0038	1092.0067 5790
R(46)	3276 6062.8469	0.0039	1092.9582 1067
R(48)	3279 3838.9297	0.0043	1093.8847 2107
R(50)	3282 0872.4368	0.0055	1094.7864 6180
R(52)	3284 7168.7402	0.0081	1095.6636 1206
R(54)	3287 2733.3987	0.0127	1096.5163 5728
R(56)	3289 7572.1515	0.0199	1097.3448 8889
R(58)	3292 1690.9108	0.0305	1098.1494 0411

[a]Reproduced with permission from Bradley *et al.* [37]. © 1986 IEEE.

TABLE 3 Molecular Constants and Frequencies Calculated for 636[a]

$^{16}O\ ^{13}C\ ^{16}O$

NUMBER	SYMBOL		CONSTANTS (MHZ)	STD.DEV. (MHZ)
15	V(001-I)	=	2.738 379 258 341 D+07	4.5D-03
16	V(001-II)	=	3.050 865 923 183 D+07	4.6D-03
17	B(001)	=	1.161 016 490 148 D+04	1.1D-04
18	B(I)	=	1.168 344 168 872 D+04	1.2D-04
19	B(II)	=	1.171 936 491 647 D+04	1.2D-04
20	D(001)	=	3.984 584 753 D-03	1.4D-07
21	D(I)	=	3.604 500 429 D-03	1.5D-07
22	D(II)	=	4.747 234 294 D-03	1.5D-07
23	H(001)	=	0.495 934 D-09	7.2D-11
24	H(I)	=	6.338 964 D-09	7.6D-11
25	H(II)	=	8.203 342 D-09	7.8D-11
26	L(001)	=	-2.29 763 D-14	1.3D-14
27	L(I)	=	5.77 901 D-14	1.4D-14
28	L(II)	=	-7.93 174 D-14	1.5D-14

BAND I

LINE	FREQUENCY (MHZ)	STD.DEV. (MHZ)	VAC.WAVE NO. (CM-1)
P(60)	2572 0428.2139	0.1461	857.9411 3653
P(58)	2578 4672.4669	0.0893	860.0840 9414
P(56)	2584 8281.2715	0.0506	862.2058 5547
P(54)	2591 1259.2641	0.0254	864.3065 7519
P(52)	2597 3610.8059	0.0104	866.3863 9875
P(50)	2603 5339.9930	0.0046	868.4454 6280
P(48)	2609 6450.6662	0.0060	870.4838 9544
P(46)	2615 6946.4203	0.0071	872.5018 1658
P(44)	2621 6830.6129	0.0069	874.4993 3824
P(42)	2627 6106.3727	0.0062	876.4765 6475
P(40)	2633 4776.6070	0.0055	878.4335 9311
P(38)	2639 2844.0093	0.0050	880.3705 1317
P(36)	2645 0311.0659	0.0048	882.2874 0784
P(34)	2650 7180.0624	0.0047	884.1843 5338
P(32)	2656 3453.0895	0.0047	886.0614 1951
P(30)	2661 9132.0488	0.0046	887.9186 6968
P(28)	2667 4218.6576	0.0045	889.7561 6117
P(26)	2672 8714.4542	0.0044	891.5739 4527

(continues)

TABLE 3 *(continued)*

LINE	FREQUENCY (MHZ)	STD.DEV. (MHZ)	VAC.WAVE NO. (CM-1)
		BAND I *(continued)*	
P(24)	2678 2620.8016	0.0045	893.3720 6747
P(22)	2683 5938.8924	0.0046	895.1505 6754
P(20)	2688 8669.7518	0.0048	896.9094 7969
P(18)	2694 0814.2416	0.0049	898.6488 3264
P(16)	2699 2373.0626	0.0051	900.3686 4979
P(14)	2704 3346.7581	0.0051	902.0689 4925
P(12)	2709 3735.7157	0.0051	903.7497 4396
P(10)	2714 3540.1700	0.0051	905.4110 4173
P(8)	2719 2760.2041	0.0050	907.0528 4534
P(6)	2724 1395.7513	0.0049	908.6751 5257
P(4)	2728 9446.5964	0.0048	910.2779 5624
P(2)	2733 6912.3769	0.0046	911.8612 4425
V(0)	2738 3792.5834	0.0045	913.4249 9962
R(0)	2740 7012.8973	0.0044	914.1995 4592
R(2)	2745 3013.4681	0.0042	915.7339 5979
R(4)	2749 8426.5523	0.0041	917.2487 7723
R(6)	2754 3251.1293	0.0039	918.7439 6418
R(8)	2758 7486.0315	0.0038	920.2194 8169
R(10)	2763 1129.9444	0.0037	921.6752 8592
R(12)	2767 4181.4046	0.0037	923.1113 2806
R(14)	2771 6638.7995	0.0037	924.5275 5431
R(16)	2775 8500.3648	0.0037	925.9239 0583
R(18)	2779 9764.1836	0.0037	927.3003 1866
R(20)	2784 0428.1832	0.0037	928.6567 2369
R(22)	2788 0490.1338	0.0037	929.9930 4651
R(24)	2791 9947.6446	0.0036	931.3092 0741
R(26)	2795 8798.1618	0.0036	932.6051 2117
R(28)	2799 7038.9645	0.0036	933.8806 9704
R(30)	2803 4667.1610	0.0036	935.1358 3858
R(32)	2807 1679.6853	0.0036	936.3704 4349
R(34)	2810 8073.2921	0.0037	937.5844 0354
R(36)	2814 3844.5522	0.0037	938.7776 0434
R(38)	2817 8989.8473	0.0037	939.9499 2520
R(40)	2821 3505.3647	0.0038	941.1012 3893
R(42)	2824 7387.0908	0.0039	942.2314 1167
R(44)	2828 0630.8053	0.0047	943.3403 0262
R(46)	2831 3232.0738	0.0075	944.4277 6388
R(48)	2834 5186.2410	0.0138	945.4936 4017
R(50)	2837 6488.4223	0.0251	946.5377 6855
R(52)	2840 7133.4961	0.0432	947.5599 7818
R(54)	2843 7116.0949	0.0708	948.5600 9002
R(56)	2846 6430.5956	0.1112	949.5379 1651
R(58)	2849 5071.1098	0.1688	950.4932 6124
		BAND II	
P(60)	2872 9056.6508	0.2555	958.2981 7876
P(58)	2879 9935.4314	0.1690	960.6624 4039
P(56)	2887 0077.7355	0.1079	963.0021 3581
P(54)	2893 9475.6922	0.0660	965.3170 0248
P(52)	2900 8121.5973	0.0383	967.6067 8340
P(50)	2907 6007.9210	0.0208	969.8712 2741
P(48)	2914 3127.3153	0.0108	972.1100 8942
P(46)	2920 9472.6220	0.0060	974.3231 3064
P(44)	2927 5036.8795	0.0046	976.5101 1886

(continues)

TABLE 3 *(continued)*

BAND II *(continued)*

LINE	FREQUENCY (MHZ)	STD.DEV. (MHZ)	VAC.WAVE NO. (CM-1)
P(42)	2933 9813.3301	0.0042	978.6708 2867
P(40)	2940 3795.4270	0.0040	980.8050 4170
P(38)	2946 6976.8409	0.0037	982.9125 4682
P(36)	2952 9351.4664	0.0036	984.9931 4037
P(34)	2959 0913.4284	0.0035	987.0466 2638
P(32)	2965 1657.0881	0.0034	989.0728 1677
P(30)	2971 1577.0489	0.0034	991.0715 3152
P(28)	2977 0668.1613	0.0035	993.0425 9887
P(26)	2982 8925.5288	0.0037	994.9858 5548
P(24)	2988 6344.5126	0.0039	996.9011 4661
P(22)	2994 2920.7360	0.0043	998.7883 2629
P(20)	2999 8650.0890	0.0046	1000.6472 5741
P(18)	3005 3528.7321	0.0048	1002.4778 1190
P(16)	3010 7553.1003	0.0050	1004.2798 7085
P(14)	3016 0719.9062	0.0050	1006.0533 2460
P(12)	3021 3026.1432	0.0050	1007.7980 7286
P(10)	3026 4469.0880	0.0050	1009.5140 2480
P(8)	3031 5046.3034	0.0049	1011.2010 9911
P(6)	3036 4755.6398	0.0048	1012.8592 2409
P(4)	3041 3595.2374	0.0048	1014.4883 3771
P(2)	3046 1563.5271	0.0047	1016.0883 8762
V(0)	3050 8659.2318	0.0046	1017.6593 3124
R(0)	3053 1879.5457	0.0046	1018.4338 7754
R(2)	3057 7664.6183	0.0045	1019.9611 0317
R(4)	3062 2575.1933	0.0044	1021.4591 5870
R(6)	3066 6611.0178	0.0042	1022.9280 3569
R(8)	3070 9772.1308	0.0041	1024.3677 3546
R(10)	3075 2058.8624	0.0041	1025.7782 6899
R(12)	3079 3471.8321	0.0040	1027.1596 5697
R(14)	3083 4011.9476	0.0040	1028.5119 2966
R(16)	3087 3680.4026	0.0040	1029.8351 2689
R(18)	3091 2478.6741	0.0040	1031.1292 9793
R(20)	3095 0408.5204	0.0040	1032.3945 0141
R(22)	3098 7471.9774	0.0040	1033.6308 0526
R(24)	3102 3671.3557	0.0039	1034.8382 8655
R(26)	3105 9009.2365	0.0039	1036.0170 3137
R(28)	3109 3488.4681	0.0040	1037.1671 3474
R(30)	3112 7112.1611	0.0040	1038.2887 0042
R(32)	3115 9883.6840	0.0040	1039.3818 4075
R(34)	3119 1806.6581	0.0041	1040.4466 7655
R(36)	3122 2884.9526	0.0041	1041.4833 3687
R(38)	3125 3122.6789	0.0043	1042.4919 5885
R(40)	3128 2524.1847	0.0047	1043.4726 8752
R(42)	3131 1094.0483	0.0054	1044.4256 7559
R(44)	3133 8837.0719	0.0071	1045.3510 8324
R(46)	3136 5758.2755	0.0112	1046.2490 7794
R(48)	3139 1862.8900	0.0193	1047.1198 3415
R(50)	3141 7156.3502	0.0332	1047.9635 3316
R(52)	3144 1644.2875	0.0555	1048.7803 6283
R(54)	3146 5332.5230	0.0892	1049.5705 1732
R(56)	3148 8227.0596	0.1386	1050.3341 9685
R(58)	3151 0334.0742	0.2089	1051.0716 0749

[a]Reproduced with permission from Bradley *et al.* [37]. © 1986 IEEE.

TABLE 4 Molecular Constants and Frequencies Calculated for 628[a]

16 12 18
O C O

NUMBER	SYMBOL		CONSTANTS (MHZ)	STD.DEV. (MHZ)
29	V(001-I)	=	2.896 801 233 901 D+07	1.0D-02
30	V(001-II)	=	3.215 835 064 653 D+07	2.3D-02
31	B(001)	=	1.095 102 264 016 D+04	2.8D-04
32	B(I)	=	1.104 772 438 281 D+04	3.0D-04
33	B(II)	=	1.103 600 443 963 D+04	2.8D-04
34	D(001)	=	3.550 909 355 D-03	5.2D-07
35	D(I)	=	3.064 795 497 D-03	5.5D-07
36	D(II)	=	4.096 110 317 D-03	6.3D-07
37	H(001)	=	0.074 060 D-09	4.0D-10
38	H(I)	=	2.945 673 D-09	4.2D-10
39	H(II)	=	4.419 934 D-09	6.2D-10
40	L(001)	=	5.56 243 D-14	1.1D-13
41	L(I)	=	7.69 066 D-14	1.1D-13
42	L(II)	=	64.89 108 D-14	2.1D-13

BAND I

LINE	FREQUENCY (MHZ)	STD.DEV. (MHZ)	VAC.WAVE NO. (CM-1)
P(60)	2729 6371.2432	2.7312	910.5089 3759
P(59)	2733 0160.6851	2.2947	911.6360 3206
P(58)	2736 3739.9515	1.9182	912.7561 1582
P(57)	2739 7109.7225	1.5948	913.8692 1156
P(56)	2743 0270.6628	1.3182	914.9753 4147
P(55)	2746 3223.4212	1.0828	916.0745 2717
P(54)	2749 5968.6313	0.8834	917.1667 8981
P(53)	2752 8506.9114	0.7153	918.2521 5000
P(52)	2756 0838.8646	0.5746	919.3306 2788
P(51)	2759 2965.0793	0.4575	920.4022 4305
P(50)	2762 4886.1287	0.3606	921.4670 1465
P(49)	2765 6602.5715	0.2812	922.5249 6130
P(48)	2768 8114.9518	0.2165	923.5761 0116
P(47)	2771 9423.7991	0.1644	924.6204 5190
P(46)	2775 0529.6287	0.1229	925.6580 3069
P(45)	2778 1432.9417	0.0901	926.6888 5425
P(44)	2781 2134.2250	0.0647	927.7129 3883
P(43)	2784 2633.9515	0.0453	928.7303 0020

(continues)

TABLE 4 *(continued)*

BAND I *(continued)*

LINE	FREQUENCY (MHZ)	STD.DEV. (MHZ)	VAC.WAVE NO. (CM-1)
P(42)	2787 2932.5802	0.0308	929.7409 5366
P(41)	2790 3030.5565	0.0203	930.7449 1409
P(40)	2793 2928.3119	0.0130	931.7421 9586
P(39)	2796 2626.2643	0.0084	932.7328 1292
P(38)	2799 2124.8184	0.0059	933.7167 7877
P(37)	2802 1424.3652	0.0050	934.6941 0645
P(36)	2805 0525.2826	0.0048	935.6648 0857
P(35)	2807 9427.9351	0.0047	936.6288 9729
P(34)	2810 8132.6743	0.0045	937.5863 8432
P(33)	2813 6639.8385	0.0044	938.5372 8096
P(32)	2816 4949.7533	0.0043	939.4815 9808
P(31)	2819 3062.7312	0.0042	940.4193 4608
P(30)	2822 0979.0720	0.0041	941.3505 3498
P(29)	2824 8699.0627	0.0041	942.2751 7434
P(28)	2827 6222.9778	0.0041	943.1932 7332
P(27)	2830 3551.0789	0.0041	944.1048 4065
P(26)	2833 0683.6152	0.0041	945.0098 8464
P(25)	2835 7620.8235	0.0040	945.9084 1320
P(24)	2838 4362.9282	0.0040	946.8004 3379
P(23)	2841 0910.1411	0.0040	947.6859 5350
P(22)	2843 7262.6619	0.0039	948.5649 7897
P(21)	2846 3420.6781	0.0039	949.4375 1647
P(20)	2848 9384.3647	0.0040	950.3035 7184
P(19)	2851 5153.8849	0.0040	951.1631 5050
P(18)	2854 0729.3895	0.0039	952.0162 5751
P(17)	2856 6111.0174	0.0039	952.8628 9749
P(16)	2859 1298.8955	0.0039	953.7030 7466
P(15)	2861 6293.1385	0.0039	954.5367 9287
P(14)	2864 1093.8494	0.0039	955.3640 5553
P(13)	2866 5701.1190	0.0040	956.1848 6570
P(12)	2869 0115.0266	0.0041	956.9992 2600
P(11)	2871 4335.6392	0.0044	957.8071 3867
P(10)	2873 8363.0123	0.0047	958.6086 0557
P(9)	2876 2197.1895	0.0052	959.4036 2814
P(8)	2878 5838.2025	0.0057	960.1922 0745
P(7)	2880 9286.0713	0.0063	960.9743 4417
P(6)	2883 2540.8044	0.0069	961.7500 3857
P(5)	2885 5602.3982	0.0075	962.5192 9054
P(4)	2887 8470.8376	0.0081	963.2820 9957
P(3)	2890 1146.0958	0.0087	964.0384 6476
P(2)	2892 3628.1341	0.0093	964.7883 8484
P(1)	2894 5916.9025	0.0097	965.5318 5813
V(0)	2896 8012.3390	0.0101	966.2688 8256
R(0)	2898 9914.3701	0.0104	966.9994 5567
R(1)	2901 1622.9105	0.0106	967.7235 7464
R(2)	2903 3137.8634	0.0108	968.4412 3622
R(3)	2905 4459.1202	0.0108	969.1524 3679
R(4)	2907 5586.5606	0.0108	969.8571 7235
R(5)	2909 6520.0529	0.0107	970.5554 3848
R(6)	2911 7259.4532	0.0105	971.2472 3042
R(7)	2913 7804.6065	0.0103	971.9325 4296

(continues)

TABLE 4 *(continued)*

BAND I *(continued)*

LINE	FREQUENCY (MHZ)	STD.DEV. (MHZ)	VAC.WAVE NO. (CM-1)
R(8)	2915 8155.3456	0.0100	972.6113 7055
R(9)	2917 8311.4918	0.0096	973.2837 0722
R(10)	2919 8272.8546	0.0093	973.9495 4661
R(11)	2921 8039.2319	0.0089	974.6088 8199
R(12)	2923 7610.4096	0.0084	975.2617 0620
R(13)	2925 6986.1619	0.0080	975.9080 1173
R(14)	2927 6166.2511	0.0075	976.5477 9064
R(15)	2929 5150.4278	0.0071	977.1810 3461
R(16)	2931 3938.4306	0.0066	977.8077 3493
R(17)	2933 2529.9861	0.0062	978.4278 8247
R(18)	2935 0924.8091	0.0057	979.0414 6772
R(19)	2936 9122.6024	0.0053	979.6484 8076
R(20)	2938 7123.0568	0.0050	980.2489 1129
R(21)	2940 4925.8509	0.0047	980.8427 4858
R(22)	2942 2530.6513	0.0044	981.4299 8152
R(23)	2943 9937.1125	0.0043	982.0105 9856
R(24)	2945 7144.8766	0.0041	982.5845 8779
R(25)	2947 4153.5738	0.0041	983.1519 3686
R(26)	2949 0962.8216	0.0040	983.7126 3301
R(27)	2950 7572.2255	0.0040	984.2666 6309
R(28)	2952 3981.3785	0.0039	984.8140 1352
R(29)	2954 0189.8609	0.0039	985.3546 7029
R(30)	2955 6197.2409	0.0039	985.8886 1901
R(31)	2957 2003.0737	0.0040	986.4158 4485
R(32)	2958 7606.9022	0.0042	986.9363 3254
R(33)	2960 3008.2564	0.0044	987.4500 6642
R(34)	2961 8206.6535	0.0047	987.9570 3038
R(35)	2963 3201.5979	0.0049	988.4572 0788
R(36)	2964 7992.5812	0.0052	988.9505 8198
R(37)	2966 2579.0817	0.0058	989.4371 3526
R(38)	2967 6960.5648	0.0074	989.9168 4990
R(39)	2969 1136.4828	0.0109	990.3897 0763
R(40)	2970 5106.2746	0.0168	990.8556 8972
R(41)	2971 8869.3657	0.0256	991.3147 7703
R(42)	2973 2425.1684	0.0381	991.7669 4994
R(43)	2974 5773.0814	0.0549	992.2121 8839
R(44)	2975 8912.4896	0.0772	992.6504 7187
R(45)	2977 1842.7644	0.1060	993.0817 7941
R(46)	2978 4563.2633	0.1428	993.5060 8958
R(47)	2979 7073.3299	0.1892	993.9233 8048
R(48)	2980 9372.2936	0.2469	994.3336 2975
R(49)	2982 1459.4700	0.3181	994.7368 1456
R(50)	2983 3334.1601	0.4052	995.1329 1159
R(51)	2984 4995.6509	0.5108	995.5218 9705
R(52)	2985 6443.2145	0.6381	995.9037 4667
R(53)	2986 7676.1087	0.7903	996.2784 3569
R(54)	2987 8693.5765	0.9714	996.6459 3886
R(55)	2988 9494.8460	1.1856	997.0062 3042
R(56)	2990 0079.1304	1.4377	997.3592 8415
R(57)	2991 0445.6275	1.7331	997.7050 7327
R(58)	2992 0593.5203	2.0776	998.0435 7054
R(59)	2993 0521.9760	2.4777	998.3747 4817

(continues)

TABLE 4 *(continued)*

BAND II

LINE	FREQUENCY (MHZ)	STD.DEV. (MHZ)	VAC.WAVE NO. (CM-1)
P(60)	3054 3244.7021	15.2104	1018.8129 7835
P(59)	3057 4756.3872	12.8533	1019.8640 9502
P(58)	3060 6123.1746	10.8119	1020.9103 7843
P(57)	3063 7344.4579	9.0504	1021.9518 0834
P(56)	3066 8419.6268	7.5364	1022.9883 6440
P(55)	3069 9348.0678	6.2405	1024.0200 2614
P(54)	3073 0129.1655	5.1363	1025.0467 7304
P(53)	3076 0762.3030	4.1999	1026.0685 8452
P(52)	3079 1246.8631	3.4099	1027.0854 3999
P(51)	3082 1582.2290	2.7471	1028.0973 1888
P(50)	3085 1767.7849	2.1943	1029.1042 0064
P(49)	3088 1802.9170	1.7363	1030.1060 6481
P(48)	3091 1687.0141	1.3596	1031.1028 9099
P(47)	3094 1419.4680	1.0521	1032.0946 5890
P(46)	3097 0999.6746	0.8032	1033.0813 4838
P(45)	3100 0427.0340	0.6039	1034.0629 3943
P(44)	3102 9700.9514	0.4459	1035.0394 1221
P(43)	3105 8820.8376	0.3222	1036.0107 4706
P(42)	3108 7786.1094	0.2268	1036.9769 2453
P(41)	3111 6596.1900	0.1545	1037.9379 2538
P(40)	3114 5250.5098	0.1008	1038.8937 3060
P(39)	3117 3748.5064	0.0620	1039.8443 2145
P(38)	3120 2089.6253	0.0350	1040.7896 7942
P(37)	3123 0273.3202	0.0177	1041.7297 8628
P(36)	3125 8299.0533	0.0093	1042.6646 2411
P(35)	3128 6166.2956	0.0090	1043.5941 7526
P(34)	3131 3874.5277	0.0104	1044.5184 2240
P(33)	3134 1423.2391	0.0107	1045.4373 4850
P(32)	3136 8811.9297	0.0101	1046.3509 3688
P(31)	3139 6040.1090	0.0088	1047.2591 7118
P(30)	3142 3107.2971	0.0075	1048.1620 3539
P(29)	3145 0013.0245	0.0065	1049.0595 1385
P(28)	3147 6756.8324	0.0058	1049.9515 9126
P(27)	3150 3338.2731	0.0055	1050.8382 5268
P(26)	3152 9756.9100	0.0054	1051.7194 8355
P(25)	3155 6012.3177	0.0053	1052.5952 6968
P(24)	3158 2104.0824	0.0052	1053.4655 9727
P(23)	3160 8031.8019	0.0050	1054.3304 5290
P(22)	3163 3795.0859	0.0049	1055.1898 2355
P(21)	3165 9393.5558	0.0048	1056.0436 9660
P(20)	3168 4826.8453	0.0048	1056.8920 5981
P(19)	3171 0094.5998	0.0050	1057.7349 0138
P(18)	3173 5196.4775	0.0052	1058.5722 0989
P(17)	3176 0132.1485	0.0056	1059.4039 7435
P(16)	3178 4901.2955	0.0060	1060.2301 8416
P(15)	3180 9503.6138	0.0065	1061.0508 2917
P(14)	3183 3938.8112	0.0071	1061.8658 9961
P(13)	3185 8206.6080	0.0079	1062.6753 8618
P(12)	3188 2306.7374	0.0090	1063.4792 7997
P(11)	3190 6238.9453	0.0102	1064.2775 7250
P(10)	3193 0002.9904	0.0116	1065.0702 5572
P(9)	3195 3598.6444	0.0132	1065.8573 2201

(continues)

TABLE 4 *(continued)*

BAND II *(continued)*

LINE	FREQUENCY (MHZ)	STD.DEV. (MHZ)	VAC.WAVE NO. (CM-1)
P(8)	3197 7025.6917	0.0148	1066.6387 6420
P(7)	3200 0283.9296	0.0164	1067.4145 7551
P(6)	3202 3373.1687	0.0180	1068.1847 4962
P(5)	3204 6293.2322	0.0195	1068.9492 8064
P(4)	3206 9043.9565	0.0208	1069.7081 6312
P(3)	3209 1625.1911	0.0218	1070.4613 9203
P(2)	3211 4036.7984	0.0226	1071.2089 6278
P(1)	3213 6278.6540	0.0230	1071.9508 7123
V(0)	3215 8350.6465	0.0231	1072.6871 1365
R(0)	3218 0252.6776	0.0228	1073.4176 8677
R(1)	3220 1984.6620	0.0222	1074.1425 8774
R(2)	3222 3546.5277	0.0213	1074.8618 1416
R(3)	3224 4938.2155	0.0201	1075.5753 6406
R(4)	3226 6159.6795	0.0186	1076.2832 3590
R(5)	3228 7210.8868	0.0169	1076.9854 2859
R(6)	3230 8091.8175	0.0150	1077.6819 4147
R(7)	3232 8802.4647	0.0131	1078.3727 7430
R(8)	3234 9342.8347	0.0112	1079.0579 2729
R(9)	3236 9712.9467	0.0094	1079.7374 0109
R(10)	3238 9912.8328	0.0078	1080.4111 9676
R(11)	3240 9942.5380	0.0065	1081.0793 1581
R(12)	3242 9802.1204	0.0056	1081.7417 6018
R(13)	3244 9491.6508	0.0051	1082.3985 3222
R(14)	3246 9011.2129	0.0050	1083.0496 3472
R(15)	3248 8360.9032	0.0051	1083.6950 7091
R(16)	3250 7540.8306	0.0052	1084.3348 4443
R(17)	3252 6551.1172	0.0052	1084.9689 5933
R(18)	3254 5391.8971	0.0052	1085.5974 2010
R(19)	3256 4063.3174	0.0051	1086.2202 3164
R(20)	3258 2565.5374	0.0050	1086.8373 9927
R(21)	3260 0898.7287	0.0049	1087.4489 2871
R(22)	3261 9063.0753	0.0050	1088.0548 2609
R(23)	3263 7058.7733	0.0051	1088.6550 9797
R(24)	3265 4886.0308	0.0053	1089.2497 5127
R(25)	3267 2545.0679	0.0055	1089.8387 9334
R(26)	3269 0036.1164	0.0056	1090.4222 3192
R(27)	3270 7359.4198	0.0057	1091.0000 7512
R(28)	3272 4515.2331	0.0061	1091.5723 3145
R(29)	3274 1503.8227	0.0068	1092.1390 0980
R(30)	3275 8325.4660	0.0079	1092.7001 1943
R(31)	3277 4980.4516	0.0093	1093.2556 6995
R(32)	3279 1469.0786	0.0106	1093.8056 7134
R(33)	3280 7791.6570	0.0114	1094.3501 3395
R(34)	3282 3948.5069	0.0113	1094.8890 6845
R(35)	3283 9939.9585	0.0101	1095.4224 8586
R(36)	3285 5766.3518	0.0106	1095.9503 9752
R(37)	3287 1428.0366	0.0187	1096.4728 1509
R(38)	3288 6925.3717	0.0360	1096.9897 5055
R(39)	3290 2258.7249	0.0634	1097.5012 1615
R(40)	3291 7428.4725	0.1029	1098.0072 2447
R(41)	3293 2434.9992	0.1577	1098.5077 8832
R(42)	3294 7278.6976	0.2316	1099.0029 2080
R(43)	3296 1959.9675	0.3291	1099.4926 3525

(continues)

TABLE 4 *(continued)*

BAND II *(continued)*

LINE	FREQUENCY (MHZ)	STD.DEV. (MHZ)	VAC.WAVE NO. (CM-1)
R(44)	3297 6479.2160	0.4554	1099.9769 4525
R(45)	3299 0836.8567	0.6169	1100.4558 6459
R(46)	3300 5033.3092	0.8207	1100.9294 0728
R(47)	3301 9068.9988	1.0750	1101.3975 8749
R(48)	3303 2944.3560	1.3893	1101.8604 1958
R(49)	3304 6659.8155	1.7743	1102.3179 1807
R(50)	3306 0215.8163	2.2423	1102.7700 9758
R(51)	3307 3612.8006	2.8069	1103.2169 7288
R(52)	3308 6851.2130	3.4839	1103.6585 5878
R(53)	3309 9931.5003	4.2906	1104.0948 7020
R(54)	3311 2854.1107	5.2465	1104.5259 2209
R(55)	3312 5619.4927	6.3736	1104.9517 2939
R(56)	3313 8228.0944	7.6959	1105.3723 0708
R(57)	3315 0680.3629	9.2405	1105.7876 7005
R(58)	3316 2976.7434	11.0373	1106.1978 3315
R(59)	3317 5117.6781	13.1190	1106.6028 1114

TABLE 5 Molecular Constants and Frequencies Calculated for 828[a]

$^{18}O\ ^{12}C\ ^{18}O$

NUMBER	SYMBOL		CONSTANTS (MHZ)	STD.DEV. (MHZ)
43	V(001-I)	=	2.898 859 706 882 D+07	3.6D-03
44	V(001-II)	=	3.248 919 295 228 D+07	3.9D-03
45	B(001)	=	1.031 555 954 654 D+04	3.7D-05
46	B(I)	=	1.041 489 423 454 D+04	3.4D-05
47	B(II)	=	1.038 852 773 874 D+04	3.6D-05

(continues)

TABLE 5 *(continued)*

$^{18}O\ ^{12}C\ ^{18}O$

NUMBER	SYMBOL		CONSTANTS (MHZ)	STD.DEV. (MHZ)
48	D(001)	=	3.150 554 563 D-03	5.9D-08
49	D(I)	=	2.768 029 928 D-03	5.4D-08
50	D(II)	=	3.518 236 015 D-03	5.8D-08
51	H(001)	=	0.267 825 D-09	3.9D-11
52	H(I)	=	2.501 922 D-09	3.5D-11
53	H(II)	=	4.744 762 D-09	3.7D-11
54	L(001)	=	0.52 648 D-14	9.2D-15
55	L(I)	=	-0.28 458 D-14	7.8D-15
56	L(II)	=	-3.21 944 D-14	8.3D-15

BAND I

LINE	FREQUENCY (MHZ)	STD.DEV. (MHZ)	VAC.WAVE NO. (CM-1)
P(60)	2738 4653.4520	0.0476	913.4537 1510
P(58)	2744 9958.7473	0.0308	915.6320 6528
P(56)	2751 4420.9601	0.0193	917.7822 9325
P(54)	2757 8044.1062	0.0117	919.9045 3296
P(52)	2764 0832.0154	0.0071	921.9989 1218
P(50)	2770 2788.3340	0.0047	924.0655 5251
P(48)	2776 3916.5272	0.0038	926.1045 6955
P(46)	2782 4219.8818	0.0036	928.1160 7295
P(44)	2788 3701.5085	0.0036	930.1001 6644
P(42)	2794 2364.3439	0.0035	932.0569 4801
P(40)	2800 0211.1532	0.0035	933.9865 0987
P(38)	2805 7244.5316	0.0035	935.8889 3859
P(36)	2811 3466.9070	0.0036	937.7643 1517
P(34)	2816 8880.5416	0.0036	939.6127 1506
P(32)	2822 3487.5337	0.0036	941.4342 0825
P(30)	2827 7289.8196	0.0036	943.2288 5933
P(28)	2833 0289.1753	0.0036	944.9967 2755
P(26)	2838 2487.2180	0.0036	946.7378 6683
P(24)	2843 3885.4075	0.0035	948.4523 2589
P(22)	2848 4485.0477	0.0035	950.1401 4821
P(20)	2853 4287.2879	0.0035	951.8013 7213

(continues)

TABLE 5 *(continued)*

BAND I *(continued)*

LINE	FREQUENCY (MHZ)	STD.DEV. (MHZ)	VAC.WAVE NO. (CM-1)
P(18)	2858 3293.1241	0.0035	953.4360 3087
P(16)	2863 1503.3996	0.0035	955.0441 5256
P(14)	2867 8918.8066	0.0036	956.6257 6030
P(12)	2872 5539.8870	0.0036	958.1808 7215
P(10)	2877 1367.0327	0.0036	959.7095 0119
P(8)	2881 6400.4870	0.0036	961.2116 5553
P(6)	2886 0640.3445	0.0036	962.6873 3834
P(4)	2890 4086.5522	0.0036	964.1365 4783
P(2)	2894 6738.9096	0.0036	965.5592 7733
V(0)	2898 8597.0688	0.0036	966.9555 1523
R(0)	2900 9228.1753	0.0035	967.6436 9487
R(2)	2904 9894.0639	0.0035	969.0001 6290
R(4)	2908 9764.2422	0.0034	970.3300 8890
R(6)	2912 8837.8481	0.0034	971.6334 4410
R(8)	2916 7113.8724	0.0033	972.9101 9484
R(10)	2920 4591.1584	0.0033	974.1603 0254
R(12)	2924 1268.4016	0.0032	975.3837 2368
R(14)	2927 7144.1495	0.0032	976.5804 0982
R(16)	2931 2216.8003	0.0032	977.7503 0752
R(18)	2934 6484.6028	0.0032	978.8933 5838
R(20)	2937 9945.6557	0.0031	980.0094 9896
R(22)	2941 2597.9062	0.0031	981.0986 6080
R(24)	2944 4439.1493	0.0031	982.1607 7034
R(26)	2947 5467.0268	0.0031	983.1957 4893
R(28)	2950 5679.0262	0.0032	984.2035 1276
R(30)	2953 5072.4789	0.0032	985.1839 7280
R(32)	2956 3644.5594	0.0032	986.1370 3482
R(34)	2959 1392.2837	0.0033	987.0625 9928
R(36)	2961 8312.5075	0.0034	987.9605 6129
R(38)	2964 4401.9249	0.0035	988.8308 1058
R(40)	2966 9657.0662	0.0038	989.6732 3141
R(42)	2969 4074.2966	0.0045	990.4877 0255
R(44)	2971 7649.8141	0.0063	991.2740 9717
R(46)	2974 0379.6472	0.0100	992.0322 8279
R(48)	2976 2259.6531	0.0162	992.7621 2122
R(50)	2978 3285.5157	0.0260	993.4634 6851
R(52)	2980 3452.7430	0.0404	994.1361 7480
R(54)	2982 2756.6650	0.0610	994.7800 8433
R(56)	2984 1192.4311	0.0898	995.3950 3529
R(58)	2985 8755.0078	0.1292	995.9808 5979

BAND II

P(60)	3099 1695.4754	0.0052	1033.7716 8599
P(58)	3104 9479.9052	0.0041	1035.6991 6710
P(56)	3110 6752.5492	0.0039	1037.6095 7686
P(54)	3116 3509.5006	0.0038	1039.5027 8498
P(52)	3121 9746.9218	0.0038	1041.3786 6343
P(50)	3127 5461.0484	0.0038	1043.2370 8665
P(48)	3133 0648.1932	0.0038	1045.0779 3166
P(46)	3138 5304.7512	0.0038	1046.9010 7818

(continues)

TABLE 5 *(continued)*

BAND II *(continued)*

LINE	FREQUENCY (MHZ)	STD.DEV. (MHZ)	VAC.WAVE NO. (CM-1)
P(44)	3143 9427.2028	0.0038	1048.7064 0885
P(42)	3149 3012.1187	0.0038	1050.4938 0924
P(40)	3154 6056.1633	0.0038	1052.2631 6812
P(38)	3159 8556.0987	0.0037	1054.0143 7746
P(36)	3165 0508.7885	0.0037	1055.7473 3266
P(34)	3170 1911.2012	0.0037	1057.4619 3259
P(32)	3175 2760.4139	0.0037	1059.1580 7975
P(30)	3180 3053.6153	0.0037	1060.8356 8037
P(28)	3185 2788.1092	0.0037	1062.4946 4452
P(26)	3190 1961.3173	0.0037	1064.1348 8618
P(24)	3195 0570.7820	0.0037	1065.7563 2339
P(22)	3199 8614.1691	0.0037	1067.3588 7829
P(20)	3204 6089.2707	0.0037	1068.9424 7722
P(18)	3209 2994.0069	0.0037	1070.5070 5081
P(16)	3213 9326.4282	0.0037	1072.0525 3403
P(14)	3218 5084.7176	0.0037	1073.5788 6627
P(12)	3223 0267.1923	0.0037	1075.0859 9140
P(10)	3227 4872.3053	0.0038	1076.5738 5781
P(8)	3231 8898.6464	0.0038	1078.0424 1848
P(6)	3236 2344.9440	0.0038	1079.4916 3097
P(4)	3240 5210.0656	0.0039	1080.9214 5753
P(2)	3244 7493.0190	0.0039	1082.3318 6503
V(0)	3248 9192.9523	0.0039	1083.7228 2508
R(0)	3250 9824.0588	0.0039	1084.4110 0472
R(2)	3255 0648.1734	0.0039	1085.7727 5061
R(4)	3259 0887.7557	0.0039	1087.1149 9859
R(6)	3263 0542.4476	0.0039	1088.4377 3674
R(8)	3266 9612.0317	0.0039	1089.7409 5778
R(10)	3270 8096.4309	0.0039	1091.0246 5916
R(12)	3274 5995.7070	0.0039	1092.2888 4294
R(14)	3278 3310.0604	0.0039	1093.5335 1579
R(16)	3282 0039.8288	0.0039	1094.7586 8899
R(18)	3285 6185.4856	0.0039	1095.9643 7832
R(20)	3289 1747.6385	0.0040	1097.1506 0405
R(22)	3292 6727.0276	0.0040	1098.3173 9088
R(24)	3296 1124.5237	0.0040	1099.4647 6785
R(26)	3299 4941.1261	0.0040	1100.5927 6828
R(28)	3302 8177.9601	0.0040	1101.7014 2973
R(30)	3306 0836.2746	0.0040	1102.7907 9384
R(32)	3309 2917.4396	0.0040	1103.8609 0632
R(34)	3312 4422.9433	0.0041	1104.9118 1680
R(36)	3315 5354.3890	0.0041	1105.9435 7877
R(38)	3318 5713.4920	0.0042	1106.9562 4945
R(40)	3321 5502.0763	0.0044	1107.9498 8966
R(42)	3324 4722.0714	0.0051	1108.9245 6379
R(44)	3327 3375.5084	0.0069	1109.8803 3957
R(46)	3330 1464.5166	0.0104	1110.8172 8802
R(48)	3332 8991.3192	0.0163	1111.7354 8333

(continues)

TABLE 5 *(continued)*

BAND II *(continued)*

LINE	FREQUENCY (MHZ)	STD.DEV. (MHZ)	VAC.WAVE NO. (CM-1)
R(50)	3335 5958.2301	0.0252	1112.6350 0265
R(52)	3338 2367.6494	0.0382	1113.5159 2605
R(54)	3340 8222.0593	0.0564	1114.3783 3634
R(56)	3343 3524.0201	0.0812	1115.2223 1891
R(58)	3345 8276.1658	0.1145	1116.0479 6161

[a]Reproduced with permission from Bradley *et al.* [37]. © 1986 IEEE.

TABLE 6 Molecular Constants and Frequencies Calculated for 838[a]

$^{18}O\ ^{13}C\ ^{18}O$

NUMBER	SYMBOL		CONSTANTS (MHZ)	STD.DEV. (MHZ)
57	V(001-I)	=	2.783 855 114 188 D+07	3.8D-03
58	V(001-II)	=	3.078 588 436 561 D+07	4.1D-03
59	B(001)	=	1.031 909 579 289 D+04	4.3D-05
60	B(I)	=	1.040 347 357 162 D+04	4.5D-05
61	B(II)	=	1.039 898 242 205 D+04	4.2D-05
62	D(001)	=	3.148 155 581 D-03	7.2D-08
63	D(I)	=	2.717 913 129 D-03	7.5D-08
64	D(II)	=	3.657 050 669 D-03	6.7D-08
65	H(001)	=	0.317 872 D-09	3.9D-11
66	H(I)	=	3.111 016 D-09	4.2D-11
67	H(II)	=	5.173 276 D-09	3.6D-11
68	L(001)	=	-0.13 805 D-14	6.7D-15
69	L(I)	=	0.34 339 D-14	7.5D-15
70	L(II)	=	-1.95 866 D-14	6.0D-15

(continues)

TABLE 6 *(continued)*

BAND I

LINE	FREQUENCY (MHZ)	STD.DEV. (MHZ)	VAC.WAVE NO. (CM-1)
P(60)	2628 8254.3691	0.1107	876.8817 7830
P(58)	2635 0100.2532	0.0715	878.9447 3493
P(56)	2641 1213.9553	0.0444	880.9832 6861
P(54)	2647 1600.1418	0.0263	882.9975 3498
P(52)	2653 1263.2613	0.0148	884.9876 8242
P(50)	2659 0207.5479	0.0083	886.9538 5218
P(48)	2664 8437.0249	0.0053	888.8961 7847
P(46)	2670 5955.5086	0.0046	890.8147 8856
P(44)	2676 2766.6111	0.0045	892.7098 0296
P(42)	2681 8873.7438	0.0046	894.5813 3546
P(40)	2687 4280.1203	0.0048	896.4294 9324
P(38)	2692 8988.7594	0.0050	898.2543 7701
P(36)	2698 3002.4878	0.0051	900.0560 8106
P(34)	2703 6323.9427	0.0052	901.8346 9334
P(32)	2708 8955.5742	0.0052	903.5902 9560
P(30)	2714 0899.6478	0.0051	905.3229 6339
P(28)	2719 2158.2464	0.0049	907.0327 6620
P(26)	2724 2733.2727	0.0048	908.7197 6748
P(24)	2729 2626.4506	0.0046	910.3840 2476
P(22)	2734 1839.3276	0.0044	912.0255 8964
P(20)	2739 0373.2761	0.0042	913.6445 0790
P(18)	2743 8229.4949	0.0041	915.2408 1953
P(16)	2748 5409.0108	0.0039	916.8145 5878
P(14)	2753 1912.6797	0.0038	918.3657 5421
P(12)	2757 7741.1880	0.0038	919.8944 2870
P(10)	2762 2895.0531	0.0037	921.4005 9952
P(8)	2766 7374.6251	0.0037	922.8842 7833
P(6)	2771 1180.0865	0.0038	924.3454 7124
P(4)	2775 4311.4538	0.0038	925.7841 7879
P(2)	2779 6768.5773	0.0038	927.2003 9599
V(0)	2783 8551.1419	0.0038	928.5941 1233
R(0)	2785 9189.3209	0.0038	929.2825 2788
R(2)	2789 9959.0945	0.0038	930.6424 6114
R(4)	2794 0052.7980	0.0037	931.9798 4314
R(6)	2797 9469.5379	0.0037	933.2946 4405
R(8)	2801 8208.2548	0.0036	934.5868 2856
R(10)	2805 6267.7235	0.0036	935.8563 5578
R(12)	2809 3646.5527	0.0036	937.1031 7932
R(14)	2813 0343.1839	0.0036	938.3272 4718
R(16)	2816 6355.8909	0.0037	939.5285 0178
R(18)	2820 1682.7789	0.0037	940.7068 7992
R(20)	2823 6321.7838	0.0037	941.8623 1275
R(22)	2827 0270.6704	0.0037	942.9947 2572
R(24)	2830 3527.0319	0.0037	944.1040 3853
R(26)	2833 6088.2880	0.0037	945.1901 6513
R(28)	2836 7951.6837	0.0037	946.2530 1360
R(30)	2839 9114.2873	0.0037	947.2924 8617
R(32)	2842 9572.9890	0.0037	948.3084 7909
R(34)	2845 9324.4986	0.0037	949.3008 8263

(continues)

TABLE 6 *(continued)*

BAND I *(continued)*

LINE	FREQUENCY (MHZ)	STD.DEV. (MHZ)	VAC.WAVE NO. (CM-1)
R(36)	2848 8365.3438	0.0038	950.2695 8096
R(38)	2851 6691.8679	0.0038	951.2144 5210
R(40)	2854 4300.2272	0.0038	952.1353 6783
R(42)	2857 1186.3889	0.0039	953.0321 9366
R(44)	2859 7346.1285	0.0039	953.9047 8864
R(46)	2862 2775.0267	0.0040	954.7530 0539
R(48)	2864 7468.4669	0.0052	955.5766 8989
R(50)	2867 1421.6320	0.0090	956.3756 8147
R(52)	2869 4629.5011	0.0166	957.1498 1266
R(54)	2871 7086.8467	0.0292	957.8989 0907
R(56)	2873 8788.2305	0.0486	958.6227 8932
R(58)	2875 9728.0006	0.0773	959.3212 6487

BAND II

P(60)	2926 4508.5336	0.0293	976.1589 3104
P(58)	2932 3720.0883	0.0169	978.1340 1591
P(56)	2938 2386.9924	0.0092	980.0909 3319
P(54)	2944 0503.8821	0.0051	982.0295 0396
P(52)	2949 8065.5045	0.0038	983.9495 5301
P(50)	2955 5066.7231	0.0036	985.8509 0900
P(48)	2961 1502.5235	0.0035	987.7334 0467
P(46)	2966 7368.0181	0.0035	989.5968 7699
P(44)	2972 2658.4516	0.0036	991.4411 6733
P(42)	2977 7369.2056	0.0037	993.2661 2164
P(40)	2983 1495.8037	0.0040	995.0715 9062
P(38)	2988 5033.9156	0.0043	996.8574 2980
P(36)	2993 7979.3620	0.0045	998.6234 9979
P(34)	2999 0328.1180	0.0047	1000.3696 6634
P(32)	3004 2076.3181	0.0048	1002.0958 0049
P(30)	3009 3220.2591	0.0049	1003.8017 7873
P(28)	3014 3756.4042	0.0049	1005.4874 8308
P(26)	3019 3681.3863	0.0048	1007.1528 0123
P(24)	3024 2992.0111	0.0047	1008.7976 2663
P(22)	3029 1685.2604	0.0046	1010.4218 5859
P(20)	3033 9758.2945	0.0044	1012.0254 0240
P(18)	3038 7208.4549	0.0043	1013.6081 6939
P(16)	3043 4033.2670	0.0042	1015.1700 7699
P(14)	3048 0230.4418	0.0041	1016.7110 4887
P(12)	3052 5797.8781	0.0040	1018.2310 1494
P(10)	3057 0733.6641	0.0040	1019.7299 1142
P(8)	3061 5036.0793	0.0040	1021.2076 8092
P(6)	3065 8703.5950	0.0040	1022.6642 7246
P(4)	3070 1734.8761	0.0041	1024.0996 4150
P(2)	3074 4128.7817	0.0041	1025.5137 4997
V(0)	3078 5884.3656	0.0041	1026.9065 6633
R(0)	3080 6522.5446	0.0041	1027.5949 8188
R(2)	3084 7319.2989	0.0040	1028.9558 1512
R(4)	3088 7476.2204	0.0040	1030.2953 0584
R(6)	3092 6993.0464	0.0039	1031.6134 4527
R(8)	3096 5869.7090	0.0039	1032.9102 3115

(continues)

TABLE 6 *(continued)*

BAND II *(continued)*

LINE	FREQUENCY (MHZ)	STD.DEV. (MHZ)	VAC.WAVE NO. (CM-1)
R(10)	3100 4106.3345	0.0039	1034.1856 6769
R(12)	3104 1703.2428	0.0039	1035.4397 6556
R(14)	3107 8660.9460	0.0039	1036.6725 4184
R(16)	3111 4980.1471	0.0039	1037.8840 1999
R(18)	3115 0661.7389	0.0039	1039.0742 2978
R(20)	3118 5706.8021	0.0040	1040.2432 0726
R(22)	3122 0116.6032	0.0040	1041.3909 9467
R(24)	3125 3892.5924	0.0040	1042.5176 4040
R(26)	3128 7036.4017	0.0040	1043.6231 9888
R(28)	3131 9549.8415	0.0040	1044.7077 3049
R(30)	3135 1434.8987	0.0040	1045.7713 0151
R(32)	3138 2693.7329	0.0039	1046.8139 8399
R(34)	3141 3328.6739	0.0039	1047.8358 5563
R(36)	3144 3342.2180	0.0039	1048.8369 9969
R(38)	3147 2737.0241	0.0038	1049.8175 0489
R(40)	3150 1515.9106	0.0038	1050.7774 6521
R(42)	3152 9681.8507	0.0039	1051.7169 7984
R(44)	3155 7237.9690	0.0039	1052.6361 5301
R(46)	3158 4187.5362	0.0041	1053.5350 9381
R(48)	3161 0533.9655	0.0045	1054.4139 1609
R(50)	3163 6280.8072	0.0061	1055.2727 3829
R(52)	3166 1431.7443	0.0100	1056.1116 8325
R(54)	3168 5990.5869	0.0172	1056.9308 7806
R(56)	3170 9961.2676	0.0288	1057.7304 5390
R(58)	3173 3347.8356	0.0462	1058.5105 4584

[a]Reproduced with permission from Bradley *et al.* [37]. © 1986 IEEE.

TABLE 7 Molecular Constants and Frequencies Calculated for 646[a]

$^{16}O\ ^{14}C\ ^{16}O$

NUMBER	SYMBOL		CONSTANTS (MHZ)	STD.DEV. (MHZ)
71	V(001-I)	=	2.596 591 761 827 D+07	1.3D-02
72	V(001-II)	=	2.946 000 239 110 D+07	4.9D-03
73	B(001)	=	1.161 366 771 367 D+04	1.4D-04
74	B(I)	=	1.167 472 474 237 D+04	1.6D-04
75	B(II)	=	1.172 705 299 921 D+04	1.5D-04
76	D(001)	=	3.979 815 697 D-03	3.6D-07
77	D(I)	=	3.776 614 494 D-03	4.2D-07
78	D(II)	=	4.821 389 232 D-03	4.0D-07

(continues)

TABLE 7 *(continued)*

$^{16}O\ ^{14}C\ ^{16}O$

NUMBER	SYMBOL		CONSTANTS (MHZ)	STD.DEV. (MHZ)
79	H(001)	=	-0.922 033 D-09	3.4D-10
80	H(I)	=	2.658 350 D-09	3.6D-10
81	H(II)	=	11.449 041 D-09	4.1D-10
82	L(001)	=	37.29 216 D-14	1.1D-13
83	L(I)	=	41.84 717 D-14	1.0D-13
84	L(II)	=	45.06 891 D-14	1.4D-13

BAND I

LINE	FREQUENCY (MHZ)	STD.DEV. (MHZ)	VAC.WAVE NO. (CM-1)
P(60)	2434 9337.5625	1.0707	812.2064 7527
P(58)	2441 0368.8707	0.6772	814.2422 6058
P(56)	2447 0894.8065	0.4100	816.2611 8848
P(54)	2453 0917.6246	0.2378	818.2633 3418
P(52)	2459 0439.4169	0.1379	820.2487 6746
P(50)	2464 9462.1194	0.0923	822.2175 5290
P(48)	2470 7987.5190	0.0790	824.1697 5009
P(46)	2476 6017.2592	0.0755	826.1054 1387
P(44)	2482 3552.8462	0.0722	828.0245 9447
P(42)	2488 0595.6546	0.0676	829.9273 3775
P(40)	2493 7146.9321	0.0624	831.8136 8532
P(38)	2499 3207.8048	0.0570	833.6836 7475
P(36)	2504 8779.2812	0.0514	835.5373 3967
P(34)	2510 3862.2568	0.0453	837.3747 0997
P(32)	2515 8457.5180	0.0389	839.1958 1186
P(30)	2521 2565.7453	0.0322	841.0006 6805
P(28)	2526 6187.5174	0.0257	842.7892 9784
P(26)	2531 9323.3137	0.0197	844.5617 1722
P(24)	2537 1973.5173	0.0148	846.3179 3897
P(22)	2542 4138.4181	0.0114	848.0579 7276
P(20)	2547 5818.2143	0.0096	849.7818 2521
P(18)	2552 7013.0155	0.0090	851.4894 9996
P(16)	2557 7722.8440	0.0088	853.1809 9777
P(14)	2562 7947.6370	0.0087	854.8563 1653
P(12)	2567 7687.2477	0.0086	856.5154 5136
P(10)	2572 6941.4471	0.0089	858.1583 9460
P(8)	2577 5709.9249	0.0096	859.7851 3592
P(6)	2582 3992.2904	0.0107	861.3956 6227
P(4)	2587 1788.0735	0.0117	862.9899 5799
P(2)	2591 9096.7253	0.0125	864.5680 0475
V(0)	2596 5917.6183	0.0128	866.1297 8163
R(0)	2598 9144.9378	0.0128	866.9045 6161

(continues)

TABLE 7 *(continued)*

BAND I *(continued)*

LINE	FREQUENCY (MHZ)	STD.DEV. (MHZ)	VAC.WAVE NO. (CM-1)
R(2)	2603 5232.8452	0.0123	868.4418 8873
R(4)	2608 0831.0836	0.0113	869.9628 8224
R(6)	2612 5938.7519	0.0101	871.4675 1210
R(8)	2617 0554.8709	0.0089	872.9557 4563
R(10)	2621 4678.3819	0.0082	874.4275 4754
R(12)	2625 8308.1471	0.0079	875.8828 7985
R(14)	2630 1442.9480	0.0079	877.3217 0194
R(16)	2634 4081.4848	0.0080	878.7439 7043
R(18)	2638 6222.3752	0.0079	880.1496 3923
R(20)	2642 7864.1533	0.0083	881.5386 5943
R(22)	2646 9005.2678	0.0099	882.9109 7929
R(24)	2650 9644.0807	0.0135	884.2665 4418
R(26)	2654 9778.8656	0.0186	885.6052 9650
R(28)	2658 9407.8053	0.0249	886.9271 7564
R(30)	2662 8528.9901	0.0318	888.2321 1790
R(32)	2666 7140.4154	0.0387	889.5200 5642
R(34)	2670 5239.9791	0.0452	890.7909 2107
R(36)	2674 2825.4789	0.0514	892.0446 3839
R(38)	2677 9894.6097	0.0587	893.2811 3150
R(40)	2681 6444.9602	0.0707	894.5003 1996
R(42)	2685 2474.0097	0.0941	895.7021 1969
R(44)	2688 7979.1248	0.1369	896.8864 4285
R(46)	2692 2957.5553	0.2076	898.0531 9770
R(48)	2695 7406.4307	0.3157	899.2022 8849
R(50)	2699 1322.7556	0.4740	900.3336 1532
R(52)	2702 4703.4056	0.6993	901.4470 7395
R(54)	2705 7545.1223	1.0137	902.5425 5570
R(56)	2708 9844.5086	1.4453	903.6199 4726
R(58)	2712 1598.0232	2.0293	904.6791 3049

BAND II

P(60)	2766 5459.5295	4.1144	922.8203 9762
P(58)	2773 7264.0710	2.9602	925.2155 3931
P(56)	2780 8303.6083	2.0915	927.5851 6321
P(54)	2787 8570.5221	1.4473	929.9290 1516
P(52)	2794 8057.2612	0.9777	932.2468 4329
P(50)	2801 6756.3611	0.6420	934.5383 9860
P(48)	2808 4660.4634	0.4074	936.8034 3564
P(46)	2815 1762.3327	0.2478	939.0417 1307
P(44)	2821 8054.8734	0.1428	941.2529 9421
P(42)	2828 3531.1460	0.0764	943.4370 4757
P(40)	2834 8184.3816	0.0368	945.5936 4737
P(38)	2841 2007.9961	0.0152	947.7225 7400
P(36)	2847 4995.6042	0.0059	949.8236 1445
P(34)	2853 7141.0312	0.0049	951.8965 6276
P(32)	2859 8438.3257	0.0051	953.9412 2042
P(30)	2865 8881.7700	0.0049	955.9573 9670
P(28)	2871 8465.8912	0.0048	957.9449 0905
P(26)	2877 7185.4704	0.0048	959.9035 8338

(continues)

TABLE 7 *(continued)*

BAND II *(continued)*

LINE	FREQUENCY (MHZ)	STD.DEV. (MHZ)	VAC.WAVE NO. (CM-1)
P(24)	2883 5035.5520	0.0048	961.8332 5439
P(22)	2889 2011.4519	0.0046	963.7337 6584
P(20)	2894 8108.7652	0.0044	965.6049 7080
P(18)	2900 3323.3734	0.0042	967.4467 3188
P(16)	2905 7651.4505	0.0041	969.2589 2147
P(14)	2911 1089.4690	0.0040	971.0414 2189
P(12)	2916 3634.2047	0.0041	972.7941 2562
P(10)	2921 5282.7418	0.0042	974.5169 3537
P(8)	2926 6032.4761	0.0043	976.2097 6429
P(6)	2931 5881.1188	0.0045	977.8725 3603
P(4)	2936 4826.6991	0.0047	979.5051 8485
P(2)	2941 2867.5662	0.0048	981.1076 5569
V(0)	2946 0002.3911	0.0049	982.6799 0421
R(0)	2948 3229.7106	0.0048	983.4546 8419
R(2)	2952 9003.6861	0.0047	984.9815 3967
R(4)	2957 3869.7091	0.0044	986.4781 0910
R(6)	2961 7827.5803	0.0041	987.9443 8586
R(8)	2966 0877.4220	0.0038	989.3803 7401
R(10)	2970 3019.6766	0.0037	990.7860 8831
R(12)	2974 4255.1041	0.0037	992.1615 5412
R(14)	2978 4584.7800	0.0039	993.5068 0730
R(16)	2982 4010.0913	0.0040	994.8218 9413
R(18)	2986 2532.7332	0.0042	996.1068 7115
R(20)	2990 0154.7042	0.0044	997.3618 0502
R(22)	2993 6878.3016	0.0045	998.5867 7237
R(24)	2997 2706.1154	0.0047	999.7818 5960
R(26)	3000 7641.0223	0.0049	1000.9471 6266
R(28)	3004 1686.1791	0.0050	1002.0827 8686
R(30)	3007 4845.0148	0.0051	1003.1888 4656
R(32)	3010 7121.2231	0.0053	1004.2654 6498
R(34)	3013 8518.7535	0.0054	1005.3127 7386
R(36)	3016 9041.8019	0.0055	1006.3309 1316
R(38)	3019 8694.8011	0.0072	1007.3200 3075
R(40)	3022 7482.4096	0.0154	1008.2802 8201
R(42)	3025 5409.5012	0.0343	1009.2118 2951
R(44)	3028 2481.1520	0.0692	1010.1148 4258
R(46)	3030 8702.6288	0.1280	1010.9894 9690
R(48)	3033 4079.3751	0.2216	1011.8359 7404
R(50)	3035 8616.9973	0.3644	1012.6544 6102
R(52)	3038 2321.2499	0.5755	1013.4451 4977
R(54)	3040 5198.0199	0.8788	1014.2082 3668
R(56)	3042 7253.3104	1.3049	1014.9439 2198
R(58)	3044 8493.2235	1.8916	1015.6524 0922

[a]Reproduced with permission from Bradley *et al.* [37]. © 1986 IEEE.

TABLE 8 Molecular Constants and Frequencies Calculated for 848[a]

$^{18}O\ ^{14}C\ ^{18}O$

NUMBER	SYMBOL		CONSTANTS (MHZ)	STD.DEV. (MHZ)
85	V(001-I)	=	2.665 794 012 522 D+07	5.1D-01
86	V(001-II)	=	2.945 628 336 884 D+07	4.3D-03
87	B(001)	=	1.032 222 210 875 D+04	1.5D-04
88	B(I)	=	1.039 139 637 214 D+04	2.8D-03
89	B(II)	=	1.041 017 017 924 D+04	1.4D-04
90	D(001)	=	3.145 791 088 D-03	3.1D-07
91	D(I)	=	2.762 860 020 D-03	4.9D-06
92	D(II)	=	3.717 259 657 D-03	2.9D-07
93	H(001)	=	0.074 897 D-09	2.5D-10
94	H(I)	=	-3.624 392 D-09	3.3D-09
95	H(II)	=	4.503 216 D-09	2.2D-10
96	L(001)	=	9.77 438 D-14	6.6D-14
97	L(I)	=	176.77 976 D-14	7.3D-13
98	L(II)	=	7.33 773 D-14	5.7D-14

BAND I

LINE	FREQUENCY (MHZ)	STD.DEV. (MHZ)	VAC.WAVE NO. (CM-1)
P(60)	2516 3563.1916	24.9722	839.3661 1880
P(58)	2522 1736.2103	16.1045	841.3065 6183
P(56)	2527 9300.5125	9.9374	843.2267 0027
P(54)	2533 6261.8905	5.7850	845.1267 2732
P(52)	2539 2625.5971	3.1031	847.0068 1820
P(50)	2544 8396.4026	1.4677	848.8671 3203
P(48)	2550 3578.6456	0.5603	850.7078 1352
P(46)	2555 8176.2776	0.1907	852.5289 9449
P(44)	2561 2192.9029	0.1915	854.3307 9517
P(42)	2566 5631.8132	0.1816	856.1133 2535
P(40)	2571 8496.0177	0.1304	857.8766 8540
P(38)	2577 0788.2691	0.1036	859.6209 6715
P(36)	2582 2511.0860	0.1289	861.3462 5461
P(34)	2587 3666.7717	0.1595	863.0526 2462
P(32)	2592 4257.4305	0.1718	864.7401 4735
P(30)	2597 4284.9803	0.1655	866.4088 8679
P(28)	2602 3751.1638	0.1484	868.0589 0106
P(26)	2607 2657.5569	0.1306	869.6902 4274

(continues)

TABLE 8 *(continued)*

BAND I *(continued)*

LINE	FREQUENCY (MHZ)	STD.DEV. (MHZ)	VAC.WAVE NO. (CM-1)
P(24)	2612 1005.5759	0.1194	871.3029 5906
P(22)	2616 8796.4821	0.1155	872.8970 9210
P(20)	2621 6031.3862	0.1159	874.4726 7890
P(18)	2626 2711.2509	0.1210	876.0297 5159
P(16)	2630 8836.8926	0.1375	877.5683 3738
P(14)	2635 4408.9825	0.1719	879.0884 5867
P(12)	2639 9428.0471	0.2234	880.5901 3303
P(10)	2644 3894.4684	0.2855	882.0733 7319
P(8)	2648 7808.4833	0.3503	883.5381 8705
P(6)	2653 1170.1836	0.4107	884.9845 7768
P(4)	2657 3979.5153	0.4603	886.4125 4328
P(2)	2661 6236.2781	0.4944	887.8220 7717
V(0)	2665 7940.1252	0.5095	889.2131 6777
R(0)	2667 8584.5569	0.5096	889.9017 9189
R(2)	2671 9458.0588	0.4944	891.2651 8516
R(4)	2675 9777.1350	0.4603	892.6100 8477
R(6)	2679 9540.9244	0.4107	893.9364 6202
R(8)	2683 8748.4193	0.3503	895.2442 8327
R(10)	2687 7398.4657	0.2855	896.5335 1005
R(12)	2691 5489.7640	0.2234	897.8040 9899
R(14)	2695 3020.8692	0.1719	899.0560 0191
R(16)	2698 9990.1917	0.1375	900.2891 6577
R(18)	2702 6395.9971	0.1211	901.5035 3273
R(20)	2706 2236.4068	0.1160	902.6990 4011
R(22)	2709 7509.3968	0.1156	903.8756 2041
R(24)	2713 2212.7973	0.1195	905.0332 0124
R(26)	2716 6344.2906	0.1307	906.1717 0531
R(28)	2719 9901.4088	0.1485	907.2910 5029
R(30)	2723 2881.5295	0.1656	908.3911 4870
R(32)	2726 5281.8713	0.1720	909.4719 0777
R(34)	2729 7099.4864	0.1597	910.5332 2917
R(36)	2732 8331.2527	0.1290	911.5750 0876
R(38)	2735 8973.8628	0.1037	912.5971 3621
R(40)	2738 9023.8112	0.1307	913.5994 9460
R(42)	2741 8477.3784	0.1828	914.5819 5985
R(44)	2744 7330.6123	0.1953	915.5444 0013
R(46)	2747 5579.3060	0.1998	916.4866 7512
R(48)	2750 3218.9719	0.5659	917.4086 3514
R(50)	2753 0244.8124	1.4700	918.3101 2014
R(52)	2755 6651.6845	3.1024	919.1909 5858
R(54)	2758 2434.0616	5.7807	920.0509 6611
R(56)	2760 7585.9881	9.9284	920.8899 4407
R(58)	2763 2101.0296	16.0893	921.7076 7783

BAND II

P(60)	2790 5884.6278	0.1963	930.8401 1566
P(58)	2796 6918.2463	0.1219	932.8759 7803
P(56)	2802 7353.5817	0.0718	934.8918 8383
P(54)	2808 7184.5030	0.0394	936.8876 2854
P(52)	2814 6405.0223	0.0198	938.8630 1243
P(50)	2820 5009.2992	0.0093	940.8178 4069

(continues)

TABLE 8 *(continued)*

BAND II *(continued)*

LINE	FREQUENCY (MHZ)	STD.DEV. (MHZ)	VAC.WAVE NO. (CM-1)
P(48)	2826 2991.6460	0.0056	942.7519 2360
P(46)	2832 0346.5324	0.0052	944.6650 7668
P(44)	2837 7068.5896	0.0050	946.5571 2085
P(42)	2843 3152.6154	0.0047	948.4278 8258
P(40)	2848 8593.5779	0.0045	950.2771 9403
P(38)	2854 3386.6201	0.0045	952.1048 9318
P(36)	2859 7527.0634	0.0045	953.9108 2398
P(34)	2865 1010.4118	0.0046	955.6948 3645
P(32)	2870 3832.3553	0.0047	957.4567 8683
P(30)	2875 5988.7736	0.0047	959.1965 3768
P(28)	2880 7475.7389	0.0047	960.9139 5798
P(26)	2885 8289.5197	0.0047	962.6089 2326
P(24)	2890 8426.5831	0.0046	964.2813 1568
P(22)	2895 7883.5981	0.0046	965.9310 2412
P(20)	2900 6657.4375	0.0045	967.5579 4429
P(18)	2905 4745.1809	0.0043	969.1619 7875
P(16)	2910 2144.1167	0.0042	970.7430 3706
P(14)	2914 8851.7437	0.0042	972.3010 3579
P(12)	2919 4865.7733	0.0042	973.8358 9861
P(10)	2924 0184.1309	0.0042	975.3475 5631
P(8)	2928 4804.9574	0.0043	976.8359 4687
P(6)	2932 8726.6103	0.0044	978.3010 1551
P(4)	2937 1947.6644	0.0044	979.7427 1469
P(2)	2941 4466.9132	0.0044	981.1610 0416
V(0)	2945 6283.3688	0.0043	982.5558 5098
R(0)	2947 6927.8005	0.0043	983.2444 7510
R(2)	2951 7688.6939	0.0042	984.6041 1215
R(4)	2955 7745.2842	0.0041	985.9402 5618
R(6)	2959 7097.3511	0.0040	987.2528 9984
R(8)	2963 5744.8935	0.0040	988.5420 4309
R(10)	2967 3688.1283	0.0041	989.8076 9317
R(12)	2971 0927.4901	0.0041	991.0498 6457
R(14)	2974 7463.6304	0.0043	992.2685 7903
R(16)	2978 3297.4158	0.0044	993.4638 6545
R(18)	2981 8429.9272	0.0046	994.6357 5989
R(20)	2985 2862.4581	0.0049	995.7843 0549
R(22)	2988 6596.5128	0.0051	996.9095 5243
R(24)	2991 9633.8045	0.0052	998.0115 5787
R(26)	2995 1976.2534	0.0053	999.0903 8584
R(28)	2998 3625.9839	0.0055	1000.1461 0721
R(30)	3001 4585.3228	0.0058	1001.1787 9960
R(32)	3004 4856.7961	0.0063	1002.1885 4726
R(34)	3007 4443.1264	0.0068	1003.1754 4101
R(36)	3010 3347.2301	0.0069	1004.1395 7812
R(38)	3013 1572.2138	0.0063	1005.0810 6224
R(40)	3015 9121.3714	0.0078	1006.0000 0322
R(42)	3018 5998.1806	0.0173	1006.8965 1708
R(44)	3021 2206.2990	0.0371	1007.7707 2581
R(46)	3023 7749.5608	0.0703	1008.6227 5731
R(48)	3026 2631.9724	0.1219	1009.4527 4522
R(50)	3028 6857.7089	0.1988	1010.2608 2881
R(52)	3031 0431.1097	0.3096	1011.0471 5282
R(54)	3033 3356.6741	0.4650	1011.8118 6733
R(56)	3035 5639.0573	0.6783	1012.5551 2763
R(58)	3037 7283.0656	0.9658	1013.2770 9404

[a]Reproduced with permission from Bradley *et al.* [37]. © 1986 IEEE.

TABLE 9 Molecular Constants and Frequencies Calculated for 638[a]

$^{16}O\ ^{13}C\ ^{18}O$

NUMBER	SYMBOL		CONSTANTS (MHZ)	STD.DEV. (MHZ)
99	V(001-I)	=	2.769 166 220 212 D+07	4.9D-02
100	V(001-II)	=	3.061 096 273 608 D+07	9.9D-02
101	B(001)	=	1.095 417 207 032 D+04	5.1D-04
102	B(I)	=	1.103 309 137 756 D+04	8.1D-04
103	B(II)	=	1.104 838 028 891 D+04	8.8D-04
104	D(001)	=	3.553 496 537 D-03	1.7D-06
105	D(I)	=	3.099 388 259 D-03	2.8D-06
106	D(II)	=	4.206 493 331 D-03	2.5D-06
107	H(001)	=	5.818 906 D-09	2.2D-09
108	H(I)	=	6.110 893 D-09	3.8D-09
109	H(II)	=	17.600 347 D-09	3.0D-09
110	L(001)	=	-201.16 254 D-14	1.0D-12
111	L(I)	=	7.84 555 D-14	1.8D-12
112	L(II)	=	-507.39 778 D-14	1.2D-12

BAND I

LINE	FREQUENCY (MHZ)	STD.DEV. (MHZ)	VAC.WAVE NO. (CM-1)
P(60)	2608 4932.6048	98.3718	870.0996 9426
P(59)	2611 6598.0182	84.2242	871.1559 3876
P(58)	2614 8086.3664	71.8523	872.2062 7700
P(57)	2617 9398.6843	61.0659	873.2507 4350
P(56)	2621 0535.9568	51.6916	874.2893 7111
P(55)	2624 1499.1212	43.5718	875.3221 9110
P(54)	2627 2289.0702	36.5633	876.3492 3325
P(53)	2630 2906.6539	30.5366	877.3705 2591
P(52)	2633 3352.6819	25.3746	878.3860 9609
P(51)	2636 3627.9259	20.9716	879.3959 6952
P(50)	2639 3733.1212	17.2329	880.4001 7075
P(49)	2642 3668.9688	14.0733	881.3987 2314
P(48)	2645 3436.1373	11.4166	882.3916 4900
P(47)	2648 3035.2642	9.1949	883.3789 6960
P(46)	2651 2466.9580	7.3480	884.3607 0523
P(45)	2654 1731.7991	5.8222	885.3368 7526
P(44)	2657 0830.3416	4.5705	886.3074 9816
P(43)	2659 9763.1145	3.5512	887.2725 9158

(continues)

TABLE 9 *(continued)*

BAND I *(continued)*

LINE	FREQUENCY (MHZ)	STD.DEV. (MHZ)	VAC.WAVE NO. (CM-1)
P(42)	2662 8530.6229	2.7280	888.2321 7237
P(41)	2665 7133.3489	2.0692	889.1862 5661
P(40)	2668 5571.7531	1.5471	890.1348 5967
P(39)	2671 3846.2752	1.1381	891.0779 9621
P(38)	2674 1957.3353	0.8216	892.0156 8024
P(37)	2676 9905.3343	0.5802	892.9479 2514
P(36)	2679 7690.6549	0.3991	893.8747 4367
P(35)	2682 5313.6624	0.2658	894.7961 4802
P(34)	2685 2774.7054	0.1701	895.7121 4982
P(33)	2688 0074.1161	0.1031	896.6227 6014
P(32)	2690 7212.2113	0.0581	897.5279 8956
P(31)	2693 4189.2925	0.0293	898.4278 4813
P(30)	2696 1005.6468	0.0127	899.3223 4542
P(29)	2698 7661.5470	0.0066	900.2114 9054
P(28)	2701 4157.2519	0.0071	901.0952 9213
P(27)	2704 0493.0072	0.0075	901.9737 5837
P(26)	2706 6669.0452	0.0071	902.8468 9701
P(25)	2709 2685.5857	0.0064	903.7147 1539
P(24)	2711 8542.8354	0.0059	904.5772 2040
P(23)	2714 4240.9891	0.0057	905.4344 1854
P(22)	2716 9780.2293	0.0057	906.2863 1589
P(21)	2719 5160.7266	0.0056	907.1329 1815
P(20)	2722 0382.6396	0.0055	907.9742 3061
P(19)	2724 5446.1155	0.0054	908.8102 5818
P(18)	2727 0351.2897	0.0054	909.6410 0537
P(17)	2729 5098.2865	0.0055	910.4664 7633
P(16)	2731 9687.2184	0.0056	911.2866 7481
P(15)	2734 4118.1871	0.0057	912.1016 0421
P(14)	2736 8391.2828	0.0059	912.9112 6753
P(13)	2739 2506.5846	0.0066	913.7156 6741
P(12)	2741 6464.1606	0.0081	914.5148 0613
P(11)	2744 0264.0678	0.0105	915.3086 8558
P(10)	2746 3906.3522	0.0136	916.0973 0730
P(9)	2748 7391.0486	0.0174	916.8806 7245
P(8)	2751 0718.1811	0.0216	917.6587 8183
P(7)	2753 3887.7626	0.0260	918.4316 3588
P(6)	2755 6899.7953	0.0305	919.1992 3467
P(5)	2757 9754.2701	0.0349	919.9615 7789
P(4)	2760 2451.1674	0.0389	920.7186 6489
P(3)	2762 4990.4564	0.0424	921.4704 9464
P(2)	2764 7372.0954	0.0453	922.2170 6576
P(1)	2766 9596.0318	0.0474	922.9583 7648
V(0)	2769 1662.2021	0.0486	923.6944 2470
R(0)	2771 3570.5320	0.0489	924.4252 0792
R(1)	2773 5320.9363	0.0484	925.1507 2331
R(2)	2775 6913.3186	0.0469	925.8709 6766
R(3)	2777 8347.5719	0.0445	926.5859 3739
R(4)	2779 9623.5784	0.0414	927.2956 2858

(continues)

TABLE 9 *(continued)*

BAND I *(continued)*

LINE	FREQUENCY (MHZ)	STD.DEV. (MHZ)	VAC.WAVE NO. (CM-1)
R(5)	2782 0741.2091	0.0376	928.0000 3692
R(6)	2784 1700.3243	0.0333	928.6991 5775
R(7)	2786 2500.7734	0.0287	929.3929 8605
R(8)	2788 3142.3950	0.0239	930.0815 1643
R(9)	2790 3625.0166	0.0192	930.7647 4314
R(10)	2792 3948.4550	0.0148	931.4426 6007
R(11)	2794 4112.5159	0.0109	932.1152 6075
R(12)	2796 4116.9943	0.0078	932.7825 3832
R(13)	2798 3961.6742	0.0059	933.4444 8559
R(14)	2800 3646.3284	0.0053	934.1010 9498
R(15)	2802 3170.7189	0.0055	934.7523 5854
R(16)	2804 2534.5966	0.0058	935.3982 6798
R(17)	2806 1737.7013	0.0057	936.0388 1460
R(18)	2808 0779.7615	0.0054	936.6739 8936
R(19)	2809 9660.4946	0.0049	937.3037 8283
R(20)	2811 8379.6066	0.0045	937.9281 8519
R(21)	2813 6936.7919	0.0044	938.5471 8626
R(22)	2815 5331.7334	0.0046	939.1607 7546
R(23)	2817 3564.1022	0.0050	939.7689 4183
R(24)	2819 1633.5576	0.0054	940.3716 7398
R(25)	2820 9539.7466	0.0056	940.9689 6015
R(26)	2822 7282.3040	0.0058	941.5607 8816
R(27)	2824 4860.8519	0.0062	942.1471 4541
R(28)	2826 2274.9998	0.0069	942.7280 1885
R(29)	2827 9524.3435	0.0078	943.3033 9503
R(30)	2829 6608.4660	0.0097	943.8732 6001
R(31)	2831 3526.9357	0.0148	944.4375 9942
R(32)	2833 0279.3072	0.0268	944.9963 9838
R(33)	2834 6865.1200	0.0490	945.5496 4155
R(34)	2836 3283.8986	0.0853	946.0973 1305
R(35)	2837 9535.1515	0.1405	946.6393 9649
R(36)	2839 5618.3707	0.2211	947.1758 7494
R(37)	2841 1533.0311	0.3349	947.7067 3087
R(38)	2842 7278.5901	0.4914	948.2319 4619
R(39)	2844 2854.4862	0.7021	948.7515 0215
R(40)	2845 8260.1385	0.9808	949.2653 7940
R(41)	2847 3494.9459	1.3437	949.7735 5787
R(42)	2848 8558.2859	1.8099	950.2760 1681
R(43)	2850 3449.5139	2.4017	950.7727 3471
R(44)	2851 8167.9616	3.1450	951.2636 8928
R(45)	2853 2712.9361	4.0697	951.7488 5741
R(46)	2854 7083.7186	5.2100	952.2282 1511
R(47)	2856 1279.5630	6.6054	952.7017 3751
R(48)	2857 5299.6945	8.3004	953.1693 9876
R(49)	2858 9143.3078	10.3459	953.6311 7200
R(50)	2860 2809.5658	12.7992	954.0870 2930
R(51)	2861 6297.5977	15.7249	954.5369 4161
R(52)	2862 9606.4969	19.1957	954.9808 7870
R(53)	2864 2735.3193	23.2928	955.4188 0908

(continues)

TABLE 9 *(continued)*

BAND I *(continued)*

LINE	FREQUENCY (MHZ)	STD.DEV. (MHZ)	VAC.WAVE NO. (CM-1)
R(54)	2865 5683.0813	28.1068	955.8506 9993
R(55)	2866 8448.7571	33.7388	956.2765 1704
R(56)	2868 1031.2769	40.3009	956.6962 2472
R(57)	2869 3429.5242	47.9175	957.1097 8574
R(58)	2870 5642.3331	56.7257	957.5171 6119
R(59)	2871 7668.4857	66.8772	957.9183 1046

BAND II

P(60)	2896 3467.3195	86.8068	966.1172 7702
P(59)	2899 5949.0536	73.6194	967.2007 5105
P(58)	2902 8278.6677	62.1727	968.2791 5090
P(57)	2906 0454.6740	52.2716	969.3524 2694
P(56)	2909 2475.6481	43.7390	970.4205 3166
P(55)	2912 4340.2262	36.4145	971.4834 1958
P(54)	2915 6047.1010	30.1535	972.5410 4708
P(53)	2918 7595.0185	24.8251	973.5933 7234
P(52)	2921 8982.7755	20.3120	974.6403 5521
P(51)	2925 0209.2160	16.5089	975.6819 5715
P(50)	2928 1273.2288	13.3216	976.7181 4108
P(49)	2931 2173.7450	10.6662	977.7488 7135
P(48)	2934 2909.7356	8.4680	978.7741 1364
P(47)	2937 3480.2089	6.6610	979.7938 3487
P(46)	2940 3884.2089	5.1870	980.8080 0315
P(45)	2943 4120.8131	3.9946	981.8165 8770
P(44)	2946 4189.1307	3.0391	982.8195 5881
P(43)	2949 4088.3007	2.2814	983.8168 8777
P(42)	2952 3817.4909	1.6877	984.8085 4681
P(41)	2955 3375.8957	1.2287	985.7945 0907
P(40)	2958 2762.7353	0.8797	986.7747 4853
P(39)	2961 1977.2545	0.6192	987.7492 3999
P(38)	2964 1018.7210	0.4293	988.7179 5904
P(37)	2966 9886.4250	0.2950	989.6808 8200
P(36)	2969 8579.6778	0.2032	990.6379 8589
P(35)	2972 7097.8114	0.1430	991.5892 4843
P(34)	2975 5440.1771	0.1043	992.5346 4799
P(33)	2978 3606.1454	0.0790	993.4741 6356
P(32)	2981 1595.1050	0.0608	994.4077 7476
P(31)	2983 9406.4623	0.0463	995.3354 6178
P(30)	2986 7039.6411	0.0342	996.2572 0541
P(29)	2989 4494.0818	0.0242	997.1729 8698
P(28)	2992 1769.2416	0.0166	998.0827 8838
P(27)	2994 8864.5933	0.0118	998.9865 9203
P(26)	2997 5779.6258	0.0099	999.8843 8087
P(25)	3000 2513.8436	0.0096	1000.7761 3839
P(24)	3002 9066.7664	0.0096	1001.6618 4856
P(23)	3005 5437.9293	0.0092	1002.5414 9587
P(22)	3008 1626.8822	0.0086	1003.4150 6530
P(21)	3010 7633.1902	0.0082	1004.2825 4236
P(20)	3013 3456.4332	0.0081	1005.1439 1303

(continues)

TABLE 9 *(continued)*

BAND II *(continued)*

LINE	FREQUENCY (MHZ)	STD.DEV. (MHZ)	VAC.WAVE NO. (CM-1)
P(19)	3015 9096.2061	0.0083	1005.9991 6380
P(18)	3018 4552.1183	0.0085	1006.8482 8163
P(17)	3020 9823.7944	0.0084	1007.6912 5401
P(16)	3023 4910.8735	0.0081	1008.5280 6889
P(15)	3025 9813.0098	0.0081	1009.3587 1475
P(14)	3028 4529.8723	0.0097	1010.1831 8054
P(13)	3030 9061.1448	0.0134	1011.0014 5571
P(12)	3033 3406.5264	0.0191	1011.8135 3022
P(11)	3035 7565.7308	0.0261	1012.6193 9454
P(10)	3038 1538.4873	0.0341	1013.4190 3962
P(9)	3040 5324.5400	0.0428	1014.2124 5694
P(8)	3042 8923.6485	0.0518	1014.9996 3847
P(7)	3045 2335.5874	0.0607	1015.7805 7669
P(6)	3047 5560.1470	0.0693	1016.5552 6461
P(5)	3049 8597.1328	0.0773	1017.3236 9574
P(4)	3052 1446.3659	0.0844	1018.0858 6412
P(3)	3054 4107.6828	0.0904	1018.8417 6429
P(2)	3056 6580.9357	0.0949	1019.5913 9131
P(1)	3058 8865.9923	0.0980	1020.3347 4079
V(0)	3061 0962.7361	0.0994	1021.0718 0882
R(0)	3063 2871.0660	0.0992	1021.8025 9205
R(1)	3065 4590.8968	0.0972	1022.5270 8762
R(2)	3067 6122.1589	0.0937	1023.2452 9321
R(3)	3069 7464.7984	0.0888	1023.9572 0703
R(4)	3071 8618.7769	0.0825	1024.6628 2780
R(5)	3073 9584.0718	0.0752	1025.3621 5477
R(6)	3076 0360.6761	0.0670	1026.0551 8769
R(7)	3078 0948.5983	0.0582	1026.7419 2685
R(8)	3080 1347.8624	0.0493	1027.4223 7306
R(9)	3082 1558.5081	0.0403	1028.0965 2763
R(10)	3084 1580.5901	0.0318	1028.7643 9240
R(11)	3086 1414.1789	0.0239	1029.4259 6971
R(12)	3088 1059.3601	0.0169	1030.0812 6242
R(13)	3090 0516.2344	0.0113	1030.7302 7389
R(14)	3091 9784.9179	0.0074	1031.3730 0799
R(15)	3093 8865.5416	0.0059	1032.0094 6908
R(16)	3095 7758.2517	0.0061	1032.6396 6206
R(17)	3097 6463.2092	0.0068	1033.2635 9228
R(18)	3099 4980.5901	0.0072	1033.8812 6562
R(19)	3101 3310.5852	0.0073	1034.4926 8845
R(20)	3103 1453.4002	0.0075	1035.0978 6761
R(21)	3104 9409.2555	0.0080	1035.6968 1047
R(22)	3106 7178.3862	0.0087	1036.2895 2488
R(23)	3108 4761.0423	0.0095	1036.8760 1915
R(24)	3110 2157.4886	0.0102	1037.4563 0214
R(25)	3111 9368.0045	0.0107	1038.0303 8316
R(26)	3113 6392.8845	0.0115	1038.5982 7203
R(27)	3115 3232.4380	0.0135	1039.1599 7907
R(28)	3116 9886.9894	0.0180	1039.7155 1511
R(29)	3118 6356.8784	0.0254	1040.2648 9147
R(30)	3120 2642.4602	0.0363	1040.8081 2000
R(31)	3121 8744.1055	0.0520	1041.3452 1308

(continues)

TABLE 9 *(continued)*

BAND II *(continued)*

LINE	FREQUENCY (MHZ)	STD.DEV. (MHZ)	VAC.WAVE NO. (CM-1)
R(32)	3123 4662.2009	0.0748	1041.8761 8359
R(33)	3125 0397.1494	0.1084	1042.4010 4497
R(34)	3126 5949.3704	0.1581	1042.9198 1122
R(35)	3128 1319.3005	0.2308	1043.4324 9691
R(36)	3129 6507.3936	0.3348	1043.9391 1716
R(37)	3131 1514.1219	0.4804	1044.4396 8773
R(38)	3132 6339.9758	0.6798	1044.9342 2499
R(39)	3134 0985.4654	0.9478	1045.4227 4594
R(40)	3135 5451.1207	1.3018	1045.9052 6826
R(41)	3136 9737.4926	1.7624	1046.3818 1033
R(42)	3138 3845.1539	2.3539	1046.8523 9126
R(43)	3139 7774.7001	3.1045	1047.3170 3091
R(44)	3141 1526.7506	4.0470	1047.7757 4994
R(45)	3142 5101.9501	5.2193	1048.2285 6985
R(46)	3143 8500.9695	6.6649	1048.6755 1303
R(47)	3145 1724.5076	8.4334	1049.1166 0278
R(48)	3146 4773.2927	10.5813	1049.5518 6340
R(49)	3147 7648.0840	13.1728	1049.9813 2021
R(50)	3149 0349.6734	16.2804	1050.4049 9963
R(51)	3150 2878.8878	19.9855	1050.8229 2923
R(52)	3151 5236.5905	24.3797	1051.2351 3783
R(53)	3152 7423.6840	29.5654	1051.6416 5551
R(54)	3153 9441.1120	35.6568	1052.0425 1376
R(55)	3155 1289.8621	42.7811	1052.4377 4552
R(56)	3156 2970.9683	51.0791	1052.8273 8528
R(57)	3157 4485.5139	60.7073	1053.2114 6918
R(58)	3158 5834.6344	71.8380	1053.5900 3509
R(59)	3159 7019.5211	84.6613	1053.9631 2275

[a]Reproduced with permission from Bradley *et al.* [37]. © 1986 IEEE.

TABLE 10 Molecular Constants and Frequencies Calculated for 727[a]

$^{17}O\,^{12}C\,^{17}O$

NUMBER	SYMBOL		CONSTANTS (MHZ)	STD.DEV. (MHZ)
113	V(001-I)	=	2.894 953 245 732 D+07	1.0D-02
114	V(001-II)	=	3.214 846 174 949 D+07	6.1D-03
115	B(001)	=	1.092 153 560 997 D+04	1.2D-04
116	B(I)	=	1.101 834 696 644 D+04	1.5D-04
117	B(II)	=	1.100 609 965 843 D+04	1.1D-04

(continues)

TABLE 10 *(continued)*

$^{17}O\ ^{12}C\ ^{17}O$

NUMBER	SYMBOL		CONSTANTS (MHZ)	STD.DEV. (MHZ)
118	D(001)	=	3.530 964 947 D-03	2.1D-07
119	D(I)	=	3.049 684 815 D-03	3.1D-07
120	D(II)	=	4.069 984 195 D-03	1.9D-07
121	H(001)	=	-0.086 853 D-09	1.5D-10
122	H(I)	=	3.143 802 D-09	3.0D-10
123	H(II)	=	5.840 864 D-09	1.4D-10
124	L(001)	=	10.84 024 D-14	3.8D-14
125	L(I)	=	-1.29 247 D-14	1.0D-13
126	L(II)	=	6.45 892 D-14	3.3D-14

BAND I

LINE	FREQUENCY (MHZ)	STD.DEV. (MHZ)	VAC.WAVE NO. (CM-1)
P(60)	2728 1083.6929	7.6946	909.9989 9981
P(59)	2731 4822.5368	6.5234	911.1244 0650
P(58)	2734 8351.3738	5.5069	912.2428 0812
P(57)	2738 1670.8532	4.6277	913.3542 2632
P(56)	2741 4781.6111	3.8702	914.4586 8232
P(55)	2744 7684.2700	3.2200	915.5561 9688
P(54)	2748 0379.4394	2.6644	916.6467 9034
P(53)	2751 2867.7152	2.1917	917.7304 8257
P(52)	2754 5149.6802	1.7914	918.8072 9302
P(51)	2757 7225.9038	1.4542	919.8772 4067
P(50)	2760 9096.9421	1.1718	920.9403 4407
P(49)	2764 0763.3380	0.9366	921.9966 2134
P(48)	2767 2225.6209	0.7420	923.0460 9014
P(47)	2770 3484.3071	0.5821	924.0887 6767
P(46)	2773 4539.8997	0.4519	925.1246 7074
P(45)	2776 5392.8885	0.3466	926.1538 1567
P(44)	2779 6043.7501	0.2623	927.1762 1836
P(43)	2782 6492.9481	0.1955	928.1918 9428
P(42)	2785 6740.9328	0.1433	929.2008 5844
P(41)	2788 6788.1415	0.1029	930.2031 2544
P(40)	2791 6634.9985	0.0723	931.1987 0943
P(39)	2794 6281.9151	0.0495	932.1876 2412
P(38)	2797 5729.2897	0.0330	933.1698 8280
P(37)	2800 4977.5075	0.0214	934.1454 9833
P(36)	2803 4026.9412	0.0136	935.1144 8314
P(35)	2806 2877.9504	0.0088	936.0768 4922

(continues)

TABLE 10 *(continued)*

BAND I *(continued)*

LINE	FREQUENCY (MHZ)	STD.DEV. (MHZ)	VAC.WAVE NO. (CM-1)
P(34)	2809 1530.8823	0.0063	937.0326 0815
P(33)	2811 9986.0709	0.0052	937.9817 7107
P(32)	2814 8243.8379	0.0047	938.9243 4872
P(31)	2817 6304.4921	0.0044	939.8603 5139
P(30)	2820 4168.3301	0.0042	940.7897 8898
P(29)	2823 1835.6355	0.0040	941.7126 7095
P(28)	2825 9306.6799	0.0040	942.6290 0636
P(27)	2828 6581.7220	0.0039	943.5388 0384
P(26)	2831 3661.0086	0.0039	944.4420 7161
P(25)	2834 0544.7738	0.0039	945.3388 1749
P(24)	2836 7233.2396	0.0039	946.2290 4889
P(23)	2839 3726.6158	0.0039	947.1127 7279
P(22)	2842 0025.0999	0.0039	947.9899 9579
P(21)	2844 6128.8772	0.0039	948.8607 2408
P(20)	2847 2038.1213	0.0040	949.7249 6344
P(19)	2849 7752.9932	0.0041	950.5827 1923
P(18)	2852 3273.6422	0.0042	951.4339 9646
P(17)	2854 8600.2058	0.0043	952.2787 9968
P(16)	2857 3732.8091	0.0043	953.1171 3309
P(15)	2859 8671.5658	0.0044	953.9490 0047
P(14)	2862 3416.5773	0.0045	954.7744 0521
P(13)	2864 7967.9336	0.0046	955.5933 5030
P(12)	2867 2325.7126	0.0048	956.4058 3835
P(11)	2869 6489.9806	0.0051	957.2118 7157
P(10)	2872 0460.7920	0.0055	958.0114 5178
P(9)	2874 4238.1899	0.0060	958.8045 8040
P(8)	2876 7822.2052	0.0066	959.5912 5847
P(7)	2879 1212.8575	0.0073	960.3714 8665
P(6)	2881 4410.1546	0.0079	961.1452 6519
P(5)	2883 7414.0928	0.0086	961.9125 9397
P(4)	2886 0224.6567	0.0091	962.6734 7248
P(3)	2888 2841.8194	0.0096	963.4278 9982
P(2)	2890 5265.5424	0.0100	964.1758 7471
P(1)	2892 7495.7756	0.0103	964.9173 9547
V(0)	2894 9532.4573	0.0104	965.6524 6005
R(0)	2897 1375.5144	0.0104	966.3810 6601
R(1)	2899 3024.8621	0.0103	967.1032 1052
R(2)	2901 4480.4042	0.0100	967.8188 9037
R(3)	2903 5742.0327	0.0096	968.5281 0195
R(4)	2905 6809.6283	0.0090	969.2308 4130
R(5)	2907 7683.0600	0.0084	969.9271 0404
R(6)	2909 8362.1852	0.0077	970.6168 8540
R(7)	2911 8846.8498	0.0070	971.3001 8027
R(8)	2913 9136.8882	0.0063	971.9769 8310
R(9)	2915 9232.1228	0.0057	972.6472 8797
R(10)	2917 9132.3648	0.0051	973.3110 8859
R(11)	2919 8837.4136	0.0046	973.9683 7827
R(12)	2921 8347.0567	0.0042	974.6191 4992

(continues)

TABLE 10 *(continued)*

BAND I *(continued)*

LINE	FREQUENCY (MHZ)	STD.DEV. (MHZ)	VAC.WAVE NO. (CM-1)
R(13)	2923 7661.0702	0.0040	975.2633 9606
R(14)	2925 6779.2184	0.0038	975.9011 0884
R(15)	2927 5701.2537	0.0037	976.5322 8000
R(16)	2929 4426.9168	0.0037	977.1569 0089
R(17)	2931 2955.9368	0.0036	977.7749 6246
R(18)	2933 1288.0305	0.0036	978.3864 5529
R(19)	2934 9422.9032	0.0035	978.9913 6953
R(20)	2936 7360.2482	0.0035	979.5896 9496
R(21)	2938 5099.7467	0.0034	980.1814 2093
R(22)	2940 2641.0680	0.0034	980.7665 3643
R(23)	2941 9983.8693	0.0034	981.3450 3001
R(24)	2943 7127.7959	0.0035	981.9168 8985
R(25)	2945 4072.4807	0.0035	982.4821 0369
R(26)	2947 0817.5447	0.0035	983.0406 5891
R(27)	2948 7362.5966	0.0036	983.5925 4243
R(28)	2950 3707.2326	0.0037	984.1377 4080
R(29)	2951 9851.0371	0.0038	984.6762 4016
R(30)	2953 5793.5817	0.0040	985.2080 2620
R(31)	2955 1534.4257	0.0043	985.7330 8424
R(32)	2956 7073.1163	0.0046	986.2513 9917
R(33)	2958 2409.1878	0.0050	986.7629 5545
R(34)	2959 7542.1621	0.0059	987.2677 3714
R(35)	2961 2471.5487	0.0082	987.7657 2787
R(36)	2962 7196.8443	0.0128	988.2569 1086
R(37)	2964 1717.5329	0.0206	988.7412 6890
R(38)	2965 6033.0860	0.0322	989.2187 8435
R(39)	2967 0142.9621	0.0489	989.6894 3916
R(40)	2968 4046.6072	0.0718	990.1532 1483
R(41)	2969 7743.4542	0.1026	990.6100 9247
R(42)	2971 1232.9234	0.1431	991.0600 5273
R(43)	2972 4514.4219	0.1957	991.5030 7584
R(44)	2973 7587.3442	0.2628	991.9391 4159
R(45)	2975 0451.0716	0.3476	992.3682 2934
R(46)	2976 3104.9725	0.4534	992.7903 1804
R(47)	2977 5548.4022	0.5844	993.2053 8618
R(48)	2978 7780.7031	0.7450	993.6134 1182
R(49)	2979 9801.2044	0.9406	994.0143 7258
R(50)	2981 1609.2224	1.1769	994.4082 4567
R(51)	2982 3204.0601	1.4606	994.7950 0782
R(52)	2983 4585.0076	1.7992	995.1746 3537
R(53)	2984 5751.3418	2.2012	995.5471 0418
R(54)	2985 6702.3264	2.6758	995.9123 8971
R(55)	2986 7437.2121	3.2337	996.2704 6696
R(56)	2987 7955.2367	3.8863	996.6213 1049
R(57)	2988 8255.6246	4.6466	996.9648 9445
R(58)	2989 8337.5873	5.5289	997.3011 9252
R(59)	2990 8200.3233	6.5490	997.6301 7799

(continues)

TABLE 10 *(continued)*

BAND II

LINE	FREQUENCY (MHZ)	STD.DEV. (MHZ)	VAC.WAVE NO. (CM-1)
P(60)	3053 8359.5142	0.4634	1018.6500 2602
P(59)	3056 9761.4634	0.3777	1019.6974 8230
P(58)	3060 1020.0398	0.3054	1020.7401 5617
P(57)	3063 2134.5330	0.2448	1021.7780 2395
P(56)	3066 3104.2389	0.1942	1022.8110 6214
P(55)	3069 3928.4602	0.1524	1023.8392 4749
P(54)	3072 4606.5061	0.1182	1024.8625 5695
P(53)	3075 5137.6927	0.0904	1025.8809 6772
P(52)	3078 5521.3436	0.0680	1026.8944 5722
P(51)	3081 5756.7892	0.0503	1027.9030 0313
P(50)	3084 5843.3680	0.0366	1028.9065 8337
P(49)	3087 5780.4257	0.0261	1029.9051 7612
P(48)	3090 5567.3161	0.0184	1030.8987 5984
P(47)	3093 5203.4011	0.0131	1031.8873 1323
P(46)	3096 4688.0508	0.0098	1032.8708 1527
P(45)	3099 4020.6437	0.0080	1033.8492 4526
P(44)	3102 3200.5669	0.0071	1034.8225 8272
P(43)	3105 2227.2163	0.0066	1035.7908 0753
P(42)	3108 1099.9967	0.0063	1036.7538 9982
P(41)	3110 9818.3221	0.0059	1037.7118 4004
P(40)	3113 8381.6157	0.0056	1038.6646 0896
P(39)	3116 6789.3101	0.0052	1039.6121 8765
P(38)	3119 5040.8476	0.0049	1040.5545 5750
P(37)	3122 3135.6800	0.0047	1041.4917 0024
P(36)	3125 1073.2694	0.0045	1042.4235 9791
P(35)	3127 8853.0875	0.0044	1043.3502 3290
P(34)	3130 6474.6165	0.0044	1044.2715 8793
P(33)	3133 3937.3489	0.0044	1045.1876 4608
P(32)	3136 1240.7875	0.0043	1046.0983 9076
P(31)	3138 8384.4458	0.0043	1047.0038 0574
P(30)	3141 5367.8482	0.0043	1047.9038 7516
P(29)	3144 2190.5298	0.0042	1048.7985 8351
P(28)	3146 8852.0367	0.0042	1049.6879 1566
P(27)	3149 5351.9262	0.0042	1050.5718 5682
P(26)	3152 1689.7667	0.0042	1051.4503 9262
P(25)	3154 7865.1382	0.0042	1052.3235 0902
P(24)	3157 3877.6318	0.0042	1053.1911 9241
P(23)	3159 9726.8505	0.0042	1054.0534 2954
P(22)	3162 5412.4088	0.0042	1054.9102 0754
P(21)	3165 0933.9330	0.0042	1055.7615 1395
P(20)	3167 6291.0614	0.0043	1056.6073 3671
P(19)	3170 1483.4440	0.0043	1057.4476 6414
P(18)	3172 6510.7431	0.0043	1058.2824 8498
P(17)	3175 1372.6330	0.0043	1059.1117 8836
P(16)	3177 6068.8002	0.0044	1059.9355 6383
P(15)	3180 0598.9435	0.0044	1060.7538 0134
P(14)	3182 4962.7742	0.0045	1061.5664 9125
P(13)	3184 9160.0159	0.0045	1062.3736 2435
P(12)	3187 3190.4045	0.0046	1063.1751 9184

(continues)

TABLE 10 *(continued)*

BAND II *(continued)*

LINE	FREQUENCY (MHZ)	STD.DEV. (MHZ)	VAC.WAVE NO. (CM-1)
P(11)	3189 7053.6889	0.0048	1063.9711 8532
P(10)	3192 0749.6301	0.0049	1064.7615 9684
P(9)	3194 4278.0022	0.0051	1065.5464 1886
P(8)	3196 7638.5917	0.0053	1066.3256 4425
P(7)	3199 0831.1981	0.0055	1067.0992 6632
P(6)	3201 3855.6333	0.0056	1067.8672 7881
P(5)	3203 6711.7224	0.0058	1068.6296 7588
P(4)	3205 9399.3031	0.0059	1069.3864 5211
P(3)	3208 1918.2262	0.0060	1070.1376 0253
P(2)	3210 4268.3552	0.0061	1070.8831 2259
P(1)	3212 6449.5665	0.0061	1071.6230 0816
V(0)	3214 8461.7495	0.0061	1072.3572 5555
R(0)	3217 0304.8066	0.0060	1073.0858 6151
R(1)	3219 1978.6530	0.0059	1073.8088 2320
R(2)	3221 3483.2169	0.0058	1074.5261 3824
R(3)	3223 4818.4395	0.0056	1075.2378 0466
R(4)	3225 5984.2747	0.0054	1075.9438 2093
R(5)	3227 6980.6896	0.0052	1076.6441 8594
R(6)	3229 7807.6639	0.0051	1077.3388 9903
R(7)	3231 8465.1904	0.0049	1078.0279 5994
R(8)	3233 8953.2747	0.0047	1078.7113 6887
R(9)	3235 9271.9352	0.0046	1079.3891 2643
R(10)	3237 9421.2029	0.0045	1080.0612 3366
R(11)	3239 9401.1219	0.0045	1080.7276 9202
R(12)	3241 9211.7486	0.0044	1081.3885 0340
R(13)	3243 8853.1525	0.0044	1082.0436 7011
R(14)	3245 8325.4153	0.0044	1082.6931 9488
R(15)	3247 7628.6314	0.0044	1083.3370 8086
R(16)	3249 6762.9079	0.0044	1083.9753 3162
R(17)	3251 5728.3640	0.0045	1084.6079 5114
R(18)	3253 4525.1314	0.0045	1085.2349 4381
R(19)	3255 3153.3541	0.0044	1085.8563 1444
R(20)	3257 1613.1883	0.0044	1086.4720 6823
R(21)	3258 9904.8024	0.0044	1087.0822 1080
R(22)	3260 8028.3769	0.0044	1087.6867 4817
R(23)	3262 5984.1040	0.0043	1088.2856 8676
R(24)	3264 3772.1880	0.0043	1088.8790 3338
R(25)	3266 1392.8451	0.0043	1089.4667 9523
R(26)	3267 8846.3029	0.0043	1090.0489 7991
R(27)	3269 6132.8008	0.0043	1090.6255 9542
R(28)	3271 3252.5895	0.0044	1091.1966 5010
R(29)	3273 0205.9314	0.0044	1091.7621 5272
R(30)	3274 6993.0998	0.0045	1092.3221 1238
R(31)	3276 3614.3794	0.0046	1092.8765 3859
R(32)	3278 0070.0659	0.0048	1093.4254 4121
R(33)	3279 6360.4658	0.0050	1093.9688 3046
R(34)	3281 2485.8964	0.0052	1094.5067 1692
R(35)	3282 8446.6858	0.0054	1095.0391 1155
R(36)	3284 4243.1725	0.0056	1095.5660 2563

(continues)

TABLE 10 *(continued)*

BAND II *(continued)*

LINE	FREQUENCY (MHZ)	STD.DEV. (MHZ)	VAC.WAVE NO. (CM-1)
R(37)	3285 9875.7055	0.0059	1096.0874 7080
R(38)	3287 5344.6439	0.0061	1096.6034 5905
R(39)	3289 0650.3571	0.0065	1097.1140 0268
R(40)	3290 5793.2244	0.0071	1097.6191 1437
R(41)	3292 0773.6349	0.0083	1098.1188 0707
R(42)	3293 5591.9873	0.0105	1098.6130 9411
R(43)	3295 0248.6901	0.0142	1099.1019 8909
R(44)	3296 4744.1609	0.0196	1099.5855 0595
R(45)	3297 9078.8267	0.0271	1100.0636 5893
R(46)	3299 3253.1235	0.0372	1100.5364 6258
R(47)	3300 7267.4961	0.0502	1101.0039 3173
R(48)	3302 1122.3983	0.0668	1101.4660 8152
R(49)	3303 4818.2921	0.0876	1101.9229 2736
R(50)	3304 8355.6482	0.1135	1102.3744 8496
R(51)	3306 1734.9456	0.1452	1102.8207 7028
R(52)	3307 4956.6710	0.1838	1103.2617 9957
R(53)	3308 8021.3193	0.2304	1103.6975 8933
R(54)	3310 0929.3931	0.2863	1104.1281 5632
R(55)	3311 3681.4023	0.3529	1104.5535 1756
R(56)	3312 6277.8646	0.4317	1104.9736 9032
R(57)	3313 8719.3043	0.5246	1105.3886 9208
R(58)	3315 1006.2533	0.6335	1105.7985 4058
R(59)	3316 3139.2500	0.7606	1106.2032 5379

[a]Reproduced with permission from Bradley *et al.* [37]. © 1986 IEEE.

[37] the NIST group included all the measurements that applied to laser transitions of $^{12}C^{16}O_2$, $^{13}C^{16}O_2$, $^{12}C^{18}O_2$, $^{13}C^{18}O_2$, and $^{12}C^{17}O_2$. The uncertainties Maki *et al.* used in the fitting procedure were those given by Bradley *et al.* or those by the other papers cited before. Furthermore, several new absolute frequency measurements of the I-P(12), I-P(14), I-R(10), I-R(30), and II-R(12) lines in the regular band of $^{12}C^{16}O_2$ have been reported [104–107] and were included by Maki *et al.* in their database. Finally more accurate recent measurements [108–110] of the methane line required that the I-R(30) $^{12}C^{16}O_2$ laser line frequency be corrected by −2.9 kHz when compared to the value originally given by Petersen *et al.* [99]. Remember, that it is precisely this I-R(30) $^{12}C^{16}O_2$ regular band transition that was used by Bradley *et al.* [37] as the best single absolute CO_2 reference line available at that time, as previously shown in Table 1.

In the new paper, Maki *et al.* [38] list the improved molecular constants and frequencies for the regular bands of $^{12}C^{16}O_2$, $^{13}C^{16}O_2$, $^{12}C^{18}O_2$, and $^{13}C^{18}O_2$ and for the 01^11—$[11^10, 03^10]_{I,II}$ hot bands of $^{12}C^{16}O_2$, but do not give any new values for the other five CO_2 isotopes listed in Bradley *et al.* [37]

To assess the frequency differences between the results published by Bradley *et al.* [37] and those to be published by Maki *et al.* [38], I compiled Table 11, which shows the frequency differences in kilohertz for the regular band lasing transitions (differing by $\Delta J = 8$ or 10) in the four CO_2 isotopic species to be published by Maki *et al.* [38]. Similar to the case in Tables 2 through 10, the horizontal lines in Table 11 demarcate the boundaries in each vibrational-rotational branch beyond which higher J lines were not measured in the Bradley *et al.* database.

Table 11 clearly indicates that within the database given in Bradley *et al.* only one transition, the II-$R(50)$ of $^{12}C^{18}O_2$, differs by more than 11 kHz. For most other transitions within the measured database in [37] the frequency differences are only a few kilohertz and would be even less had we taken into account the −2.9-kHz correction to be applied to the I-$R(30)$ $^{12}C^{16}O_2$ absolute frequency reference used in Bradley *et al.* [37].

At this stage of development it appears that even more refined techniques will be necessary to attain another order of magnitude improvement in the precision and accuracy of CO_2 beat frequency measurements than was obtained with the relatively simple two-channel heterodyne system depicted in Fig. 13. Such an improved system was developed at MIT Lincoln Laboratory in order to obtain reliable measurements of pressure shifts in the CO_2 laser system [76,111,112]. A brief outline of the improved heterodyne setup and the results of pressure shift measurements is given in the next section. However, before leaving the subject of absolute frequency calibration of CO_2 laser transitions, I would like to repeat here the dedication written for the paper by Bradley *et al.* [37]:

> The authors would like to dedicate this work to the memory of the late Russell Petersen, who did so much for the measurement of absolute frequencies at optical wavelengths, and whose work has been an essential foundation stone for this paper. Russ was also a true friend, and his premature death leaves a large gap in the lives of people who were privileged to know him.

I was gratified to see a very similar dedication to F. R. Petersen in the forthcoming paper by Maki *et al.* [38].

10. PRESSURE SHIFTS IN LINE-CENTER-STABILIZED CO_2 LASERS

In the very first publication on the standing-wave saturation resonances observed in the 4.3-μm fluorescence band of CO_2, Freed and Javan drew attention to the phenomenon (see Fig. 1 in [48]) that the center frequency of the standing-wave saturation resonance shifted by about 0.33 MHz on the low-frequency side of the peak in the broad background curve. (Note that in the actual *Appl. Phys. Lett.* publication exactly the reverse direction was stated and indicated by the arrows. This error was caught shortly after publication and a correction erratum was included with reprints.) The two-mirror laser (shown in Fig. 9)

TABLE 11 Frequency Differences in kHz between Results Published in References [37] and [38]

CO_2 laser		$\Delta\nu$ (kHz) = ν [37] − ν [38]			
Band	Transition	$^{12}C^{16}O_2$	$^{13}C^{16}O_2$	$^{12}C^{18}O_2$	$^{13}C^{18}O_2$
	P(60)	−65.3	−40.2	86.0	−72.9
	P(50)	10.7	6.9	9.1	3.4
	P(40)	6.5	6.0	6.4	6.3
I	P(30)	6.4	5.6	7.5	9.6
	P(20)	7.5	7.0	5.2	10.8
	P(10)	4.9	8.1	4.1	7.5
	P(2)	3.0	9.0	4.9	5.4
	$\nu_o = \nu(o)$	3.0	9.2	5.0	5.4
	R(0)	3.0	9.3	5.1	5.4
	R(10)	4.8	8.7	5.3	7.1
	R(20)	5.3	5.8	3.9	7.7
I	R(30)	2.8	5.6	3.5	4.9
	R(40)	5.9	8.8	8.9	6.3
	R(50)	−3.1	−50.1	31.3	−9.7
	R(58)	−129.4	−23.8	85.1	−149.1
	P(60)	71.3	−0.4	3.5	−44.4
	P(50)	5.8	8.9	3.4	6.0
	P(40)	4.4	2.7	3.0	3.4
II	P(30)	4.6	4.4	4.4	6.3
	P(20)	2.9	4.7	3.5	8.0
	P(10)	3.6	4.7	1.5	5.0
	P(2)	4.8	4.3	1.0	3.2
	$\nu_o = \nu(o)$	5.0	4.4	1.2	3.1
	R(0)	5.0	4.5	1.3	3.1
	R(10)	3.6	5.3	2.6	4.7
	R(20)	0.7	4.5	2.1	4.8
II	R(30)	1.0	4.4	0.3	1.7
	R(40)	3.9	5.5	5.5	3.4
	R(50)	8.2	−48.2	25.5	−7.1
	R(58)	−52.2	−296.2	33.0	−128.9

used in the experiment was filled with 2 Torr CO_2, 2 Torr N_2, and 7 Torr He partial pressures, and the fill pressure of the internal CO_2 absorption cell was 0.02 Torr. Thus the effective pressure shift appeared to be about 330 kHz/11 Torr ~ 30

kHz/Torr of the laser's gas mixture. Because the typical CO_2 fill pressures in the saturable absorber cells used to line-center-stabilize the lasers in the two-channel calibration system were about 40 mTorr, a first-order guess-estimate indicated an approximately 1.2-kHz systematic error in the beat measurements. The magnitude of such an error was too small to worry about too much during the first few years of calibrating the CO_2 laser transitions. When the uncertainties in the measured results diminished from about 20 to 25 kHz to about 5 kHz or less, it seemed prudent to initiate a more precise theoretical and experimental endeavor for evaluating the effect of pressure shift on the frequency calibration of CO_2 laser transitions. Thus "Pressure Shifts in Carbon Dioxide and Its Isotopes" became the topic of the PhD dissertation of SooHoo who then proceeded to compile a vast amount of experimental data and all available theoretical interpretations that took years of assiduous work [112]. The in many ways surprising outcome of this research was summarized in two publications by SooHoo *et al.*

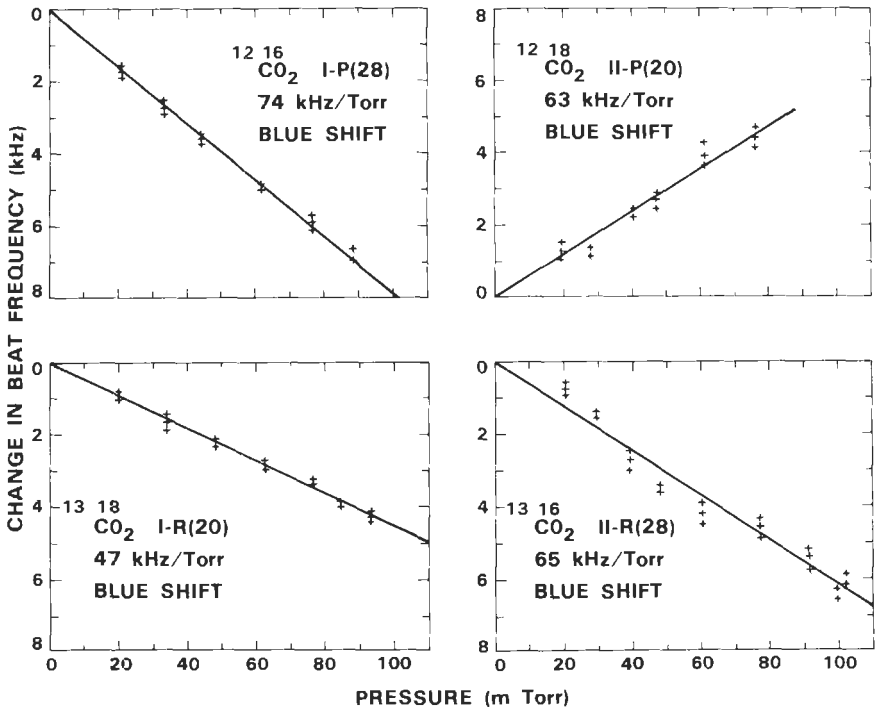

FIGURE 19 Typical pressure shift data sequences, all "blue" shifts, one for each CO_2 isotope and rotational-vibrational branch transition. Note that a "blue shift" sequence may have either a positive or a negative slope depending on whether the fixed reference line was above or below the frequency of the transition that was pressure shifted. (Reprinted with permission from SooHoo *et al.* [76]. © 1985 IEEE.)

in 1984 [111] and 1985 [76], respectively. Here I can only give a few glimpses into some of the findings.

In [76,111,112] we find anomalous blue shifts of CO_2 absorptions with pressure that were in the range of 40 to 90 kHz/Torr for the 626, 636, 828, and 838 CO_2 isotopic species (see Table 1 of [78] or [111]). Figure 19 shows a sample of the plots of typical pressure shift data sequences, all "blue" shifts, one for each of the four CO_2 isotopic species that were measured. Because the CO_2 pressures used in the frequency stabilization cells were typically in the 50 ± 15 mTorr range, the implication is that there is a systematic 3.6 ± 2.2 kHz frequency shift that we chose to ignore when generating the predicted [37] absolute frequencies. Our decision not to take into account pressure shift was based on the considerations that follow.

The anomalous blue pressure shifts we measured could not be explained by any of the theories that we explored [112] or that were suggested to us because all of them predict red pressure shifts. The pressure shifts we measured were very small and necessitated the improvement of our experimental apparatus and measurement technique well beyond what was available when most of our data were gathered for the database given in Bradley *et al.* [37].

Consistent and reproducible pressure shifts were only obtained after we initiated a new measurement technique in order to eliminate frequency-offset errors caused by the nonzero slope of the power-versus-frequency characteristics of the lasers over the frequency range of the nonlinear saturation resonance dip. This nonzero power slope is a universal problem in most stabilization schemes used with lasers. Furthermore, this so-called "instrumental" frequency shift has a quadratic dependence on pressure and may easily dominate over the true pressure shift at stabilization cell pressures greater than about 60 mTorr. Moreover, the sense of this "instrumental" frequency shift can be either red or blue, depending on the adjustment of the grating position in the CO_2 laser as illustrated by the data shown in Fig. 20.

Figure 21 shows the block diagram of the two-channel line-center-stabilized CO_2 heterodyne laser system we used in our experiments for the purpose of determining pressure shift. This system is an expanded version of the one previously described in Fig. 13 and Sec. 8.

Comparison of Figs. 21 and 13 will indicate the addition of a power slope detection channel consisting of a relatively large AuGe detector (in order to detect a portion of the entire combined beam cross section) and a phase-sensitive lock-in amplifier. The power slope signal is already present in the saturated absorption-stabilized system shown in Fig. 21 since the PZT is dithered to recover the first derivative of the 4.3-μm fluorescence signal. By synchronously detecting the laser power output at 9 or 10 μm with an additional detector (a 0.3-cm-diameter gold-doped germanium detector in our system), the slope of the laser power can be measured with a large degree of reliability. In our system the asymmetry in the resonant dip originates from the net dispersive profile, and is the sum total of the

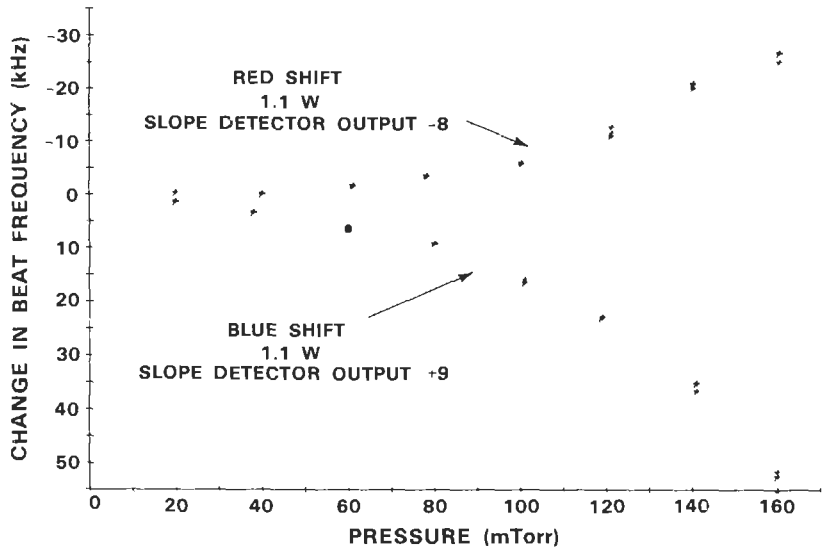

FIGURE 20 Two runs with the grating positions deliberately offset in order to produce both "blue" and "red" shifts. Note that these "instrumental" pseudo pressure shifts may easily dominate over true pressure shift, especially for pressures greater than about 60 mTorr. (Reprinted with permission from SooHoo *et al.* [76]. © 1985 IEEE.)

dispersion due to the laser configuration, cavity alignment, components, and lasing and absorption medium. Even with an ideal cavity configuration, there are physical and mechanical limitations on designing and building a perfectly centered and a perfectly aligned laser cavity, especially since the PZT, with a nonlinear hysteresis response to a symmetric signal, can easily distort any alignment of the cavity as a function of the applied voltage, and may also introduce dither-caused asymmetry in the derivative signal. In grating-controlled lasers, such as are used in our system, there is the additional inherent dispersion of the grating itself. Consequently, the laser power peak for any J line will almost never coincide perfectly with the corresponding saturated resonance dip, and the error will depend on the existing laser power profile and cavity configuration. It turns out that for each J line there is a certain angular tuning range of the grating for which that line and a particular longitudinal mode dominate the laser gain. Because the gain profile depends on the cavity arrangement, including the grating position, slightly tilting the grating creates a different cavity configuration and consequently a different gain profile, which generally varies from J line to J line. Figure 20 is an illustration of both blue and red "instrumental" pseudo pressure shifts that were obtained by deliberately offsetting the grating positions first in one and then in the other direction. Note that the power slope offset error varies quadratically with pressure and its

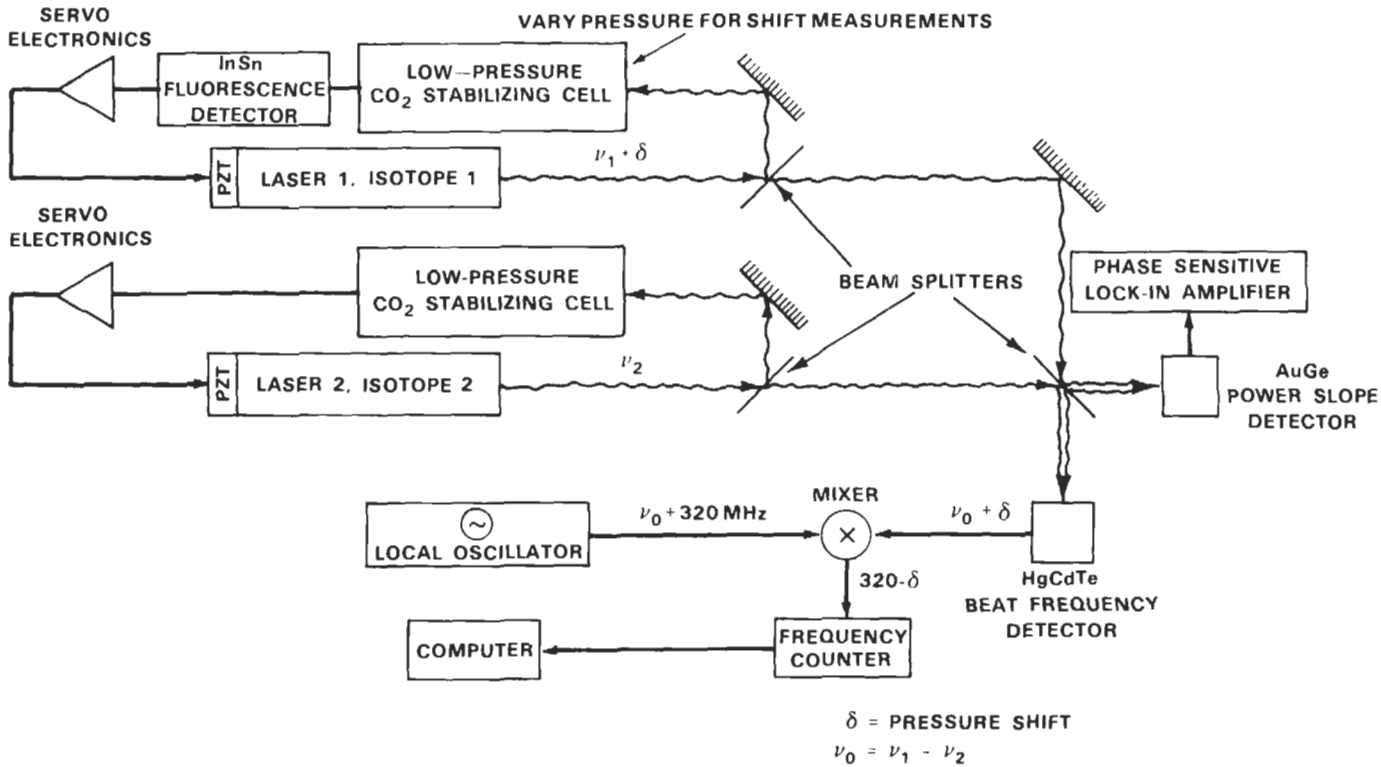

FIGURE 21 Block diagram of the improved two-channel line-center-stabilized CO_2 laser heterodyne system used to measure pressure shifts. (Reprinted with permission from SooHoo *et al.* [76]. © 1985 IEEE.)

magnitude will also depend on the power incident on the stabilization cells. Note, however, that by shychronously detecting the laser output, the power slope can be monitored and adjusted (by incrementally tilting the diffraction grating) to obtain as close to zero slope as possible at the center of the Doppler-free saturation resonance. By using this technique, reliable pressure shift measurements could be taken without the overriding errors so frequently encountered as a result of the power slope variations.

Another way to solve the background slope problem is through the use of the so-called third derivative detection method. In most saturated absorption experiments, the laser signal is dithered (frequency modulated) and the first derivative signal ($1f$) is detected and used as a frequency discriminator. If one assumes a parabolic power profile, then the background slope error can be eliminated if the third derivative signal is detected and used as a frequency discriminator. This third derivative ($3f$) method of stabilization has been utilized in several saturated absorption systems using CH_4 [113], OSO_4, and SF_6 [114], where the $3f$ absorption signal is large enough to eliminate or at least reduce the power slope error without sacrificing the stability provided by the much larger SNR of the $1f$ technique. However, potentially serious errors may be introduced by third harmonic distortions [115–117] due to both the motion of the laser mirror (caused by distortion in the modulation drive voltage or nonlinearities in the PZT driver) and in the optical detector and associated $3f$ phase-sensitive electronics. In our system, the frequency stability using the $3f$ technique was worse than that obtained with the $1f$ technique. We have, therefore, devised the new power slope detection method to eliminate the background slope and retain the SNR advantage of the $1f$ stabilization technique.

By using the new technique we were able to reliably measure the "true" pressure shifts both in pure CO_2 and with the admixture of various perturber gases.

Several possible explanations for the anomalous behavior of the pressure shifts obtained in our experiments were considered [112], none of which could explain the blue shift.

The effect of different perturber gases on the pressure shift of CO_2 was also studied. Here the frequency shift for fixed CO_2 (20 to 30 mTorr) pressure as a function of different perturber gas additives (up to about 80-mTorr perturber gas pressure) including Xe, Ar, N_2, He, H_2, and CH_3F were measured. Xenon, Ar, N_2, and CH_3F gave blue shifts, and He and H_2 gave red shifts. The magnitudes of the shifts scaled roughly with their corresponding polarizabilities except for the change in sign.

Similarly anomalous results have been obtained by Bagaev and Chebotayev [118,119] for a CH_4-stabilized HeNe system in which extremely small blue shifts were measured for CH_4 perturbed by Xe, He, or Kr at pressures less than 10 mTorr; on the other hand red shifts were measured for the same transitions for nobel gas perturbers (Xe, Kr, Ar, Ne, He) at pressures greater than 10 Torr [120]. Again, the blue shift at low pressures was measured using saturated absorption techniques, whereas linear techniques were used in the high-pressure regime.

11. SMALL-SIGNAL GAIN AND SATURATION INTENSITY OF REGULAR BAND LASING TRANSITIONS IN SEALED-OFF CO_2 ISOTOPE LASERS

The stability and most other operational characteristics of rare CO_2 isotope lasers are generally similar to the commonly used $^{12}C^{16}O_2$ lasers. However, the small-signal gain coefficient α_o and saturation intensity I_s of the rare CO_2 lasing transitions can be significantly different from corresponding lines of $^{12}C^{16}O_2$. It can be shown that the power output of a laser may be approximated [121] by

$$P_0 = 2 I_s A t_r \left(\frac{\alpha_0 L}{l_i + t_r} - 1 \right) , \tag{19}$$

where l_i is the internal cavity loss per pass, t_r is the transmittance of the output mirror, and L and A are the length and effective cross-section area of the gain medium, respectively. Equation (19) clearly shows that the small-signal gain coefficient α_o and saturation intensity I_s are the two salient parameters to be measured in order to optimize a laser design for a desired output power P_o.

The measured values of small-signal gain coefficient α_o and saturation intensity I_s will, to a very large degree, depend on a number of experimental parameters, such as excitation currents, gas pressures, mixtures and mixing ratios, wall temperatures, and discharge tube diameters. CO_2 dissociation and recombination rates and impurity buildup will also critically affect both α_o and I_s, and thus output power and CO_2 laser lifetime. Recirculating gas flow can lead to very large increases of the small-signal gain coefficient and saturation intensity by a complex combination of effects involving not only convective cooling, but also better control of CO_2 dissociation and recombination rates and impurity cleanup by means of appropriately chosen catalytic converters. Clearly, any meaningful measurement of small-signal gain and saturation intensity in a CO_2 amplifier should be accompanied by a detailed description of the experimental method and associated parameters. Note that the gas-discharge scaling laws and other results described by Abrams and Bridges [122] may be of great value in extrapolation from a given set of data.

Effects due to Fermi resonance play a major role in determining the very significant variations in gain for the I and II bands in the various CO_2 isotopes. This was both theoretically and experimentally demonstrated for the first time by Silver *et al.* [123] in 1970. To show the effect of Fermi resonance on the laser gain, it is only necessary to form the gain ratio of the transitions. Silver *et al.* used the gains measured for the $^{12}C^{18}O_2$, $^{12}C^{16}O_2$, and $^{13}C^{16}O_2$ I and II band $P(20)$ transitions to obtain their results. The ratios of gain and absorption coefficients depend directly on the matrix element ratio, which they calculated from the vibrational state wave functions. Thus, the ratio of gain was given [123] as $g(00^01\text{–I})/g(00^01\text{–II}) = K(00^01\text{–I})/K(00^01\text{–II})$ where K denoted the J-independent portion of the matrix element ratio inferred from gain and loss measurements. The final result obtained for the matrix element ratio was [123]:

$$\frac{K\left(00^0 1 - I\right)}{K\left(00^0 1 - II\right)} = \left|\frac{a + 0.13b}{b - 0.13a}\right|^2 , \tag{20}$$

where the coefficients a and b were calculated from tabulated [124] unperturbed energy-level splittings δ and the energy-level splittings Δ, including Fermi resonance effects, as

$$a = \left[\left(\Delta + \delta\right) / 2\Delta\right]^{1/2}; \; b = \left(1 - a^2\right)^{1/2}. \tag{21}$$

Table 12 summarizes the results Silver *et al.* obtained [123] for $^{12}C^{16}O_2$, $^{12}C^{18}O_2$, and $^{13}C^{16}O_2$.

In their 1970 paper, Silver *et al.* [123] gave results only for the ratios of the measured $P(20)$ gain values but not for the individual gain coefficients. More comprehensive experiments were carried out at MIT Lincoln Laboratory by Freed *et al.* in 1981 in which both the small-signal gain coefficients α_o and the saturation parameters I_s were determined [125] for five laser transitions in each of the four rotational branches of the (00^01–I) and (00^01–II) vibrational bands. Some of the results associated with the $P(20)$ transitions are listed in Table 13

TABLE 12 Results of Silver *et al.* [123]

$\frac{10^00-I}{10^00-II}$ ratios	$^{12}C^{16}O_2$	$^{12}C^{18}O_2$	$^{13}C^{16}O_2$
Matrix element	1.4	0.48	3.2
Absorption coefficient	1.0	0.3	1.8
Gain coefficient	1.3	0.4	2.5

TABLE 13 Comparison of the Small-Signal Gain Coefficients and Saturation Parameters of the $P(20)$ Transitions in Five CO_2 Species[a]

Band	Parameter	$^{12}C^{16}O_2$	$^{12}C^{18}O_2$	$^{13}C^{16}O_2$	$^{13}C^{18}O_2$	$^{14}C^{16}O_2$
I	α_o (% cm^{-1})	1.07	0.30	0.64	0.42	0.55
	I_s (W-cm^{-2})	47	30	38	39	56
II	α_o (% cm^{-1})	0.9	0.73	0.26	0.42	0.099
	I_s (W-cm^{-2})	25	39	9	32	~3
Measured	$\frac{\alpha_o\text{–I}}{\alpha_o\text{–II}}$	1.2	0.4	2.5	1.0	5.6
Calculated	$\frac{K\text{–I}}{K\text{–II}}$	1.4	0.5	3.2	1.0	7.1

[a]Reprinted with permission from Freed *et al.* [125]. © 1982 IEEE.

and show excellent agreement with the corresponding values of Silver *et al.* More importantly, however, Table 13 gives a quick preview of the significant differences between corresponding I and II band transitions of a given isotope and also among corresponding transitions of the various CO_2 isotopic species. The procedure followed by Freed *et al.* in the Lincoln Laboratory experiments in 1981 was based on the method developed by Christensen *et al.* in 1969 [126].

In a typical gain measurement sequence, the laser oscillator was first frequency locked to the line center of the transition to be measured, and the amplifier gain was then determined for several input power levels.

The TEM_{00q} mode output beam of the CO_2 oscillator was recollimated into the amplifier in a confocal configuration, with the position of the beamwaist at the center of the amplifier. The water-cooled, sealed-off amplifier had an inside diameter of 1.3 cm and an active length of 203 cm. The computed average probe-beam diameter within the amplifier was $2\bar{r} = 0.35$ cm at the e^{-1} point of intensity. Under these conditions typically 85% of the probe beam was transmitted through the unexcited amplifier. About half of the insertion loss could be attributed to attenuation of the gas mix. The remaining attenuation was caused by window loss, aperturing, and scatter in the amplifier bore due to slight misalignments.

The gas mixtures used were identical for all CO_2 isotopes and consisted of 59.2% He, 20% CO_2, 14.5% N_2, 5.5% Xe, and ~1.3% H_2 at a total pressure of 11.75 Torr. The sealed-off volume of the amplifier was 830 cm^3, of which 310 cm^3 (37% of the entire volume) was occupied by the excited discharge. After a fresh fill of the amplifier, the discharge was turned on for at least several hours to allow the CO_2 dissociation-recombination process and gas mixing to come to equilibrium before commencing with the measurements.

The gain was determined by taking the ratio of the output power measured with the amplifier discharge on, to the output power with the discharge off. True amplifier gain is, of course, defined as the ratio of power output to power input and in this sense the values of gain we determined are overestimated, but by no more than a few percent. This overestimate of the measured gain is probably more than counterbalanced by the fact that the experimental parameters were not optimized for each individual transition of the various isotopic gas mixtures.

The gain was measured for five transitions ($J = 12, 16, 20, 24, 28$) in each of the four rotational branches of the (00^01)—$[10^00, 02^00]_{I,II}$ vibrational bands. Thus, 20 individual vibrational-rotational transitions were measured for each CO_2 isotopic gas mixture.

The data gathering for a given isotopic mixture was carried to completion with a single gas fill of the amplifier. The amplifier power output readings were taken within about 2 min after turning on the amplifier discharge. The measured gain had excellent day-to-day repeatability.

The 10 ± 1 mA excitation current in our experiments was optimized for maximum small-signal gain and was substantially lower than one would find in

TABLE 14 Small-Signal Gain Coefficients α_o and Saturation Parameters I_s for a ^4He—$^{12}C^{16}O_2$—$^{14}N_2$—Xe Mixture[a]

Band	Transition	α_o (% cm^{-1} or m^{-1})	I_s (W-cm^{-2})	$\alpha_o I_s$ (W-cm^{-3})
	P(28)	0.90	32	0.28
	P(24)	1.01	34	0.34
	P(20)	1.07	47	0.50
	P(16)	1.00	42	0.42
	P(12)	0.88	38	0.34
I				
	R(12)	0.88	24	0.21
	R(16)	0.96	29	0.28
	R(20)	0.96	29	0.28
	R(24)	0.88	33	0.29
	R(28)	0.77	26	0.20
	P(28)	0.79	22	0.18
	P(24)	0.88	22	0.20
	P(20)	0.90	25	0.23
	P(16)	0.87	22	0.19
	P(12)	0.74	20	0.15
II				
	R(12)	0.74	22	0.16
	R(16)	0.84	23	0.19
	R(20)	0.84	23	0.19
	R(24)	0.85	22	0.19
	R(28)	0.70	20	0.14

[a]Reprinted with permission of Freed *et al.* [125]. © 1982 IEEE.

trying to maximize the power output of an oscillator with the same discharge tube diameter. CO_2 laser oscillators, which are usually optimized for maximum power output, operate under highly saturated conditions. The saturation parameter is generally proportional to pressure squared [127], $I_s \propto p^2$, and therefore CO_2 laser oscillators are filled to higher pressures than amplifiers, which are usually optimized for maximum small-signal gain.

Our measurements of the small gain coefficients and saturation parameters for 20 transitions in each of the five high-purity isotopic species—$^{12}C^{16}O_2$, $^{12}C^{18}O_2$, $^{13}C^{16}O_2$, $^{13}C^{18}O_2$, and $^{14}C^{16}O_2$—are summarized in Tables 14 through 18. The large variations measured for corresponding I and II band transitions of a given isotope were due to the Fermi-resonance coupling of the (10^00) and

TABLE 15 Small-Signal Gain Coefficients α_o and Saturation Parameters I_s for a $^4He—^{12}C^{18}O_2—^{14}N_2—Xe$ Mixture[a]

Band	Transition	α_o (% cm^{-1} or m^{-1})	I_s (W-cm^{-2})	$\alpha_o I_s$ (W-cm^{-3})
	P(28)	0.27	22	0.060
	P(24)	0.30	24	0.071
	P(20)	0.30	30	0.091
	P(16)	0.28	24	0.069
	P(12)	0.24	22	0.052
I				
	R(12)	0.24	23	0.054
	R(16)	0.26	27	0.071
	R(20)	0.27	29	0.079
	R(24)	0.26	22	0.059
	R(28)	0.23	20	0.047
	P(28)	0.66	30	0.20
	P(24)	0.71	34	0.24
	P(20)	0.73	39	0.28
	P(16)	0.67	36	0.24
	P(12)	0.60	25	0.15
II				
	R(12)	0.60	28	0.17
	R(16)	0.64	30	0.19
	R(20)	0.64	33	0.21
	R(24)	0.62	31	0.19
	R(28)	0.50	28	0.14

[a]Reprinted with permission from Freed *et al.* [125]. © 1982 IEEE.

(02^00) levels. The gain coefficient ratios measured experimentally were in good agreement with matrix element calculations. Substitution of $^{15}N_2$ instead of $^{14}N_2$ did not significantly improve the results obtained for $^{13}C^{16}O_2$ and $^{14}C^{16}O_2$. The small-signal gain coefficients and saturation parameters tabulated in Tables 14 through 18 may only serve as guidelines in the design of sealed-off CO_2 isotope lasers and amplifiers. The actual values that may be obtained would depend on the optimization procedure since the design parameters required for maximum gain, highest power, greatest efficiency, and longest sealed-off life are generally quite different. The products $\alpha_o I_s$ listed in the tables give a conservative but good indication of the fundamental mode power per unit length that can be achieved with sealed-off CO_2 lasers.

TABLE 16 Small-Signal Gain Coefficients α_o and Saturation Parameters I_s for a ^4He—$^{13}C^{16}O_2$—$^{14}N_2$—Xe Mixture[a]

Band	Transition	α_o (% cm^{-1} or m^{-1})	I_s (W-cm^{-2})	$\alpha_o I_s$ (W-cm^{-3})
	P(28)	0.55	28	0.15
	P(24)	0.61	35	0.22
	P(20)	0.64	38	0.25
	P(16)	0.61	36	0.22
	P(12)	0.53	24	0.13
I				
	R(12)	0.52	25	0.13
	R(16)	0.57	30	0.17
	R(20)	0.56	32	0.18
	R(24)	0.51	33	0.17
	R(28)	0.44	25	0.11
	P(28)	0.23	7.7	0.018
	P(24)	0.26	8.4	0.022
	P(20)	0.26	8.7	0.023
	P(16)	0.25	7.2	0.018
	P(12)	0.21	5.6	0.012
II				
	R(12)	0.21	4.6	0.010
	R(16)	0.23	5.4	0.012
	R(20)	0.23	6.0	0.014
	R(24)	0.23	4.8	0.011
	R(28)	0.19	2.1	0.004

[a]Reprinted with permission from Freed *et al.* [125]. © 1982 IEEE.

12. LASER DESIGN

All of the experimental results described in this chapter that were carried out at MIT Lincoln Laboratory were obtained with ultrastable lasers and amplifiers that were designed and constructed at MIT Lincoln Laboratory. However, copies of the designs were also sent to qualified researchers outside the MIT community, and many of the lasers were reproduced elsewhere.

The most important aspects of the design were based on the He–Ne laser design of Javan *et al.* [128], which demonstrated superb frequency stability [129]. Departure from the original He–Ne designs occurred in three stages between 1966 and 1968 as described in [56]. Additional details on the evolution

TABLE 17 Small-Signal Gain Coefficients α_o and Saturation Parameters I_s for a ^4He—$^{13}C^{18}O_2$—$^{14}N_2$—Xe Mixture[a]

Band	Transition	α_o (% cm^{-1} or m^{-1})	I_s (W-cm^{-2})	$\alpha_o I_s$ (W-cm^{-3})
	P(28)	0.37	33	0.12
	P(24)	0.40	35	0.14
	P(20)	0.42	39	0.17
	P(16)	0.37	30	0.11
	P(12)	0.32	18	0.057
I				
	R(12)	0.30	23	0.070
	R(16)	0.34	24	0.081
	R(20)	0.34	27	0.091
	R(24)	0.33	23	0.077
	R(28)	0.31	16	0.051
	P(28)	0.38	23	0.087
	P(24)	0.42	29	0.12
	P(20)	0.42	32	0.13
	P(16)	0.39	30	0.12
	P(12)	0.32	19	0.063
II				
	R(12)	0.28	15	0.044
	R(16)	0.34	23	0.079
	R(20)	0.37	27	0.10
	R(24)	0.37	26	0.096
	R(28)	0.34	23	0.078

[a]Reprinted with permission from Freed *et al.* [125]. © 1982 IEEE.

and output characteristics of the various designs may be found (in chronological order) in [130,55,72,16,77,56,63]. Virtually all experimental results described in this chapter were obtained with the (so-called) third-generation lasers [72,56] that have been in use at Lincoln Laboratory since the beginning of 1968. Most of the stable CO_2 (and CO) laser oscillators that were designed and constructed at Lincoln Laboratory have several common features, described as follows.

A nearly semiconfocal optical cavity configuration is used, which yields a ratio of relative diffraction loss of about 10 to 1 between the low-loss off-axis TEM_{10q} mode and the desired fundamental TEM_{00q} mode. In general, only fundamental TEM_{00q} mode operation can overcome the combined losses, which are due to output coupling and diffraction. The lasers are dc-excited internal-mirror

TABLE 18 Small-Signal Gain Coefficients α_o and Saturation Parameters I_s for a ^4He—$^{14}C^{16}O_2$—$^{14}N_2$—Xe Mixture[a]

Band	Transition	α_o (% cm^{-1} or m^{-1})	I_s (W-cm^{-2})	$\alpha_o I_s$ (W-cm^{-3})
	P(28)	0.37	30	0.11
	P(24)	0.42	32	0.13
	P(20)	0.45	44	0.20
	P(16)	0.43	34	0.15
	P(12)	0.36	26	0.094
I				
	R(12)	0.35	26	0.091
	R(16)	0.39	29	0.11
	R(20)	0.39	30	0.12
	R(24)	0.36	23	0.083
	R(28)	0.30	19	0.057
	P(28)	0.076		
	P(24)	0.084		
	P(20)	0.086	~3	0.0026
	P(16)	0.083		
	P(12)	0.071		
II				
	R(12)	0.064		
	R(16)	0.074		
	R(20)	0.076		
	R(24)	0.065		
	R(28)	0.048		

[a]Reprinted with permission from Freed *et al.* [125]. © 1982 IEEE.

tubes in which four superinvar or other very low coefficient of expansion invar alloy rods rigidly space the mirror holders to achieve maximum open-loop stability. To the best of my knowledge, this was the first use of superinvar for the optical resonator of a laser. Furthermore, acoustic damping, magnetic shielding, and thermal insulation of the optical cavity was achieved by a variety of materials surrounding each superinvar rod in a concentrically layered arrangement. Viscous damping compounds, insulating foam, lead, Mu-metal and Co-netic magnetic shields, and aluminum foil provided this isolation of the rods. The shielded superinvar cavity lasers yielded more than a factor-of-100 improvement in short-term stability compared to the first-generation stable CO_2 lasers built at Lincoln Laboratory.

In the third-generation design careful choices of materials and techniques are employed for enhancing the open-loop stability of the optical cavity. However, in spite of the rigid structure, the laser design is entirely modular and can be rapidly disassembled and reassembled; mirrors can be interchanged, and mirror holders can be replaced by piezoelectric and grating-controlled tuners. The stainless steel endplates and the eight differential-alignment screws of the first- and second-generation designs were replaced by much more stable black diabase endplates and a novel internal mirror-alignment mechanism that is not accessible from the outside. The third-generation lasers are not only more stable, but also much easier to align and less costly to manufacture compared to the older designs.

In the simplest configuration the laser has two mirrors, one of which is piezoelectrically tunable. Two-mirror lasers come in various lengths, depending on the output power requirements, and are used primarily in CO_2 optical radars as local and power oscillators. However, for applications in spectroscopy, grating-controlled lasers are much more suitable than the simpler two-mirror lasers.

Figure 22 is a close-up photograph of a grating-controlled stable TEM_{00q} mode laser. Many variants of this basic design exist both at Lincoln Laboratory and elsewhere. This particular unit was built for a relatively high-power application such as optical pumping and frequency shifting. In the laser shown in Fig. 22 the first-order reflection of the grating was coupled through a partially reflecting output mirror. For heterodyne spectroscopy, purely zero-order output coupling from the grating is preferable because many more laser transitions can be obtained with such lasers.

Three grating-controlled lasers with zero-order output coupling are contained in Fig. 23, a photograph of the two-channel heterodyne measurement system, the block diagram of which was previously shown in Fig. 13. The two external frequency-stabilization cells, used for the individual line-center locking of lasers in pairs, are also clearly visible in Fig. 23.

Some of the lasers have short intracavity absorption cells that can be used either for frequency stabilization or for very stable high-repetition-rate passive Q-switching. Such a laser was previously illustrated in Fig. 9, which shows a 50-cm two-mirror laser with a short (3-cm) internal absorption cell. This laser was the

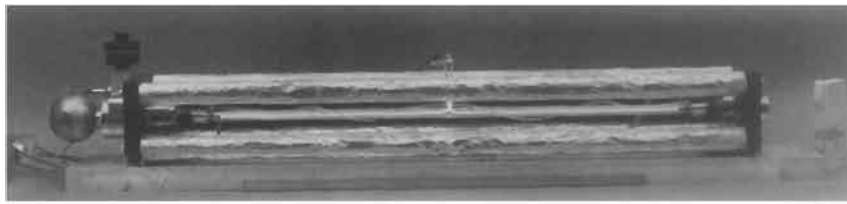

FIGURE 22 Basic grating-controlled stable TEM_{00q} mode CO_2 laser. (Reprinted with permission from Freed [75]. © 1982 IEEE.)

one with which the 4.3-μm standing-wave saturation resonance and the subsequent line-center stabilization of a CO_2 laser were first demonstrated through the use of the 4.3-μm fluorescence signal in 1970, as was discussed in Sec. 8 of this chapter.

For more than 25 years the dual requirements of modularity of laser design and interchangeability of parts have provided a vast amount of convenience and savings both in time and cost. But such requirements have perforce introduced certain limitations in design and performance. Moreover, the laser designs and components were developed more than 25 years ago. Extensive experience gained by working with these lasers clearly indicates that updated designs could easily improve the short-term and long-term stabilities by at least one to two orders of magnitude. However, the instrumentation currently available is not sufficient to measure definitively even the stabilities of our present lasers.

In the research, technology, and calibration of CO_2 laser transitions the main emphasis was on the regular bands of the rare CO_2 isotopes at MIT Lincoln Laboratory. The primary calibration of the regular bands of the most abundant $^{12}C^{16}O_2$ species was first carried out at the NBS (now NIST) in Boulder, Colorado. Calibration of hot bands with line-center-stabilized lasers was started at NRC in Canada in 1977 [100] and continued at NBS/NIST [101], much of it only very recently in 1994 [80,81,83]. Precise calibration of the sequence bands transitions

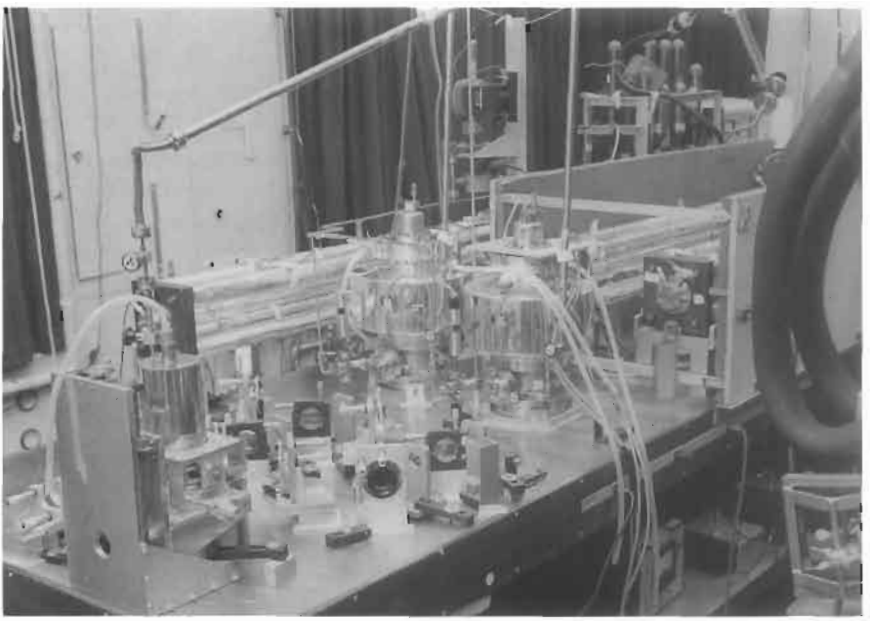

FIGURE 23 The optical portion of the two-channel CO_2 calibration system. (Reprinted with permission from Freed [75]. © 1982 IEEE.)

with line-center-stabilized lasers just began in 1994 [87,88] even though they were first identified in 1973 [94] and extensively studied from 1976 on [89,90].

Most of the sequence band and many of the hot band lasing transitions are very close to the frequencies of those of the much higher gain regular band laser lines. Thus if the laser cavity does not have sufficient frequency discrimination, the regular band laser transitions will dominate as a result of gain competition. As an initial approach to overcome this problem, one can use higher resolution gratings than the 80 line/mm gratings used in the measurements of regular band lasing transitions at MIT Lincoln Laboratory. Indeed, groove densities as high as 171 line/mm were employed in some of the recent work carried out at NIST [80,81,83].

A more effective way of suppressing the oscillation of regular band lasing transitions was achieved by the addition of an intracavity hot CO_2 absorption cell to prevent the buildup of radiation at the regular band transition frequencies. This technique was first used by Reid and Siemsen [89,90] in their comprehensive study of sequence band laser transitions in CO_2. An additional improvement was introduced only very recently by Evenson *et al.* by the addition of a ribbed tube to inhibit the waveguide (or wall-bounce) modes of regular band lasing transitions [80,81].

13. SPANNING THE FREQUENCY RANGE BETWEEN LINE-CENTER STABILIZED CO_2 LASER TRANSITIONS

This section briefly outlines three methods that can provide continuously tunable cw signal sources to either partially or completely span the frequency ranges between adjacent line-center-stabilized isotopic CO_2 laser transitions.

The first of these methods uses small-bore (1- to 2.5-mm circular or rectangular cross section) relatively high-pressure (100- to 400-Torr) CO_2 lasers that could (theoretically at least) provide a tuning range of a few hundred megahertz with relative ease and perhaps as much as 2 to 3 GHz with a great deal of difficulty. Such lasers would have to be relatively long (for a small-bore tube) in order to provide adequate gain to operate in other than the highest gain lasing transitions. Thus they would have to operate in a waveguide mode and their cavity design would be rather complex to provide single axial mode selectivity. An excellent comprehensive review of multimirror (interferometric) laser cavities and other optical resonator mode control methods was published by Smith in 1972 [131,18,19]. The development of waveguide mode CO_2 lasers has taken great strides during the past decade or so, and nowadays probably the majority of small commercially produced CO_2 lasers are waveguide mode lasers. However, at the present at least, I am not aware of a commercially available, high-pressure, single-mode CO_2 laser that could provide more than a few hundred megahertz tuning range in other than the most powerful laser transitions.

Electro-optic waveguide modulators for frequency tuning of CO_2 (and other infrared) lasers provide a second method of obtaining a continuously tunable cw signal source between adjacent CO_2 lasing transitions. The development of such modulators was pioneered by Cheo, who in 1984 reported as much as a 30-GHz total frequency tuning range in two sidebands from a line-selectable CO_2 laser by phase modulation of an optical guided wave in a thin GaAs slab active layer at microwave frequencies [132–135]. More recent advances in electro-optic waveguide modulators for generating tunable sideband power from infrared lasers was also published by Cheo in 1994 [136]. Some of the high-resolution spectroscopic measurements obtained with these modulators are described in [137,138].

The third type of continuously tunable cw signal source is provided by a family of lead-salt tunable diode lasers (TDLs). Undoubtedly, these lasers are by far the most versatile and widely used sources of tunable IR radiation; however, their power output is rather limited, usually below a few milliwatts. Also, their use requires cryogenic cooling, and achieving tunable single-frequency output is often a problem. On the other hand, even a single TDL can provide an enormous tuning range.

The first lead-salt TDLs were made at MIT Lincoln Laboratory by Butler *et al.* in 1964 [139,140]. An excellent short review of the MIT Lincoln Laboratory work on TDLs was written by Melngailis in 1990 [141].

The early MIT Lincoln Laboratory work included the first optical heterodyne detection of beat frequencies between a tunable $Pb_{0.88}Sn_{0.12}Te$ diode laser and a (second-generation) ultrastable CO_2 laser by Hinkley *et al.* in 1968 [142]. Shortly thereafter the first direct observation and experimental verification of the quantum-phase-noise-limited linewidth predicted by Schawlow and Townes in 1958 [57] was demonstrated by Hinkley and Freed also using a $Pb_{0.88}Sn_{0.12}Te$ TDL heterodyned with the same CO_2 laser as described earlier [143]. This fundamental quantum-phase-noise-limited Schawlow–Townes linewidth was subsequently reaffirmed from spectral analysis of the beat frequencies between a solitary $PbS_{1-x}Se_x$ TDL and an ultrastable (third-generation) CO laser by Freed *et al.* at MIT Lincoln Laboratory in 1983 [144]. Linewidths as narrow as ~54 kHz at 10.5 μm [143] and ~22 kHz at 5.3 μm [144] were achieved with the above-mentioned lead-salt TDLs. Figure 24 illustrates the emission wavelength (wave number) range of lead-salt TDLs and some of the compounds used to fabricate such devices.

The reasonably narrow linewidths, the ability to produce devices at any required wavelength to match molecular absorption lines, and the capability of short-range tuning through variation of the injection current opened up semiconductor laser applications in high-resolution spectroscopy and air pollution monitoring. These applications provided the impetus for the creation in 1974 of the first spin-off from Lincoln Laboratory in the laser area, Laser Analytics (presently known as Analytics Division of Laser Photonics, Inc.). To the best of my knowledge this company is the sole U.S. manufacturer of lead-salt TDLs, since MIT Lincoln Laboratory

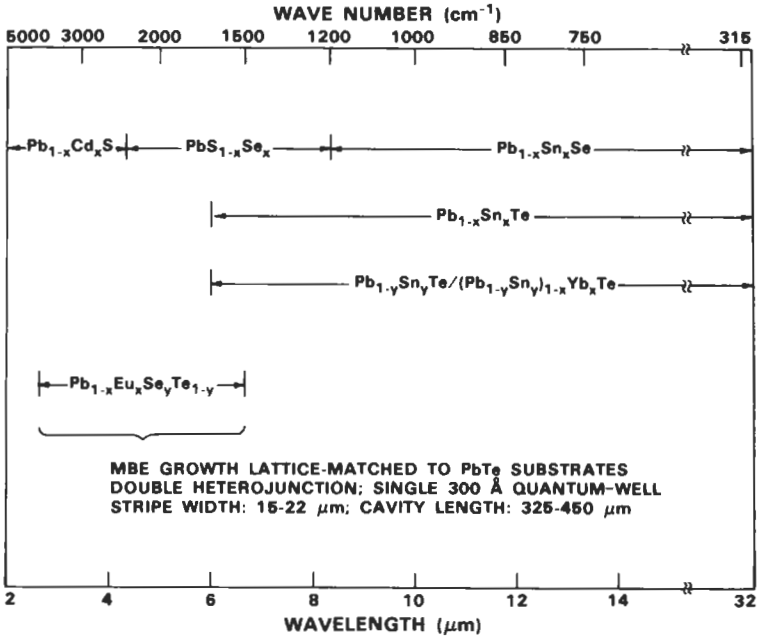

FIGURE 24 Emission wavelength range of various lead-salt TDLs.

discontinued further development of lead-salt lasers shortly after the spin-off by Laser Analytics. A periodically updated list of review articles and IR laser spectroscopy applications and techniques may be obtained from the company.

The remainder of this section describes two high-resolution spectroscopic applications of TDLs in conjunction with the line-center-stabilized CO_2 (or CO) lasers. Figure 25 illustrates a calibration method for locating and precisely calibrating reference lines that was used to determine the absorption spectra of UF_6 isotopes in the vicinity of 12 μm [145,98]. In this experimental arrangement, a beamsplitter combines the output of a lead-salt TDL and that of a $^{14}C^{16}O_2$ laser. A fast HgCdTe varactor photodiode [74] heterodynes one part of the combined radiation, the beat note of which is displayed and measured by a microwave spectrum analyzer (or frequency counter). The other part of the combined laser radiation is used to probe an absorption cell that, in this particular experiment, is filled with NH_3 gas at a pressure of 5 Torr. With the CO_2 laser stabilized to its line center and the diode laser locked to the absorption line to be measured, heterodyne calibration provides an accuracy not currently available by any other method. As an example, Fig. 26 shows a heterodyne beat frequency of 6775 MHz between a $^{14}C^{16}O_2$ laser and a diode laser tuned to one of the NH_3 absorption lines near 12.1 μm [145,98].

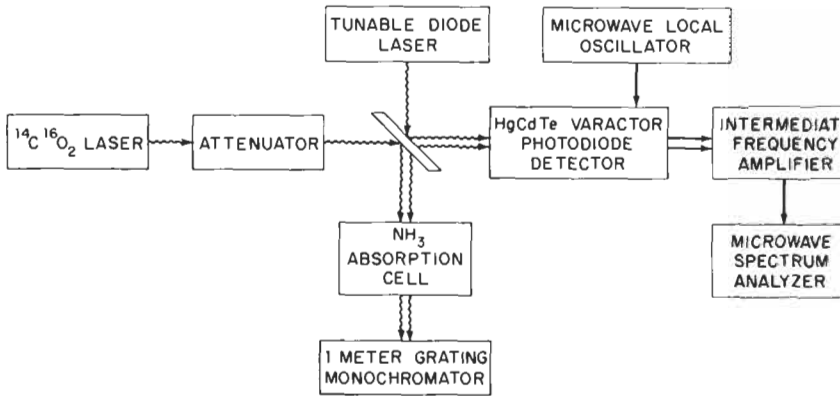

FIGURE 25 High-accuracy calibration method for heterodyne spectroscopy with tunable lasers. In the figure, wavy and solid lines denote optical and electrical paths, respectively. (Reprinted with permission from Freed [75]. © 1982 IEEE.)

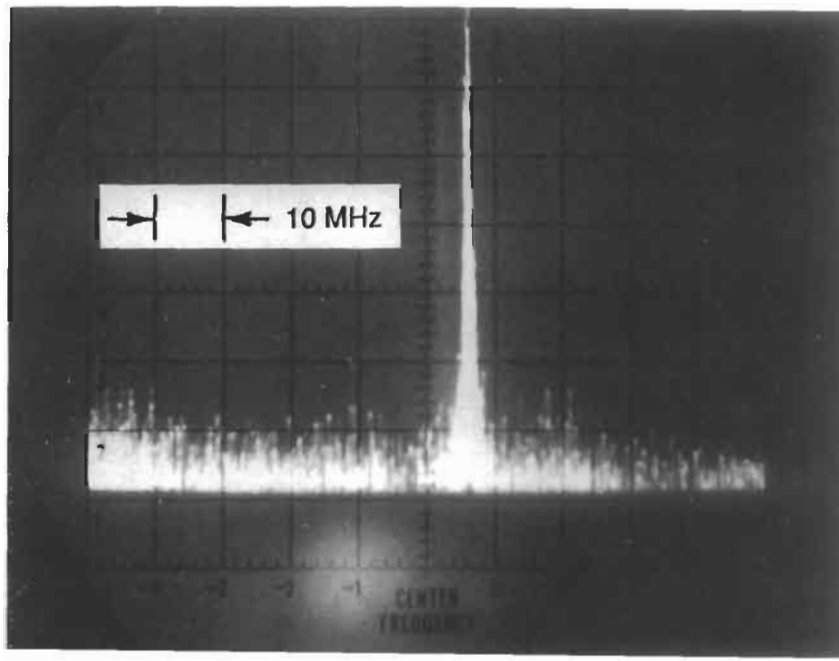

FIGURE 26 The 6775-MHz beat note of a $^{14}C^{16}O_2$ laser (00^{01})—[10^{00}, 02^{00}] I-band *P*-transition and a diode laser tuned to an ammonia absorption line at 12.1 μm. (Reprinted with permission from Freed [75]. © 1982 IEEE.)

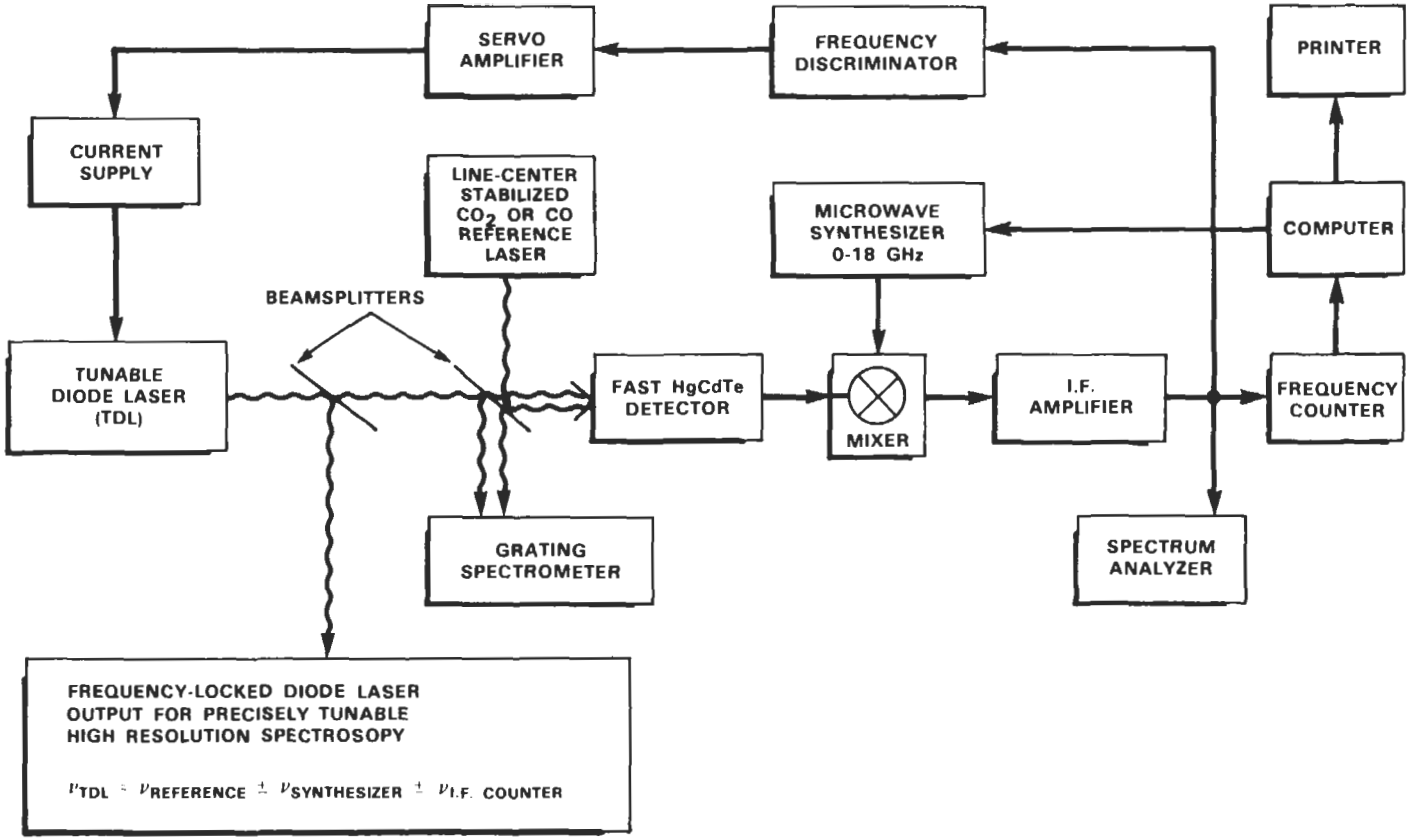

FIGURE 27 Block diagram of an accurate, continuously tunable, computer-controlled, kilohertz-resolution IR-frequency synthesizer.

In another project at Lincoln Laboratory, we demonstrated the equivalent of a programmable and highly accurate tunable IR synthesizer, as shown in Fig. 27 [146,147,56]. In Figure 27 the IR synthesizer is derived from a lead-salt TDL; a small portion of the TDL output is heterodyned against a line-center stabilized grating-controlled CO_2 or CO molecular laser. A high-speed HgCdTe varactor photodiode detects the beat note of the two lasers. The detected beat frequency, which is generally in the 0- to 18-GHz range, is further heterodyned to some convenient intermediate frequency (IF) through the use of readily available commercial rf/microwave-frequency synthesizers and wideband double-balanced mixers. The IF output is amplified and amplitude limited by means of low-noise wideband amplifiers and limiters. The limiter output is, in turn, used as input to a wideband delay-line-type frequency discriminator (200- to 600-MHz typical bandwidth). A servoamplifier/integrator further amplifies the output of the frequency discriminator, and the amplified output is then used to control the TDL current, which determines the TDL output frequency. Closing the servoloop in this fashion frequency-offset-locks the TDL output to the combination of CO_2 (or CO) laser, rf/microwave synthesizer, and the center frequency of the wideband IF discriminator, which a frequency counter accurately monitors.

A computer controls the entire IR synthesizer system shown in Fig. 27. If, for instance, the microwave synthesizer is frequency swept under computer control, the IR output frequency of the TDL would also be swept in synchronism with the microwave synthesizer because the frequency-offset-locking servoloop forces the TDL output to maintain the following frequency relationship:

$$f_{TDL} = f_{CO_2;CO} \pm f_{synthesizer} \pm f_{IF\ counter} \ . \tag{22}$$

Either the operator or the computer program predetermines the frequency of the rf/microwave synthesizer in Eq. (22). The IF is very accurately measured, and averaged if so desired, even in the presence of appreciable frequency modulation, which may be necessary to line-center-lock either one or both lasers. Thus to a great extent the absolute accuracy of the TDL output frequency f_{TDL} will depend on the absolute accuracy, resettability, and long-term stability of the reference molecular gas laser(s). To date, the most accurate results have been achieved with the use of CO_2 reference lasers.

14. SPECTROSCOPIC USE OF CO_2 LASERS OUTSIDE THEIR FUNDAMENTAL 8.9- TO 12.4-μM WAVELENGTH RANGE

We can utilize harmonics and the difference frequencies of CO_2 lasing transitions to synthesize precisely known reference frequencies well beyond the 8.9- to 12.4-μm range of the CO_2-isotope laser transition frequencies illustrated

TABLE 19 An Example of IR Synthesis at 16 μm with Regular Band CO_2 Transitions. Wave Number = (2 × Transition 1) − (Transition 2)[a]

Wave number (cm^{-1})	Transition 1	Transition 2
624.906042	$^{14}C^{16}O_2$ I-*P*(40)	$^{13}C^{16}O_2$ II-*R*(30)
624.915792	$^{14}C^{16}O_2$ I-*P*(28)	$^{12}C^{16}O^{18}O$ II-*P*(16)
624.917820	$^{14}C^{16}O_2$ I-*P*(48)	$^{12}C^{16}O^{18}O$ II-*P*(56)
624.937049	$^{14}C^{16}O_2$ I-*P*(56)	$^{13}C^{18}O_2$ II-*P*(26)
624.945145	$^{14}C^{16}O_2$ I-*P*(14)	$^{12}C^{16}O^{18}O$ II-*R*(16)
624.954490	$^{14}C^{16}O_2$ I-*P*(4)	$^{12}C^{18}O_2$ II-*R*(26)
624.978786	$^{14}C^{16}O_2$ I-*P*(48)	$^{13}C^{16}O_2$ II-*R*(6)
624.988389	$^{14}C^{16}O_2$ I-*P*(20)	$^{12}C^{16}O^{18}O$ II-*R*(1)
625.007851	$^{14}C^{16}O_2$ I-*P*(16)	$^{12}C^{18}O_2$ II-*P*(4)
625.013741	$^{14}C^{16}O_2$ I-*P*(6)	$^{12}C^{16}O_2$ II-*R*(56)
625.044477	$^{14}C^{16}O_2$ I-*P*(2)	$^{12}C^{16}O^{18}O$ II-*R*(52)
625.046863	$^{14}C^{16}O_2$ I-*P*(54)	$^{14}C^{18}O_2$ II-*R*(52)
625.091263	$^{14}C^{16}O_2$ I-*P*(4)	$^{12}C^{16}O^{18}O$ II-*R*(45)

[a]Reprinted with permission from Freed [75]. ©1982 IEEE.

in Fig. 18. For instance, heterodyne comparisons with the second harmonics of appropriately selected CO_2 laser transitions have achieved the first accurate determination of several CO-isotope laser lines in the 5- to 6-μm range. This work was carried out by Eng *et al.* at MIT Lincoln Laboratory in 1974 [17] with the use of (third-generation) ultrastable CO_2 and CO lasers [148,149] and high-quality crystals of the calcopyrites $CdGdH_2$ and HgGaSe.

Yet another example of ultraprecise IR synthesis at 16 μm (625 cm^{-1}) is illustrated in Table 19 [16]. To generate Table 19 we gave a computer the task of finding the CO_2-isotope laser transitions for which the difference frequency between a frequency-doubled $^{14}C^{16}O_2$ laser transition and any other CO_2-isotope laser transition fell within the 625.0 ± 0.1 cm^{-1} frequency range. Synthesized frequency tables very similar to Table 19 have been used for the accurate determination of absorption lines in isotopes of uranium hexafluoride (UF_6) near 16 μm.

ACKNOWLEDGMENTS

In compiling this chapter I most often used results and examples of research at MIT Lincoln Laboratory because this was the work with which I was most familiar. However, my own contributions to the results are due to the active encouragement and cumulative efforts of many individuals in the MIT/Lincoln

Laboratory community. In particular, I wish to thank the following individuals (listed in alphabetical order): J. W. Bielinski, L. C. Bradley, C. P. Christensen, J. A. Daley, L. E. Freed, T. R. Gurski, H. A. Haus, E. D. Hinkley, A. Javan, R. H. Kingston, D. G. Kocher, R. G. O'Donnell, K. L. SooHoo, D. L. Spears, L. J. Sullivan, J. E. Thomas, S. A. Tirrell, and C. H. Townes. I also received much appreciated help and cooperation from K. M. Evenson and F. R. Petersen (NBS/NIST), K. J. Siemsen (NRC), K. Nill (Laser Analytics), W. Lo (General Motors Research Labs), and P. K. Cheo (University of Connecticut). Finally, I want to express my deepest appreciation to Barbara A. Raymond for a wonderful job in typing the manuscript of this chapter.

REFERENCES

1. C. K. N. Patel, *Phys. Rev. Lett.* **12,** 588 (1964).
2. C. K. N. Patel, *Phys. Rev.* **136,** A1187 (1964).
3. T. H. Maiman, *Phys. Rev. Lett.* **4,** 564 (1960).
4. C. K. N. Patel, *Sci. Am.* **219**(2), 22 (1968).
5. C. K. N. Patel, *Proc. SPIE* **1042,** 112, SPIE, Bellingham, WA (1989).
6. N. G. Basov, E. M. Belenov, V. A. Danilychev, O. M. Kerimov, A. S. Podsosonnyi, and A. F. Suchkov, *Kratk. Soobshch. Fiz.* **5,** 44 (1972).
7. A. J. Alcock, K. Leopold, and M. C. Richardson, *Appl. Phys. Lett.* **23,** 562 (1973).
8. V. N. Bagratashvili, I. N. Knyazev, YU.A. Kudryavtsev, and V. S. Letokhov, *Opt. Commun.* **9,** 135 (1973).
9. T. Y. Chang and O. R. Wood, *Appl. Phys. Lett.* **23,** 370 (1973).
10. N. G. Basov, E. M. Belenov, V. A. Danilychev, O. M. Kerimov, I. B. Kovsh, A. S. Podsosonnyi, and A. F. Suchkov, *Sov. Phys. JETP,* **37,** 58 (1973).
11. N. G. Basov, V. A. Danilychev, O. M. Kerimov, and A. S. Podsosonnyi, *JETP Lett.* **17,** 102 (1973).
12. N. W. Harris, F. O'Neill, and W. T. Whitney, *Appl. Phys. Lett.* **25,** 148 (1974).
13. F. O'Neill and W. T. Whitney, *Appl. Phys. Lett.* **26,** 454 (1975).
14. N. W. Harris, F. O'Neill, and W. T. Whitney, *Opt. Commun.* **16,** 57 (1976).
15. R. B. Gibson, A. Javan, and K. Boyer, *Appl. Phys. Lett.* **32,** 726 (1978).
16. C. Freed, *IEEE J. Quantum Electron.* **18,** 1220 (1982).
17. R. S. Eng, H. Kildal, J. C. Mikkelsen, and D. L. Spears, *Appl. Phys. Lett.* **24,** 231 (1974).
18. A. E. Siegman, in *Lasers,* University Science Books, Mill Valley, CA (1986).
19. A. Yariv, in *Quantum Electronics,* John Wiley & Sons, New York (1989).
20. W. J. Witteman, in *The CO_2 Laser,* Springer Series in Optical Sciences, p. 53, Springer-Verlag, New York (1987).
21. P. K. Cheo, in *Lasers, Vol. III* (A. K. Levine and A. J. DeMaria, Eds.), pp. 111–267, Marcel Dekker, New York (1971).
22. P. K. Cheo, in *Handbook of Molecular Lasers,* Marcel Dekker, New York (1987).
23. T. S. Hartwick, in *CO_2 Laser Devices,* Proc. SPIE **227,** SPIE, Bellingham, WA (1980).
24. D. W. Trainor and E. P. Chickliss, in *Laser Research and Development in the Northeast, Proc. SPIE* **709,** 35–52, SPIE, Bellingham, WA (1986).
25. R. A. Sauerbrey, J. H. Tillotson, and P. P. Chenausky, in *Gas Laser Technology, Proc. SPIE* **894,** 77–106, SPIE, Bellingham, WA (1988).
26. J. D. Evans and E. V. Locke, in *CO_2 Lasers and Applications, Proc. SPIE* **1042,** SPIE, Bellingham, WA (1989).

27. P. V. Avizonis, C. Freed, J. J. Kim, and F. K. Tittel, in *High Power Gas Lasers, Proc. SPIE* **1225,** 318–400, SPIE, Bellingham, WA (1990).
28. H. Opower, in *CO_2 Lasers and Applications II, Proc. SPIE* **1276,** SPIE, Bellingham, WA (1990).
29. A. M. Robinson and D. C. Johnson, *IEEE J. Quantum Electron.* **6,** 590 (1970).
30. J. D. Evans, in *Selected Papers on CO_2 Lasers,* Milestone Series, **22,** SPIE, Bellingham, WA (1990).
31. G. Herzberg, in *Infrared and Raman Spectra,* Van Nostrand, New York (1945).
32. E. Fermi, *Z. Physik* **71,** 250 (1931).
33. G. Amat and M. Pimbert, *J. Mol. Spectrosc.* **19,** 278 (1965).
34. H. R. Gordon and T. K. McCubbin, Jr., *J. Mol. Spectrosc.* **19,** 137 (1966).
35. H. E. Howard-Lock and B. P. Stoicheff, *J. Mol. Spectrosc.* **37,** 321 (1971).
36. C. Freed, L. C. Bradley, and R. G. O'Donnell, *IEEE J. Quantum Electron.* **16,** 1195 (1980).
37. L. C. Bradley, K. L. SooHoo, and C. Freed, *IEEE J. Quantum Electron.* **22,** 234 (1986).
38. A. G. Maki, C. C. Chou, K. M. Evenson, L. R. Zink, and J. T. Shy, *J. Mol. Spectrosc.* **167,** 211 (1994).
39. C. K. N. Patel, P. K. Tien, and J. H. McFee, *Appl. Phys. Lett.* **7,** 290 (1965).
40. W. J. Witteman, *Appl. Phys. Lett.* **11,** 337 (1967).
41. R. J. Carbone, *IEEE J. Quantum Electron.* **3,** 373 (1967).
42. R. A. Paananen, *Proc. IEEE* **55,** 2036 (1967).
43. P. O. Clark and J. Y. Wada, *IEEE J. Quantum Electron.* **4,** 236 (1968).
44. I. Wieder and G. B. McCurdy, *Phys. Rev. Lett.* **16,** 565 (1966).
45. C. Freed in *Proc. 3rd Int. DRA/NASA Conf. Long-Life CO_2 Laser Technology,* Malvern, UK, pp. 35–51 (1992).
46. NASA in *Closed-Cycle, Frequency-Stable CO_2 Laser Technology Conf. Publication,* 2456, Hampton, VA (1986).
47. NASA in *Low-Temperature CO-Oxidation Catalysts for Long-Life CO_2 Lasers Conf. Publication,* 3076, Hampton, VA (1989).
48. C. Freed and A. Javan, *Appl. Phys. Lett.* **17,** 53 (1970).
49. O. R. Wood, *Proc. IEEE* **62,** 355 (1974).
50. R. L. Abrams, *Appl. Phys. Lett.* **25,** 609 (1974).
51. I. M. Beterov, V. P. Chebotayev, and A. S. Provorov, *Opt. Commun.* **7,** 410 (1973).
52. V. P. Chebotayev, *Dokl. Akad. Nauk SSSR* **206,** 334 (1972).
53. I. M. Beterov, V. P. Chebotoyev, and S. A. Provorov, *IEEE J. Quantum Electron.* **10,** 245 (1974).
54. R. B. Gibson, K. Boyer, and A. Javan, *IEEE J. Quantum Electron.* **15,** 1224 (1979).
55. C. Freed, *IEEE J. Quantum Electron.* **4,** 404 (1968).
56. C. Freed, "Ultrastable CO_2 Lasers," *Lincoln Lab. J.* **3**(3), 479–500 (1990).
57. A. L. Schawlow and C. H. Townes, *Phys. Rev.* **112,** 1940 (1958).
58. T. R. Gurski, *J. Opt. Soc. Am.* **66,** 1133A (1976).
59. L. J. Sullivan in *CO_2 Laser Devices and Applications, Proc. SPIE,* **227,** 148, SPIE, Bellingham, WA (1980).
60. L. J. Sullivan, B. E. Edwards, and W. E. Keicher, *Proc. Int. Conf. Radar,* Paris, France, **353,** (1989).
61. K. I. Schultz and S. Fisher, *Appl. Opt.* **31,** 7690 (1992).
62. K. I. Schultz, D. G. Kocher, J. A. Daley, J. R. Theriault, Jr., J. Spinks, and S. Fisher, *Appl. Opt.* **33,** 2349 (1994).
63. C. Freed, R. S. Eng., and C. L. Summers, *Proc. Int. Conf. Lasers '93,* December 6–10, Lake Tahoe, NV, p. 100 (1993).
64. W. E. Lamb, Jr., *Phys. Rev.* **134,** A1429 (1964).
65. W. E. Lamb, Jr., in seminar presented at MIT, Cambridge, MA (1963).
66. A. Szöke and A. Javan, *Phys. Rev. Lett.* **10,** 512 (1963).

67. P. H. Lee and M. L. Skolnick, *Appl. Phys. Lett.* **10,** 303 (1967).
68. K. Shimoda, *IEEE Trans. Instrum. Meas.* **17,** 343 (1968).
69. R. L. Barger and J. L. Hall, *Phys. Rev. Lett.* **22,** 4 (1969).
70. C. Bordé and L. Henry, *IEEE J. Quantum Electron.* **4,** 874 (1968).
71. H. T. Powell and G. J. Wolga, *Bull. Am. Phys. Soc.* **15,** 423 (1970).
72. C. Freed, "Designs and Experiments Relating to Stable Gas Lasers," in *Proc. Frequency Standards and Metrology Seminar.* Quebec, Canada. National Research Council of Canada and Université Laval, pp. 226–261 (1971).
73. C. Freed and R. G. O'Donnell, *Metrologia* **13,** 151 (1977).
74. D. L. Spears and C. Freed, *Appl. Phys. Lett.* **23,** 445 (1973).
75. C. Freed, *IEEE J. Quantum Electron.* **18,** 1220 (1982).
76. K. L. SooHoo, C. Freed, J. E. Thomas, and H. A. Haus, *IEEE J. Quantum Electron.* **21,** 1159 (1985).
77. C. Freed, "Ultrastable Carbon Dioxide (CO_2) Lasers," in *Laser Research and Development in the Northeast. Proc. SPIE* **709,** pp. 36–45, SPIE, Bellingham, WA (1986).
78. B. G. Whitford, K. J. Siemsen, and J. Reid, *Opt. Commun.* **22,** 261 (1977).
79. F. R. Petersen, J. S. Wells, K. J. Siemsen, A. M. Robertson, and A. G. Maki, *J. Mol. Spectrosc.* **105,** 324 (1984).
80. K. M. Evenson, C. C. Chou, B. W. Bach, and K. G. Bach, *IEEE J. Quantum Electron.* **5,** 1187 (1994).
81. C. C. Chou, K. M. Evenson, L. R. Zink, A. G. Maki, and J. T. Shy, *IEEE J. Quantum Electron.* **31,** 343 (1995).
82. M. A. Kovacs and A. Javan, *J. Chem. Phys.* **50,** 411 (1969).
83. R. K. Huddleston, G. J. Fujimoto, and E. Weitz, *J. Chem. Phys.* **76,** 3839 (1982).
84. A. LeFloch, J. Lenormand, G. Jezequel, and R. LeNour, *Opt. Lett.* **6,** 48 (1981).
85. B. W. Peuse, M. G. Prentiss, and S. Ezekiel, *Opt. Lett.* **8,** 154 (1983).
86. M. J. Kelly in "Lineshapes of Narrow Doppler-Free Saturation Resonance and Observation of Anomalous Zeeman Splitting Arising from Magnetic Moment in $^1\Sigma CO_2$ and N_2O Molecules," PhD dissertation, Massachusetts Institute of Technology, Cambridge, MA (Feb. 1976).
87. C. C. Chou, J. T. Shy, and T. C. Yen, *Opt. Lett.* **17,** 967 (1992).
88. C. C. Chou, S. J. Tochitsky, J. T. Shy, A. G. Maki, and K. M. Evenson, *J. Molec. Spectrosc.* in press.
89. J. Reid and K. J. Siemsen, *Appl. Phys. Lett.* **29,** 250 (1976).
90. J. Reid and K. J. Siemsen, *J. Appl. Phys.* **48,** 2712 (1977).
91. A. Javan and C. Freed, "Method of Stabilizing a Gas Laser," U.S. Patent 3686585 (issued Aug. 22, 1972).
92. T. J. Bridges and T. Y. Chang, *Phys. Rev. Lett.* **22,** 811 (1969).
93. F. R. Petersen, D. G. McDonald, J. D. Cupp, and B. L. Danielson, *Phys. Rev. Lett.* **31,** 573 (1973).
94. K. M. Evenson, J. S. Wells, F. R. Petersen, B. L. Danielson, and G. W. Day, *Appl. Phys. Lett.* **22,** 192 (1973).
95. F. R. Petersen, D. G. McDonald, J. D. Cupp, and B. L. Danielson, "Accurate Rotational Constants, Frequencies, and Wavelengths from $^{12}C^{16}O_2$ Laser Stabilized by Saturated Absorption," in *Laser Spectroscopy* (R. G. Brewer and A. Mooradian, Eds.), pp. 555–569, Plenum, New York (1974).
96. C. Freed, D. L. Spears, R. G. O'Donnell, and A. H. M. Ross, "Precision Heterodyne Calibration," in *Proc. Laser Spectrosc. Conf.,* June 25–29, 1973, Vail, CO; also in *Laser Spectroscopy* (R. G. Brewer and A. Mooradian, Eds.), pp. 171–191, Plenum, New York (1974).
97. C. Freed, A. H. M. Ross, and R. G. O'Donnell, *J. Molec. Spectrosc.* **49,** 439 (1974).
98. C. Freed, R. G. O'Donnell, and A. H. M. Ross, *IEEE Trans. Instrum. Meas.* **25,** 431 (1976).
99. F. R. Petersen, E. C. Beaty, and C. R. Pollack, *J. Molec. Spectrosc.* **102,** 112 (1983).
100. K. J. Siemsen and B. G. Whitford, *Opt. Commun.* **22,** 11 (1977).

101. F. R. Petersen, J. S. Wells, K. J. Siemsen, A. M. Robinson, and A. G. Maki, *J. Molec. Spectrosc.* **105,** 324 (1984).
102. F. R. Petersen, J. S. Wells, A. G. Maki, and K. J. Siemsen. *Appl. Opt.* **20,** 3635 (1981).
103. K. J. Siemsen, *Opt. Commun.* **34,** 447 (1980).
104. T. G. Blaney, C. C. Bradley, G. J. Edwards, B. W. Jolliffe, D. J. E. Knight, W. R. C. Rowley, K. C. Shotten, and P. T. Woods, *Proc. R. Soc. London A* **355,** 61 (1977).
105. A. Clairon, B. Dahmani, and J. Rutman, *IEEE Trans. Instrum. Meas.* **29,** 268 (1980).
106. Ch. Chardonnet, A. VanLerberghe, and C. J. Bordé, *Opt. Commun.* **58,** 333 (1986).
107. A. Clairon, O. Acef, C. Chardonnet, and C. J. Bordé, in *Frequency Standards and Metrology,* (A. DeMarchi, Ed.), p. 212, Springer-Verlag, Berlin/Heidelberg (1989).
108. A. Clairon, B. Dahmani, A. Filimon, and J. Rutman, *IEEE Trans. Instrum. Meas.* **34,** 265 (1988).
109. C. O. Weiss, G. Kramer, B. Lipphardt, and E. Garcia, *IEEE J. Quantum Electron.* **24,** 1970 (1988).
110. S. N. Bagayev, A. E. Baklanov, V. P. Chebotayev, and A. S. Dychkov, *Appl. Phys. B* **48,** 31 (1989).
111. K. L. SooHoo, C. Freed, J. E. Thomas, and H. A. Haus. *Phys. Rev. Lett.* **53,** 1437 (1984).
112. K. L. SooHoo, "Pressure Shifts in Carbon Dioxide and Its Isotopes," PhD dissertation, Massachusetts Institute of Technology, MIT, Cambridge, MA (Jan. 1984).
113. S. N. Bagaev, A. S. Dychkov, A. K. Dmitriev, and V. P. Chebotayev, *JETP* **52,** 586 (1980).
114. V. M. Gusev, O. N. Kompanets, A. R. Kukudzhanov, L. S. Letokhov, and E. L. Mikhailov, *Sov. JQE* **4,** 1370 (1975).
115. G. R. Hanes, K. M. Baird, and J. DeRemigis, *Appl. Opt.* **12,** 1600 (1973).
116. D. P. Blair. *Appl. Phys. Lett.* **25,** 71 (1974).
117. B. P. J. vanOorshot, *J. Phys. D* **10,** 1117 (1977).
118. S. N. Bagaev, V. P. Chebotayev, *JETP Lett.* **16,** 243 (1972).
119. S. N. Bagaev, S. V. Maltsev, V. P. Chebotayev, *JETP Lett.* **37,** 590 (1983).
120. H. Goldring, A. Szöke, E. Zasmir, and A. Ben-Reuven, *JCP* **49,** 4235 (1968).
121. A. Yariv in *Introduction to Optical Electronics,* Holt, Rinehart and Winston, Inc., New York (1971); for a more exact analytical study see L. W. Casperson, *Appl. Opt.* **19,** 422 (1980).
122. R. L. Abrams and W. B. Bridges, *IEEE J. Quantum Electron.* **9,** 940 (1973).
123. M. Silver, T. S. Hartwick, and M. J. Posakony, *J. Appl. Phys.* **41,** 4566 (1970).
124. P. K. L. Yin, in "Studies on CO_2 Isotope Molecules and Atmospheric Transmission of $^{12}C^{18}O_2$ Laser Radiation," T.R. 2384-6, Ohio State University Electro Science Laboratory (1968).
125. L. E. Freed, C. Freed, and R. G. O'Donnell, *IEEE J. Quantum Electron.* **18,** 1229 (1982).
126. C. P. Christensen, C. Freed, and H. A. Haus, *IEEE J. Quantum Electron.* **5,** 276 (1969).
127. Y. Nachshon and U. P. Oppenheim, *Appl. Opt.* **12,** 1934 (1973).
128. A. Javan, W. B. Bennett, Jr., and D. R. Herriott, *Phys. Rev. Lett.* **6,** 106 (1961).
129. T. S. Jaseja, A. Javan, and C. H. Townes, *Phys. Rev. Lett.* **10,** 165 (1963).
130. C. Freed, *IEEE J. Quantum Electron.* **4,** 404 (1967).
131. P. W. Smith. *Proc. IEEE* **60,** 422 (1972).
132. P. K. Cheo. *IEEE J. Quantum Electron.* **20,** 700 (1984).
133. P. K. Cheo, "Generation and Applications of 16 GHz Tunable Sidebands from a CO_2 Laser," in *Laser Spectroscopy III* (J. L. Hall and J. L. Carlsten, Eds.), pp. 394–401, Springer-Verlag, New York (1977).
134. P. K. Cheo and M. Gilden, *Opt. Lett.* **1,** 38 (1977).
135. G. Sachse, "Microwave Tunable Laser Source: A Stable, Precision Tunable Heterodyne Local Oscillator," in *Proc. Heterodyne Systems and Technology Conf.,* Mar. 25–27, 1980, Williamsburg, VA.
136. P. K. Cheo, *J. Quant. Spectrosc. Radiat. Transfer* **51,** 579 (1994).
137. P. K. Cheo, Z. Chu, L. Chen, and Y. Zhou, *Appl. Opt.* **32,** 836 (1993).
138. Z. Cheo, L. Chen, and P. K. Cheo, *J. Quantum. Spectrosc. Radiat. Transfer* **51,** 591 (1994).

139. J. F. Butler, A. R. Calawa, R. J. Phelan, T. C. Harman, A. J. Strauss and R. H. Rediker, *Appl. Phys. Lett.* **5,** 75 (1964).
140. J. F. Butler, A. R. Calawa, R. J. Phelan, A. J. Strauss, and R. H. Rediker, *Solid State Commun.* **2,** 303 (1964).
141. I. Melngailis, *Lincoln Lab. J.* **3,** 347 (1990).
142. E. D. Hinkley, T. C. Harman, and C. Freed. *Appl. Phys. Lett.* **13,** 49 (1968).
143. E. D. Hinkley and C. Freed, *Phys. Rev. Lett.* **23,** 277 (1969).
144. C. Freed, J. W. Bielinski, and W. Lo, *Appl. Phys. Lett.* **43,** 629 (1983).
145. C. Freed and K. Nill, "12.2 μm Wavelength Calibration," in *Semiannual Report in Support of the Jumper Program for Laser Isotope Separation*, pp. 70–78, Lincoln Lab (Dec. 1975).
146. C. Freed, "Programmable, Secondary Frequency Standards Based Infrared Synthesizer Using Tunable Lead-Salt Diode Lasers," in *Tunable Diode Laser Development and Spectroscopy Applications, Proc. SPIE* **438,** 119 (1983).
147. C. Freed, "Programmable Secondary Frequency Standards Based Infrared Synthesizers for High Resolution Spectroscopy," in *Methods of Laser Spectroscopy* (Y. Prior, A. Ben-Reuven, and M. Rosenbluh, Eds.), pp. 151–161, Plenum Press, New York (1986).
148. C. Freed, *Appl. Phys. Lett.* **18,** 458 (1971).
149. C. Freed and H. A. Haus, *IEEE J. Quantum Electron.* **9,** 219 (1973).

5 Dye Lasers

F. J. Duarte
Eastman Kodak Company
Rochester, New York

1. INTRODUCTION

Dye lasers are unique sources of tunable coherent radiation that offer unparalleled operational flexibility. Broad tunability, from the near ultraviolet to the near infrared (Fig. 1), is facilitated by the existence of hundreds of laser dye molecular species. The tuning range of pulsed narrow-bandwidth emission achievable with a single dye can be up to 50 nm. Significantly broader tuning ranges (up to 100 nm) can be obtained with some dyes under pulsed broadband and continuous wave (cw) operation.

In addition to tunability, an intrinsic feature of dye lasers is their inherent ability to yield high-pulse energies and high-average powers in the visible [1]. Single-pulse energies in excess of several hundred joules and average powers in excess of 2.5 kW have been reported [2]. This unparalleled performance is greatly facilitated by the heat dissipating ability of the gain medium in the liquid phase.

On the other hand, highly stabilized single-longitudinal-mode cw dye lasers can yield frequency drift rates below 1 Hz/sec [3,4]. In the ultrashort-pulse regime dye lasers have demonstrated pulses as short as 19 fs [5] and extra cavity prism-grating compressors have yielded 6-fs pulses [6]. In this regard, dye lasers have been an important vehicle in the development of many pioneering

Tunable Lasers Handbook
Copyright © 1995 by Academic Press, Inc. All rights of reproduction in any form reserved.

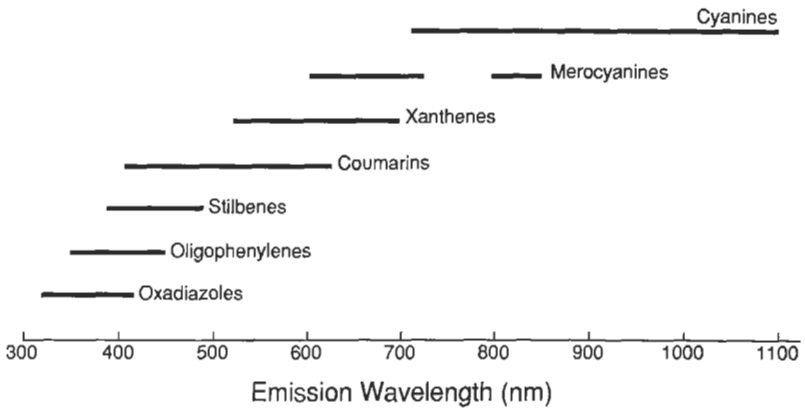

FIGURE 1 Approximate wavelength coverage achieved with different classes of laser dye molecules.

techniques that have now found wide applicability in lasers in general. Important contributions to the laser field first demonstrated in dye lasers include frequency stabilization techniques, pulse compression techniques, dispersive oscillator configurations, and numerous cavity and resonator innovations.

Although dye molecules have been demonstrated to lase in the three states of matter, it is in the liquid phase that dye lasers have made their most significant impact. Recently, however, there has been a resurgence of work in solid-state dye lasers. Hence a section of this chapter is especially devoted to this topic.

This chapter is intended to provide an expeditious guide to the performance and basic features of dye lasers. For an in-depth approach to the subject, the reader should consult the references provided in the various sections and the following books: *High Power Dye Lasers* [1], *Dye Laser Principles* [7], *Dye Lasers* [8], and *Selected Papers on Dye Lasers* [9]. These works should also be consulted for a historical perspective on the subject.

1.1 The Molecular Gain Media

Laser dye molecules are large, with atomic weights in the 175- to 1000-amu range (see the Appendix at the end of this chapter). These molecules exhibit a wide absorption spectrum with broad and strong absorption maxima corresponding to $S_0 \rightarrow S_n$ electronic transitions (Fig. 2). Here, dye molecules are considered simply from an energetic perspective with an excitation dynamics involving several energy levels. A feature of dye laser molecules is that each electronic state contains a multitude of overlapping vibrational-rotational levels. This plethora of closely lying vibrational levels gives origin to the broadband gain and tunability features that are so characteristic of dye lasers.

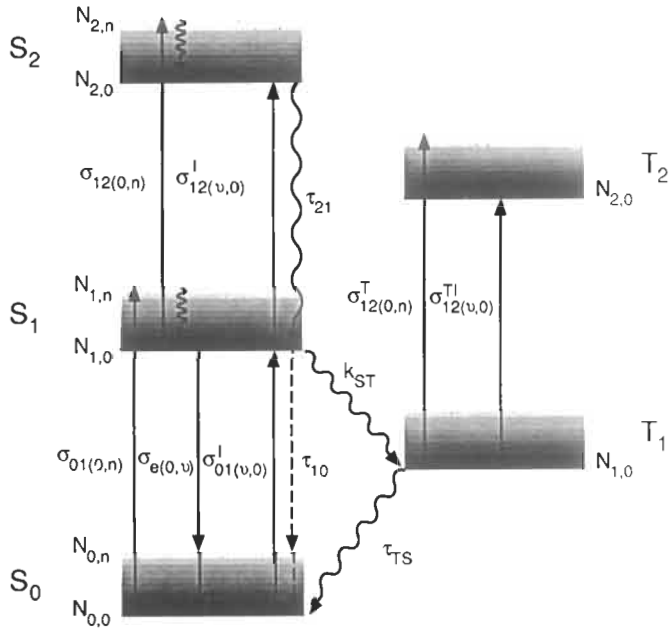

FIGURE 2 Energy-level diagram illustrating excitation and emission transitions of laser dye molecules. Absorption cross sections are written as $\sigma_{v''S'(v'',v')}$ and the emission cross section as $\sigma_{e(v',v'')}$.

The literature on rate equations for dye lasers is quite extensive. Representative and detailed treatments on the subject have been given by [10–19]. Here, a set of rate equations, applicable to transverse laser excitation and intrinsic broadband emission, is considered. In reference to the energy diagram of Fig. 2, the population equation can be written as

$$N = \sum_{S=0}^{n} \sum_{v=0}^{n} N_{S,v} + \sum_{T=1}^{n} \sum_{v=0}^{n} N_{T,v} , \tag{1}$$

where summation over S refers to the electronic states and summation over v considers all the vibrational levels within each electronic state. A similar description applies to the summation over the triplet states $N_{T,v}$.

Pump laser intensity $I_p(t)$, at a wavelength compatible with the $S_0 \rightarrow S_1$ transition, populates a higher vibrational level $(1,n)$ at the first excited electronic state. The cross section corresponding to this transition is $\sigma_{01(0,n)}$. This is followed by rapid intraband radiationless deexcitation to the $N_{1,0}$ vibrational level from where transitions to a vibrational manifold at the ground electronic state give origin to broadband emission $I_l(x,t,\lambda)$. The emission cross section is $\sigma_{e(0,v)}$. Intensity $I_p(t)$ excitation of S_2 may occur with a cross section $\sigma_{12(0,n)}$ and emission reabsorption

by the ground, and first excited electronic states are represented by cross sections $\sigma^{l}_{01(v,0)}$ and $\sigma^{l}_{12(v,0)}$, respectively. The decay lifetime of $N_{2,0}$ toward the first excited electronic state (τ_{21}) is very fast relative to the other processes, such as τ_{10}, that occur in the nanosecond regime. The singlet to triplet intersystem crossing occurs at a rate k_{ST} and is a loss process detrimental to laser action, because it may deplete the available population at the ground electronic state. Decay from T_1 to S_0 occurs at a rate $1/\tau_{TS}$ mainly through collision deactivation but also by a weak radiative transition called phosphorescence.

Thus, the dynamics of the upper laser level $N_{1,0}$, the laser pumping intensity $I_p(t)$, and the broadband emission intensity $I_l(x,t,\lambda)$ can be described by the following set of equations:

$$\begin{aligned}\frac{\partial N_{1,0}}{\partial t} \approx{}& N_{0,0}\sigma_{01(0,n)} I_p(t) + \sum_{v=0}^{n} N_{0,v}\sigma^{l}_{01(v,0)} I_l(x,t,\lambda_v) \\ &+ \frac{N_{2,0}}{\tau_{21}} - N_{1,0}\sigma_{12(0,n)} I_p(t) \\ &- N_{1,0}\sum_{v=0}^{n} \sigma_{e(0,v)} I_l(x,t,\lambda_v) \\ &- N_{1,0}\sum_{v=0}^{n} \sigma^{l}_{12(v,0)} I_l(x,t,\lambda_v) - N_{1,0}\left(k_{ST} + \frac{1}{\tau_{10}}\right),\end{aligned} \tag{2}$$

$$\begin{aligned}\frac{\partial N_{1,0}}{\partial t} \approx{}& N_{1,0}\, k_{ST} - \frac{N_{0,0}}{\tau_{TS}} - N_{1,0}\sigma^{T}_{12(0,n)} I_p(t) \\ &- N_{1,0}\sum_{v=0}^{n} \sigma^{Tl}_{12(v,0)} I_l(x,t,\lambda_v),\end{aligned} \tag{3}$$

$$\frac{1}{c}\frac{\partial I_p(t)}{\partial t} \approx -\left[N_{0,0}\,\sigma_{01(0,n)} + N_{1,0}\,\sigma_{12(0,n)} + N_{1,0}\sigma^{T}_{12(0,n)}\right] I_p(t), \tag{4}$$

$$\begin{aligned}\frac{1}{c}\frac{\partial I_l(x,t,\lambda)}{\partial t} + \frac{\partial I_l(x,t,\lambda)}{\partial x} \approx{}& N_{1,0}\sum_{v=0}^{n} \sigma_{e(0,v)} I_l(x,t,\lambda_v) \\ &- \sum_{v=0}^{n} N_{0,v}\,\sigma^{l}_{01(v,0)} I_l(x,t,\lambda_v) \\ &- N_{1,0}\sum_{v=0}^{n} \sigma^{l}_{12(v,0)} I_l(x,t,\lambda_v), \\ &- N_{1,0}\sum_{v=0}^{n} \sigma^{Tl}_{12(v,0)} I_l(x,t,\lambda_v),\end{aligned} \tag{5}$$

$$I_l(x,t,\lambda) = \sum_{v=0}^{n} I_l(x,t,\lambda_v), \tag{6}$$

and

$$I_l(x,t,\lambda) = I_l^+(x,t,\lambda) + I_l^-(x,t,\lambda). \tag{7}$$

where the various coefficients are described in Fig. 2. In Eq. (7) $I_l^+(x,t,\lambda)$ represents propagation in the positive x direction and $I_l^-(x,t,\lambda)$ refers to propagation in the opposite direction. The units are molecules cm^{-3} for populations, photons $cm^{-2}\ s^{-1}$ for intensities, square centimeters for cross sections, and seconds for time.

The broadband nature of the emission is a consequence of the involvement of the vibrational manifold of the ground electronic state represented by the summation terms of Eqs. (2), (5), and (6). Because the gain medium exhibits homogeneous broadening, the introduction of intracavity dispersive elements (see Chapter 2) enables all the excited molecules to contribute efficiently to narrow-linewidth emission.

Replacing the vibronic manifolds by single levels and neglecting absorptive depopulations of $N_{1,0}$ and $N_{1,0}$, Eqs. (1) to (5) reduce to

$$N = N_{0,0} + N_{1,0} + N_{1,0}\ , \tag{8}$$

$$\begin{aligned}\frac{\partial N_{1,0}}{\partial t} \approx\ & N_{0,0}\,\sigma_{01}\,I_p(t) + N_{0,0}\,\sigma_{01}^{l}\,I_l(x,t,\lambda) \\ & - N_{1,0}\,\sigma_e\,I_l(x,t,\lambda) - N_{1,0}\left(k_{ST} + \frac{1}{\tau_{10}}\right),\end{aligned} \tag{9}$$

$$\frac{\partial N_{1,0}}{\partial t} \approx N_{1,0}\,k_{ST} - \frac{N_{1,0}}{\tau_{TS}}\ , \tag{10}$$

$$\frac{1}{c}\frac{\partial I_p(t)}{\partial t} \approx -\left(N_{0,0}\,\sigma_{01} + N_{1,0}\,\sigma_{12}\right) I_p(t)\,, \tag{11}$$

and

$$\frac{1}{c}\frac{\partial I_l(x,t,\lambda)}{\partial t} + \frac{\partial I_l(x,t,\lambda)}{\partial x} \approx \left(N_{1,0}\,\sigma_e - N_{0,0}\,\sigma_{01}^{l} - N_{1,0}\,\sigma_{12}^{l} - N_{1,0}\,\sigma_{12}^{Tl}\right) I_l(x,t,\lambda)\,. \tag{12}$$

This simplified set of equations is similar to the rate equation system considered by Teschke *et al.* [11]. Using available excitation parameters from the literature, Eqs. (8) to (12) can be solved numerically for the case of pulsed excitation.

The numerical approach is particularly relevant for pulsed excitation in the nanosecond range because the dynamic occurs in the transient regime. Also, excitation in the nanosecond domain allows for some simplification because the triplet states can be neglected. Examples of numerical solutions considering

transitions from single levels, rather than manifolds, are given by [10,11,18]. Long-pulse or cw excitation enables further simplification because time derivatives can be neglected, although the triplet state now has to be considered. Also, because cw emission tends to be intrinsically narrow linewidth, the use of single levels rather than manifolds is justified. Consequently, rate equations to describe the cw dynamics can be sufficiently simplified, thus enabling the use of analytical methods in their solutions. Examples of analytical solutions to rate equations in the cw regime are given by [3,20].

The cross sections and rates for the transitions depicted in Fig. 2 are given in Tables 1 and 2 for rhodamine 6G. It is important to emphasize that these cross sections are derived from spectroscopic measurements and that they can vary with different solvents. The dependence of the emission cross section on the wavelength and refractive index of the dye solution is discussed by [20,24]. In addition to the values given in Table 1, [7] and [26] provide further information on cross sections and transition rates for rhodamine 6G. Jensen [18] gives relevant cross sections and transition rates for the dye TBS under excimer laser excitation.

2. LASER-PUMPED PULSED DYE LASERS

Laser excitation of pulsed dye lasers is practiced in a variety of geometries. Suitable lasers for optical excitation of pulsed dye lasers are listed in Table 3. Here only the most important features of these lasers are considered, such as their spectral characteristics. Further details on the emission and operational characteristics of these lasers are given by Duarte [37]. Important excitation sources for dye lasers are the excimer lasers and copper vapor lasers; these sources are described in detail by Tallman and Tennant [38] and Webb [39], respectively.

Ultraviolet lasers such as excimer lasers, or nitrogen lasers, can be used to excite a large number of dyes whose emissions span the spectrum from the near ultraviolet to the near infrared. Nitrogen lasers offer simplicity and low cost, at typical energies in the 1- to 10-mJ range, and pulse durations of 5 to 10 ns. Excimer lasers on the other hand, can routinely yield energies approaching 1 J/pulse at pulse lengths in the 10- to 30-ns range. More recently, pulse lengths >200 ns have become available. Pulse repetition frequencies (prfs) can be typically a few hundred hertz and approach the kilohertz range.

In the low prf domain, excimer-laser pumped dye lasers have demonstrated large pulse energies. For instance, using an electron-beam-excited XeCl laser pump, ~800 J/pulse, in a 500-ns pulse, have been reported for coumarin 480 [40]. By contrast, conventional XeCl lasers have been used to excite dye lasers yielding hundreds of millijoules per pulse at a prf of a few hundred hertz. In this regard, Tallman and Tennant [38] discuss the design and construction of a XeCl laser-pumped dye laser system capable of yielding some 74 W of average power

TABLE 1 Transition Cross Sections for Rhodamine 6G

Symbol	Cross section (cm^2)	Wavelength (nm)	Reference
σ_{0N}	0.34×10^{-16}	308	[20]
σ_{0N}	0.34×10^{-16}	337	[20]
σ_{01}	1.66×10^{-16}	510	[21]
	2.68×10^{-16}	514.5	[20]
	4.5×10^{-16}	530	[19]
σ_{12}	$\sim 0.4 \times 10^{-16}$	510	[22]
	0.4×10^{-16}	530	[23]
σe	1.86×10^{-16}	572	[21]
	1.32×10^{-16}	590	[20]
	1.3×10^{-16}	600	[19]
σ^{l}_{01}	$\leq 1 \times 10^{-17}$	580	[15,23]
	1×10^{-19}	600	[19]
σ^{l}_{12}	1×10^{-17}	600	[19]
σ^{T}_{12}	1×10^{-17}	530	[19]
σ^{TT}_{12}	6×10^{-17}	590	[20]
	4×10^{-17}	600	[19]

TABLE 2 Transition Rates and Decay Times for Rhodamine 6G

Symbol	Rate (sec^{-1})	Decay time (sec)	Reference
k_{ST}	2×10^{7}		[19]
	3.4×10^{6}		[24]
	8.2×10^{6}		[25]
τ_{TS}		2.5×10^{-7}	[24]
		1.1×10^{-7}	[25]
		0.5×10^{-7}	[19]
τ_{10}		4.8×10^{-9}	[25]
		3.5×10^{-9}	[19]
τ_{21}		$\sim 10^{-12}$	[21]

[38,41]. The dye used by these authors was TBS and emission was near 400 nm. For blue dyes such as coumarin 120 efficiencies of up to 41% have been reported under XeCl laser excitation [42].

Copper vapor lasers (CVLs) can operate up to prfs in excess of 30 kHz [39]. Furthermore, the spectral emission from those lasers is ideally suited for the efficient excitation of orange-red dyes such as the rhodamine class. Indeed, Bass *et al.* [2] report average powers in excess of 2.5 kW for a CVL-pumped dye laser system capable of efficiencies better than 50%.

As discussed by Duarte [37] conversion efficiencies are optimized when the emission wavelength of the pump laser corresponds to the maximum absorption wavelength of the $S_0 \rightarrow S_1$ electronic transition of the dye. Hence, excitation lasers emitting in the ultraviolet are most suitable to excite dyes emitting in the blue-green. Pump lasers emitting in the green yield the best conversion efficien-

TABLE 3 Available Lasers for Excitation of Pulsed Dye Lasers[a]

Lasers	Transition	λ (nm)	prf[b]	~Bandwidth (GHz)	Reference[c]
KrF	$B^2\Sigma^+_{1/2}-X^2\Sigma^+_{1/2}$	248	200 Hz	10500[d]	[27]
				2583[d]	[28]
XeCl		308	500 Hz	374	[29]
				204	[30]
		308.2		397	[29]
				223	[30]
XeF		351	200 Hz	187	[31]
		353		330	[31]
N_2	$C^3\Pi_u-B^3\Pi_g$	337.1	100 Hz	203	[32]
HgBr	$B^2\Sigma^+_{1/2}-X^2\Sigma^+_{1/2}$	502	<100 Hz	918	[33]
		504		1012	[33]
Ca^+	$5^2S_{1/2}-4^2P_{3/2}$	373.7			
Sr^+	$6^2S_{1/2}-5^2P_{3/2}$	430.5	0.5–15 kHz	2–12[e]	[34]
Cd^+	$4^2F_{5/2}-5^2D_{3/2}$	533.7			
Cu	$^2P_{1/2}-^2D_{3/2}$	510.5	5–30 kHz	7	[35]
Cu	$^2P_{1/2}-^2D_{3/2}$	578.2	5–30 kHz	11	[35]
Au	$^2P_{1/2}-^2D_{3/2}$	627.8	5–20 kHz		
$Al_2O_3:Cr^{3+}$	$\bar{E}(^2E)-^4A_2$	694.3	1 Hz	7	[36]
Nd:YAG	$^4F_{3/2}-^4I_{11/2}$	1064	10–50 Hz	15–30	
	Second harmonic	532			
	Third harmonic	355			
	Fourth harmonic	266			

[a]Adapted from Duarte [37]; with permission.
[b]The prf figures do not represent absolute limits.
[c]References relate to the full-width bandwidth exclusively.
[d]Tuning range.
[e]Range of variable linewidth.

cies when used to excite dyes such as the rhodamines. Performance of some high-power laser-pumped dye lasers are listed in Table 4.

Excitation of dye lasers using GaAlAs diode lasers has been reported by Wang and Webb [43] and dye laser pumping using electron-beam-excited semiconductor lasers has been reported by Bogdankevich *et al.* [44]. These authors report an efficiency of 50% for rhodamine 6G at a pump energy of 100 mJ.

2.1 Excitation Geometries

Excitation geometries used in dye lasers are shown schematically in Fig. 3. Three avenues of excitation are the single-transverse excitation geometry (Fig. 3a), the double-transverse excitation geometry (Fig. 3b), and the semilongitudinal excitation geometry (Fig. 3c). All of these pumping geometries are applicable to amplification stages. The oscillator stage utilizes mainly the single-transverse excitation geometry and the semilongitudinal excitation geometry. These optical pumping geometries are equally applicable to dye lasers in the solid-state and/or liquid phase.

In the case of oscillator excitation, the beamwaist of the laser emission should be determined by the diffraction conditions necessary to restrict emission to a single-transverse mode (see Chapter 2). This implies that for a 10-cm oscillator cavity length the beamwaist should not be greater than ≈ 150 μm at $\lambda \approx 580$ nm. In the case of single-transverse excitation the pump beam is shaped using cylindrical lenses or a combination of a multiple-prism beam expander and a convex lens to yield a very thin and wide excitation beam, often of dimensions 10×0.1 mm. The width of the beam is determined by the length of the dye's active region. In the case of the semilongitudinal excitation the pump beam is shaped to maintain the desired radius of ≈ 150 μm over most of the propagation distance at the active region. In both cases care should be taken not to exceed limits on incident energy density. In the case of liquid dye lasers, this limit is a few joules per square centimeter and is determined by the damage threshold of the dye cell (usually quartz) and the dye solution. For solid-state dye lasers the incident excitation energy can be limited to ≤ 1 J/cm^2.

TABLE 4 Performance of Laser-Pumped Dye Lasers

Excitation laser	Pulse length	Pulse energy	prf	Average power	% Conversion efficiency	Dye	Reference
XeCl	500 ns	~800 J	Very low	—	27	Coumarin 480	[40]
XeCl		200 mJ	250 Hz	50 W	20	TBS	[38]
CVL	40 ns		13.2 kHz	>2.5 kW	>50	Rhodamine	[2]

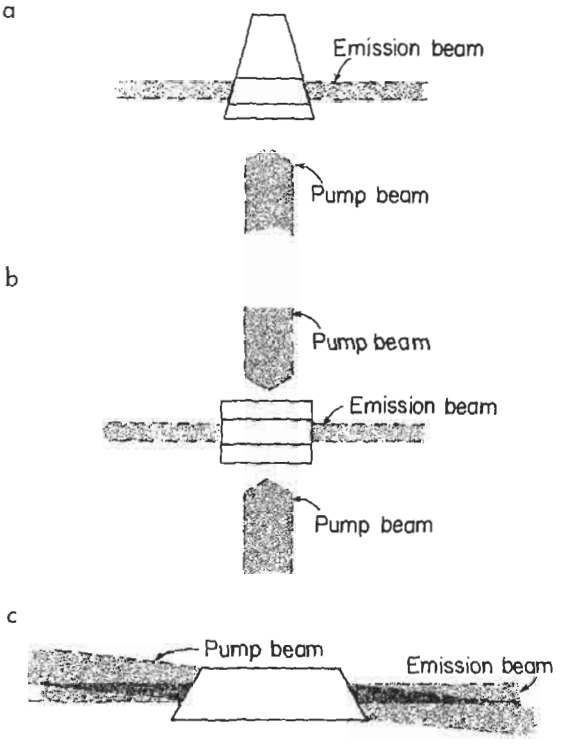

FIGURE 3 Excitation geometries utilized in pulsed dye lasers. (a) Transverse excitation. (b) Collinear two-sided transverse excitation. (c) Semilongitudinal excitation. (Reproduced with permission from Duarte [37].)

At the amplification stages the dimensions of the pump beam are determined by the need to match the propagation geometry of the oscillator beam.

Dye laser cells are of trapezoidal, parallelogrammatic, and rectangular geometries [37] (Fig. 4). Trapezoidal and parallelogrammatic geometries are used to reduce parasitic broadband emission. For high-prf laser oscillators the cross-sectional area of the dye passage is usually about 10 mm in length and a fraction of a millimeter in width to help achieve dye flow speeds of a few $m\text{–}s^{-1}$. The length quoted here is along the optical axis of the cavity. Trapezoidal geometries are also used in solid-state dye laser matrices for either transverse and/or semilongitudinal excitation [45,46].

2.2 Oscillators

Single-transverse-mode narrow-linewidth dispersive oscillators used in dye laser systems are discussed in Chapter 2. The performances of representative

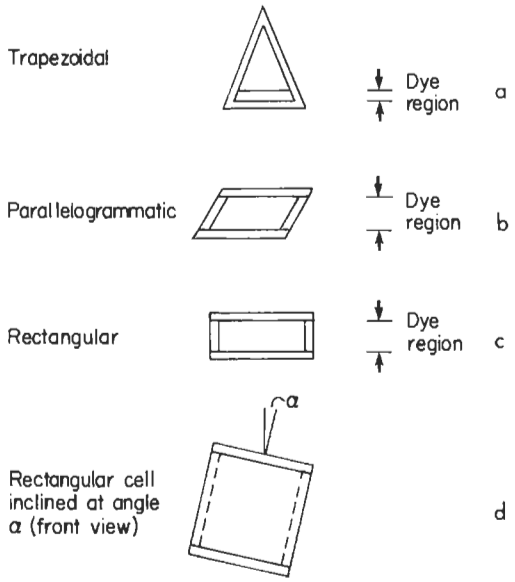

FIGURE 4 Dye laser cell geometries: (a) Trapezoidal. (b) Parallelogrammatic. (c) Rectangular. Here the cross sections of the dye cells are shown parallel to the plane of propagation (that is, top view). (d) Rectangular geometry cells are often used inclined at a few-degree angle. (Reproduced with permission from Duarte [37].)

oscillator configurations including telescopic, grazing-incidence, multiple-prism Littrow (MPL), and hybrid multiple-prism grazing-incidence (HMPGI) grating oscillators are listed in Table 1 of Chapter 2. Parameters considered in this table include tuning range, laser linewidth, and conversion efficiency.

A very important parameter in narrow-linewidth dye laser oscillators is the amplified spontaneous emission (ASE) level. One approach to quantify the ASE level is to measure the ASE % present in the output. Although this is a useful approach used by many authors, it does not provide information on the spectral brightness of the laser. A measure of ASE that does include information on spectral density is [37]:

$$\rho_{ASE}/\rho_l \approx \left[(\Delta\Lambda)^{-1}\int_{\Lambda_1}^{\Lambda_2} W(\Lambda)\,d\Lambda\right]\left[(\Delta\lambda)^{-1}\int_{\lambda_1}^{\lambda_2} E(\lambda)\,d\lambda\right]^{-1}. \qquad (13)$$

Here $\Delta\Lambda$ is the full width of the ASE emission energy $W(\Lambda)$, and $\Delta\lambda$ is the linewidth of the laser emission energy $E(\lambda)$. For the special case of identical energy distributions for the ASE and laser emission, Eq. (13) reduces to the ratio of the maximum intensities (I_{ASE}/I_l). The ASE % can be obtained by multiplying

TABLE 5 ASE Levels of Multiple-Prism Grating Oscillators[a]

Excitation source	Cavity	E_0 (mJ)	$\Delta\nu$ (MHz)	I_{ASE}/I_l	ρ_{ASE}/ρ_l	C (mM)	Reference
Coaxial flashlamp	MPL	2.6–4.2	≤360	7×10^{-9}	1.2×10^{-9}	0.0125	[47]
Coaxial flashlamp	MPL[b]	~3	≤360	6×10^{-10}	1.7×10^{-10}	0.0125	[47]
Linear flashlamp	HMPGI	3.6	≤138	6×10^{-11}	2.9×10^{-11}	~0.01	[47]
CVL	MPL[c]		60	2×10^{-7}		0.6	[48]
CVL	HMPGI		~400	5×10^{-7}		2.0	[49]

[a]Adapted from Duarte *et al.* [47], with permission.
[b]Uses of intracavity polarizer next to the output coupler.
[c]Uses an intracavity etalon.

(ρ_{ASE}/ρ_l) by ($\Delta\Lambda/\Delta\lambda$). Information on ASE levels for multiple-prism grating oscillators is given in Table 5. Measures to reduce the level of ASE at the oscillator stage include the use of low dye concentrations, deployment of multiple-prism beam expanders in a nonorthogonal beam exit configuration [1,50], the use of antireflection coatings at the dye cell windows and the prismatic expander, and the use of a polarizer output coupler [51] (see Chapter 2). Further information on ASE reduction techniques and the measurement of ASE are given in [52–58]. For further details on the design and physics of dye oscillators, see Duarte [1,50].

2.3 Oscillator–Amplifiers

The theory of dye laser amplifiers has been considered by several authors [10, 14, 21]. In Table 6 the performance of several transversely excited oscillator–amplifier systems is listed. All these systems use a single-pass configuration at the amplification stage(s). The first three systems use single-transverse excitation. The master-oscillator power-amplifier (MOPA) chain delivering high average powers (>1.3 kW) uses double-transverse excitation at the amplification stages. A typical dye laser system utilizing multistage amplification is shown in Fig. 5. Semilongitudinal excitation of dye laser amplifiers is discussed by [21,39].

Measures to reduce ASE at the amplification stages include the use of appropriate delay factors in the excitation of the amplifier. This is due to the fact that ASE leads the narrow-linewidth emission at the oscillator stage. In the case of the system described by Dupre [61], the excitation of the amplifiers is delayed by ~9 ns. A simple approach to induce optical delay is illustrated in Fig. 5. Other ASE suppression methods exploit the broadband and high-divergence characteristics of this emission by using spectral and spatial filters between amplification stages [63]. For further discussion on this topic, see Duarte [1,37].

TABLE 6 Laser-Pumped Oscillator–Amplifiers[a]

Oscillator	Number of amplification stages	Total gain	Δν	Output energy	Average power	% Efficiency	Reference
Littrow grating and two etalons	One[b]	10–100	~2.4 GHz	0.25 mJ		25 at 460 nm	[59]
Telescope and Littrow grating plus etalon	Three	229	320 MHz	165 mJ		55 at 590 nm	[60]
HMPGI	Two	~700	650 MHz	3.5 mJ		~9 at 440 nm	[61]
MPL plus etalon	Four[c,d]		0.05–5 GHz		>1.3 kW	>50	[2]

[a]Adapted from Duarte [37], with permission.
[b]Oscillator and amplifier synchronously pumped by two N_2 lasers.
[c]These results correspond to a single MOPA chain of the system.
[d]This system uses double-transverse excitation of the amplifier stages.

In addition to the dispersive oscillators listed on Table 6 some authors have also used cw or quasi-cw lasers as injection sources [64,65].

3. FLASHLAMP-PUMPED DYE LASERS

This section is intended to be an expeditious guide to the performance of flashlamp-pumped dye lasers. For a detailed and thorough review on this subject the reader is referred to the work of Everett [19].

3.1 Excitation Configurations

Flashlamp-pumped dye lasers can be excited using linear, coaxial, and transverse configurations. Linear and coaxial excitation configurations are illustrated in Fig. 6. Linear flashlamp pumping utilizes two or more flashlamps deployed symmetrically around the active region (Fig. 6a). The aim here is to provide concentric illumination of the dye region and thus obtain a uniform beam profile. In this regard, high-energy linear pumping arrangements can involve up to 18 or more lamps.

Coaxial flashlamp excitation provides uniform and inherently concentric optical pumping of the dye region (Fig. 6b). In both methods of excitation the dye is illuminated through the cooling fluid and an outer reflector surrounds the flashlamp(s) (Fig. 6).

Other common features of coaxial and linear excitation include a linear dye flow, along the optical axis, and the use of relatively low dye concentrations

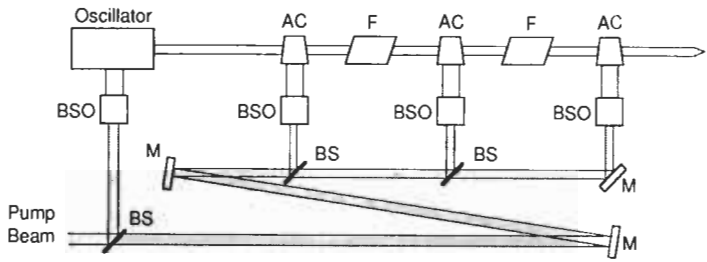

FIGURE 5 Dye laser system illustrating multistage amplification. AC, amplifier cell; BS, beam-splitter; BSO, beam-shaping optics; F, spectral filter; M, mirror. (Reprinted with permission from Duarte and Foster [62].)

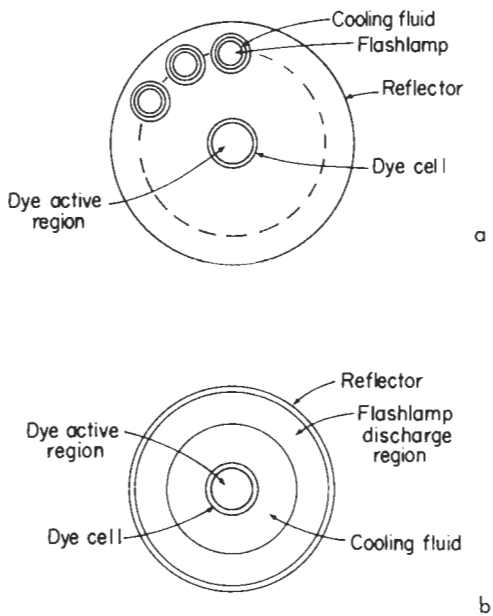

FIGURE 6 (a) Cross section of a linear excitation configuration using multiple flashlamps. (b) Cross section of a coaxial flashlamp excited dye laser. (Reprinted with permission from Duarte [37].)

typically in the 0.01- to 0.1-mM range. The diameter of active volumes vary from a few millimeters to a centimeters. The active lengths range from ~10 up to ~100 cm.

Because flashlamps emit a significant amount of radiation in the 200- to 300-nm region of the spectrum [19], it is necessary to shield the dye solution against UV-induced photodegradation. One approach is to use passive filters such as Pyrex dye cells or additives in the cooling fluid such as caffeine, ethanol,

or $CuSO_4$. An alternative approach is to use an active filter that absorbs the damaging ultraviolet radiation and emit at longer wavelengths compatible with the absorption band of the laser dye. The use of the dye converter stilbene 420 is reported to enhance efficiency of coumarin 504 by up to 75% [66].

A third excitation configuration uses linear flashlamps to excite the dye region transversely (Fig. 7). This transverse excitation configuration uses two rows of linear lamps to excite a narrow dye region channel. The dimensions of the active region volume depicted in Fig. 7 are a 0.5-mm width, a 55-mm height, and a 150-mm length [67]. This transverse excitation geometry allows the use of higher dye concentrations and more importantly the rapid flow of the dye solution. Also note that dye converters are also used in the cooling fluid. Using this type of excitation geometry, with eight lamps at each side, Klimek *et al.* [68] report an average power of 1.4 kW. The performance of various flashlamp-pumped dye lasers is listed on Table 7.

3.2 Multiple-Prism Grating Master Oscillators

Important features for master oscillators are narrow-linewidth emission, good beam quality, and very low ASE levels. Given the geometrical and excitation characteristics of flashlamp-pumped dye lasers it is a particular challenge to achieve stable narrow-linewidth oscillation. MPL and HMPGI oscillator configurations coupled with thermal and fluid flow controls have been crucial to the demonstration of stable long-term narrow-linewidth emission in this class of master oscillators [47,72]. In this subsection the physics and technological elements central to this topic are surveyed.

The first step in the design of a high-performance dispersive oscillator is to apply the generalized interference equation [Eq. (2) in Chapter 2] to determine the aperture necessary to yield a single-transverse mode for a given cavity length. Then, for a given grating and grating configuration the necessary intracavity beam expansion is calculated followed by an estimate of the dispersive linewidth. If the dispersive linewidth is within the desired range, then the multiple-prism beam expander is designed. In the event that the dispersive linewidth is not appropriate, then a higher dispersion grating should be considered. In this approach Eqs. (8) to (12) of Chapter 2 should be applied.

The multiple prism should be designed for near-orthogonal beam exit and $(\partial\Phi/\partial\lambda)_p \approx 0$. This approach reduces significantly back reflections of ASE and minimizes frequency detuning due to thermal change. Equations (22) and (23) of Chapter 2 are then utilized to determine the transmission efficiency of the multiple-prism beam expander. Here the quest for efficiency must be balanced against the length of the prism expander and its cost. Duarte [1,50] provides a detailed and explicit discussion on the design of multiple-prism beam expanders.

Further avenues in the reduction of ASE include the use of very low dye concentrations ~0.01 mM and the use of a polarizer output coupler [47,72].

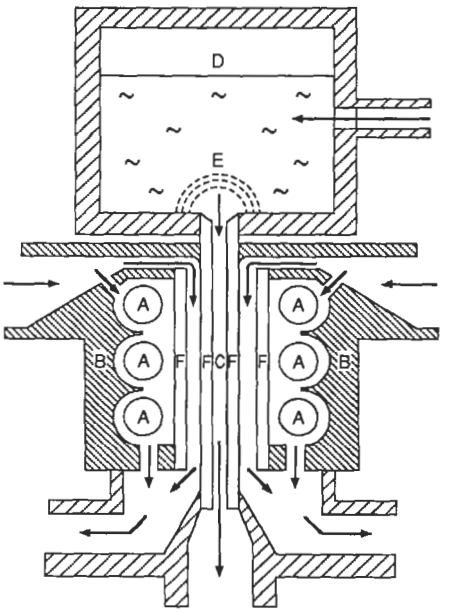

FIGURE 7 Cross section of transverse-flow flashlamp-pumped dye laser. Here the plane of propagation is perpendicular to the page and the arrows indicate the direction of flow of the dye and cooling fluid. A, flashlamp; B, reflector; C, dye channel; D, dye expansion channel; E, filters; F, glass plates. (Reprinted with permission from Mazzinghi *et al.* [67]. © 1981 IEEE.)

In 1987–1988 Duarte *et al.* [73,74] reported on the measurement of dynamic linewidth instabilities in dispersive dye laser oscillators yielding double-longitudinal-mode emission. Subsequent studies [47,72] revealed that these dynamic linewidth instabilities, that were characterized by a low-frequency modulation of the double-longitudinal-mode oscillation, originated from inhomogeneities of the active medium because of dye flow turbulence and radial thermal gradients. The radial thermal gradient has its origin on the temperature difference between the cooling fluid and the dye solution.

Multiple-prism grating master-oscillators with optimized dispersive configurations, intracavity Glan-Thompson polarizer, optimized fluid flow control and thermal control were demonstrated by Duarte *et al.* [72]. For instance, the temperatures were controlled to better than 0.01°C. In addition this master oscillator was constructed of superinvar material to minimize thermal expansion. The schematics for these dispersive oscillators are shown in Fig. 8 and a partial view of the MPL oscillator is shown in Fig. 9. The superinvar structure rests on four pneumatic mounts, each used with an air pressure of 1.72×10^5 N-m^{-2}.

The optimum performance of the ruggedized multiple-prism dye laser oscillator is given in Table 8. This oscillator was displaced on a vehicle over a rugged

TABLE 7 Performance of Flashlamp-Pumped Dye Laser[a]

Excitation	Dye	Converter dye	Output energy	Pulse duration	% Efficiency	Reference
Linear						
2	Coumarin 504	Stilbene 420				
	0.19 mM	0.25 mM	7J	~3 μs	1.0	[66]
12	Rhodamine 6G					
	0.08 mM		40 J	7 μs	0.4	[69]
Coaxial						
	Rhodamine 6G.					
	0.25 mM		8 J	5 μs	0.3	[70]
	0.022 mM		400 J	10 μs	0.8	[71]
Transverse						
6	Rhodamine 6G					
	0.8 mM		~5 J[b]	~12 ms	0.6	[67]
16	0.025 mM	Coumarin 480				
		0.2 mM	140 J[c]	5 μs	1.8	[68]

[a]Adapted from Duarte [37], with permission.
[b]Provides an average power of 200 W at a prf of 50 Hz.
[c]Provides an average power of 1.4 kW at a prf of 10 Hz.

terrain at a speed of 16 km/hour for a distance of 3.5 km. The performance measured prior and following the displacement test is given in Table 9.

Note that the fluid system was composed of a stainless steel reservoir and all connections are made of Teflon tubing. The Teflon tubing connecting the reservoir and the laser chassis is concentric with an outer flexible stainless steel protective sleeve. The dye flows through the laser head at a linear speed of 2.75 ms. Single solutions of rhodamine 590 have been used in this system for periods *in excess of one year.*

3.3 Master-Oscillator/Forced-Oscillator Configurations

In flashlamp-pumped dye lasers, amplification of the master-oscillator emission is often accomplished using forced oscillators rather than single-pass amplifiers. Forced oscillators comprise stable or unstable resonator optics in the absence of frequency selective optical components. The frequency information is provided by the master oscillator (Fig. 10).

Requirements for successful excitation of forced oscillators include very low ASE levels at the master-oscillator stage and excellent triggering synchronization.

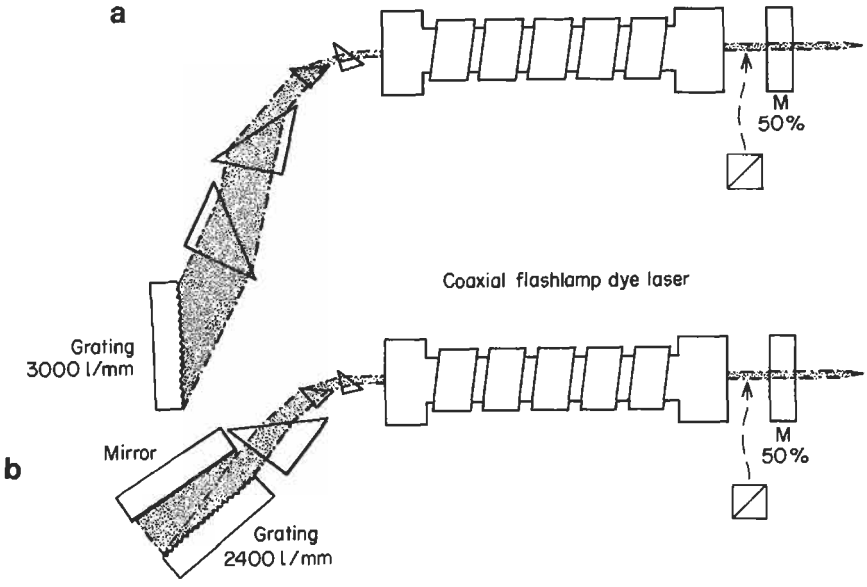

FIGURE 8 Schematics of (a) flashlamp-pumped MPL oscillator and (b) HMPGI oscillator. (Reprinted with permission from Duarte *et al.* [72] and Elsevier Science.)

In this regard, the narrow-linewidth emission pulse must be synchronized to arrive during the buildup period of the forced-oscillator pulse. In the case of forced oscillators using unstable resonator optics, the magnification of the optics must be optimized relative to the beam dimensions of the master oscillator to completely fill the active volume of the forced oscillator. Also, the injection beam should be aligned exactly for concentric propagation along the optical axis of the forced oscillator. The performance of flashlamp-pumped master-oscillator/forced-oscillator systems is listed in Table 10. In addition to those results, energy gains as high as 478 have been reported for an MPL master oscillator and a forced oscillator with a magnification factor of 5 [62].

The use of cw dye laser oscillators as injection sources of amplification stages utilizing ring cavity configurations is discussed by Blit *et al.* [78] and Trehin *et al.* [79].

4. cw LASER-PUMPED DYE LASERS

The cw dye lasers span the spectrum from ~370 to ~1000 nm. Frequency doubling extends their emission range into the 260- to 390-nm region. An important feature of cw dye lasers has been their ability to yield extremely stable emissions and very narrow linewidths. These qualities have made cw dye lasers

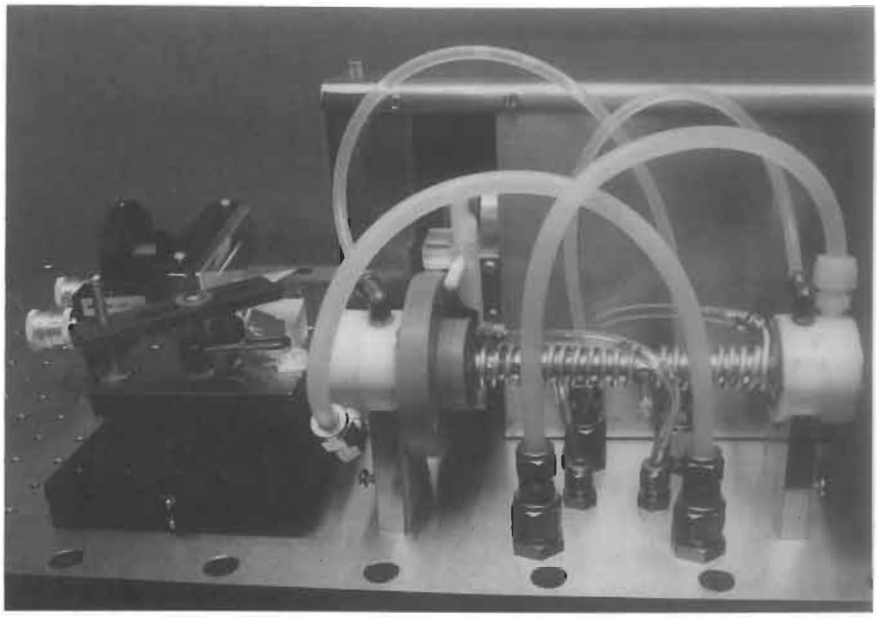

FIGURE 9 Partial view of ruggedized multiple-prism grating oscillator. (Reprinted with permission from Duarte *et al.* [72] and Elsevier Science.)

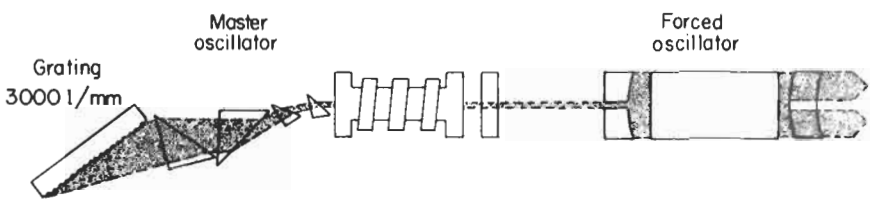

FIGURE 10 Master-oscillator/forced-oscillator system. (Reprinted with permission from Duarte and Conrad [73].)

extremely important to applications in physics, spectroscopy, and other sciences. A thorough and extensive description of this branch of dye lasers is given by Hollberg [3]. Here some of the most important features of cw dye lasers and their emission characteristics are surveyed.

4.1 Excitation Sources for cw Dye Lasers

The main sources of excitation for cw dye lasers are the argon ion (Ar^+) and the krypton ion (Kr^+) lasers. These are conventional discharge lasers that emit

TABLE 8 Optimum Performance of Ruggedized Multiple-Prism Grating Master Oscillator[a]

Output energy (mJ)	$\Delta\nu$ (MHz)	$\delta\lambda/\lambda$	$\Delta\theta$ (mrad)	C (mM)
2.2–3.6	300	4.63×10^{-7}	0.35	0.01

[a]From Duarte *et al.* [72], with permission.

TABLE 9 Performance of Ruggedized Multiple-Prism Grating Master Oscillator Prior (First Row) and Following (Second Row) Field Test[a]

Output energy (mJ)	$\Delta\nu$ (MHz)	$\delta\lambda/\lambda$	$\Delta\theta$ (mrad)	C (mM)
2–3	300	1.45×10^{-6}	0.51	0.01
2–3	300	1.18×10^{-6}	0.45	0.01

[a]From Duarte *et al.* [72], with permission.

TABLE 10 Performance of Flashlamp-Pumped Master-Oscillator/Forced-Oscillator Systems[a]

Master oscillator	Forced-oscillator configuration	Output energy	Energy gain	Reference
Two etalons $\Delta\nu \approx 8.65$ GHz	Flat-mirror cavity	600 mJ at 589 nm	200	[75]
Three etalons $\Delta\nu = 4$ GHz	Planoconcave resonator	4J	~267	[76]
Two etalons $\Delta\nu = 346$ MHz	Flat-mirror cavity	300 mJ at 590 nm		[77]
MPL $\Delta\nu \leq 375$ MHz	Positive-branch unstable resonator	600 mJ at 590 nm	60	[73]

[a]Adapted from Duarte [37], with permission.

via excitation mechanisms such as Penning ionization [80]. Table 11 lists some of the most widely used transitions in dye laser excitation. Note that the quoted powers are representative of devices available commercially. It should also be indicated that not all transitions may be available simultaneously and that more than one set of mirrors may be required to achieve lasing in different regions of the spectrum. Also, for a mirror set covering a given spectral region, lasing of individual lines may be accomplished using intracavity prism tuners.

TABLE 11 Excitation Lasers of cw Dye Lasers

Laser	Transition[a]	Wavelength (nm)	Power[b] (W)
Ar^+	$4p^4D^0_{5/2} - 4s^2P_{1/2}$	528.69	1.5
	$4p^4D^0_{3/2} - 4s^2P_{3/2}$	514.53	10.0
	$4p'^2F^0_{5/2} - 3d^2D_{3/2}$	501.72	1.5
	$4p^2D^0_{3/2} - 4s^2P_{1/2}$	496.51	2.5
	$4p^2D^0_{5/2} - 4s^2D_{3/2}$	487.99	7.0
	$4p^2P^0_{3/2} - 4s^2P_{1/2}$	476.49	2.8
	$4p^2D^0_{3/2} - 4s^2P_{3/2}$	472.69	1.2
	$4p^2P^0_{1/2} - 4s^2P_{1/2}$	465.79	0.75
	$4p^2S^0_{1/2} - 4s^2P_{1/2}$	457.93	1.4
	$4p^2P^0_{3/2} - 4s^2P_{3/2}$	454.50	1.0
Kr^+	$5p^4P^0_{3/2} - 4d^4D_{1/2}$	799.32	0.1
	$5p^4P^0_{5/2} - 5s^2P_{3/2}$	752.55	0.35
		676.4	0.2
	$5p^4P^0_{5/2} - 5s^2P_{3/2}$	647.09	1.4
	$5p^4D^0_{5/2} - 5s^2P_{3/2}$	568.19	0.53
	$5p^4P^0_{3/2} - 5s^4P_{5/2}$	530.87	0.7
	$5p^4P^0_{5/2} - 5s^4P_{3/2}$	520.83	0.25

[a]Transition identification from [80].
[b]Ar^+ laser power from [3] and Kr^+ laser powers from [81].

Given the relatively long cavity length of these lasers (typically ~1 m), and their narrow beamwaists (~1 mm), the output beam characteristics are excellent. In this regard these lasers can offer single-transverse-mode outputs and beam divergence's approaching the diffraction limit.

In addition to the output powers listed in Table 11, higher powers are available. For instance, Baving *et al.* [82] reports the use of a 200-W multiwavelength Ar^+ laser in the excitation of a linear cw dye laser. The Ar^+ laser oscillated simultaneously at 457.93, 476.49, 487.99, 496.51, 501.72, and 514.53 nm. Other lasers useful in the excitation of cw dye lasers include HeNe [83,84], frequency-doubled cw Nd:YAG [3], and semiconductor lasers.

4.2 cw Dye Laser Cavities

The cw dye laser cavities evolved from the simple and compact linear cavity first demonstrated by Peterson *et al.* [85]. External mirrors and intracavity tuning prisms were introduced by Hercher and Pike [86] and Tuccio and Strome [25] (Fig. 11). An important innovation in cw dye lasers was the introduction of the dye jet [83]. Fast flow of the dye solution at speeds of a few m-s^{-1} is important

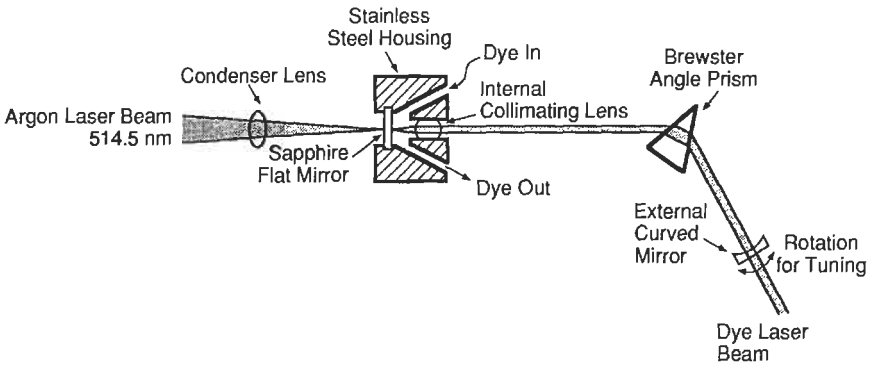

FIGURE 11 Linear cw dye laser cavity configuration. (Reprinted with permission from Tuccio and Strome [25].)

to induce heat dissipation and hence reduce thermally induced optical inhomogeneities in the active medium [85].

Widely used configurations of cw dye laser cavities include the three-mirror folded linear cavity (see, for example, [20] and references therein) and ring-dye laser cavities (see, for example, [3] and references therein). These two configurations are shown in Fig. 12. In both cases excitation from a cw laser is accomplished semilongitudinally to the optical axis defined by M_1 and M_2. Tuning elements, or frequency-selective elements (FSEs), are deployed between M_2 and M_3 in the linear cavity, and between M_3 and M_4 in the ring cavity. The unidirectional device (UDD) depicted in Fig. 12(b) is an optical diode that controls the direction of propagation in the ring cavity [3].

Ring-dye laser cavities circumvent the problem of spatial hole burning associated with linear cavities [3]. Also ring cavities are reported to yield higher single-longitudinal-mode power than linear cavities [3]. However, linear configurations offer greater optical simplicity and lower oscillation thresholds.

Diels [87] discusses the use of propagation matrices, applicable for Gaussian beam propagation analysis, to characterize stability conditions and astigmatism in cw dye laser cavities.

Linewidth narrowing and FSEs used in cw dye lasers are birefringent crystals, prisms, gratings, and Fabry-Perot etalons. Often two or more FSEs are necessary to achieve single-longitudinal-mode oscillation. The first stage in the frequency narrowing usually consists of utilizing prisms or birefringement filters to yield a bandwidth compatible with the free spectral range (FSR) of the first of two etalons. In turn, the second etalon has a FSR and finesse necessary to restrict oscillation in the cavity to a single-longitudinal mode [3]. Alternative approaches may replace the second etalon by an interferometer [88]. The performance of various linear and ring cw dye lasers is listed in Table 12.

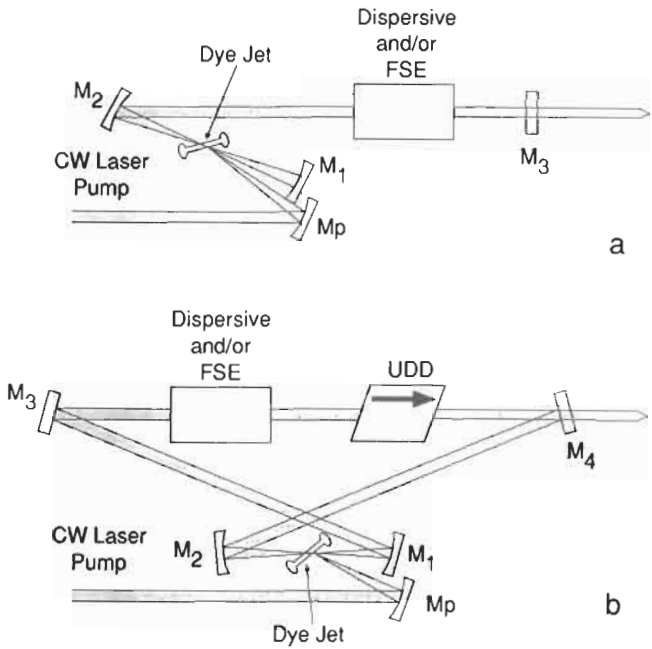

FIGURE 12 (a) Three mirror-folded linear cw dye laser cavity. (b) A cw ring dye laser cavity (see text for details). (Reprinted with permission from Hollberg [3].)

4.3 Frequency Stabilization

Intrinsic linewidths in single-longitudinal-mode cw ring-dye lasers, utilizing intracavity FSE, can be in the 1- to 3-MHz range [3,92]. Further reduction in linewidth requires the use of frequency stabilization techniques. This subject is reviewed in detail by Hollberg [3].

Frequency fluctuations in single-longitudinal-mode cw dye lasers are the result of minute dynamic variations in cavity length. These changes can be the consequence of very small mechanical displacement of cavity components, changes in the dye jet optical length, and optical inhomogeneities in the active medium. Hall and Hänsch [92] have estimated that a change in thickness of the dye jet by a few molecular monolayers can cause phase shifts of several radians in about 3 μs. Hence, frequency stabilization techniques should offer rapid response.

Hollberg [3] lists and describes in detail a number of frequency stabilization techniques:

Cavity side lock [3,93]: A beamsplitter directs a fraction of the laser output toward a second beamsplitter that distributes the signal toward a detector and a reference Fabry-Perot interferometer. The difference between the

TABLE 12 Performance of cw Dye Lasers[a]

Cavity	Spectral coverage (nm)	Output power (W)	Linewidth	% Efficiency	Reference
Linear		33[b] Using rhodamine 6G at 0.7 mM		30	[89]
Linear	560–650	33[c] Using rhodamine 6G at 0.94 mM		17	[82]
Ring	407–887 using 11 dyes	5.6 Using rhodamine 6G	SLM[d]	23.3	[90]
Ring	364–524 using 4 dyes	0.43 Using coumarin 102	SLM[d]	10.2	[91]

[a]Under Ar^+ laser excitation.
[b]Maximum cw power quoted was 52 W for a pump power of 175 W.
[c]Output power without intracavity tuning prism is quoted at 43 W for a pump power of 200 W.
[d]Single-longitudinal mode (SLM). Linewidth values can be in the few megahertz range.

direct signal and the signal from the reference cavity is used to drive the laser cavity servocontrol amplifier.

Modulation lock [3]: A beamsplitter sends part of the emission beam toward a reference Fabry-Perot interferometer. The transmitted signal from the reference cavity is compared at a lock-in amplifier with the signal modulating the dye laser frequency. The resulting error signal is used to drive the dye laser cavity servo control.

rf-optical heterodyne lock [3,94]: A beamsplitter sends portion of the dye laser output toward a phase modulator (electro-optics transducer). The phase-modulated radiation then propagates toward a reference cavity via a Thompson prism in series with a Faraday rotator. The return beam from the reference cavity is reflected by the Thompson prism toward a detector. The signal from the detector is sent to a set of filters followed by a balanced mixer. At this stage the signal from the reference cavity is mixed with the signal from the phase modulator to produce an error signal that drives the dye laser cavity servocontrol.

Post-laser stabilization [3,92]: This method changes the frequency of the dye laser emission outside the cavity. The technique combines an electro-optic modulator (EOM) and an acousto-optic modulator (AOM) to yield a fast frequency transducer. The EOM and the AOM are deployed in series with the EOM in between two mirrors whose optical axis is at a slight angle relative to the propagation axis of the laser beam. The aim of the mirrors is to provide an optical delay line (the beam

undergoes three single passes inside the EOM) prior to illumination of the AOM. At the EOM a voltage is applied to change the phase of the radiation. A frequency shift is induced when the voltage changes as a function of time. Voltage limitations restrict the time over which the frequency shift can be sustained. Thus the function of the slower AOM is to relieve the EOM soon after a pertubation. The EOM used by Hall and Hänsch is an AD*P crystal, in a triple-pass configuration, and their AOM used TeO_2.

Further frequency stabilization methods use molecular media, such as iodine, to provide frequency reference [95]. Performance of frequency-stabilized cw dye lasers is tabulated in Table 13.

5. FEMTOSECOND-PULSE DYE LASERS

The dye laser with its continuous and wide frequency gain profile is an inherent source of ultrashort temporal pulses. Indeed, the development of femtosecond-pulsed dye lasers has been essential to the development and advancement of ultrashort-pulse laser science. An excellent review on this subject, including a historical perspective, is given by Diels [87]. In this section the performance of femtosecond-pulsed dye lasers is presented together with a description of technical elements relevant to the technology of ultrashort-pulse laser emission.

For a comprehensive discussion on ultrashort-pulse-measuring techniques the reader should refer to Diels [87]. Also, for alternative methods of ultrashort-pulse generation utilizing distributed feedback dye laser configurations, the review given by Schäfer [98] is suggested.

The principles and theory of femtosecond-pulse generation has been discussed by many authors [99–109]. Notable among these works are the papers by Zhakarov and Shabat [99], Diels *et al.* [100], and Salin *et al.* [101], which discuss nonlinear effects and the subject of solitons. Pulse evolution is discussed by New [102]. An important contribution of general interest is that of Penzkofer and Bäumler [103]. This comprehensive work includes excitation parameters and cross sections relevant to the saturable absorber DODCI and the gain dye rhodamine 6G.

5.1 Femtosecond-Pulse Dye Laser Cavities

Mode locking in dye lasers using an intracavity saturable absorber dye cell was first demonstrated in a flashlamp-pumped dye laser [110]. This development was followed by the demonstration of passive mode locking in a linear cw dye laser [111].

A development of crucial importance to the generation of ultrashort pulses was the introduction of the concept of colliding-pulse mode locking (CPM) by

TABLE 13 Performance of Frequency-Stabilized cw Dye Lasers

Stabilization method	Linewidth	Frequency drift	Limiting factors	Reference
Cavity side lock: Uses two Fabry-Perot interferometers	150 kHz[a] (rms)	50 MHz/hour		[96]
rf-optical heterodyne lock: Uses signals reflected from a reference cavity	100 Hz		Servo electronics	[94]
	<750 Hz[a]	720 Hz/sec	Mechanical noise	[97]
Post-laser: Uses acousto-optic and electro-optic modulators[b]	20 kHz[a]			[92]

[a]Emission source: ring-dye laser.
[b]For dye lasers with intrinsic linewidths of ~1 MHz, this method has produced linewidths of ~1 kHz [3].

Ruddock and Bradley [112]. Subsequently, Fork *et al.* [113] incorporated the CPM concept to ring cavities, thus demonstrating pulses as short as 90 fs.

CPM is established when a *collision* between two counterpropagating pulses is induced at the saturable absorber. The interaction of the two counterpropagating pulses gives origin to interference that induces a reduction in the pulse duration.

Two of the most widely used cavities in femtosecond dye lasers are the cw linear and ring cavity configurations modified to incorporate CPM. Linear and ring femtosecond dye laser cavities incorporating the saturable absorber region in its counterpropagating arrangement is shown in Fig. 13. In both cavities the gain region is configured in the optical axis defined by M_1 and M_2, whereas the saturable absorber is deployed in the optical path defined by M_3 and M_4. Note that in both instances these ultrashort-pulse cavities are equivalent to the linear and ring cw dye laser cavities shown in Fig. 12 with M_3 replaced by the CPM arrangement.

An additional feature of these cavities is the use of intracavity prisms to induce pulse compression. In dye lasers, pulse broadening by positive group velocity dispersion (GVD) is induced at the dye gain and absorber regions. Multiple-prism arrangements can be configured to provide net positive dispersion, no dispersion, or negative dispersion [1,107]. In femtosecond dye lasers, intracavity prisms are deployed to provide negative GVD and hence compensate for the positive GVD generated at the dye regions.

Gordon and Fork [104] provide an expression for the group velocity dispersion constant in a prism array:

$$D = \left(\frac{\lambda}{cL}\right)\frac{d^2P}{d\lambda^2} , \tag{14}$$

where L is the physical length of the light path, and P is the optical path length through the prism array. By differentiating

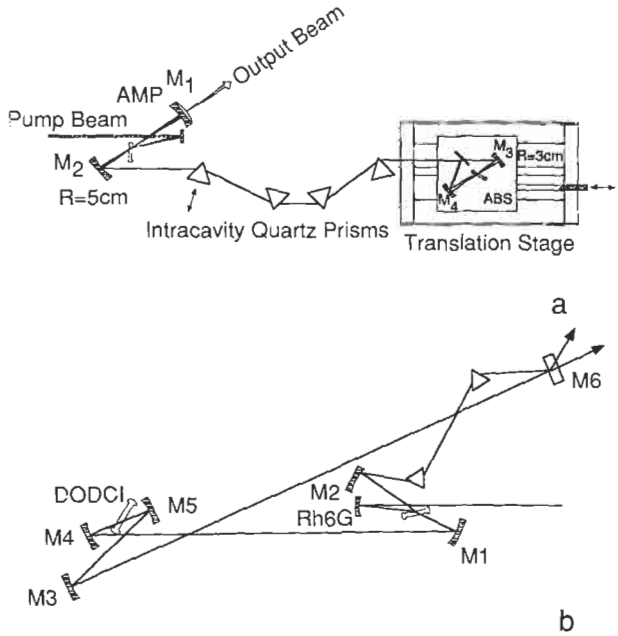

FIGURE 13 (a) Linear femtosecond dye laser cavity deploying the saturable absorber within a counterpropagating ring. GVD compensation is provided by a four-prism array (from Jamasbi *et al.* [114]). (b) Ring femtosecond dye laser cavity using a two-prism pulse compressor. (Reprinted with permission from Diels *et al.* [100].)

$$\frac{dP}{d\lambda} = \frac{dn}{d\lambda}\frac{d\phi}{dn}\frac{dP}{d\phi} \,. \tag{15}$$

Fork *et al.* [105] have shown that

$$\frac{d^2P}{d\lambda^2} = \left[\frac{d^2n}{d\lambda^2}\frac{d\phi}{dn} + \left(\frac{dn}{d\lambda}\right)^2\frac{d^2\phi}{dn^2}\right]\frac{dP}{d\phi} + \left(\frac{dn}{d\lambda}\right)^2\left(\frac{d\phi}{dn}\right)^2\frac{d^2P}{d\phi^2} \,, \tag{16}$$

which shows the dependence of $d^2P/d\lambda^2$ on $d\phi/dn$ and $d^2\phi/dn^2$. It is these two derivatives, $d\phi/dn$ and $d^2\phi/dn^2$, that depend on the overall prismatic dispersion. A negative value for $d^2P/d\lambda^2$ can be achieved by adjusting the interprism separation. The effect of minute geometrical perturbations and/or beam deviations on overall dispersion was quantified by [107]. This work demonstrated that very small angular deviations induced changes in dispersion that can only be assessed using the generalized multiple-prism dispersion theory. Generalized expressions for $d\phi/dn$ and $d^2\phi/dn^2$ are given in Chapter 2.

Kafka and Baer [108] and Duarte [107] have discussed the effect of variations of beam angle of exit and incidence on overall dispersion. Bor [109] has considered the distortion of femtosecond pulses following transmission in lens systems.

The first use of intracavity prismatic dispersion to achieve pulse compression was reported by Dietel *et al.* [115]. These authors reported pulse lengths of less than 60 fs. A collinear four-prism sequence was introduced by Fork *et al.* [105] and a single prism pair was used by Diels *et al.* [100]. The dispersion theory of multiple-prism arrays has been discussed by Duarte [1,106,107]. Table 14 lists the performance of several prismatic configurations. Table 15 tabulates relevant values of $dn/d\lambda$ and $d^2n/d\lambda^2$ for several prism materials. Note that some materials such as LaSF9 and ZnSe provide significantly higher $dn/d\lambda$ and $d^2n/d\lambda^2$ values that enable the design of very compact multiple-prism pulse compressors [50].

An alternative and/or complementary avenue to prismatic pulse compression is the use of grating pairs. In this regard, Fork *et al.* [6] report the use of an extracavity four-prism compressor in conjunction with two grating pairs to achieve pulses as short as 6 fs. These authors note that the shortest pulse measured using the grating pairs alone, in the external compressor, was 8 fs. An additional feature of this work was the preamplification of 50-fs pulses, generated in a cavity including CPM and prismatic GVD compensation, to energy levels of ~1 mJ and a prf of 8 kHz. The amplification pump source was a CVL laser [6].

Amplification of 70-fs pulses to gigawatt power levels has been reported by Fork *et al.* [118]. These authors employed an extracavity grating pair following the multiple-amplification stages.

Diels [87] has tabulated a comprehensive performance listing of ultra-fast dye lasers utilizing passive and hybrid mode locking. This listing is reproduced on Tables 16 and 17.

TABLE 14 Performance of Intracavity Prismatic GVD Compensation

Number of prisms	Cavity configuration	Pulse width	Reference
1	Ring[a]	53 fs	[115]
2	Ring[b]	85 fs	[100]
4	Ring[c]	65 fs	[105]
4	Ring	19 fs	[5]
4	Linear	29 fs	[116]

[a]First report on the use of prismatic intracavity dispersion to achieve GVD compensation (1983).
[b]First report on the use of a compensating prism pair to achieve GVD compensation (1985).
[c]First report on the use of two compensating prism pairs to achieve GVD compensation (1984).

6. SOLID-STATE DYE LASERS

Solid-state dye lasers were first demonstrated by Soffer and McFarland [139] in 1967 using rhodamine-doped polymethyl methacrylate (PMMA) under laser excitation. Lasing of rhodamine-doped PMMA under flashlamp excitation was demonstrated by Peterson and Snavely [140].

Table 18 lists available matrices used in solid-state dye lasers. Modified PMMA (MPMMA) [141,142] is an improved form of PMMA with high damage thresholds and excellent optical properties. MPMMA results from purifying the initial monomer compositions and by doping PMMA with low molecular additives [142]. Gromov *et al.* [141] report that MPMMA has an energy damage thresholds of 13 J/cm^2. Further, these authors report that the threshold for photobleaching of rhodamine 6G in MPMMA is ~1.6 J/cm^2. Duarte [46] reports that for a beam radius of 200 μm no evidence of photobleaching in rhodamine-doped MPMMA was evident at energy densities of ~0.7 J/cm^2. The measured refractive index for rhodamine-6G-doped MPMMA at a concentration of 0.1 mM is 1.453 at $\lambda = 594.48$ nm.

Gromov *et al.* [141] report that at an incident energy density of 1 J/cm^2 photobleaching occurs in 2000 pulses for dye 11B and in 1100 pulses for rhodamine 111. Hermes *et al.* [143] quotes a useful lifetime of more than 20,000 pulses for PM-570-doped hydroxypropyl acrylate/MMA at an incident energy density of 0.6 J/cm^2.

For ORMOSIL, Duarte *et al.* [45] report on long-pulse lasing under dye laser excitation. This ORMOSIL was synthesized using the method of Dunn *et al.* [144] and was composed by a 1:1:1:3.5 molar ratio of TMOS/MMA/3-(trimethoxysilyl) propyl MA/0.04 N HCl [145]. The dye concentration used in

TABLE 15 Dispersion Characteristics of Prism Materials for Pulse Compression[a]

Material	n	λ (μm)	$dn/d\lambda$ (μm^{-1})	$d^2n/d\lambda^2$ (μm^{-2})	Reference
Quartz	1.457	0.62	−0.03059	0.1267	[105]
BK7	1.51554	0.62	−0.03613	0.15509	
F2	1.61747	0.62	−0.07357	0.34332	[87]
SF10	1.72444	0.62	−0.10873	0.53819	[87]
LaSF9	1.84629	0.62	−0.11189	0.57778	
	1.83257	0.80	−0.05201	0.18023	
ZnSe[b]	2.586	0.62	−0.698	5.068	
	2.511	0.80	−0.246	1.163	

[a]Adapted from Diels [87], with permission.
[b]Calculated using data from Marple [117].

TABLE 16 Passive Mode Locking[a]

Gain dye	Absorber[b]	Wavelength range (nm)	Minimum width (fs)	at (nm)	Remarks	Reference
Coumarin 102	DOCI	493–502	93	497	Ring cavity	[119]
Coumarin 102	D9MOCI	488–512			UV argon laser	
Coumarin 102	DPQI	494–512			pump	
Coumarin 102	DQTI	492–512				
Coumarin 6H	DOCI	492–507	110	497	Ring cavity	[120]
Rh 110	DASBTI	553–570	210	561	Linear cavity	[121]
	HICI	553–570	80	581	Ring cavity	[122]
Rh 6G	DASTBI	570–600	500		Linear cavity	[123]
Rh B	DQTCI	616–658	220	635	Linear cavity	[124]
Rh 6G/SRh 101	DQTCI	652–681	120	666	Linear cavity,	[125]
	DCCI	652–694	240		energy transfer	
DCM	DQTCI	655–673	680	670	Linear cavity	[126]
Rh 700	(DOTCI + DCI)	727–740	350	740	Linear cavity, krypton laser	[127]
	HITCI	762–778	850	770	pump	
Rh 700/DCM	DDI	742–754	110	754	Ring cavity, energy transfer	[128]

[a]Adapted from Diels [87], with permission.
[b]See Appendix for abbreviations.

TABLE 17 Hybrid Mode Locking[a]

Gain dye	Absorber[b]	Wavelength range (nm)	Minimum width (fs) at (nm)		Remarks	Reference
Disodium fluorescein	Rh B	535–575	450	545		[129]
Rh 110	Rh B	545–585	250	560		
Rh 6G	DODCI	574–611	300	603		[130]
Rh 6G	DODCI		110	620	Ring cavity	[131]
Rh 6G	DODCI		60	620	Antiresonant ring cavity	[132]
Kiton red S	DODCI		29	615	Linear cavity	[116]
	DQOCI					
RhB	Oxazine 720		187	650		[133]
SRh 101	DQTCI		55	675	Direct pumping with doubled Nd:YAG, linear cavity	[133]
Pyridine 1	DDI		103	695	Linear cavity	[134]
Rh 700	DOTCI	710–718	470	713	Linear cavity	[135]
Pyridine 2	DDI, DOTCI		263	733	Linear cavity	[134]
Rh 700	HITCI	770–781	550	776	Linear cavity	[135]
LDS-751	HITCI	790–810	100		Linear cavity	[136]
Styryl 8	HITCI		70	800	Linear cavity	[134]
Styryl 9	IR 140		65	840	Linear cavity	[134]
		840–880	65	865	Ring cavity	[137]
Styryl 14	DaQTeC		228	974	Linear cavity	[138]

[a]Adapted from Diels [87], with permission.
[b]See Appendix for abbreviations.

TABLE 18 Matrices for Solid-State Dye Lasers

Matrix	Abbreviation
Polymethyl methacrylate[a]	PMMA
Modified polymethyl methacrylate	MPMMA
Tetraethoxysilane [$Si(OC_2H_5)_4$]	TEOS
Tetramethoxysilane [$Si(OCH_3)_4$]	TMOS
Organically modified silicate	ORMOSIL
Silica-PMMA nanocomposites	

[a]Methyl methacrylate (MMA) is $CH_2{=}C(CH_3)COOCH_3$.

these experiments was 2 mM and the excitation laser was a flashlamp-pumped dye laser with a 170-ns pulse duration [45].

An alternative to ORMOSILs are the transparent silica-PMMA nanocomposites [146]. Although these nanocomposites have a number of similarities with ORMOSILs, including very high transparencies, they also have a number of synthetic differences [146]. These nanocomposites can be optically polished to yield high-quality optical surfaces. This feature, coupled to their high transparency, offers a very attractive optical material. Silica-PMMA nanocomposites doped with rhodamine 6G and rhodamine B have been made to lase under transverse excitation from a coumarin 152 dye laser [147].

An important difference between PMMA-type matrices and silicate matrices is the internal structure of the latter. This structure can induce refractive index variations that leads to optical inhomogeneities of the active medium. These inhomogeneities can be characterized by propagating a narrow-linewidth laser through the matrix and then observing the far-field interferometric pattern thus produced [147].

The energetic and efficiency performances of solid-state dye lasers using a variety of host matrices are listed in Table 19.

The performance of solid-state dispersive dye laser oscillators is given in Chapter 2 for MPMMA matrices. In addition to those results, Duarte *et al.* [45] reports an output energy of ~ 1 mJ at $\Delta\nu \approx 3$ GHz for a multiple-prism grating oscillator using TEOS doped with rhodamine 6G at 2 mM. The same oscillator yielded <1 mJ/pulse for ORMOSIL doped with rhodamine 6G at the same concentration. In an extension of the work published in [46], Duarte [153] has optimized the architecture of the solid-state multiple-prism grating dye laser oscillators and has demonstrated a very compact dispersive oscillator. This dispersive oscillator has a cavity length in the 55–60 mm range and yields efficient single-longitudinal-mode lasing at $\Delta\nu \approx 420$ MHz with a near-Gaussian temporal profile 3–4 ns in duration (FWHM).

TABLE 19 Performance of Solid-State Dye Lasers

Matrix	Dye	Excitation source	Output energy	% Efficiency	Concentration (mM)	Reference
PMMA	Rhodamine 590	flashlamp	50 mJ		0.11	[148]
PMMA	Coumarin 540	flashlamp	50 mJ		0.14	[148]
MPMMA	Rhodamine 6G	Nd:glass laser[a]		50		[141]
MPMMA	11B			52		[141]
Hydroxypropyl acrylate/MMA	PM-570[b]	Nd:YAG laser[a]	128 mJ	85	0.32	[143]
TMOS	Sulforhodamine 640	Nd:YAG laser[a]	10 μJ	20		[149]
TEOS	Rhodamine 6G	Nd laser[a]	~240 μJ	~40		[150]
TEOS	Rhodamine 6G	Flashlamp-pumped dye laser[c]	2.5 mJ[d]		2.0	[45]
ORMOSIL	Rhodamine 6G	Nd:YAG laser[a]	150 μJ	30		[151]
	Rhodamine 6G	Nd:YAG laser[a]	3.5 mJ	35%	0.086	[152]

[a]Second harmonic.
[b]1,3,5,7,8-pentamethyl-2, 6-di-n-butylpyrromethene-BF_2.
[c]The dye used was coumarin 525.
[d]The pulse length was 60 ns (FWHM).

APPENDIX OF LASER DYES

Name	Molecular weight (au)	Maximum absorption l(nm)	Maximum fluorescence l(nm)	Maximum lansing l (nm) (pump laser)	Tuning range[a] (nm)	Solvents	Molecular Structure
p-Terphenyl (PTP)	230.31	276	354	338 (XeCl)	330–355	cyclohexane	
p-Quaterphenyl (PQP)	306.41	300	363	378 (XeCl)	360–394	toluene	
Carbostyril 124 (Carbostyril 7; 7-Amino-4-methylcarbostyril)	174.20	349	405	417 (N_2)	400–430	methanol	
POPOP	364.40	358	415	419 (N_2)	412–426	cyclohexane	

Coumarin 120 (Coumarin 440; 7-Amino-4-methylcoumarin)	175.19	352	428	444 (N_2)	418–498	methanol, ethanol	
Coumarin 2 (Coumarin 450; 4,6-Dimethyl-7-ethylaminocoumarin)	217.27	365	435	450 (N_2)	430–478	methanol, ethanol	
Coumarin 339	215.25	377	447	460 (N_2)	437–492	methanol	
Coumarin 1 (Coumarin 47; Coumarin 460; 7-Diethylamino-4-methylcoumarin)	231.30	374	450	464 (N_2)	438–510	methanol, ethanol	

(continues)

APPENDIX OF LASER DYES (*continued*)

Name	Molecular weight (au)	Maximum absorption l(nm)	Maximum fluorescence l(nm)	Maximum lansing l (nm) (pump laser)	Tuning range[a] (nm)	Solvents	Molecular Structure
Coumarin 138 (7-Dimethylamino cyclopenta[c]-coumarin)	229.28	365	447	464 (N_2)	441–489	methanol	
Coumarin 102T (Coumarin 480T)	311.32	385	–	475 (XeCl)[1]	450–511	ethanol, methanol, ethanol/water	
Coumarin 102 (Coumarin 480)	255.32	390	468	481 (N_2)	460–515	methanol, ethanol	
Coumarin 338T	397.41	–	–	491 (XeCl)[1]	477–526	ethanol, methanol, ethanol/water	

Coumarin 151 (Coumarin 490; 7-Amino-4-trifluoro-methylcoumarin)	229.16	377	479	493 (N_2)	465–533	methanol, ethanol	
Coumarin 4 (Umbelliferon 47; 7-Hydroxy-4-methylcoumarin)	176.17	322	386	494 (N_2)	464–534	methanol	
Coumarin 314 (Coumarin 504)	313.35	437	478	495 (N_2)	488–504	methanol, ethanol	
Coumarin 30 (Coumarin 515)	347.42	413	478	497 (N_2)	478–518	methanol, ethanol	

(continues)

APPENDIX OF LASER DYES (*continued*)

Name	Molecular weight (au)	Maximum absorption l(nm)	Maximum fluorescence l(nm)	Maximum lansing l (nm) (pump laser)	Tuning range[a] (nm)	Solvents	Molecular Structure
Coumarin 314T (Coumarin 504T)	369.35	435	478	506 (XeCl)[1]	478–525	ethanol, methanol, ethanol/water	
Coumarin 307 (Coumarin 503; 7-Ethylamino-6-methyl-4-trifluoro methylcoumarin)	271.24	395	488	510 (N_2)	480–552	methanol, ethanol	
Coumarin 334 (Coumarin 521)	283.33	452	491	511 (N_2)	504–522	methanol, ethanol	
Coumarin 334T (Coumarin 521T)	339.33	–	–	515 (XeCl)[1]	500–546	ethanol, methanol, ethanol/water	

Coumarin 343 (Coumarin 519)	285.30	440	482	–	–	methanol, ethanol	
Coumarin 7 (Coumarin 535; 3-(2'-Benzimidazolyl)-7-N,N-diethylamino coumarin)	333.39	437	488	518 (N_2)	507–531	methanol, ethanol	
Coumarin 6 (Coumarin 540)	350.44	458	497	523 (Nd:YAG)[b]	506–544	methanol, ethanol	
Coumarin 152 (Coumarin 485; 7-Dimethylamino-4-trifluoromethylcoumarin)	257.21	394	496	530 (N_2)	492–572	methanol, ethanol	

(continues)

APPENDIX OF LASER DYES (*continued*)

Name	Molecular weight (au)	Maximum absorption l(nm)	Maximum fluorescence l(nm)	Maximum lansing l (nm) (pump laser)	Tuning range[a] (nm)	Solvents	Molecular Structure
Coumarin 153T	365.29	–	–	535 (XeCl)[1]	508–588	ethanol, methanol, ethanol/water	
PMP-BF_2	262	492.5	504	542.5 (FL)[2]	523–580	methanol	
Fluorescein (Fluorescein 548; Fluorescein 27)	332.31	498	518	545 (Nd:YAG)[b]	533–575	methanol + 2% base	
Rhodamine 110 (Rhodamine 560)	366.80	498	520	554 (N_2)	538–584	methanol, ethanol	

PMPDS-BF_2	484	496.5	521	555 (FL)[2]	537–605	methanol	
2',7'-Dichlorofluorescein	401.20	512	526	557 (Nd:YAG)[b]	544–584	methanol + 2% base	
Rhodamine 6G Tetrafluoroborate (Rhodamine 590 Tetrafluoroborate)	530.37	528	547	581 (N_2) 563 (Nd:YAG)[c]	566–610	methanol, ethanol	
Rhodamine 6G Perchlorate (Rhodamine 590 Perchlorate)	543.02	528	547	581 (N_2) 563 (Nd:YAG)[c]	564–611	methanol, ethanol	

(continues)

APPENDIX OF LASER DYES (*continued*)

Name	Molecular weight (au)	Maximum absorption l(nm)	Maximum fluorescence l(nm)	Maximum lansing l (nm) (pump laser)	Tuning range[a] (nm)	Solvents	Molecular Structure
Rhodamine 6G (Rhodamine 590)	479.00	528	555	586 (N_2) 568 (Nd:YAG)[c]	568–618	methanol, ethanol	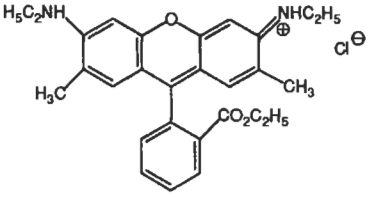
Rhodamine B (Rhodamine 610)	479.02	545	565	609 (N_2) 588 (Nd:YAG)[c]	595–639	methanol, ethanol	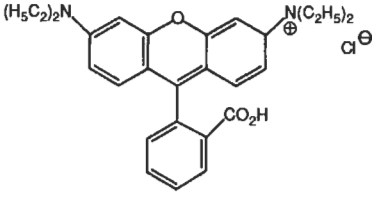
Sulforhodamine B (Kiton Red 620; Xylene Red B)	558.66	556	572	624 (N_2) 589 (Nd:YAG)[c]	595–641	methanol, ethanol	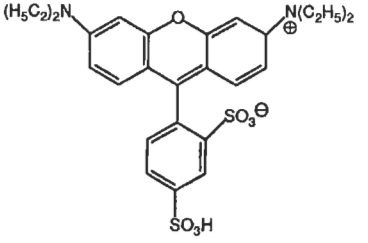

DODC Iodide (DODCI; 3,3'-Diethyloxadi carbocyanine Iodide)	486.35	578	605	647 (Nd:YAG)[C]	639–659	methanol	
Sulforhodamine 101 (Sulforhodamine 640)	606.00	578	605	649 (N_2) 614 (Nd:YAG)[C]	620–678	methanol, ethanol	
DCM (4-(Dicyanomethylene)-2-methyl-6-(p-dimethyl-aminostyryl)-4H-pyran)	303.37	480	627	663 (N_2) 661 (Nd:YAG)[C]	640–691	DMSO, methanol, ethanol	
Oxazine 4 Perchlorate (LD690 Perchlorate)	395.84	610	625	667 (N_2) 651 (Nd:YAG)[C]	653–681	methanol	

(continues)

APPENDIX OF LASER DYES (*continued*)

Name	Molecular weight (au)	Maximum absorption l(nm)	Maximum fluorescence l(nm)	Maximum lansing l (nm) (pump laser)	Tuning range[a] (nm)	Solvents	Molecular Structure
DTDC Iodide (DTDCI; 3,3'-Diethylthiadi carbocyanine Iodide	518.48	662	679	743 (N_2) 698 (Nd:YAG)[c]	725–761	DMSO	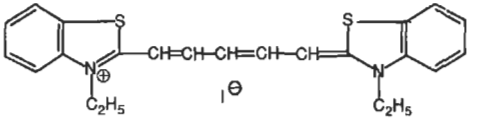
DOTC Iodide (DOTCI; 3,3'-Diethyloxatri-carbocyanine Iodide)	512.39	695	719	762 (Nd:YAG)[c]	750–770	DMSO	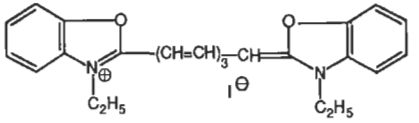
HITC Perchlorate (HITCP; 1,1',3,3,3',3'-Hexamethyl-indotricarbocyanine Perchlorate)	509.05	750	790	837 (N_2) 826 (Nd:YAG)[c]	823–875	DMSO	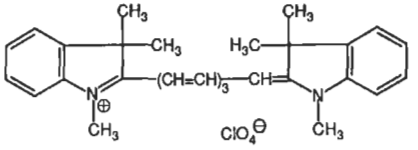
HITC Iodide (HITCI; 1,1',3,3,3',3'-Hexa-methylindotricarbo-cyanine Iodide)	536.00	750	790	841 (N_2) 832 (Nd:YAG)[c]	816–880	DMSO	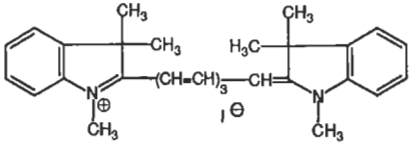

DTTC Iodide (DTTCI 3,3'-Diethylthiatri carbocyanine Iodide)	544.00	772	820	856 (N_2) 850 (Nd:YAG)[c]	843–890	DMSO	
DTTC Perchlorate (DTTCP 3,3'-Diethylthiatri carbocyanine Perchlorate)	517.06	772	818	863 (N_2) 846 (Nd:YAG)[c]	843–900	DMSO	
IR-144	1008.00	745	825	878 (N_2) 867 (Nd:YAG)[c]	865–895	DMSO	

(continues)

APPENDIX OF LASER DYES (*continued*)

Name	Molecular weight (au)	Maximum absorption l(nm)	Maximum fluorescence l(nm)	Maximum lansing l (nm) (pump laser)	Tuning range[a] (nm)	Solvents	Molecular Structure
HDITC Perchlorate (HDITCP; 1,1',3,3,3',3'-Hexamethyl-4,4',5,5'-dibenzo-2,2'-indotricarbocyanine Perchlorate)	609.17	780	828	913 (N_2) 886 (Nd:YAG)[c]	883–946 866–938	DMSO	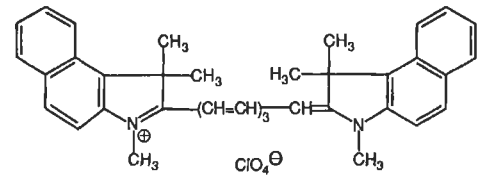
IR-125	774.00	795	833	914 (N_2) 915 (Nd:YAG)[c]	880–943	DMSO	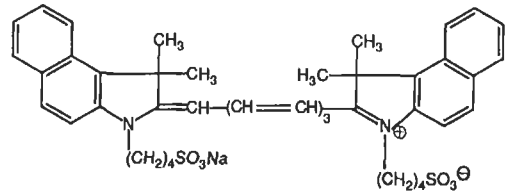

IR-132	954.55	832	905	918 (N_2) 914 (Nd:YAG)[C]	900–940	DMSO

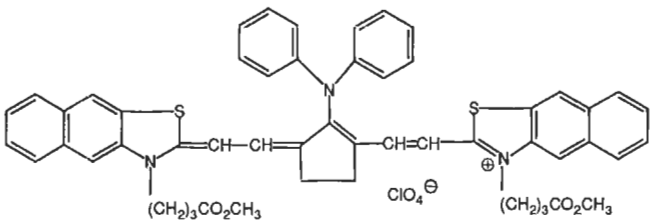

IR-140	779.00	826	882	943 (N_2) 897 (Nd:YAG)[C]	913–986 889–930	DMSO

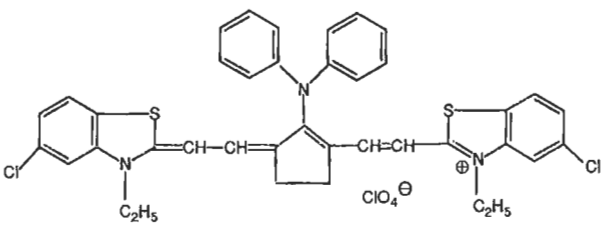

(continues)

Emission data obtained with solvent listed in first place. For further alternative solvents, see Rfs. 3 and 4. Most of the information given in this table has been adapted from *KODAK Laser Dyes*[5] courtesy of Eastman Kodak Company and originally published in *Dye Laser Principles*.[6]

[a]These are approximate values since the tuning range depends on solvent, pump source, and resonator characteristics.

[b]Third Harmonic from Nd:YAG at 355 nm.

[c]Second Harmonic from Nd:YAG at 532 nm.

References

1. C. H. Chen, J. L. Fox, F J. Duarte, and J. J. Ehrlich, *Appl. Opt.* 27, 443 (1988).
2. W. E. Davenport, J. J. Ehrlich, and S. E. Neister, in *Proceedings of the International Conference on Laser '89* (D. G. Harris and T. M. Shay, Eds.), pp. 408–414, STS Press, McLean, VA, (1990).
3. K. H. Drexhage, in *Dye Lasers* (F. P. Schäfer, Ed.), pp. 155–200, Springer-Verlag, Berlin, 1990.
4. M. Maeda, *Laser Dyes*, Academic, New York, 1984.
5. R. R. Birge, *KODAK Laser Dyes*, Kodak Publication JJ-169, Eastman Kodak Company, Rochester, NY, (1987).
6. F. J. Duarte and L. W. Hillman, "*Dye Laser Principles*", Academic, New York, (1990).

Abbreviations: DASBTI, 2-(p-dimethylaminostryl)-benzothiazolylethyl iodide; DaQTeC, 1,1'-diethyl-13-acetoxy-2, 2'-quinotetracarbocyanine iodide; DCM, 4-dicyanomethylene-2-methyl-6-p-dimethylaminostryl-4H-pyran; DCCI, 1,1'-diethyl-2, 4'-carbocyanine iodide; =DCI, 1,1'-diethyl-2, 4'-carbocyanine iodide; DCCI*, 1,1'-diethyl-2, 2'-carbocyanine iodide; =DDI, DOCI, 3,3'-diethyl oxacarbocyanine iodide; DODCI, 3,3'-diethyl oxadicarbocyanine iodide; DOTCI, 3,3'-diethyl oxatricarbocyanine iodide; DQOCI, 1,3'-diethyl-4, 2'-quinolyoxacarbocyanine iodide; HICI, 1,1'3,3,3',3'-hexamethylindocarbocyanine iodide; HITCI, 1,1'3,3,3',3'-hexamethylindotricarbocyanine iodide; MNA, 2-methyl-4-nitroaniline.

*Cryptocyanine 1,1'-Diethyl-4, 4'-carbocyanine iodide; DTDCI, 3,3'-Diethyl thiadicarbocyanine iodide; DQTCI, 1,3'-Diethyl-4,2'-quinolthiacarbocyanine iodide.

REFERENCES

1. F. J. Duarte. in *High Power Dye Lasers* (F. J. Duarte, Ed.), pp. 7–43, Springer-Verlag, Berlin (1991).
2. I. L. Bass, R. E. Bonanno, R. P. Hackel, and P. R. Hammond, *Appl. Opt.* **31,** 6993 (1992).
3. L. Hollberg, in *Dye Laser Principles* (F. J. Duarte and L. W. Hillman, Eds.), pp. 185–238, Academic, New York (1990).
4. C. Salomon, D. Hils, and J. L. Hall, *J. Opt. Soc. Am. B* **5,** 1576 (1988).
5. A. Finch, G. Chen, W. Sleat, and W. Sibbett, *J. Mod. Opt.* **35,** 345 (1988).
6. R. L. Fork, C. H. Brito Cruz, P. C. Becker, and C. V. Shank, *Opt. Lett.* **12,** 483 (1987).
7. F. J. Duarte and L. W. Hillman (Eds.), *Dye Laser Principles,* Academic, New York (1990).
8. F. P. Schäfer (Ed.), *Dye Lasers,* Springer-Verlag, Berlin (1990).
9. F. J. Duarte (Ed.), *Selected Papers on Dye Lasers,* Milestone Series, SPIE, Bellingham, WA (1992).
10. U. Ganiel, A. Hardy, G. Newmann, and D. Treves, *IEEE J. Quantum Electron.* **QE-11,** 881 (1975).
11. O. Teschke, A. Dienes, and J. R. Whinnery, *IEEE J. Quantum Electron.* **QE-12,** 383 (1976).
12. G. Dujardin and P. Flamant, *Opt. Commun.* **24,** 243 (1978).
13. A. Penzkofer and W. Falkenstein, *Opt. Quantum Electron.* **10,** 399 (1978).
14. G. Haag, M. Munz, and G. Marowsky, *IEEE J. Quantum Electron.* **QE-19,** 1149 (1983).
15. M. Munz, G. Haag, and G. Marowsky, *Appl. Phys.* **22,** 175 (1980).
16. L. G. Nair and G. Dasgupta, *IEEE J. Quantum Electron.* **QE-21,** 1782 (1985).
17. A. A. Hnilo and O. E. Martinez, *IEEE J. Quantum Electron.* **QE-23,** 593 (1987).
18. C. Jensen, in *High Power Dye Lasers* (F. J. Duarte, Ed.), pp. 45–91, Springer-Verlag, Berlin (1991).
19. P. N. Everett, in *High Power Dye Lasers* (F. J. Duarte, Ed.), pp. 183–245, Springer-Verlag, Berlin (1991).
20. O. G. Peterson, in *Methods of Experimental Physics* (C. L. Tang, Ed.), Vol. 15, pp. 251–359, Academic, New York (1979).
21. R. S. Hargrove and T. Kan, *IEEE J. Quantum Electron.* **QE-16,** 1108 (1980).
22. P. R. Hammond, *IEEE J. Quantum Electron.* **QE-15,** 624 (1979).
23. L. W. Hillman, in *Dye Laser Principles* (F. J. Duarte and L. W. Hillman, Eds.), pp. 17–39, Academic, New York (1990).
24. J. P. Webb, W. C. McColgin, O. G. Peterson, D. L. Stockman, and J. H. Eberly, *Chem. Phys.* **53,** 4227 (1970).
25. S. A. Tuccio and F. C. Strome, *Appl. Opt.* **11.** 64 (1972).
26. B. B. Snavely, in *Dye Lasers* (F. P. Schäfer, Ed.), pp. 91–120, Springer-Verlag, Berlin (1990).
27. T. R. Loree, K. B. Butterfield, and D. L. Barker, *Appl. Phys. Lett.* **32,** 171 (1978).
28. R. G. Caro, M. C. Gower, and C. E. Webb, *J. Phys. D: Appl. Phys.* **15,** 767 (1982).
29. V. L. Lyutskanov, K. G. Khristov, and I. V. Tomov, *Sov. J. Quantum Electron.* **10,** 1456 (1980).
30. T. J. McKee, *Can. J. Phys.* **63,** 214 (1985).
31. T. T. Yang, D. H. Burde, G. A. Merry, D. G. Harris, L. A. Pugh, J. H. Tillotson, C. E. Turner, and D. A. Copeland, *Appl. Opt.* **27,** 49 (1988).
32. B. W. Woodward, V. J. Ehlers, and W. C. Lineberger, *Rev. Sci. Instrum.* **44,** 882 (1973).
33. T. M. Shay, F. E. Hanson, D. Gookin, and E. J. Schimitschek, *Appl. Phys. Lett.* **39,** 783 (1981).
34. L. M. Bukshpun, V. V. Zhukov, E. L. Latush, and M. F. Sem, *Sov. J. Quantum Electron.* **11,** 804 (1981).
35. J. Tenenbaum, I. Smilanski, S. Gabay, L. A. Levin, G. Erez, and S. Lavi, *Opt. Commun.* **32,** 473 (1980).
36. I. J. D'Haenens and C. K. Asawa, *J. Appl. Phys.* **33,** 3201 (1962).

37. F. J. Duarte, in *Dye Laser Principles* (F. J. Duarte and L. W. Hillman, Eds.), pp. 239–285, Academic, New York (1990).
38. C. Tallman and R. Tennant, in *High Power Dye Lasers* (F. J. Duarte, Ed.), pp. 93–142, Springer-Verlag, Berlin (1991).
39. C. E. Webb, in *High Power Dye Lasers* (F. J. Duarte, Ed.), pp. 143–182, Springer-Verlag, Berlin (1991).
40. K. Y. Tang, T. O'Keefe, B. Treacy, L. Rottler, and C. White, in *Proc. Dye Laser/Laser Dye Technical Exchange Meeting* (J. H. Bentley, Ed.), pp. 490–502, U.S. Army Missile Command, Redstone Arsenal, AL (1987).
41. R. A. Tennant, M. C. Whitehead, C. R. Tallman, and R. W. Basinger, in *Proc. Int. Conf. Lasers '88* (R. C. Sze and F. J. Duarte, Eds.), pp. 420–424, STS, McLean, VA (1989).
42. O. Uchino, T. Mizumani, M. Maeda, and Y. Miyazoe, *Appl. Phys.* **19,** 35 (1979).
43. G. Wang and J. P. Webb, *IEEE J. Quantum Electron.* **QE-10,** 722 (1974).
44. O. V. Bogdankevich, M. M. Zverev, E. M. Krasavina, I. V. Kryukova, and V. F. Pevtsov, *Sov. J. Quantum Electron.* **17,** 133 (1987).
45. F. J. Duarte, J. J. Ehrlich, W. E. Davenport, T. S. Taylor, and J. C. McDonald, in *Proc. Int. Conf. Lasers '92* (C. P. Wang, Ed.), pp. 293–296, STS, McLean, VA (1993).
46. F. J. Duarte, *Appl. Opt.* **33,** 3857 (1994).
47. F. J. Duarte, J. J. Ehrlich, W. E. Davenport, and T. S. Taylor, *Appl. Opt.* **29,** 3176 (1990).
48. A. F. Bernhardt and P. Rasmussen, *Appl. Phys. B* **26,** 141 (1981).
49. F. J. Duarte and J. A. Piper, *Appl. Opt.* 23, 1391 (1984).
50. F. J. Duarte, in *Dye Laser Principles* (F. J. Duarte and L. W. Hillman, Eds.), pp. 133–183, Academic, New York (1990).
51. F. J. Duarte, U.S. Patent 5,181,222 (Jan. 19, 1993).
52. F. J. Duarte and J. A. Piper, *Opt. Commun.* **35,** 100 (1980).
53. F. J. Duarte and J. A. Piper, *Appl. Opt.* **20,** 2113 (1981).
54. Z. Bor, *Opt. Commun.* **39,** 383 (1981).
55. T. J. McKee, J. Lobin, and W. A. Young, *Appl. Opt.* **21,** 725 (1982).
56. I. A. McIntyre and M. H. Dunn, *Opt. Commun.* **50,** 169 (1984).
57. E. Berik, B. Davidenko, V. Mihkelsoo, P. Apanasevich, A. Grabchikov, and V. Orlovich, *Opt. Commun.* **56,** 283 (1985).
58. M. R. Gorbal and M. I. Savadatti, *Pramana J. Phys.* **31,** 205 (1988).
59. I. Itzkan and F. W. Cunningham, *IEEE J. Quantum Electron.* **QE-8,** 101 (1972).
60. F. Bos, *Appl. Opt.* **20,** 1886 (1981).
61. P. Dupre, *Appl. Opt.* **26,** 860 (1987).
62. F. J. Duarte and D. R. Foster, in *Encyclopedia of Applied Physics* (G. L. Trigg, Ed.), Vol. 8, pp. 331–352, VCH, New York (1994).
63. R. Wallenstein and T. W. Hänsch, *Opt. Commun.* **14,** 353 (1975).
64. L. E. Erickson and A. Szabo, *Appl. Phys. Lett.* **18,** 433 (1971).
65. Q. H. F. Vrehen and A. J. Breimer, *Opt. Commun.* **4,** 416 (1972).
66. P. N. Everett, H. R. Aldag, J. J. Ehrlich, G. S. Janes, D. E. Klimek, F. M. Landers, and D. P. Pacheco, *Appl. Opt.* **25,** 2142 (1986).
67. P. Mazzinghi, P. Burlamacchi, M. Matera, H. F. Ranea-Sandoval, R. Salimbeni, and U. Vanni, *IEEE J. Quantum Electron.* **QE-17,** 2245 (1981).
68. D. E. Klimek, H. R. Aldag, and J. Russell, in *Conf. Lasers and Electro-Optics*, OSA Technical Digest Series, Vol. 12, p. 332, Optical Society of America, Washington, DC (1992).
69. J. Fort and C. Moulin, *Appl. Opt.* **26,** 1246 (1987).
70. B. A. Knyazev, S. V. Lebedev, and E. P. Fokin, *Sov. J. Quantum Electron.* **13,** 146 (1983).
71. F. N. Baltakov, B. A. Barikhin, and L. V. Sukhanov, *JETP Lett.* **19,** 174 (1974).
72. F. J. Duarte, W. E. Davenport, J. J. Ehrlich, and T. S. Taylor, *Opt. Commun.* **84,** 310 (1991).
73. F. J. Duarte and R. W. Conrad, *Appl. Opt.* **26,** 2567 (1987).

74. F. J. Duarte, J. J. Ehrlich, S. P. Patterson, S. D. Russell, and J. E. Adams, *Appl. Opt.* **27,** 843 (1988).
75. G. Magyar and H. J. Schneider-Muntau, *Appl. Phys. Lett.* **20,** 406 (1972).
76. M. Maeda, O. Uchino, T. Okada, and Y. Miyazoe, *Jpn. J. Appl. Phys.* **14,** 1975 (1975).
77. P. H. Flamant, D. Josse, and M. Maillard, *Opt. Quantum Electron.* **16,** 179 (1984).
78. S. Blit, U. Ganiel, and D. Treves, *Appl. Phys.* **12,** 69 (1977).
79. F. Trehin, F. Biraben, B. Cagnac, and G. Grynberg, *Opt. Commun.* **31,** 76 (1979).
80. C. S. Willett, *An Introduction to Gas Lasers: Population Inversion Mechanisms*, Pergamon, New York (1974).
81. "The Tungsten-Bore Ion-Gas Laser," Laser Ionics Inc., Orlando, FL (1982).
82. H. J. Baving, H. Muuss, and W. Skolaut, *Appl. Phys. B* **29,** 19 (1982).
83. P. K. Runge and R. Rosenberg, *IEEE J. Quantum Electron.* **QE-8,** 910 (1972).
84. E. Thiel, C. Zander, and K. H. Drexhage, *Opt. Commun.* **60,** 396 (1986).
85. O. G. Peterson, S. A. Tuccio, and B. B. Snavely, *Appl. Phys. Lett.* **17,** 245 (1970).
86. M. Hercher and H. A. Pike, *Opt. Commun.* **3,** 346 (1971).
87. J.-C. Diels, in *Dye Laser Principles* (F. J. Duarte and L. W. Hillman, Eds.), pp. 41–132, Academic, New York (1990).
88. J. C. Bergquist and L. Burkins, *Opt. Commun.* **50,** 379 (1984).
89. P. Anliker, H. R. Luthi, W. Seelig, J. Steinger, H. P. Weber, S. Leutwyler, E. Schumacher, and L. Woste, *IEEE J. Quantum Electron.* **QE-13,** 547 (1977).
90. T. F. Johnston, R. H. Brady, and W. Proffitt, *Appl. Opt.* **21,** 2307 (1982).
91. T. Johnston, *Opt. Commun.* **69,** 147 (1988).
92. J. L. Hall and T. W. Hänsch, *Opt. Lett.* **9,** 502 (1984).
93. J. Helmcke, S. A. Lee, and J. L. Hall, *Appl. Opt.* **21,** 1686 (1982).
94. R. W. P. Drever, J. L. Hall, F. V. Kowalski, T. Hough, G. M. Ford, A. J. Munley, and H. Ward, *Appl. Phys. B* **31,** 97 (1983).
95. D. J. E. Knight, G. J. Edwards, P. R. Pearce, K. I. Pharaoh, G. P. Barwood, N. R. Cross, and F. Xi-Sheng, *Sov. J. Quantum Electron.* **15,** 1374 (1985).
96. W. G. Divens and S. M. Jarrett, *Rev. Sci. Instrum.* **53,** 1363 (1982).
97. J. Hough, D. Hils, M. D. Rayman, L. S. Ma, L. Hollberg, and J. L. Hall, *Appl. Phys. B* **33,** 179 (1984).
98. F. P. Schäfer, in *Dye Lasers* (F. P. Schäfer, Ed.), pp. 1–89, Springer-Verlag, Berlin (1990).
99. V. E. Zakharov and A. B. Shabat, *Sov. Phys. JEPT* **34,** 62 (1972).
100. J.-C. Diels, W. Dietel, J. J. Fontaine, W. Rudolph, and B. Wilhelmi, *J. Opt. Soc. Am. B* **2,** 680 (1985).
101. F. Salin, P. Grangier, G. Roger, and A. Brun, *Phys. Rev. Lett.* **56,** 1132 (1986).
102. G. H. New, *IEEE J. Quantum Electron.* **QE-10,** 115 (1974).
103. A. Penzkofer and W. Baümler, *Opt. Quantum Electron.* **23,** 727 (1991).
104. J. P. Gordon and R. L. Fork, *Opt. Lett.* **9,** 153 (1984).
105. R. L. Fork, O. E. Martinez, and J. P. Gordon, *Opt. Lett.* **9,** 150 (1984).
106. F. J. Duarte and J. A. Piper, *Opt. Commun.* **43,** 303 (1982).
107. F. J. Duarte, *Opt. Quantum Electron.* **22,** 467 (1990).
108. J. D. Kafka and T. Baer, *Opt. Lett.* **12,** 401 (1987).
109. Z. Bor, *J. Mod. Opt.* **35,** 1907 (1988).
110. W. Schmidt and F. P. Schäfer, *Phys. Lett.* **26A,** 558 (1968).
111. E. P. Ippen, C. V. Shank, and A. Dienes, *Appl. Phys. Lett.* **21,** 348 (1972).
112. I. S. Ruddock and D. J. Bradley, *Appl. Phys. Lett.* **29,** 296 (1976).
113. R. L. Fork, B. I. Greene, and C. V. Shank, *Appl. Phys. Lett.* **38,** 671 (1981).
114. N. Jamasbi, J. C. Diels, and L. Sarger, *J. Mod. Opt.* **35,** 1891 (1988).
115. W. Dietel, J. J. Fontaine, and J.-C. Diels, *Opt. Lett.* **8,** 4 (1983).
116. H. Kubota, K. Kurokawa, and M. Nakazawa, *Opt. Lett.* **13,** 749 (1988).

117. D. T. F. Marple, *J. Appl. Phys.* **35,** 539 (1964).
118. R. L. Fork, C. V. Shank, and R. T. Yen, *Appl. Phys. Lett.* **41,** 223 (1982).
119. P. M. W. French and J. R. Taylor, *Opt. Lett.* **13,** 470 (1988).
120. P. M. W. French and J. R. Taylor, *Opt. Commun.* **67,** 51 (1988).
121. P. M. W. French and J. R. Taylor, *Opt. Lett.* **11,** 297 (1986).
122. P. M. W. French and J. R. Taylor, *Opt. Commun.* **61,** 224 (1987).
123. P. M. W. French and J. R. Taylor, in *Ultrafast Phenomena V* (G. R. Fleming and A. E. Siegman, Eds.), pp. 11–13, Springer-Verlag, Berlin (1986).
124. P. M. W. French and J. R. Taylor, *Opt. Commun.* **58,** 53 (1986).
125. P. M. W. French and J. R. Taylor, *IEEE J. Quantum Electron.* **QE-22,** 1162 (1986).
126. P. M. W. French and J. R. Taylor, *Appl. Phys. B* **41,** 53 (1986).
127. K. Smith, N. Langford, W. Sibbett, and J. R. Taylor, *Opt. Lett.* **10,** 559 (1985).
128. P. M. W. French, J. A. R. Williams, and J. R. Taylor, *Opt. Lett.* **12,** 684 (1987).
129. Y. Ishida, K. Naganuma, and T. Yajima, *Jpn. J. Appl. Phys.* **21,** L312 (1982).
130. Y. Ishida, T. Yajima, and K. Naganuma, *Jpn. J. Appl. Phys.* **19,** L717 (1980).
131. M. C. Nuss, R. Leonhardt, and W. Zinth, *Opt. Lett.* **10,** 16 (1985).
132. J. C. Diels, N. Jamasbi, and L. Sarger, in *Ultrafast Phenomena V* (G. R. Fleming and A. E. Siegman, Eds.), pp. 2–4, Springer-Verlag, Berlin (1986).
133. M. D. Dawson, T. F. Boggess, D. W. Garvey, and A. L. Smirl, *IEEE J. Quantum Electron.* **QE-23,** 290 (1987).
134. M. D. Dawson, T. F. Doggess, and A. L. Smirl, *Opt. Lett.* **12,** 254 (1987).
135. N. Langford, K. Smith, W. Sibbett, and J. R. Taylor, *Opt. Commun.* **58,** 56 (1986).
136. W. H. Knox, in *Conf. Lasers and Electro-Optics,* OSA Technical Digest Series, Vol. 14, p. 368, Optical Society of America, Washington, DC (1987).
137. J. Dobler, H. H. Schulz, and W. Zinth, *Opt. Commun.* **57,** 407 (1986).
138. M. D. Dawson, T. F. Boggess, and A. L. Smirl, *Opt. Lett.* **12,** 590 (1987).
139. B. H. Soffer and B. B. McFarland, *Appl. Phys. Lett.* **10,** 266 (1967).
140. O. G. Peterson and B. B. Snavely, *Appl. Phys. Lett.* **12,** 238 (1968).
141. D. A. Gromov, K. M. Dyumaev, A. A. Manenkov, A. P. Maslyukov, G. A. Matyushin, V. S. Nechitailo, and A. M. Prokhorov, *J. Opt. Soc. Am. B* **2,** 1028 (1985).
142. K. M. Dyumaev, A. A. Manenkov, A. P. Maslyukov, G. A. Matyushin, V. S. Nechitailo, and A. M. Prokhorov, *J. Opt. Soc. Am. B* **9,** 143 (1992).
143. R. E. Hermes, T. H. Allik, S. Chandra, and J. A. Hutchinson, *Appl. Phys. Lett.* **63,** 877 (1993).
144. B. Dunn, J. D. Mackenzie, J. I. Zink, and O. M. Stafsudd, in *Proc. SPIE* **1328,** 174–182, SPIE, Bellingham, WA (1990).
145. S. Melpolder, private communication (1992).
146. E. J. A. Pope, M. Asami, and J. D. Mackenzie, *J. Mater. Res.* **4,** 1018 (1989).
147. F. J. Duarte, in *Proc. Int. Conf. Lasers '93* (V. J. Corcoran and T. A. Goldman, Eds.), pp. 400–404, STS, McLean, VA (1994).
148. D. P. Pacheco, H. R. Aldag, I. Itzkan, and P. S. Rostler, in *Proc. Int. Conf. Lasers '87* (F. J. Duarte, Ed.), pp. 330–337, STS, McLean, VA (1988).
149. F. Salin, G. LeSaux, P. Georges, A. Brun, C. Bagnall, and J. Zarzycki, *Opt. Lett.* **14,** 785 (1989).
150. G. B. Altshuler, V. A. Bakhanov, E. G. Dulneva, A. V. Erofeev, O. V. Mazurin, G. P. Roskova, and T. S. Tsekhomskaya, *Opt. Spectrosc.* **62,** 709 (1987).
151. J. C. Altman, R. E. Stone, B. Dunn, and F. Nishida, *IEEE Photon. Technol. Lett.* **3,** 189 (1991).
152. D. Larrue, J. Zarzycki, M. Canva, P. Georges, F. Bentivegna, and A. Brun, *Opt. Commun.* **110,** 125 (1994).
153. F. J. Duarte, *Opt. Commun.,* **117,** 480 (1995).

6 Transition Metal Solid-State Lasers

Norman P. Barnes
NASA Langley Research Center
Hampton, Virginia

1. INTRODUCTION

Solid-state lasers are becoming the laser of choice for many diverse applications. Selection of solid-state lasers is based on their performance capabilities, such as available wavelengths, efficiency, tuning range, reliability, and pulse format flexibility. These performance capabilities can be directly attributed to spectroscopic properties that are often unique to solid-state lasers.

Solid-state lasers can be subdivided into two broad categories, transition metal lasers and lanthanide series lasers. The spectroscopic and performance properties of these two broad categories of solid-state lasers are considerably different. Transition metal lasers have active atoms that come from the fourth row in the periodic table of the elements, whereas lanthanide series lasers have active atoms that come from the sixth row. Although many properties of these two categories are similar, spectral absorption and emission characteristics and, thus, tunability are significantly different. Transition metal lasers are usually tunable over a relatively wide spectral range, whereas the tuning range of lanthanide series lasers is relatively limited. It is the intent of this chapter to concentrate on the transition metal lasers.

Tunable Lasers Handbook
Copyright © 1995 by Academic Press, Inc. All rights of reproduction in any form reserved.

Tunability of transition metal solid-state lasers, a prime reason for their selection, results from the interaction of the transition metal active atom with the crystal field of the laser material. The electrons that participate in the lasing process in transition metal lasers are the 3*d* electrons; the electrons that participate in the lasing process in lanthanide series lasers are the 4*f* electrons. Because of the electronic configuration, the 3*d* electrons interact strongly with the crystal field of the laser material, whereas the 4*f* electrons do not. It is the strong interaction of the electrons with the crystal field that produces the tunability. Tuning ranges can be a very large fraction of the center wavelength. For example, the ratio of the tuning range to the peak gain wavelength of $Ti:Al_2O_3$ is about 0.5, providing one of the largest tuning ranges of any laser.

Solid-state lasers operate best in the near-infrared region of the spectrum, from about 0.7 to 2.1 μm. Operation at shorter wavelengths tends to be limited by the lifetime of the upper laser level and laser material considerations. Material considerations are associated with the pumping process because solid-state lasers are optically pumped almost exclusively. Because the pump wavelength is almost always shorter than the laser wavelength, the laser material must be transparent at wavelengths considerably shorter than the laser wavelength. Because most optical materials begin absorbing in the near ultraviolet, finding a laser material with the requisite transparency becomes increasingly difficult as the laser wavelength moves from the near infrared into the visible. On the other extreme, long-wavelength operation of solid-state lasers is limited primarily by lifetime and quantum efficiency considerations. As the laser wavelength becomes longer, an increasing fraction of the excited laser atoms is lost to nonradiative decay processes. Nonradiative decay processes deplete the upper laser level population density without the emission of a photon, which, in turn, decreases the lifetime and quantum efficiency. Nonradiative decay processes make it increasingly more difficult to create a high upper laser level population density and thus reach threshold. High thresholds limit the laser efficiency and if the thresholds are too high, eventually prevent operation of solid state at the longer wavelengths lasers altogether.

Solid-state lasers offer a large variety of pulse formats, ranging from single pulses with very large energies to continuous wave (cw) operation. At low pulse repetition frequencies (prfs), solid-state lasers can be excited or pumped with a pulsed source. Laser output pulse lengths can range from time intervals commensurate with the pump pulse length to pulse lengths that are a tiny fraction of the pump pulse length. When the laser operates with pulse lengths controlled by the pump pulse length, the mode of operation is referred to as *normal mode*. To obtain the short laser pulse lengths, and the high peak power associated with them, an optical switch or *Q*-switch is employed. During most of the pump pulse the *Q*-switch prevents lasing. However, because of the long lifetime of the upper laser level, the pump energy can be stored in the upper laser level efficiently. Near the end of the pump pulse, the *Q*-switch is opened and the majority of the

energy stored in the laser material can be extracted in a single pulse. Pulsed pumping and Q-switching can generate pulses at prfs up to frequencies on the order of a kilohertz. To produce even higher prfs, a continuous pump source can be used. Transition from a pulsed pump to a continuous pump source usually occurs at a prf on the order of the inverse of the upper laser level lifetime. By using the appropriate optical switching technique, a train of pulses can be obtained even though a continuous pump source is used.

At frequencies above the kilohertz range, continuous pumping and repetitive optical switching can produce a train of laser pulses. At pulse repetition frequencies on the order of kilohertz, continuous pumping and repetitive Q-switching can be employed to produce the desired prf. If even higher prfs are desired—up to about a megaHertz frequency—a technique known as *cavity dumping* can be used. Energy storage methods are the primary difference between these two techniques. With repetitive Q-switching, the energy is stored in the laser material, whereas with cavity dumping the energy is stored in the optical field. If even higher prfs are desired, mode locking can be employed. Mode locking produces pulses by coupling the various frequencies or modes comprising the laser output. By coupling the modes, pulses with short pulse lengths are produced at a frequency associated with the round-trip time interval of the laser resonator. These coupled modes can produce prfs on the order of 100 MHz. Finally, cw operation of many solid-state lasers is possible using cw pumping.

Long upper laser level lifetimes, characteristic of most solid-state lasers, are the key to the large variety of possible pulse formats. The upper laser level lifetimes for solid-state lasers can be as long as many milliseconds. Virtually all other types of lasers have short upper laser level lifetimes, on the order of nanoseconds. A long upper laser level lifetime allows the optical pump pulse for the solid-state laser to be long, yet still maintain efficient storage of the pump energy in the upper laser level. In other types of lasers, the stored energy escapes from the upper laser level virtually as fast as the pump puts it in. Thus, when other types of lasers operate pulsed, they act much like a quasi cw laser that is only operating for a short time interval. On the other hand, having a long upper laser level lifetime allows solid-state lasers to store the pump energy and extract it in a pulse that is short compared with the pumping time interval.

Having a long upper laser level can also lower the threshold for cw operation. Analysis shows that the threshold for cw operation is proportional to the inverse of the lifetime. Thus, if this were the only variable, threshold would be lower for longer lifetime lasers. Offsetting this is the relationship between the lifetime and the stimulated emission cross section. In many instances, the product of these two factors is approximately constant for a particular laser atom. In these cases, an increase in the lifetime indicates a decrease in the stimulated emission cross section. Consequently, in these cases, the threshold tends to be independent of the lifetime to first order.

Solid-state lasers can operate with reasonable efficiency, even if conventional optical pumping techniques are employed. Solid-state lasers were initially optically pumped by flashlamps. The very first laser [1], a $Cr:Al_2O_3$ or ruby laser, was pumped with a flashlamp similar to the flashlamps used for photographic purposes. The first lasers were very inefficient, but substantial progress has been made even with these optical pump sources. Commercial Nd:YAG lasers, using flashlamp or arc lamp optical pumping, operate with an electrical to optical efficiency in the approximate range of 0.01 to 0.05. A primary reason for this limitation to the efficiency is the poor spectral match of the flashlamp emission spectrum with the absorption spectrum of the laser material. Because of the poor spectral match, much of the flashlamp radiation is not absorbed by the laser material and therefore does not contribute to the laser output. Transition metal lasers can be more efficient than lanthanide series lasers in this respect because they can have broad absorption as well as broad emission bands. Broad absorption bands are more efficient absorbers of the wide spectral bandwidth emission from the lamps used for optical pumping.

Efficient absorption of flashlamp radiation can be enhanced by using more than one species of atom in a laser material. Absorption of the optical pump radiation can be performed by one type of atom and the absorbed energy can be efficiently transferred to another type of atom that participates in the lasing process. The former is referred to as a *sensitizer* and the latter is referred to as the *active atom*. Through the use of sensitizers, often transition metal atoms, the efficiencies of solid-state lasers can be increased by a factor of 2 or more. One example of such a laser is the Nd:Cr:GSGG laser [2]. Cr, with its broad absorption bands, is the sensitizer and Nd is the active atom.

With the advent of light-emitting and laser diodes, the prospect of even more efficient solid-state lasers was realized [3–5]. While light-emitting diodes were used initially; laser diodes, with their narrower spectral bandwidth and emission angles, have become the norm. Laser diodes have an advantage over flashlamps by concentrating the optical pump radiation in a relatively narrow spectral band. By matching the laser diode emission with the absorption bands of the solid-state laser material, virtually all of the optical pump radiation from the laser diode can be absorbed by the laser material. Using laser diodes for optical pumping can increase the efficiency of solid-state lasers, particularly lanthanide series lasers, by a factor that may approach an order of magnitude. Because lanthanide series lasers are often used as optical pumps for transition metal lasers, increases in the efficiency of the former can have a beneficial effect on the latter.

The efficiency of solid-state lasers, both in cw and pulsed modes of operation, is enhanced by the favorable stimulated emission cross section. Efficient lasers should have stimulated emission cross sections in the midrange, about 10^{-23} m^2. Many solid-state lasers can meet these requirements. If the stimulated emission cross section of a laser is too large, energy stored in the laser material

is lost through a process referred to as *amplified spontaneous emission* (ASE). In this process, a photon emitted spontaneously in the laser material will stimulate several other active atoms in the upper laser level to emit their quantum of stored energy before it can escape from the laser material. Thus, a single spontaneously emitted photon can cause several other atoms in the upper laser level to lose their energy in a process that does not contribute to the laser output. As such, lasers with high stimulated emission cross sections can be inefficient in the pulsed mode. Conversely, lasers with low stimulated emission cross sections also tend to be inefficient. In this case, the stimulated emission cross section is so low that even the photons destined for laser output have difficulty stimulating the active atoms in the upper laser level to emit. Although this can be overcome to a degree by having a high density of laser photons, this high density of laser photons tends to aggravate laser induced damage problems.

Solid-state lasers can also have favorable size and reliability properties. Solid-state lasers can be compact. A solid-state laser head, which is the optical portion of the laser device, capable of producing an average output of several watts, either pulsed or continuous wave, can be a hand-held item. The reliability of solid-state lasers is primarily limited by the lifetime of the optical pump. Continuously operating arc lamps have lifetimes in the range of several hundred hours. Pulsed flashlamps can have a lifetime from 10^7 to 10^9 shots. With diode-pumped lasers, these lifetimes can increase one or more orders of magnitude.

Because some of the improvements in solid-state lasers are predicated on the use of laser diode pumping, it is reasonable to ask whether laser diodes should be used directly. In many cases, the direct use of laser diodes is appropriate. However, a primary advantage of the solid-state lasers is their utility as an optical integrator. Laser diodes are devices with a short upper laser level lifetime and a limited amount of power. To obtain a high peak power or a large energy per pulse requires many laser diodes to operate in concert. In addition, if good beam quality or narrow spectral bandwidth is desired, all of the individual laser diodes must be operated coherently, complicating the design of the laser diode arrays.

Solid-state lasers on the other hand can integrate the output of many laser diodes or laser diode arrays, both spatially and temporally, in a single optical device. Moreover, the solid-state laser material can store the power output of the laser diodes efficiently, making the production of high-peak-power pulses possible. This spatial and temporal optical integration ability makes it substantially easier to achieve a high peak power pulse or an output with particular beam quality or spectral bandwidth properties. Having the optical energy concentrated in a single optical device, such as a laser rod, facilitates the production of a single-transverse-mode, high-peak-power device.

In the following sections, transition metal and lanthanide series solid-state lasers are compared and the physics germane to transition metal solid-state lasers is outlined. Thereafter, a section is devoted to each of the more common

transition metal solid-state lasers. Basic material properties and laser performance details are given for each laser material. Oscillator performance, as well as amplifier performance where appropriate, is also presented.

Laser performance will be characterized by a threshold and slope efficiency. If the laser output energy is plotted versus the pump energy, very often a linear relationship can be obtained. That is, the laser output energy E_{LO} is approximately related to the pump energy, E_p, by a relationship of the form

$$E_{LO} = \sigma_s \left(E_P - E_{Pth} \right), \tag{1}$$

where σ_s is the slope efficiency and E_{Pth} is the threshold energy. Pumping of the transition metal solid-state lasers can be accomplished using either a flashlamp or another laser. In either case, the linear relationship is approximately true. For some laser materials, both types of optical pumping have been successfully employed. Furthermore, this approximate relation is true for either normal mode or Q-switched operation of the laser. Thus, rather than presenting typical laser output energy versus pump energy data, the threshold and slope efficiency are given.

When selecting a laser for a particular application, several factors need to be considered including tuning range, threshold, slope efficiency, energy per pulse, and average power. Tuning range is often the first selection criterion, that is, the laser must be able to produce the desired wavelength. Toward this end, the emission spectra for the various laser materials are given.

A low threshold is necessary to efficient laser operation, particularly if cw operation is desired. A primary consideration is whether the laser operates as a three- or four-level laser, the latter being vastly preferred. Threshold depends on the absorption efficiency of the laser material and the product of the effective stimulated emission cross section and the lifetime. Absorption efficiency depends on the characteristics of the optical pump and the absorption properties of the laser material. If a narrow spectral bandwidth optical pump is used, such as a laser diode or another laser, relatively narrow absorption features can be used to advantage. However, if a broad spectral bandwidth pump is used, such as a flashlamp, broad absorption features become advantageous. To assess the absorption efficiency, absorption spectra have been included. Threshold is roughly inversely proportional to the product of the effective stimulated emission cross section and the upper laser level lifetime. Both parameters are given in this chapter for the various laser materials.

Slope efficiency depends on the absorption efficiency, as does the threshold, and on the overlap of the laser mode volume with the pumped volume as well as the losses. Overlap of the laser mode volume and the pumped volume is particularly important if good beam quality is also important. Good overlap is dependent on the particular laser design but as a general rule is easier to achieve when

laser pumping is used rather than flashlamp pumping. Slope efficiency also depends on the losses, including excited state absorption.

Energy per pulse depends on the pump source and the effective stimulated emission cross section. A high energy per pulse usually favors flashlamp pumping over laser pumping, primarily because of the higher optical pump energies available. An effective stimulated emission cross section limits the amount of energy per pulse that can be extracted from a single device. If the effective stimulated emission cross section is high, the resulting high gain will promote ASE, as mentioned earlier. In essence, a photon emitted because of natural spontaneous emission will cause the emission of several other photons before it can escape from the laser material. Because both the amount of fluorescence and the gain increase as the stored energy increases, ASE rapidly becomes a limiting mechanism in high-energy-per-pulse or high gain applications. Thus, a high energy per pulse favors moderate effective stimulated emission cross sections when long optical pump pulses are used.

Average power limitations are limited by the thermal, optical, and mechanical properties of the laser material. Ultimately, the average power is limited by thermally induced fracture in the laser material. To mitigate this effect, a laser material should be durable and have a high thermal conductivity. Such properties are discussed for the laser materials appearing in the following sections. Before the laser material fails because of thermally induced fracture, thermally induced lensing and thermally induced birefringence tend to degrade beam quality. An analysis of these problems is available but is beyond the scope of this chapter.

2. TRANSITION METAL AND LANTHANIDE SERIES LASERS

In transition metal lasers, electrons in the $3d$ subshell participate in the lasing process. Transition metal atoms that have demonstrated laser action reside in the fourth row of the periodic table of the elements. Electronic configurations of these atoms, derived from quantum mechanics, are shown in the Fig. 1. The first two shells, consisting of the $1s$ subshell as well as the $2s$ and $2p$ subshells, are completely filled. In this notation, the first digit is the radial quantum number and the letter represents the angular quantum number; s representing 0, p representing 1, d representing 2, f representing 3, and so forth. As electrons continue to be added, the first two subshells of the third shell, the $3s$ and $3p$ subshells, are filled. In the free atom configuration, the next two electrons are added to the $4s$ fourth subshell. After this, the $3d$ subshell begins to fill. When the transition metal atom is put into the laser material, the $4s$ electrons and possibly one or more of the $3d$ electrons are used to form the chemical bonds associated with the laser material. This leaves the remaining $3d$ electrons exposed to the electric forces of the neighboring atoms, that is, the crystal field associated with the laser material. As such, the $3d$ electrons are strongly affected by the crystal field.

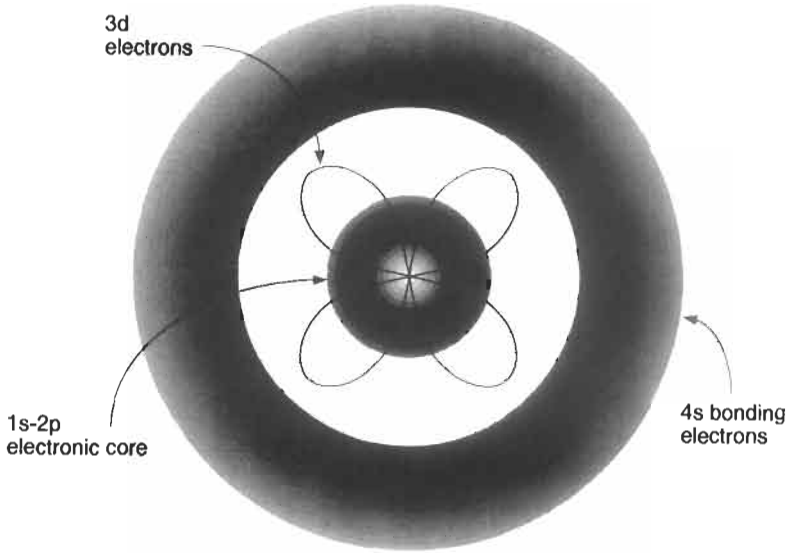

FIGURE 1 Transition metal electronic configuration.

Crystal field effects contribute strongly to the energy levels of the $3d$ electrons of a transition metal atom embedded in a laser material. The results of turning on the various interactions that contribute to the energy levels of $2d$ electrons, in order of their magnitude, are shown schematically in Fig. 2 [6]. Protons in the nucleus and filled subshells form a spherically symmetric central potential for the $3d$ electrons. A net positive charge exists on the central potential because the nucleus has more protons than there are electrons in the surrounding cloud at this point. This net positive charge binds the $3d$ electrons to the transition metal atom. In many cases, next in importance is the mutual repulsion of the individual electrons. To avoid each other and thus minimize mutual repulsion effects, the $3d$ electrons tend to fill subshells in such a way that the spins of the electrons are opposed. Thus the spins of the electrons couple together; making the total spin quantum number, S, approximately a good quantum number. After the mutual repulsion effects, the crystal field effects become important. Crystal field effects tend to split the energy levels remaining after the spin coupling. Levels are split into those that have orbitals which are directed toward the nearest neighbors in the lattice and those that have orbitals directed between the nearest neighbors.

Although this simple picture is useful to describe the situation, the calculation of the energy levels involve many more contributions than the effect of the nearest neighbors. In some laser materials, the relative size of the mutual repulsion and the crystal field effects are roughly similar or the crystal field effects

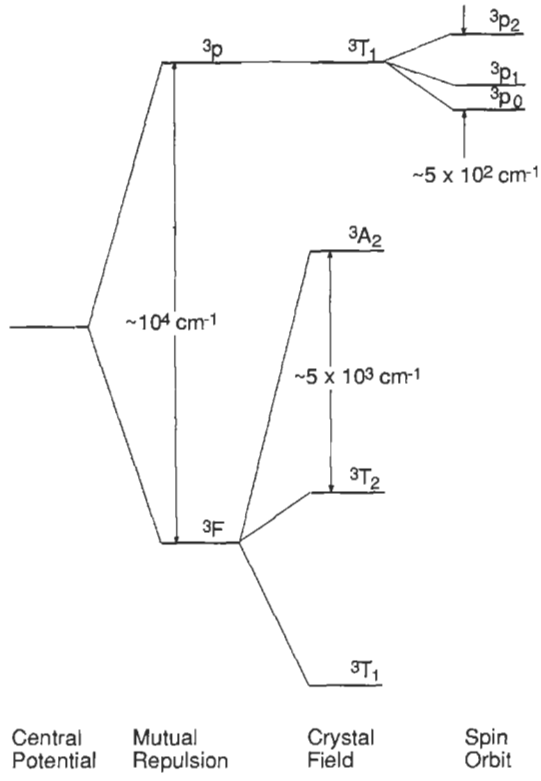

FIGURE 2 Effect of various interactions on transition metal atoms.

may even be larger than mutual repulsion. Consequently, the mutual repulsion and the crystal field effects are often considered together rather than using successive perturbations to the electron configuration.

Finally, the spin orbit interaction also contributes to the energy. Spin orbit interaction arises from the interaction of the magnetic forces associated with the spin of the electron and the orbit of the electron. Magnetic forces arise since both the spin and the angular momentum involve moving charges or currents. Currents, in turn, produce magnetic fields. Magnetic fields can alter the energy by orienting their magnetic poles to be parallel or antiparallel. Usually the spin orbit interaction has only a small contribution to the energy of the various levels. The nomenclature associated with the energy levels of the transition metal lasers reflects the forces that determine them. A typical energy level is designated as

$$^{(2S+1)}A \ .$$

In this notation, S is the spin quantum number and A is a letter associated with the symmetry of the site of the active atom. These letters come from group theory and are associated with character tables describing the group. For example, if the active atom occupied a site in the center of a cube and the nearest neighbors occupy sites in the center of the faces of the cube, the site is said to have octahedral symmetry. Octahedral symmetry describes the situation because the nearest neighbors form an octahedron. Octahedral designations include A_1, A_2, E. T_1, and T_2.

Absorption and emission of the transition metals in a laser material are characterized primarily by band structures. That is, the absorption and emission spectra are characterized by broad spectral features. It is the broad absorption features that allow transition metal atoms to be efficient absorbers of broadband flashlamp radiation. Superimposed on the broad absorption and emission bands may be some relatively narrow line features. For example, the $Cr:Al_2O_3$ laser (the ruby laser) utilizes the broad absorption features for efficient absorption of flashlamp radiation and the narrow emission features associated with the transition from the ^2E upper laser level to the $^4A_2$ ground level for the lasing process.

Interactions of the transition metal active atom with the laser material create the broad absorption and emission features. Absorption or emission of a photon by a transition metal atom can change the crystal lattice and the number of phonons in the lattice. Reasons for the change in the lattice can be explained by considering the size and orientation of the orbits of the electrons in the excited state and ground state of the transition metal. In the ground state, the $3d$ electrons tend to be closer to the active atom, whereas in the excited state the electrons tend to be farther away. A resulting difference in size causes shifts in the positions of the nearest neighbors. Thus, associated with an electronic transition, is a shift in the position of the nearest neighbors. That is, the absorption or emission of a photon can cause a shift in the crystal lattice as shown in Fig. 3. Transitions can also occur with the emission or absorption of both a photon and phonon. Energy differences between the initial and final energy levels can be shared between the photon and the phonon. Because the phonon spectrum can be wide, a wide variation of the phonon energies is possible. A wide variation of photon energies is thus possible since only the sum of the photon and phonon energies must add up to the energy difference between the energy levels involved. Transitions that involve the simultaneous absorption or emission of both photons and phonons are referred to as *vibronic transitions*.

Since the laser material is strongly involved in the absorption and emission processes, the nature of the transition metal lasers depends strongly on the laser material. Putting the same active atom in another laser material can, for example, change the symmetry of the site of the active atom. With a change in symmetry, the entire nature of the energy levels and thus the absorption and emission can change. Even if two laser materials with the same site symmetry are compared,

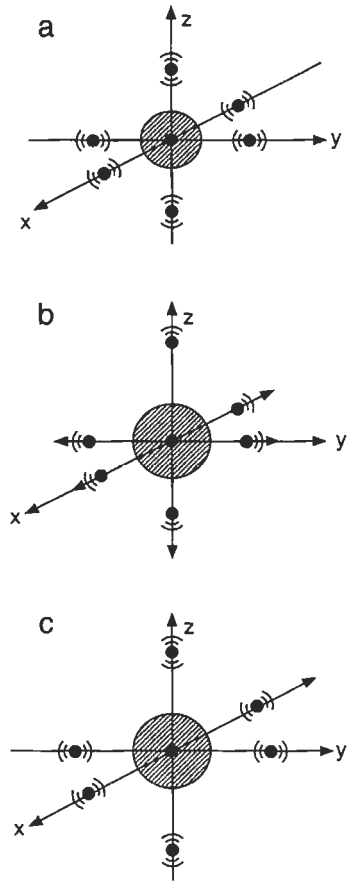

FIGURE 3 Transition metal atom undergoing absorption of a photon. (a) Transition metal atom in ground level before absorption. (b) Transition metal atom in excited level immediately after absorption. (c) Transition metal atom in excited level. Nearest neighbors vibrating around new positions.

changes in the strength of the crystal field can substantially shift the position of the energy levels.

In lanthanide series lasers, electrons in the $4f$ subshell participate in the lasing process. Lanthanide series atoms that have demonstrated lasing appear in the sixth row of the periodic table of the elements. The electronic configuration of these atoms, shown in Fig. 4, has all of the subshells of the first three shells filled; that is, $1s$, $2s$, and $2p$, as well as $3s$, $3p$, and $3d$ are filled. In addition, the $4s$, $4p$, and $4d$ subshells and the $5s$ and $5p$ subshells are filled. The next two electrons added to this structure go into the $6s$ subshell before the $4f$ subshell begins to fill. When incorporated into a laser material, the lanthanide atoms

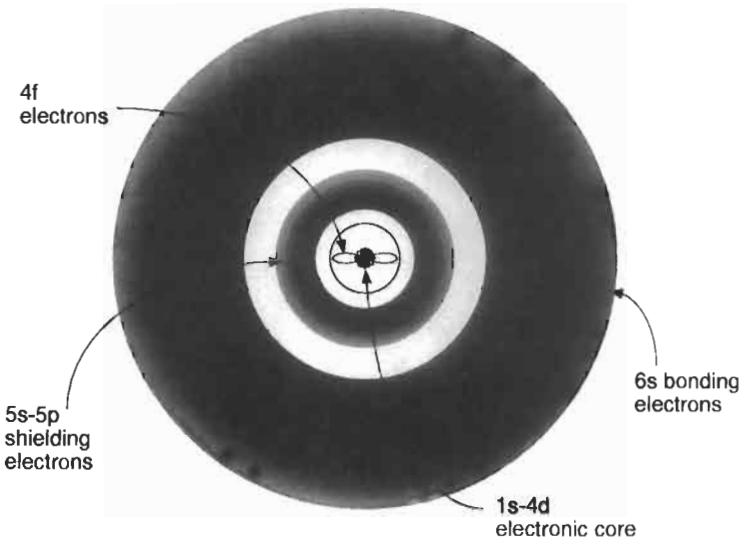

FIGURE 4 Lanthanide series atom electronic configuration.

usually enter the crystal lattice by sharing three electrons, one from the 4*f* subshell and the two 6*s* electrons. Electrons from the first three shells and the electrons from the first three subshells of the fourth shell form a spherically symmetric potential, which binds the 4*f* electrons to the lanthanide series atom. Electrons from the 5*s* and 5*p* subshells form a shield for the 4*f* electrons from the crystal field. Hence, the crystal field does not have a strong interaction with the 4*f* electrons. Consequently, the absorption and emission spectra of the lanthanide series elements resemble the spectra of the corresponding triply ionized atom in free space.

As with many of the transition metals, the central potential and mutual repulsion are dominant interactions [7]. The results of turning on the various interactions when considering the energy levels of the lanthanide series atoms appear in Fig. 5. The central potential is the strongest force, binding the 4*f* electrons to the lanthanide series atom. Next in order of importance is the mutual repulsion of the electrons. As before, the spins of the electrons couple to minimize the mutual repulsion forces, making the total spin S a good quantum number. However, unlike the transition metal atoms, the mutual repulsion also couples the orbital momentum of the various electrons. By coupling the orbital momentum associated with each electron, the total orbital momentum L becomes a good quantum number. In essence, this is the same as the Russel Saunders coupling associated with atomic spectroscopy.

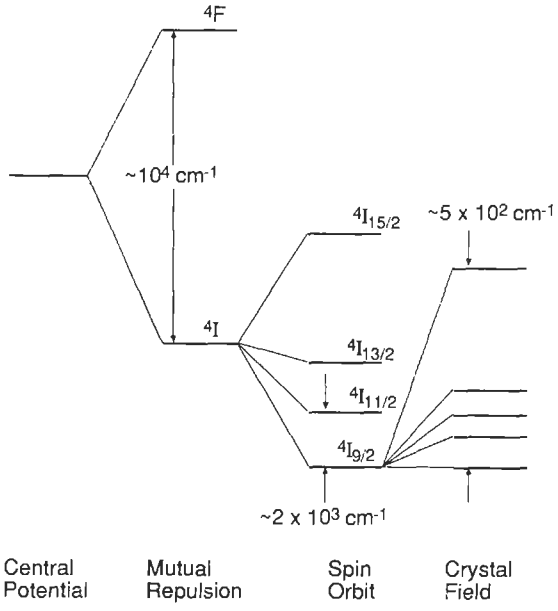

FIGURE 5 Effect of various interactions on lanthanide series atoms.

With lanthanide series elements, the spin orbit interaction is next in order of importance, sometimes equalling the strength of the mutual repulsion of the electrons. Through the spin orbit interaction, the total spin momentum and the total orbital momentum are coupled to produce the total angular momentum, characterized by the quantum number J. In cases where the mutual repulsion and the spin orbit interaction are comparable, the same Russel Saunders nomenclature is used to designate the states. Although J is an approximately good quantum number, actual states can be composed of various combinations of states. For the lower levels, however, the states are primarily composed of states having the same L and S quantum numbers.

Crystal field effects contribute only weakly to the energy levels of the lanthanide series atoms embedded in a laser material. Although crystal field interactions have a relatively small effect on the energy levels, they do split the levels associated with a particular level, lifting much of the degeneracy left after the spin orbit coupling. Groups of energy levels, associated with a particular J quantum number, are referred to as *manifolds*.

The nomenclature for the lanthanide series elements is similar to the notation used for Russel Saunders coupling. Energy manifolds, that is, closely spaced groups of energy levels, are labeled

$$^{(2S+1)}L_J,$$

where L denotes the total orbital angular momentum with S representing 0, P representing 1, D representing 2, F representing 3, and so forth. In accordance with the notation used here, S is the total spin quantum number and J is the total angular momentum quantum number. Therefore, the superscript and subscript are numbers, but the angular momentum is represented by a letter.

Absorption and emission from lanthanide series atoms embedded in a laser material are characterized by line structure. Linewidths of individual transitions are on the order of 10^{11} Hz wide. By way of comparison, the frequency of the transition is on the order of 3×10^{14} Hz. Thus, unlike the transition metals lasers, the lanthanide series lasers are tunable over a fairly narrow range. Tuning can be extended in some cases. One of these cases is where the number of energy levels within a manifold is high. An example of this is the Ho $^5I_7$ to $^5I_8$ transition. Fifteen levels exist in the upper manifold; 17 in the lower manifold. Taken in combination, this produces hundreds of possible transitions between pairs of individual levels. Thus, as the laser is tuned off of one transition, it can be tuned onto another, making continuous tuning possible. Vibronic transitions in lanthanide series atoms are possible but the effect is much weaker than in transition metal atoms.

Because the crystal field has a relatively small effect on the lanthanide series atoms, wavelengths of the transitions are less dependent on the laser material. By knowing the energy levels of a particular lanthanide series atom in one laser material, the energy levels of this atom in any laser can be estimated. This has led to a useful representation of the energy levels of all of the lanthanide series elements. An energy-level diagram showing the positions of the various energy manifolds for all of the lanthanide series atoms is often referred to as a Dieke diagram [8].

3. PHYSICS OF TRANSITION METAL LASERS

Energy levels associated with transition metal atoms in laser materials can be interpreted in terms of a theory developed by Tanabe and Sugano [9]. Tanabe and Sugano developed the theory for transition metal active atoms subjected to octahedral crystal fields. Active atoms in octahedral sites are common, including such combinations as Cr:YAG and Cr:GSGG. Active atoms in other laser materials are often approximated as residing in octahedral sites. For example, Cr:Al_2O_3 and Ti:Al_2O_3 are often approximated as octahedral sites having a slight trigonal distortion. By following a procedure similar to that outlined in the initial Tanabe and Sugano paper, energy levels of active atoms in other site symmetries can be calculated.

In octahedrally coordinated crystal fields, the $3d$ energy levels split into two levels. One set of these levels, denoted by $3d\varepsilon$, is lower than the initial $3d$ level by amount $-4Dq$. These levels are triply degenerate. The other set of these levels, denoted by $3d\Gamma$, is higher than the initial $3d$ levels by amount $6Dq$. These levels are doubly degenerate. The term Dq is referred to as the crystalline field parameter. It can be regarded as the measure of the overlap of the $3d$ electron orbits with the electron orbits of the neighboring atoms comprising the laser material. Even though Tanabe and Sugano refer to Dq as the crystalline field parameter, some authors refer to the process of computing the energy levels as ligand field theory.

In essence, the Tanabe–Sugano theory treats the active atom and the six nearest neighbors as a molecule. The initial $3d$ orbits of the active atom are now combined to form orbits associated with the formation of molecular bonds. That is, the atomic electron orbits are combined so that the electron can follow complex orbits that can take them in the vicinity of some of the atoms in the molecule. For the $3d\Gamma$ orbits, the departure of the molecular bounding orbits from the atomic $3d$ orbits of the active atom can be significant. Energy differences between any of the levels can be determined by calculating all of the various terms in an energy matrix. Thus, the energies of the various interactions, specifically the mutual repulsion of the electrons and the crystal field effects, are calculated using all possible combinations of orbits of the electrons and arranged in a matrix. Energy levels are then computed by diagonalizing the resulting matrix.

Even though the departure of the orbits from the atomic orbits can be significant, the orbits can be composed of a sum of atomic orbits. Atomic orbits can be described as the product of a radial function $R(r)$ and angular function $Y_{nm}(\theta, \phi)$. The functions $Y_{nm}(\theta, \phi)$ are referred to as the spherical harmonics and are composed of a product of sine and cosine functions involving θ and ϕ. Functions describing the $3d\Gamma$ orbits are the linear combinations

$$u = R(r)Y_{20}(\theta,\phi) \ , \tag{2}$$

$$v = R(r)\left(Y_{22}(\theta,\phi) + Y_{2-2}(\theta,\phi)\right)/2^{1/2} \ . \tag{3}$$

On the other hand, functions describing the $3d\varepsilon$ orbits are the linear combinations

$$x = -iR(r)\left(Y_{21}(\theta,\phi) - Y_{2-1}(\theta,\phi)\right)/2^{1/2} \ . \tag{4}$$

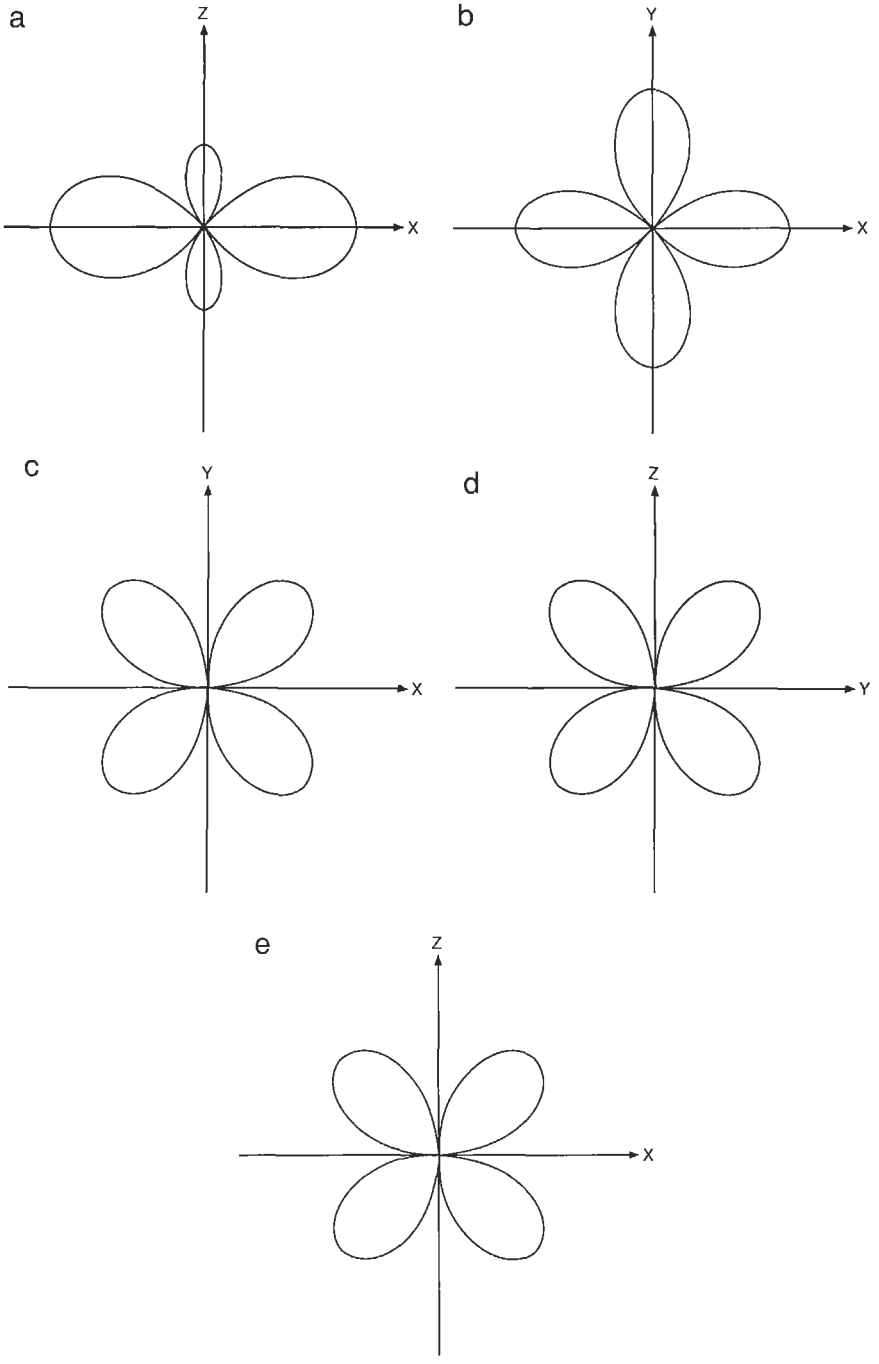

FIGURE 6 Orbits in octahedral symmetry. (a) u orbit. (b) v orbit. (c) x orbit. (d) y orbit. (e) z orbit.

$$y = -R(r)\left(Y_{21}(\theta,\phi) + Y_{2-1}(\theta,\phi)\right)/2^{1/2} \ , \tag{5}$$

$$z = iR(r)\left(Y_{22}(\theta,\phi) - Y_{2-2}(\theta,\phi)\right)/2^{1/2} \ . \tag{6}$$

Electron orbits described by these linear combinations of functions are graphed in Fig. 6. As can be seen, the $3d\Gamma$ orbits are maximized along the x, y, and z axes, that is, the orbits are directed toward the positions of the nearest neighbors. On the other hand, the $3d\varepsilon$ orbits are maximized at angles directed between the nearest neighbors. Because the nearest neighbors usually have a net negative charge, it is logical that the orbits directed toward the nearest neighbors would have a higher energy. In essence, the electrons are being forced to go where they are being repulsed.

A calculation of the energies of the molecular bonding orbits must include the effects of the mutual repulsion. Mutual repulsion energy contributions can be expressed in terms of the Racah parameters, A, B, and C. Racah parameters, in turn, are expressed in terms of Slater integrals; however, it is beyond the scope of this chapter to delve into the details. Suffice it to say that the A term is an additive term on all of the diagonal elements. When only energy differences are to be calculated, this term drops out. The B and C energy terms occur on many off-diagonal elements. However, Tanabe and Sugano observed that the ratio of C/B is nearly constant and in the range of 4 to 5. A slight increase of this ratio is noted as the nuclear charge increases while the number of electrons remains constant. A ratio of C/B of 3.97 was expected based on Slater integral formalism. Thus, the mutual repulsion contribution to the energy levels can be approximated if only a single parameter is known. Usually this parameter is the Racah parameter B. Hence, many of the Tanabe–Sugano calculations are normalized by this parameter.

Crystal field contributions to the energy of the molecular orbits can be described by the parameter Dq. Remember that $10Dq$ is the energy difference between the $3d\Gamma$ and the $3d\varepsilon$ levels for a single $3d$ electron. Consider the case where there are N electrons. These electrons can be split between the $3d\Gamma$ and $3d\varepsilon$ orbits. Suppose n of these electrons are in the $3d\varepsilon$ orbits, leaving $N-n$ of them in the $3d\Gamma$ orbits. Crystal field effect contributions to the energy can be approximated as $(6N - 10n)Dq$. Crystal field energy contributions, in this simplified approach, occur only for diagonal energy matrix elements.

Energy differences between the various levels have been calculated for all combinations of electrons in octahedral symmetry and are presented in Tanabe–Sugano diagrams. Such diagrams often plot the energy difference between various energy levels, normalized by the Racah B parameter, as a function of the crystal field parameter, again normalized by the Racah B parameter. A Tanabe–Sugano diagram for three electrons in the $3d$ subshell is presented in

Fig. 7. For this diagram, the ratio of C/B was assumed to be 4.5. Triply ionized Cr is an example of an active atom with three electrons in the $3d$ subshell. Energies are calculated by diagonalizing the energy matrix. However, as the Dq term becomes large, the energy differences asymptotically approach a constant or a term that is linearly increasing with the parameter Dq. Such behavior would be expected since, for large values of Dq, the diagonal terms dominate and the crystal field energy contributions only appear on diagonal terms. Note that a Tanabe–Sugano diagram is valid only for one particular active atom since other active atoms may not have the same ratio of C/B.

Absorption and emission occur when an electron makes a transition between levels. The energy difference between the initial and final levels of the electron is related to the energy of the absorbed or emitted photon. In purely electronic transitions, all of the energy between the two levels is taken up with the emitted or absorbed photon. However, as will be explained in more detail, some of the energy can appear as vibrations associated with the crystal lattice, that is, phonons, in the vicinity of the active atom.

Selection rules indicate the strength of the transition between two levels of different energy. Obviously, a transition that is allowed will have stronger absorption and emission spectra than a transition that is not allowed. Two selection rules are particularly germane to the transition metals, the spin selection

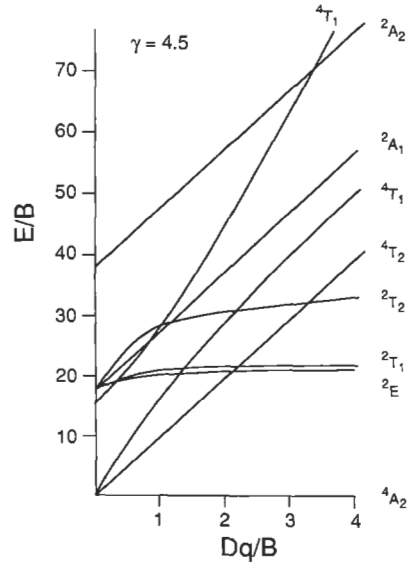

FIGURE 7 Tanabe–Sugano diagram for d^3 electrons.

rule and the Laporte selection rule. According to the spin selection rule, a transition can only occur between levels in which the number of unpaired electrons in the initial and final levels is the same. In cases where a single electron undergoes a transition, the spin must be the same for the initial and final levels. According to one formulation of the Laporte selection rule, a transition is forbidden if it involves only a redistribution of electrons having similar orbitals within a single quantum shell. This formulation is particularly relevant to transition metals because transitions tend to be between different $3d$ levels but within the same quantum shell. For example, transitions involving only a rotary charge displacement in one plane would be forbidden by this selection rule.

Selection rules were also considered by Tanabe and Sugano. Usually the strong interaction that allows a transition between levels with the emission of a photon is the electric dipole interaction. However, for the $3d$ electrons, all transitions between the various levels are forbidden since all levels have the same parity. Consequently, three other transition interactions were considered: the electric dipole interaction coupled with a vibration, the electric quadrupole interaction, and the magnetic dipole interaction. The strengths of these various interactions were estimated. From these estimations, it was concluded that the electric dipole transition coupled with vibration, that is, a vibronic transition, was the strongest interaction. Vibronic transitions involve emission or absorption of a photon and a quantized amount of lattice vibrations referred to as a phonon. Vibronic interactions were estimated to be about 2 orders of magnitude stronger than the next strongest interaction, the magnetic dipole interaction.

McCumber [10] investigated the absorption and emission that results from vibronic interactions. Terminology used in the original paper refers to phonon-terminated absorption and emission rather than vibronic transitions. McCumber analyzed the absorption, emission, and gain of the transition metal Ni in the initial paper. Emission spectra from Ni:MgF_2 were characterized by sharp emission lines and a broad emission spectra on the long-wavelength side of the sharp emission lines. Sharp lines were associated with electronic transitions, whereas the long-wavelength emission was associated with vibronic emission. Since then, this general analysis has been extended to many of the transition metals.

Through the use of an analysis similar to the McCumber analysis, the gain characteristics of an active atom can be related to the absorption and emission spectra. Relating the gain to the absorption and emission spectra is of considerable practical importance since the gain as a function of wavelength is a more difficult measurement than the absorption and emission. Emission and absorption spectra often display relatively sharp electronic, or no phonon, transitions accompanied by adjacent broad vibronic transitions associated with the emission and absorption of phonons. General absorption and emission processes appear in Fig. 8. At reduced temperatures only phonon emission is observed since the average phonon population is low. In this case, the vibronic emission spectra

extends to the long-wavelength side of the electronic transitions. On the other hand, the vibronic absorption spectra extends to the short-wavelength side of the electronic transition. In some cases, the absorption spectra and emission spectra are mirror images of each other. Although in general this is not true, at any wavelength the absorption, emission, and gain are related by the principle of detailed balance.

Several assumptions must be met in order for the McCumber analysis to be valid. Consider a system consisting of an upper manifold and a lower manifold. As before, the term *manifold* will be used to describe a set of closely spaced levels. To first order approximation, levels within the manifold can be associated with a simple harmonic motion of the active atom and its surrounding atoms. While the simple harmonic oscillator energy level spacings of the upper and lower manifolds may be the same, in general they do not have to be. Furthermore, the position of the minimum of the simple harmonic potential wells may be spatially offset from each other due to the difference in size of the active atom in the ground level and the excited level. Population densities of these manifolds are denoted by N_1 and N_2. One of the assumptions used by the theory is that a single lattice temperature can describe the population densities of these manifolds. For example, suppose the upper manifold consists of a series of levels commencing with the lowest energy level which is an energy $h\nu_{zp}$ above the ground level. Levels within the manifold are separated by an energy $h\nu_v$ where this energy represents a quantum of vibrational energy associated with the simple harmonic motion of the upper level. According to this assumption, the active atoms in the upper manifold will be distributed among the various vibrational levels associated with the upper manifold according to a simple Boltzmann distribution. In turn, the Boltzmann distribution can be characterized by a single temperature T. Thus, with all of the vibrational levels equally degenerate, the population of any particular vibrational level will be given by $N_2 \exp(-Jh\nu_v/kT)(1 - \exp(-h\nu_v/kT))$ where J is the integer denoting the energy level, k is Boltzmann's constant, and T is the lattice temperature. The last factor simply normalizes the distribution since it represents the summation over all levels within the manifold. Furthermore, the same temperature can describe the relative population of the levels comprising the lower manifold. Another assumption is that the time interval required for thermal equilibrium for the various population densities is very short compared with the lifetime of the upper level. For example, suppose all of the population of the upper manifold may be put initially in a single level by utilizing laser pumping. The second assumption says, in essence, that the closely spaced levels achieve thermal equilibrium in a time interval short with respect to the lifetime of the upper manifold. A third assumption is that nonradiative transitions are negligible compared with the transitions that produce the absorption or emission of a photon. Although this is not always true, the lifetime of the upper level may be

decomposed into components representing a radiative lifetime and a nonradiative lifetime.

Given the population densities of the upper and lower manifolds, the absorption and emission cross sections can be related to the absorption and emission coefficients, $a_p(k,\nu)$ and $e_p(k,\nu)$, respectively. In these expressions, k is the wave vector indicating the direction of propagation and ν is the frequency. A subscript p is utilized since the absorption and emission may depend on the polarization p. Given the absorption and emission coefficients, absorption and emission cross sections can be defined by the relations

$$\sigma_{ap}(k,\nu) = a_p(k,\nu) / N_1 \ , \tag{7}$$

$$\sigma_{ep}(k,\nu) = e_p(k,\nu) / N_2 \ . \tag{8}$$

Using the principle of detailed balance, the absorption and emission cross sections are related by

$$\sigma_{ap}(k,\nu) = \sigma_{ep}(k,\nu) \exp\left(\frac{h(\nu-\mu)}{kT}\right). \tag{9}$$

In this expression, $h\mu$ is the energy required to excite one active atom from the lower level to the upper level while maintaining the lattice temperature T. In the low-temperature limit for any system and for any temperature in a mirror image type of system, the parameter μ is the frequency of the no phonon transition.

Using these relations, the gain coefficient $g_{0p}(k,\nu)$ as a function of wavelength is given by

$$\begin{aligned} g_{0p}(k,\nu) &= \sigma_{ep}(k,\nu)\left[N_2 - N_1 \exp\left(\frac{h(\nu-\mu)}{kT}\right)\right]. \\ &= \sigma_{ap}(k,\nu)\left[N_2 \exp\left(\frac{-h(\nu-\mu)}{kT}\right) - N_1\right]. \end{aligned} \tag{10}$$

While either of these expressions could be utilized to determine the gain coefficient, the relation using the emission cross section is usually of the greater practical importance. In general, the absorption cross section is too small to be measured in a practical situation. On the other hand, the stimulated emission cross

section can be readily deduced from a single fluorescence spectrum if the laser material is isotropic or fluorescence spectra if the material is not isotropic.

McCumber's theory yields a practical method of deducing the emission cross section from the emission spectrum or spectra. To establish this relation, a function $f_p(k,\nu)$ is introduced. When multiplied by an incremental solid angle $d\Omega_{kp}$ and a unit frequency interval $d\nu$, this function represents the average intensity of emitted photons/second in the direction k, with frequency ν, and with polarization p. One of the prime values of this function is that it can be easily measured and normalized. Normalization can be obtained through another easily measured quantity, the radiative lifetime of the upper manifold, τ, by the relation

$$\frac{1}{\tau} = \Sigma_p \int_0^{4\pi} d\Omega_{kp} \int_0^{\infty} f_p(k,\nu)\, d,\nu \quad . \tag{11}$$

Using this function, the stimulated emission cross section can be expressed as

$$\sigma_{ep}(k,\nu) = f_p(k,\nu)\left(\frac{c}{\nu n}\right)^2 . \tag{12}$$

In this expression, c is the speed of light and n is the refractive index. In general, the refractive index will depend on the direction of propagation k, as well as the polarization. Combining these equations leads to the primary result of the McCumber analysis,

$$g_{0p}(k,\nu) = \left[N_2 - N_1 \exp\left(\frac{h(\nu-\mu)}{kT}\right)\right] f_p(k,\nu)\left(\frac{c}{\nu n}\right)^2 . \tag{13}$$

That is, the gain can be related to the measurable quantities, the fluorescence spectrum or spectra, and the radiative lifetime.

Although McCumber's theory laid the foundation for the determination of the gain, most experimental measurements are made in terms of watts per unit wavelength interval rather than photons per second per unit frequency interval. However, the change can be made in a straightforward manner. To change from $f_p(k,\nu)$ in units of photons per second per unit frequency interval to $g_p(k,\nu)$ in units of watts per unit wavelength interval,

$$f_p(k,\nu) = g_p(k,\lambda)\left(\frac{\lambda^3}{hc^2}\right), \tag{14}$$

where λ is the wavelength associated with the frequency ν. In a practical laboratory system, only a fraction of the emitted radiation is collected by the fluorescence measurement device. If this fraction collected, Ω, is independent of the wavelength, then

$$\Omega g_p(k,\lambda) = G_p(k,\lambda) \ , \tag{15}$$

where $G_p(k,\nu)$ is the measured quantity. Using the preceding relations, the quantity Ω can be determined using the relation between the radiative lifetime and the fluorescence spectrum. With the measured spectrum, the emission cross section becomes

$$\sigma_{ep}(k,\lambda) = \lambda^5 G_p(k,\lambda)/(8\pi n^2 c\tau I_w) \ , \tag{16}$$

where I_w is defined by the relation

$$I_w = \int_{\infty}^{0} \lambda G_p(k,\lambda)\, d\lambda \ . \tag{17}$$

In Eq. (17), it has been tacitly assumed that the material is isotropic. If the material is not isotropic, the extension to take into account the effects of anisotropy is straightforward.

While McCumber related the gain of a transition metal to the absorption or emission spectra, Struck and Fonger [11] presented a unified theory of both the radiative emission and nonradiative decay processes. Previously, two disparate theories had described nonradiative decay processes. One of these theories, referred to as the *activation energy relation*, described the nonradiative decay process by the relation

$$\frac{1}{\tau_{nr}} = A_m \exp\left(-\frac{E_x}{kT}\right) \ . \tag{18}$$

In this expression, τ_{nr} is the nonradiative lifetime, A_m is a rate constant, E_x is an activation energy, k is Boltzmann's constant, and T is the temperature. It can be loosely interpreted as the number of times per second that the excited active atom tries to escape from a potential well times the probability that it will have energy to effect its escape.

Another theory is referred to as the *multiphonon emission formula*. In this formulation, the nonradiative decay rate is given by

$$\frac{1}{\tau_{nr}} = A_k \varepsilon^p (1 + \langle m \rangle)^p \ , \tag{19}$$

where A_k is a rate constant, ε is a coupling constant, p is the number of phonons required to span the gap between the manifolds, and

$$<m> = \left[\exp\left(\frac{h\nu_p}{kT}\right) - 1\right]^{-1} \tag{20}$$

is the thermal occupation factor for the phonons, ν_p being the phonon frequency. In this formulation, the first two factors are nominally temperature independent so that the temperature dependence is carried by the thermal occupation factor for the phonons.

To reconcile these two theories, Struck and Fonger relied on a single configurational coordinate model. In the simplest application of the single configurational coordinate model, the interaction of the active atom and its nearest neighbors is considered to be described by a single configurational parameter. A configurational parameter can describe one aspect of the geometrical configuration of the active atom with its nearest neighbors. As an example, a configurational parameter for an active atom in a position of octahedral symmetry could be the average distance between the active atom and its six nearest neighbors. As the single configurational coordinate changes, the average distance between the active atom and its six nearest neighbors expands or contracts. In this case, the expansion and contraction is reminiscent of the breathing motion; consequently, it is often referred to as the breathing mode.

Energies associated with different manifolds are dependent on this single configurational coordinate. Typically, energy as a function of the configuration coordinate appears as a parabola as shown in Fig. 8. Equilibrium positions are found near the lowest point in the parabola. That is, it would require energy to either expand or contract the configurational coordinate. For example, as the length between the active atom and its nearest neighbors contracts, the mutual repulsion of like charges would tend to dominate and push the nearest neighbors away. The strength of the interaction can be gauged from the shape of the parabolic curves. If the energy depends strongly on the configurational coordinate, the parabola will be more strongly curved. Conversely, if the parabola is weakly curved, the energy depends only weakly on the configurational coordinate. Although the curvature of the parabolas for different manifolds can be different, a case can be made for them being roughly equal.

The curvature of the parabolas describing the energy versus configurational coordinate determines the energy spacing between adjacent energy levels within the manifold. If a particle is trapped in a potential well described by a parabolic form, the particle will undergo simple harmonic motion. For the atoms involved in the configurational coordinate model, the harmonic motion must be described using quantum mechanics. For this reason, Struck and Fonger refer to a quantum mechanical single configurational coordinate. Quantizing the simple harmonic motion introduces two effects not found in classical simple harmonic oscillators,

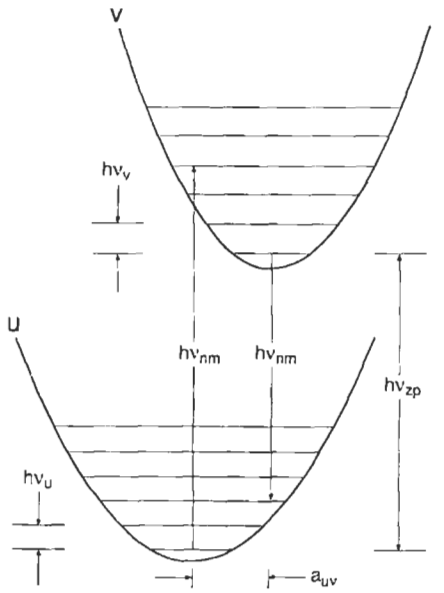

FIGURE 8 Configuration coordinate energy-level diagram.

discrete energy levels and a zero point energy. Differences between discrete energy levels associated with a quantum mechanical parabola are $h\nu_v$ where h is Planck's constant and ν_v is a frequency. Parabolas associated with different manifolds can have different curvatures with different frequencies. To describe the different curvatures, an angle θ is introduced and defined by

$$\tan^2 \theta = \frac{h\nu_v}{h\nu_u}, \tag{21}$$

where the subscripts v and u denote the upper and lower parabolas, respectively. In terms of the discrete energy difference, the zero point energy associated with the v parabola is $h\nu_v/2$.

Parabolas for manifolds with different energies may be offset from each other. Manifolds having different energies have different electronic charge configurations. For these different electronic charge configurations, the equilibrium position of the nearest neighbors can be different. For example, an electronic charge distribution that has the electrons appear between the active atom and its nearest neighbors may result in a stronger repulsion and consequently a longer distance between them. A difference in the equilibrium position can affect the energy of the manifold. In general, the active atom and its surrounding neighbors will prefer to reside in a configurational coordinate position, which minimizes

the energy. Thus, the equilibrium position of the configurational coordinate may be different for different manifolds. Struck and Fonger refer to the offset between the equilibrium position of the configurational coordinate of different manifolds as the Franck–Condon [11] offset. Offsets are the difference in the configurational coordinate for the two parabolas normalized by the amplitude of the zero point motion of the quantum mechanical simple harmonic oscillator. This normalized distance is denoted by a_{uv}.

Parabolas describing the different energy manifolds are also described by an energy offset corresponding approximately to the energy required to raise the active atom to the excited manifold. Energy offsets are represented as a vertical difference in Fig. 8 in contrast to the horizontal difference corresponding to an offset in the configurational coordinate. An exact definition of the energy offset is the energy difference between the zero point energy of the upper manifold and the zero point energy of the lower manifold. This energy difference is characterized by a zero point energy, $h\nu_{zp}$. If the simple harmonic oscillator were not quantized, the zero point energy would be zero and the equilibrium position would be at the minimum of the parabola.

Energy absorption and emission between manifolds with an offset can now be associated with a change in the motion of the simple harmonic oscillator. For example, consider transitions shown in Fig. 8. A transition from the zero point level of the lower manifold, designated with the letter u, does not go to the zero point level of the upper manifold, designated with the letter v. Rather, the transition is to a higher level of the simple harmonic oscillator. Consequently, the several quanta of simple harmonic motion become available. Quanta of simple harmonic motion can be readily identified as phonons, establishing the correspondence between the Struck and Fonger model and the McCumber model. Phonons, as referred to here, are localized to the vicinity of the active atom. However, phonons may also refer to simple harmonic motion of the entire crystal. Although localized and distributed phonons are obviously not the same, the concept of quantized simple harmonic oscillation will be referred to as phonons.

Using the single configurational coordinate model, energy balances for radiative and nonradiative transitions can be expressed as

$$h\nu_{zp} = mh\nu_v - nh\nu_u + h\nu_{nm} \quad , \tag{22}$$

$$h\nu_{zp} = mh\nu_v - nh\nu_u = 0 \quad , \tag{23}$$

respectively. In this expression, ν_{nm} is the frequency of the emitted photon. Energy differences between the zero point or zero phonon energy and the emitted photon energy are taken up by the creation or annihilation of phonons, designated as $h\nu_u$ and $h\nu_v$ for the u and v manifolds, respectively. Using this concept, the cause of the wide absorption and emission spectra can be attributed to the multitude of phonon levels associated with the configurational coordinate parabolas. In emission, for example, the electron can start from any of the phonon levels in the

upper manifold and end on any of the phonon levels in the lower manifold. It is the variety of initial and final phonons levels that allows a wide spectrum of phonon energies to be produced. Because the total energy associated with the transition is distributed between the photon and the phonons, the photon energy, and thus the frequency, can vary over a wide range.

Shifts of the frequency from the zero phonon frequency are related to the offset associated with the configurational coordinate. Transitions between the upper and lower manifolds are represented by vertical lines in Fig. 8. Consider the transition from the lowest energy level in the upper manifold to the lower manifold. In the lowest level, the most likely position of the configurational coordinate is in the center of the parabola. Consequently, a transition from the lowest energy level in the upper manifold to the lowest energy in the lower manifold is not probable since the overlap of their respective wave functions is small. Far more likely is a transition to one of the higher energy levels in the lower manifold. These levels are associated with the creation of more phonons, and the photon energy will be lower. Thus, the emission spectra will be on the long-wavelength side of the zero phonon line. Conversely, the absorption spectra will be on the short-wavelength side of the zero phonon line.

Radiative and nonradiative transition rates for these processes, characterized by the radiative and nonradiative lifetimes τ_r and τ_{nr}, respectively, can be expressed as

$$\frac{1}{\tau_r} = R_{uv}\left[1 - \exp\left(\frac{-h\nu_v}{kT}\right)\right]\exp\left(\frac{-mh\nu_v}{kT}\right)<u_n|\,v_m>^2 \ . \tag{24}$$

$$\frac{1}{\tau_{nr}} = N_{uv}\left[1 - \exp\left(\frac{-h\nu_v}{kT}\right)\right]\exp\left(\frac{-mh\nu_v}{kT}\right)<u_n|\,v_m>^2 \ . \tag{25}$$

In these expressions, R_{uv} and N_{uv} are constants from the electronic portion of the transition integral and $<u_n \mid v_m>^2$ is the squared overlap of the quantum-mechanical wave functions. As the offset becomes larger, the overlap of the quantum-mechanical wave functions decreases since the wave functions are physically displaced. This expression is valid for a single set of levels in the manifolds, but the total transition rates are the summation of the rates corresponding to transitions between all of the levels in the manifold.

To determine the total radiative and nonradiative transition rates, a summation over all of the possible energy levels in both the upper and lower manifolds must be taken into account. For arbitrary curvatures of the parabolas, the summation becomes more complicated and is beyond the scope of this chapter. However, in the case where the parabolas have the same curvature, the radiative and nonradiative transition rates reduce to

$$\frac{1}{\tau_r} = R_{uv}\,W_{pu} \ , \tag{26}$$

$$\frac{1}{\tau_{nr}} = N_{uv} W_{pu} \quad , \tag{27}$$

where the quantity W_{pu} can be computed exactly. If, in addition, the offset is small, that is, a_{uv} is smaller than unity, then

$$W_{pu} = \frac{\exp\left(-S_0 < 2m+1 >\right)\left(S_0 < 1+m >\right)^{p_u}}{p_u!} \text{ for } p_u > 0 \quad , \tag{28}$$

$$\frac{\exp\left(-S_0 < 2m+1 >\right)\left(S_0 < m >\right)^{|p_u|}}{|p_u|!} \text{ for } p_u < 0 \quad . \tag{29}$$

In these expressions, S_0 is proportional to the square of the offset, that is, $a_{uv}/4$, and

$$<m> = \left[\exp\left(\frac{-h\nu_v}{kT}\right) - 1\right]^{-1} \quad . \tag{30}$$

According to this expression, the shape of the absorption and emission features tends to be given by a Poisson distribution. In fact, emission lines can often be approximated by such a line shape. In addition, the similarity between this expression and the multiphonon theory can be observed. Thus, the multiphonon theory appears to be valid when the approximations just given are valid.

Struck and Fonger also compared this derived theory to the activation energy theory. Although the activation energy theory can approximate the preceding equations (28 and 29), in the cases of a relatively large offset, the fit was only valid over relatively small temperature ranges. As such, the more complex Struck and Fonger theory may be required to describe the radiative and nonradiative decay for the large offset cases.

4. $Cr:Al_2O_3$

$Cr:Al_2O_3$, a transition metal solid-state laser, was the first laser of any type to be demonstrated [12]. $Cr:Al_2O_3$, commonly referred to as ruby, has several advantages, which are currently being put to use. Its principal advantage is the wavelength at which it is usually operated, 0.694 μm. Although this wavelength is near the limit of the response of the human eye, it is plainly visible. Part of its easy visibility is due to its high intensity. Most other solid-state lasers operate further into the near infrared and are not visible to the human eye. Other desirable properties of ruby include wide absorption bands, a long upper laser level lifetime, a narrow linewidth, and a high quantum efficiency.

A primary disadvantage of $Cr:Al_2O_3$ is its three-level operating scheme. In a three-level scheme, the levels are the ground level, the pump level, and the upper laser level. Figure 9 depicts the situation. In this scheme, the lower laser level is the ground level. For lasing to occur, the population density of the upper laser level has to be greater than the population density of the lower laser level. If the population density of the upper laser level is higher than the population density of the lower laser level, a *population inversion* is said to exist. To achieve a population inversion, roughly half of the Cr atoms must be pumped to the upper laser level. Pumping levels must be high in order for this to occur. If a population inversion is achieved, laser action can only be sustained as long as the population inversion is maintained. Consequently, when lasing terminates, all of the remaining energy stored in the upper laser level is lost. A three-level laser is relatively inefficient because of this. First, a great deal of pump energy is expended to store enough energy in the upper laser level to achieve population inversion or threshold. Second, of the energy stored in the upper laser level, only that portion of it which is above threshold is available for laser output. Despite this limitation on the efficiency of the $Cr:Al_2O_3$, the use of these lasers continues to this day.

Al_2O_3, or sapphire, is a crystal composed of alternate hexagonal layers of Al and O atoms, as shown in the Fig. 10. Oxygen atoms fill a layer in a close-packed hexagonal arrangement. On top of this layer is a layer of Al atoms, which nestle in the depressions between three adjacent O atoms of the lower layer. In a filled layer, one-third of the potential Al sites is left unfilled. A third layer is composed of O atoms, again in a close-packed hexagonal arrangement. However, this layer is displaced from the first layer. To first-order approximation, each Al atom has six O neighbors in an octahedral arrangement. However, since the distance between the O layers is larger than the distance between O atoms within a layer,

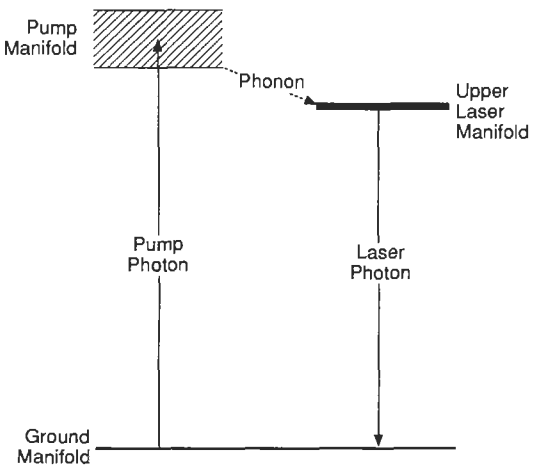

FIGURE 9 Three-level laser energy-level diagram.

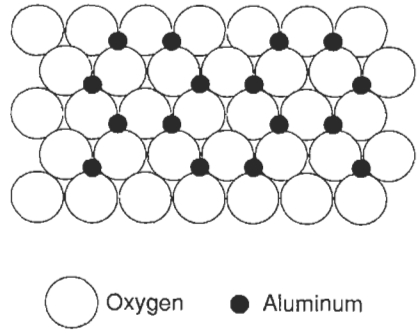

FIGURE 10 Crystal structure of Al_2O_3.

there is an elongation of the octahedron in the vertical direction. This elongation gives rise to a trigonal distortion.

$Cr:Al_2O_3$ is produced by replacing a small fraction of the Al atoms with Cr. Through this replacement, sapphire becomes ruby. Typically, the fraction of the Al atoms replaced is small. In the production of $Cr:Al_2O_3$, about 0.0005 by weight of the Al_2O_3 is replaced by Cr_2O_3. In the laser material, Cr takes the place of some of the Al atoms and therefore sees the same symmetry as the Al atoms. Replacement is straightforward since the Al and Cr have the same valence and are roughly the same size, Cr being somewhat larger.

Al_2O_3 is a good material from which to make a laser. It is transparent from about 0.2 to about 6.0 μm. Good transparency in the visible and near ultraviolet allows a wide spectral region for efficient pump bands. It is a hard material, which permits it to take a good polish, and it has a relatively high laser-induced damage threshold. It has a very high thermal conductivity for a crystalline material. High thermal conductivity is important in the design of high-average-power laser systems. Other physical properties of this material are listed in Table 1 [13].

Al_2O_3 is a birefringent material with a relatively high refractive index. It is also a uniaxial material, that is, it has an unique optical axis. For directions of propagation other than along the optic axis, this material has two refractive indices. One refractive index is associated with radiation polarized in the optic plane, that is, the plane defined by the direction of the optic axis and the direction of propagation. Another refractive index is associated with the normal to the optic plane. These refractive indices are referred to as the extraordinary and ordinary refractive indices, respectively. Refractive indices of this material do not change significantly when doped with Cr. Birefringence, the difference between these two refractive indices, is relatively small, about 0.008. However, the differences in the optical properties of these two polarizations are sufficient to make the $Cr:Al_2O_3$ laser operate in polarized modes.

$Cr:Al_2O_3$ has two strong absorption bands, which differ slightly depending on the polarization [12,14]. One of these absorption bands lies in the blue region

TABLE 1 Physical Properties of Al_2O_3

Parameter	Value	Units
Lattice constants		pm
a axis	476.3	
c axis	1300.3	
Density	3990	kg/m³
Heat capacity	775	J/kg-K
Thermal conductivity		W/m-K
a axis	33	
c axis	35	
Thermal expansion		10^{-6}/K
a axis	4.8	
c axis	5.3	
Refractive index		
a axis	1.7654	
c axis	1.7573	
Refractive index variation		10^{-6}/K
a axis	13.1	
c axis	17.5	
Optical transparency	0.14–6.5	μm
Melting point	2040	°C

of the spectrum, being centered at about 0.405 μm; the other absorption band lies in the green region of the spectrum, being centered at about 0.551 μm, as shown in Fig. 11. The spectral bandwidths of these bands are about 0.05 and 0.07 μm, respectively. Absorption features are associated with transitions between the $^4T_1$ and $^4T_2$ levels and the $^4A_2$ ground level. Absorption coefficients associated with these bands are relatively strong and yield absorption coefficients on the order of 200 m^{-1} for common $Cr:Al_2O_3$ laser material. Because of the presence of two relatively strong and spectrally wide absorption features, Cr can be an efficient absorber of blackbody radiation in the visible region of the spectrum.

Having absorbed flashlamp radiation in the pump bands, absorbed energy can be transferred to the upper laser level with a high quantum efficiency. That is, a quantum of energy absorbed in the pump band has a high probability of producing a Cr atom in the upper laser level. For $Cr:Al_2O_3$ operating at 0.694 μm, the upper laser level is the ^2E level. Quantum efficiency has been experimentally demonstrated to be a function of temperature. At reduced temperatures, the quantum efficiency has been measured to be about 1.0; however, it begins to decrease as the temperature increases. Near room temperature, it has been estimated to be between 0.7 and 1.0 [14,15].

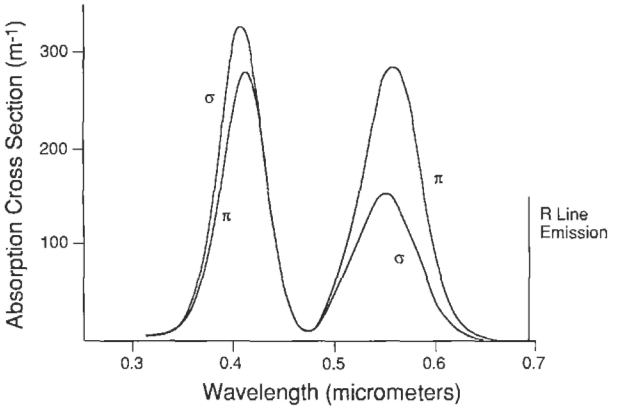

FIGURE 11 Absorption spectra of $Cr:Al_2O_3$.

The upper laser level lifetime of this material is relatively long, being about 3.0 ms at room temperature. Lifetimes of standard concentrations of Cr are about 4.3 ms at 78 K [13]. Having a long upper laser level lifetime allows long pump pulses to be employed, thereby facilitating the intense pumping required for this material.

Polarized emission spectra of $Cr:Al_2O_3$ display two line features, usually referred to as the R_1 and R_2 lines. The existence of two lines arises from the fact that the ^2E level is split into two narrowly separated levels. Separation of these levels is only 29 cm^{-1}. Lasing naturally occurs on the R_1 line, which has its origin on the lower of these two levels. Lasing occurs on this line for two reasons. First, the lower level has a somewhat larger fraction of the population of the inverted population density by virtue of its lower energy. Second, because the stimulated emission cross section of this line is higher than of the R_2 line, the gain is higher. The emission cross section is higher for radiation polarized perpendicular to the optic axis than for radiation polarized parallel to the optic axis. As such, the laser output from a $Cr:Al_2O_3$ laser is polarized.

Even though the strongest radiation from $Cr:Al_2O_3$ is associated with the R_1 and R_2 lines, sidebands had been noted early in the development of this material. The fraction of the radiation appearing in the R bands is approximately constant up to a temperature of about 275 K. As expected when considering the vibronic transitions, the majority of the sideband radiation existed on the long-wavelength side of the R lines. It is interesting to note that lasing was observed in $Cr:Al_2O_3$ at 0.767 μm [16]. However, at the time it was not ascribed to lasing on a vibronic transition and its appearance was treated mostly as a curiosity.

Although the threshold of a $Cr:Al_2O_3$ laser can be quite high, performance of this laser above threshold can be relatively efficient. Operation of a laser can be characterized by two parameters, the threshold and the slope efficiency. Consider a plot of laser output energy as a function of electrical energy used for pumping the laser. Electrical energy is usually associated with the energy stored

on the capacitor in a pulse-forming network, which drives the flashlamp. Electrical energy stored on the capacitor is easily determined by measuring the voltage to which the capacitor is charged. A plot of the laser output energy as a function of the electrical energy usually can be well approximated by a linear relationship. Threshold is defined by the intersection of a linear fit with the abscissa, and slope efficiency is simply the slope of the line. Threshold occurs for energies on the order of 2000 to 3000 J. Slope efficiencies can be in excess of 0.01. Consequently, tens of joules can be generated from a single $Cr:Al_2O_3$ laser oscillator when operating in the normal mode.

Threshold and slope efficiency are a function of the concentration of Cr in the Al_2O_3 [17]. Threshold depends on the Cr concentration for two reasons, the absorption efficiency and the population density of the lower laser level. Absorption efficiency is the fraction of the pump radiation that is transmitted into the laser material and subsequently absorbed. Obviously, if there is no Cr in the Al_2O_3, there will be no absorption. Absorption efficiency increases with increasing Cr concentration. However, as the laser material becomes opaque, increases in the Cr concentration further produce diminishingly smaller increases in absorption efficiency. For efficient operation, absorption of the pump radiation should be high, favoring higher Cr concentrations. Conversely, as the Cr concentration increases, more energy needs to be absorbed to overcome the population density in the lower laser level, that is to produce an inversion. Thus, threshold depends on these two competing effects. As these two effects compete, the threshold is not critically dependent on the exact Cr concentration as long as it is near the optimum concentration. Slope efficiency, on the other hand, tends to favor higher concentrations as slope efficiency describes what happens above threshold. However, for the concentrations commonly used, the absorption efficiency is relatively high. Thus, only modest increases in the slope efficiency are obtained as the Cr concentration increases. For a particular application, the Cr concentration can be optimized. Many of the problems associated with the $Cr:Al_2O_3$ laser can be obviated by finding a laser material where Cr can act like a four-level laser.

$Cr:Al_2O_3$ has achieved cw operation at room temperature despite the fact that it is a three-level laser [18,19]. Typically, a mercury-arc lamp was used to optically pump the laser rod. Threshold depends on the size of the laser rod, being lower for the shorter laser rods [19]. Typically, thresholds are on the order of 1000 W and slope efficiencies are about 0.001.

5. $Cr:BeAl_2O_4$

$Cr:BeAl_2O_4$ is a laser material that overcame the primary difficulty associated with $Cr:Al_2O_3$ lasers, namely, three-level operation. $Cr:BeAl_2O_4$ is commonly referred to as alexandrite, a gemstone that has the same chemical composition and structure as the laser material. Although not a true four-level laser, the vibronic transition on which this laser usually operates, permits four-level-like

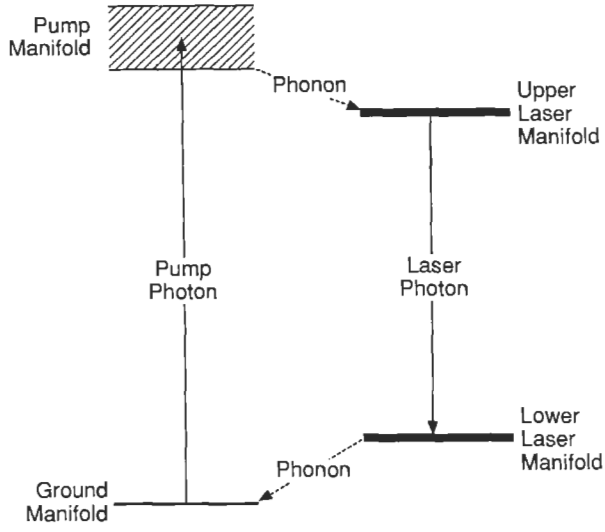

FIGURE 12 Four-level laser energy-level diagram.

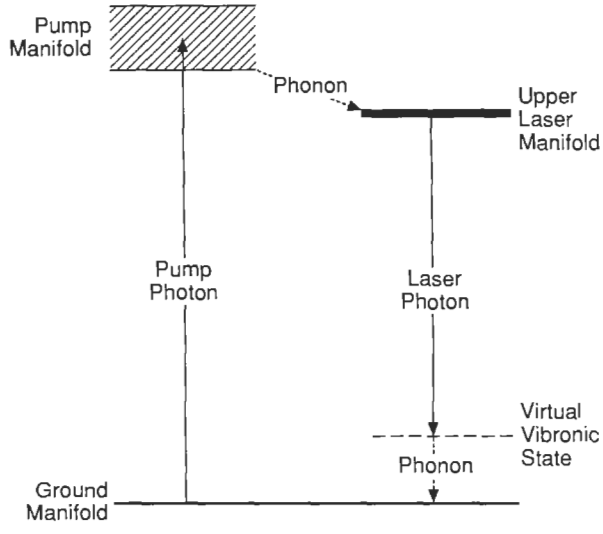

FIGURE 13 Vibronic laser energy-level diagram.

operation. A four-level laser, depicted in Fig. 12, has a ground manifold, a pump manifold, and an upper laser manifold, similar to the three-level laser. However, in contrast to the three-level system, there is a fourth manifold, the lower laser manifold, in which the lower laser level resides. As with the three-level laser, lasing occurs between a level in the upper laser manifold to a level in the lower

laser manifold. For four-level laser operation, the lower laser manifold is well above the ground manifold. Thus, the lower laser level has virtually no population density at its operating temperature. A virtually empty lower laser level makes threshold much easier to achieve since a high lower laser level population density does not have to be overcome. Cr:$BeAl_2O_4$, on the other hand, operates on a vibronic transition (see Fig. 13). As such, the population density of the ground level does not have to be overcome in order to reach threshold. In short, since the population density of the ground level does not have to be overcome, Cr:$BeAl_2O_4$ operating on a vibronic transition resembles the operation of a four-level laser.

Even though the overall symmetry of the $BeAl_2O_4$ crystal is considerably different than the Al_2O_3 crystal, the approximate octahedral symmetry for the active atom prevails. As in the case of Cr:Al_2O_3, the Cr in Cr:$BeAl_2O_4$ substitutes for the Al. Typical concentrations of Cr are in the range from 0.0005 to 0.003 atomic. That is, between 0.0005 and 0.003 of the Al atoms are replaced by Cr atoms. However, there are two different Al sites in this material. One site has mirror symmetry; the other has inversion symmetry. Most of the Cr substitutes for Al in the slightly larger mirror site, about 0.78 of the Cr is found in this site [20]. This is fortunate because this site is by far the dominant site for laser action. Both Al sites are approximated as being octahedral. That is, the Cr atom is surrounded by six O atoms forming an approximate octahedron. However, distortions to the approximate octahedron provide for different optical properties along three axes.

$BeAl_2O_4$, like Al_2O_3, has excellent mechanical and thermal properties for a laser material [21]. Thermal conductivity is about half that of Al_2O_3 but still larger than the thermal conductivity of most other laser materials. It is also a hard material, conducive to taking a good optical polish. The laser induced damage threshold for this material is very high. Excellent thermal and optical damage thresholds are important since this material is generally subjected to higher thermal and optical energy densities than higher gain materials. Germane physical properties are listed in Table 2.

$BeAl_2O_4$ is a birefringent material; however, it is a biaxial material rather than an uniaxial material. That is, there are two directions in this material for which the index of refraction is independent of the polarization. The refractive indices of this material are about 1.74. Difference between the refractive indices along the *a* and *c* axes is relatively small, about 0.002, whereas the difference between the *a* and *b* axes is significantly larger, about 0.005.

Because of its biaxial nature, there are three absorption and emission spectra, associated with the *a*, *b*, and *c* axes of the laser material. In general, absorption along any of these directions displays two broad absorption features. Absorption peaks occur at approximately 0.42 and 0.56 μm as shown in Fig. 14. The second absorption peak for radiation polarized along the *b* axis occurs at a somewhat longer wavelength, about 0.59 μm. Linewidths for the absorption features are about 0.05 and 0.08 μm, respectively. Absorption peaks are associated with the transitions between the $^4T_1$ and $^4T_2$ levels and the $^4A_2$ ground level. Even for lightly doped laser material, the absorption coefficients at the peak are

TABLE 2 Physical Properties of $BeAl_2O_4$

Parameter	Value	Units
Lattice constants		pm
a axis	940.4	
b axis	547.6	
c axis	442.7	
Density	3700	kg/m^3
Heat capacity	830	J/kg-K
Thermal conductivity	23	W/m-K
Thermal expansion		10^{-6}
a axis	4.4	
b axis	6.8	
c axis	6.9	
Refractive index		
a axis	1.7422	
b axis	1.7478	
c axis	1.7401	
Refractive index variation		10^{-6}/K
a axis	9.4	
b axis	8.3	
c axis	15.7	
Optical transparency	0.23–*	μm
Melting point	1870	°C

*Long wavelength cut off is unavailable.

on the order of 200 m^{-1}. Typical of the Cr absorption spectra, these broad absorption bands cover much of the visible portion of the spectrum. Wide absorption features permit efficient absorption of flashlamp radiation.

However, as the pumping proceeds to create a substantial population in the upper laser manifold, excited state absorption of the pump radiation can occur [22]. That is, pump radiation can be absorbed by the Cr atoms in the upper laser manifold. Absorption cross sections are approximately equal for the two absorption processes. Obviously, excited state absorption competes with ground state absorption for pump radiation and tends to limit the level of population inversion. However since the population density of the upper laser manifold is often low, excited state absorption may not be serious. Eventually at high levels of excitation, competition for the pump radiation leads to a decrease in the efficiency of the device. Decreases in the efficiency are less pronounced when the laser is operating in the normal mode, as opposed to the *Q*-switched mode, because less energy is stored in the upper laser manifold with normal mode operation.

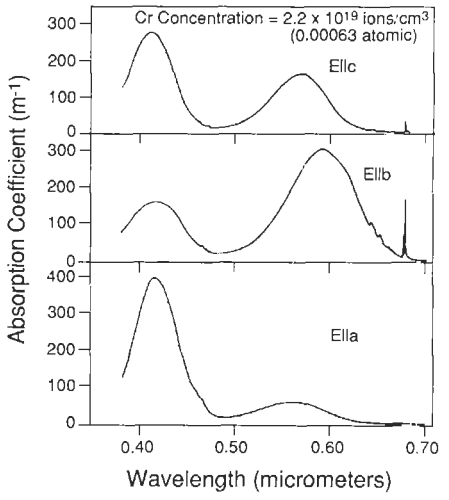

FIGURE 14 Absorption spectra of Cr:$BeAl_2O_4$. (a) *a* axis absorption. (b) *b* axis absorption (c) *c* axis absorption. (Courtesy of M. L. Shand, Allied Signal Corporation.)

Quantum efficiency of Cr:$BeAl_2O_4$ is high, about 0.95 at room temperature [23]. Quantum efficiency was measured using a sophisticated photoacoustic technique, which measures the phase shift between a modulated pump source and the photoacoustic signal. The high quantum efficiency of this laser material promotes efficient laser operation.

The upper laser level lifetime of Cr:$BeAl_2O_4$ is strongly temperature dependent [21]. Temperature-dependent effects can be successfully modeled by considering the population of the upper laser manifold to be divided between two manifolds, the ^2E and the $^4T_2$. Lifetimes of these two manifolds are 1.54 ms and 6.6 μs, respectively [20]. In comparison, the lifetime of the $^2T_1$ manifold is assumed to have an arbitrarily long lifetime. Assuming thermal equilibrium among the various manifolds near the ^2E level, the fractional population of the various manifolds can be calculated using Boltzmann's statistics. If f_E and f_T are the fractional populations of these two manifolds, the fluorescent lifetime can be approximated as

$$\frac{1}{\tau_2} = \frac{f_E}{\tau_E} + \frac{f_T}{\tau_T} .$$

A plot of this lifetime appears in Fig. 15. Near room temperature, efficient energy storage under flashlamp pumping is feasible with lifetimes available in this laser material.

Polarized emission spectra of Cr:$BeAl_2O_4$ have both *R* line features and the vibronic sidebands. Emission spectra are shown in Fig. 16. Vibronic spectra exist from the *R* lines, about 0.68 μm, to beyond 0.82 μm. Of the three emission spectra, the strongest emission is associated with radiation polarized along the *b* axis. Consequently, laser rods are usually cut so that the *b* axis is perpendicular to the axis of the

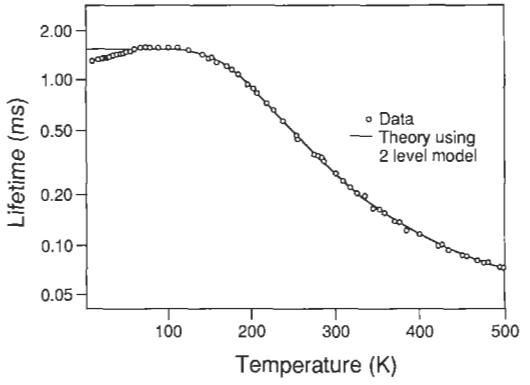

FIGURE 15 Upper laser level lifetime of $Cr:BeAl_2O_4$ versus temperature. (Courtesy of M. L. Shand, Allied Signal Corporation.)

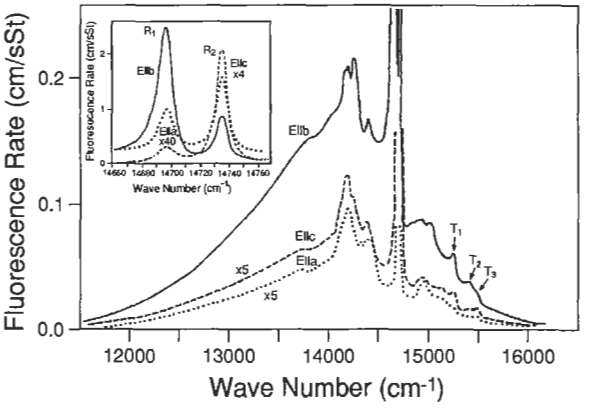

FIGURE 16 Emission spectra of $Cr:BeAl_2O_4$. (Courtesy of M. L. Shand, Allied Signal Corporation.)

laser rod. Use of this cut produces the highest gain operation of the laser. If the *b* axis is perpendicular to the laser rod axis, the laser rod axis could be along either the *a* or the *c* axis. c axis rods are often utilized based on the growth properties of $Cr:BeAl_2O_4$.

Although the emission spectra suggest a relatively wide tuning range for $Cr:BeAl_2O_4$, ground state absorption and excited state absorption restrict the tuning range. Ground state absorption affects primarily the short-wavelength operation of this material [24]. Experimentally, the ground state absorption cross section varies nearly exponentially with the energy of the transition. At 0.7 μm, the cross section is a little over 10^{-25} m^2, whereas at 0.8 μm the cross section has decreased to a little less than 10^{-29} m^2. For wavelengths longer than 0.7 μm, ground state absorption is a rapidly decreasing effect. Excited state absorption, on the other hand, affects both the long- and short-wavelength operations of this laser material [25]. A plot of the excited state cross section appears in Fig. 17. At about 0.77 μm, the excited state absorption reaches a minimum. A minimum in the excited state

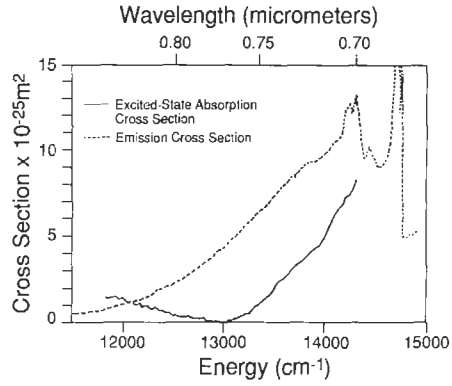

FIGURE 17 Excited state absorption of $Cr:BeAl_2O_4$. (Courtesy of M. L. Shand, Allied Signal Corporation.)

absorption is one of the reasons why this laser operates most efficiently around this wavelength. On the long-wavelength side, about 0.83 μm, the emission cross section and the excited state cross section are equal. Lasing at wavelengths longer than this is not possible under these conditions. On the short-wavelength side, the emission cross section and the excited state absorption cross section again become equal slightly on the short-wavelength side of the *R* lines, about 0.68 μm. Although excited state absorption does not prevent laser operation of the *R* lines, it does significantly reduce the laser performance.

Effective stimulated emission cross sections were determined by using the McCumber theory for the analysis [25]. At room temperature, the effective stimulated emission cross section at the wavelength of peak gain, about 0.77 μm, was calculated to be about 0.6×10^{-24} m^2. As the operating temperature increases, the effective stimulated emission cross section increases, nearly linearly. At 200°C, the effective stimulated emission cross section has increased to about 2.0×10^{-24} m^2. Increases in this parameter result from the increased population of the $^4T_2$ level. However, the increased effective stimulated emission cross section is balanced by the concomitant decrease in the upper laser level lifetime. For normal mode operation, the shortening of the upper laser level lifetime is not as serious as it is for *Q*-switched operation. Excited state absorption of the laser radiation will have the effect of decreasing the effective emission cross section.

Due to the relatively low effective stimulated emission cross section and competition from other absorption mechanisms, $Cr:BeAl_2O_4$ is usually pumped at high levels. High pump levels are usually achieved by using two flashlamps to pump a single laser rod. Although high pumping levels cause thermal problems in many materials, they are compensated to some degree by the excellent thermal properties of the laser material. However, because of the high pump levels, it becomes more difficult to achieve good beam quality and narrow spectral bandwidth operation at high prfs.

Since the Cr:$BeAl_2O_4$ laser does not operate like a three-level laser, the thresholds can be modest at room temperature. Modest thresholds for this device are associated with the relatively low effective stimulated emission cross section. Threshold will, of course, depend on the reflectivity of the output mirror and the losses. Using relatively high reflectivity mirrors, in excess of 0.8, normal mode thresholds are on the order of 20 J. While output mirror reflectivities this high are satisfactory for normal mode operation, they can lead to high-peak-power densities within the laser resonator for Q-switched operation. Thresholds can be decreased by operating the laser at elevated temperatures where the effective stimulated emission cross section is higher.

Slope efficiencies of Cr:$BeAl_2O_4$ laser can be relatively high, primarily due to the efficient absorption of the flashlamp radiation. Slope efficiencies for normal mode operation can be on the order of 0.02. Slope efficiencies with Q-switched operation are usually lower due to the loss associated with the insertion of the Q-switch into the resonator and the less than unity storage efficiency. Storage efficiency in this case is the fraction of Cr atoms pumped to the upper laser manifold, which remains in the upper laser manifold at the time of the opening of the Q-switch. Since the pump pulse is a fair fraction of the upper laser level lifetime, some of the energy stored in the upper laser manifold decays during the pump pulse. Losses associated with the insertion of the Q-switch are especially significant for low-gain lasers. Because of the relatively low gain, components selected for spectral or spatial mode control must be selected carefully in order to minimize loss.

Even though the gain of Cr:$BeAl_2O_4$ is relatively low, this material can be made into an amplifier. A small-signal gain of about 4.5 has been achieved [20]. However, to achieve this gain, the operating temperature of the laser rod was maintained at about 270 K and the laser rod was pumped very hard, about 1.9 MJ/m^3. In this case the pump level refers to the electrical energy supplied to the flashlamps divided by the volume of the laser rod. To achieve this pump level, 280 J/pulse was supplied to each of two flashlamps. Higher amplifier efficiency can be achieved by using multiple passes through the amplifier. However, this raises the optical energy density on the laser material.

Continuous wave oscillation of Cr:$BeAl_2O_4$ has been achieved around the peak gain wavelength of this laser material [26]. As in the case of Cr:Al_2O_3, mercury-arc lamps were employed. Threshold was high, somewhat over 2000 W, but the slope efficiency was also reasonably high, about 0.01. In this case, the laser could be tuned from less than 0.74 μm to beyond 0.78 μm.

6. Ti:Al_2O_3

Ti:Al_2O_3 is a laser material, tunable over much of the near infrared, which has both a high gain and freedom from excited state absorption. Because Ti has

only one *d* electron, to first-order approximation, there are only two levels. In a strict sense, a two-level laser would not lase since a population inversion could not be achieved. However, because the Ti:Al_2O_3 laser operates on a vibronic transition, it can operate much like a four-level laser. In addition, an extremely wide tuning range is available with this material. Full width at half-maximum (FWHM) spectral bandwidth is roughly one-third of the peak emission wavelength. Such a wide spectral bandwidth gives this laser material one of the widest tuning ranges of any laser.

Many of the desirable properties of Ti:Al_2O_3 result from the single electron in the 3*d* level. Since there is only one electron available, the mutual repulsion effects are zero. Consequently, only the spin orbit and crystal field effects remain. Crystal field effects split the degenerate levels associated with the central field approximation into two levels. With only two levels, deleterious excited state absorption is negligible. Crystal field effects are the same as those associated with the Cr:Al_2O_3, namely, a strong octahedral field with a triginol distortion. Since there is only a single 3*d* electron, rather than the three 3*d* electrons associated with Cr, the levels are labeled differently. Neglecting the triginol distortion, the triply degenerate ground level is labeled as $^2T_2$ and the doubly degenerate excited state is labeled as ^2E. Triginol distortion further splits the $^2T_2$ ground level into two relatively closely spaced levels and the spin orbit interaction further splits the lower of these into two levels [27].

Ti:Al_2O_3 is produced by replacing a small fraction of the Al atoms with Ti atoms. Concentrations of Ti are relatively low, often less than 0.0015 by weight. Although higher concentrations are possible, considerations such as optical quality tend to limit the Ti concentration. Ti sees the same symmetry as the Al atoms in Al_2O_3.

Since only a small fraction of the Al is replaced with either Cr for Cr:Al_2O_3 or Ti for Ti:Al_2O_3, the optical and mechanical properties of Ti:Al_2O_3 are very nearly the same as Cr:Al_2O_3. However, addition of Ti tends to produce a harder crystal than undoped Al_2O_3.

Ti:Al_2O_3 displays polarization-dependent absorption bands that peak about 0.49 μm. Absorption of radiation polarized along the optic axis, π polarized, is more than twice as strong as absorption of radiation polarized perpendicular to the optic axis, σ polarized [28]. For both polarizations, a shoulder in the absorption spectra appears at about 0.54 μm. Because absorption occurs from wavelengths shorter than 0.45 μm to wavelengths longer than 0.60 μm, a wide range of pump wavelengths is possible. However, even with relatively low Ti concentrations, peak absorption coefficients on the order of 200 m^{-1} are common.

Quantum efficiency can be deduced from the measurement of the lifetime of the upper laser level as a function of temperature. At cryogenic temperatures, the upper laser level lifetime has been measured to be 3.87 μs [29]. Lifetime is nominally independent of temperature to about 200 K. At room temperature the lifetime is nominally 3.2 μs and it decreases rapidly as the temperature decreases.

The experimental data of lifetime as a function of temperature can be well represented by using the Struck and Fonger theory as shown in Fig. 18. Ratioing the lifetime at room temperature to the lifetime at cryogenic temperatures yields an estimate of the quantum efficiency of 0.83. A short upper laser level lifetime complicates flashlamp pumping of this material. Consequently, the majority of the systems developed to date use laser pumping.

Polarized emission spectra of $Ti:Al_2O_3$ display a single broad emission band for both polarizations. As expected, the π polarization displays considerably more intensity than the σ polarization, approximately in the ratio of 3:1 [28]. Again using the Struck and Fonger theory, the emission spectra follows the expected lineshape [30]. A curve fit of the π polarized experimental data to the expected fluorescent spectrum, as shown in Fig. 19, yields a good fit with the zero phonon line at about 15968 cm^{-1}. Using the McCumber theory to predict the gain indicates that gain exists well beyond 1.0 μm. Peak stimulated emission cross section occurs at 0.795 μm and is about 4.3×10^{-23} m^2. A large effective stimulated emission cross section makes $Ti:Al_2O_3$ an extremely useful laser material.

Although excited state absorption is negligible, initially $Ti:Al_2O_3$ suffered from absorption losses at the lasing wavelengths. Experimental evidence indicated this absorption was caused by quadruply ionized Ti [31]. Ti substitutes for the Al, which is triply ionized. However, Ti has a predilection for the quadruply ionized state. Consequently, some of the Ti in Al_2O_3 was found in this state. To overcome the loss associated with the quadruply ionized Ti, different growth techniques were tried and postgrowth annealing was implemented. Both of these techniques resulted in substantial decreases in the loss.

Loss at the lasing wavelength in $Ti:Al_2O_3$ was characterized by a figure of merit that related the loss to the Ti concentration. More than one figure of merit has been proposed, but the figure of merit used here will be defined as the absorption coefficient at the peak of the pump absorption, about 0.49 μm, to the absorption coefficient at the peak of the gain, about 0.80 μm. Experimental evidence indicated that the absorption at the lasing wavelength increased quadratically with the Ti concentration [31]. A log–log plot of the absorption coefficient at the lasing wavelength versus the absorption coefficient at the pump wavelength showed a linear dependence with a slope of 2.0. A quadratic dependence was explained on the basis of Ti pair formation, one triply ionized and the other quadruply ionized. As much as 0.03 of the Ti was found to occur in the quadruply ionized state. Early samples of $Ti:Al_2O_3$ had figures of merit of about 5. However with improvements in growth and annealing, $Ti:Al_2O_3$ with figures of merit well in excess of 100 are now available.

Using laser pumping, arbitrarily low thresholds can be obtained. For pulsed operation, the most commonly used pump laser is the frequency-doubled Nd:YAG laser. Absorption coefficients on the order of 100 m^{-1} are common at 0.532 μm. To obtain efficient absorption of the pump radiation, longitudinal pumping is often employed. Because the beam quality of the pump can be relatively good, the pump

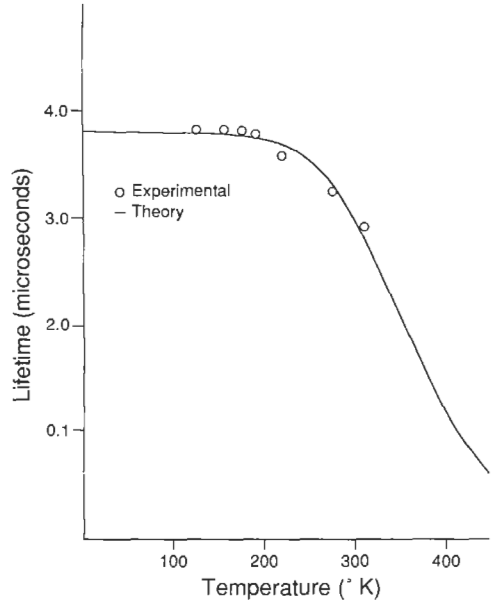

FIGURE 18 Upper laser level lifetime of $Ti:Al_2O_3$ versus temperature.

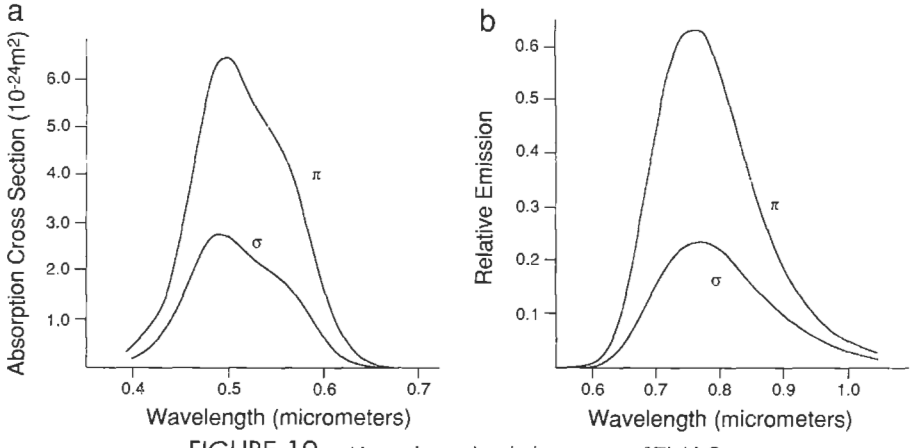

FIGURE 19 Absorption and emission spectra of $Ti:Al_2O_3$.

radiation can be focused to a small beam radius. Thus, in the volume of the pumped region, the inversion can be high even at relatively low pump energies.

Coupled with a high effective stimulated emission cross section, gain in the pumped volume can be high. By matching the mode radius of the $Ti:Al_2O_3$

oscillator to the pumped region, the gain of the lasing mode can be high and thus the threshold can be low [28]. However, use of a small pump beam radius will limit the amount of energy available from the Ti:Al_2O_3 laser. Output from a Ti:Al_2O_3 laser with a tightly focused pump beam will be limited by the laser induced damage threshold of the laser material. It is simply not feasible to expose very small areas of the Ti:Al_2O_3 laser material to high energy pump pulses without incurring laser induced damage. Although the laser induced damage threshold of this material is relatively high, the small pump beam radii will limit the amount of pump energy that can be used and thus the amount of laser output energy. Consequently, the pumped beam radius is adjusted to accommodate the desired laser output energy without incurring laser induced damage.

Using a frequency-doubled Nd:YAG pump laser has the additional benefit of producing a short Ti:Al_2O_3 laser output pulse, much like a Q-switched pulse. To achieve efficient frequency doubling, the Nd:YAG laser is usually Q-switched. As such, the pump pulse is short compared with the pulse evolution time interval of the Ti:Al_2O_3 laser. A short pump pulse produces gain-switched operation. Gain switching is different than Q-switching; however, the effect is the same. With gain switching, the gain varies quickly while with Q-switching the loss varies quickly. In either case, a short laser output pulse is produced. For all practical purposes, the dynamics of the pulse evolution for gain-switched or Q-switched operation can be described using the same formalism. The desirability of a short gain-switched pulse often excludes pumping of a Ti:Al_2O_3 with a flashlamp pumped dye laser even though they could be tuned to the absorption peak of Ti:Al_2O_3. The pulse lengths of these devices are relatively long in comparison to either the upper laser level lifetime or the pulse evolution time interval, making either Q-switching or gain switching less efficient.

The slope efficiency of a frequency-doubled Nd:YAG laser-pumped Ti:Al_2O_3 laser is limited primarily by the ratio of the photon energies. In the ideal case, one pump photon, with a wavelength of 0.532 μm, produces one photon with a wavelength of about 0.795 μm. Slope efficiencies are limited by the ratio of photon energies to about 0.67. In actuality, not all of the pump beam will be absorbed, not all of the population inversion will be extracted, and not all of the extracted energy appears as laser output energy. In many situations, the slope efficiency is only about 0.4, somewhat more than half of the maximum slope efficiency.

Flashlamp-pumped Ti:Al_2O_3 lasers can be achieved in spite of the short upper laser level lifetime [32,33]. For most solid-state lasers, efficient pumping can occur over time intervals on the order of 100 μs or more. Efficient energy storage over a time interval this long facilitates the achievement of threshold by allowing high population inversions to be attained. However, pumping longer than a few times the upper laser level lifetime produces a negligible increase in the population inversion. Thus the pump intensity must be high enough to produce threshold in Ti:Al_2O_3 in about 10 μs. Flashlamp pulses this short can be produced, but careful attention must be given to the inductance in the pulse-forming

network. In addition, the radiation from the flashlamp tends to be blue shifted to wavelengths shorter than ideal for pumping $Ti:Al_2O_3$. Nevertheless, flashlamp pumping has been achieved by utilizing long, low-loss $Ti:Al_2O_3$ laser rods. Sometimes a fluorescent converter will be used to increase the pumping efficiency. A fluorescent converter can absorb ultraviolet radiation and fluoresce in the wavelength region where the $Ti:Al_2O_3$ laser material can absorb. Other methods include using long laser rods so that higher gain can be achieved while the effective blackbody temperature of the flashlamp can be decreased. Using this arrangement, a slope efficiency threshold of 20 J and of 0.01 have been achieved.

One of the advantages of the $Ti:Al_2O_3$ laser is the ability to make efficient amplifiers. Efficient amplifiers can be obtained if the laser induced damage threshold energy density is several times larger than the saturation energy density. A large effective stimulated emission cross section provides $Ti:Al_2O_3$ with a low saturation energy density while the material properties allow operation at high energy densities. As such, $Ti:Al_2O_3$ can operate as an efficient amplifier. Amplifier studies have demonstrated the need for low-loss laser material, matching the pump beam and laser beam radii, and for control of parasitic lasing and ASE [34]. Small-signal gains of 25 were achieved as well as large-signal gains of 3.0 [35]. In this case high efficiency was not achieved primarily due to the limited amount of probe energy and the low figure of merit of the material. However, an analysis of the $Ti:Al_2O_3$ laser performance indicated that high efficiency would be achieved if these limitations were removed.

Continuous wave oscillation of $Ti:Al_2O_3$ can be achieved using laser pumping [36]. Either Ar ion or frequency-doubled Nd:YAG can be used as the pump source. Because single-longitudinal-mode operation is often sought, ring resonators are often employed. Pump beam radii in the $Ti:Al_2O_3$ are kept small, on the order of tens of micrometers, to keep the threshold low. To achieve the small beam radii, careful attention is given to minimizing astigmatism. By doing this, thresholds can be well under 1.0 W, and slope efficiencies can be on the order of 0.1.

7. $Cr:LiCaAlF_6$ AND $Cr:LiSrAlF_6$

$Cr:LiCaAlF_6$ and $Cr:LiSrAlF_6$ fill an important niche between $Cr:BeAl_2O_4$ and $Ti:Al_2O_3$. Although the former material can be flashlamp pumped, the gain of this material is low. A primary reason for this is that most of the excited Cr atoms reside in the ^2E manifold rather than the $^4T_2$ manifold. It is the latter manifold from which most of the laser action occurs. On the other hand, the latter material has a high gain but its short upper laser level lifetime makes flashlamp pumping difficult. $Cr:LiCaAlF_6$ and $Cr:LiSrAlF_6$ represent a good compromise between these materials, that is, reasonably high gain but an upper laser level lifetime long enough for flashlamp pumping. Such a compromise is possible by selecting a material with a Dq/B ratio of approximately 2.15. In this case, the ^2E

and $^4T_2$ manifold have approximately the same energy. By bringing these manifolds together, a significantly larger fraction of the excited Cr atoms resides in the $^4T_2$ manifold. Hence, the effective stimulated emission cross section is larger, which, in turn, increases the gain. However, the high fraction of the population residing in the $^4T_2$ manifold does decrease the upper laser level lifetime.

In $LiCaAlF_6$ and $LiSrAlF_6$, the active atom resides in a position of near octahedral symmetry. In essence, the crystal structure is formed by planes containing the Ca or Sr atoms [37]. Sandwiched between these planes are the Li and Al atoms, each surrounded by six F atoms forming an approximate regular octahedron. However, important deviations from the regular octahedron exist. Referring to Fig. 20, the planes containing the six F atoms above and below the Al atom are brought slightly closer to the plane containing the Al atoms than they would be in a regular octahedron. Such a distortion tends to produce a trigonal distortion of the octahedral symmetry. Another distortion of the octahedron consists of a slight clockwise rotation of the three F atoms in the upper plane while the three F atoms in the lower plane experience a slight counterclockwise rotation. Such a shift in the position of the F atoms eliminates the inversion symmetry.

As with the other laser materials, the Cr substitutes for the Al atoms. Concentrations of Cr in excess of 0.05 have been incorporated into the $LiCaAlF_6$ material. Similar concentrations are expected in $LiSrAlF_6$. Quenching effects

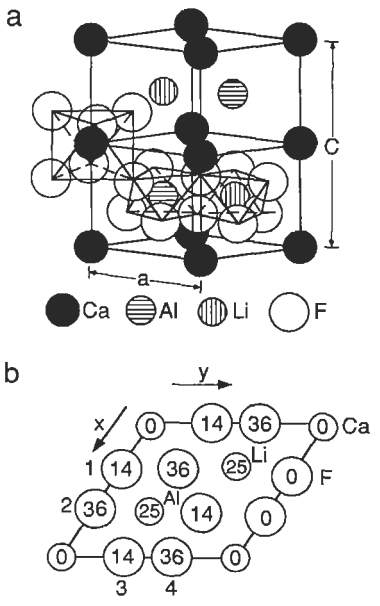

FIGURE 20 Configuration of $LiCaAlF_6$. (Courtesy of S. A. Payne, Lawrence Livermore National Laboratory.)

have not been observed up to concentrations as high as 0.05. It has been suggested that this is possible because the adjacent substitutional sites do not share F atoms and consequently are somewhat isolated. Such isolation tends to minimize pair effects associated with concentration quenching.

The thermal and mechanical properties of these laser materials are not as favorable as they are for oxide materials but this tends to be compensated by their good thermo-optic properties. Thermal conductivity for $LiCaAlF_6$ is about one-fourth of the thermal conductivity of $BeAl_2O_4$ [38]. Still, the thermal conductivity is sufficiently large to keep thermal gradients at reasonable levels. More debilitating is that the coefficients of thermal expansion for the two axes of $LiCaAlF_6$ are, unfortunately, significantly different, as noted in Table 3. However, the variation of the refractive index with temperature is negative, similar to $LiYF_4$ or YLF. A negative variation of the refractive index with temperature mitigates the effects of thermally induced lensing. Thus, the thermal and mechanical properties limit the amount of average power available from these laser materials but do not produce the thermal lensing and depolarization found with some other laser materials.

TABLE 3 Physical Properties of $LiCaAlF_6$

Parameter	Value	Units
Lattice constants		pm
a axis	499.6	
c axis	963.6	
Density	2989	kg/m^3
Heat capacity	938	J/kg-K
Thermal conductivity		W/m-K
a axis	4.6	
c axis	5.1	
Thermal expansion		10^{-6}/K
a axis	22	
c axis	3.6	
Refractive index		
a axis	1.3902	
c axis	1.3889	
Refractive index variation		10^{-6}/K
a axis	−4.2	
c axis	−4.6	
Optical transparency		μm
Melting point	825	°C

$LiCaAlF_6$ and $LiSrAlF_6$ are birefringent materials with relatively low refractive indices. Refractive indices have been measured for $LiCaAlF_6$ at nine wavelengths in the visible and near infrared [39]. Ordinary and extraordinary refractive indices at laser wavelengths are 1.390 and 1.389, respectively, leaving a difference in the refractive indices of only 0.0013. Variation of the refractive indices with temperature for $LiCaAlF_6$ is negative and relatively small, -4.2×10^{-6}/K and -4.6×10^{-6}/K for the ordinary and extraordinary waves, respectively. This small variation of the refractive indices with temperature tends to minimize the thermally induced focusing. In essence, the negative variation of the refractive index with temperature tends to compensate for the positive variation of the refractive index caused by the stress optic effect. In most oxide materials, these two effects are both positive, which tends to exacerbate the thermal focusing problem.

Absorption spectra of $LiCaAlF_6$ and $LiSrAlF_6$ are quite similar. Similarities are expected since the exchange of Sr for Ca is a relatively minor substitution. Both laser materials exhibit the double-peaked absorption spectra characteristic of Cr [40]. Because both materials are uniaxial, absorption spectra are recorded for both the π and σ polarizations. At room temperature, the absorption peaks for the π polarization are approximately at 0.425 and 0.628 μm. Absorption peaks for the σ polarization are approximately at 0.423 and 0.622 μm. The long-wavelength peak is stronger for the π polarization, and the short wavelength peak is stronger for the σ polarization. Linewidth of the short wavelength peak is about 0.064 μm, and the linewidth of the long wavelength peak is about 0.093 μm. With the concentrations available with $LiCaAlF_6$, typical absorption coefficients can be on the order of a few hundred per meter. In combination, large absorption coefficients and wide spectral bandwidths leads to efficient flashlamp pumping. Absorption spectra for Cr:$LiSrAlF_6$ are quite similar to absorption spectra for Cr:$LiCaAlF_6$. Peaks occur at nearly the same wavelengths and the relative strengths of the peaks are also similar. However, the absolute strengths for Cr:$LiSrAlF_6$ are roughly twice as strong as the strengths of Cr:$LiSrAlF_6$. Absorption spectra are shown in Fig. 21 and 22 for these two laser materials.

The upper laser level lifetimes of $LiCaAlF_6$ and $LiSrAlF_6$ are sufficiently long to allow flashlamp pumping. Lifetime has been measured as a function of Cr concentration in $LiCaAlF_6$ for concentrations exceeding 0.05. Up to this concentration, the lifetime was virtually independent of the concentration. Lifetime has also been measured as a function of the temperature for both laser materials [40]. Lifetimes of these laser materials are shown as a function of temperature in Fig. 23. Cr:$LiSrAlF_6$ has a lifetime of 67 μs, which is independent of temperature up to 300 K. In contrast, the upper laser level lifetime of Cr:$LiCaAlF_6$ is independent of temperature to only about 100 K. Above this temperature, the lifetime decreases slowly, dropping from 215 μs at low temperatures to 172 μs at room temperature. This decrease in the lifetime is attributed to a dynamic effect of the crystal field on the transition probability.

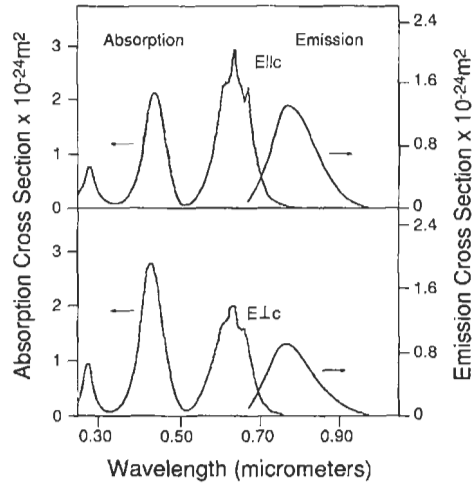

FIGURE 21 Absorption and emission spectra of $Cr:LiCaAlF_6$. (Courtesy of S. A. Payne, Lawrence Livermore National Laboratory.)

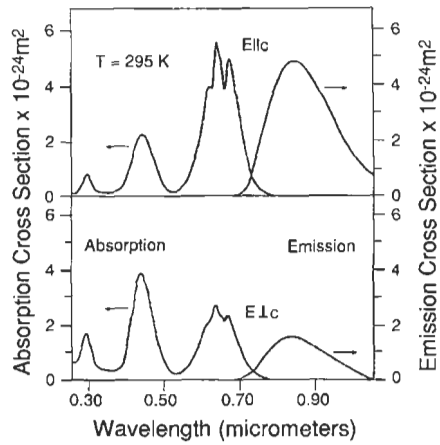

FIGURE 22 Absorption and emission spectra of $Cr:LiSrAlF_6$. (Courtesy of S. A. Payne, Lawrence Livermore National Laboratory.)

Although $Cr:LiCaAlF_6$ and $Cr:LiSrAlF_6$ have quite similar absorption spectra, the emission spectra are somewhat different. Emission from $Cr:LiCaAlF_6$ peaks about at 0.76 μm and has a linewidth of about 0.132 μm for both polarizations [41]. On the other hand, emission from $Cr:LiSrAlF_6$ peaks about at 0.84 μm and has a linewidth of about 0.197 μm for both polarizations [42]. For $Cr:LiCaAlF_6$, the π polarized emission is approximately 1.5 times as intense as the σ polarization. The π polarized emission spectrum for $Cr:LiSrAlF_6$ is approximately three times as intense as the σ polarized emission. Emission spectra are shown in Figs. 21 and 22 for $Cr:LiCaAlF_6$ and $Cr:LiSrAlF_6$, respectively.

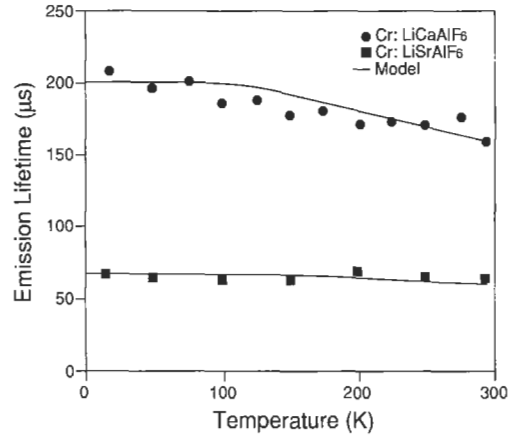

FIGURE 23 Upper laser level lifetimes of Cr:LiCaAlF$_6$ and Cr:LiSrAlF$_6$. (Courtesy of S. A. Payne, Lawrence Livermore National Laboratory.)

Ground state and excited state absorption both exist for Cr:LiCaAlF$_6$ and Cr:LiSrAlF$_6$. Ground state absorption for these laser materials can be observed in Fig. 21. Ground state absorption can seriously affect the laser performance for wavelengths shorter than 0.75 μm. Single-pass absorption depends, of course, on the length of the laser rod and concentration of Cr. However, even at low concentrations, absorptions of 0.05 have been observed at 0.725 μm. At long wavelengths, ground absorption becomes an increasingly smaller effect. Because Cr:LiCaAlF$_6$ emission peaks at shorter wavelengths, ground state absorption is a more serious effect for this laser material. Excited state absorption can occur between the $^4T_2$ and $^4T_1$ manifolds. Because more than one manifold is designated as the $^4T_1$ manifold, a further designation is given. On the Tanabe–Sugano diagram, the manifold that originates at the origin is designated the $^4T_1$a manifold, and the manifold that originates at an E/B ratio of about 15 is designated the ^4T_1b manifold. In Cr:LiCaAlF$_6$, the excited state absorption between the $^4T_2$ and the ^4T_1b manifold peaks around 0.51 μm and stretches across much the visible [37]. Excited state absorption in this region is non-negligible and will limit the level of inversion if flashlamp pumping is employed. However, if laser or laser diode array pumping is utilized, this problem can be mitigated. Excited state absorption between the $^4T_2$ and the ^4T_1a manifolds occurs at wavelengths at which lasing can occur. Excited state absorption has been measured in Cr:LiCaAlF$_6$ for wavelengths longer than 1.0 μm. Experimental difficulties made measurements at shorter wavelengths difficult. Through extrapolation of the measured data, it was determined that the peak of this absorption occurred at 0.997 μm and the linewidth was estimated to be 0.243 μm. An excited state absorption cross section at the peak was inferred to be at 0.17×10^{-24} m^2. Peak effective stimulated emission cross section is 1.3×10^{-24} m^2. Thus, near the peak emission wavelengths, excited state absorption is a small effect.

Normal mode thresholds for flashlamp-pumped Cr:LiSrAlF$_6$ are considerably lower than they are for Cr:LiCaAlF$_6$, reflecting the higher gain of the former laser material. Experimental results are available for 6.35-mm-diameter laser rods. The length of the Cr:LiCaAlF$_6$ was 80 mm; the length of the Cr:LiSrAlF$_6$ was 100 mm. Although the experimental arrangements are somewhat different, including the exact pump cavity, there are enough similarities for a comparison. Threshold for Cr:LiCaAlF$_6$ varied from about 55 to 82 J as the output mirror reflectivity decreased from 0.944 to 0.62 [43]. On the other hand, the threshold for Cr:LiSrAlF$_6$ varied from 15 to 32 J as the output mirror reflectivity decreased from 0.985 to 0.43 [44]. From these measurements, the double-pass loss was deduced as 0.49 for Cr:LiCaAlF$_6$ and 0.39 for the Cr:LiSrAlF$_6$. Considerably lower thresholds can be expected if this relatively high loss can be reduced. Because both of these laser materials can be considered to be new materials at this time, a relatively high loss is not surprising.

Even at this stage of development, normal mode slope efficiencies can be relatively high. Slope efficiency of a normal mode Cr:LiCaAlF$_6$ increased monotonically with a decrease in the output mirror reflectivity. As the output mirror reflectivity decreased from 0.944 to 0.62, the slope efficiency increased from 0.0035 to 0.0155 [43]. Such an increase is consistent with a nonsaturable passive loss. Slope efficiency of a normal mode Cr:LiSrAlF$_6$ also displayed a monotonic increase in the slope efficiency as the output mirror reflectivity decreased. For this laser material, the slope efficiency increased from 0.0043 to 0.050 as the output mirror reflectivity decreased from 0.985 to 0.43 [44]. Slope efficiency is expected to increase as the quality of the laser material increases and more nearly optimum configurations are developed.

Tuning of these laser materials has been demonstrated over wide spectral regions. Cr:LiCaAlF$_6$ has operated between about 0.72 and 0.85 μm [45]. Short-wavelength operation appears to be limited primarily by ground state absorption. Long-wavelength operation is limited by a combination of effects including the decreasing effective stimulated emission cross section and the increasing excited state absorption. Cr:LiSrAlF$_6$ has lased over the approximate range between 0.78 and 1.01 μm [44]. Limits on the short-wavelength operation are probably caused by ground state absorption, a decrease in effective stimulated emission cross section, and possibly excited state absorption. Long-wavelength operation is also limited by a decreasing effective stimulated emission cross section.

Continuous wave operation of these laser materials has been demonstrated using a 0.647-μm Kr ion laser pump. Slope efficiencies for Cr:LiCaAlF$_6$ and Cr:LiSrAlF$_6$ were measured as 0.54 and 0.36, respectively [42]. Slope efficiency is limited by the ratio of the pump wavelength to the lasing wavelength. Based on this, slope efficiencies should be 0.83 and 0.78, respectively. Part of the difference between the observed slope efficiency and the maximum slope efficiency can be attributed to the losses in the resonator. However, because the observed slope efficiency of Cr:LiSrAlF$_6$ is less than half of the limit, an excited state absorption mechanism has been used to explain the difference.

8. Cr:GSGG, Cr:YSAG, AND Cr:GSAG

Of the plethora of laser materials into which Cr can be incorporated, Cr:GSGG, Cr:YSAG, and Cr:GSAG are three of the laser materials with the highest demonstrated potential. An experimental survey of the possible materials into which Cr could be incorporated was conducted by using laser pumping [46]. Such a procedure has several advantages including the requirement for only small samples and facile determination of the amount of pump radiation absorbed by the laser material. Because the amount of pump power absorbed by the laser material can be determined to good accuracy, the efficiencies of the various laser materials can be compared on a more nearly equitable basis. Furthermore, by measuring the laser performance as a function of the output mirror reflectivity, the losses in the laser material can be determined. If these losses are determined, the effects of laser material quality can also be factored out. Factoring out the losses tends to compensate for the level of development and leaves an intrinsic slope efficiency. Comparing the intrinsic slope efficiency gives a good estimate of the potential of various laser materials. Laser material, peak emission wavelength, and laser-pumped slope efficiency are listed in Table 4. Only the top 10 candidates are listed in the table.

Some of the most promising Cr-doped laser materials appearing in Table 4 are not currently finding wide acceptance for a variety of reasons. $Be_3Al_2(SiO_3)_6$ or emerald appears to be the most promising material. However, this laser material is a difficult material to grow. Much of the crystal growth has been by the hydrothermal method. Hydrothermal growth is not widely employed as a method for large commercial crystal growth and crystal quality has been limited to date. The next three laser materials, $LiCaAlF_6$, $BeAl_2O_4$, and $LiSrAlF_6$ have been covered in previous sections. $ScBeAlO_4$ and $ScBO_3$ both appear attractive, however they have not received as much attention as the next group of laser materials, possibly because of limited availability. Appearing next are four garnet laser materials: $Gd_3Sc_2Ga_3O_{12}$ or GSGG, $Na_3Ga_2Li_3F_6$ or GFG, $Y_3Sc_2Al_3O_{12}$ or YSAG, and $Gd_3Sc_2Al_3O_{12}$ or GSAG. Of these, oxide crystals tend to be easier to grow than fluoride crystals. Ease of growth is dependent on material purity as well as good mechanical and thermal properties. Fluoride materials are often contaminated, usually with oxides, and tend to have poorer thermal and mechanical properties when compared with oxides. Furthermore, the oxide garnet materials are available from a variety of vendors. This combination of circumstances has led to more exploration of GSGG, YSAG, and GSAG than some of the other laser materials appearing above them in Table 4.

All three of these garnet laser materials have the general chemical formula $A_3B_2C_3O_{12}$. Although in oxide garnets, the three sites have the same valence, the site symmetry is completely different. Site symmetry of the *A* site is dodecahedral. In contrast, site symmetry of the *B* site is octahedral, and site symmetry of the *C* site is tetrahedral. Cr has a proclivity to substitute into octahedrally

TABLE 4 Measured Slope Efficiencies of Cr Lasers

Laser material	Peak wavelength	Slope efficiency
$Be_3Al_2(SiO_3)_6$	0.768	0.64
$LiCaAlF_6$	0.780	0.54
$BeAl_2O_4$	0.752	0.51
$LiSrAlF_6$	0.825	0.36
$ScBeAlO_4$	0.792	0.30
$ScBO_3$	0.843	0.29
$Gd_3Sc_2Ga_3O_{12}$	0.785	0.28
$Na_3Ga_2Li_3F_{12}$	0.791	0.23
$Y_3Sc_2Al_3O_{12}$	0.767	0.22
$Gd_3Sc_2Al_3O_{12}$	0.784	0.19

coordinated sites. Thus, Cr tends to occupy the *B* site, which enjoys the octahedral symmetry. The *Dq/B* parameters have been estimated for GSGG and GSAG to be 2.45 and 2.55, respectively. Consequently, the $^4T_2$ manifold appears above the ^2E manifold for these laser materials. However, both laser materials are expected to have a larger fraction of the excited Cr atoms in the $^4T_2$ manifold than Cr:$BeAl_2O_4$. Because laser action usually occurs from this manifold, having a larger fraction of the excited state population increases the gain of the laser material. All three of these materials utilize Sc in the octahedral site rather than Al to provide a better lattice match for the Cr. Cr usually substitutes for Sc, however, it can also substitute for Ga in GSGG. By expanding the octahedral site with Sc atoms, crystals with reasonable concentrations of Cr can be grown with high optical quality. Availability of high optical quality laser material is a contributing factor to the interest in these laser materials. Although a variety of Cr concentrations is available in these laser materials, absorption bands are strong enough so that concentrations are usually kept in the range of 0.01 atomic or less.

Garnets are desirable materials from which to make lasers, however, the thermal and mechanical properties are not usually as good as YAG. Transparency of these garnets in the ultraviolet is less than that of YAG; typically substantial absorption occurs at wavelengths shorter than 0.3 μm. Lack of good ultraviolet transmission is not surprising in view of the strong absorption of Gd in this region. Low ultraviolet transmission does not seriously degrade the absorption of Cr. However, absorption of short-wavelength flashlamp radiation by the laser material may detract seriously from the laser performance as described later. Substitution of Gd, Sc, and Ga for Y and Al in YAG degrades the thermal properties of these materials. Specifically, the thermal conductivity is considerably

lower, which limits the average power available from these laser materials. Some of the physical properties of these laser materials are listed in Table 5.

Garnet materials are isotropic materials with a relatively high refractive index. As expected, the refractive index of these materials is higher than that of YAG. Specifically, the refractive indices of GSGG, YSAG, and GSAG are 1.952, 1.867, and 1.890, respectively. Because these materials are isotropic, laser output is not polarized in general. If polarizers are included in the laser resonator, depolarization losses can be expected at high average powers [47,48]. Depolarization losses are due to the thermally induced birefringence in normally isotropic materials and are exacerbated by the reduced thermal conductivity when compared to YAG.

When Cr is incorporated into these materials, the two absorption bands characteristic of Cr are readily identified. Absorption peaks for the short-wavelength absorption are approximately 1.5 times stronger than the absorption peaks for the long wavelength. Spectra of Cr:GSGG and Cr:GSAG appear in Figs. 24 and 25, respectively. Short-wavelength absorption peaks occur at 0.46 and 0.45 μm; widths are 0.09 and 0.12 μm for GSGG and GSAG, respectively [49,50]. Long-wavelength absorption peaks occur at 0.64 and 0.63 μm; widths are 0.12 and 0.09 μm for the same laser materials. These absorption features are strong enough to produce absorption coefficients on the order of 200 m^{-1} even with concentrations below 0.01 atomic. Efficient flashlamp pumping is possible with these materials because of these strong absorption features. However, the shorter wavelengths, shorter than about 0.4 μm, should be filtered out since these wavelengths are absorbed primarily by the laser material itself. Short pump wavelengths thus contribute to heating of the laser material while producing little population in the upper laser level. Worse still is the creation of detrimental flashlamp-induced loss.

TABLE 5 Physical Properties of Garnets

Parameter	YAG	GSGG	Units
Lattice constants	1201	1256	pm
Density	4550	6439	kg/m^3
Heat capacity	620	402	J/kg-K
Thermal conductivity	13.0	5.78	W/m-K
Thermal expansion	7.0	7.5	10^{-6}/K
Refractive index	1.8289	1.9518	
Refractive index variation	10.4	10.1	10^{-6}/K
Optical transparency	0.24–5.5	0.3–6.5	μm
Melting point	1940	≈1830	°C

Flashlamp radiation has been shown to induce both transient and stable losses in GSGG and GSAG. Losses have been measured as a function of wavelength, flashlamp energy, and time [50,51]. Some of the losses induced by the flashlamp will disappear spontaneously as a function of time, whereas others remain for long periods of time. In general, the flashlamp-induced loss is more severe in GSGG than in GSAG. Higher losses are associated with the higher volatility of Ga_2O_3 in the laser material growth process when compared with Al_2O_3. Higher volatility of the former has been shown to result in O vacancies in the laser material. Vacancies can contribute to color center formation, which could explain the losses. In general flashlamp-induced losses are more severe at shorter wavelengths than they are at longer wavelengths. For example, stable flashlamp-induced loss was low at the lasing wavelength and progressively became worse as short wavelengths were approached. Although flashlamp-induced loss increased as the flashlamp energy increased, considerable saturation in this effect has been noted, especially at the shorter wavelengths where the problem is more severe. Flashlamp-induced losses tend to decrease as a function of the time interval between the flashlamp pulse and the measurement. No single exponential decay constant could be associated with the process, possibly indicating the formation of several types of loss mechanisms.

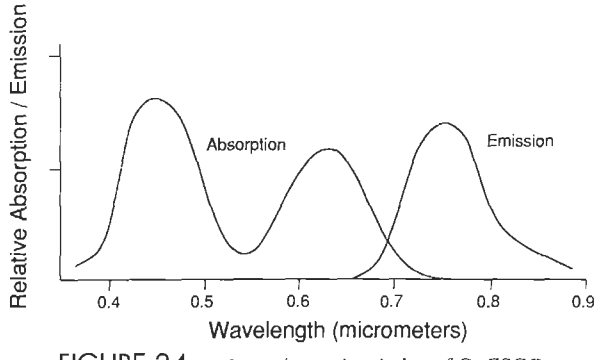

FIGURE 24 Absorption and emission of Cr:GSGG.

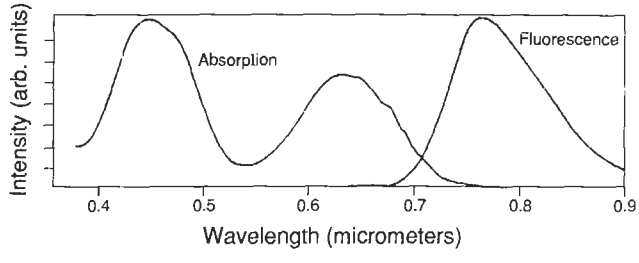

FIGURE 25 Absorption and emission of Cr:GSAG.

As the quality of laser materials increases, more nearly stoichiometric laser material should become available, which should mitigate this problem.

The quantum efficiency of these materials is relatively high. Quantum efficiency has been measured for GSGG and found to be nearly unity [52]. Little evidence of concentration quenching for either GSGG or GSAG has been reported.

Upper laser level lifetimes are compatible with flashlamp pumping. Upper laser level lifetimes at room temperature are 120 and 160 μs for GSGG and GSAG, respectively [49,50]. Upper laser level lifetime was measured as a function of temperature for GSAG and appears in Fig. 26. Lack of a precipitous decrease in the upper laser level lifetime as a function of temperature tends to support the contention that nonradiative decay effects are small. A two-level model can represent the data well. From this curve fit, the lifetime of the $^4T_2$ and the weighted average of the ^2E and $^4T_1$ levels are 57 and 304 μs, respectively.

Emission spectra from these materials display a single broad peak with little evidence of *R* line emission at room temperature. Emission peaks for GSGG and GSAG occur at about 0.760 and 0.765 μm with widths of about 0.10 and 0.11 μm, respectively [49,50]. Emission spectra also appear in Figs. 24 and 25. Because of the ground state absorption, the wavelengths corresponding to peak laser emission are somewhat longer. Peak laser emission wavelengths for GSGG, YSAG, and GSAG are 0.785, 0.767, and 0.784 μm, respectively [53]. At reduced temperatures, *R* line emission can be observed at wavelengths slightly shorter than about 0.7 μm.

Normal mode lasing has been achieved using flashlamp pumping of GSGG and GSAG. Initial results using GSGG produced a threshold of about 25 J and a slope efficiency of about 0.0005 [49]. However by filtering the flashlamp radiation with a K_2CrO_4 solution, performance was substantially increased [5]. The threshold did not vary significantly, but the slope efficiency increased to about

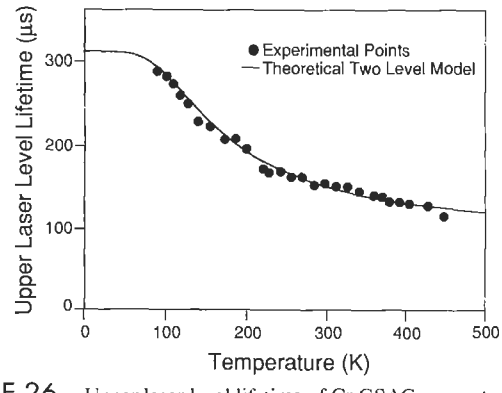

FIGURE 26 Upper laser level lifetime of Cr:GSAG versus temperature.

0.003. Threshold and slope efficiency for GSAG are 45 J and 0.0012, respectively [50]. Effects of filtering the flashlamp were not performed with this material although increases in performance are expected based on the measured flashlamp-induced loss. Gain in flashlamp-pumped YSAG has been observed but the gain was insufficient to produce lasing [53].

Laser-pumped lasing has been achieved in GSGG, YSAG, and GSAG. Commonly a Kr ion laser is used as the pump source [46,54,55]. Its wavelength, 0.647 μm, corresponds well to the long-wavelength absorption band of these laser materials. Low thresholds are achieved using laser pumping by focusing the pump laser to a small beam radius, often to a pump beam radius as small as 25 μm. As such, the threshold is a critical function of the degree of focusing. A more fundamental parameter of these laser materials is the slope efficiency. Slope efficiencies of GSGG, YSAG, and GSAG are 0.28, 0.22, and 0.19 as listed in Table 4. Slope efficiency will be limited by the ratio of the pump wavelength to the lasing wavelength, about 0.83 for these materials. Because these laser materials have a slope efficiency so much lower than the limiting value, a serious loss mechanism is indicated. Excited state absorption has been identified as a possible source of this loss mechanism.

9. Co:MgF_2, Ni:MgF_2, AND V:MgF_2

Co:MgF_2, Ni:MgF_2, and V:MgF_2 are among the earliest solid-state lasers discovered; however, a low effective stimulated emission cross section contributed to their slow development. Initial laser experiments performed with these laser materials utilized flashlamp pumping and were conducted at cryogenic temperatures, ≈80 K [56]. Low-temperature operation increased the upper laser level lifetime and the gain of these laser materials, which promoted laser operation. While low-temperature operation is feasible, room-temperature operation is vastly preferred. The advent of laser pumping refocused attention on these laser materials. By using laser pumping, the pump radiation could be focused into small volumes, thus compensating in part for the low effective stimulated emission cross section. In addition, the use of laser pumping allowed for rapid increases in the population inversion. A rapid increase in the population inversion mitigates the effect of the decrease in the upper laser level lifetime with increasing temperature.

Co:MgF_2, Ni:MgF_2, and V:MgF_2 have manifolds that are labeled using a nomenclature associated with octahedral symmetry. A strong interaction of the active atoms with the crystal field is in effect. One result of this strong interaction is a difference in the lattice configuration of the laser material for the ground and excited states in some instances. Even though the crystal field does not have strict octahedral symmetry, the states are still labeled using the octahedral nomenclature. Doubly ionized V has the same energy-level diagram of triply ionized Cr. As

such, the lower laser manifold is the $^4A_2$ manifold, and the upper laser manifold is the $^4T_2$. For V, the ratio of Dq/B is lower than Dq/B values usually associated with Cr. A direct result of the lower value of Dq/B is that the $^4T_2$ manifold is lower than the ^2E manifold. In doubly ionized Ni the lower laser manifold is the $^4T_1$ and the upper laser manifold is the $^4T_2$. In doubly ionized Co the lower laser manifold is the $^3A_2$ and the upper laser manifold is the $^3T_2$.

Co:MgF_2, Ni:MgF_2 and V:MgF_2 can have both electronic and vibronic transitions. For example, consider the energy levels of Co:MgF_2. Here the lower laser manifold is split into six levels by the spin orbit interaction and the crystal field effects. Each of these levels has Kramer's degeneracy. Splitting of the lower laser manifold is quite large, about 1400 cm^{-1} for Co:MgF_2. Because of the large splitting, electronic transitions can occur between the upper and lower laser manifolds. These electronic transitions produce relatively narrow and strong peaks in the fluorescence spectrum. If a transition occurs in the vicinity of these peaks, the lower laser level can have a significant population density, leading to three-level-like operation. On the other hand, far from these peaks, the transitions are vibronic, leading to four-level-like operation.

Laser materials are produced by replacing some of the Mg with the proper active atom—Co, Ni, or V. Although there is some size discrepancy between Mg and the active atoms, laser materials having concentrations above 0.01 atomic and high optical quality can be produced. Because of the size discrepancy and the strong interaction between the active atom and the crystal field, a shift in the position of some of the spectral features can occur at higher concentrations. At concentrations of 0.01 atomic, these effects are minimal.

MgF_2 is a good material from which to make a laser, primarily because of its relatively high thermal conductivity. MgF_2 has a wide range of transparency, extending from the ultraviolet through the midinfrared, about 6.5 μm. As such, the losses at the laser wavelength can be low. Its wide range of transparency has led to its use as a window material; consequently, polishing techniques have been developed for this material. Thermal conductivity is high, approaching that of YAG. This, coupled with the refractive index properties, allows the use of the high power densities often associated with laser pumping. The physical properties of MgF_2 are listed on Table 6.

MgF_2 is a birefringent material with a relatively low refractive index. This crystal is uniaxial, producing differences in the refractive index and spectra depending on the polarization. The refractive index is only about 1.38, whereas the difference between the ordinary and extraordinary indices of refraction is about 0.011. A refractive index this low makes a conventional single-layer broadband antireflection coating impractical. As such, Brewster's angle laser materials are often employed where operation over a broad spectral band is desired.

Of the three laser materials, V:MgF_2 has, to date, not been developed because of relatively inefficient performance. The lifetime of the upper laser level of this laser material is 2.3 ms at 77 K. However, relatively poor perfor-

TABLE 6 Physical Properties of MgF_2

Parameter	Value	Units
Lattice constants		pm
a axis	462.3	
c axis	305.2	
Density	3170	kg/m³
Heat capacity	989	J/kg-K
Thermal conductivity	20.6	W/m-K
Thermal expansion		10^{-6}/K
a axis	13.1	
c axis	8.8	
Refractive index		
a axis	1.3768	
c axis	1.3886	
Refractive index variation		10^{-6}/K
a axis	1.12	
c axis	0.58	
Optical transparency	0.12–6.5	μm
Melting point	1263	°C

mance has been achieved so far. One reason for this is excited state absorption [57]. Excited state absorption might be expected by considering its similarities with Cr. In general, excited state absorption occurs in Cr materials as laser operation shifts toward longer wavelengths. Doubly ionized V is similar to triply ionized Cr and V:MgF_2 operates around 1.12 μm, so excited state absorption is probable. Excited state absorption would likely occur between the $^4T_2$ and the $^4T_1$ manifolds. Although excited state absorption occurs for Ni:MgF_2, its effects do not preclude reasonable operation of this material.

Absorption bands in Ni:MgF_2 are strong enough to allow flashlamp or laser pumping. Absorption bands for Ni peak in the vicinity of 1.35 and 0.79 μm for the $^3A_2$ to $^3T_2$ and the $^3A_2$ to $^3T_1$ manifolds, respectively, as shown in Fig. 27. Absorption between these manifolds is relatively weak, producing π polarized absorption coefficients on the order of 100 m^{-1} for a Ni concentration of 0.01. Stronger absorption is associated with the $^3T_1$ manifold in the blue region of the spectrum. Laser pumping is enabled by utilizing the long-wavelength absorption band around 1.35 μm.

Strong absorption bands in Co:MgF_2 occur between the $^4T_1$ and $^4A_2$ manifolds, which peak at about 1.35 μm for both π and σ polarizations as shown in Fig. 28. The spectral bandwidths of both of these features are about 0.26 μm [58].

As with Ni:MgF_2, this long-wavelength absorption feature allows laser pumping. Strong absorption bands also occur between the $^4T_1$ and $^4A_2$ manifolds. For the σ polarized radiation, this feature peaks about 0.51 μm and has a width of about 0.05 μm. Absorption is skewed toward shorter wavelengths for this feature. For the σ polarized radiation, the absorption peak occurs at about 0.49 μm and has a linewidth of about 0.10 μm. The strengths of the shorter wavelength absorption peaks are similar for both polarizations, but the strength of the longer wavelength absorption feature is about twice as strong for the π polarization. This difference in the absorption coefficients translates into a preference for a polarized pump laser. Weaker absorption features are observable around 0.68 μm.

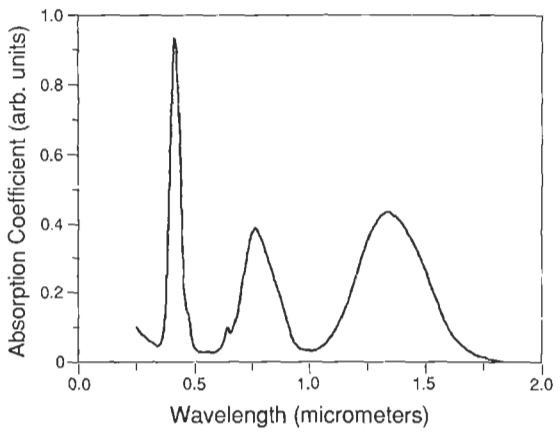

FIGURE 27 Absorption spectrum of Ni:MgF_2. (Courtesy of P. F. Moulton, Schwartz Electo-Optics.)

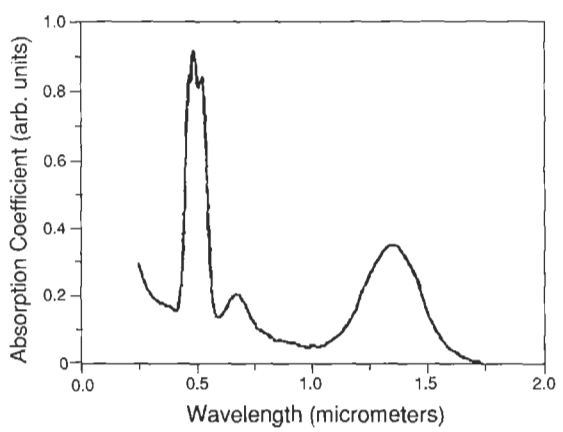

FIGURE 28 Absorption spectrum of Co:MgF_2. (Courtesy of P. F. Moulton, Schwartz Electo-Optics.)

Quantum efficiency data for these laser materials are complicated by the varying definitions found in the literature. However, quantum efficiency, defined as the fraction of the active atoms in the upper laser manifold that decay by direct emission of a photon, is expected to be low. For example, for a similar laser material, Co:$KMgF_3$, the quantum efficiency even at cryogenic temperatures has been estimated as only 0.7 [59]. Low values of the quantum efficiency tend to indicate the presence of strong nonradiative decay.

Upper laser level lifetime is strongly temperature dependent. For Ni:MgF_2, the upper laser level lifetime drops precipitously as the temperature increases. Lifetimes are 12.8, 11.5, and 3.7 ms at 20, 77, and 295 K, respectively [60]. At very low temperatures, the upper laser level lifetime of Co:MgF_2 is relatively long, about 1.8 ms. However, above about 80 K, the lifetime begins to fall as shown in Fig. 29 [61]. At room temperature, the upper laser level lifetime is only about 36 μs.

Polarized emission spectra of Ni:MgF_2 (Fig. 30) extend between 1.5 and 1.9 μm. At cryogenic temperatures, a strong emission feature occurs for both polarizations at about 1.54 μm [62]. This emission feature is associated with a pure electronic transition. On the long-wavelength side of the electronic transition are vibronic transitions. At low temperatures the π polarized spectra is stronger than the σ polarized spectra. Relatively broad peaks can be observed in the nominal vibronic transitions. As the temperature increases, these peaks tend to disappear and the emission spectra become smoother.

Polarized emission spectra of Co:MgF_2 (Fig. 31) display broad peaks around 1.9 μm and relatively sharp line spectra only at cryogenic temperatures. At cryogenic temperatures, around 80 K, six peaks in the fluorescence can be observed. These peaks are associated with the six components of the ground

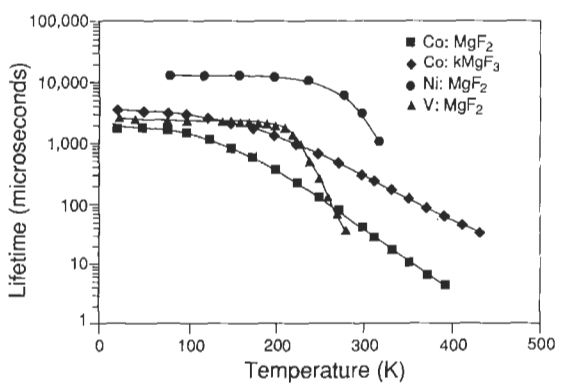

FIGURE 29 Upper laser level lifetime of Co:MgF_2, Co:$KMgF_3$, Ni:MgF_2, and V:MgF_2 versus temperature. (Courtesy of P. F. Moulton, Schwartz Electro-Optics.)

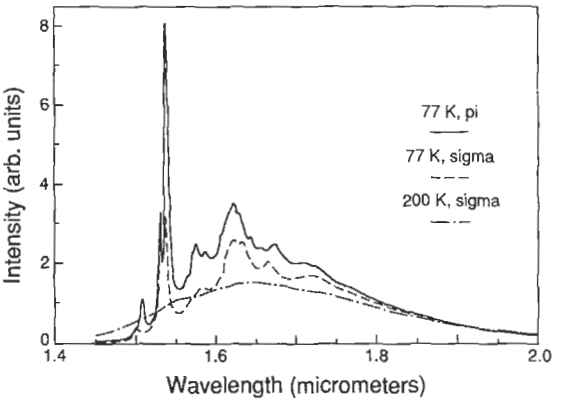

FIGURE 30 Polarized emission spectra of Ni:MgF_2. (Courtesy of P. F. Moulton, Schwartz Electo-Optics.)

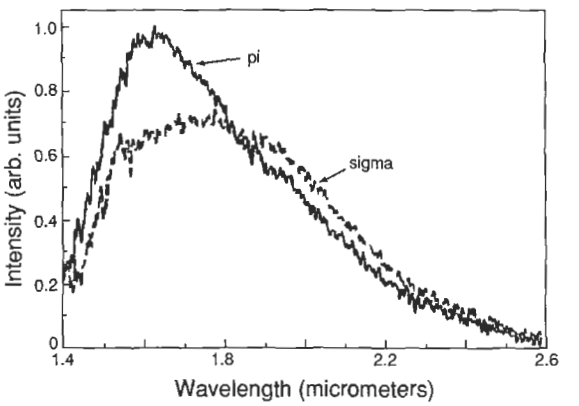

FIGURE 31 Polarized emission spectra of Co:MgF_2. (Courtesy of P. F. Moulton, Schwartz Electo-Optics.)

manifold [62]. As the temperature is increased, these peaks disappear. Near room temperature, a broad emission peak remains. Emission for the π polarization is peaked at shorter wavelengths, about 1.65 μm, and continues out to beyond 2.4 μm. Emission for the σ polarization is significantly flatter and not as strong as the π polarized emission. Due to decreased quantum efficiency, room-temperature fluorescence is about 0.02 as strong as fluorescence at cryogenic temperatures, roughly in proportion with the decrease in the upper laser level lifetime. Emission spectra from Ni:MgF_2 occur at somewhat shorter wavelengths. Again, relatively narrow emission features occur at cryogenic temperatures and disappear as room temperature is approached. A broad emission peak, extending from about 1.5 to 1.9 μm, occurs for both the σ and π polarizations.

Flashlamp-pumped laser performance of $Co:MgF_2$, $Ni:MgF_2$, and $V:MgF_2$ have all been achieved at cryogenic temperatures [56]. $V:MgF_2$ did little more than achieve threshold. Even at cryogenic temperatures, the threshold for flashlamp-pumped operation occurred at flashlamp energies of about 1150 J. Part of this high threshold is associated with the low concentration of V in the sample. On the other hand, thresholds for $Co:MgF_2$ and $Ni:MgF_2$ devices were achieved at somewhat lower flashlamp energies, around 690 and 150 J, respectively. Slope efficiencies for these materials were not quoted. Peak emission wavelengths were 1.750 and 1.623 μm for these two laser materials.

Laser-pumped performance of $Co:MgF_2$ has been achieved at temperatures up to room temperature. Laser pumping can utilize a Nd:YAG laser operating at 1.33 μm [62]. As an example, with an output mirror reflectivity of 0.98 and at a temperature of 248 K, slope efficiencies of 0.59 have been achieved for both π and σ polarizations. The threshold for the σ polarization was 17 mJ, whereas threshold for the π polarization was 27 mJ. At a temperature of 299 K, slope efficiencies of the σ and π polarizations decreased to 0.48 and 0.39, respectively. Thresholds increased to 28 and 41 mJ at this temperature for the two polarizations. To achieve this performance, low-loss laser material was essential to achieve the low threshold and high slope efficiency. Note that the high slope efficiency was achieved despite the high output mirror reflectivity. Using laser pumping, cw operation has been achieved in both $Co:MgF_2$ and $Ni:MgF_2$ [63,64].

Dr. Peter Moulton kindly provided figures for this subsection, some of which have not been published previously.

10. WAVELENGTH CONTROL METHODS

Most applications of transition metal solid-state lasers benefit from the tuning characteristics of these devices. However, to capitalize on the tuning characteristics, wavelength control devices are needed. Wavelength control of solid-state lasers falls into three general categories: broadband wavelength control, narrowband wavelength control, and injection wavelength control. For broad tuning, only a coarse wavelength control device is required. It may be noted that with lanthanide series lasers, broad wavelength control devices are usually not required. Broad wavelength control devices include prisms, gratings, and birefringent filters. With these devices, the spectral bandwidth of the transition metal laser can be reduced to the order of a nanometer. For narrow tuning, a narrow wavelength control device must be utilized in addition to the broad wavelength control device. Narrow wavelength control devices are primarily etalons. The transmission peaks of these devices are approximately cyclic with wavelength, so they are usually used in conjunction with a broad wavelength control device. With these devices, the spectral bandwidth of the transition can be reduced to the order of a picometer or less. With injection control, a narrow spectral bandwidth

source is injected into the resonator to control the wavelength. Using this technique, the spectral bandwidth of the laser is usually restricted to one or two longitudinal modes. If a single longitudinal mode is produced, the spectral bandwidth is on the order of tens of femtometers.

Prisms are broad wavelength control devices that can achieve a low loss when set at Brewster's angle but they tend to polarize the laser. If an optical material, such as fused silica, is fabricated into a prismatic shape, as shown in Fig. 32, an incident ray is deviated by propagating through the prism. Deviation is characterized by a deviation angle ε. Deviation is dependent on the incident angle and the refractive index n [65]. For many applications, the incident angle is set at Brewster's angle to minimize losses. By selecting the apex angle of the prism, α, Brewster's angle can be achieved at both the input and output surfaces of the prism. Although the reflection loss associated with a prism in this configuration can be very low, the use of a prism usually polarizes the laser. If the laser is not naturally polarized, restricting operation to a polarized mode can significantly increase the losses. If the laser is naturally polarized, losses associated with the use of a Brewster's angle prism can be very small if aligned correctly.

Wavelength control by a prism is achieved because the angle of deviation depends on the wavelength. If a Brewster's angle prism is used, the angle of deviation depends only on the refractive index. Since the refractive index depends on wavelength, the angle of deviation depends on the wavelength. With a prism in the laser resonator, the resonator will be aligned correctly only for one wavelength. It is the dependence on the angle of deviation with wavelength that allows the prism to tune the laser. Wavelength control can be achieved by varying the orientation of the resonator mirrors.

The spectral bandwidth of a single-pass prism can be estimated by calculating the variation of the angle of deviation with wavelength. To estimate the angle of deviation, this quantity can be expanded in a Taylor series, that is

$$\varepsilon = \varepsilon_0 + \frac{d\varepsilon}{d\lambda}\Delta\lambda \ . \tag{31}$$

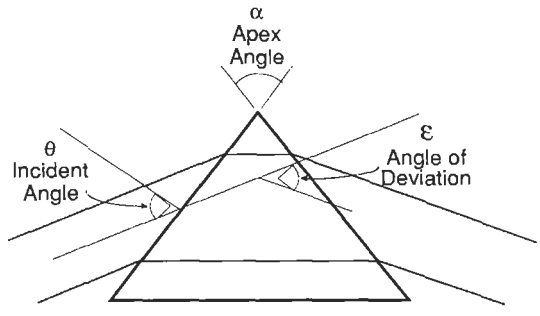

FIGURE 32 Dispersive prism.

For a Brewster's angle prism at the angle of minimum deviation, the variation of the angle of deviation can be readily related to the variation of the refractive index with the wavelength. Thus, the above expression becomes

$$\varepsilon = \varepsilon_0 + 2\frac{dn}{d\lambda}\Delta\lambda \ . \tag{32}$$

An estimate of the allowable variation of the angle of deviation can be obtained from the beam divergence. For a TEM_{00} mode Gaussian beam, the beam divergence θ_0 is given by $\lambda/\pi w_0$ where w_0 is the beam radius. Thus, for a single pass, the spectral bandwidth can be estimated as

$$\frac{\Delta\lambda}{\lambda} = \frac{1}{2\pi w_0} \Big/ \frac{dn}{d\lambda} \ . \tag{33}$$

For a material like fused silica, the variation of the index of refraction with wavelength, that is, the dispersion, is on the order of 2.0×20^4 m^{-1}. However, materials with higher dispersion are available. For example, the dispersion of SF6 glass is 9.8×10^4 m^{-1}. Materials such as SF6 glass are satisfactory for low-power applications, but they are susceptible to laser induced damage at higher power densities. On the other hand, the simple fused silica prism can be extremely damage resistant.

Gratings can produce significantly smaller spectral bandwidths than prisms since they can have a greater variation of the angle of deviation with wavelength. Gratings can be used in either a Littrow or a grazing-incidence configuration [66,67]. In a Littrow configuration, the radiation at the selected wavelength is retroreflected. As such, the grating can be used as one of the mirrors of the resonator. In most cases, plane gratings are used. In this configuration, the output mirror is often a curved mirror so that a stable resonator can be formed. In the grazing-incidence configuration, the grating is used as a mirror internal to the resonator. One of the incident angles associated with the grating is a grazing angle, as shown in Fig. 33. A grazing-incidence angle produces two useful results. One result is that the radiation is spread over larger area of the grating, reducing the energy density on the grating and consequently the probability of laser induced damage. Another result is the increase in the number of illuminated grooves. With a higher number of illuminated grooves, the wavelength selectivity of the grating is enhanced.

Single-pass spectral bandwidth can be estimated by calculating the variation of the reflected angle with wavelength. Using the grating equation, the angles of incidence θ_i and reflection θ_r are related to the groove spacing d_g by the relation

$$\sin(\theta_i) + \sin(\theta_r) = N\lambda/d_g \ , \tag{34}$$

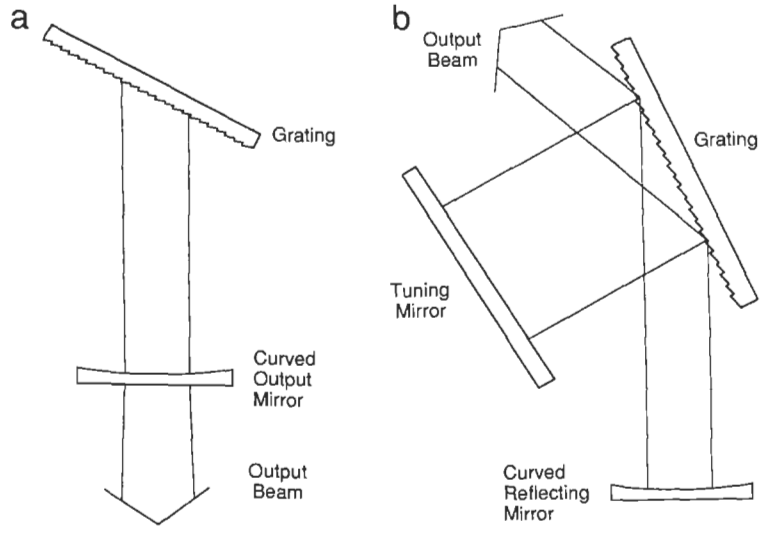

FIGURE 33 Littrow and Grazing-incidence grating configurations. (a) Littrow configuration. (b) Grazing-incidence configuration.

where N is the order of the reflection. For gratings used in a laser resonator, the orders are limited to 1 so that the losses associated with the higher orders are avoided. In the following, we assume that the first-order reflection is always utilized. If a grating is used in the Littrow configuration, the incident and reflected angles are equal. In this case, the variation of the angle with wavelength is

$$\frac{d\lambda}{d\theta} = \frac{1}{2d_g \cos\left(\theta_i\right)} \ . \tag{35}$$

Using the same expression for the beam divergence, the single-pass spectral bandwidth is

$$\frac{\Delta\lambda}{\lambda} = \left[2\pi d_g\, w_0 \cos\left(\theta_i\right)\right]^{-1} \ . \tag{36}$$

Since $d_g \cos(\theta_i)$ can be much larger than $dn/d\lambda$, the spectral narrowing achieved with a grating can be much larger by employing a grating rather than a prism.

Although greater spectral resolution can be achieved with a grating, the losses of a grating tend to be higher. Losses are associated with both finite reflectivity of the coating, usually a metal, and less than unity grating efficiency. Higher losses are particularly pronounced at shorter wavelengths where the

reflectivity of the grating is lower since the reflectivity of the metal is lower. In addition, gratings tend to be more damage prone as compared with prisms. Note that a grating will, in general, polarize a laser. Consequently, the same comments regarding the losses associated with restricting the laser to operate in a polarized mode apply. The dispersive characteristics of multiple-prism grating systems are described in Chapter 2.

Birefringent filters achieve wavelength control by utilizing the variation of the phase retardation of a wave plate with wavelength. For normal incidence, the phase difference Φ between the ordinary and extraordinary wave of a wave plate is

$$\Phi = 2\pi\left(n_o - n_e \right)d/\lambda \ , \tag{37}$$

where n_o and n_e are the ordinary and extraordinary refractive indices, respectively, d is the thickness of the wave plate, and λ is the wavelength. If a polychromatic polarized wave is incident on the wave plate, only some of the wavelengths will have a phase difference, which is an integer multiple of 2π. These wavelengths will interfere constructively as they exit from the wave plate and emerge with the same polarization as the incident polarization. If a polarization discrimination device is used after the wave plate, only the wavelengths that have the correct polarization will suffer no loss. By using this wavelength varying loss, a wavelength selective device can be made.

Both birefringent filters and Lyot filters can be made using this principle. Lyot filters [68] employ several wave plates to achieve better spectral resolution. Between each wave plate is a polarizer. By using these polarizers, good wavelength resolution can be achieved. However, this leads to a filter with high transmission losses. High losses are incompatible with efficient lasers. To obviate these losses, birefringent filters were created [69,70]. These devices are wave plates oriented at Brewster's angle. In this configuration, the Brewster's angle surfaces act as the polarizer, eliminating the polarizer as a loss element. Since the degree of polarization of a Brewster's angle surface is not as high as that of a polarizer, the wavelength resolution is not as high as that of a Lyot filter. Phase difference between the ordinary and extraordinary waves can be calculated for a wave plate at Brewster's angle by taking into account the variation of the refractive index with orientation and the birefringence. Because birefringent filters consist only of wave plates oriented at Brewster's angle, they can have low loss, assuming a polarized laser, and can be damage resistant.

Etalons, like birefringent filters, operate on a principle of constructive interference. An etalon consists of two parallel reflective surfaces separated by a distance d. Wavelengths that fill the distance between the mirrors with an integer multiple of half-wavelengths will be resonant; that is, resonance occurs when

$$\Phi = 4\pi nd \cos\left(\theta\right)/\lambda = 2\pi N \ , \tag{38}$$

where θ is the angle of propagation, N is an integer, and n is the refractive index of the material between the mirrors [65]. Note that since n occurs in these relations rather than $n_o - n_e$, resonances are much closer together. Because the resonances are closer together and the resolution is related to the wavelength interval between the resonances, etalons tend to have much better spectral resolution than birefringent filters.

Spectral resolution of the etalon is a function of the free spectral range (FSR) and the finesse. FSR is defined as the spectral interval between the transmission maxima. If λ_1 corresponds to N half-wavelengths between the reflective surfaces and λ_2 corresponds to $(N + 1)$ half-wavelengths, the difference between the wavelengths is the FSR. It can be easily shown that

$$\lambda_{\mathrm{FSR}} = \frac{\lambda}{2d} \ . \tag{39}$$

Finesse F is related to the reflectivity of the mirror surfaces R by

$$F = \frac{\pi R^{1/2}}{\left(1 - R\right)} \ . \tag{40}$$

Single-pass spectral resolution, $\Delta\lambda$, is then $\Delta\lambda_{\mathrm{FSR}}/F$. To obtain good spectral resolution, either the FSR can be made small or the finesse can be made large. Unfortunately, both of these options involve compromises. If the FSR is made small, laser operation on two adjacent resonances of the etalon is more likely. To avoid this, multiple etalons may have to be employed. If the finesse is made large, the reflectivity of the mirrors must be made close to unity. As the reflectivity is increased, the power density internal to the etalon increases approximately as $(1 + R)/(1 - R)$. Increased power density increases the probability of laser induced damage. In general, laser induced damage is usually a concern for etalons employed in pulsed lasers. In addition, as the reflectivity increases, the losses associated with the etalon also increase.

Losses in etalons are related to the incident angle used with the etalon. In practice, etalons are used internal to the laser resonator and are oriented somewhat away from normal incidence. Tuning is achieved by varying the orientation of the etalon, although temperature tuning is sometimes utilized. When the etalon is not oriented at normal incidence, the transmitted beam is distorted by the multiple reflections occurring in the etalon. This beam distortion leads to losses that increase as the angle of incidence is increased. Consequently, etalons are usually operated near normal incidence. Typically, angles of incidence range around a few times the beam divergence. However, as the orientation of the etalon is varied to tune the laser, care must be taken to avoid normal or near normal incidence. Additional losses in etalons are associated with losses in the reflective coatings and with nonparallel reflective surfaces.

When wavelength control devices are utilized in laser resonators, the resolution is higher than predicted by using the single-pass approximation. For example, in a pulsed laser the pulse propagates through the wavelength control device several times as it evolves. Theory indicates and experiments have verified that the resolution increases as the number of passes through the wavelength control device increases [71]. If p is the number of passes through the wavelength control device that the pulse makes during the pulse evolution time interval, the resolution is increased by the factor $p^{-\frac{1}{2}}$. Thus, when estimating the spectral bandwidth of the laser output, the resolution of the wavelength control devices must be known as well as the pulse evolution time interval.

Injection wavelength control utilizes a low-power or low-energy laser, referred to as a seed oscillator, to control the wavelength of a more energetic oscillator referred to as a power oscillator. Either a pulsed or a cw single-longitudinal-mode oscillator, that is, a single-wavelength oscillator, may be used to produce the laser output needed for injection control [72–74]. Injection seeding can utilize length control of the power oscillator for high finesse resonators or length control may be omitted for low finesse resonators. If length control is not utilized, the seed laser resonator is not necessarily matched to the resonances of the power oscillator. However, the output of the power oscillator will tend to occur at a resonance of the power oscillator resonator nearest to the seed laser. Because this may not correspond exactly to the injected wavelength, some wavelength pulling effects may occur. In some cases, the injected wavelength will occur almost exactly between two adjacent resonances of the power oscillator. In this case, the power oscillator will tend to oscillate at two wavelengths. On the other hand, if length control is utilized, the resonances of the power oscillator match the resonances of the seed oscillator. In this case, operation at a single wavelength is more likely. However, the power oscillator must be actively matched to the resonances of the seed oscillator, complicating the system.

Injection seeding has several advantages over passive wavelength control. By eliminating or minimizing the wavelength control devices in the power oscillator, losses in this device are decreased. Concomitant with a decrease in the losses is the attainment of higher efficiency. In addition, wavelength control of the low-power or low-energy seed laser is usually better than that of the wavelength control of a high-power or high-energy device. Finally, optical devices that are prone to laser induced damage are eliminated from the high-energy laser device, therefore higher reliability is possible. However, the system is complicated by the necessity of a separate wavelength-controlled oscillator.

Power or energy required from the seed oscillator to injection lock or injection seed a power oscillator can be estimated [75]. Power requirements for injection seeding are lower if length control is utilized. However, for low-finesse resonators, the difference is not great. The power or energy required for injection seeding depends on the degree of spectral purity required. In essence, the pulse evolving from the seed must extract the stored energy before the pulse evolving

from noise can extract a significant amount of the stored energy. Power or energy requirements depend critically on the net gain of the power oscillator. In addition, the alignment of the seed laser to the power oscillator is critical. Especially critical are the transverse overlap of the seed with the mode of the power oscillator and the direction of propagation of the seed with respect to the power oscillator. A full analysis of the power required can be found in the literature as well as an analysis of the critical alignment.

For single-wavelength operation of a solid-state laser, ring resonators are often preferred to standing-wave resonators. Standing-wave resonators are formed by two reflective surfaces facing each other, similar to a Fabry–Perot etalon. As such, waves in a standing-wave resonator propagates both in a forward and a reverse direction. If the propagation in the forward direction is characterized by the propagation term $\exp(-jkz)$, then the propagation in the reverse direction is characterized by the propagation term $\exp(+jkz)$. In these expressions, j is the square root of -1, k is the wave vector, and z is the spatial coordinate along the direction of propagation. Waves propagating in the forward and reverse directions interfere to create an intensity pattern characterized by $\cos^2(kz)$. If the laser operates at a single wavelength, the power density is zero at the nulls of the cosine squared term. At these positions, the energy stored in the active atoms will not be extracted. Unextracted stored energy will increase the gain for wavelengths that do not have nulls at the same spatial position as the first wavelength. Increased gain may be sufficient to overcome the effects of homogeneous gain saturation and allow a second wavelength to lase. Conversely, no standing-wave patterns exist in a ring resonator. By eliminating the standing-wave pattern, homogeneous broadening will help discriminate against other wavelengths and thus promote laser operation at a single wavelength. For this reason, ring resonators are often preferred for single-wavelength operation of a solid-state laser.

REFERENCES

1. T. H. Maiman, "Stimulated Optical Radiation in Ruby," *Nature* **187,** 493–494 (1960).
2. D. Pruss, G. Huber, A. Beimowski, V. V. Lapetev, I. A. Shcherbakov, and Y. V. Zharikov, "Efficient Cr^{3+} Sensitized Nd^{3+} GdScGa-Garnet Laser at 1.06 μm," *Appl. Phys. B* **28,** 355–358 (1982).
3. R. B. Allen and S. J. Scalise, "Continuous Operation of a YAlG:Nd Diode Pumped Solid State Laser," *Appl. Phys. Lett.* **14,** 188–190 (1969).
4. N. P. Barnes, "Diode Pumped Solid State Lasers," *J. Appl. Phys.* **44,** 230–237 (1973).
5. L. J. Rosenkrantz, "GaAs Diode-Pumped Nd:YAG Laser," *J. Appl. Phys.* **43,** 4603–4605 (1972).
6. D. Sutton, *Electronic Spectra of Transition Metal Complexes,* McGraw-Hill, London (1968).
7. A. Kaminskii, *Laser Crystals,* Springer Verlag, Berlin (1981).
8. G. H. Dieke and H. M. Crosswhite, "The Spectra of the Doubly and Triply Ionized Rare Earths," *Appl. Opt.* **2,** 675–686 (1963).
9. Y. Tanabe and S. Sugano, "On the Absorption Spectra of Complex Ions," *J. Phys. Soc. Japan* **9,** 753–779 (1954).

10. D. E. McCumber, "Theory of Phonon-Terminated Optical Masers," *Phys. Rev.* **134,** A299–A306 (1964).
11. C. W. Struck and W. H. Fonger, "Unified Model of the Temperature Quenching of Narrow-Line and Broad-Band Emissions," *J. Luminescence* **10,** 1–30 (1975).
12. T. H. Maiman, "Stimulated Optical Radiation in Ruby," *Nature,* **187,** 493–494 (1960).
13. D. C. Cronemeyer, "Optical Absorption Characteristics of Pink Ruby," *J. Opt. Soc. Am.* **56,** 1703–1706 (1966).
14. G. Burns and M. I. Nathan, "Quantum Efficiency of Ruby," *J. Appl. Phys.* **34,** 703–705 (1963).
15. W. Koechner, *Solid State Laser Engineering,* Springer-Verlag, New York (1971).
16. E. J. Woodbury and W. K. Ng, "Ruby Laser Operation in the Near IR," *Proc. IRE* **50,** 2369 (1962).
17. T. H. Maiman, R. H. Hoskins, I. J. D'Haenens, C. K. Asawa, and V. Evtuhov, "Stimulated Optical Emission in Fluorescent Solids. II. Spectroscopy and Stimulated Emission in Ruby," *Phys. Rev.* **123,** 1151–1157 (1961).
18. V. Evtuhov and J. K. Neeland, "Continuous Operation of a Ruby Laser at Room Temperature," *Appl. Phys. Lett.* **6,** 75–76 (1965).
19. D. Roess, "Analysis of Room Temperature CW Ruby Lasers," *IEEE J. Quantum Electron.* **QE-2,** 208–214 (1966).
20. J. C. Walling, D. F. Heller, H. Samuelson, D. J. Harter, J. A. Pete, and R. C. Morris, "Tunable Alexandrite Lasers: Development and Performance," *IEEE J. Quantum Electron.* **QE-21,** 1568–1580 (1985).
21. J. C. Walling, O. G. Peterson, H. P. Jenssen, R. C. Morris, and E. W. O'Dell, "Tunable Alexandrite Lasers," *IEEE J. Quantum Electron.* **QE-16,** 1302–1314 (1980).
22. M. L. Shand, J. C. Walling, and R. C. Morris, "Excited-State Absorption in the Pump Region of Alexandrite," *J. Appl. Phys.* **52,** 953–955 (1981).
23. M. L. Shand, "The Quantum Efficiency of Alexandrite," *J. Appl. Phys.* **54,** 2602–2604 (1983).
24. M. L. Shand, J. C. Walling, and H. P. Jenssen, "Ground State Absorption in the Lasing Region of Alexandrite: Theory and Experiment," *IEEE J. Quantum Electron.* ***QE-18,*** 167–169 (1982).
25. M. L. Shand and H. P. Jenssen, "Temperature Dependence of the Excited State Absorption of Alexandrite," *IEEE J. Quantum Electron.* **QE-19,** 480–484 (1983).
26. J. C. Walling, O. G. Peterson, and R. C. Morris, "Tunable CW Alexandrite Laser," *IEEE J. Quantum Electron.* **QE-16,** 120–121 (1980).
27. R. L. Aggarwal, A. Sanchez, R. E. Fahey, and A. J. Strauss, "Magnetic and Optical Measurements on Ti:Al_2O_3 Crystal for Laser Applications," *Appl. Phys. Lett.* **48,** 1345–1347 (1986).
28. P. F. Moulton, "Spectroscopic and Laser Characteristics of Ti:Al_2O_3," *J. Opt. Soc. Am. B* **3,** 125–133 (1986).
29. P. Albers, E. Stark, and G. Huber, "Continuous-Wave Laser Operation and Quantum Efficiency of Titanium Doped Sapphire," *J. Opt. Soc. Am. B* **3,** 134–139 (1986).
30. L. G. DeShazer, J. M. Eggleston, and K. W. Kangas, "Oscillator And Amplifier Performance of Ti:Sapphire," in *Tunable Solid State Lasers II* (A. B. Budgor, L. Esterowitz, and L. G. DeShazer, Eds.), Springer Verlag, Berlin (1986).
31. A. Sanchez, A. J. Strauss, R. L. Aggarwal, and R. E. Fahey, "Crystal Growth, Spectroscopy, and Laser Characteristics Of Ti:Al_2O_3," *IEEE J. Quantum Electron.* **QE-24,** 995–1002 (1988).
32. P. Lacovara, L. Esterowitz, and R. Allen, "Flashlamp Pumped Ti:Al_2O_3 Using Fluorescent Conversion," *Opt. Lett.* **10,** 273–275 (1985).
33. E. G. Erickson, "The Flashlamp Pumped Titanium Sapphire Laser," in *Tunable Solid State Laser Conf.* May 1989, North Falmouth, MA.
34. N. P. Barnes and D. K. Remelius, "Amplifier and Line Narrowed Oscillator Performance of Ti:Al_2O_3," in *Tunable Solid State Lasers II* (A. B. Budgor, L. Esterowitz, and L. G. DeShazer, Eds.), Springer Verlag, Berlin (1986).
35. J. C. Barnes, N. P. Barnes, and G. E. Miller, "Master Oscillator Power Amplifier Performance of Ti:Al_2O_3," *IEEE J. Quantum Electron.* **QE-24,** 1029–1038 (1988).

36. A. Sanchez, R. E. Fahey, A. J. Strauss, and R. L. Aggarwal, "Room Temperature CW Operation of the Ti:Al_2O_3 Laser," in *Tunable Solid State Lasers II* (A. B. Budgor, L. Esterowitz, and L. G. DeShazer, Eds.), Springer Verlag, Berlin (1986).
37. H. W. Lee, S. A. Payne, and L. L. Chase, "Excited State Absorption of Cr^{3+} In $LiCaAlF_6$: Effects of Asymmetric Distortions And Intensity Selection Rules," *Phys. Rev. B* **39,** 8907–8914 (1989).
38. S. A. Payne, L. L. Chase, L. J. Atherton, J. A. Caird, W. L. Kway, M. D. Shinn, R. S. Hughes, and L. K. Smith, "Properties and Performance Of The $LiCaAlF_6$:Cr^{3+} Laser Material," *Proc. SPIE* **1223**, 84–93 (1990).
39. B. W. Woods, S. A. Payne, J. E. Marvin, R. S. Hughes, and L. E. Davis, "Thermomechanical and Thermo-optical Properties of the $LiCaAlF_6$:Cr^{3+} Laser Material," *J. Opt. Soc. Am. B* **8,** 970–977 (1991).
40. S. A. Payne, L. L. Chase, and G. D. Wilke, "Optical Spectroscopy of the New Laser Material, $LiSrAlF_6$:Cr^{3+} and $LiCaAlF_6$:Cr^{3+}," *J. Luminescence* **44,** 167–176 (1989).
41. L. L. Chase and S. A. Payne, "New Tunable Solid State Lasers, Cr^{3+}:$LiCaAlF_6$ and Cr^{3+}:Li-$SrAlF_6$," *Opt. Photon. News*, pp. 16–18 (1990).
42. S. A. Payne, L. L. Chase, L. K. Smith, W. L. Kway, and H. W. Newkirk, "Laser Performance of $LiSrAlF_6$:Cr^{3+}," *J. Appl. Phys.* **66,** 1051–1056 (1989).
43. S. A. Payne, L. L. Chase, L. K. Smith, and B. H. Chai, "Flashlamp Pumped Laser Performance of $LiCaAlF_6$:Cr^{3+}," *Opt. Quantum Electron.* **21,** 1–10 (1990).
44. M. Stalder, B. H. Chai, M. Bass, "Flashlamp Pumped Cr:$LiSrAlF_6$ Laser," *Appl. Phys. Lett.* **58,** 216–218 (1991).
45. S. A. Payne, L. L. Chase, H. W. Newkirk, L. K. Smith, and W. F. Krupke, "$LiCaAlF_6$:Cr^{3+}:" A Promising New Solid State Laser Material," *IEEE J. Quantum Electron.* **QE-24,** 2243–2252 (1988).
46. S. A. Payne, L. L. Chase, L. K. Smith, W. L. Kway, and H. W. Newkirk, "Laser Performance of $LiSrAlF_6$:Cr^{3+}:" *J. Appl. Phys.* **66,** 1051–1056 (1989).
47. W. Koechner, *Solid State Laser Engineering*, Springer Verlag, New York (1971).
48. J. A. Williams-Byrd and N. P. Barnes, "Laser Performance, Thermal Focusing, and Depolarization Effects In Nd:Cr:GSGG And Nd:YAG," *Proc. SPIE* **1223,** 237–246 (1990).
49. E. V. Zharikov, N. N. Il'ichev, S. P. Kalitin, V. V. Lapetev, A. A. Malyutin *et al.*, "Tunable Laser Utilizing an Electric-Vibrational Transition in Chromium in Gadolinium Scandium Gallium Garnet Crystal," *Sov. J. Quantum Electron.* **13,** 1274–127 (1983).
50. J. V. Meier, N. P. Barnes, D. K. Remelius, and M. R. Kokta, "Flashlamp-Pumped Cr^{3+}:GSAG Laser," *IEEE J. Quantum Electron.* **QE-22,** 2058–2063 (1986).
51. E. V. Zharikov, N. N. Il'ichev, S. P. Kalitin, V. V. Lapetev, A. A. Malyutin *et al.*, "Color Centers and Absorption From Cr^{3+} Excited State in a GSGG Crystal," *Izvestia Akademii Nauk. USSR, Seriya Fizicheskaya*, **48,** 1354–1358 (1984).
52. E. V. Zharikov, V. V. Laptev, E. I. Sidorova, Yu. P. Timofeev, and I. A. Shcherbakov, "Absolute Quantum Efficiency of the Luminescence of Cr^{3+}+ Ions in Gadolinium Gallium and Gadolinium Scandium Gallium Garnet Crystals," *Sov. J. Quantum Electron.* **12,** 1124–1125 (1982).
53. N. P. Barnes, D. K. Remelius, D. J. Gettemy, and M. R. Kokta, "Cr:YSAG-A Tunable Near Infrared Laser Material," in *Tunable Solid State Lasers II* (A. B. Budgor, L. Esterowitz, and L. G. DeShazer, Eds.), Springer Verlag, Berlin (1986).
54. B. Struve and G. Huber, "Tunable Room-Temperature CW Laser Action in Cr^{3+}:GdScGaGarnet," *Appl. Phys. B* **30,** 117–120 (1983).
55. J. Drube, B. Struve, and G. Huber, "Tunable Room Temperature CW Laser Action in Cr^{3+}:GdScAlGarnet," *Opt. Commun.* **50,** 45–48 (1984).
56. L. F. Johnson, H. J. Guggenheim, and R. A. Thomas, "Phonon-Terminated Optical Masers," *Phys. Rev.* **149,** 179–185 (1966).
57. S. A. Payne, L. L. Chase, and G. D. Wilke, "Excited State Absorption Spectra of V^{2+} in $KMgF_3$ and MgF_2," *Phys. Rev. B* **37,** 998–1006 (1988).

58. D. Welford and P. F. Moulton, "Room Temperature Operation of a Co:MgF_2 Laser." *Opt. Lett.* **13,** 975–977 (1988).
59. M. D. Sturge, "Temperature Dependence of Multiphonon Nonradiative Decay at an Isolated Impurity." *Phys. Rev. B* **8,** 6–14 (1973).
60. L. F. Johnson, H. J. Guggenheim, and D. Bahnck, "Phonon-Terminated Laser Emission from Ni^{2+} Ions in $KMgF_3$." *Opt. Lett.* **8,** 371–373 (1983).
61. P. F. Moulton, "An Investigation of the Co:MgF_2 Laser System," *IEEE J. Quantum Electron.* **QE-21,** 1582–1595 (1985).
62. P. F. Moulton kindly provided these absorption spectra.
63. P. F. Moulton and A. Mooradian, "Broadly Tunable CW Operation of Ni:MgF_2 and Co:MgF_2 Lasers." *Appl. Phys Lett.* **35,** 838–840 (1971).
64. P. F. Moulton, A. Mooradian, and T. B. Reed, "Efficient CW Optically Pumped Ni:MgF_2 Laser," *Opt. Lett.* **3,** 164–166 (1978).
65. M. Born and E. Wolf, *Principles of Optics*, Pergamon Press, New York (1964).
66. M. Littman, and H. Metcalf, "Spectrally Narrow Pulsed Dye Laser Without Beam Expander," *Appl. Opt.* **17,** 2224–2227 (1978).
67. K. Liu and M. Littman, "Novel Geometry for Single-Mode Scanning of Tunable Lasers." *Opt. Lett.* **6,** 117–118 (1981).
68. B. Lyot "Un Monochromateur a Grand Champ Utilisant les Interferences en Lumiere Polarisee" *Compt. Rend.* **197,** 1593 (1933).
69. J. W. Evans, "The Birefringent Filter," *J. Opt. Soc. Am.* **39,** 229–242 (1949).
70. A. L. Bloom, "Modes of a Laser Resonator Containing Tilted Birefringent Plates." *J. Opt. Soc. Am.* **64,** 447–452 (1974).
71. N. P. Barnes, J. A. Williams, J. C. Barnes, and G. E. Lockard, "A Self Injection Locked, Q-Switched, Line Narrowed Ti:Al_2O_3 Laser," *IEEE J. Quantum Electron.* **QE-24,** 1021–1028 (1988).
72. A. N. Bondarenko, K. G. Folin, V. A. Smirnov, and V. V. Antsiferov, "Generation Induced in a Q-Switched Ruby Laser by an External Signal." *JETP Lett.* **6,** 178–180 (1967).
73. Y. K. Park, G. Giuliani, and R. L. Byer, "Stable Single Axial Mode Operation Of A Q-Switched Nd:YAG Oscillator By Injection Locking," *Opt. Lett.* **5,** 96–98 (1980).
74. N. P. Barnes and J. P. Barnes, "Injection Seeding: Model," and J. C. Barnes, N. P. Barnes, L. G. Wang, and W. C. Edwards, "Injection Seeding: Ti:Al_2O_3 Experiments," *IEEE J. Quantum Electron.* **QE-29,** 2670–2683 (1993).
75. J. C. Barnes, N. P. Barnes, L. G. Wang, and W. Edwards, "Injection Seeding: Ti:Al_2O_3 Experiments." *IEEE J. Quantum Electron.* **29,** 2684 (1993).

7 Optical Parametric Oscillators

Norman P. Barnes
NASA Langley Research Center
Hampton, Virginia

1. INTRODUCTION

Optical parametric oscillators are a convenient method to create a widely tunable source of laser radiation. An optical parametric oscillator begins with a pump laser. In many cases the pump laser is a well-behaved solid-state laser such as a Nd:YAG laser or a frequency-doubled Nd:YAG laser. To complete the system, a nonlinear crystal between a set of mirrors is required. As such, the optical parametric oscillator by itself is an extremely simple device. Using an optical parametric oscillator, any wavelength longer than the pump wavelength and nominally within the transparency region of the nonlinear crystal can be created. However, practical problems limit the range of generated wavelengths to those that are somewhat longer than the pump wavelength, nominally a factor of 1.2 or so.

Optical parametric oscillators may be regarded as photon splitters. That is, a pump photon is split into two photons or one photon divides itself to create two photons. To satisfy conservation of energy, the sum of the energy of the two created photons must equal the energy of the pump photon. With the energy of a photon given by $h\nu$ where h is Planck's constant and ν is the frequency of the photon, the conservation of energy can be written as

Tunable Lasers Handbook
Copyright © 1995 by Academic Press, Inc. All rights of reproduction in any form reserved.

$$\nu_1 = \nu_2 + \nu_3 \ . \tag{1}$$

In this expression, the subscript 1 denotes the pump, 2 denotes the signal, and 3 denotes the idler. By convention, the signal is the higher of the two generated frequencies. Any pair of frequencies can be generated, but only frequencies that satisfy the conservation of momentum will be generated efficiently. Conservation of momentum can be expressed as

$$\mathbf{k}_1 = \mathbf{k}_2 + \mathbf{k}_3 \ . \tag{2}$$

In this expression, $\mathbf{k}_i$ is the wave vector at frequency ν_i. For the most common situation where the interacting beams are collinear, the vector relation simplifies to an algebraic relation. Substituting $2\pi n_i h\nu_i$ for the wave vector, the relation becomes

$$n_1 \nu_1 = n_2 \nu_2 + n_3 \nu_3 \ , \tag{3}$$

where n_i is the refractive index at the i'th frequency. In practice, the conservation of momentum will limit the generated wavelengths to a relatively narrow spectral bandwidth.

Optical parametric oscillators have several desirable features including a wide range of tunability. In practice, the ultimate tuning range of the optical parametric oscillator is limited only by the conservation of momentum or the range of transparency of the nonlinear material. Consequently, the practical range of tuning is usually very wide and is set by the available transmission properties of the ancillary optics. Not only is the tuning range wide, the gain is relatively flat. To first-order approximation, the gain of the optical parametric device is maximized at the degenerate wavelength, which is where the signal and idler are equal. Away from the degenerate wavelength, gain decreases relatively slowly as the wavelength of the device is tuned to other wavelengths. Another advantage of this device is the inherent wavelength selectivity of the device. Although lasers with wide spectral bandwidths are available, several wavelength control devices are often used to effect the tuning. Optical parametric oscillators, on the other hand, have a built-in wavelength control mechanism, namely, the requirement to satisfy the conservation of momentum. Conservation of momentum does not provide fine wavelength control, but it does provide broad wavelength control.

Optical parametric oscillators have several other desirable features including a compact size, good beam quality, and the potential of high-gain amplifiers. A simple optical parametric oscillator consists of a nonlinear crystal in a resonator. As such, these devices can easily be hand-held items. In principle, the mirrors could be coated on the nonlinear crystal if a more compact device is required, however, this would limit the flexibility of the system. The beam qual-

ity of the device is usually good although it does depend on the beam quality of the pump laser. Heat loads on the optical parametric oscillator are usually quite small, thus minimizing the effects of thermally induced distortions on the beam quality. In addition, optical parametric amplifiers are available by simply deleting the mirrors forming the resonator. By utilizing optical parametric amplifiers, the output of an optical parametric oscillator can be amplified to the desired level. Optical parametric amplifiers are especially attractive because they are usually high-gain devices.

Optical parametric oscillators do require a pump laser, often with good beam quality. Although optical parametric devices are usually compact, the size of the system does depend on the size of the pump laser. Because optical parametric oscillators are so small, the size of the system is essentially the size of the ancillary pump laser. With the maturation of diode-pumped solid-state lasers, the size of the pump laser should decrease considerably. As optical parametric oscillators convert pump photons, the system efficiency is limited by the efficiency of the pump laser. In general, the evolution of diode-pumped solid-state lasers will also make a significant increase in the system efficiency. In addition to the limitation of the efficiency set by the efficiency of the pump laser, the optical parametric oscillator is limited by the ratio of the photon energy of the generated wavelength to the photon energy of the pump wavelength. For efficient systems, thus, the generated wavelength should be relatively close to the pump wavelength.

Although optical parametric oscillators have many desirable features, they have been limited in application to date primarily by the limited nonlinear crystal selection and the availability of damage-resistant optics. Even though nonlinear crystals have been investigated nearly as long as lasers themselves, the crystal selection was limited. However, a recent interest in these devices has been spurred by the introduction of several new nonlinear crystals, which have improved the performance of optical parametric oscillators. The efficiency of these devices is dependent on the power density incident on the nonlinear crystal. A high power density is required for efficient operation. Usually, the power density is limited by laser induced damage considerations. Initially, the laser induced damage threshold limited the performance of existing nonlinear crystals. However, some of the newer nonlinear crystals have demonstrated higher laser induced damage thresholds. In addition, advances in optical fabrication and coating technology should further improve the laser induced damage threshold. With these advances, optical parametric devices should become more efficient.

Optical parametric oscillators were demonstrated only a few years after the first demonstration of the laser itself [1]. For this demonstration, a Q-switched and frequency-doubled $Nd:CaWO_4$ laser served as a pump for a $LiNbO_3$ optical parametric oscillator. Tuning was accomplished by varying the temperature of the device, and the device was tuned between about 0.96 to 1.16 μm. However, the output power was low, about 15 W of peak power. From this initial demonstration, the state of the art has improved to where peak powers well above 1.0 MW

are available and the tuning is limited essentially by the range of transparency of the nonlinear crystal.

Nonlinear optics devices in general and optical parametric oscillators in particular have received a significant amount of theoretical attention. Nonlinear interactions between three waves have been investigated by several authors [2,3]. In the first, the interaction between planes waves was considered. A treatment that allowed a variable phase between the interacting plane waves and also a depletion of the various waves provided a description where complete conversion could be achieved under ideal conditions. However, in reality, a plane wave is a mathematical fiction. Consequently, in the second of these treatments, the effects of a finite beam size were considered under the approximation of negligible depletion of the pump wave. In actual situations, the effects of both finite beam size and pump depletion should be taken into account.

A comprehensive review of the progress to date on optical parametric oscillators was given several years after the first introduction of the optical parametric oscillator [4]. In this review, the effects of Gaussian beam radii on the interaction were considered as well as the effects of singly resonant and doubly resonant optical parametric oscillator resonators. In addition, a calculation of the threshold pumping power was included and an estimate of the saturation and power output was given, A figure of merit to characterize the utility of nonlinear crystals was also introduced.

A later investigation of optical parametric oscillators focused on both the threshold and the linewidth of the device. Dependence of the threshold on the resonator length, the nonlinear crystal length, and the pump beam radius was measured and compared with the model developed to describe the operation of the device [5,6]. Linewidth was controlled by means of gratings, etalons, and the natural frequency-selective properties of the optical parametric interaction, including the aperture effect imposed by the finite pump beam radius. Combining these effects by using a square root of the sum of the squares technique, good agreement was obtained between the measured linewidth and the combination of the calculated linewidths. It has also been shown that calculations of the linewidths require an expansion of the phase mismatch retaining terms through second order [7].

Another treatment investigated the average power limit imposed on the optical parametric oscillator imposed by crystal heating that was caused by absorption of the interacting waves. Because absorption occurs throughout the volume of the nonlinear crystal while cooling occurs at the surface, thermal gradients within the nonlinear crystal are established. Because the refractive index depends on the temperature, phase matching cannot be maintained over the entire interaction volume. As the average power increases, the thermal gradients also increase, thereby limiting the volume over which the nonlinear interaction is effective. As the volume of the interaction decreases, the efficiency of the interaction also decreases. Average power limits have been estimated for the optical parametric interaction for both Gaussian and circular beam profiles [8].

2. PARAMETRIC INTERACTIONS

Optical parametric oscillators and amplifiers can be created by using the frequency mixing properties in nonlinear crystals. Nonlinearity in crystals can be characterized through a set of nonlinear coefficients. In general, the polarization of a crystal can be expanded in a power series of the applied electric field. For most materials, the components of polarization vector P_i are linearly related to the components of the applied electric field vector E_i. Subscripts refer to the vector components of the polarization and the electric field and are usually expressed in Cartesian coordinates. Nonlinear crystals have a significant nonlinear response to the electric field which can be described by

$$P_{i,NL} = \varepsilon_0 \sum_j d_{ij} (EE)_j \ , \tag{4}$$

where ε_0 is the permittivity of free space, d_{ij} are components of a 3×6 tensor, and $(EE)_j$ is the product of the applied electric fields creating the nonlinear polarization. Because the polarization depends on the product of the applied electric fields, frequency mixing can occur. That is, the product of the two electric fields will contain terms at both sum and difference frequencies. Sum and difference frequencies are obtained by expanding the product of two sine waves using trigonometric identities. Optical parametric oscillators use this effect to generate new frequencies or wavelengths from the pump.

Components of the nonlinear tensor depend on the symmetry of the nonlinear crystal. For a nonlinear crystal with very low symmetry, all 18 components of the nonlinear tensor may exist. However, in general, crystal symmetry minimizes the number of independent components. Depending on the symmetry, some of the components are zero while other components may be simply related to each other. For example, some components may be equal to a given component or equal to the negative of a given component. Which components exist depends on the point group of the nonlinear crystal. Given the point group, the nonzero components and the relations between them can be determined by referring to tables [9].

To satisfy conservation of momentum, the nonlinear interaction usually occurs in a birefringent crystal. Over the range of transparency, the refractive index of a crystal is usually a monotonically decreasing function of wavelength. If this is the case, the crystal is said to have *normal dispersion*. Thus, in isotropic materials where there is only one refractive index, conservation of momentum cannot be satisfied. To satisfy conservation of momentum, a birefringent nonlinear crystal is utilized since, in these crystals, two indices of refraction are available.

In birefringent crystals the refractive index depends on the polarization as well as the direction of propagation. In uniaxial birefringent crystals, at a given wavelength, the two refractive indices are given by [10]

$$n = n_0 \quad , \tag{5}$$

$$n = \left[\frac{\cos^2(\theta)}{n_o^2} + \frac{\sin^2(\theta)}{n_e^2} \right]^{-1/2} \quad , \tag{6}$$

In this expression, n_o is the ordinary refractive index, n_e is the extraordinary refractive index, and θ is the direction of propagation with respect to the optic axis. For propagation normal to the optic axis, the extraordinary refractive index becomes n_e. Thus, the extraordinary refractive index varies from n_o to n_e as the direction of propagation varies from 0° to 90°. If there is a large enough difference in the ordinary and extraordinary refractive indices, the dispersion can be overcome and the conservation of momentum can be satisfied. A similar, but somewhat more complicated, situation exists in biaxial birefringent crystals.

Given the point group of the nonlinear crystal, an effective nonlinear coefficient can be defined. To calculate the effective nonlinear coefficient, the polarization and the direction of propagation of each of the interacting waves must be determined. Components of the interacting electric fields can then be determined by using trigonometric relations. If the signal and idler have the same polarization, the interaction is referred to as a Type I interaction. If, on the other hand, the signal and idler have different polarizations, the interaction is referred to as a Type II interaction. By resolving the interacting fields into their respective components, the nonlinear polarization can be computed. With the nonlinear polarization computed, the projection of the nonlinear polarization on the generated field can be computed, again using trigonometric relations. These trigonometric factors can be combined with the components of the nonlinear tensor to define an effective nonlinear coefficient. With a knowledge of the point group and the polarization of the interacting fields, the effective nonlinear coefficient can be found in several references [11]. Tables 7.2 and 7.3 tabulate the effective nonlinear coefficient for several point groups.

Given an effective nonlinear coefficient, the gain at the generated wavelengths can be computed. To do this, the parametric approximation is usually utilized. In the parametric approximation, the amplitudes of the interacting electric fields are assumed to vary slowly compared with the spatial variation associated with the traveling waves. At optical wavelengths, this is an excellent approximation. If, in addition, the amplitude of the pump is nearly constant, the equation describing the growth of the signal and the idler assumes a particularly simple form [12–14]:

$$\frac{\partial E_2}{\partial z} = -2\pi j \eta_2 \nu_2 d_e E_1 E_3^* \exp\left(-j\Delta k z\right) \quad , \tag{7}$$

$$\frac{\partial E_3^*}{\partial z} = -2\pi j \eta_3 \nu_3 d_e E_1 E_2 \exp\left(-j\Delta k z\right) . \tag{8}$$

In these expressions E_i is the electric field, η_i is the impedence, ν_i is the frequency, d_e is the effective nonlinear coefficient, Δk is the phase mismatch, and j is the square root of -1. Subscripts 1, 2, and 3 refer to the pump, the signal, and the idler, respectively. Phase mismatch is the deviation from ideal conservation of momentum, or

$$\Delta k = 2\pi \left(\frac{n_1}{\lambda_1} - \frac{n_2}{\lambda_2} - \frac{n_3}{\lambda_3} \right) . \tag{9}$$

When the idler is initially zero but the signal is not, the coupled equations can be solved exactly to yield

$$S_2 = S_{20} \left(1 + (\Gamma l)^2 \sinh^2 \left[(\Gamma l)^2 - \left(\frac{\Delta k l}{2} \right)^2 \right]^{1/2} / \left[(\Gamma l)^2 - \left(\frac{\Delta k l}{2} \right)^2 \right] \right) . \tag{10}$$

In this expression, S_2 is the intensity of the signal, S_{20} is the initial intensity of the signal, l is the length of the nonlinear crystal, and

$$\Gamma = \frac{4\pi^2 d_e^2 |E_1|^2}{n_2 n_3 \lambda_2 \lambda_3} . \tag{11}$$

Although this expression describes the growth of plane waves well, in reality the interacting beams are not plane waves but are more likely to be Gaussian beams. When the interacting beams are Gaussian, the gain must be averaged over the spatial profile of the laser beam.

Two common approximations are available for this expression that demonstrate the limiting performance of parametric amplification. If the mismatch is small compared with the gain, that is, if Δk is much smaller than Γ, this term can be neglected. In this case

$$S_2 = S_2 \cosh^2 \left[\Gamma l \right] . \tag{12}$$

Thus, the signal will enjoy exponential gain as long as the pump is not depleted. On the other hand if the gain is small compared with the mismatch, that is, if Γ is much smaller than Δk, this term can be neglected. In this case,

$$S_2 = S_2\left[1 + (\Gamma l)^2 \sin^2(\Delta kl/2)/(\Delta kl/2)^2\right] . \tag{13}$$

In this case, energy can be transferred between the pump and the signal and idler beams and back again.

When a Gaussian beam enjoys a gain profile created by a Gaussian pump beam, an average-gain concept can accurately describe the situation. An average gain can be computed by integrating the product of the initial signal and the gain created by a Gaussian pump beam. With a Gaussian pump beam, the square of the electric field can be expressed as

$$|E_2|^2 = \frac{2}{c\varepsilon_0 n_1}\frac{2P_1}{\pi w_1^2}\exp\left(\frac{-2\rho^2}{w_1^2}\right) , \tag{14}$$

where c is the speed of light, P_1 is the power of the pump beam, w_1 is the beam radius, and ρ is the radial coordinate. When the electric field of the pump varies with radial position, the gain also varies radially since Γ depends on the electric field of the pump. An average gain G_a can be defined as [15]

$$G_a = \int_0^\infty \frac{2}{\pi w_2^2}\exp\left(\frac{-2\rho^2}{w_2^2}\right)\cosh^2(\Gamma l)2\pi\rho d\rho . \tag{15}$$

Although this expression cannot be integrated in closed form, it is readily amenable to integration using numerical techniques. Note that this expression represents a power gain. Energy gain can then be readily computed by integrating this expression over time.

Gain in parametric amplifiers has been characterized experimentally and found to agree with the predictions of the model. For these experiments, a continuous wave (cw) HeNe laser operating at 3.39 μm was used as the signal, and a pulsed Er:YLF laser, operating at 1.73 μm, was used as the pump. Both the energy and the pulse length of the pump laser were measured to determine the power of the laser. Beam radii of both the pump and the signal beam were measured using a translating knife-edge technique. Pump energies ranged up to 15 mJ, and the pulse lengths, represented by τ_1, were typically around 180 ns. Even with this relatively low power, single-pass gains in excess of 13 were observed. In Fig. 1, the experimental gain of the signal versus $(E_1/\tau_1)^{1/2}$ is plotted along with the average gain computed from Eq. (15). To within experimental error, the agreement between the experiment and the prediction of the average gain is found to be reasonable. High single-pass gains available with optical parametric amplifiers make their use attractive in high-energy-per-pulse situations.

While high-gain optical parametric amplifiers are possible, amplified spontaneous emission (ASE) does not affect these devices like it affects laser amplifiers.

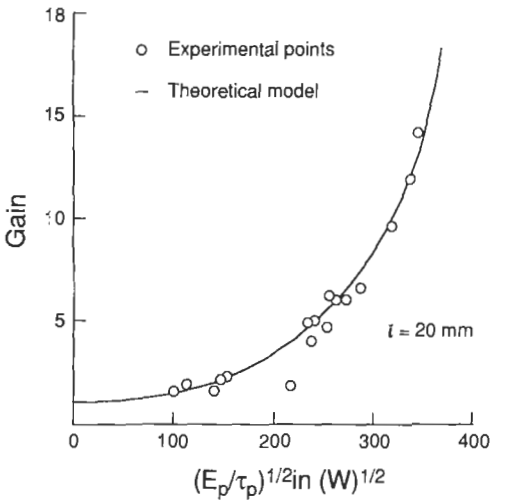

FIGURE 1 Average gain of 3.39-μm HeNe laser as a function of pump power.

In a laser amplifier, energy is stored in the laser material for long time intervals, on the order of 100 μs. During this time interval, spontaneous emission can deplete the stored energy, thus reducing the gain. In an optical parametric amplifier, energy is not stored in the nonlinear material. In addition, gain is only present while the pump pulse traverses the nonlinear crystal, a time interval on the order of 10 ns or less. As such, ASE does not detract from the gain significantly.

3. PARAMETRIC OSCILLATION

Whereas parametric amplification occurs at any pump level, parametric oscillation exhibits a threshold effect. The threshold of a parametric oscillator can be determined for either pulsed or cw operation of the device. In a cw parametric oscillator, threshold will occur when gain exceeds losses in the resonator even though the time interval required to achieve steady state may be relatively long. In a pulsed parametric oscillator, on the other hand, gain may exceed the losses with no measurable output. In these cases, the pump pulse may become powerful enough to produce a net positive gain. However, before the generated signal reaches a measurable level, the pump power falls below the level at which positive gain is achieved. Consequently, to describe this situation both an instantaneous threshold and an observable threshold are defined. Pulsed gain is shown in Fig. 2 with a threshold set by the losses in the parametric oscillator resonator. Although an observable threshold depends on the detection system, it remains a useful concept. As the signal grows below observable threshold, it will enjoy

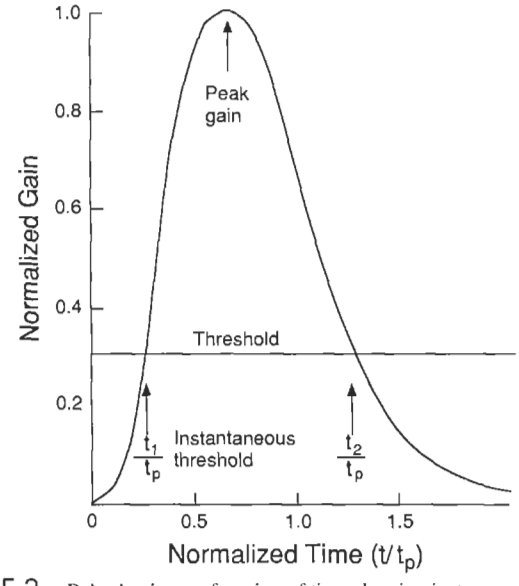

FIGURE 2 Pulsed gain as a function of time showing instantaneous threshold.

exponential gain. Because of this large gain, the difference between an observable threshold that produces 1.0 or 10.0 μJ is relatively small.

In the cw parametric oscillator, a mode gain can be determined under threshold conditions. Because the pump beam will not be significantly depleted at threshold, the longitudinal variation of the pump beam may be neglected. Because the product of two Gaussian beams is another Gaussian beam, interacting beams will generate a nonlinear polarization, which is also a Gaussian. If the electric fields at wavelengths λ_i and λ_j interact, they will generate a nonlinear polarization at wavelength λ_k, which will have a spatial variation characterized by a beam radius given by

$$\frac{1}{w_{kg}^2} = \frac{1}{w_i^2} + \frac{1}{w_j^2} \ . \tag{16}$$

Note that the generated nonlinear polarization does not necessarily have the same spatial variation as the incident field at λ_k. Because of the potential mismatch between the incident electric field and the generated electric field, the gain coefficient will have an additional term to account for this effect [6]. Including this term in the gain expression yields

$$(\Gamma l)^2 = \frac{8\pi^2 d_e^2 l^2 P_1}{n_1 n_2 n_3 \lambda_2 \lambda_3 c \varepsilon_0} \frac{8}{\pi} \left(\frac{w_1 w_2 w_3}{w_1^2 w_2^2 + w_1^2 w_3^2 + w_2^2 w_3^2} \right)^2 \ . \tag{17}$$

Considerable simplification can result in this expression depending on whether the optical parametric oscillator is singly or doubly resonant.

In singly resonant oscillators, only one of the generated waves is resonant. Either the signal or the idler could be the resonant wave. In general, singly resonant oscillators are preferred for pulsed applications where the gain is high. In doubly resonant oscillators, both the signal and the idler are resonant. Doubly resonant oscillators are often used for cw applications because of the lower threshold. Doubly resonant oscillators are often more challenging to control spectrally because generated wavelengths must satisfy conservation of energy, conservation of momentum, and the resonant condition. If the parametric oscillator is a singly resonant device, only one of the generated waves has a beam radius determined by the configuration of the resonator. If, for example, the signal is resonant, the idler beam radius will be given by

$$\frac{1}{w_3^2} = \frac{1}{w_1^2} + \frac{1}{w_2^2} \ . \tag{18}$$

In this situation, the gain coefficient simplifies to

$$(\Gamma l)^2 = \frac{8\pi^2 d_e^2 l^2 P_1}{n_1 n_2 n_3 \lambda_2 \lambda_3 c \varepsilon_0} \frac{2}{\pi\left(w_1^2 + w_2^2\right)} \ . \tag{19}$$

A similar expression can be obtained if the idler is resonant by interchanging the subscripts. To maximize the gain, the pump beam radius and the resonant beam radius can be minimized. However, eventually laser induced damage or birefringence effects will limit the minimum practical size for the beam radii.

If the parametric oscillator is a doubly resonant device, both of the generated waves have a beam radius determined by the configuration of the resonator. To maximize the gain for a doubly resonant device, the beam radius of the pump can be optimized. Performing the optimization yields a beam radius for the pump, which is given by

$$\frac{1}{w_1^2} = \frac{1}{w_2^2} + \frac{1}{w_3^2} \ . \tag{20}$$

Utilizing the optimum pump beam radius yields a gain coefficient given by

$$(\Gamma l)^2 = \frac{8\pi^2 d_e^2 l^2 P_1}{n_1 n_2 n_3 \lambda_2 \lambda_3 c \varepsilon_0} \frac{2}{\pi\left(w_2^2 + w_3^2\right)} . \tag{21}$$

As in the case of the singly resonant oscillator, gain can be increased by decreasing the beam radii of the resonant beams. However, also as in the singly resonant

device, laser induced damage and birefringence will limit the minimum size of the resonant beam radii.

Given the expressions for the gain, threshold can be defined by equating the gain and the losses. For cw operation, threshold will occur when [4]

$$\cosh\left(\Gamma l\right) = 1 + \frac{\alpha_2\alpha_3}{2 - \alpha_2 - \alpha_3} \ , \tag{22}$$

where α_2 is the round trip field loss at the signal wavelength and α_3 is the round trip field loss at the idler wavelength. In the singly resonant case and under small gain, α_2 is near unity and α_3 is near zero. Under these circumstances, the threshold for the singly resonant signal becomes approximately

$$\left(\Gamma l\right)^2 = 2\alpha_3 \ . \tag{23}$$

A similar expression exists for the situation where the signal is resonant. Again under the small-gain approximation but in the doubly resonant situation where both effective reflectivities are close to unity, the approximate expression for threshold becomes

$$\left(\Gamma l\right)^2 = \alpha_2\alpha_3 \ . \tag{24}$$

By employing a doubly resonant parametric oscillator, the threshold can be reduced substantially since α_2 can be an order of magnitude smaller than 2.0.

An observable threshold can be defined for pulsed parametric oscillators. An instantaneous threshold for a pulsed parametric oscillator is similar to the threshold for the cw case just defined. To define the observable threshold, Fig. 2 can be utilized. At time t_1, a net positive gain exists. At this time, the signal and the idler begin to evolve from the zero point energy. At time t_2 the pump power decreases to a point where the net gain is no longer positive. In the interim, as the signal and idler evolve, they are initially too small to be observed. For an observable threshold to be achieved, the power level in the resonator must increase essentially from a single circulating photon to a level that is amenable to measurement. To accomplish this, the gain must be on the order of exp(33).

Observable threshold depends on the time interval over which a net positive gain exists as well as how much the pump power exceeds the pump power required for threshold. For a circular pump beam, the observable threshold can be approximated by a closed-form expression [8]. In this approximation, a gain coefficient can be defined as

$$\left(\Gamma_0 l\right)^2 = \frac{8\pi^2 d_e^2 l^2}{n_1 n_2 n_3 \lambda_2 \lambda_3 c\varepsilon_0} \frac{2E_1}{\pi w_1^2 r_1} \frac{2^{1/2}}{\pi} \ . \tag{25}$$

Using the gain defined in Eq. (25), the number of times over threshold, N, can be defined by using

$$\frac{1}{N} = \frac{-ln\left(R_m T_c\right)}{2\Gamma_0 l} \ , \tag{26}$$

where R_m is the mean reflectivity of the mirrors at the resonant wavelength and T_c is the transmission of the nonlinear crystal. With these definitions, an observable threshold will be achieved at an approximate time when

$$33 = \frac{c\Gamma_0 l\tau_1}{l_c}\left[1 - \exp\left(\frac{-t^2}{\tau_1^2}\right) - \frac{2t}{N\tau_1} + \frac{2}{N^2}\right] \ . \tag{27}$$

In this expression, the pump pulse length τ_1 is related to the full width at half-maximum (FWHM) pulse length τ_{pl} through the relation

$$\tau_{pl} = 0.82\tau_1 \ . \tag{28}$$

If time t is less than the time at which the gain falls below the positive value, that is, t_2, an observable threshold will be achieved.

A slope efficiency can also be estimated for an optical parametric oscillator. Eventually, the slope efficiency will be limited by the ratio of the photon energies. At best, each pump photon will produce a single photon at both the signal and idler wavelengths. Thus, the energy conversion efficiency will be limited by the ratio of the photon energy at the output wavelength to the photon energy at the pump wavelength; that is, the slope efficiency will be limited to λ_1/λ_2 when the output is at the signal. In a singly resonant oscillator, in essence, all of the generated signal photons will be available for the output. However, for a doubly resonant oscillator, some of the generated photons will be dissipated by losses within the resonator. Consequently, for a double resonant oscillator, the ultimate slope efficiency will be limited by the ratio of the fractional output to the total losses in the resonator. If R_{2m} represents the output mirror reflectivity wavelength and R_{2l} represents the other losses at the signal wavelength, the ultimate slope efficiency will be further limited by the ratio of the output to the total losses, that is $ln(R_{2m})/ln(R_{2m}R_{2l})$. In many instances the losses in the parametric oscillator resonator can be kept small so that this ratio can be relatively high.

Experiments have demonstrated the validity of the basic approach [16,17]. For one set of experiments, an Er:YLF pump laser was used with a singly resonant

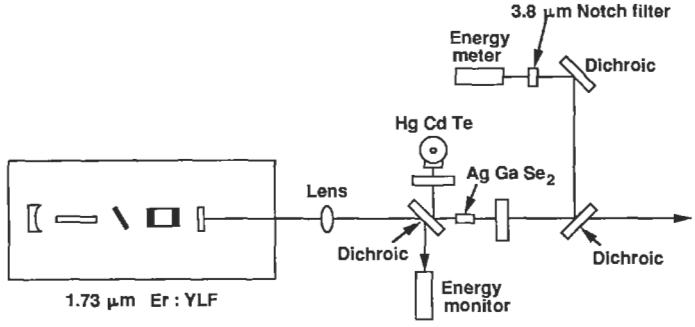

FIGURE 3 An $AgGaSe_2$ optical parametric oscillator experimental arrangement utilizing an Er:YLF pump laser.

$AgGaSe_2$ optical parametric oscillator. For these experiments, the signal was resonant rather than the idler, as shown in Fig. 3. The idler wavelength was 3.82 μm. A pump beam was introduced through a folding mirror within the optical parametric oscillator resonator. Output energy of the optical parametric oscillator was measured as a function of the pump energy for various lengths of the resonator. A typical plot of the results appears in Fig. 4. Data were extrapolated to define a threshold, and a slope efficiency was determined at an input energy 1.5 times the threshold.

Because the threshold depends on the number of passes the evolving signal can make through the gain medium, it can be reduced by decreasing the length of the parametric oscillator resonator. A shorter resonator length also improves the slope efficiency. By providing a shorter pulse evolution time interval, more of the pump pulse is available to be converted to useful output. Thus, both the threshold and the slope efficiency will benefit from a shorter resonator.

Benefits of a shorter resonator are displayed in Fig. 5. Data in this figure are presented for the same experimental configuration described previously. Threshold decreases, perhaps linearly, as the resonator length is decreased. For the shortest resonator length, the slope efficiency reaches 0.31. It may be noted that the ratio of the photon energies for this situation is 0.45. Thus, the observed slope efficiency is about ⅔ of the maximum slope efficiency.

4. SPECTRAL BANDWIDTH AND ACCEPTANCE ANGLES

Spectral bandwidth, acceptance angles, and allowable temperature variations are determined from the conservation of momentum or phase-matching condition. To satisfy the conservation of energy and momentum simultaneously requires a precise relation among the refractive indices at the various wavelengths. Referring to the previous section on parametric amplification, it can be shown that the efficiency of a low-gain and low-conversion nonlinear interaction

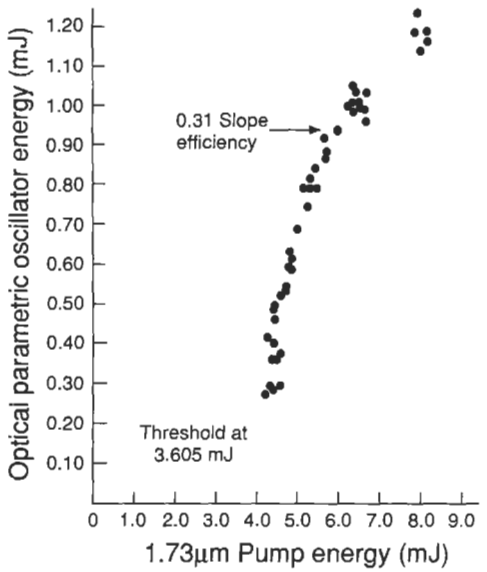

FIGURE 4 The $AgGaSe_2$ optical parametric oscillator output energy versus Er:YLF pump energy.

decreases according to a $\sin^2(x)/x^2$ relation. An allowable mismatch can be defined as

$$\Delta kl/2 = \pi/2 \ . \tag{29}$$

At this point, a nonlinear interaction decreases to about $(4/\pi^2)$ the efficiency of the ideally phase-matched interaction. For nonlinear interactions in the optical region of the spectrum, the ratio of the length of the nonlinear crystal to the wavelength is a large number. Thus to make the phase mismatch small, the relation among the three refractive indices becomes relatively strict. Because the refractive indices depend on the direction of propagation and temperature as well as the wavelengths, rather small variances are set for these parameters in order to satisfy the phase-matching condition.

Allowable variances for these parameters can be calculated by expanding the phase-matching condition in a Taylor series about the phase-matching condition. In general, if x is the parameter of interest, the mismatch can be expanded as follows [7]

$$\Delta k = \Delta k_0 + \frac{\partial \Delta k}{\partial x}\Delta x + \frac{1}{2}\frac{\partial^2 \Delta k}{\partial x^2}\Delta x^2 \ . \tag{30}$$

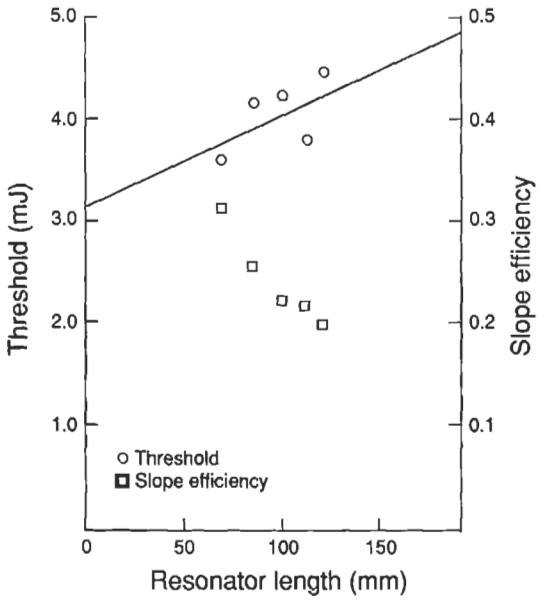

FIGURE 5 The $AgGaSe_2$ optical parametric oscillator threshold and slope efficiency versus resonator length.

By evaluating the expression at the phase-matching condition, the zeroth-order term vanishes. In most cases, the first term then dominates. When this is the case, the allowable variance of the parameter of interest is simply

$$\Delta x = \frac{\pi/l}{\partial \Delta k/\partial x} \ . \tag{31}$$

However, in many cases, the first-order term vanishes or is comparable to the second-order term. For example, the first-order derivative with respect to angle vanishes for noncritical phase matching. First-order derivatives with respect to wavelength can also vanish, often when the generated wavelengths are in the mid-infrared region [7]. In these cases, both the first- and second-order terms must be evaluated and the resulting quadratic equation must be solved to determine the allowable variance.

Acceptance angles should be calculated for orthogonal input angles. Consider the case where the ideally phase-matched condition defines a direction of propagation. For now, consideration will be restricted to uniaxial crystals. For the situation shown in Fig. 6 the ideally phase-matched direction and the optic axis of the crystal will define a plane referred to as the *optic plane*. For an arbitrary direction of propagation, two angles can be defined, one in the optic plane and the other orthogonal to the optic plane. In an uniaxial crystal, the refractive

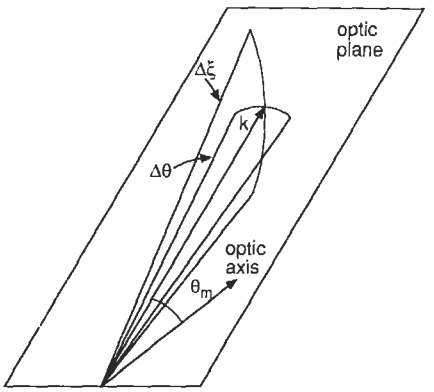

FIGURE 6 Definition of orthogonal acceptance angles for a uniaxial crystal.

index varies as the angle in the optic plane varies but is independent, to first order, of a variation of the angle orthogonal to the optic plane. In the optic plane, the derivative of the refractive index with angle is

$$\frac{\partial n}{\partial \theta} = \frac{n^3\left(n_0^2 - n_e^2\right)}{n_0^2\, n_e^2} \sin\left(\theta\right) \cos\left(\theta\right) . \tag{32}$$

Having evaluated the derivative of the refractive index with angle, the variation of the wave vector for extraordinary waves is

$$\frac{\partial k}{\partial \theta} = \frac{2\pi}{\lambda} \frac{\partial n}{\partial \theta} . \tag{33}$$

For ordinary waves, this derivative is, of course, zero. In most cases, the first-order derivative will dominate. As such, the acceptance angle will be determined using the first-order approximation. However, orthogonal to the optic plane, the first-order term vanishes. Here, the acceptance angle is determined by the second-order term. Usually, the first-order term will restrict the acceptance angle an order of magnitude more than the second-order term. First-order acceptance angles are often on the order of a few milliradians, comparable to the beam divergence of the laser in many cases. Because the second-order term is so much less restrictive, the acceptance angle orthogonal to the optic plane is often ignored. In biaxial crystals, the acceptance angles in orthogonal directions assume much more importance. In these crystals, the refractive index will, in general, depend critically on variations in the direction of propagation in both directions.

Measured acceptance angles agree well with the acceptance angles predicted using the preceding analysis. Although many examples are available, only

one will be presented [15]. Measurement of the acceptance angle can be performed using parametric amplifier experiments. Amplifier experiments can be used directly since the interacting wavelengths are fixed in these experiments. In parametric oscillator experiments, changing the angle at which the nonlinear crystal is oriented will tend to change the wavelength. As such, a measurement of the parametric oscillator output as a function of the orientation of the nonlinear crystal is likely to produce a tuning curve rather than a measurement of the acceptance angle. Data on the parametric amplifier presented here are for an $AgGaSe_2$ parametric amplifier pumped by a Ho:YAG laser. In this case, the $AgGaSe_2$ is ≈20 mm in length and oriented at ≈48° to the direction of propagation. A 3.39-μm HeNe laser is being amplified. Measured amplification as a function of the angular orientation of the crystal is shown in Fig. 7. Also shown is the predicted relative amplification as a function of the orientation of the crystal. To obtain the predicted relative amplification versus angle a relation of the form $\sinh^2[(\Gamma l)^2 - (\Delta kl/2)^2]/[(\Gamma l)^2 - (\Delta kl/2)^2]$ is used since the low-gain approximation is not valid in this case. Results of this experiment, as well as many others cited in the literature, tend to confirm the validity of this analysis.

The spectral bandwidth of the nonlinear interaction will be determined much like the acceptance angle in some respects. For optical parametric oscillators, the pump wavelength is usually fixed. However, as the signal wavelength varies, the idler wavelength can vary in order to satisfy conservation of energy or vice versa. Thus, a variation in one of these wavelengths will produce a com-

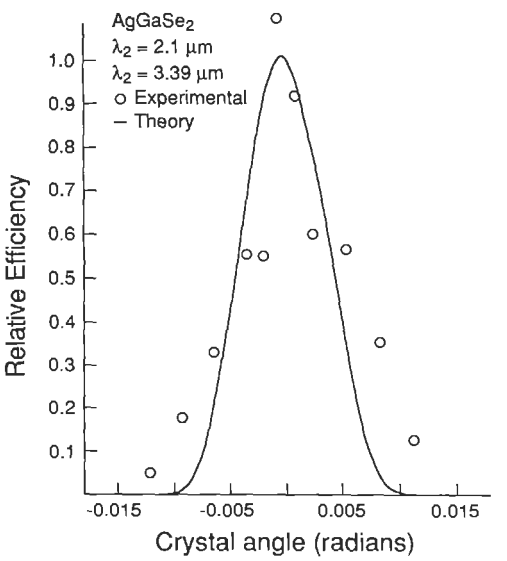

FIGURE 7 Measured acceptance angle.

pensating variation in the other wavelength. Keeping the pump wavelength fixed and taking the derivative of the mismatch with respect to the signal wavelength produces

$$\frac{d\Delta k}{d\lambda_2} = \frac{\partial \Delta k}{\partial \lambda_2} - \frac{\lambda_3^2}{\lambda_2^2}\frac{\partial \Delta k}{\partial \lambda_3} \quad . \tag{34}$$

When taking the derivatives of the phase mismatch with respect to the wavelength, the pump wavelength can be considered to be fixed. Evaluating the partial derivatives in Eq. (34) yields

$$\frac{\partial \Delta k_i}{\partial \lambda_i} = \frac{2\pi}{\lambda_i}\frac{\partial n_i}{\partial \lambda_i} - \frac{n_i}{\lambda_i} \quad . \tag{35}$$

Derivatives of the refractive index with respect to wavelength can be determined using experimental refractive index data or curve fits to the experimental refractive index data. If a standard two-pole Sellmeier expression is used, then

$$\frac{\partial n}{\partial \lambda} = -\frac{\lambda}{n}\left[\frac{BC}{\left(\lambda^2 - C\right)^2} + \frac{DE}{\left(\lambda^2 - E\right)^2}\right] \quad . \tag{36}$$

With these expressions, the single-pass spectral bandwidth of a difference frequency interaction can be calculated.

To calculate the spectral bandwidth of an optical parametric oscillator, the number of passes of the signal through the nonlinear crystal must be taken into account. Calculated using equations 31 and 34 is the spectral bandwidth for a single pass. However, during the pulse evolution, the signal makes repeated passes through the nonlinear crystal. Subsequent passes through the nonlinear crystal will continue to narrow the spectral bandwidth of the parametric oscillator. It has been shown [17–19] that the spectral bandwidth depends on the number of passes the radiation makes through the spectral narrowing device, in this case the nonlinear crystal. To take this effect into account, the calculated single-pass spectral bandwidth should be divided by the $p^{1/2}$, where p is the number of passes that occur during the pulse evolution time interval. An estimate of the number of passes the signal makes through the nonlinear crystal can be obtained from the pulse evolution time interval τ_e using the relation

$$p = c\tau_e / 2l_c \quad . \tag{37}$$

where c is the speed of light and l_c is the length of the parametric oscillator resonator.

The spectral bandwidth of the parametric oscillator depends on the spectral bandwidth of the pump laser as well as the spectral bandwidth of the interaction. Consider the situation in a singly resonant oscillator where, in addition, only a single resonant wavelength exists. If the pump laser consists of several wavelengths, each wavelength of the pump laser would mix with the single resonant wavelength of the parametric oscillator. As a result, each pump wavelength of the pump would produce a corresponding wavelength around the nonresonant wavelength. If $\Delta\lambda_1$ is the spectral bandwidth of the pump, the corresponding spectral bandwidth of the nonresonant wavelength is given by

$$\Delta\lambda_2 = \Delta\lambda_1 \lambda_2^2/\lambda_1^2 \ . \tag{38}$$

If the singly resonant oscillator does not restrict itself to a single wavelength but consists of a distribution of wavelengths with a spectral bandwidth of $\Delta\lambda_3$, then each resonant wavelength would mix with each pump wavelength to produce a corresponding wavelength around the nonresonant wavelength. In this case, the spectral bandwidth of the nonresonant wavelength can be approximated as

$$\Delta\lambda_2 = \lambda_2^2 \left(\Delta\lambda_1^2/\lambda_1^4 + \Delta\lambda_3^2/\lambda_3^4\right)^{1/2} . \tag{39}$$

For equal spectral bandwidths of the pump and the resonant wavelength, the spectral bandwidth of the pump is weighted more heavily since the pump wavelength is shorter.

The spectral bandwidth of the parametric oscillator can also depend on the beam divergence of the pump. Heretofore, the phase mismatch has been expanded using a single variable. However, this parameter can be expanded as a function of two variables; for example, the wavelength and the propagation of direction. For each direction of propagation there is a combination of the signal and idler that minimizes the phase mismatch. Because a pump beam with finite divergence can be decomposed into a distribution of plane waves, each having a slightly different direction of propagation, a variety of wavelengths could result. To estimate this effect, the phase mismatch can be expanded in a Taylor series of two variables. Keeping terms only through first order and expanding around the ideal phase-matching direction yields

$$\Delta k = \frac{\partial \Delta k}{\partial \lambda}\Delta\lambda + \frac{\partial \Delta k}{\partial \theta}\Delta\theta \ , \tag{40}$$

where θ is an angle in the optic plane of an uniaxial crystal. For a beam with a divergence of $\Delta\theta$, the corresponding spectral bandwidth becomes

$$2\Delta\lambda = \frac{2\left(\partial\Delta k/\partial\theta\right)\Delta\theta}{\partial\Delta k/\partial\lambda} \ . \tag{41}$$

For TEM_{00} mode pump beams, the divergence internal to the nonlinear crystal is

$$\Delta\theta = \lambda_1 / n_1 \pi w_1 \quad . \tag{42}$$

Using this for the beam divergence and evaluating the partial derivatives, the magnitude of this effect can be estimated.

Experimental results appear in agreement with this analysis of the spectral bandwidth. The spectral bandwidths of parametric oscillators have been determined experimentally for several situations [17,18]. In one instance, a Nd:YAG pump laser was utilized with a $LiNbO_3$ parametric oscillator. In this study, the wavelength control exerted by the nonlinear crystal was compared with wavelength control exerted by other wavelength control elements such as gratings and etalons. In the other instance, an Er:YLF laser was used to pump an $AgGaSe_2$ optical parametric oscillator. In this study the effects of the pump divergence on the spectral bandwidth are compared with the effects of the pump spectral bandwidth and the spectral bandwidth of the nonlinear interaction. Results are shown in Fig. 8. It is of interest that in both cases the spectral bandwidth is significantly increased by the pump beam divergence.

An allowable variation of the temperature can also be defined in a similar manner by expanding the phase-matching condition as a function of temperature. Expanding the phase mismatch as a function of the temperature T yields

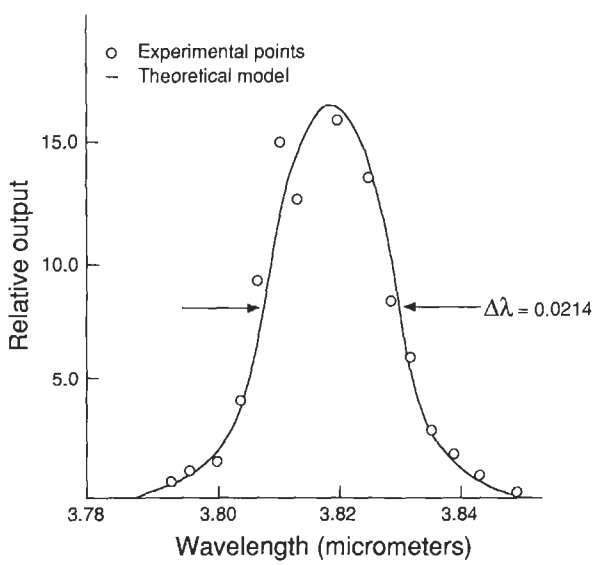

FIGURE 8 Measured spectral bandwidth.

$$\Delta k = \Delta k_0 + \frac{\partial \Delta k}{\partial T} \Delta T \quad . \tag{43}$$

Expansion is usually limited to first order because the variation of the refractive index with temperature is usually known only to first order. Expanding the first-order term yields

$$\frac{\partial \Delta k}{\partial T} = 2\pi \left(\frac{1}{\lambda_1} \frac{\partial n_1}{\partial T} - \frac{1}{\lambda_2} \frac{\partial n_2}{\partial T} - \frac{1}{\lambda_3} \frac{\partial n_3}{\partial T} \right) \quad . \tag{44}$$

For ordinary waves in uniaxial crystals, values for the variation of the refractive index with temperature can be used directly. For extraordinary waves, in general, the variation of the refractive index with temperature depends on the variation of the refractive index with temperature of both the ordinary and extraordinary waves. In uniaxial crystals this becomes

$$\frac{\partial n}{\partial T} = \frac{n^3 \cos^2(\theta)}{n_o^3} \frac{\partial n_o}{\partial T} + \frac{n^3 \sin^2(\theta)}{n_e^3} \frac{\partial n_e}{\partial T} \quad . \tag{45}$$

Substituting these expressions into the allowable phase mismatch yields the allowable temperature variation. Allowable temperature variation also enters into the calculation of the average power limit for a nonlinear interaction as well as the temperature tuning rate.

5. BIREFRINGENCE EFFECTS

Even though birefringence is necessary to produce an efficient interaction by compensating for dispersion, birefringence will eventually limit the efficiency of the interaction. Efficiency limitations can arise since the direction of energy propagation of ordinary beams and extraordinary beams is not, in general, collinear in a birefringent crystal. Even when both the ordinary and extraordinary beams are normally incident on the birefringent crystal, a difference in the direction of the energy propagation exists. The direction of energy propagation of a normally incident ordinary beam does not suffer any deviation when entering the crystal. On the other hand, the direction of energy propagation of a normally incident extraordinary beam occurs at an angle to the normal, denoted by ρ. For non-normal angles of incidence, both the ordinary and extraordinary beams are deviated by refraction, in accordance with Snell's law. However, in addition, the extraordinary beam still experiences the effects of the birefringence, again characterized by the birefringence angle ρ. To satisfy the phase-matching condition, at least one of the interacting beams is an ordinary beam and at least one is an extraordinary beam. Thus, eventually the interacting beams separate, causing a decrease in the efficiency of the nonlinear interaction.

Birefringence angles can be calculated in uniaxial crystals given the ordinary and extraordinary indices of refraction, n_o and n_e, respectively [20]. In a given direction of propagation, there are two refractive indices for the two polarizations. Specifying a direction of propagation θ and the two refractive indices, denoted by n_o and n_e, a refractive index for the extraordinary polarized ray can be calculated, similar to the calculations used for phase matching. With these, the birefringence angle in an uniaxial crystal can be expressed as

$$\tan(\rho) = n^2 \left(n_e^2 - n_o^2\right) \sin(\theta) \cos(\theta) / n_o^2 n_e^2 \ . \tag{46}$$

In an uniaxial crystal, the angle ρ is measured in the optic plane. In a biaxial crystal, a similar analysis can yield the birefringence angle.

Birefringence eventually limits the region of overlap of interacting beams and therefore the efficiency of the nonlinear interaction. To obtain an estimate of the limitation, the region of the overlap can be calculated for the situation depicted in Fig. 9. Considering the overlap, an effective length l_e can be calculated by considering the following

$$l_e = \left. \frac{\int_{-\infty}^{\infty} \int_{-\infty}^{\infty} \int_0^l E_3 E_1 E_2 \, dx \, dy \, dz}{\int_{-\infty}^{\infty} \int_{-\infty}^{\infty} E_3 E_1 E_2 \, dx \, dy} \right|_0 . \tag{47}$$

For extraordinary beams, the electric field can be represented as

$$E_i = \left(\frac{2}{\pi w_i^2}\right)^{1/2} \exp\left[\frac{-(x + \rho z)^2 - y^2}{w_i^2}\right] , \tag{48}$$

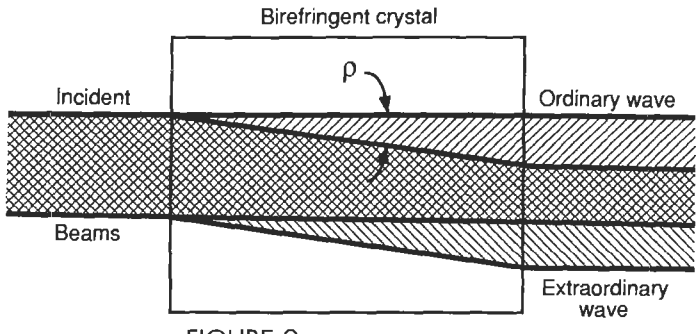

FIGURE 9 Birefringence effects.

where E_i is the electric field of the interacting wave and w_i is the beam radius. For ordinary waves, the expression for the electric field is similar but the birefringence angle is zero.

In the case of a singly resonant oscillator, an effective length for the nonlinear crystal can be calculated using the preceding expressions. As an example, consider the case where the signal is resonant. In this case, the beam radius of the nonresonant idler w_3 is given by

$$\frac{1}{w_3^2} = \frac{1}{w_1^2} + \frac{1}{w_2^2} \ . \tag{49}$$

With this nonresonant beam radius, the integral can be evaluated to obtain an effective length l_e for the nonlinear crystal:

$$l_e = l_w \operatorname{erf}\left(\pi^{1/2} l / 2 l_w\right) \ . \tag{50}$$

Here, erf(x) is the error function and l_w is a parameter that depends on the beam radii of the pump beam and signal beam as well as birefringence.

In general, the parameter l_w is sensitive to which beams are ordinary and extraordinary as well as which waves are resonant and nonresonant. If the pump beam is an extraordinary beam and the signal and idler are both ordinary beams while the signal is resonant, l_w can be expressed as [21]

$$l_w = \frac{\pi^{1/2} w_1}{2\rho_1}\left(\frac{w_1^2 + w_2^2}{w_1^2 + w_2^2/2}\right)^{1/2} \ . \tag{51}$$

If the pump beam and the resonant wave are extraordinary waves, the expression for l_w becomes [8]

$$l_w = \frac{\pi^{1/2}}{2}\left[\frac{2w_1^2 + w_2^2\left(w_1^2 + w_2^2\right)}{w_1^2 + w_2^2\left(\rho_1^2 - \rho_1\rho_2 + \rho_2^2\right) + \rho_1^2 w_2^4 + \rho_2^2 w_1^4}\right]^{1/2} \ . \tag{52}$$

For other combinations of ordinary and extraordinary beams as well as resonant and nonresonant waves, the parameter l_w can be calculated using the same approach.

Because birefringence is needed to effect phase matching, but the birefringence angle eventually limits the effective length of the nonlinear crystal, it is of interest to explore methods of achieving the former while minimizing the latter. One method of reaching this end is phase matching at 90° to the optic axis. If this

can be effected, it is often referred to as *noncritical phase matching*. If noncritical phase matching is achieved, the birefringence angles become zero leading to an infinite effective length for the nonlinear crystal. In addition, the acceptance angle for the nonlinear interaction becomes much larger since the first-order term in the expansion of the phase mismatch vanishes. Since the ordinary and extraordinary indices of refraction have different dependencies on the temperature, noncritical phase matching may be possible by varying the temperature. However, if this is not possible, it is advantageous to select a nonlinear crystal that minimizes the deleterious effects of birefringence. Minimization can be accomplished by minimizing the difference in the ordinary and extraordinary index of refraction, that is, the birefringence, without compromising phase matching. Thus, it is of interest to determine how much birefringence is required.

An estimate of the required birefringence is dependent on the dispersion of the nonlinear crystal. Dispersion of the nonlinear crystal is characterized by the first derivative of the index of refraction with respect to the wavelength—$\partial n/\partial\lambda$. If the interacting wavelengths are far from the absorption edges of the nonlinear crystal, the dispersion can be approximated as being nearly independent of wavelength. As a natural extension of this, birefringence also tends to be independent of wavelength. Within these constraints, the required birefringence Δn can be estimated for the various types of interactions. For Type I interactions, the required birefringence can be approximated as

$$|\Delta n| = |n_o - n_e| \approx -\lambda_1 \frac{\partial n_1}{\partial \lambda} \ . \tag{53}$$

For Type II interactions, a similar expression exists with the signal or idler wavelength replacing the pump wavelength, depending on which of these wavelengths has a different polarization compared to the pump wavelength. Birefringence in excess of this tends to limit the acceptance angle. In addition, more birefringence than required for phase matching exacerbates birefringence angle effects and thus the interaction length.

6. AVERAGE POWER LIMITATIONS

Thermally induced changes in the phase matching will limit the average power available from a nonlinear interaction. For all practical nonlinear crystals, significant absorption of the interacting wavelengths occurs even if the interacting waves are nominally in a transmitting region of the crystal. Absorption of the interacting wavelengths deposits heat throughout the volume of the nonlinear crystal. However, to dissipate the deposited heat, it must be conducted to the surface of the nonlinear crystal. Volumetric heating and surface cooling establish thermal gradients in the nonlinear crystal. Because the ordinary and extraordinary indices of refraction, in general, behave differently with temperature, the phase-matching condition cannot be maintained throughout the volume of the

nonlinear crystal. As the average power increases, the generated heat and the concomitant thermal gradients increase. Consequently, the effective volume of the nonlinear crystal decreases, which, in turn, eventually limits the average power that can be produced.

Average power limitations will depend on the geometry of the nonlinear crystal and the interacting beams. When considering the geometry of the nonlinear crystal, actual cooling conditions in many instances can be approximated by two limiting situations. In most common situations, the lateral surfaces of the nonlinear crystal are in thermal contact with a heat sink while the entrance and exit surfaces are essentially insulated. In this case, the thermal gradients can be approximated as being radial. However, it is also feasible to insulate the lateral surface on the nonlinear crystal and extract the heat through the entrance and exit surfaces. Heat extraction could be accomplished by flowing a transparent fluid with high heat capacity over these surfaces. Gaseous He is an attractive candidate for such a fluid. In this case, the thermal gradients would be approximately along the direction of propagation of the beams or longitudinal. Both cases are depicted in Fig. 10.

Thermal gradients in the nonlinear crystal also depend on the beam profiles of the interacting beams. Again two approximations are commonly used. If the beam has a constant intensity out to some limiting radius and is essentially zero elsewhere, the beam profile is referred to as a circular beam profile. Such beam profiles can approximate beam profiles from laser resonators with graded reflected mirrors or from saturated amplifiers. If, on the other hand, the interacting beams are constrained to TEM_{00} modes, the beam profile is referred to as a Gaussian beam profile. Initially, the average power limit was calculated for a Gaussian beam profile and with lateral heat extraction [22]. However, similar analyses have been performed for several combinations of beam profiles and heat extraction methods [23].

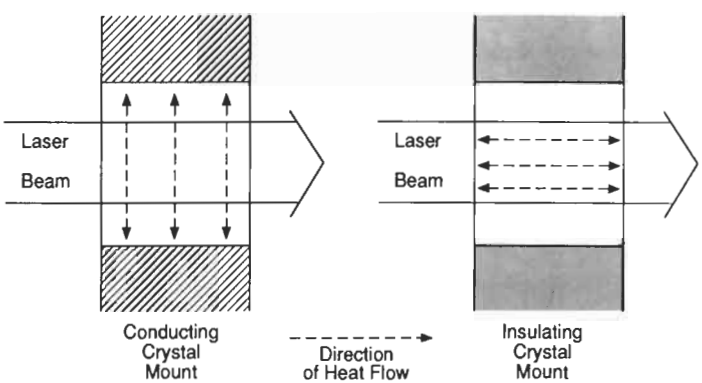

FIGURE 10 Heat flow in transversely and longitudinally cooled nonlinear crystals.

Under the assumption of radial crystal symmetry and lateral heat extraction, the phase mismatch can be approximated as a function of radial position, that is,

$$\Delta k = \Delta k_0 - a_{rc}\rho^2/w^2 \ , \tag{54}$$

$$\Delta k = \Delta k_0 - a_{rg}\left[1 - \exp\left(-\rho^2/w^2\right)\right] , \tag{55}$$

for a circular and a Gaussian beam profile, respectively. In these expressions a_{rc} and a_{rg} can be defined as

$$a_{rc} = \left(\frac{1}{\lambda_1}\frac{\partial n_1}{\partial T} - \frac{1}{\lambda_2}\frac{\partial n_2}{\partial T} - \frac{1}{\lambda_3}\frac{\partial n_3}{\partial T}\right)\frac{\beta_a P_a}{2k_c} \ , \tag{56}$$

$$a_{rg} = \left(\frac{1}{\lambda_1}\frac{\partial n_1}{\partial T} - \frac{1}{\lambda_2}\frac{\partial n_2}{\partial T} - \frac{1}{\lambda_3}\frac{\partial n_3}{\partial T}\right)\frac{\beta_a P_a}{k_c} \ , \tag{57}$$

In these expressions, $\partial n_i/\partial T$ is the variation with temperature of the refractive index n_i at wavelength λ_i, β_a is the average absorption coefficient, P_a is the average power, and k_c is the thermal conductivity. With the mismatch known as a function of the radial position, the conversion efficiency can be integrated over the cross section of the nonlinear crystal.

To explore this effect, a simple example can be investigated that illuminates the salient features. Effects of phase mismatch on parametric generation, under the low conversion efficiency approximation, can be described in terms of a $\sin^2(x)/x^2$ function. A relative efficiency η_R can be defined as the fractional decrease in the conversion efficiency caused by the effects of crystal heating. Integrating this over the cross section of the nonlinear crystal yields

$$\eta_R = \left(1/\pi w_c^2\right)\int_0^{2\pi}\int_0^{w_c} \sin^2\left(\Delta kl/2\right)/\left(\Delta kl/2\right)^2 \rho d\rho d\theta \tag{58}$$

Evaluation of this integral is straightforward using numerical techniques. Referring back to the expressions for Δk, it can be seen that there are two contributions, a zeroth-order term that does not depend on the average power and another term that does. The zeroth-order term represents the residual phase mismatch in the absence of average power heating effects. For cases where there is no average power heating effects, the residual phase mismatch is minimized. However, with average power heating effects, this term can be optimized for maximum efficiency.

Relative efficiency can be calculated as a function of the heating parameter for the cases of no zeroth-order phase mismatch and optimum zeroth-order phase mismatch. A heating parameter ($al/2$) can be defined substituting the definitions of a_{rc} and a_{rg} for a. In this expression, l is the length of the nonlinear crystal. Relative efficiency is plotted in Fig. 11 for two cases, one where the zeroth-order term is zero and one where the zeroth-order term is optimized. A negligible zeroth-order phase mismatch would occur if the nonlinear interaction were optimized at a low average power and then the average power were increased. An optimized zeroth-order phase mismatch would occur when the nonlinear interaction were optimized at the final average power. Note that the optimum value depends on the value of the heating parameter. As can be seen in the figure, by using an optimum zeroth-order term the average power term can be doubled. A similar calculation has been performed under the approximation of Gaussian beam profiles and the results are similar [23].

Average power limits depend on the absorption coefficients of the nonlinear crystal. Absorption coefficients depend on the wavelength; wavelengths nearer the transmission limits of the nonlinear crystal tend to be absorbed more

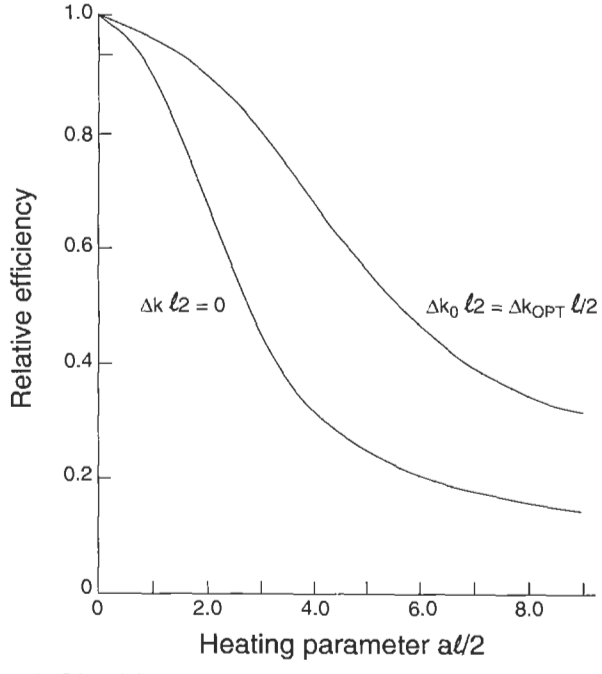

FIGURE 11 Relative efficiency versus heating parameter.

strongly. Absorption coefficients also depend strongly on purity of the crystal and the growth conditions. As such, the absorption coefficients can vary significantly from vendor to vendor and can also vary as a function of the date of purchase even if the crystals are from the same vendor. For many commercially available nonlinear crystals, absorption coefficients are on the order of 1.0 m^{-1} [24]. With absorption coefficients on this order, average power limits on the order of several watts appear feasible. However, optical materials with larger commercial demand can have significantly lower absorption coefficients. Because the heating parameter depends on the product of the average absorption coefficient and the average power, an order of magnitude decrease in the absorption implies an order of magnitude increase in the average power. Although absorption effects can impose practical limits, they can be mitigated through nonlinear crystal selection and crystal growth development efforts.

Pulse repetition frequency (prf) does not enter into the preceding estimate of the average power limit. As defined, the absorbed power which creates a thermal gradient large enough to limit the effective volume of the nonlinear crystal is estimated If absorption of the pump power is the primary contribution to the heating, then the average power of the pump rather than the prf per se is the primary factor. However, if the absorption of the signal or idler is the primary contribution to the heating, then the prf can have more of an effect. With a constant average power and a high prf, the pump energy per pulse decreases. If this in turn decreases the conversion efficiency, less heating can occur. As such, as the prf increases, the average power heating decreases. However, the signal and idler power still decrease because of the lower conversion efficiency of even the ideally phase-matched interaction.

If even higher average power is required, the nonlinear crystal can be fabricated into a series of thin plates. The thin plates could be cooled by flowing gas between them. In essence, this decreases the thermal gradient by increasing the surface to volume ratio of the nonlinear crystal [25]. For a geometry like this, the longitudinal heat extraction technique is appropriate. While this technique will work, antireflection coatings on the surfaces will be required. A practical limit on the thickness of the plates will be set by the fabrication process.

7. NONLINEAR CRYSTALS

Many good nonlinear crystals are currently available for optical parametric oscillators and amplifiers and new nonlinear crystals are being developed constantly. In the early days of the development of optical parametric oscillators and amplifiers, only a relatively few nonlinear crystals were available. In addition, the available nonlinear crystals had limited utility, either because of fundamental reasons or because of limited size and optical quality. Lack of good nonlinear crystals limited development of practical devices utilizing nonlinear crystals in these situations. Since then, many more nonlinear crystals have been discovered

and the size and optical quality has improved. With continued improvements, optical parametric oscillators and amplifiers should find increasing use.

Selection of the best nonlinear crystal for a particular application depends on several basic crystal parameters including the transparency. In approximate order of consideration, the nonlinear crystal parameters that must be considered in the selection process include range of transparency, phase matching, nonlinearity, birefringence, and temperature sensitivity. The rationale for nonlinear crystal selection using these parameters is presented in some detail in the following paragraphs. Germane parameters, where available, are listed for select nonlinear crystals in Table 1.

Transparency is an obvious requirement for the nonlinear crystal. However, it has been shown that a nonlinear interaction can occur even if one of the interacting waves is strongly absorbed [26]. Beyond the obvious, it is preferable to avoid the absorption edges of the crystal from an average power point of view. In addition, in cases where the crystal has limited birefringence, phase matching cannot be effected near either the ultraviolet or the infrared absorption edges since the absorption edges exhibit increased dispersion.

For efficient interactions, phase matching must be effected. Phase matching allows the entire length of the nonlinear crystal to contribute positively to the conversion efficiency. Nonlinear interactions can occur in situations where the phase-matching conditions can only be approximated by using plates cut to the coherence length. However, these situations require approximate phase matching in order to have reasonable lengths for the nonlinear crystal [27]. If approximate phase matching cannot be met, the coherence length and thus the nonlinear crystal length become short. In the low-conversion-efficiency regime, the conversion efficiency of a parametric interaction increases as the square of the length of the nonlinear crystal. Thus, phase matching must be possible in order to obtain long coherence lengths, and the concomitant long nonlinear crystal lengths, and therefore reasonable efficiencies.

Efficiency of the optical parametric oscillator or amplifier also depends critically on the effective nonlinearity. Again in the low-conversion-efficiency regime, the conversion efficiency depends on the effective nonlinearity squared. Because the effective nonlinearity depends on the orientation of the nonlinear crystal, the effective nonlinearity is dependent on the phase-matching conditions and the interacting wavelengths. Inspection of the gain coefficient shows that the effective nonlinearity is divided by the refractive indices. Consequently, a commonly used figure of merit for nonlinear crystal selection is $d_e^2/n_1n_2n_3$. Often this figure of merit is plotted as a constant over the range of transparency of the nonlinear crystal. That is, the variation of the effective nonlinearity with wavelength is neglected. Because conversion efficiency is directly proportional to the figure of merit in the low-conversion approximation, a high figure of merit is desirable.

Effective nonlinear coefficients depend on the direction of propagation, polarization of the interacting wavelengths, and the point group. Given this

TABLE 1 Physical Properties of Selected Nonlinear Crystals[a]

Crystal	Point group	Transmission	Index	Variation of index	Thermal conduction
ADP *o*	$\bar{4}2m$	0.18–1.5	1.5065	−49.3	1.26
e			1.4681	≈0.0	0.71
KDP *o*	$\bar{4}2m$	0.18–1.7	1.4938	−34.0	1.34
e			1.4599	−28.7	1.21
CD*A *o*	$\bar{4}2m$	0.27–1.7	1.5499	−23.3	1.5
e			1.5341	−16.7	
$LiNbO_3$ *o*	3m	0.33–5.5	2.2340	0.2	4.6
e			2.1554	40.9	4.8
BBO *o*	3m	0.20–2.2	1.6551	−16.6	1.2
e			1.5426	−9.3	1.6
KTP *x*	mm2	0.35–4.5	1.7386	22.0	2.0
y			1.7458	25.9	3.0
z			1.8287	42.8	3.3
LBO *x*	mm2	0.16–2.3	1.5656	−1.9	3.5
y			1.5905	−13.0	3.6
z			1.6055	−8.3	
$AgGaS_2$ *o*	42m	0.50–13	2.4508	17.2	1.5
e			2.2924	18.3	1.4
$AgGaSe_2$ *o*	42m	0.71–18	2.7005	77	1.1
e			2.6759	45	1.0
CdSe *o*	6mm	0.75–20	2.5375	120	12.0
e			2.5572	141	
$ZnGeP_2$ *o*	42m	0.74–12	3.2324	204.9	35
e			3.2786	223.5	36
Tl_3AsSe_3 *o*	3m	1.30–13	3.3799	−45.2	1.8
e			3.1899	35.5	
Units		μm		10^{-6}/K	W/m K

[a]Refractive indices and the variation of the refractive indices with temperature evaluated at 1.064 μm except for TAS, which is evaluated at 2.1 μm. Thermal conductivities are quoted for the different crystallographic directions where available. In some cases, only a single value for the thermal conductivity was available.

information, the effective nonlinear coefficient can be obtained by decomposing the interacting electric field vectors into the coordinate system of the nonlinear crystal and performing the matrix multiplication indicated in the previous sections. However, this has already been done and the effective nonlinear coefficient

TABLE 2 Effective Nonlinear Coefficient for Uniaxial Crystals[a]

Point group	Interactions 001, 010, 100	Interactions 110, 101, 011
3	$(d_{11}\cos 3\phi - d_{22}\sin 3\phi)\cos\theta + d15\sin\theta$	$(d_{11}\sin 3\phi + d_{22}\cos 3\phi)\cos^2\theta$
32	$d_{11}\cos\theta\cos 3\phi$	$d_{11}\cos^2\theta\sin 3\phi$
3m	$d_{15}\sin\theta - d_{22}\cos^2\theta\sin 3\phi$	$d_{22}\cos^2\theta\cos 3\phi$
4, 4mm	$d_{15}\sin\theta$	0
4	$(d_{14}\sin 2\theta + d_{15}\cos 2\phi)\sin\theta$	$(d_{14}\cos 2\phi - d_{15}\sin 2\phi)\sin 2\theta\}$
42m	$d_{36}\sin\theta\sin 2\phi$	$d_{36}\sin 2\theta\cos 2\phi$
6, 6mm	$d_{15}\sin\theta$	0
6	$(d_{11}\cos 3\phi - d_{22}\sin 3\phi)\cos\theta$	$(d_{11}\sin 3\phi + d_{22}\cos 3\phi)\cos^2\theta$
6m2	$d_{22}\cos\theta\sin 3\phi$	$d_{22}\cos^2\theta\cos\phi$

[a]In this notation, 0 represents an ordinary wave and 1 represents an extraordinary wave.

TABLE 3 Effective Nonlinear Coefficient in Biaxial Crystals

Point group	Plane	Interaction 001, 010, 100	Interaction 110, 101, 011
2	xy	$d_{23}\cos\phi$	$d_{36}\sin 2\phi$
	yz	$d_{12}\cos\theta$	$d_{36}\sin 2\theta$
	xz	0	$d_{21}\cos^2\theta + d_{23}\sin^2\theta + d_{36}\sin 2\theta$
222	xy	0	$d_{36}\sin 2\phi$
	yz	0	$d_{36}\sin 2\theta$
	xz	0	$d_{36}\sin 2\theta$
m	xy	$d_{13}\sin\phi$	$d_{31}\sin^2\phi + d_{32}\cos^2\phi$
	yz	$d_{31}\sin\theta$	$d_{13}\sin^2\theta + d_{12}\cos^2\theta$
	xz	$d_{12}\cos\theta - d_{32}\sin\theta$	0
mm2	xy	0	$d_{31}\sin^2\phi + d_{32}\cos^2\phi$
	yz	$d_{31}\sin\theta$	0
	xz	$d_{32}\sin\theta$	0

[a]In this notation, 0 represents an ordinary wave and 1 represents an extraordinary wave.

can be obtained by evaluating the expressions given in tables, such as Tables 2 and 3 [28,29]. For these tables, Kleinman's symmetry condition has been assumed. Values for the nonlinear coefficients of several common nonlinear crystals are found in Table 4 [30–32].

Kleinman's symmetry condition reduces the number of independent contributions to the nonlinear matrix and thus simplifies the expressions. Kleinman's symmetry condition assumes that the components of the nonlinear matrix which

TABLE 4 Nonlinear Coefficients for Selected Nonlinear Materials[a]

Crystal	Point group	Nonlinear Coefficients
ADP	42m	$d_{36} = 0.53$
KDP	42m	$d_{36} = 0.44$
CD*A	42m	$d_{36} = 0.40$
$LiNbO_3$	3m	$d_{22} = 2.76$ $d_{31} = -5.44$
BBO	3m	$d_{22} = 2.22$ $d_{31} = 0.16$
KTP	mm2	$d_{31} = 6.5$ $d_{32} = 5.0$ $d_{33} = 13.7$
		$d_{24} = 7.6$ $d_{15} = 6.1$
LBO	mm2	$d_{31} = -1.09$ $d_{32} = 1.17$ $d_{33} = 0.065$
$AgGaS_2$	42m	$d_{36} = 13.4$
$AgGaSe_2$	42m	$d_{36} = 37.4$
CdSe	6mm	$d_{15}5 = 18.0$
$ZnGeP_2$	42m	$d_{14} = 75.4$
Tl_3AsSe_3	3m	$d_{22} = 16.0$ $d_{31} = 15.0$

[a]Units of the nonlinear coefficients are 10^{-12} m/V.

merely permute the subscripts are equal. Conditions where this is valid can be met in cases where the dispersion of the electronic polarizability is negligible. Such conditions exist in a majority of practical crystals. Assumption of this symmetry condition simplifies the expressions for the nonlinear coefficient.

Birefringence must be sufficient to achieve phase matching and adequate tuning but beyond that more birefringence is not usually desirable. A large birefringence usually indicates a restricted acceptance angle and a large birefringence angle. Both of these effects can limit the efficiency of the parametric interaction. However, there are instances where angular tuning rates can benefit from a large birefringence.

Temperature sensitivity arises through the variation of the refractive indices with temperature. Because, in general, the variations of the ordinary and the extraordinary refractive index with temperature are different, the phase-matching condition varies with temperature. If this difference is large, a small variation in the ambient temperature changes the phase-matching condition and adversely affects the efficiency. Thus, to maintain the efficiency, temperature control of the nonlinear crystal may be required. Although temperature control is straightforward it adds complexity to the system. In high-power situations, a large difference in the variation of the refractive indices adversely affects the average power limits of a given nonlinear interaction. On the other hand, a large difference in the variation of the refractive indices with temperature may allow 90°

phase matching to be effected with a concomitant increase in the acceptance angle and possibly in the efficiency.

Several of the available nonlinear crystals can be evaluated by considering the factors just outlined. Because of space limitations, such a survey cannot evaluate all of the known nonlinear crystals. Consequently, only a few select nonlinear crystals are evaluated here. More nearly complete surveys can be found in the literature. In general, the nonlinear crystals can be divided into two categories, depending on their range of transparency. Oxide crystals will generally transmit in the visible and near infrared while the semiconductor materials can transmit from the near infrared through much of the mid-infrared region. Tables 1 and 4 summarize the important properties of the select nonlinear crystals for facile reference.

ADP, or $NH_4H_2PO_4$, was one of the earliest nonlinear crystals to be used. ADP existed before lasers were invented and was useful because of its piezoelectric properties. As such, nonlinear crystals large enough for practical devices were available immediately. However, it does have relatively low nonlinear coefficients, a somewhat limited acceptance angle, and is hygroscopic. To avoid degrading the optical faces of a hygroscopic crystal by exposure to a humid atmosphere, it is often kept in a sealed container that may be heated. Because of the large difference in the variation of the refractive indices with temperature, ADP can be temperature tuned over a relatively large range. Even though several useful nonlinear devices have been demonstrated using this material, its use has been declining, primarily because of the availability of better materials.

KDP, or KH_2PO_4, was also available before the invention of the laser. KD*P, an isomorph where the hydrogen is replaced by deuterium, has nearly identical nonlinear coefficients and refractive indices but better transmission in the near infrared, especially beyond about 1.0 μm. As such, KD*P is often preferred in cases where a high average power is required. Use of this material as a second harmonic generator for Nd:YAG lasers is common. However, like ADP, this crystal also has relatively low nonlinear coefficients and somewhat limited acceptance angle. KDP is also hygroscopic and therefore often kept in a crystal oven.

CD*A, or CsD_2AsO_4, is an isomorph of KDP and was developed primarily as a harmonic generator for Nd:YAG lasers. Its nonlinear coefficients are about the same as the previous two nonlinear crystals, but this material can achieve nearly noncritical phase matching for second harmonic generation of Nd:YAG lasers. Noncritical phase matching provides for a significantly enhanced acceptance angle and negligible birefringence angle effects. As with other KDP isomorphs, CD*A is hygroscopic.

$LiNbO_3$ was the first nonlinear crystal to demonstrate optical parametric oscillation. Nonlinear coefficients of this material are significantly larger than the previous three materials. However, this material suffered from optically induced refractive index inhomogeneities when irradiated with short-wavelength laser radiation. This deleterious effect can be mitigated by growing very pure materials, but it has not yet been eliminated. However, it has been discovered that this

effect could be annealed out if the temperature were high enough. Annealing temperatures range from about 100 to 200°C, depending on the purity of the nonlinear crystal. Another option to avoid this effect was to confine operation to long wavelengths, roughly longer than 1.0 μm. $LiNbO_3$ displays a relatively large difference in the variation of the ordinary and extraordinary refractive indices with temperature making temperature tuning of nonlinear devices practical.

KTP, or $KTiOPO_4$, properties allow it to overcome many of the shortcomings of the previous nonlinear crystals. KTP has large nonlinear coefficients, and can be phase matched to have a large acceptance angle. It is a biaxial material, unlike the previous materials, which are all uniaxial. Being biaxial allows a greater variety of phase-matching conditions to be explored in order to find a larger effective nonlinear coefficient, a larger acceptance angle, or both. Its initial acceptance was hindered by the availability of sufficiently large crystals, a problem that has been largely ameliorated. Its ultraviolet absorption edge tends to limit the use of this crystal in the visible region.

BBO, or the β phase of BaB_2O_4, is a nonlinear crystal that is finding applications in the visible and near infrared. It has relatively large nonlinear coefficients, good transmission in the visible region, and its large birefringence allows phase matching throughout the visible region of the spectrum. However, this large birefringence leads to birefringence angle and acceptance angle problems in some cases. It does appear that this material is slightly hygroscopic.

LBO, or LiB_3O_5, is also a nonlinear crystal that will have applications in the visible region of the spectrum. It has similar transmission as BBO, but it does not display nonlinear coefficients as large as BBO. However, they are larger than those available with the KDP isomorphs. It does not suffer from the large birefringent angle effects of BBO and its biaxial nature allows a wider range of phase-matching conditions to be explored. It does not appear that this material is hygroscopic.

CdSe has a wide range of transparency in the mid-infrared region and is one of the first of the mid-infrared nonlinear crystals to be useful for optical parametric oscillator applications. CdSe has large nonlinear coefficients that allow efficient interactions to occur despite the fact that the interactions occur at longer wavelengths. However, it has a relatively low birefringence that can allow long interactions lengths, but not all desired interactions can be phase matched in this material.

$AgGaS_2$ is an interesting crystal for several reasons other than its nonlinear properties. Although it is birefringent, its birefringence vanishes at one particular wavelength in the visible. Vanishing of the birefringence has led to other applications such as optical filters. If near-infrared as well as mid-infrared transmission is desired, this nonlinear crystal is a good choice. It has large nonlinear coefficients, but not as large as $AgGaSe_2$. Consequently, the latter crystal is often selected in preference to this crystal except in cases where better visible and near-infrared transmission is desired.

$AgGaSe_2$ has large nonlinear coefficients but suffered initially from limited transmission in the near infrared. Absorption in the near infrared has been mitigated to a large extent by an annealing process. Because of the large vapor pressure of Se, this material often grows Se deficient. To overcome this, grown crystals have been annealed in Se-rich atmospheres. By doing this, the absorption in the near infrared is substantially reduced. Birefringence of this material is sufficient to effect phase matching but not so large as to impose severe acceptance angle problems. Both optical parametric oscillators and amplifiers have been demonstrated using this material.

$ZnGeP_2$ has an even larger nonlinearity than $AgGaSe_2$. It too suffers from absorption problems in the near infrared. As this material has a high vapor pressure during growth, an absorption analogy with $AgGaSe_2$ is possible. Several approaches to lowering this absorption have been tried with varying degrees of success. Birefringence of this material allows phase matching of a wide variety of nonlinearity interactions without incurring severe birefringence effects. In addition, this material has better thermal characteristics than $AgGaSe_2$.

TAS, or Tl_3AsSe_3, is a mid-infrared nonlinear crystal with sufficient birefringence to allow phase matching of a wide variety of nonlinear interactions. It has reasonably large nonlinear coefficients that have allowed its use as a nonlinear crystal. However, as mid-infrared nonlinear crystals with even larger nonlinear coefficients are available, this material also has seen somewhat limited use.

8. PHASE-MATCHING CALCULATIONS

Phase-matching curves are used to describe the orientation of the nonlinear crystal for which phase matching will be achieved. In uniaxial crystals, the angle for which phase matching is achieved is usually displayed as a function of the interacting wavelengths. In biaxial crystals, two angles are needed to describe the orientation of the nonlinear crystal. Consequently, phase matching can be achieved at a locus of points. Thus, for a given set of interacting wavelengths, the locus of the phase matching angles is usually described in terms of the polar and azimuthal angles. To determine the phase-matching angle or angles, the refractive indices at the interacting wavelengths must be determined.

A Sellmeier equation can be used to describe the variation of the refractive indices with wavelength. Historically several equations have been used to describe the variation of the refractive index as a function of wavelength. However, the Sellmeier equation has several advantages, including a physical basis and the ability to describe accurately the refractive index over relatively large wavelength intervals. Several forms of the Sellmeier equation have been reported, but the form that is most usually associated with a physical basis is expressed as

$$n^2 = A + B\lambda^2/\left(\lambda^2 - C\right) + D\lambda^2/\left(\lambda^2 - E\right) . \tag{59}$$

In this expression, C represents the ultraviolet resonance wavelength squared and E represents the infrared resonance wavelength squared. In the same context, B and D represent the strengths of the ultraviolet and infrared absorption resonances, respectively.

If the ultraviolet or infrared resonances are not approached too closely, this form can represent the refractive index quite accurately. As the resonances are approached, effects such as the finite width of the resonance and the possibility of multiple resonances can detract from the accuracy. Typically, by adding a second ultraviolet resonance, the fit may be improved; especially as the ultraviolet resonance is approached. For example, the refractive index of Al_2O_3 has been accurately expressed using two ultraviolet resonances and an unity value for A [33]. However, away from the resonance, a nonunity value for A can be used to satisfactorily describe the refractive index without the added complexity of a double ultraviolet resonance.

Although the Sellmeier equation [given in Eq. (59)] has many desirable features, it is not universally utilized. However, to compute the refractive indices as well as the first and second derivatives of the refractive index with respect to wavelength, it is convenient to have a standard form for the expression relating the refractive index with the wavelength. Toward this end, original measurements of the refractive index as a function of wavelength were found and fitted to the standard form [34–44]. Results of the curve-fitting procedure are found in Table 5 for visible and mid-infrared crystals. In addition, the root mean square deviation between the calculated experimental values appears in Table 5. Typically, the experimental values are presented with four significant figures beyond the decimal point. Except for LBO, the root mean square deviation is in the fourth place after the decimal point. In cases where five significant figures were quoted in the cited literature (specifically ADP, KDP, and BBO), the fit is much better. The accuracy of this approach in describing the phase-matching angle has been demonstrated [17].

It is useful to have the temperature dependence of the refractive index built into the Sellmeier equation. With this feature, temperature tuning of the nonlinear interaction can be computed in a straightforward manner. In one case, this is possible since the refractive indices were measured accurately at two temperatures [36]. It is very convenient to have this information for $LiNbO_3$ because this nonlinear crystal is often operated at elevated temperatures when short wavelengths are among the interacting wavelengths. Operation of this nonlinear crystal at elevated temperatures helps control the optically induced refractive index inhomogeneities associated with the short wavelengths. If the material can be grown with close attention to the impurities, the optically induced refractive index inhomogeneities are annealed at about 105°C. Consequently, when a short-wavelength pump is used with this material, such as a 0.532-μm frequency-doubled Nd:YAG laser, the refractive indices associated with an elevated temperature should be used. Appropriate Sellmeier coefficients can be determined from the following relations.

$$A = 2.33907 + 8.20 \times 10^{-5} (T - 25)$$

$$B = 2.58395 - 10.47 \times 10^{-5} (T - 25)$$

$$C = 0.4588 + 1.13 \times 10^{-5} (T - 25)$$

$$D = 13.8169 + 7.73 \times 10^{-5} (T - 25)$$

$$E = 519.66$$

$$A = 2.35084 - 100.78 \times 10^{-5} (T - 25)$$

$$B = 2.22518 + 114.47 \times 10^{-5} (T - 25)$$

$$C = 0.04371 - 0.24 \times 10^{-5} (T - 25)$$

$$D = 15.9773 - 107.60 \times 10^{-5} (T - 25)$$

$$E = 741.15$$

for the ordinary and extraordinary Sellmeier refractive indices, respectively. In these expressions, temperature T is given in degrees centigrade. Operation at 105°C is only a small extrapolation of the refractive index data, taken at 25 and 80°C.

In cases where insufficient data are available for complete temperature-dependent Sellmeier coefficients, the variations of the ordinary and extraordinary refractive indices are given for selected wavelengths [35,37,41,45–47]. Far from the absorption features of the nonlinear crystal, the variation of the refractive index with temperature is relatively insensitive to the wavelength. Values for the variation of the ordinary and extraordinary refractive index with temperature are tabulated in Table 1.

Using the Sellmeier constants listed in Table 5, the phase-matching curves for Type I phase matching have been calculated for the selected uniaxial nonlinear crystals listed. For these calculations, pump wavelengths are 0.355, 0.532, 1.064, and 2.10 μm. Solid-state lasers make convenient pump sources for optical parametric oscillators because these lasers can operate either in a cw or a Q-switched mode. In particular, the Q-switched mode, with its short pulse lengths and concomitant high peak powers, is conducive to the operation of optical parametric oscillators and amplifiers. Pump lasers operating at these wavelengths can be obtained from a Nd:YAG laser and its harmonics or from either a Ho:Tm:Cr:YAG or Ho:Tm:Er:YLF laser. Phase-matching curves generated in this manner are not intended to be an exhaustive compilation of the possibilities but rather are intended to suggest some of the more common situations. Other possible

TABLE 5 Sellmeier Coefficients for Selected Nonlinear Crystals[a]

Crystal		A	B	C	D	E	σ_{rms}
ADP	*o*	1.37892	0.91996	0.01249	0.15771	5.7600	0.00015
	e	1.35302	0.80752	0.01227	0.02612	3.3156	0.00014
KDP	*o*	1.41344	0.84308	0.01229	0.26923	10.2480	0.00014
	e	1.40442	0.72733	0.01201	0.07974	12.4840	0.00007
CD*A	*o*	1.65075	0.75762	0.02218	0.03942	4.4399	0.00072
	e	1.69749	0.65313	0.02365	0.01710	7.5095	0.00065
$LiNbO_3$	*o*	2.33907	2.58395	0.04588	13.8169	519.658	0.00022
	e	2.35084	2.22518	0.04371	15.9773	741.146	0.00025
BBO	*o*	1.71283	1.02790	0.01790	2.23130	138.650	0.00013
	e	1.50569	0.86544	0.01512	0.56478	248.360	0.00014
KTP	*x*	2.22237	0.78681	0.04746	0.67167	54.90	0.00039
	y	2.30590	0.72572	0.05387	1.00870	77.50	0.00043
	z	2.35249	0.96655	0.05812	1.24674	77.50	0.00065
LBO	*x*	2.07557	0.38193	0.02597	2.60858	191.04	0.00052
	y	1.61856	0.92347	0.01355	4.48336	204.16	0.00109
	z	2.00372	0.58147	0.02176	2.55777	155.84	0.00077
$AgGaS_2$	*o*	3.02917	2.76318	0.08343	2.03585	910.181	0.00055
	e	3.31265	2.22509	0.10048	2.01258	911.484	0.00051
$AgGaSe_2$	*o*	4.08904	2.76132	0.15669	11.72170	9502.6	0.00065
	e	4.44502	2.23490	0.20592	8.64984	7054.4	0.00032
CdSe	*o*	4.16222	1.82886	0.22148	2.48631	3840.03	0.00014
	e	4.01216	2.07364	0.20209	13.8169	2235.17	0.00022
$ZnGeP_2$	*o*	4.64467	5.10087	0.13656	4.27777	1653.89	0.00048
	e	4.71534	5.26358	0.14386	2.39310	1000.82	0.00058
T13AsSe3	*o*	1.0	9.977	0.18923	0.067	400.0	
	e	1.0	8.782	0.18923	0.051	400.0	

[a]Wavelengths are in micrometers.

combinations can be obtained in a straightforward manner once the Sellmeier constants are known.

ADP, KDP, and CD*A can be used to generate output at wavelengths in the visible and near infrared, to about 1.1 μm or somewhat beyond. ADP and KDP are very similar, even to the shape of the phase-matching curve (Fig. 12). CD*A, on the other hand, does not have enough birefringence to be pumped by a 0.355-μm pump. However, by using a 0.532-μm pump, a parametric device tunable at wavelengths longer than about 0.85 μm is possible (Fig. 13). As phase matching can be obtained very near 90°, long nonlinear crystals may be employed without seriously affecting efficiency through the deleterious effects of birefringence.

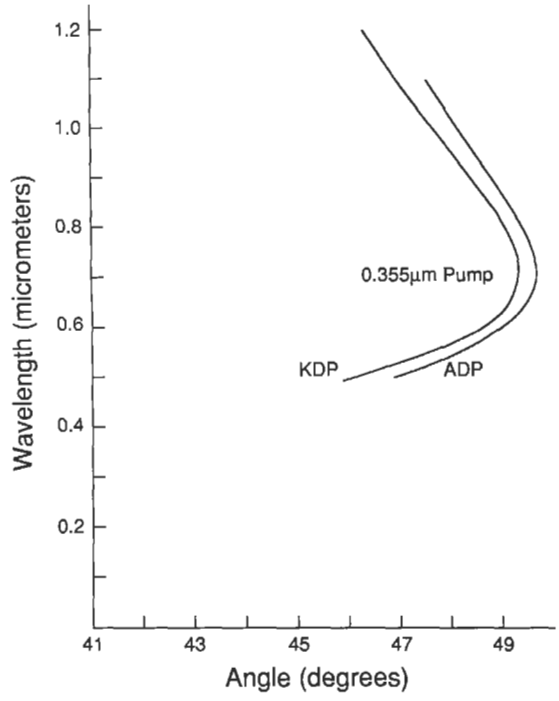

FIGURE 12 Phase-matching curves for ADP and KDP for a 0.355-μm pump.

Tunable radiation in the near infrared can be obtained from an optical parametric oscillator using a 0.532-μm pump and a $LiNbO_3$ or BBO nonlinear crystal (Figs. 14, 15, and 16). Operation at somewhat longer wavelengths than shown in the figures may be possible, depending on the infrared absorption properties of the particular nonlinear crystal. Because of absorption, calculations were not carried out beyond 2.2 μm in BBO and 4.0 μm in $LiNbO_3$. A device based on BBO would be attractive because a single crystal could be used to tune over a very large wavelength range. On the other hand, a device based on $LiNbO_3$ would be attractive if a narrow spectral bandwidth device were desired.

A Nd:YAG laser can be used directly as a pump source for at least three different nonlinear crystals, $LiNbO_3$, BBO, and $AgGaS_2$ (as shown in Figs. 15, 16, and 17). In the first case, the range from about 1.4 μm to beyond 4.0 μm could be covered with a single $LiNbO_3$ crystal. BBO could not cover the same range due to transparency limitations. On the other hand, $AgGaS_2$ could be tuned over a much wider range, from about 2.0 to beyond 10.0 μm. However, this tuning range would require a variation in the phase-matching angle of about 20°. Since the Nd:YAG laser has enjoyed a significant amount of development, such a system appears to be very attractive.

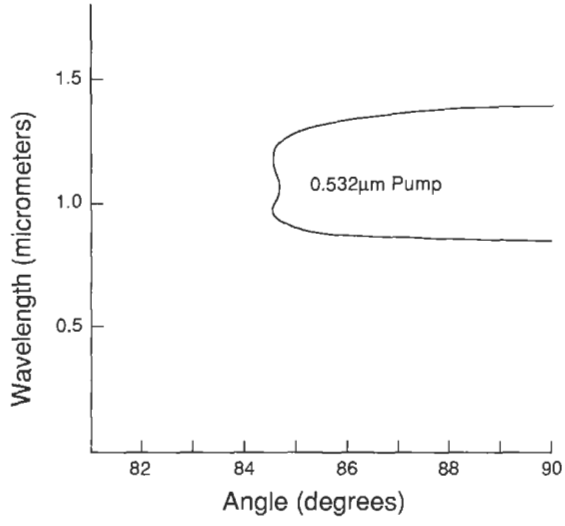

FIGURE 13 Phase-matching curve for CD*A for a 0.532-μm pump.

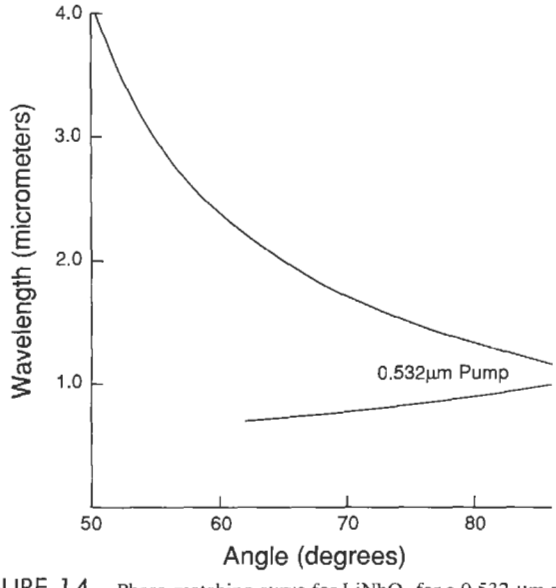

FIGURE 14 Phase-matching curve for $LiNbO_3$ for a 0.532-μm pump.

At least five different optical parametric oscillators can be made using a 2.10-μm pump. A device that could tune between about 2.5 μm to beyond 10.0 μm could be based on $AgGaS_2$, $AgGaSe_2$, CdSe, $ZnGeP_2$, or Tl_3AsSe_3 (Figs. 19

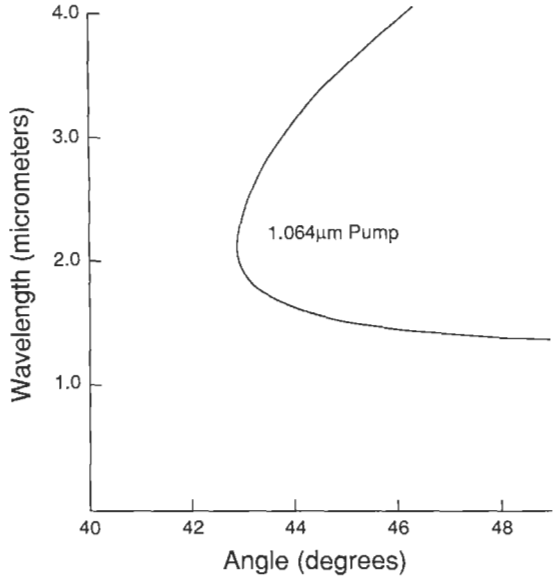

FIGURE 15 Phase-matching curve for $LiNbO_3$ for a 1.064-μm pump.

through 22). $ZnGeP_2$ could tune over this range with a variation of about 4°, the smallest angular range; CdSe would require about 14°, the largest angular range. $AgGaS_2$ does display an unusually flat tuning range about 4.2 μm. Besides this, the tuning curves are in general similar, except for the direction of the curvature. As such, selection of the best nonlinear crystal would probably be based on considerations other than the phase matching curves.

9. PERFORMANCE

Optical parametric oscillators have developed from their initial stage where they were little more than a curiosity. Initial performance was limited by lack of high optical quality nonlinear crystals, nonlinear crystals with relatively small nonlinear coefficients, and limited pump laser performance. In addition, optical parametric oscillators were in competition with dye lasers in the visible and near infrared. Pulsed dye lasers have an advantage because laser-pumped dye lasers do not necessarily require high beam quality from the pump laser. In essence, dye lasers can serve as an optical integrator, converting a fixed-wavelength pump laser with relatively poor beam quality into a tunable laser with a better beam quality. In the face of these difficulties, optical parametric oscillators enjoyed limited commercial applications for a considerable time. However, several increases in optical parametric oscillator technology have improved the viability of these devices.

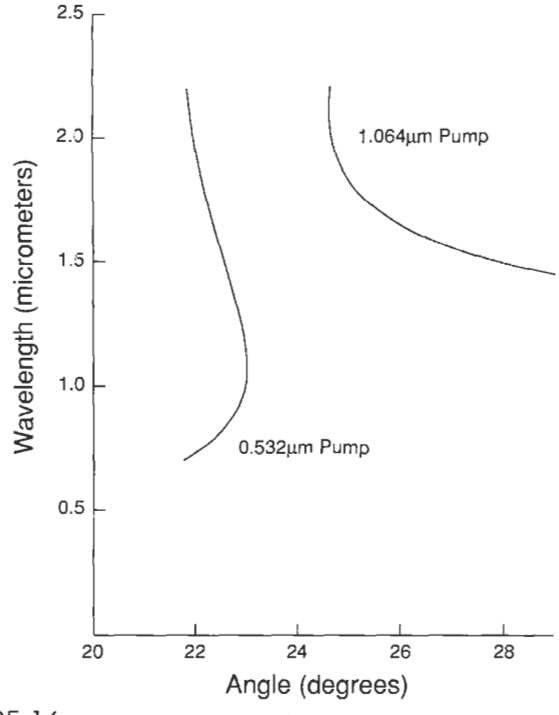

FIGURE 16 Phase-matching curve for BBO for 0.532- and 1.064-μm pumps.

Optical quality of the nonlinear crystals has improved. Optical quality improvements have occurred both in the form of decreased absorption and decreased distortion. For example, $LiNbO_3$ crystals were found to suffer from optically induced refractive index inhomogeneities. It was found that, in part, these problems could be traced to Fe impurities. By decreasing the Fe impurities, the susceptibility of optically induced refractive index inhomogeneities was decreased. Similarly, the short-wavelength absorption in $AgGaSe_2$ was correlated with a deficiency of Se. By annealing these crystals in an atmosphere rich in Se, the short-wavelength transmission of these crystals improved. Initially some nonlinear crystals were deliberately doped with impurities to reduce growth time and therefore cost. While some impurities are benign, others can cause unwanted absorption. Increased absorption can limit the efficiency and average power limit available with a given nonlinear crystal. In addition, some crystals tended to grow multidomain. That is, not all of the nonlinear crystal was oriented in the same manner. Multidomain crystals limit efficiency by limiting the effective length of the nonlinear crystal. As growth technology improved, many of these problems were resolved.

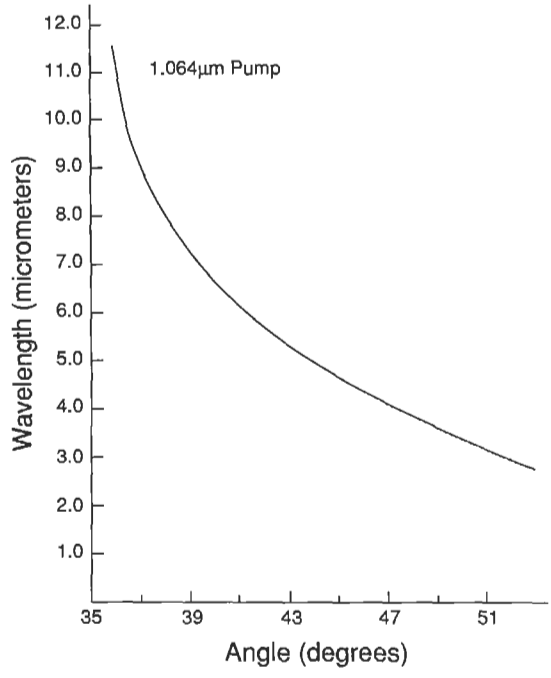

FIGURE 17 Phase-matching curve for $AgGaS_2$ for a 1.064-μm pump.

Of perhaps more significance is the introduction of better nonlinear crystals, particularly ones with a larger nonlinear coefficient. Of particular note in the way of visible crystals are KTP, BBO, and LBO. Crystals with nonlinear coefficients as large as those available with these more recent crystals were not generally available in the early developmental stages of optical parametric oscillators. In the infrared, $AgGaSe_2$ has developed to the point where it is presently commercially available for applications in the mid-infrared region. Although this crystal has been known for some time, the availability and the absorption in the near-infrared region limited its utility. In addition, substantial progress has also been made with the commercialization of $ZnGeP_2$.

Pump lasers have also improved both in power and beam quality, a definite advantage when nonlinear optics are being used. Improvements such as unstable resonators and graded reflectivity output mirrors have made pump lasers with good beam quality as well as high energy per pulse available. The beam quality of pump lasers is often limited by thermal effects. However, as laser diode array pumping of solid-state lasers becomes more common, the beam quality should improve even more since the thermal load on a laser diode array-pumped solid-state laser is less than a similar lamp-pumped solid-state laser at the same average output power. In addition, injection seeding techniques have narrowed the linewidth of the pump

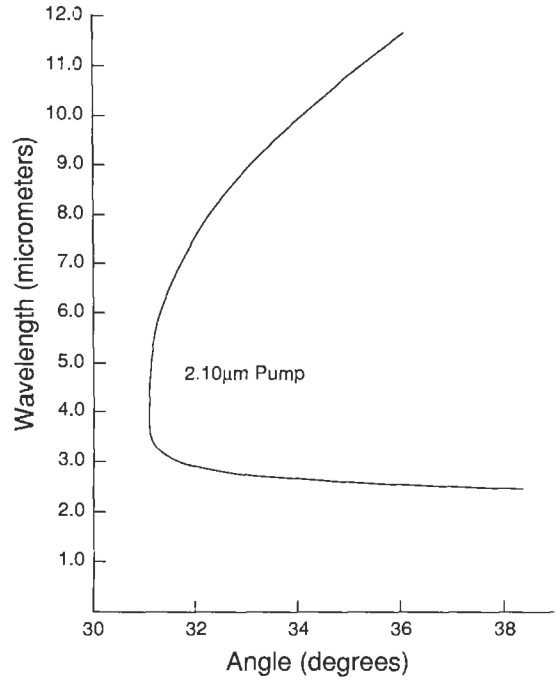

FIGURE 18 Phase-matching curve for $AgGaS_2$ for a 2.10-μm pump.

lasers. Both increased beam quality and decreased linewidth can lead to an increased performance for the optical parametric oscillator.

Several different concepts are involved in the assessment of the performance of an optical parametric oscillator including threshold, slope efficiency, total efficiency, photon efficiency, and pump depletion. Optical parametric oscillators can be operated either in a cw or a pulsed mode. Of the two modes of operation, the pulsed mode is much more common since the operation of an optical parametric oscillator is enhanced by a high power density. The threshold in the cw mode is straightforward to define as the amount of pump power required to achieve optical parametric oscillation. In the pulsed mode, the observable threshold, rather than the instantaneous threshold, is usually quoted; however, this is not always made clear. While slope efficiency is sometimes quoted, it could represent either the ratio of the increase in power at the output wavelength to the increase in power at the pump wavelength or the increase in power of both the signal and idler wavelengths to the increase in power at the pump wavelength. In the pulsed mode, it could be quoted at the instant of peak power or it could be quoted for the total output energy. Although laser theory usually predicts a nearly linear increase in the output with increases in the input, optical parametric oscillator theory does not necessarily predict the same approximation. However, in practice, a linear

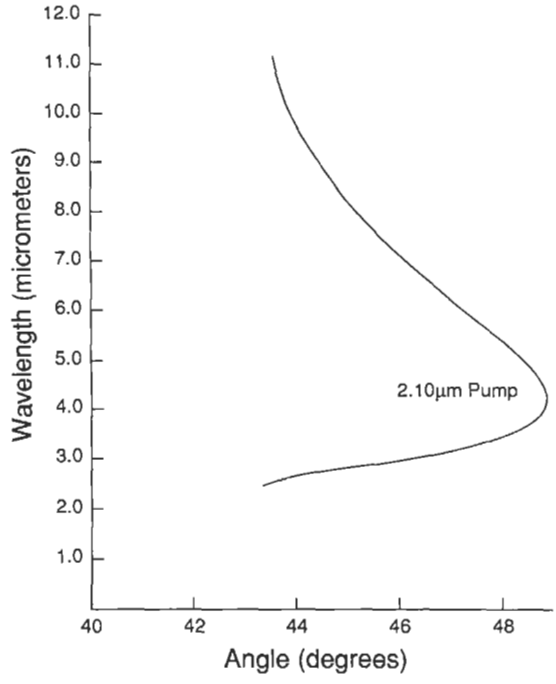

FIGURE 19 Phase-matching curve for $AgGaSe_2$ for a 2.10-μm pump.

increase of the output with the input is often observed. Total efficiency suffers from many of the same ambiguities as slope efficiency. It could imply the output power or energy at one or both of the signal and idler wavelengths divided by the pump power or energy. Photon efficiency normalizes the pump power and energy and the output power or energy by the energy of the pump and output photon, respectively. Thus, a unity photon efficiency would imply that the power or energy efficiency would be in the ratio of the pump wavelength to the output wavelength. Pump depletion usually compares the pump pulse transmitted through the optical parametric oscillator with and without oscillation occurring. As such, it is closest to the efficiency calculated using both the signal and idler as outputs.

Optical parametric oscillation was first demonstrated using a pulsed pump laser, a frequency-doubled Nd:$CaWO_4$ laser [50]. The threshold was reported to be sharp and well defined at 6.7 kW, but was only achieved on about one in five shots. A peak output power of 15 W at a signal wavelength of 0.984 μm was reported, yielding an efficiency of about 0.002.

Continuous wave optical parametric oscillation was reported by using a $Ba_2NaNb_5O_{15}$ crystal [51]. It was pumped by a frequency-doubled Nd:YAG laser. A threshold of 45 mW was observed when the wavelengths available

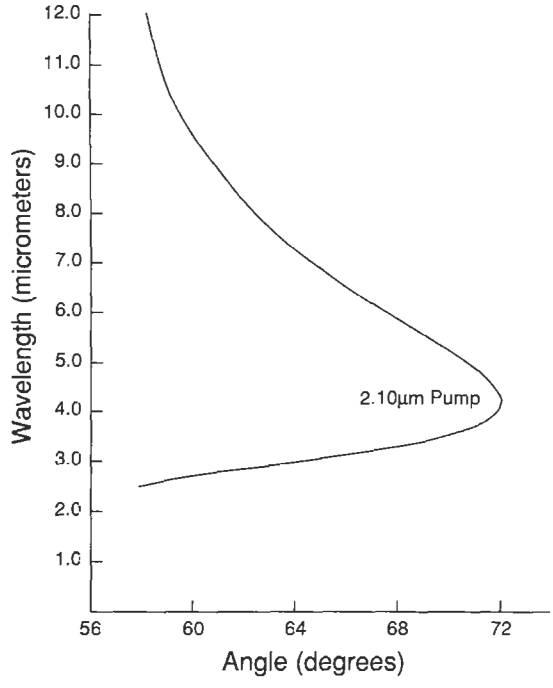

FIGURE 20 Phase-matching curve for CdSe for a 2.10-μm pump.

ranged from 0.98 to 1.16 μm. With 0.3 W of pump power, the available power at both the signal and idler wavelengths was estimated at 0.003 W, yielding an efficiency of 0.01. Later, by using a cw Ar ion laser for a pump laser, a threshold as low as 2.0 mW was achieved. A power output of about 0.0015 W was achieved at about 2.8 times threshold. While a continuous pump was employed, the output consisted of a series of pulses with pulse lengths ranging from 0.1 to 1.0 ms in length [52].

More efficient operation in the near infrared was obtained by two researchers both using $LiNbO_3$ as the nonlinear crystal. In one case, a frequency-doubled Nd:glass laser was used as the pump source [53], and the other used a Q-switched $Cr:Al_2O_3$ laser [54]. In the first case, a threshold of about 5.0 kW was required for a 8.0-mm crystal length. At twice threshold, a peak output power of 1.8 kW was achieved yielding an efficiency of 0.18. In the second case a threshold of 65 kW was achieved in a doubly resonant arrangement with a 9.35-mm crystal length. With the doubly resonant arrangement, 0.22 of the peak pump power was converted to the signal at 1.04 μm. On the other hand, with a singly resonant arrangement, only 0.06 of the peak pump power was converted to the signal. Although the efficiencies reported in these experiments are impressive, the output energy of these devices is in the millijoule range or less.

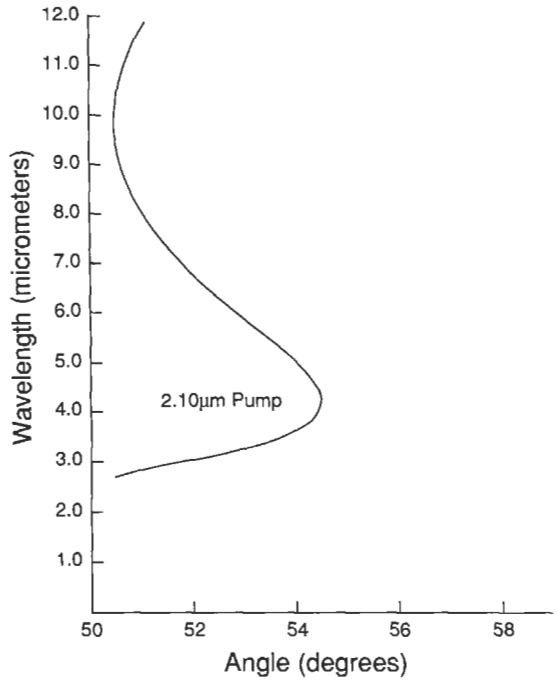

FIGURE 21 Phase-matching curve for $ZnGeP_2$ for a 2.10-μm pump.

A device tunable across the visible region of the spectrum was produced by using ADP as the nonlinear crystal [55]. A frequency-quadrupled Nd:YAG laser, yielding about 1.0 mJ/pulse at 0.266 μm, was utilized as the pump. Gains were high enough with this configuration that external mirrors were not necessary to obtain significant conversion. With the 50-mm ADP crystal oriented normal to the pump beam, an average power conversion of the pump to the outputs in the visible region of the spectrum was as high as 0.25. Temperature tuning the crystal from 50 to 105°C allowed the region from 0.42 to 0.73 μm to be covered.

A cw optical parametric oscillator tunable in the red region of the spectrum, from 0.680 to 0.705 μm, was demonstrated using an Ar ion laser operating at 0.5145 μm in conjunction with a 16.5-mm $LiNbO_3$ crystal [52]. To avoid optically induced refractive index inhomogeneities, the crystal was operated at elevated temperatures, nominally 240°C. A threshold of 410 mW was possible. At 2.8 times threshold, 1.5 mW of output power was available even though the output mirror only had a transmission of approximately 0.0004.

An optical parametric oscillator tunable in the mid-infrared region was obtained by using a Nd:YAG laser directly as the pump and a $LiNbO_3$ crystal [56]. Operation in this region of the spectrum is more difficult because the gain

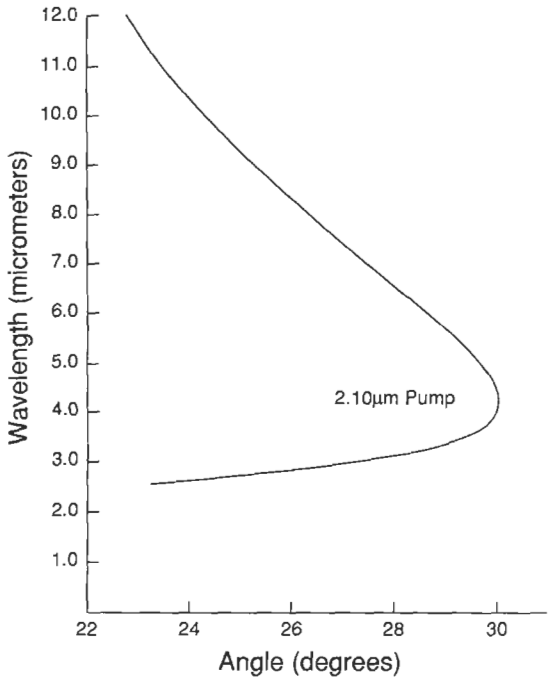

FIGURE 22 Phase-matching curve for Tl_3AsSe_3 for a 2.10-μm pump.

coefficient is inversely proportional to the product of the signal and idler wavelengths. To help compensate for the low gain, a 50-mm-long crystal was used. Using angle tuning, the spectral range from 1.4 to 4.5 μm could be covered. The threshold was 4.0 mJ when the oscillator was operating near 1.7 μm. An energy conversion efficiency of 0.15 was reported.

Optical parametric oscillation further into the mid-infrared region was possible by using a CdSe crystal. Initially, a Nd:YAG laser operating at 1.83 μm was used as the pump [57]. Later, a HF laser, operating around 2.87 μm was used for a pump [58]. In the former case, threshold for a 21-mm crystal length was observed to be between 0.55 and 0.77 kW. A power conversion efficiency of 0.40 was inferred by measuring the depletion of the transmitted pump. In the latter case, threshold for a 28-mm crystal length was found to be 2.25 kW. At about twice threshold, a signal power of 0.8 kW was observed that indicated a power efficiency of 0.15. By employing angle tuning, a signal was generated over the range from 4.3 to 4.5 μm. Corresponding to this, the idler was tuned between 8.1 to 8.3 μm.

Optical parametric oscillator operation can be enhanced by utilizing a mode-locked pump [59]. For one set of experiments, a mode-locked Nd:glass laser, operating at 1.058 μm, was amplified to produce an output of 0.55 J. By using an

etalon in the Nd:glass laser resonator, the pulse length could change from 7 to 60 ps. Using a KDP crystal, this produced about 0.15 J of second harmonic. A $LiNbO_3$ crystal with a length of 20 mm was utilized as the nonlinear crystal. It was housed in an oven to allow temperature tuning. With the optical parametric oscillator tuned to 0.72 μm, an output of 6 mJ was achieved. To utilize the peak power associated with the pump, the length of the optical parametric oscillator had to be adjusted so that the circulating pulse was in synchronism with the incident pump pulse train. With a 7.0-ps pulse length, a change in the length of the resonator in the range of 0.1 mm produced a factor of 10 change in the output energy. In a different experiment, a mode-locked Ho:YAG laser was used to pump a CdSe optical parametric oscillator [60]. A similar enhancement in the conversion was effected by using the mode-locked pump pulse train.

An attractive optical parametric oscillator for use in the mid-infrared region was demonstrated using $AgGaSe_2$ as the crystal. Although CdSe could cover much of the mid infrared, its limited birefringence limited its tuning capability. However, much of the mid infrared could be covered using long-wavelength pump lasers including a 2.04-μm Ho:YLF [61] or a 1.73-μm Er:YLF [17] laser. Use of a 23-mm crystal length with the 1.73-μm pump resulted in a threshold of 3.6 mJ. A slope efficiency, measuring only the signal at 3.8 μm, of 0.31 at 1.5 times threshold was achieved simultaneously. On the other hand, with the 2.05-μm pump, a threshold of 4.0 mJ was achieved along with an energy conversion into both the signal and idler of 0.18.

Substantial energy conversion has been demonstrated using BBO as the nonlinear conversion by two different groups. Both groups used the third harmonic of a Nd:YAG as the pump. In one case, two opposed crystals, one 11.5 mm in length with the other 9.5 mm in length, were used to minimize birefringence angle effects [62]. Efficiency in this case is defined as the sum of the signal and idler energy output divided by the incident pump energy. Here significant saturation in the conversion efficiency was observed, nearly 0.32; that is, 7 mJ of output energy for 21 mJ of pump. In the other case, a 10-mm crystal length yielded a quantum conversion efficiency as high as 0.57 at a signal wavelength of 0.49 μm by double passing the pump through the nonlinear crystal [63].

By simply using more energetic pump lasers, more output energy can be obtained. By using a Nd:YAG oscillator and amplifier, a pump energy of about 0.35 J/pulse could be obtained. Using two opposed KTP crystals 10 mm in length, for birefringence angle compensation, a nearly degenerate optical parametric oscillator was demonstrated [64]. Signal and idler wavelengths were 1.98 and 2.31 μm, respectively. The threshold for this arrangement was about 100 mJ and the slope efficiency was as high as 0.48. At the full input energy, 0.115 J/pulse was produced. Even higher energy per pulse could be obtained by simply scaling the device in cross section while retaining the same energy density.

10. TUNING

Tuning of the optical parametric oscillator can be handled using the same techniques as described in the chapter on solid-state lasers (Chapter 6; see also Chapter 2). However, significant differences do exist that can be attributed to the difference in the operating principles of the two devices. Some of these differences are manifest in the coarse tuning available with phase matching of the optical parametric oscillator and in the time-varying instantaneous gain, which has to be taken into account if injection seeding is to be utilized. However, because many of the tuning and line narrowing elements are discussed in Chapter 6, they will not be discussed here. Rather, the tuning aspects unique to the optical parametric oscillator will be emphasized.

Coarse tuning of the optical parametric oscillator can be accomplished using either angular or temperature tuning. In fact, any effect that causes a differential change in the refractive indices at the pump, signal, and idler wavelengths could be used to effect tuning. For example, tuning could be achieved using an applied pressure through the stress optic effect. However, to date, only angular or temperature tuning has received wide application. To calculate the tuning rate, the partial derivatives of the phase mismatch can be used. According to a theorem in partial differential calculus,

$$\frac{\partial x}{\partial y}\Big|_z \frac{\partial y}{\partial z}\Big|_x \frac{\partial z}{\partial x}\Big|_y = -1 \quad . \tag{60}$$

Using this relation, the tuning rate can be approximated by

$$\frac{\partial \lambda}{\partial \theta} = -\frac{\partial \Delta k/\partial \theta}{\partial \Delta k/\partial \lambda} \tag{61}$$

for angular tuning and

$$\frac{\partial \lambda}{\partial T} = -\frac{\partial \Delta k/\partial T}{\partial \Delta k/\partial \lambda} \tag{62}$$

for temperature tuning. To evaluate the derivatives of Δk with respect to the direction of propagation and temperature, the results of Sec. 4 can be used. Thus,

$$\frac{\partial \Delta k}{\partial \theta} = 2\pi\left(\frac{1}{\lambda_1}\frac{\partial n_1}{\partial \theta} - \frac{1}{\lambda_2}\frac{\partial n_2}{\partial \theta} - \frac{1}{\lambda_3}\frac{\partial n_3}{\partial \theta}\right) \tag{63}$$

in general. Of course, the partial derivative with respect to angle for ordinary waves is zero in uniaxial crystals. For temperature tuning,

$$\frac{\partial \Delta k}{\partial T} = 2\pi\left(\frac{1}{\lambda_1}\frac{\partial n_1}{\partial T} - \frac{1}{\lambda_2}\frac{\partial n_2}{\partial T} - \frac{1}{\lambda_3}\frac{\partial n_3}{\partial T}\right) \tag{64}$$

Individual partial derivatives with respect to angle are evaluated in Section 4. Partial derivatives of the index of refraction with respect to temperature are listed for the more common crystal in Section 8. Thus, to determine the particular wavelength that will be generated, the phase-matching condition can be calculated as done for a variety of situations in Section 8. Tuning near the phase-matching condition can then be found by using the preceding equations. Linewidth can be determined by using the approach also described in Section 4.

Injection seeding of an optical parametric oscillator can be accomplished in much the same way as injection seeding of a solid-state laser. Injection seeding has been demonstrated for several optical parametric oscillators operating in the visible and mid-infrared regions [65–67]. However, there are several significant differences between seeding an optical parametric oscillator and injection seeding a solid-state laser [67]. One of these differences occurs during the critical pulse evolution time interval. During this phase of the development, not much energy is extracted. However, the spectral properties of the output are determined by the competition between the seeded and unseeded modes. In a solid-state laser, the gain is nearly constant since the stored energy or the population inversion density is nearly constant. In an optical parametric oscillator, the gain varies with the pump power. Thus, for a pulsed pump, the gain varies with time. Although this makes the description of the competition more complex, it does not prevent seeding. A second difference is in the extraction of the energy. In a solid-state laser, as the seeded mode extracts the energy stored in the upper laser level, it hinders the development of the unseeded mode by decreasing its gain. However, in an optical parametric oscillator, there is no stored energy. Thus for injection seeding to be highly successful, the seeded pulse should continue to extract the energy from the pump pulse as fast as it arrives at the crystal. A third difference exists in the saturation effect. In a solid-state laser the laser pulse extracts the energy stored in the upper laser level to the point where the gain falls to zero. However, in an optical parametric oscillator, the gain may not fall to zero in the presence on the seeded pulse. A nonzero gain allows the unseeded modes to continue to extract energy from the pump and thus decrease the efficacy of the seeding process.

In doubly resonant optical parametric oscillators, spectral output of the device may be unstable due to an effect referred to as the cluster effect. If both the signal and idler are resonant, oscillation can only occur at frequencies that satisfy both the conservation of energy and the resonance condition. Because of these simultaneous requirements, the frequencies that oscillate may not occur at the minimum phase mismatch as shown in Fig. 23. By operating away from the point at minimum phase mismatch, the output can be significantly reduced. Worse still, the

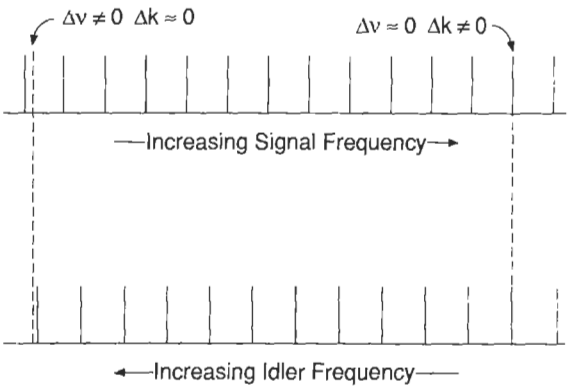

FIGURE 23 Cluster effects in doubly resonant devices.

closest set of frequencies that satisfies both the resonance condition and the conservation of energy can vary on a shot-to-shot basis. For example, the pump frequency may experience small variations caused by small variations in the level of excitation of the pump laser. A small variation in the pump frequency may cause a much larger difference in the frequencies that satisfy both the conservation of energy and the resonance condition. Due to instabilities associated with the cluster effect, the doubly resonant optical parametric oscillator is often avoided.

REFERENCES

1. J. A. Giordmaine and R. C. Miller. "Tunable Coherent Parametric Oscillation in $LiNbO_3$ at Optical Frequencies," *Phys. Rev. Lett.* **14,** 973–976 (1965).
2. J. A. Armstrong, N. Bloembergen. J. Ducuing, and P. S. Pershan, "Interactions between Light Waves in a Nonlinear Dielectric," *Phys. Rev.* **127,** 1918–1938 (1962).
3. G. D. Boyd and D. A. Kleinman, "Parametric Interaction of Focused Gaussian Light Beams," *J. Appl. Phys.* **39,** 3597–3639 (1968).
4. S. E. Harris. "Tunable Optical Parametric Oscillators," *Proc. IEEE* **57,** 2096–2113 (1969).
5. S. J. Brosnan and R. L. Byer, "Optical Parametric Oscillator Threshold and Linewidth Studies," *IEEE J. Quantum Electron.* **QE-15,** 415–431 (1979).
6. R. L. Byer and S. E. Harris, "Observation of Tunable Optical Parametric Fluorescence," *Phys. Rev. Lett.* **18,** 732–734 (1968).
7. N. P. Barnes and V. J. Corcoran, "Acceptance Angles and Spectral Bandwidths of Nonlinear Interactions," *Appl. Opt.* **15,** 696–699 (1976).
8. N. P. Barnes. "Tunable Mid Infrared Sources Using Second Order Nonlinearities," *Int. J. Nonlinear Opt.* **1,** 639–672 (1992).
9. P. N. Butcher, *Nonlinear Optical Phenomena,* Bulletin 200 Ohio State University, Columbus, OH (1965).
10. M. Born and E. Wolf, *Principles Of Optics,* Pergamon Press. New York (1964).
11. F. Zernike and J. E. Midwinter, *Applied Nonlinear Optics.* Wiley, New York (1973).

12. J. A. Armstrong, N. Bloembergen, J. Ducuing, and P. S. Pershan, "Interactions Between Light Waves in a Nonlinear Dielectric," *Phys. Rev.* **127,** 1918–1938 (1962).
13. G. D. Boyd and D. A. Kleinman, "Parametric Interactions of Focused Gaussian Light Beams," *J. Appl. Phys.* **39,** 3597–3639 (1968).
14. R. A. Baumgartner and R. L. Byer, "Optical Parametric Amplification," *IEEE J. Quantum Electron.* **QE-15,** 432–444 (1979).
15. N. P. Barnes, D. J. Gettemy, J. R. Hietanen, and R. A. Iannini, "Parametric Amplification in $AgGaSe_2$," *Appl. Opt.* **28,** 5162–5168 (1989).
16. S. J. Brosnan and R. L. Byer, "Optical Parametric Oscillator Threshold and Linewidth Studies," *IEEE J. Quantum Electron.* **QE-15,** 415–431 (1979).
17. N. Barnes, K. E. Murray, J. R. Hietanen, and R. A. Iannini, "Er:YLF Pumped $AgGaSe_2$ Optical Parametric Oscillator," in *Proc. OSA Advanced Solid State Lasers*, OSA, Washington, D.C. 322–328 (1990).
18. S. J. Brosnan and R. L. Byer, "Optical Parametric Oscillator Threshold and Linewidth Studies," *IEEE J. Quantum Electron.* **QE-15,** 415–431 (1976).
19. N. P. Barnes, J. A. Williams, J. C. Barnes, and G. E. Lockard, "A Self Injection Locked Q-Switched Line Narrowed $Ti:Al_2O_3$ Laser," *IEEE J. Quantum Electron.* **24,** 1021–1028 (1988).
20. G. D. Boyd, A. Ashkin, J. M. Dziedzic, and D. A. Kleinman, "Second Harmonic Generation of Light with Double Refraction," *Phys. Rev.* **137,** A1305–A1319 (1965).
21. S. J. Brosnan and R. L. Byer, "Optical Parametric Oscillator Threshold and Linewidth Studies," *IEEE J. Quantum Electron.* **QE-15,** 415–431 (1979).
22. M. Okada and S. Ieiri, "Influences of Self-Induced Thermal Effects on Phase Matching in Nonlinear Optical Crystals," *IEEE J. Quantum Electron.* **QE-7,** 560–563 (1971).
23. N. P. Barnes, R. C. Eckhardt, D. J. Gettemy, and L. B. Edgett, "Heating Effects in Second Harmonic Generation," in *LIS Information Exchange Meeting*, Albuquerque, NM (May 1977).
24. D. T. Hon and H. Brusselbach, "Beam Shaping to Suppress Phase Mismatch in High Power Second Harmonic Generation," *IEEE J. Quantum Electron.* **QE-16,** 1356–1364 (1980).
25. D. Eimerl, "The Potential for Efficient Frequency Conversion at High Average Power Using Solid State Nonlinear Optical Materials," UCID-20565, University of California (Oct. 1985).
26. T. G. Giallorenzi and C. L. Tang, "CW Parametric Scattering in ADP with Strong Absorption in the Idler Band," *Appl. Phys. Lett.* **12,** 376–378 (1968).
27. J. D. McMullen, "Optical Parametric Interactions in Isotropic Materials Using a Phase Corrected Stack of Nonlinear Dielectric Plates," *J. Appl. Phys.* **46,** 3076–3081 (1975).
28. F. Zernike and J. E. Midwinter, *Applied Nonlinear Optics*, Wiley, New York (1973).
29. V. G. Dmitriev, G. G. Gurzadyan, and D. N. Nikogosyan, *Handbook of Nonlinear Optical Crystals*, Springer Verlag, New York (1991).
30. M. J. Weber, *Handbook of Laser Science and Technology, Vol. III, Optical Materials*, CRC Press, Boca Raton, FL (1986).
31. M. M. Choy and R. L. Byer, "Accurate Second Order Susceptibility Measurements of Visible and Infrared Nonlinear Crystals," *Phys. Rev. B.* **14,** 1693–1706 (1976).
32. R. C. Eckhardt, H. Masuda, Y. X. Fan, and R. L. Byer, "Absolute and Relative Nonlinear Optical Coefficients of KDP, KD*P, BaB_2O_4, $LiIO_3$, $MgO:LiNbO_3$, and KTP Measured by Phase-Matched Second-Harmonic Generation," *IEEE J. Quantum Electron.* **QE-26,** 922–933 (1990).
33. I. H. Malitson, and M. J. Dodge, "Refractive Index and Birefringence of Synthetic Sapphire," *J. Opt. Soc. Am.* **62,** 1405 (1972).
34. F. Zernike, "Refractive Indices of Ammonium Dihydrogen Phosphate and Potassium Dihydrogen Phosphate Between 2000A and 1.5 μm," *J. Opt. Soc. Am.* **54,** 1215–1220 (1964).
35. L. G. DeShazer and K. E. Wilson, "Refractive Index and Thermo-Optic Coefficients of CD*A," in *Basic Properties of Optical Materials Symp.*, NBS Special Publication 574, Gaithersburg, MD (1980).
36. G. D. Boyd, W. L. Bond, and H. L. Carter, "Refractive Index as a Function of Temperature in $LiNbO_3$," *J. Appl. Phys.* **38,** 1941 (1967).

37. D. Eimerl, L. Davis, and S. Velsko, E. K. Graham, and A. Zalkin, "Optical, Mechanical, and Thermal Properties of Barium Borate," *J. Appl. Phys.* **62,** 1968–1983 (1987).
38. C. Chen, Y. Wu, A. Jiang, B. Wu, G. You *et al.*, "New Nonlinear Optical Crystal: $LiB_3O_5$5," *J. Opt. Soc. Am. B* **6,** 616–621 (1989).
39. T. Y. Fan, C. E. Huang, R. C. Eckardt, Y. X. Fan, R. L. Byer, and R. S. Feigelson, "Second Harmonic Generation and Accurate Indices of Refraction Measurements in Glux-Crown $KTiOPO_4$," *Appl. Opt.* **26,** 2390–2394 (1987).
40. G. D. Boyd, H. Kasper, and J. H. McFee, "Linear and Nonlinear Properties of $AgGaS_2$, $CuGaS_2$ and $CuInS_2$, and Theory of the Wedge Technique for the Measurements of Nonlinear Coefficients," *IEEE J. Quantum Electron.* **QE-7,** 563–573 (1971).
41. G. D. Boyd, H. M. Kasper, J. H. McFee, and F. G. Storz, "Linear and Nonlinear Optical Properties of Some Ternary Selenides," *IEEE J. Quantum Electron.* **QE-8,** 900–908 (1972).
42. R. L. Herbst and R. L. Byer, "Efficient Parametric Mixing In CdSe," *Appl. Phys. Lett.* **19,** 527–530 (1971).
43. G. D. Boyd, E. Buehler, and F. G. Storz, "Linear and Nonlinear Properties of $ZnGeP_2$ and CdSe," *Appl. Phys. Lett.* **18,** 301–304 (1971).
44. J. D. Feichtner and G. W. Roland, "Optical Properties of a New Nonlinear Optical Material: Tl_3AsSe_3," *Appl. Opt.* **11,** 993–998 (1972).
45. N. P. Barnes, D. J. Gettemy, and R. S. Adhav, "Variation of the Refractive Indices with Temperature and the Tuning Rate for KDP Isomorphs," *J. Opt. Soc. Am.* **72,** 895–898 (1982).
46. L. G. DeShazer, C. S. Hoefer, and K. W. Kirby, "Optical Characterization of Nonlinear Crystals," Final Report to Lawrence Livermore National Laboratory, Livermore, CA (1985).
47. D. J. Gettemy, W. C. Harker, G. Lindholm, and N. P. Barnes, "Some Optical Properties of KTP, $LiIO_3$, and $LiNbO_3$," *IEEE J. Quantum Electron.* **QE-24,** 2231–2237 (1988).
48. R. L. Herbst, "Cadmium Selenide Infrared Parametric Oscillator," Microwave Laboratory Report 2125, Stanford University, Stanford, CA (1972).
49. M. D. Ewbank, P. R. Newman, N. L. Mota, S. M. Lee, W. L. Wolfe *et al.*, "The Temperature Dependence of Optical and Mechanical Properties of Tl_3AsSe_3," *J. Appl. Phys.* **51,** 3848–3852 (1980).
50. J. A. Giordmaine and R. C. Miller, "Tunable Coherent Parametric Oscillation in $LiNbO_3$ at Optical Frequencies," *Phys. Rev. Lett.* **14,** 973–976 (1968).
51. R. G. Smith, J. E. Geusic, H. J. Levinstein, J. J. Rubin, S. Singh, and L. G. Van Uitert, "Continuous Optical Parametric Oscillation in $Ba_2NaNb_5O_{15}$," *Appl. Phys. Lett.* **12,** 308–309 (1968).
52. R. L. Byer, M. K. Oshman, J. F. Young, and S. E. Harris, "Visible CW Parametric Oscillator," *Appl. Phys. Lett.* **12,** 109–111 (1968).
53. L. B. Kreuzer, "High Efficiency Optical Parametric Oscillator And Power Limiting In $LiNbO_3$," *Appl. Phys. Lett.* **13,** 57–59 (1968).
54. J. E. Bjorkholm, "Efficient Optical Parametric Oscillation Using Doubly Resonant and Singly Resonant Cavities," *Appl. Phys. Lett.* **13,** 53–56 (1968).
55. J. M. Yarborough and G. A. Massey, "Efficient High Gain Parametric Generation in ADP Continuously Tunable across the Visible Spectrum," *Appl. Phys. Lett.* **18,** 438–440 (1971).
56. R. H. Herbst, R. N. Fleming, and R. L. Byer, "A 1.4–4.0 μm High Energy Angle Tuned $LiNbO_3$ Optical Oscillator," *Appl. Phys. Lett.* **25,** 520–522 (1974).
57. R. L. Herbst and R. L. Byer, "Singly Resonant CdSe Infrared Parametric Oscillator," *Appl. Phys. Lett.* **21,** 189–191 (1972).
58. J. A. Weiss and L. S. Goldberg, "Singly Resonant CdSe Parametric Oscillator Pumped by an HF Laser," *Appl. Phys. Lett.* **24,** 389–391 (1974).
59. T. Kushida, Y. Tanaka, and M. Ojima, "Tunable Picosecond Pulse Generation by Optical Parametric Oscillator," *Jap. J. App. Phys.* **16,** 2227–2235 (1977).
60. G. P. Arnold, N. P. Barnes, and D. J. Gettemy, and R. G. Wenzel, "Anomalous Behavior of Some Synchronously Pumped Mode Locked Parametric Oscillators," in *Lasers 80,* New Orleans, LA (Dec. 1980).

61. R. C. Eckhardt, Y. X. Fan, R. L. Byer, C. L. Marquardt, M. E. Storm, and L. Esterowitz, "Broadly Tunable Infrared Parametric Oscillator Using $AgGaSe_2$," *Appl. Phys. Lett.* **49,** 608–610 (1986).
62. W. R. Bosenberg, W. S. Pelouch, and C. L. Tang, "High Efficiency and Narrow Linewidth Operation of a Two Crystal β–BaB_2O_4 Optical Parametric Oscillator," *Appl. Phys. Lett.* **58,** 1461–1463 (1991).
63. Y. Wang, Z. Xu, D. Deng, W. Zheng, X. Liu *et al.*, "Highly Efficient Visible and Infrared β–BaB_2O_4 Optical Parametric Oscillator With Pump Reflection," *Appl. Phys. Lett.* **58,** 1461–1463 (1991).
64. S. Chandra, M. J. Ferry, and G. Daunt, "115 mJ, 2-Micron Pulses by OPO in KTP," in *Advanced Solid State Laser Conf.*, Santa Fe, NM (Feb. 1992).
65. V. L. Boichenko, M. M. Novikov, and A. I. Kholodnykh, "Improvement in the Output Characteristics of a Pulsed Optical Parametric Oscillator on Injection of an External Signal into an Extracavity Wave," *Sov. J. Quant. Elect.* **17,** 392–393 (1987).
66. W. R. Bosenberg, D. R. Guyer, and C. E. Hamilton, "Single Frequency Optical Parametric Oscillators," in *CLEO Conf.*, Baltimore, MD (May, 1993).
67. N. P. Barnes, G. H. Watson, and K. E. Murray, "Injection Seeded Optical Parametric Oscillator," in *Advanced Solid State Laser Conf.*, Santa Fe, NM (Feb. 1992).

8 Tunable External-Cavity Semiconductor Lasers

Paul Zorabedian
Photonics Technology Department
Hewlett-Packard Laboratories
Palo Alto, California

1. INTRODUCTION

1.1 What Is an External-Cavity Laser?

A tunable external-cavity laser (ECL) (Fig. 1) comprises an optical gain medium (a laser diode with antireflection coatings on one or both facets), optics for coupling the output of the gain-medium waveguide to the free-space mode of the external cavity, one or more wavelength-selective filters, and one or more mirrors for defining an external feedback path, possibly with a piezoelectric translator (PZT) for fine tuning. The external cavity may also contain additional components such as polarization optics, beamsplitters, prisms, telescopes, etc.

1.2 Why Apply External Feedback to Laser Diodes?

1.2.1 Limitations of Diode Lasers

Semiconductor Fabry–Perot diode lasers are compact and easy to use, but they suffer from a number of performance limitations that are potentially serious in many applications: Solitary laser diodes are often multimode, and they exhibit large linewidths due to a short photon cavity lifetime and strong coupling

Tunable Lasers Handbook
Copyright © 1995 by Academic Press, Inc. All rights of reproduction in any form reserved.

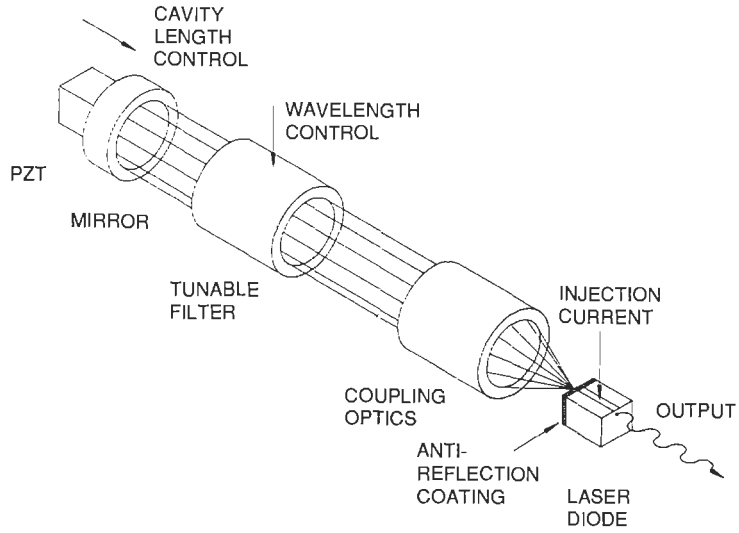

FIGURE 1 Generic tunable extended-cavity diode laser.

between the phase and amplitude of the intracavity optical field. Laser diodes are somewhat tunable by varying temperature or current, but these methods are awkward and have limited ranges, which do not fully exploit the broad semiconductor gain bandwidth.

1.2.2 Advantages of External-Cavity Lasers over Solitary Diode Lasers

ECLs retain in large measure the compactness and ease of use of solitary cavity diode lasers and in addition provide a number of performance enhancements. A typical semiconductor ECL has a volume of ~1000 cm^3. A properly designed ECL will operate on a single external-cavity longitudinal mode. The density of accessible modes is increased by the ratio of the external to solitary cavity lengths. Truly phase-continuous tuning without mode hops is also possible. The linewidth of ECLs is greatly reduced in comparison to solitary diode lasers because of the longer photon lifetime of an external cavity. The use of an external filter allows tunability across the wide gain bandwidth of the semiconductor gain medium.

1.2.3 Comparison with Other Types of Tunable Lasers

Compared to other types of tunable lasers, external-cavity semiconductor lasers are compact, are easily pumped by direct injection current excitation, have high wallplug efficiency, are air cooled, and have long lifetimes. However, their output power is generally lower (typically ~1 to 10 mW, although up to 1 W has been reported).

1.3 Brief History of ECL Development

Several papers on external cavity lasers appeared in the early 1970s. Some of these authors recognized a number of the basic issues of concern to the present-day designer and user of ECLs. In the late 1970s several papers were also published in the Soviet literature. The paper by Fleming and Mooradian in 1981 is the earliest reference cited by many authors, since they were the first to study the spectral properties of ECLs in detail.

Considerable work was done in the early to mid-1980s at British Telecom Research Laboratories, motivated by the prospect of using ECLs as transmitters and local oscillators in coherent optical communication systems. In a similar vein, the mid- to late 1980s saw a great deal of work at AT&T Bell Laboratories. Eventually, the telecommunication companies realized that distributed feedback lasers (DFBs) and distributed Bragg reflector lasers (DBRs) would better suit their needs. The end of the 1980s and early 1990s saw growing interest in ECLs as sources for spectroscopic work and in commercial fiber optic test equipment.

1.4 Scope of ECL Discussion

This chapter considers lasers operating in the strong-external-feedback regime. This generally requires devices with facets that have dielectric anti-reflection (AR) coatings or tilted-stripe devices where the light exits the facet at the Brewster angle.

This chapter deals mainly with the design and continuous wave (cw) properties of laser diodes coupled to free-space external cavities using bulk optical lenses, prisms, filters, and mirrors. Some treatment of integrated optic external cavities is also given. We exclude the treatment of the important monolithically tunable DFB and DBR lasers. The rationale for this is that the design of these lasers is very specialized and their fabrication requires sophisticated equipment that necessarily limits the number of organizations that can produce them. Broadband tuning of DFB lasers over ranges comparable to ECLs has been obtained [1]. However the linewidths of these lasers are 2 to 3 orders of magnitude broader than that obtainable with ECLs.

We also do not explicitly consider vertical-cavity surface-emitting diode lasers (VCSELs). By their structure these lasers are well suited to low-cost, high-density uses in computer networks, but their short active regions provide low gain and require very high cavity Q to achieve oscillation. At present, vertical-cavity lasers are limited to those materials systems that can be grown on GaAs substrates. This has restricted the spectral coverage to wavelengths below 1 μm. So far, the goal of the few published external-feedback studies on VCSELs is from the point of view of their applications to optical signal processing and optical communications. They have comparable feedback sensitivity [2] and behave in agreement with theory developed for edge-emitting laser diodes [3].

To the best of my knowledge, no work has been published so far with the intent of achieving tunability because their low gain will not support much insertion loss for external cavity components. However, if VCSELs continue to grow in importance as some predict, greater adaptation to their use in external cavities may follow.

2 SEMICONDUCTOR OPTICAL GAIN MEDIA

2.1 Laser Diode Basics

A semiconductor laser diode (Fig. 1) serves as the gain medium of an ECL. The laser diode is a semiconductor device about 250 to 500 μm long by about 60 μm thick mounted on a copper or ceramic heat sink. Current is injected through a top ohmic contact. Photons are generated and guided by the epitaxial layers of the structure. The thin layer in which electrons and holes recombine to produce light is called the *active region*. Stimulated emission in the active region forms the basis for laser action driven by optical feedback from the facets or from the external cavity. We start by reviewing some of the basic properties of laser diodes, which are important for the design of ECLs.

2.2 Light Output versus Current Curve

The light output versus current (L-I) curve (Fig. 2) is characterized by the threshold current I_{th} and the quantum efficiency η. Saturation at high current is caused by ohmic heating and Auger recombination. The linear portion of the L-I curve is explained by the laser diode gain model.

2.3 Gain Model

2.3.1 Gain

The optical gain g varies nearly linearly with injected carrier density N:

$$g \approx \sigma\left(N - N_T\right) , \tag{1}$$

where σ is the differential gain cross section and N_T is the carrier density required for transparency.

2.3.2 Loss

The active region contains optical losses such as free-carrier absorption, scattering, and other possible effects. These factors make up the active-region

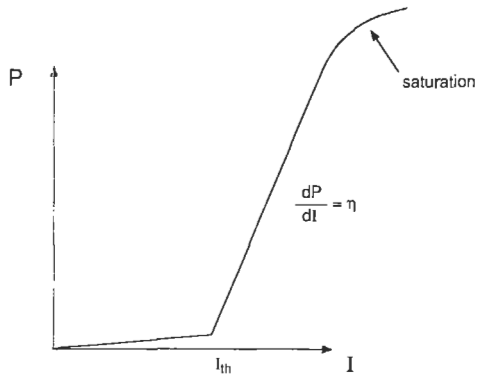

FIGURE 2 Schematic light output versus current curve.

internal loss given by α_{int}. The cleaved-facet ends of the active region constitute a mirror loss α_{mir} given by

$$\alpha_{mir} = \frac{1}{2L_{int}} ln\left(\frac{1}{R_{f1}R_{f2}}\right) , \tag{2}$$

where L_{int} is the physical length of the internal cavity bounded by the facets with power reflectances R_{f1} and R_{f2}. The Fresnel reflectance of a bare facet is

$$R = \frac{(n-1)^2}{(n+1)^2} , \tag{3}$$

where $n \approx 3.5$ is the semiconductor index of refraction.

2.3.3 Confinement Factor

Only a fraction Γ of the optical field lies within the active region and sees its gain. The factor Γ is called the confinement factor.

2.3.4 Threshold Condition

The threshold condition requires the optical field to be periodic with respect to one round-trip of the diode cavity. This leads to magnitude and phase conditions on the optical field. The magnitude part of the threshold condition requires the gain g_{th} to be equal to the total round-trip loss:

$$\Gamma g_{th} = \alpha_{int} + \alpha_{mir} . \tag{4}$$

2.3.5 Output Power and Quantum Efficiency

Below threshold, the carrier density is proportional to the injection current. Once the laser diode begins to oscillate, the carrier density is clamped at the threshold value given by

$$N_{th} = \frac{g_{th}}{\sigma} + N_T \ . \tag{5}$$

The threshold current I_{th} is given by

$$I_{th} = \frac{qN_{th}V_{act}}{\tau_c} \ , \tag{6}$$

where q is the electronic charge, V_{act} is the volume of the active region, and τ_c is the carrier lifetime. Above threshold, the relation between output power P_{out} and injection current I is given by

$$P_{out} = \eta_{ext}\left(I - I_{th}\right) \ . \tag{7}$$

The differential quantum efficiency η_{ext} is given by

$$\eta_{ext} = \frac{h\nu}{q}\eta_{int}\frac{\alpha_{mir}}{\alpha_{mir} + \alpha_{int}} \ , \tag{8}$$

where η_{int} is the probability of radiative recombination for carriers injected into the active region, which is close to unity for most semiconductor lasers [4].

2.4 Spectral Properties of Output

2.4.1 Diode Laser Axial Modes

The phase part of the threshold condition specifies the axial modes of the diode laser. The frequencies ν_m and wavelengths λ_q of the Fabry-Perot modes of the solitary diode laser are given by

$$\nu_q = \frac{qc}{2n_{eff}L_{int}} \ , \tag{9}$$

where q is an integer, c is the velocity of light, n_{eff} is the index of refraction, and L_{int} is the physical length of the active region. The frequency spacing between diode laser axial modes is thus given by

$$\Delta\nu_{int} = \frac{c}{2n_{eff}L_{int}} \ . \tag{10}$$

Assuming $n_{eff} \approx 3.5$ and $L_{int} \approx 250$–500 μm, we find $\Delta\nu_{int} \approx 85$ to 170 GHz. Many Fabry–Perot diode lasers, especially long-wavelength InGaAsP lasers, will oscillate in several axial modes simultaneously in the absence of a wavelength-selective element in the cavity.

2.4.2 Linewidth

The linewidth of a solitary single-mode laser diode is given by the modified Schawlow–Townes formula [5]:

$$\delta\nu_{int} = \frac{\upsilon_g^2 h\nu n_{sp} g_{th} \alpha_{mir}}{8\pi P_{out}} \left(1 + \alpha^2\right) , \tag{11}$$

where υ_g is the group velocity, n_{sp} for AlGaAs and InGaAsP lasers is about 2.6 and 1.6, respectively, and α is the linewidth broadening factor.

2.4.3 Linewidth Broadening Factor

The semiconductor index of refraction consists of real and imaginary parts

$$n = n' + in'' \ . \tag{12}$$

The real and imaginary parts are strongly coupled compared to other laser gain media. The strength of this coupling is characterized by the *linewidth broadening factor* α, defined as

$$\alpha = \frac{\Delta n'}{\Delta n''} \ . \tag{13}$$

The α parameter is the ratio of the changes in the real and imaginary parts of the refractive index with a change in the carrier density. The linewidth broadening factor is a positive number with typical values in the range of 4 to 7 near the middle of the optical gain band and rising steeply to values of 10 to 20 as the photon energy approaches the band gap [6]. At each wavelength, the value of α increases with higher injection current [7]. The degree of dependence of the α parameter on device geometry depends on the type of active region [8]. For index-guided lasers (see discussion later), the α parameter is not strongly dependent on device geometry; that is, it is close to the value for bulk material. For gain-guided and quantum-well laser diodes α may be geometry dependent and differ from the bulk value.

A change in the real part of the index of refraction is related to frequency chirp by

$$\Delta\nu = -\nu\upsilon_g \Delta n'/c \ . \tag{14}$$

A change in the imaginary part of the index of refraction is related to a change in the optical gain by

$$\Delta g = -2\pi\nu\Delta n''\upsilon_g/c \ . \tag{15}$$

2.5 Spatial Properties of Output

2.5.1 Transverse Modes

The beam emanating from the facet of a properly designed laser diode is a Gaussian beam. Some lasers with excessively wide active regions may emit higher order transverse modes, especially at currents well above threshold. The onset of a higher order mode is often accompanied by a telltale kink in the *L-I* curve. It is very undesirable to use a laser diode that emits in a higher order transverse mode as a gain medium in an ECL because this may degrade the coupling efficiency and the wavelength resolution of the cavity.

2.5.2 Divergence

The near-field radiation emitted from a diode facet is a few-micron spot somewhat elongated parallel to the *p-n* junction. Ideally this spot is a Gaussian beam waist at the facet surface with planar wavefronts in both the parallel and perpendicular directions. The far field is a highly divergent beam characterized by full width at half-maximum (FWHM) angles for the directions parallel and perpendicular to the junction (Fig. 3).

2.5.3 Astigmatism

In some laser diodes the facet spot has a planar wavefront perpendicular to the junction but it has convex curvature in the direction parallel to the junction. Thus the parallel rays appear to diverge from a point inside the laser (Fig. 4). This condition is known as *astigmatism*, and it depends on the waveguiding structure used in the laser diode (discussed later). Even a few microns of astigmatism is undesirable, and astigmatic laser diodes should be considered unsuitable for use as external cavity gain media.

2.5.4 Polarization

Laser diodes have modes that are polarized parallel to junction (TE) and perpendicular to the junction (TM). TE modes are usually more strongly guided

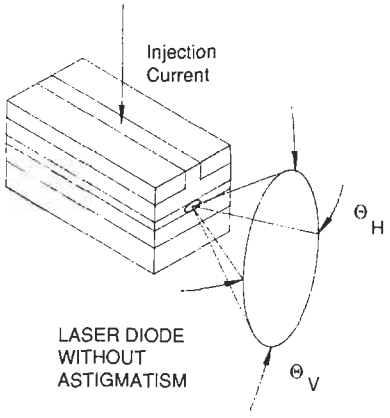

FIGURE 3 Output beam from laser diode without astigmatism.

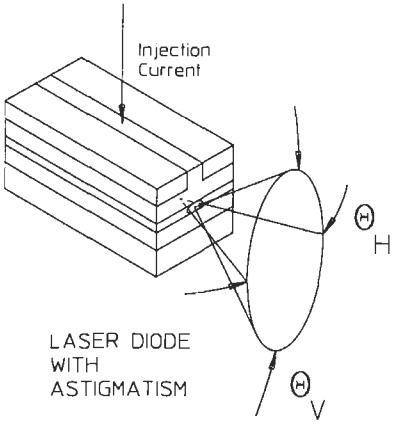

FIGURE 4 Output beam from laser diode with astigmatism.

and thus see lower internal losses. Laser diodes usually have TE polarization ratios of at least 100:1 when biased well above threshold.

2.6 Transverse Device Structures

The coupling between the active region and the external cavity occurs at the plane where the facet intersects the active region. To design efficient coupling optics for this interface, it is useful to have a rudimentary understanding of the mechanisms by which carrier confinement and optical waveguiding are achieved in the diode laser.

2.6.1 Vertical Guiding

Modern diode lasers are double heterostructures in the vertical direction. A thin active layer is sandwiched between top and bottom cladding layers, the top layer being *p*-type and the bottom *n*-type. The active layer is composed of a different semiconductor material having a lower band gap and consequently a slightly larger index of refraction than the *p* and *n* cladding layers that lie above and below it. The layers are comprised of various binary compounds and their associated lattice-matched ternary or quaternary alloys. The relative position of the materials in the sandwich depends on whether the band gap of the binary is larger or smaller than that of the alloy. For example, in the case of a GaAs/GaAlAs laser, the active layer is composed of GaAs and the cladding layers are composed of GaAlAs. In the case of an InP/GaInAsP laser, on the other hand, the active layer is GaInAsP and the cladding layers are InP. In a double-heterostructure device, the carriers are vertically confined by potential barriers and the photons are vertically confined by the refractive index gradients of the slab waveguide formed by the cladding and active layers. The active layer thickness in conventional lasers is ~0.1 μm, while in quantum-well lasers the active layer thickness is about an order of magnitude thinner—about 10 nm.

2.6.2 Active Region Vertical Structures

Laser diodes can be subdivided into two main categories according to the thickness of their active regions [9].

2.6.2.1 Bulk Active Region

Conventional lasers have active regions that are about ~0.1 μm thick. At this magnitude, the carriers in the active region material exhibit the same properties as in bulk material. The active regions of conventional laser diodes are grown either by liquid-phase epitaxy (LPE) or vapor-phase epitaxy, which is also known as metalorganic chemical vapor deposition (MOCVD). Conventional growth methods are the most amenable to low-cost, high-volume production.

2.6.2.2 Quantum-Well Active Region

When the thickness of the active region is reduced by about an order of magnitude to ~10 nm, the carriers exhibit properties that differ from the bulk because of quantum confinement. Such devices are called *quantum-well laser diodes*. Quantum-well active regions can be grown by MOCVD or by molecular-beam epitaxy (MBE). When used as gain media in ECLs, quantum-well lasers have advantages in terms of lower threshold current and increased tuning range.

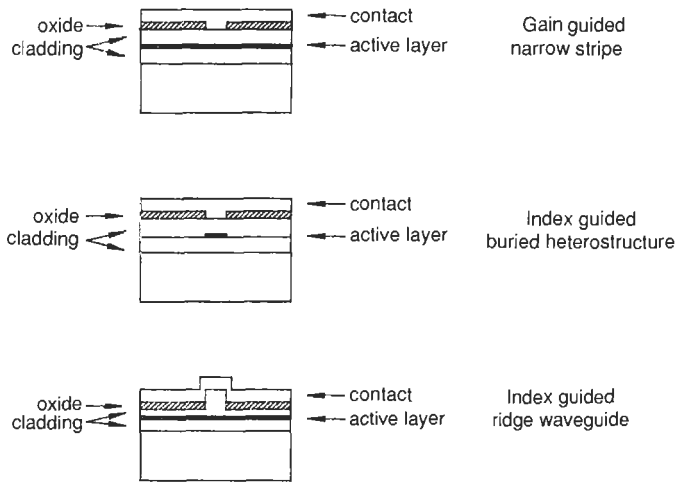

FIGURE 5 Schematic diode laser cross sections showing common waveguide structures.

2.6.3 Lateral Guiding Structures

Lateral optical guiding is necessary to confine the radiation to the region of the diode possessing optical gain. There are three basic types of guiding structures (Fig. 5): gain guiding, strong index guiding, and ridge guiding, which utilizes both gain and index guiding. The reader is cautioned that these illustrations are highly schematic and are only intended to convey the basic structure. For more detailed treatment of semiconductor laser structure, see, for example, Ref. [10]. Brief descriptions of these structures follow.

2.6.3.1 Gain-Guided Oxide Stripe Devices

In this type of laser, current is injected through a narrow (5 to 10 μm wide) opening in the top dielectric layer. Gain is laterally confined to the region around the stripe by the limited lateral diffusion of carriers. The region beyond the stripe exhibits large absorption losses, and so light is laterally confined to the region of the pumping stripe even though there is no refractive index profile. The emitting spot is approximately 1×10 μm.

Gain-guided devices are easy to fabricate and are therefore often used to test semiconductor material quality. However, they suffer from three disadvantages: (1) Because of the high absorption losses, they have a high threshold current. (2) The spot size and divergence are dependent on the pumping current. Higher order transverse modes may appear at high current. (3) Because there is no lateral index profile, gain-guided lasers have from 5 to 50 μm of astigmatism.

2.6.3.2 Index-Guided Buried-Heterostructure Devices

In an index-guided buried-heterostructure device, a stripe of active-layer material about 0.1 to 0.2 μm thick and 1.0 to 2.0 μm wide is completely buried in lower index cladding material. This guiding structure requires careful control of the fabrication process. However, almost all commercial laser diodes comprise some sort of buried heterostructure because the resulting strong index guiding results in the lowest threshold currents, typically 10 to 30 mA, good transverse mode stability, and negligible astigmatism. Typical differential quantum efficiencies are in the range of 40 to 60% for both facets. The near-field spot size is typically 0.5 to 1.0 × 2.0 μm. Beam divergence angles are typically in the range of $\theta_H \approx 30°$ to 40° and $\theta_V \approx 40°$ to 50°.

2.6.3.3 Ridge-Waveguide Laser Diodes

In a ridge-waveguide laser, thickness variation of the upper cladding layer provides optical confinement. This type of structure is simpler and easier to fabricate than a buried heterostructure. Current confinement is not as tight as in a buried heterostructure, so the threshold is also somewhat higher. Typical *L-I* characteristics are $I_{th} \approx 20$ to 30 mA and $\eta \approx 50\%$. The higher threshold is compensated by the fact that the lower current density allows higher power operation. The spot is somewhat larger than in buried heterostructure lasers, so the far-field beam is less divergent. The less divergent output beam makes it easier to couple efficiently a ridge-waveguide laser to an external cavity.

Some typical laser diode characteristics are given in Table 1.

2.7 Gain Stripe Structures

Several types of patterning of the active stripe are used in gain media for ECLs (Fig. 6).

2.7.1 Fabry-Perot Single Stripe

The basic laser diode top structure is a single contact stripe perpendicular to the cleaved-facet mirrors. The active region thus lies within a Fabry–Perot

TABLE 1 Typical Laser Diode Characteristics

Guiding mechanism	Threshold current (mA)	Differential quantum efficiency (%)	Divergence $\theta_H \times \theta_V$ FWHM	Astigmatism
Oxide stripe	>50	<50	10° × 40°	5–50 μm
Buried heterostructure	10–20	>50	30° × 40°	0 (nominal)
Ridge waveguide	20–30	~50	25° × 35°	0 (nominal)

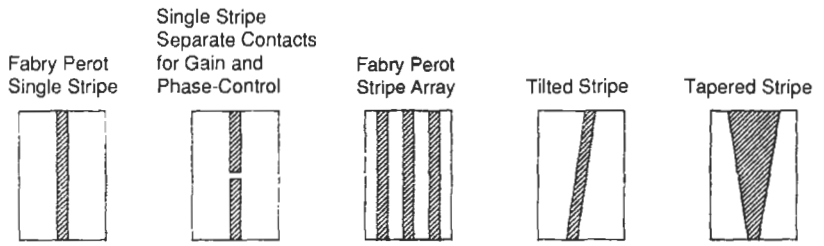

FIGURE 6 Top views of diode lasers showing different active stripe longitudinal structures.

resonator formed by the mirrors created by the Fresnel reflectance of the semiconductor–air interface at each facet.

2.7.2 Split Contact Stripe

A variation on the Fabry–Perot single stripe structure is the split contact stripe. In this structure, part of the length of the active region (gain section) is pumped above threshold. The other section (phase-control section) is biased near transparency. Whereas the carrier density in the gain section is clamped, the carrier density in the phase-control section varies linearly with respect to small changes in its bias current. This provides a means to vary the optical phase of the laser diode cavity and can be used for optical frequency stabilization and suppression of multimode oscillation.

2.7.3 Multistripe Array

Arrays of gain stripes on a single device operate either independently or in a coupled manner depending on the separation between the stripes. When the stripe separation is on the order of the stripe width (~5 to 10 μm) the optical fields from the individual active regions couple to form a supermode. In this case the near field changes phase by 180° between adjacent stripes so as to minimize the overlap with the unpumped regions. This leads to a multilobed far-field diffraction pattern. When the stripe separation is large, each individual stripe acts as an independent laser diode. Arrays of widely separated independent stripes can be used as external-cavity gain media to obtain simultaneous or rapidly switched operation at multiple output wavelengths.

2.7.4 Tilted Stripe

The gain region of a tilted-stripe amplifier is slanted with respect to the cleaved facets in order to reduce the coupling of the facet reflections back into the waveguide. This method can be used for external-cavity gain media as an alternative to the application of dielectric antireflection layers to the facets. The design of tilted-stripe amplifiers is discussed further in the section on facet reflectance reduction.

2.7.5 Tapered Gain Stripe

Tapered-stripe gain media [11] are used as optical amplifiers and in ECLs to generate high output power in a single spatial mode. The gain region is typically ~4 to 10 μm at the narrow end and tapers linearly up to ~130 to 200 μm at the wide end over a length of ~2 mm. Both ends of the amplifier are antireflection coated. The narrow end acts as a transverse-mode-limiting spatial filter. The taper allows the beam to expand by diffraction without mode conversion. The wide output end allows for the extraction of large output powers without damage caused by heat generation due to optical absorption at the output facet.

2.8 Wavelength Ranges of Laser Diode Technologies

2.8.1 Commercially Available Laser Diodes

The availability of semiconductor gain media for ECLs is for the most part dictated by the commercial availability of laser diodes. At present, commercial laser diode technologies provide optical gain over most of the wavelength range from 600 to 2000 nm (Fig. 7) [12]. The development of laser diode technologies has, in turn, been driven by several mass market applications.

The main commercial technologies and their respective applications are AlGaInP/GaAs, ~600 to 670 nm (digital optical storage and retrieval); AlGaAs/GaAs, ~750 to 870 nm (780 nm for laser printing, 850 nm for data communications); and InGaAsP/InP, ~1.1 to 1.65 μm (two separate bands at 1.3 and 1.55 μm for optical communications).

2.8.2 Laser Diode Materials at the Research Stage

In addition to the technologies presently available commercially, intensive research efforts are being carried out on new materials for shorter wavelength laser diodes in the 400 to 600-nm range, driven by desire for higher optical storage densities. These research materials are based on II-VI selenide compounds and III-V nitride compounds. In most cases, the wavelength ranges of the technologies extend beyond the main wavelengths where the applications are centered.

2.9 Gain Bandwidth of Individual Semiconductor Lasers

2.9.1 Bulk Active-Region Gain Media

Electrons and holes injected into the active region respectively begin to fill the bottom of the conduction band and the top of the valence band. The level of filling of each band is determined by the quasi-Fermi levels E_{Fc} and E_{Fv}. The tuning range is roughly determined by the separation of the quasi-Fermi levels minus the band gap ($h\Delta\nu \sim E_{Fc} - E_{Fv} - E_g$). As pumping increases, the quasi-Fermi levels are pushed farther apart. The rate of movement of the quasi-Fermi levels is determined by the density of states. In a bulk active region, the density of states is proportional to $(h\nu - E_g)^{1/2}$. Therefore, as the quasi-Fermi levels move

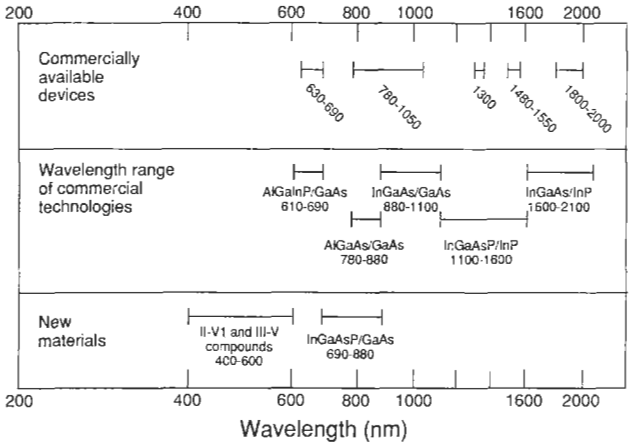

FIGURE 7 Wavelength ranges of diode laser technologies. (Reproduced with permission from Waarts [12].)

away from the band edges, there are more states to fill, and their rate of motion with respect to pumping rate slows down. This tends to limit band filling. A typical tuning range for bulk active-region gain media is roughly $h\Delta\nu_{max} \approx 50$ meV. For a more quantitative discussion of the factors determining the gain profile of a semiconductor laser, see [13].

The gain profile is experimentally determined by placing the gain chip in an external cavity laser and measuring the threshold current versus wavelength. The tuning curve typically has a "bathtub" shape with a relatively flat central region and steeply sloped sides (Fig. 8) [14]. The long-wavelength side (approaching the band edge) is quite abrupt. The roughly constant energy limit of band filling just mentioned implies a wavelength tuning range that increases roughly as the square of the center wavelength. This is born out by the data in Table 2, which gives typical tuning ranges for different active-region materials and center wavelengths. From these values the following empirical expression relating tuning range to center wavelength can be deduced:

$$\Delta\lambda \approx 4.2 \times 10^{-5} \lambda_c^2 \quad \left(\Delta\lambda \text{ and } \lambda_c \text{ in nm}\right) . \tag{16}$$

2.9.2 Quantum Well Active-Region Gain Media

Two major effects are associated with the reduction of the active region thickness from ~0.1 μm to ~10 nm. First, the injection current required to sustain transparency is reduced by about the same factor as the active-region thickness. Thus, ECLs with quantum-well gain media have lower threshold currents. Second, the quantum-well density of states is a staircase function of $(h\nu - E_g)$ that is everywhere lower than the corresponding $(h\nu - E_g)^{1/2}$ function for

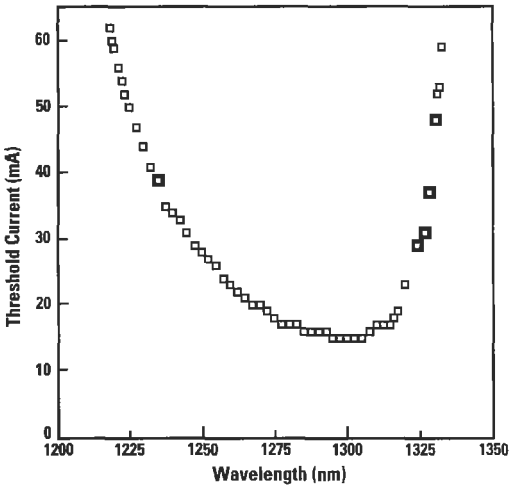

FIGURE 8 Typical diode laser threshold current versus wavelength curve. (Reproduced with permission from Zorabedian and Trutna [14].)

the bulk case. Because of the reduced density of states, for a given pumping level the quasi-Fermi levels are pushed farther apart than in bulk material, resulting in a broader tuning range [18].

Another feature of quantum-well gain media is that the thin layers need not be lattice matched to the substrate because they can sustain elastic strain without the formation of defects. Lattice-mismatch strain shifts the energy bands and can be created intentionally in order to obtain a shifted tuning range. Quantum-well active media can comprise either a single quantum well (SQW) or multiple quantum wells (MQW). SQW devices have the lowest transparency current. An MQW device has a higher transparency current but also has higher maximum gain. Furthermore, spreading the injected electrons into multiple quantum wells

TABLE 2 Tuning Ranges of Conventional Gain Media

Material system	Nominal wavelength (nm)	Typical tuning range of a single bulk DH laser (nm)	Reference
InGaAlP/GaAs	670	~15	15
GaAlAs/GaAs	780	~25	15
GaAlAs/GaAs	850	~30	16
InGaAsP/InP	1300	~70	17
InGaAsPInP	1550	~100	17

also helps reduce nonradiative losses due to Auger recombination, which is a potential problem for lasers at $\lambda > 1$ μm. Typical MQW devices have four to five wells. A basic introduction to the physics of quantum-well lasers is given in the textbook by Yariv [13]. A much more detailed treatment can be found in the articles contained in the book edited by Zory [19]. The tuning ranges of several ECLs with quantum-well gain media are tabulated in Table 3.

2.10 Facet Reflectance Control

2.10.1 Requirements and Overview of Methods

It is desirable to operate an ECL in the regime of strong external feedback in order to maintain acceptably low output power ripple, good tuning linearity, and to avoid such undesirable effects as bistability [23] and axial mode instability [24]. The requirement for strong external feedback is that the mirror losses of the solitary diode cavity are much greater than the combined mirror, filter, and coupling losses of the external cavity. At a minimum, the solitary cavity loss should exceed the external-cavity loss by at least 20 dB. For an extended-cavity configuration (Fig. 1) in which the solitary and external cavities have one mirror in common, this requirement becomes $R_{facet} < 10^{-2} \times R_{ext}$ where R_{facet} and R_{ext} are the power reflectances of the feedback-coupling facet and the external feedback optics, respectively.

For an ECL, an external feedback level of $R_{ext} \approx 0.10$ to 0.30 is typical. Therefore, a rule of thumb is that the facet reflectance should be $\sim 1 \times 10^{-3}$ or less in order to maintain good ECL performance. Because the Fresnel reflectance of the semiconductor–air interface is ~0.31, some means of facet reflectance reduction must be used. The technologies available for reducing the reflectance of gain media facets in external cavity lasers and optical amplifiers are (1) dielectric antireflection coatings, (2) tilted gain stripes, and (3) buried facets. In addition, methods (1) and (2) can be combined.

2.10.2 Antireflection-Coated Facets

2.10.2.1 Single-Layer Coating Design

The most common way to reduce facet reflectance is through the deposition of a dielectric antireflection (AR) coating. For a plane wave incident at an interface

TABLE 3 Tuning Ranges of Quantum Well Gain Media

Material	Structure	Center λ (nm)	Tuning range (nm)	Reference
GaAs/AlGaAs (GaAs substrate)	SQW	800	105	[20]
InGaAs/AlGaAs (GaAs substrate)	Strained SQW	925	170	[21]
InGaAs/InGaAsP (InP substrate)	MQW	1540	200	[22]

between an ambient with index of refraction n_0 and a substrate of index n_s, a single dielectric layer of index

$$n_1 = \sqrt{n_0 n_s} \ . \tag{17}$$

and thickness

$$t = \frac{\lambda}{4n_1} \ . \tag{18}$$

will reduce the reflectance to zero at a wavelength λ (in air). Because of the finite lateral extent of the guided optical wave in the laser diode, the optimum coating design cannot be derived analytically as for plane waves. These formulas are useful only as a guide, with n_0 replaced by unity (refractive index of air) and n_s replaced by n_m, the modal refractive index of the active-region waveguide. The modal index depends on the vertical and lateral structure of the laser diode and is between the bulk reactive indices of the materials used in the active layer and cladding layers. The design of single-layer antireflection coatings was studied by Saitoh and coworkers [25]. They found that $n_{opt} > n_m$ and that $t_{opt} > \lambda/4n_{opt}$ where n_{opt} and t_{opt} are, respectively, the optimum film index and thickness values. They also showed that the tolerances for achieving a low reflectance with single-layer coatings are quite small. To achieve a facet reflectance of 10^{-4} requires film index and thickness tolerances of ± 0.02 and ± 2 nm, respectively. However, with careful process control or real-time *in situ* monitoring of the facet emission during coating [26–28], facet reflectances on the order of 10^{-4} can be obtained reproducibly with single-layer coatings.

2.10.2.2 Multilayer Coating Design

Multilayer dielectric coatings are used to broaden the low-reflectance bandwidth and relax the thickness tolerances of the individual layers. Double-layer coatings are applied in a high–low index sequence with the higher index layer in contact with the substrate. A maximally broad double-layer coating is obtained with

$$n_1 = n_0 \left(\frac{n_m}{n_0} \right)^{3/4} , \tag{19}$$

$$n_2 = n_0 \left(\frac{n_m}{n_0} \right)^{1/4} , \tag{20}$$

$$t_1 = \frac{\lambda}{4n_1} , \tag{21}$$

$$t_2 = \frac{\lambda}{4n_2} , \tag{22}$$

where n_1 and t_1 are the index and thickness, respectively, of the inner layer and n_2 and t_2 are the index and thickness, respectively, of the outer layer. This principle can be extended to three layers by incorporating a third quarter-wave layer with an intermediate index of refraction $n_3 = n_0 (n_m/n_0)^{1/2}$ between the two layers specified above. Other index and thickness combinations for two- and three-layer antireflection coatings are also possible.

Antireflection coatings with three dielectric layers in a low–high–low sequence of refractive indices have been used to relax the tolerances and broaden the low-reflectance bandwidth [29,30].

2.10.2.3 Antireflection Coating Materials

The most widely used material for antireflection coatings on AlGaAs and InGaAsP facets is nonstoichiometric SiO_x, which can be deposited by thermal [25] or electron-beam evaporation [31]. The composition and the film index can be adjusted by varying the oxygen pressure in the deposition chamber. Sputtered Si_3N_4 films have also been used on 0.85-μm AlGaAs and 1.3 and 1.55 μm InGaAsP laser diodes, resulting in facet reflectances in the 0.01 to 0.03% range [32].

2.10.3 Passivation Layers

Commercial telecommunication and CD laser diodes are often shipped with λ/2 facet passivation layers. It is possible to etch off the passivation layer prior to coating or to deposit the antireflection coating over the passivation layer, but it is preferable to start with unpassivated devices if possible.

2.10.4 Angled Facets

An alternative to antireflection coatings is to use an optical amplifier with an angled gain stripe in an external or ring cavity. The waveguide is slanted from the cleavage plane so that the internal Fresnel reflection from the facet is not coupled back into the waveguide and lost. The effective reflectance of the lowest order TE mode decreases exponentially with the slant angle [33]. However, the reflectance of the higher modes increases with the slant angle. Therefore, caution must be exercised if the stripe is wide enough to support higher order modes. For a 2-μm stripe, the calculated facet reflectance is on the order of 10^{-3} for a slant angle of 10° [34].

Even though the internal facet reflections do not couple back to the waveguide, there are still reflections at the semiconductor–air interface that represent loss in coupling to the external cavity. The coupling loss can be reduced by applying antireflection coatings to the angled facets [35].

2.10.5 Buried Facets

Another means of facet reflectance reduction is the use of gain media with buried facets [36]. In these devices the waveguide stops several microns inside the chip, with semi-insulating material between the end of the guide and the

facet. The beam expands inside the buried-facet region since there is no waveguiding. Therefore, the reflection at the semiconductor–air interface does not couple strongly back into the waveguide. The reflectance decreases with increasing length of the buried-facet region. However, if the nonguiding region is too long, the internal beam will hit the top-surface metallization, creating a multiple-lobed far-field output and spoiling the ability to couple efficiently to the mode of the external cavity. This limits the length of the buried facet to <~15 μm and the corresponding reflectance back into the waveguide to >~−20 dB. Therefore, buried-facet gain media would probably give poor performance in a simple extended-cavity laser, but they might be useful in either a double-ended external cavity or ring laser.

3. CLASSES OF EXTERNAL-CAVITY LASERS

The term *external-cavity laser* is often used generically to describe any configuration in which the feedback path extends beyond one or both of the facets of the gain medium. However, it is useful to distinguish three distinct classes of external cavities: the extended cavity, the double-ended cavity, and the ring cavity. The following briefly describes each type.

3.1 Extended-Cavity Lasers

The extended-cavity laser (Fig. 9a) comprises a semiconductor gain chip with an antireflection coating on one facet, optically coupled through the coated facet to an external optical system that includes a retroreflecting end mirror. This configuration has also been called a *pseudo external cavity* [37]. The opposite facet, which is either uncoated or coated as a high reflector, serves as an end mirror of the cavity and is often the output coupler. The extended cavity is the most common configuration for the following reasons: (1) It requires only one antireflection coating operation. (2) An extended cavity can be built using commercial diode laser packages in which the output of only one facet is accessible. (3) The extended-cavity laser is relatively easy to align because the subthreshold emission from the gain chip is strong enough to provide an adequately bright reference beam. (4) Excellent optical performance can be obtained *provided* an excellent AR coating is applied. However, even with a high-quality facet coating, effects of the residual diode cavity resonances are still observable and are sometimes the cause of nonideal behavior.

3.2 Double-Ended External-Cavity Lasers

The double-ended external cavity laser (Fig. 9b) contains a semiconductor optical amplifier with antireflection coatings (or some other type of reflectance

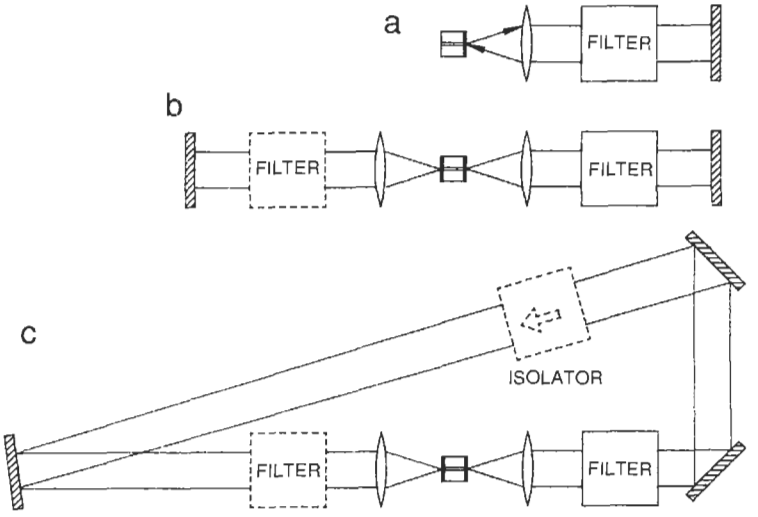

FIGURE 9 Classes of external cavities for diode lasers. (a) Extended-cavity laser. (b) Double-ended external-cavity laser. (c) Ring external-cavity laser.

reduction) on both facets. Each extended-cavity section retroreflects into its respective facet. One of the extended-cavity sections might contain all of the wavelength-selective elements, whereas the other might contain only coupling optics and a retroreflector. The most well-known example of this implementation is a linear external cavity with a Littrow-mounted diffraction grating on one end and a mirror on the other [38]. Alternatively, both extended-cavity sections could contain wavelength-selective elements such as acousto-optic tunable filters. The primary advantage of the double-ended external cavity configuration is increased suppression of diode cavity resonances obtained by reducing the reflectance on both facets. The disadvantages are the increase in the number of optical components, increased alignment difficulty, and the additional coupling loss associated with the second extended-cavity section.

3.3 Ring-External-Cavity Lasers

A ring-cavity (Fig. 9c) laser contains a semiconductor gain medium (with reflection suppression on both facets) and an external feedback path that cross-couples the outputs of the two facets. This is the most difficult type of external cavity to align. Like the double-ended external cavity, it has the advantage of increased solitary-resonance suppression because of the use of reflectance suppression on both facets. It can also be made unidirectional by inserting an optical isolator into the cavity.

4. FIRST-ORDER PROPERTIES

This section defines the main parameters and reviews the major performance features of external-cavity diode lasers.

4.1 External-Cavity Axial Modes

In the case of strong external feedback, the solitary resonances are strongly suppressed by the facet AR coating(s). In this case the axial modes of the system are the Fabry–Perot modes of the external cavity, with modal frequencies ν_q and wavelengths λ_q given by

$$\nu_q = \frac{qc}{2}\left(L_{\text{ext}} + n_{\text{eff}} L_{\text{int}}\right)^{-1} \tag{23}$$

and

$$\lambda_q = \frac{2}{q}\left(L_{\text{ext}} + n_{\text{eff}} L_{\text{int}}\right), \tag{24}$$

where L_{ext} is the total external-cavity path length and n_{eff} and L_{int} are, respectively, the effective index and physical length of the gain medium waveguide. For an extended cavity or double-ended external cavity, q is an integer; for a ring cavity q may only be an even integer. The frequency spacing between modes for an extended cavity or double-ended external cavity is given by

$$\Delta\nu_{\text{ext}} = \frac{c}{2\left(L_{\text{ext}} + n_{\text{eff}} L_{\text{int}}\right)} . \tag{25}$$

The mode spacing for a ring external cavity is given by

$$\Delta\nu_{\text{ext(ring)}} = \frac{c}{L_{\text{ext}} + n_{\text{eff}} L_{\text{int}}} . \tag{26}$$

In terms of wavelength the mode spacing is not constant but can be approximated by

$$\Delta\lambda_{\text{ext}} \approx \frac{\lambda^2}{2\left(L_{\text{ext}} + n_{\text{eff}} L_{\text{int}}\right)} \tag{27}$$

for linear configurations and

$$\Delta\lambda_{\text{ext(ring)}} \approx \frac{\lambda^2}{L_{\text{ext}} + n_{\text{eff}} L_{\text{int}}} \tag{28}$$

for a ring configuration, where λ is assumed to be the midpoint of the tuning range. It is often the case that $L_{\text{ext}} >> n_{\text{eff}} L_{\text{int}}$, and in practice the term $n_{\text{eff}} L_{\text{int}}$ is often neglected when calculating the external cavity modes. Assuming $L_{\text{ext}} \approx 5$–20 cm, we find that $\Delta\nu_{\text{ext}} \approx 1$–$3$ GHz. Thus the axial mode spectrum for an external cavity laser is about 100 times more dense than for a solitary diode laser.

4.2 Wavelength Selection

The principle of wavelength selection in an ECL can be explained with a sketch of the round-trip gain and loss terms (Fig. 10). The gain profile and the filter pass band are familiar from other types of tunable lasers such as dye lasers. However, two other features are atypical of other lasers. First, there is a sizable coupling loss (~5 to 15 dB round trip) between the guided wave in the active region and the free-space beam in the external cavity. Second, interference between the reflections from the gain-medium facets creates an additional intracavity loss that is modulated at the period of the gain-medium mode spacing $\Delta\nu_{\text{int}}$.

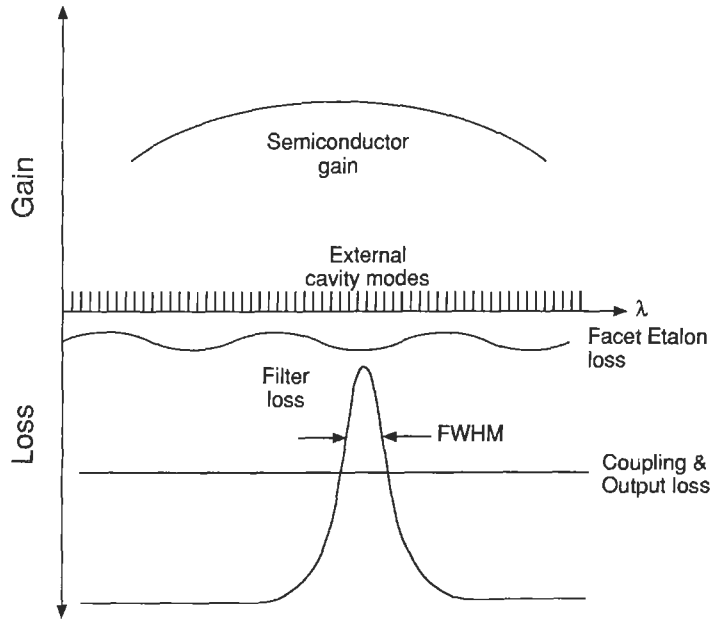

FIGURE 10 Round-trip gain and loss terms for external-cavity diode lasers.

When the gain medium is pumped sufficiently hard, oscillation will occur at the external-cavity mode that sees the lowest net cavity loss. Ideally, the loss ripple due to the facet reflections of the gain medium is weak and the filter bandwidth is narrow compared to the period of the ripple. In this case the oscillation will occur at the external-cavity mode that is closest to the loss minimum of the wavelength-selective filter. Usually the wavelengths of the external-cavity modes are fixed, that is, they do not shift as the filter is tuned. In this case, as the minimum-loss wavelength of the filter is varied, the laser oscillation repeatedly hops to the next external-cavity mode. The output wavelength tracks the filter peak wavelength in a quasi-continuous linear fashion (Fig. 11a). This type of tuning behavior is known as *stepwise* tuning. It is also sometimes called *pseudo-continuous* or *quasi-continuous* tuning. (Cautionary note: Some authors refer to stepwise tuning among external cavity modes as "continuous tuning" because the spacing is much finer than that of the solitary diode-cavity modes. However, in this chapter, this terminology is reserved for lasers that tune without any mode hops whatsoever. This type of tuning is discussed in a later section.)

In practice, the loss modulation caused by the diode-cavity etalon will cause some amount of tuning nonlinearity. Measurable tuning nonlinearity can occur even with surprisingly low facet reflectances (i.e., <1%). If the diode-etalon loss ripple is strong and the filter bandwidth is comparable to, or wider than, the solitary cavity mode spacing, then the tuning relation tends toward a staircase (Fig. 11b) with wavelength jumps approximately equal to $\Delta\nu_{int}$. Such discontinuities in the λ_{osc} vs λ_{fdbk} characteristic are called *tuning gaps*. The suppression of solitary cavity etalon effects is a major reason why the double-ended or ring external-cavity configurations are sometimes used.

4.3 Spectral Narrowing

Many solitary Fabry–Perot diode lasers, especially long-wavelength infrared lasers, run on a multiplicity of axial modes spread over several nanometers.

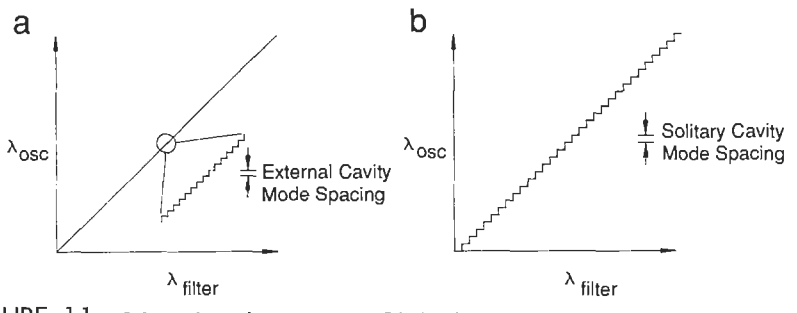

FIGURE 11 Schematic tuning curves: (a) Limit of weak facet reflectances and narrow filter bandwidth. (b) Limit of strong facet reflectances and broad filter bandwidth.

Placing the laser diode in an external cavity with wavelength-selective feedback narrows the spectral width by replacing the solitary diode spectrum with a small number of closely spaced external-cavity modes (ideally a single mode).

The width of each individual mode is also narrowed by the external cavity. The ratio of external-cavity to solitary diode linewidth is given by [39]

$$\delta\nu_{ext} = \delta\nu_{int}\left(1 + \frac{\tau_{ext}}{\tau_{int}}\right)^{-2} \tag{29}$$

where τ_{int} and τ_{ext} are, respectively, the round-trip times of the solitary and external cavities. The external-cavity linewidth is proportional to P_{out}^{-1} (Fig. 12) and L_{ext}^{-2} (Fig. 13). The power and cavity length dependencies of the linewidth have been experimentally confirmed, respectively, by workers at British Telecom [40] and at AT&T Bell Laboratories [41].

4.4 Multimoding

ECLs sometimes have a tendency to exhibit a state of multimode oscillation in which rapid hopping between several neighboring external-cavity longitudinal modes occurs. One estimate of the average mode-hopping frequency for a 1.3-μm InGaAsP laser diode in a 7.5-cm external cavity is [42]

$$f_{hop} \approx \frac{2 \times 10^{-3}}{\tau_p} \exp\left[-1.7\left(\frac{I}{I_{th}} - 1\right)\right], \tag{30}$$

where τ_p is the photon lifetime. Even though a complete theory is not available, multimoding behavior has been found to depend on a number of additional

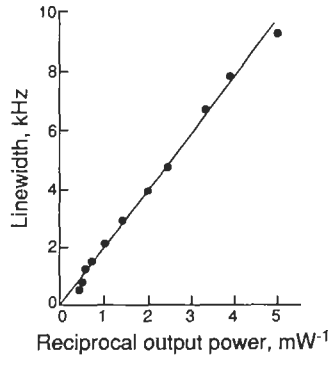

FIGURE 12 ECL linewidth versus reciprocal power dependence. (Reproduced with permission from Wyatt *et al.* [40] and Chapman and Hall Publishers.)

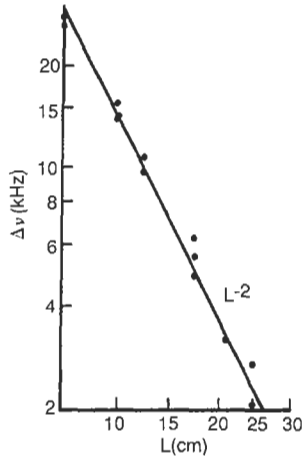

FIGURE 13 ECL linewidth versus cavity length dependence. (Reproduced with permission from Linke and Pollock [41]. © 1986 IEEE.)

factors [24]. First, it depends on the composition of the gain medium: short-wavelength (AlGaAs) lasers tend to be more stable, while lasers at 1.3 and 1.5 μm (InGaAsP) are more prone to this type of behavior. Second, it is affected by the parameters that determine the compound external cavity: the residual facet reflectance, the external reflectance, and the cavity mode selectivity. Third, the mode spectrum is strongly dependent on the wavelength to which the laser is tuned: Multimoding tends to happen at wavelengths falling within periodic bands occurring at the positions of the residual diode cavity Fabry–Perot modes.

4.5 Output Power

The output power for an ECL at a current I above the threshold current I_{th} is given by

$$P_{out} = \frac{h\nu}{q} \frac{\alpha_{mir}}{\alpha_{mir} + \alpha_{int}} \left(I - I_{th}\right) , \tag{31}$$

where α_{mir} is the mirror loss for the appropriate external-cavity configuration. Expressions for the threshold current and the mirror loss for the various external-cavity configurations are given in the next section. Typically, output powers in the range of ~1–10 mW in the lowest order transverse mode can be obtained from external-cavity lasers utilizing narrow-stripe gain media with bulk active regions. About 30–50% of the free-space output power can be coupled into a single-mode fiber pigtail. Higher output power can be obtained using quantum-well gain

media or by going to tapered-stripe gain media. Recently, up to ~1W output has been obtained from an external cavity laser with a tapered-stripe gain medium [43]. The output beam was described as diffraction-limited. The coupling efficiency to optical fiber was not reported.

5. FEEDBACK MODEL

5.1 Effective Reflectance

The basic model for an extended-cavity laser is based on a 3-mirror compound cavity (Fig. 14). The interior facet of the gain medium and the external reflector form a compound mirror. This compound mirror together with the outside facet form a Fabry–Perot resonator. The effective reflectance of the extended cavity, including multiple reflections from the inside facet, is given by [44]

$$r_{\mathrm{eff}}(\nu) = \frac{r_{f2} + r_{\mathrm{ext}}(\nu)\exp\left(i2\pi\nu\tau_{\mathrm{ext}}\right)}{1 + r_{f2}\, r_{\mathrm{ext}}(\nu)\exp\left(i2\pi\nu\tau_{\mathrm{ext}}\right)} . \tag{32}$$

In a double-ended external cavity, each extended-cavity section has its own effective reflectance, i.e.,

$$r_{\mathrm{eff}(i)}(\nu) = \frac{r_{f(i)} + r_{\mathrm{ext}(i)}(\nu)\exp\left(i2\pi\nu\tau_{\mathrm{ext}(i)}\right)}{1 + r_{f(i)}\, r_{\mathrm{ext}(i)}(\nu)\exp\left(i2\pi\nu\tau_{\mathrm{ext}(i)}\right)} \tag{33}$$

where i denotes extended-cavity section 1 or 2. The various parameters are defined in Table 4. The external feedback in a ring cavity is characterized by a wavelength-dependent coupling strength $c_{12}(\lambda)$ which gives the fraction of the field amplitude from facet 1 that is coupled into facet 2. In the absence of nonreciprocal intracavity

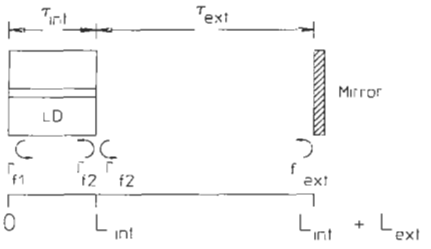

FIGURE 14 Extended-cavity laser feedback model.

elements such as an optical isolator, the coupling between the two facets obeys reciprocity, i.e., $c_{12}(\lambda) = c_{21}(\lambda)$. Multiple reflections between the facets and the external mirrors defining the ring can be neglected because there are no (intentional) standing waves in the cavity. However, sometimes spurious etalons exist between the residual reflections of the facets and the intracavity optics.

5.2 Threshold Current

The gain coefficient per unit length is given by

$$g(I,\lambda) = \gamma\left[I - I_{tr}(\lambda)\right] , \tag{34}$$

where γ is a constant independent of λ, I is the pump current, and $I_{tr}(\lambda)$ is the transparency current. Note that the previously-defined confinement factor Γ has been lumped in with the constant γ. The threshold magnitude condition states that the round-trip gain equals the total round-trip loss. This leads to the following general expression for the threshold current:

$$I_{th} = \frac{1}{\gamma}\left[\alpha_{int} + \alpha_{mir}\right] + I_{tr} , \tag{35}$$

where α_{mir} is represents the mirror loss for the appropriate cavity configuration. These are given below.

5.3 Mirror Losses

The mirror loss in an extended-cavity configuration is given by

$$\alpha_{mir} = \frac{1}{L_{int}} \ln\left(\frac{1}{r_{f1} r_{eff}(\lambda)}\right) . \tag{36}$$

TABLE 4 External Feedback Model Parameters

r_{f1}, r_{f2}	Amplitude reflectances of facets
ν	Optical frequency
$r_{ext1}(\nu)$, $r_{ext2}(\nu)$	Amplitude reflectances of extended cavity sections (lumping, coupling, filter, and mirror losses)
c	Speed of light
$\tau_{ext1} = c/2L_{ext1}$	Round-trip time of extended cavity section with length L_{ext1}
$\tau_{ext2} = c/2L_{ext2}$	Round-trip time of extended cavity section with length L_{ext2}

The mirror loss in a double-ended external-cavity configuration is given by

$$\alpha_{mir} = \frac{1}{L_{int}} \ln\left(\frac{1}{r_{eff1}(\lambda) r_{eff2}(\lambda)}\right) . \tag{37}$$

The mirror loss in a ring-external-cavity configuration is given by

$$\alpha_{mir} = \frac{1}{L_{int}} \ln\left(\frac{1}{c_{12}(\lambda)}\right) . \tag{38}$$

5.4 Strong-Feedback Regime

Because the gain of the semiconductor medium is strongly coupled to its index of refraction, threshold gain ripple caused by the diode-cavity etalon effect gives rise to a number of undesirable phenomena such as bistability, tuning nonlinearities, and in some cases axial mode instabilities [24]. To avoid these problems, it is very desirable to operate a tunable external cavity laser in the strong-feedback regime, in which $r_{ext}^2 >> r_f^2$. For a bare cleaved facet in air, $r_f^2 \approx 0.31$. Due to mode coupling losses, it is not possible to obtain external feedback much greater than $r_{ext}^2 \approx 0.40$. Therefore, operation in the strong feedback regime requires some method of facet reflectance reduction. The most common approach is to use a dielectric AR coating. Strong feedback also requires proper design of the external cavity to ensure low-loss coupling of the cavity and waveguide modes. Having previously discussed facet reflectance reduction, we now discuss external cavity optical design.

6. EXTERNAL-CAVITY DESIGN

The first subsection presents general cavity design principles that are broadly applicable regardless of the implementation. The succeeding subsections give specifications for various intracavity optical components and their positioning in the cavity.

6.1 General Design Principles

In any external-cavity design, one should try to maximize the external feedback strength and wavelength selectivity of the cavity. Brief explanations of the importance of these two conditions and definitions of their respective figures of merit are as follows. Strong external feedback is needed to obtain low output power ripple with respect to wavelength and to avoid bistability [45]. It also improves the ability to obtain single-mode oscillation without mode-hopping

instabilities [24] and the fidelity with which the oscillation wavelength tracks the peak feedback wavelength [46]. The figure of merit for external feedback strength is the *cavity loss ratio,* that is, the ratio of the mirror loss of the solitary cavity to the loss of the external cavity. Table 5 defines the cavity loss ratio for the three different external cavity classes. The cavity loss ratio should be at least 20 dB for any external cavity design.

There are two figures of merit for wavelength selectivity. The first is the *solitary cavity mode selectivity,*

$$N_{\text{int}} = \frac{\Delta\nu_{\text{FWHM}}}{\Delta\nu_{\text{int}}} \tag{39}$$

which is the ratio of the filter FWHM bandwidth to the solitary cavity axial mode spacing. Provided the cavity loss ratio is >20 dB, good tuning fidelity in the tracking between the oscillation wavelength and the peak feedback wavelength will be obtained with N_{int} less than about 0.3. For $N_{\text{int}} \approx 1$, a cavity loss ratio of at least 30 dB is needed to obtain reasonably linear tuning.

The other figure of merit for wavelength selectivity is the *external-cavity mode selectivity,*

$$N_{\text{ext}} = \frac{\Delta\nu_{\text{FWHM}}}{\Delta\nu_{\text{ext}}} , \tag{40}$$

which is the ratio of the filter FWHM bandwidth to the external cavity mode spacing. To ensure single mode operation, it is necessary to have $N_{\text{ext}} \leq 1$.

6.2 Component Throughput

The most critical component for determining the feedback strength is the intracavity collimating lens. A general requirement for strong feedback in

TABLE 5 Figures of Merit for External Feedback Strength

Cavity configuration	Cavity loss ratio
Extended	$10 \log\left(\frac{R_{eff}}{R_{f2}}\right)$
Double-ended	$10 \log\left(\frac{R_{eff1}R_{eff2}}{R_{f1}R_{f2}}\right)$
Ring	$10 \log\left(\frac{C_{12}}{R_{f1}R_{f2}}\right)$

extended-cavity or double-ended configurations is that the collimating lens must transform the Gaussian beam waist at the gain medium facet into another waist at the surface of the external mirror (Fig. 15). In ring external cavities, the intracavity optics must transform the output beam from each facet into a beam waist that matches the output beam from the opposite facet. Obtaining efficient coupling puts requirements on the numerical aperture, wavefront distortion, and attenuation of the collimating lens.

6.2.1 Numerical Aperture

Perpendicular to the junction plane the output beam from the gain medium has a divergence angle of up to $\theta_v = 40°$ FWHM. For the Gaussian intensity profile the $1/e^2$ point is 1.7 times the FWHM value. The collimating lens should have a sufficiently large numerical aperture (NA) to capture the beam out to these points, that is,

$$NA \geq \sin\left(\frac{1.7}{2}\theta_v\right) = 0.55$$

6.2.2 Wavefront Distortion

Wavefront distortion reduces the overlap integral between the waists of the output and return beams (Fig. 16) [47]. In an extended cavity, the effect of wavefront distortion is multiplied by 2 since the beam transits the collimating lens twice. A peak-to-peak wavefront distortion of $\lambda/4$ results in a 2-dB reduction in coupling efficiency. A maximum peak-to-peak wavefront distortion of $\lambda/4$ over the usable aperture of the collimating lens should be specified.

6.2.3 Attenuation

One-way coupling efficiencies for good large-aperture coupling lenses are typically in the range of 50 to 70%. Therefore, the maximum round-trip feedback efficiency is limited to the range of 25 to 50% by the coupling lens, assuming no other intracavity losses. In general, an overall feedback efficiency of >10% is desirable from an extended cavity. Therefore, the total of the additional round-trip

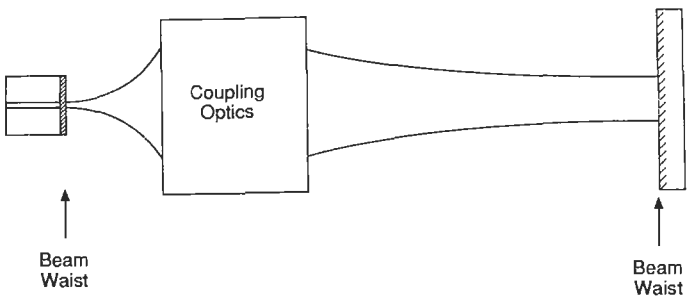

FIGURE 15 Intracavity beam transformation by coupling optics.

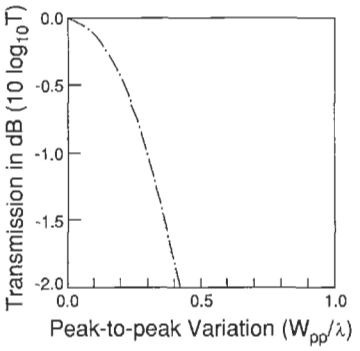

FIGURE 16 Effect of wavefront distortion on coupling efficiency (from Wagner and Tomlinson [47]).

insertion losses from all other intracavity components should not exceed 4 dB. All intracavity lenses should be AR coated to minimize losses and avoid spurious etalon effects. The round-trip insertion loss of the wavelength filter(s) should total no greater than ~3 dB.

6.3 Alignment Stability and Positioning Tolerances

In the strong-feedback approximation, the primary feedback reflection reenters the waveguide after only one round-trip through the external cavity. Therefore, in contrast to the design of conventional laser resonators, multiple-pass stability [48] is not usually an important issue. However, the tolerances for positioning and aligning the external-cavity optics can become quite severe due to the small cross section of the active area at the feedback-coupling facet. Alignment stability can be simply analyzed using Gaussian beam theory.

Consider a retroreflecting external-feedback section that is part of an extended or double-ended cavity. The extended cavity sections each contain a beam relay section, a filter, and an end reflector. The relay optics can typically be broken down into a collimation section that collimates the active-area emission and beam-shaping optics that reshape the beam incident on the filter. Without loss of generality, the relay optics can be assumed to be lossless, with the external-cavity losses being lumped into the reflectance of the end mirror. We assume that the filter is either a transmission device with no focusing power (e.g., an etalon or an acousto-optic filter) or a planar reflector (e.g., a diffraction grating). For the purposes of Gaussian beam propagation, the filter then simply modifies the path length of the cavity and changes the reflectance of the end reflector. There are therefore two requirements for strong coupling between the external cavity and the waveguide:

1. The relay optics must transform the Gaussian beam waist at the waveguide output in the facet plane into another waist at the surface of the end mirror.
2. The end reflector must be aligned so as to retroreflect the incident beam back to the active spot on the diode facet. The alignment sensitivities can be deduced using fairly simple arguments from Gaussian beam theory. Note that the sensitivities may be different in the tangential and sagittal planes of the cavity.

6.3.1 Collimating Lens Axial Position Tolerance

This refers to the sensitivity to axial positioning of the intracavity elements with respect to the diode facet. It can be shown that the axial tolerance δz_{tol} of the collimating lens is approximately given by the Rayleigh range z_R [49] of the beamwaist at the diode facet:

$$\delta z_{tol} \approx z_R = w_d^2/\lambda \ , \tag{41}$$

where w_d is the spot size at the feedback-coupling facet of the gain diode.

6.3.2 Mirror Angular Alignment Tolerance

The angular alignment tolerance $\delta\theta_{tol}$ of external mirror is approximately given by the divergence angle θ_{div} of the waist spot incident on it:

$$\delta\theta_{tol} \approx \theta_{div} = \frac{\lambda}{w_r} \ , \tag{42}$$

where w_r is the spot size at the retroreflector.

6.3.3 Gain Medium Transverse Position Tolerance

A small lateral displacement δx between the gain medium and the collimating lens is equivalent to angular misalignment of the external reflector by an angle $\delta x/f$, where f is the focal length of the lens. Thus, the lateral lens tolerance is given by

$$\delta x_{tol} \approx \frac{f\lambda}{w_r} \ . \tag{43}$$

6.4 The Degenerate Resonator

A degenerate Fabry–Perot resonator [50] comprises two end mirrors and two intracavity lenses; each lens is spaced from the adjacent mirror by its respective focal length, and the two lenses are separated from each other by the sum of their

focal lengths. In the geometric optics approximation, the degenerate resonator has the property that rays emitted from a point on either mirror return to that point after one round-trip (recycle), independent of mirror tilt or lateral displacement of the source point from the optical axis of the cavity. The degenerate-resonator concept can be usefully applied to ECL design (Fig. 17). The degenerate extended-cavity laser contains two lenses. The first lens, adjacent to the laser diode, creates a central collimation region in the cavity where the tunable filter can be inserted. The second lens refocuses the intracavity beam onto the external mirror. The combination of the second lens and the external mirror forms a cat's-eye retroreflector [51]. The retroreflecting property of the cat's eye is highly insensitive to mirror tilt. Provided the distance between the lenses is $f_1 + f_2$, the feedback from the cavity is also insensitive to lateral displacement of the active area with respect to the optic axis. If the distance between the two lenses is not equal to $f_1 + f_2$ but the distance between the second lens and the external mirror is equal to f_2, the feedback is still insensitive to mirror tilt and the cavity is called "quasi-degenerate." The degenerate-resonator concept can be independently applied in one dimension by using a cylindrical lens for refocusing onto the external mirror.

6.5 Chromatic Aberration

Chromatic aberration refers to the variation of the focal length of a lens with wavelength. Because ECLs operate over wide wavelength ranges and the position of the collimating lens is critical to laser performance, chromatic aberration can require the collimating lens working distance to be adjusted as the wavelength is varied. Multielement lenses such as microscope lenses can be corrected for chromatic aberration. Single-element lenses such as graded-index rod lenses and ball lenses cannot be corrected.

6.6 Birefringence

Some lenses, especially plastic lenses, may be birefringent due to stresses built up during the manufacturing process. Birefringence will change the polarization state of the intracavity light, reducing the external feedback.

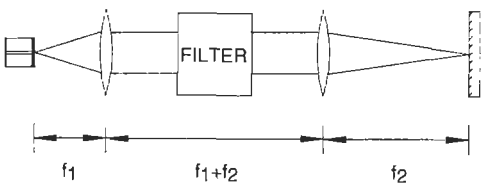

FIGURE 17 Generic laser based on a degenerate extended resonator.

7. CAVITY COMPONENTS

7.1 Coupling Optics

7.1.1 Collimating Lenses

A number of different types of lenses have been used to collimate the active-area emission in ECLs. Brief descriptions of the most common types and their properties are described in this section.

7.1.1.1 Microscope Objectives

These multiple-element spherical lens systems are available with numerical apertures as high as 0.8. To minimize loss and spurious etalon effects, all external and internal surfaces should be AR coated. Multiple-element collimating objectives specifically designed for laser diodes [52] are commercially available from vendors such as Melles Griot and Newport. Care should be used when selecting collimating objectives since many are designed to be used with a cover glass over the laser diode. Disregard for this fact will cause additional wavefront distortion.

7.1.1.2 GRIN Rod Lenses

Rod lenses with a radially graded index of refraction are manufactured by Nippon Sheet Glass and marketed under the name SELFOC [53]. These lenses are quite useful for ECLs, but they have higher wavefront distortion than the best multiple-element systems, which probably reduces somewhat the maximum external feedback that can be obtained. The plano–plano versions have numerical apertures up to ~0.45. A plano–convex version has an NA of 0.60.

7.1.1.3 Silicon Lenses

Singlet silicon lenses have lower spherical aberration for a given NA because of the high refractive index of silicon [54]. Because silicon is strongly absorbing for $\lambda < 1.1\mu m$, these lenses are only useful for ECLs operating in the 1.3- to 1.5-μm tuning bands. Material dispersion may cause significant chromatic aberration and limit the tuning range that can be achieved without working distance adjustment to less than the full gain bandwidth.

7.1.1.4 Aspheric Lenses

Molded glass and plastic aspheres can be made with low wavefront distortion and are available with numerical apertures up to 0.55 [55]. Glass is superior to plastic with respect to birefringence. Special high-index glasses reduce the severity of the aspheric curve needed to correct for spherical aberration, making the lenses easier to fabricate consistently. Molded aspherics are single-element lenses, so correction of chromatic dispersion is not possible. Dispersion in the lens material may limit the wavelength range that can be covered without working-distance adjustment. An ECL containing a molded-glass aspheric collimating lens has been reported [56].

7.1.1.5 Camera Lenses

There are at least three published reports on the use of camera lenses as collimators in ECLs. Heckscher and Rossi [57] reported the use of a TV camera lens for intracavity collimation of a Littrow grating cavity, but gave no indication of the feedback strength obtained. Sommers [58] evaluated several camera lenses from *f*/0.99 (25-mm focal length) to *f*/2.0 (50-mm focal length). The lenses gave only about 1% feedback when used with a grating, and it was concluded that spherical aberration was responsible for the poor performance since the lenses were not used in their intended geometry. Fleming and Mooradian successfully employed camera lenses in an ECL [38]. They used 50-mm focal length, *f*/1.4 seven-element lenses. All air–glass surfaces were AR coated.

7.1.1.6 Ball Lenses

Glass spheres can be used to couple the gain medium to waveguide or fiber-pigtailed external filters. However, the spherical aberrations are too great to be useful for collimation in bulk optic cavities.

7.1.1.7 Lensed Fiber

Lensed optical fiber [59] can be used to couple the gain medium to fiber-pigtailed external cavities. However, this method requires the fiber to be in very close proximity to the facet, which gives rise to the danger of facet damage. There is also a very high sensitivity of the coupling loss to lateral misalignment.

7.1.2 Optics for Beam Expansion and Shaping

7.1.2.1 Cylindrical Lenses

A cylindrical lens can be used in an ECL [60] to form a line illumination on a diffraction grating. This implements a degenerate resonator in one dimension and provides a high degree of angular misalignment tolerance while maintaining high spectral selectivity. Critical to the success of this technique is the fact that the cylinder axis can be inclined with respect to the optical axis at a large angle to match the grating angle of incidence without introducing a large amount of spherical aberration. This is because the cylinder lens has no power in this plane and appears to be a tilted plate.

7.1.2.2 Prisms

The use of prism beam expanders allows the use of a compact, high-resolution grating-tuned extended-cavity laser [61]. A particularly useful geometry is when the apex angle θ_a is cut so that

$$\theta_a = 90° - \tan^{-1}(n), \tag{44}$$

where n is the index of refraction of the prism material. For this choice of apex angle, the output beam is normal to the exit face of the prism (which is the

condition of maximum expansion) when the angle of incidence equals the Brewster angle. The magnification of each prism is then equal to the index of refraction of the prism material, that is, $M = n$.

7.2 Tunable Filters

The ideal filter for an ECL has a bandwidth that is less than the axial mode spacing of the cavity and has 0-dB insertion loss at its peak. No real filter is ideal, but a number of different types of wavelength-selective elements have been used to tune external cavity lasers. The filters are grouped according to whether they are actuated by mechanical means (e.g., have moving parts) or electronically (no moving parts).

7.2.1 Mechanically Tuned Filters

7.2.1.1 Diffraction Gratings

7.2.1.1.1 Types of Gratings

Diffraction gratings are the most common type of filter used in ECLs and have arguably the best optical performance. A diffraction grating consists of a large number of regularly spaced grooves on a substrate. The distance between adjacent grooves is called the *pitch*. If the underlying substrate is reflective, then we have a *reflection grating* [Fig. 18(a)]. If the substrate is transmissive, then the device is said to be a *transmission grating* [Fig. 18(b)].

Diffraction gratings are also classified by the way in which they are manufactured. When the grooves are created by scribing with a ruling engine, the device produced is a ruled *master* grating. Relatively few masters are produced, and these are rarely sold. The groove pattern of the master can be faithfully transferred by a contact process to a number of *replica* gratings, which are then made available commercially (e.g., by Milton Roy).

Diffraction grating groove patterns are also generated by exposing photoresist with the fringe pattern created by two interfering beams of laser light. Such gratings are called *holographic* and are also sold commercially (e.g., by American Holographic).

7.2.1.1.2 Principle of Operation

When a beam of light is incident on a grating, each groove generates a diffracted wavelet. For each wavelength component in the incident beam, the constructive interference of the diffracted components from each groove occurs at a unique set of discrete directions called the *diffraction orders* of the grating.

7.2.1.1.3 The Grating Equation

The geometry of the diffraction pattern from a grating is governed by the grating equation:

$$a\left(\sin\theta_i + \sin\varphi_m\right) = m\lambda \ , \tag{45}$$

where a is the groove spacing (pitch), θ_i is the incident angle, φ_m is the diffracted angle of the m'th order, and m is the order of diffraction. The diffracted light is dispersed according to its spectral content, with different wavelengths appearing at different angles. Differentiating the grating equation gives the angular dispersion D, which describes how much the diffraction angle changes as the wavelength varies:

$$D = \frac{d\varphi_m}{d\lambda} = \frac{m}{a\cos\varphi_m} = \frac{\left(\sin\theta_i + \sin\varphi_m\right)}{\lambda\cos\varphi_m} \ . \tag{46}$$

Diffraction gratings are usually used in first order in ECLs, that is, with $m = 1$. The zeroth-order (specular reflection) beam is sometimes used for output coupling.

The wavelength resolution of a grating-tuned external cavity is determined by the angular dispersion multiplied by the acceptance angle for coupling back into the gain medium active region. The angular dispersion can therefore be used

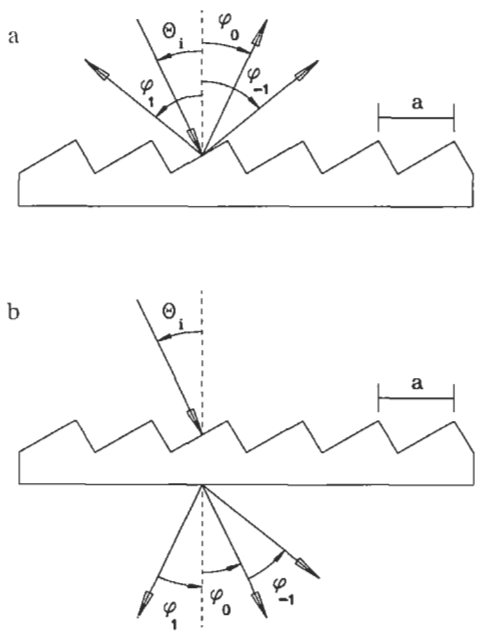

FIGURE 18 Types of plane diffraction gratings. (a) Reflection grating. (b) Transmission grating (reproduced with permission from Palmer [62]).

as a figure of merit, but it must be remembered that the parameter of ultimate importance is the grating resolution divided by the axial mode spacing of the external cavity. (For a detailed description of multiple-prism grating dispersion, see Chapter 2.)

7.2.1.1.4 Common Mountings

Diffraction gratings in external cavity lasers combine the functions of the filter and external mirror. In extended cavities, the light from the grating must be retroreflected back into the gain medium. Two common retroreflecting mounting geometries for diffraction gratings in extended-cavity lasers are the autocollimation (Littrow) configuration and the grazing-incidence (GI) configuration.

7.2.1.1.4.1 Littrow Mounting In the Littrow configuration [Fig. 19(a)], the angles of incidence and diffraction are equal: $\theta_i = \varphi_1$. The grating equation becomes

$$\lambda = 2a \sin \theta_i \ . \tag{47}$$

In this case the angular dispersion of the retroreflected beam is identical to that of the diffracted beam and is given by

$$D_{\text{Littrow}} = \frac{d\varphi_1}{d\lambda} = \frac{2 \tan \theta_i}{\lambda} \ . \tag{48}$$

A typical angle of incidence for the Littrow configuration is $\theta_i \sim 50°$.

7.2.1.1.4.2 Grazing-Incidence Mounting In the grazing-incidence configuration (Fig. 19b), the intracavity beam makes two passes at the grating. The diffracted light from the second pass is a retroflection of the incident light from

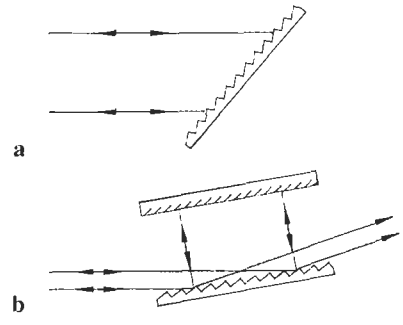

FIGURE 19 Diffraction grating mountings. (a) Littrow. (b) Grazing incidence.

the first pass. Therefore, the angular dispersion of the retroreflected light is twice that of the light diffracted on one pass:

$$D_{\mathrm{GI}} = 2\frac{d\varphi_1}{d\lambda} = \frac{4\tan\theta_i}{\lambda} = 2D_{\mathrm{Littrow}} \ . \tag{49}$$

The dispersion of the grazing-incidence configuration is therefore twice that of the Littrow configuration for the same angle of incidence. In addition, the grazing-incidence configuration is typically used with a much higher angle of incidence, for example, $\theta_i \sim 85°$.

7.2.1.1.5 Grating Efficiency

7.2.1.1.5.1 Blazed Gratings Blazing refers to an enhancement in efficiency that is obtained at a particular wavelength when the grooves on the grating surface have a triangular shape. A simple explanation for this effect is that when the specular reflection from the top surface of each groove coincides with the direction of diffraction, the reflections reinforce the diffraction effect and the efficiency is maximized. The wavelength λ_B at which this reinforcement occurs is called the "blaze wavelength." The angle θ_B of the top surface of the groove with respect to the macroscopic surface of the grating is called the "blaze angle." The terminology derives from the observation that a grating will light up or "blaze" when viewed at the correct angle.

The blaze angle of ruled gratings is defined during the process of ruling the master grating and is transferred to the replica. The simplest type of holographic grating has a sinusoidal shape. However, after interferometric recording, the grooves of holographic gratings can be shaped to approximate blazing by an ion-beam milling process.

In a Littrow mounting the blaze condition is satisfied when the tops of the grooves are perpendicular to the incident beam. The diffraction efficiency rises as the angle of incidence is increased up to $\sim\theta_B$ and falls thereafter. This simple description is only valid for low blaze angles (up to ~10°). Working near λ_B for small blaze angles implies a small diffraction angle as well, so that $\lambda \ll a$. This is the regime of validity for scalar diffraction theory, in which the diffraction efficiency is nearly independent of polarization.

7.2.1.1.5.2 Polarization Effects To obtain greater angular dispersion it is necessary to use larger blaze and diffraction angles, which implies $\lambda \sim a$. This is the regime of vector diffraction theory in which polarization effects become significant. For blaze angles above ~10°, the diffraction efficiency strongly depends on the orientation of optical polarization with respect to the direction of the grooves. A particularly useful regime for tuning ECLs is the range of blaze angles from about 22° to 38°. For this regime, there is a broad plateau of high efficiency for $\theta_i > \theta_B$ when the incident polarization is perpendicular to the

direction of the grooves on the grating (Fig. 20). The reader who desires further details on the subject of grating efficiency and polarization effects is advised to consult the excellent material in [62].

7.2.1.1.6 Wavelength Resolution

The wavelength resolution is obtained by dividing the angular spread of the beam waist at the grating (waist divergence) by the angular dispersion. The waist divergence of a Gaussian beam of radius w_g is given by

$$\Delta\theta_{\text{div}} = \frac{\lambda}{\pi w_g} \ . \tag{50}$$

The wavelength resolutions for the Littrow and grazing-incidence cases are, respectively:

$$\Delta\lambda_{\text{FWHM (Littrow)}} = \frac{\Delta\theta_{\text{div}}}{D_{\text{Littrow}}} = \frac{\lambda^2}{2\pi w_g \tan\theta_i} \ , \tag{51}$$

$$\Delta\lambda_{\text{FWHM(GI)}} = \frac{\theta_{\text{div}}}{D_{\text{GI}}} = \frac{\lambda^2}{4\pi w_g \tan\theta_i} \tag{52}$$

It is useful to relate grating resolution to the *filled depth* of the grating. The filled depth is the projection of the illuminated region of the grating onto the optical axis of the cavity. The filled depth L_g is given by

$$L_g = 2w_g \tan\theta_i \ . \tag{53}$$

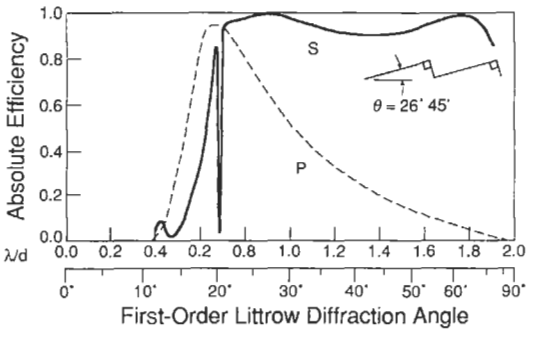

FIGURE 20 Efficiency versus angle of incidence for Littrow grating (from Palmer [62]).

For the Littrow geometry, the grating resolution can be expressed in terms of the filled depth as

$$\Delta\lambda_{\mathrm{FWHM[Littrow]}} = \frac{\lambda^2}{\pi L_g} \ . \tag{54}$$

For the grazing-incidence geometry, the resolution is

$$\Delta\lambda_{\mathrm{FWHM[GI]}} = \frac{\lambda^2}{2\pi L_g} \ . \tag{55}$$

In terms of optical frequency, the grating reflectance function for a Gaussian beam is given by [63]

$$R(\nu) = R(\nu_0)\exp\left[-2\frac{(\nu-\nu_0)^2}{\Delta\nu_{\mathrm{FWHM}}^2}\right], \tag{56}$$

where the band width is given by

$$\Delta\nu_{\mathrm{FWHM}} = \frac{c}{\pi L_g} \ . \tag{57}$$

7.2.1.2 Distributed Bragg Reflector

7.2.1.2.1 Principle of Operation

Periodic modulation of the index of refraction along the length of an optical waveguide results in a structure known as a distributed Bragg reflector. The reflection is maximized at a wavelength for which the period of the modulation is equal to $\lambda/2$. If the modulation period can be varied, then the reflected wavelength can be tuned.

7.2.1.2.2 Embodiment in Optical Fiber

A variable-wavelength distributed Bragg reflector for single-mode optical fiber has been realized in the following form [64]. An optical fiber was placed in a groove in a fused silica substrate. The substrate was then polished until part of the cladding of the fiber was removed. On a separate substrate, a fan-shaped grating consisting of slowly diverging lines of sputtered amorphous silicon was fabricated. The grating was placed face-down on the side-polished fiber with a small amount of index-matching oil between the substrates. The grating then was able to interact with the evanescent field in the fiber. The grating substrate was able to slide over the fiber substrate, thus changing the pitch of the grating

that was coupled to the fiber evanescent field. In this way, a fiber reflective grating was obtained that had a reflectance of ~60 to 80% for 1280 nm < λ < 1340 nm. The grating FWHM was between 0.7 to 1.2 nm.

7.2.1.3 Fabry–Perot Etalon

7.2.1.3.1 Principle of Operation

The filtering effect of the Fabry–Perot etalon utilizes the interference fringes produced in the transmitted light after multiple reflections between two highly reflective mirrors [65]. The Fabry–Perot etalon has periodic transmission peaks at wavelengths that satisfy the relation

$$2nd \cos\theta = m\lambda \,, \tag{58}$$

where d is the mirror spacing, n is the index of refraction of the space between the mirrors, θ is the angle of incidence, and m is an integer. Tuning can be accomplished by changing the mirror separation or by varying the angle of incidence.

7.2.1.3.2 Resolution

The ratio of the wavelength of a fringe peak to the FWHM of the peak of a Fabry–Perot etalon is called the *chromatic resolving power*. The chromatic resolving power is given by

$$\frac{\lambda}{\Delta\lambda_{\mathrm{FWHM}}} = m\frac{\pi r}{1 - r^2} \,. \tag{59}$$

where r is the amplitude reflectance of the mirrors.

7.2.1.3.3 Free Spectral Range

For a typical air-spaced or solid etalon, d is equal to a few millimeters. The wavelength spacing between maxima is given by the free spectral range.

$$\Delta\lambda_{FSR} \equiv \lambda_m - \lambda_{m+1} = \frac{2d\cos\theta}{m(m+1)} \approx \frac{\lambda^2}{2nd} \,. \tag{60}$$

For example, for λ = 1300 nm, d = 1 mm, and n = 1.5, the free spectral range is 0.56 nm.

7.2.1.3.4 Finesse

The spacing between orders relative to the width of a single order is given by the finesse f. The finesse is defined as

$$\Im = \frac{\Delta\lambda_{\mathrm{FSR}}}{\Delta\lambda_{\mathrm{FWHM}}} \,. \tag{61}$$

With special mirror coating technology, the finesse of an etalon can be as high as ≈10,000, but a finesse of a few hundred is more typically achieved with conventional coatings.

7.2.1.4 Interference Filter

A bandpass interference filter is a multilayer thin-film device [66]. The simplest type is really a Fabry–Perot etalon with $d \sim \lambda$. If the thickness of an etalon is made very small, the orders will be widely separated. This is done by evaporating dielectric-stack mirrors, separated by a half-wave spacer layer, in a continuous coating run on a substrate. Multiple reflector pairs (called cavities) can be deposited to steepen the passband. Additional metallic-layer blocking structures deposited on another plate are used to eliminate adjacent transmission orders. The plates are assembled in a sandwich that protects the deposited films. Interference filters can be made with FWHM bandwidths 2 nm or less in the near infrared and less than 1 nm in the visible. The peak transmittance can be made as high as 50 to 70%.

The interference filter is tuned by tilting it in the incident beam. For small angles (up to 5 to 10°), the wavelength of peak transmittance is given by

$$\lambda = \lambda_{max} \sqrt{\left[1 - \left(\frac{n_o}{n_e}\right)^2 \sin^2 \theta\right]^{1/2}} \quad , \tag{62}$$

where θ is the angle of incidence, n_o is the refractive index of the external medium, and n_e is the effective refractive index of the spacer.

7.2.2 Electronically Controlled Filters

7.2.2.1 Birefringent Filter

There are several forms of the birefringent filter [67,68]. They can be tuned either mechanically or electronically, with electronic tuning being the preferred means. The basic birefringent filter is called a *Lyot filter* and comprises an alternating stack of N uniaxial birefringent plates separated by polarizers. The thicknesses of the plates vary in a geometrical progression $d, 2d, 4d, \ldots, 2^{N-1}d$. The transmission axes of the polarizers are all aligned. The light propagates in a direction perpendicular to the c axis of each of the plates. Transmission through each segment (plate plus polarizer) will vary sinusoidally, with maxima at wavelengths for which the retardation of the plate is a multiple of 2π. For a plate of thickness d, the free spectral range $\Delta\lambda_{FSR}$ between successive maxima is approximated by

$$\Delta\lambda_{FSR} \approx \frac{\lambda}{d} \frac{1}{\left(\partial\Delta n/\partial\lambda - \Delta n/\lambda\right)} \quad . \tag{63}$$

For each segment, the separation between transmission maxima and the FWHM of one of the maxima is inversely proportional to the plate thickness. Thus, the resulting transmission spectrum for the entire stack will consist of narrow bands having the FWHM of the thickest plate and separated by the free spectral range of the thinnest plate. Electronically tuned birefringent filters can be realized using liquid crystal cells as the birefringent plates [69,70]. The electro-optic effect can also be used, either in bulk crystals [71] or in birefringent lithium niobate waveguides [72].

7.2.2.2 Acousto-Optic Tunable Filter

7.2.2.2.1 Principle of Operation

The acousto-optic tunable filter (AOTF) operates on the principle of anisotropic Bragg diffraction in a birefringent crystal. A piezoelectric transducer is bonded to a crystal. When the transducer is driven with an rf signal, a traveling acoustic wave is generated. The acoustic wave produces a moving refractive index grating (phase grating) in the crystal via the elasto-optic effect. Under the proper conditions, the AOTF couples a portion of the energy in a linearly polarized incident beam of light into an orthogonally polarized output beam. The interaction must satisfy the phase-matching condition $k_d = k_i \pm k_a$, where k_i, k_d, and k_a are, respectively, the momentum vectors of the incident, diffracted, and acoustic waves (Fig. 21). The AOTF is designed so that, for a given acoustic frequency, only a narrow range of optical frequencies will satisfy the phase-matching

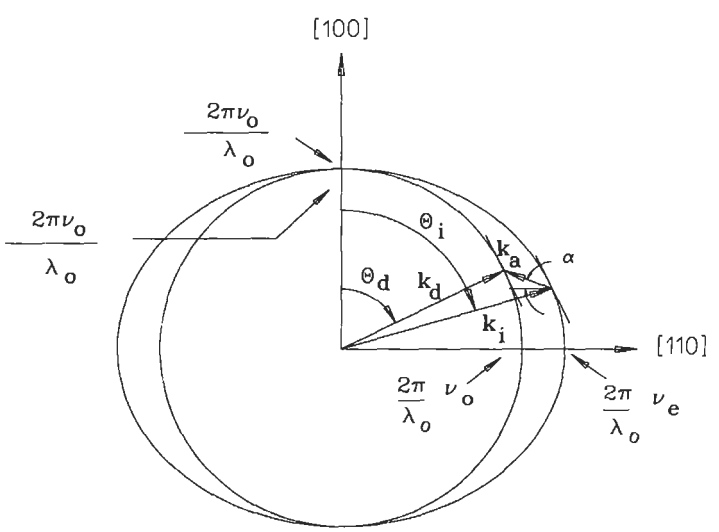

FIGURE 21 Index ellipsoids and optical and acoustic k vectors illustrating phase matching in an AOTF.

condition. Thus, the AOTF is functionally an rf-controlled narrow-band optical polarization converter. Changing the acoustic drive frequency shifts the band of optical wavelengths for which the optical polarization is flipped. Separation of the diffracted light from the residual undiffracted zeroth-order component results in an electronically controlled optical filtering operation.

7.2.2.2.2 Acousto-Optic Filter Geometries

The first AOTF was invented by Harris and Nieh [73]. This device had a geometry in which both optical beams were collinear with the acoustic beam. This necessitated immersion in index matching oil [74] in order to bring the optical and acoustic beams into collinearity and properly terminate the acoustic beam. A few years later, the noncollinear AOTF was developed by Yano and Watanabe [75], and modern AOTFs are of this type (Figs. 22 and 23). AOTFs are sold commercially by several manufacturers including Crystal Technology and Brimrose. Most designs make use of tellurium dioxide (TeO_2) as the acoustic medium, which has a transparency range extending from 0.35 to 5.0 μm and a lower acoustic power requirement than crystals used for collinear filters.

7.2.2.2.3 Filter Characteristics

For complete details on the design of noncollinear AOTFs, the comprehensive paper by Yano and Watanabe [76] should be consulted. The following expressions contain a dimensionless parameter $x \approx 1$, whose value depends on the orientations of the various beams with respect to the crystallographic axes [77].

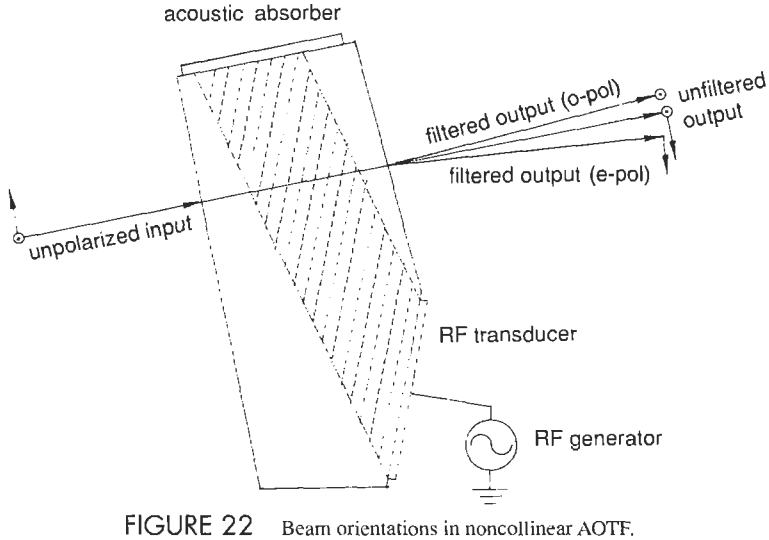

FIGURE 22 Beam orientations in noncollinear AOTF.

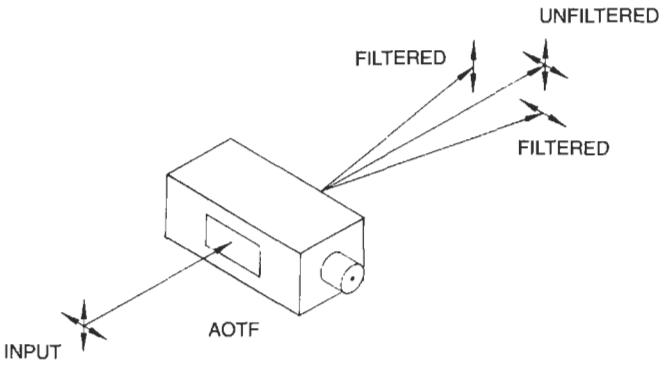

FIGURE 23 External view of AOTF.

7.2.2.2.3.1 ***Peak Wavelength*** The peak wavelength of the transmission passband λ_o is given by

$$\lambda_o = \frac{\upsilon_a \Delta n_b}{f_a} x \ . \tag{64}$$

where υ_a is the acoustic velocity, f_a is the acoustic frequency, and Δn_b is the crystal birefringence. Acousto-optic filters in principle can be made that will cover an octave of optical frequency. The practical limitation is the rf matching network for the transducer. Tuning from 1.25 to 1.6 μm with a single device is definitely possible.

7.2.2.2.3.2 ***Passband Width*** The passband width (often called the resolution) of an acousto-optic filter is given by

$$\Delta\lambda_{\text{FWHM}} \approx \frac{\lambda^2}{L_a \Delta n_b} x \ , \tag{65}$$

where L_a is the acousto-optic interaction length. Subnanometer resolution in the visible and a FWHM of ~1 nm at around 1.3 μm have been achieved (Fig. 24).

7.2.2.2.3.3 ***Diffraction Efficiency*** The diffraction efficiency is given by

$$\frac{I_d}{I_i} \approx \sin^2\left[\frac{\pi}{\sqrt{2}\lambda}\left(\frac{P_a}{h_{\text{eff}}}\right)^{1/2} M^{1/2} x\right] \ . \tag{66}$$

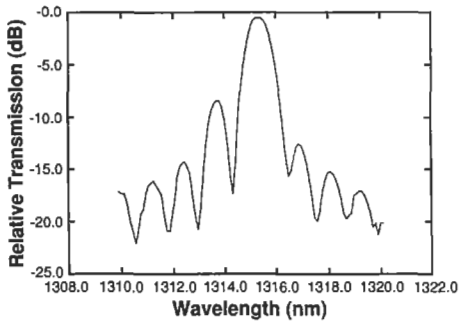

FIGURE 24 Transmission spectrum of an AOTF driven at 89.139 MHz. (Reproduced with permission from Zorabedian [46]. © 1995 IEEE.)

where I_i and I_d are, respectively, the incident and diffracted intensity, P_a is the acoustic power, h and w are, respectively, the height and width of the transducer, and M is an acousto-optic figure of merit which is $\sim 10^{21}$ sec^3/g for TeO_2. A diffraction efficiency in excess of 80% has been obtained at 1.3 μm with 2.5 W of rf drive power.

7.2.2.2.4 Design Trade-offs

The properties of acousto-optic filters can be tailored to the application by varying the angles of the optical and acoustic beams with respect to the crystal axes. Many applications of AOTFs are in spectroscopy and imaging, in which case good light-gathering efficiency requires that the filter have a wide input acceptance angle of several degrees. In contrast, laser tuning applications require narrow bandwidth and high transmission, while on the other hand a field of view of a few tenths of a degree is adequate for intracavity use. It is beyond the scope of this chapter to discuss the design trade-offs of AOTFs in detail. Some aspects of this topic are discussed in a paper by Booth and Findlay [78]. A competent manufacturer of AOTFs will understand these trade-offs and be able to design an appropriate filter once the requirements are carefully specified.

7.2.2.2.5 Frequency Chirp

Because the incident light is diffracted by a moving phase grating, all AOTFs have the property that the filtered output light is Doppler shifted with respect to the input light such that $\nu_d = \nu_i \pm f_a$, where ν_d and ν_i, are, respectively, the optical frequencies of the diffracted and incident beams. The sign of the chirp depends on the input polarization and the direction of propagation. For a given propagation direction, *e*- and *o*-polarized input beams receive opposite chirps. Similarly, reversing the direction of propagation changes the sign of the chirp for a given direction of propagation. There are two chirping and two dechirping configurations (Fig. 25).

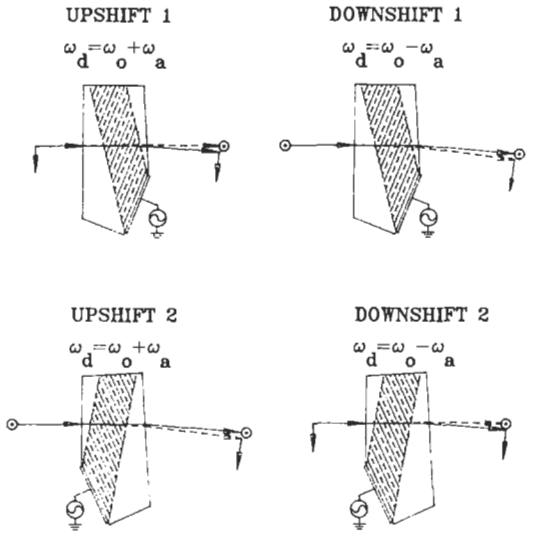

FIGURE 25 Sign of AOTF frequency chirp for various combinations of input polarization and propagation direction.

7.2.2.2.6 Acousto-Optic Tuning Speed

The wavelength switching time is given by

$$\tau_{sw} \approx \frac{\pi w_o}{\upsilon_a} , \tag{67}$$

where w_o is the Gaussian beam parameter of the input beam in the filter. The acceptance angle can be satisfied with input beams focused down to a few hundred microns in diameter. Because $\upsilon_a \sim 700$ m/sec in TeO_2, $\tau_{sw} < 1$ μs is achievable.

7.3 Optical Isolators

ECLs are sensitive to spurious optical feedback reverse-coupled through the output mirror. For very short cavities, the feedback tolerance is as high as –20 dB [79]. However, sensitivity increases with cavity length. Isolation of at least 30 dB is typically used for external-cavity lengths of 1 to 10 cm. Up the 60 dB isolation is sometimes used. High isolation from backreflections is especially important when the output of the laser is being observed with a highly reflective instrument such as a scanning Fabry–Perot interferometer. Miniature Faraday optical isolators that provide about 30 to 40 dB of isolation per stage are commercially available [80].

8. SURVEY OF EXTERNAL-CAVITY LASER DESIGNS

8.1 Grating-Tuned Lasers

In terms of optical performance, the diffraction grating is arguably the best filter for tuning an ECL, because it combines high efficiency and nearly enough resolution to resolve a single external-cavity longitudinal mode. The following examples from the literature are organized by cavity class as defined earlier.

8.1.1 Grating-Tuned Extended Cavities

The grating-tuned extended-cavity laser is by far the most commonly reported type of ECL, with dozens of papers in the literature. The design most commonly used is the "standard" Littrow configuration (Fig. 26). Table 6, which lists some published grating-tuned extended-cavity designs, is far from complete; it is a representative sampling and points out some noteworthy features and innovations.

8.1.2 Grating-Tuned Double-Ended External Cavities

A double-ended ECL based on an 830-nm AlGaAs diode was described by Fleming and Mooradian [38] (Fig. 31). Camera lenses were used as the collimators. The large-diameter beam produced by the collimators made the laser very sensitive to acoustic and thermal disturbances. A space frame constructed of superinvar rods was used for the cavity support structure, and the laser was operated inside a Lucite enclosure.

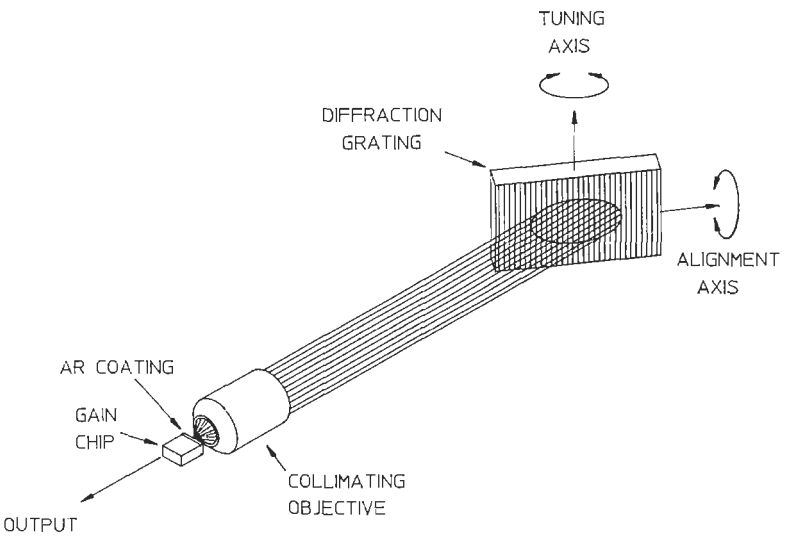

FIGURE 26 Standard Littrow-grating ECL. (Reproduced with permission from Zorabedian and Trutna [60].)

8.1.3 Grating-Tuned Ring External Cavities

The first report of a grating-tuned ring ECL operating in strong-feedback mode was by Bogatov and coworkers [86]. The active element was an AlGaAs heterojunction optical gain medium with a stripe tilt angle of 13°. The residual facet reflectance was estimated at no greater than 0.01%. The cavity comprised two 0.5 NA, 15-mm focal length collimating objectives, two mirrors, a 600 l/mm grating, and an intracavity etalon. With the grating only, the output spectrum consisted of about 20 external-cavity modes. With the insertion of the etalon, the laser operated in a single axial mode. Round-trip cavity loss was not given, and no tuning range was reported.

Oshiba and coworkers described a 1300-nm semiconductor fiber ring laser tuned with a bulk optic grating [87]. The laser contained an optical isolator to force unidirectional traveling-wave oscillation. Coupling between the 500-μm-long amplifier and the polarization-maintaining fiber was done with ball lenses. The input and output beams of the grating were coupled to the fiber using GRIN

TABLE 6 Grating-Tuned Extended-Cavity Lasers

Wavelength	Configuration	Comments	Reference
850 nm	Littrow	One of the first papers demonstrating essential features of strong, wavelength-selective feedback; cryogenic cw GaAs homojunction laser diode: $\lambda/4$ SiO AR coating, $f/2.5$ lens; 15-nm tuning range	[81] (1972)
1.55 μm	Littrow	Intracavity tilting plate for fine tuning, "shoebox-size" package	[82] (1985)
850 nm	Littrow	32-nm tuning range	[16] (1985)
1300 nm	Littrow	Short cavity; GRIN rod lens, prism grating	[83] (1987)
1.55 μm	Littrow	Lensed fiber output coupling, piezoelectric cavity length control for fine tuning; "palm-size" package served as the prototype for a product marketed by BT&D (now Fiber Optic Components Operation of Hewlett-Packard)	[84] (1988)
1.3 μm	Littrow	Use of intracavity cylinder lens to illuminate grating with narrow stripe beam for improved tolerance to angular misalignment (one-dimensional quasi-degenerate resonator) (Fig. 27)	[60] (1990)
780 nm	Grazing incidence	Grazing-incidence cavity using zeroth-order grating reflection for output coupling (Fig. 28)	[85] (1991)
1.3 μm	Littrow	GRIN rod lens collimator, intracavity silicon prism beam expanders (Fig. 29)	[61] (1992)
850 nm	Littrow	Tapered-waveguide gain chip, 1-W air beam output (Fig. 30)	[43] (1993)

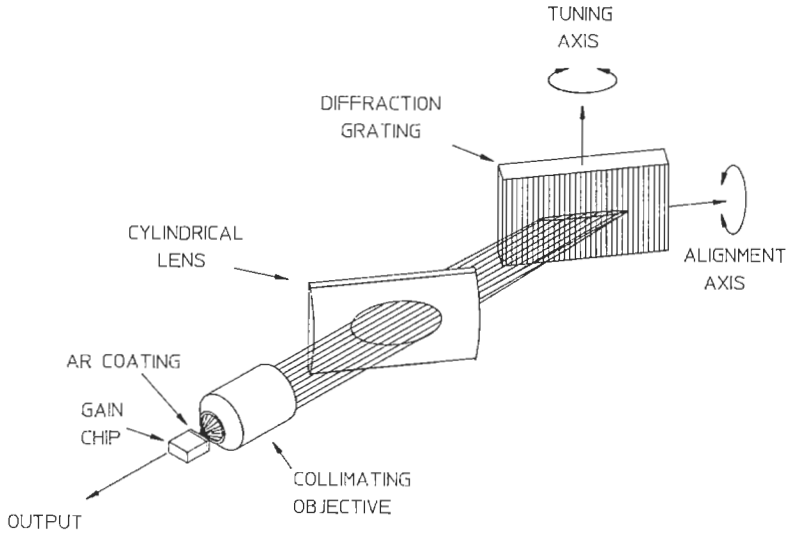

FIGURE 27 Alignment stabilization of a Littrow-grating ECL using a cylindrical lens. (Reproduced with permission from Zorabedian and Trutna [60].)

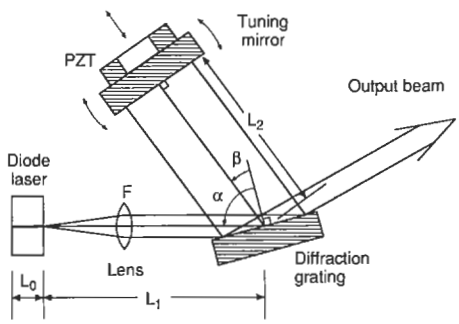

FIGURE 28 Grazing-incidence grating extended-cavity laser. (Reproduced with permission from Harvey and Myatt [85].)

rod collimating lenses attached to fiber ends. The laser's output was obtained with a 3-dB fiber directional coupler. The electron-beam-evaporated SiO_x AR coatings on the optical amplifier had a residual reflectance of less than 10^{-4} per facet. The total cavity round-trip loss was 16 dB, including 3 dB for the output coupler. The laser tuned from 1270 to 1370 nm. However, the filter bandwidth was ~5 nm because of the small spot produced on the grating by the rod lens, and single-longitudinal-mode oscillation was not obtained.

Peng and Su [88] described a 1300-nm free-space ring ECL comprising a 1000-μm-long tilted-stripe amplifier, a 600 groove/mm grating, and an optical

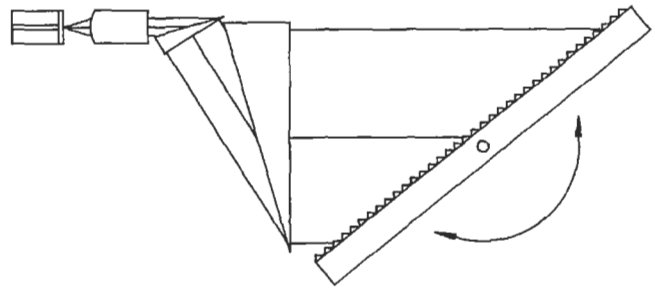

FIGURE 29 Littrow-grating extended-cavity laser with a GRIN rod lens collimator and intra-cavity silicon prism beam expanders. (Reproduced with permission from Zorabedian [61].)

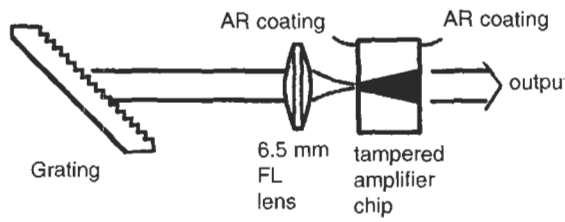

FIGURE 30 Littrow-grating extended-cavity laser with tapered-stripe gain chip. (Reproduced with permission from Mehuys *et al.* [43] and IEE Publishing.)

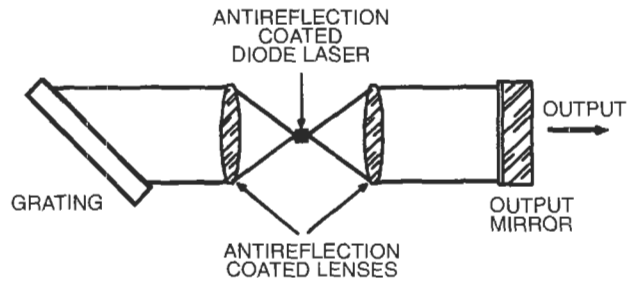

FIGURE 31 Grating-tuned double-ended extended cavity laser. (Reproduced with permission from Fleming and Mooradian [38]. © 1981 IEEE.)

isolator to force traveling-wave operation (Fig. 32). They estimated that the effective reflectance of each facet due to the 7° stripe angle was $\sim 1 \times 10^{-4}$. Total tuning range was 45 nm, with up to 24-mW cw free-space output power. A delayed-self-homodyne measurement was used to determine the longitudinal mode characteristics. Over a 35-nm range, quasi-single-mode oscillation was obtained, but the sidemode suppression was less than 20 dB, and the linewidth was ~500 kHz. A 1200 groove/mm grating increased the sidemode suppression

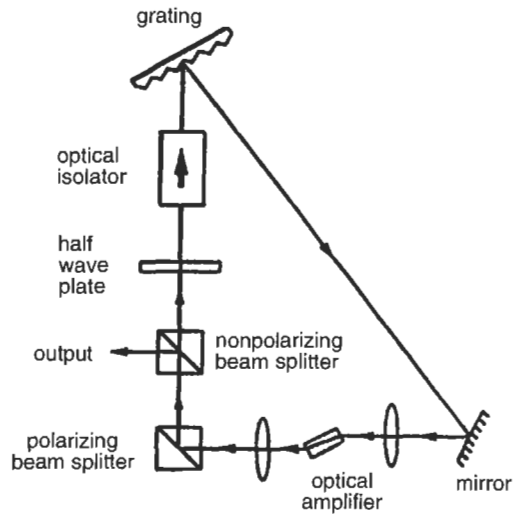

FIGURE 32 Grating-tuned ring ECL. (Reproduced with permission from Peng and Su [88].)

to ~30 dB and reduced the homodyne linewidth to ~50 kHz. The wavelength range over which these improved results could be obtained was not mentioned.

8.2 Interference-Filter Tuning

An interference filter can be used as the sole tuning element in an ECL because the blocking layers can be designed to allow only one transmission order within the gain bandwidth of the semiconductor. The advantage of an interference filter is that it is compatible with the degenerate-resonator extended cavity configuration in which the feedback strength is very insensitive to tilt of the external mirror and lateral drift of the gain diode. Interference filter tuning of a 1300-nm extended-cavity laser in a quasi-degenerate-resonator configuration with a high degree of angular misalignment tolerance has been demonstrated [14] (Fig. 33).

8.3 Etalon Tuning

By reducing the mirror spacing, the need for blocking layers is eliminated and thin etalons can be used to tune ECLs. Some examples follow.

Kahn and coworkers [89] constructed a pair of high-stability etalon-controlled ECLs. For this design, the gain element was a 400-μm-long dual-electrode buried-heterostructure InGaAsP laser diode with one HR and one AR facet. The extended cavity comprised a 100-μm air gap etalon and an output

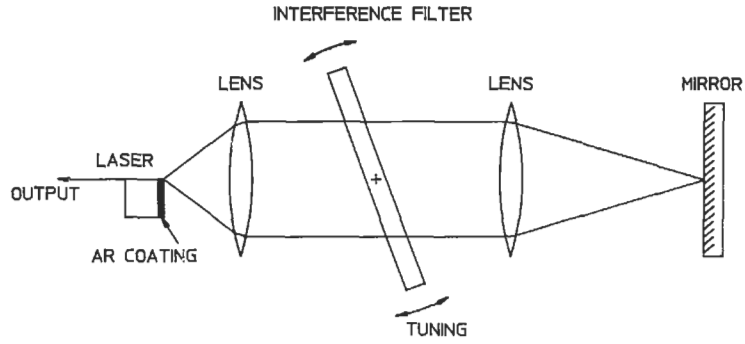

FIGURE 33 Interference filter tuned extended-cavity laser with degenerate external resonator. (Reproduced with permission from Zorabedian and Trutna [14].)

coupler mirror in an invar structure with a cavity length of ~20 cm. The lasers ran in a single longitudinal mode with sidemode suppression of >40 dB. When shielded in Plexiglas enclosures and temperature controlled to ±0.5°C, the instantaneous beat linewidth between the two lasers was 4 kHz; the total free-running relative frequency excursion over 5 min was only 600 kHz. Although the etalon had a free spectral range of 45 nm, tuning over more than one external-cavity free spectral range was not mentioned.

Liquid crystal filled Fabry–Perot filters have been used to tune ECLs. One such laser was constructed as follows [90]: The etalon comprised a sandwich of a liquid crystal layer between two glass plates on which dielectric mirrors ($R = 98.5\%$) and indium tin oxide transparent electrode layers had been deposited. A 12-μm gap (which gave a 64-nm free spectral range) was maintained by a deposited alignment layer. The bandwidth and peak transmittance depended on the spot size because of plate waviness and were found to be, respectively, 0.35 nm and 50% for a 100-μm test beam. The etalon was tuned by varying the amplitude of a 20-kHz voltage applied to the electrodes. The gain element was an AR-coated InGaAsP multiple-quantum-well laser diode with a 300-μm-long gain section and a 70-μm-long phase-control section. The extended cavity contained a coupling lens, the etalon, and an external mirror. The lens focused the intracavity beam on the mirror 3 cm from the diode. The etalon was placed near the rear focus to help improve the etalon performance. Nevertheless, the external feedback was estimated to be less than 1%. Because of the weak feedback, coordinated adjustment of the etalon voltage and phase-control current was necessary to select arbitrary external-cavity modes. By varying the plate voltage from 0 to 20 V and phase-control current by less than 1 mA, tuning from 1522 to 1563 nm was obtained, with a peak power of 5 dBm at 100-mA pump current.

A fiber Fabry–Perot etalon has also been used to tune a fiber ring ECL [91]. The filter had a 0.3-nm bandwidth and a 30-nm free spectral range. The gain

medium was a 400-μm-long, 1.5-μm semiconductor amplifier with a reflectance of $\sim 10^{-4}$ for the AR coating on each facet. The 18-m fiber loop contained two in-line optical isolators and a polarization controller. Output was obtained with a 90:10 directional coupler (90% feedback, 10% output). The cavity had an estimated loss of 12 dB. The wavelength was tunable between 1505 to 1535 nm by applying 0 to 15 V to the filter. Single-mode operation with 30-dB sidemode suppression was obtained at 0.9-nm intervals over this range in coincidence with the residual Fabry–Perot modes of the optical amplifier. The tuning range was extended to 1495 to 1544 nm by insertion of an additional Fabry–Perot filter with a broader free spectral range, but the addition of the second filter prevented single-mode operation.

8.4 Etalon-Grating Combinations

Gratings have been used in tandem with Fabry–Perot etalons to tune ECLs. There are two basic ways in which the relative spectral selectivity can be partitioned between the grating and the etalon. In the first approach, the grating is illuminated with a broad beam and provides most of the spectral selectivity. A fairly low-finesse etalon provides a resolution "boost" to the grating and improves the stability of single-mode operation [92]. In the second approach, a high-finesse etalon provides a comb of sharp transmission peaks while the grating, illuminated with a small spot, provides sufficient resolution to reject all but one interference order [93].

8.5 Birefringent Filter Tuning

Birefringent tuning lends itself to electronic tuning without the use of any moving parts by using the electro-optic effect or the birefringence of liquid crystals. A disadvantage of electro-optic birefringent tuning is that the large voltage required tends to limit the tuning to significantly less than the full semiconductor gain bandwidth.

Jopson and co-workers [94] described a 1.55-μm traveling-wave semiconductor amplifier in an optical fiber ring laser that used fiber birefringence to provide Lyot-filter-like wavelength control.

A 1.55-μm external-cavity laser comprising a InGaAsP/InP gain medium coupled by a short piece of lensed fiber to an integrated optic, birefringence-tuned, narrow-band TE-TM polarization converter/filter was built by Heissman and coworkers at AT&T Bell Laboratories [95]. The polarization converter and polarizer were integrated into a titanium-diffused waveguide on a 4-cm-long, x-cut, y-propagating lithium niobate wafer. Metallization overlaying an SiO_2 buffer layer was patterned into transverse interleaved electrodes for electro-optically tuning the wavelength of peak TE-TM conversion [72]. Metal directly overlaying the waveguide without a buffer layer provided a strong differential attenuation

for the unconverted TM-polarized light [96]. The tuning rate of the filter was ~0.05 nm/V, and its FWHM bandwidth was 1.2 nm [97]. The extended cavity did not provide much feedback, as demonstrated by the fact that its threshold current was twice that of the solitary laser diode prior to AR coating. Nevertheless, with a 1×10^{-3} AR coating on the feedback-coupling facet, the laser could oscillate on a single extended-cavity mode in 0.4-nm-wide bands around each residual solitary cavity Fabry–Perot mode for a total wavelength range to ~7 nm (limited by the voltage that could be applied to the electrodes). A linewidth of ~60 kHz and an output of more than 1 mW from the uncoated facet were measured.

Tuning of an 850-nm ECL using a single-stage electro-optically tuned birefringent filter was reported by Schremer and Tang [98]. The extended cavity comprised a collimating objective, birefringent filter, and external mirror. The external feedback was estimated to be ~30%. The reflectance of the AR-coated facet was not estimated. The filter consisted of a 38-mm-long piece of 45° y-cut ADP, with transverse electrodes, oriented so that its fast and slow axes were at 45° to the TE polarization of the laser diode and an 11-mm-long birefringent quartz plate oriented to cancel the natural birefringence of the ADP crystal. The tuning rate of the filter was 3.3 nm/kV. Oscillation could be tuned to the residual Fabry–Perot modes of the gain chip for a total range of 6.9 nm.

Andrews demonstrated tuning of an uncoated 780-nm laser diode in an extended cavity containing a two-stage birefringent filter controlled with liquid crystal cells [99]. With the laser diode operated below its solitary threshold current, the wavelength could be tuned to each of 12 adjacent diode cavity modes for a total tuning range of 2.7 nm, for a maximum applied liquid crystal voltage of 1.7 V. The power consumption of the filter was estimated to be ~50 pW. It was suggested that with optimization this laser might be useful in applications where voltage and power considerations are paramount.

8.6 Acousto-Optic Tuning

Acousto-optic filters are a very advantageous means for rapid, electronic wavelength control of ECLs. The wavelength range of an AOTF is typically much broader than the gain bandwidth of an individual diode laser, so there are no wavelength range limitations imposed by the filter, in contrast to the case of electro-optic birefringent tuning. Well-designed AOTFs have high transmittance, so an acousto-optic external cavity has the potential for providing strong feedback. The switching time between random wavelengths is equal to the transit time of the sound wave across the optical beam, which can be as little as ~1 μs. Multiple control frequencies can also be combined in the rf drive signal to generate a multiple-wavelength output.

The chief drawback of acousto-optic tuning is that the filter spectral width of the best filters (~1 nm) is about an order of magnitude greater than the width that can be readily obtained with a diffraction grating (~0.1 nm). This means that

AO-tuned ECLs must have excellent suppression of diode cavity Fabry–Perot modes in order to achieve good tuning fidelity.

An AOTF imparts a frequency chirp $\Delta\nu_{opt} = \pm f_{acoust}$ to the filtered light on each pass through the filter. The sign of the chirp depends on the polarization state of the input light and the direction of passage through the filter. The sign of the chirp is invariant with respect to simultaneous 90° rotation of the input polarization and reversal of the propagation direction. With a single intracavity AOTF, the normal modes of the laser are chirping modes [100] with normal frequencies given by

$$\nu_n(t) = \frac{c}{qL_{ext}}\left(n + qf_a t\right) . \tag{68}$$

where $q = 1$ for a ring laser and $q = 2$ for an extended-cavity laser. To obtain a set of stationary longitudinal modes, AOTFs must be arranged in chirp-compensation pairs inside the laser. There have been several reports of laser tuning using AOTFs both singly and in pairs.

Tuning of a dye laser with a single collinear AOTF was demonstrated by a Stanford group almost 25 years ago [101]. Without chirp compensation, a filter at $\lambda = 780$ nm with a bandwidth of 0.7 nm (FWHM) resulted in a laser linewidth of ~0.14 nm.

Tuning of a 0.85-μm semiconductor laser with an AOTF was reported by Coquin and Cheung [102]. They also showed that the filter chirp could be compensated with an intracavity AO modulator driven at the same frequency as the filter. Shortly thereafter, Coquin and coworkers [103] reported a 1.3-μm extended-cavity laser tuned with a chirp-compensating pair of AOTFs. Tuning over a total range of 83 nm was demonstrated. However, oscillation was restricted to the wavelengths of the residual laser diode Fabry–Perot modes, resulting in nanometer-size tuning gaps. It was pointed out that this restriction was not fundamental and that with a combination of reduced AR coating reflectance and narrower fiber bandwidth, quasi-continuous tuning would be possible.

A 1.3-μm semiconductor laser in a fiber ring cavity tuned with an AOTF was reported by Oshiba and coworkers [104]. The cavity was identical to the grating-tuned fiber ring laser described previously [87] except that the grating was replaced with an AOTF reported to have a bandwidth of <5 nm and a peak efficiency of 80%. The tuning range was about 80 nm. A minimum linewidth of 15 kHz was reported. The method of linewidth measurement was not described, but it is unlikely that 15 kHz could represent the true spectral width of the chirped-mode laser.

The elimination of nanometer-size gaps in the tuning range of acousto-optically tuned extended and ring cavity lasers has recently been demonstrated [46]. AOTFs specifically designed for tuning of 1.2- to 1.6-μm ECLs were fabricated. The devices had bandwidths of ~1.0 nm (FWHM) and peak efficiencies of

~85% when driven at 2.75 W. An extended-cavity configuration containing a pair of chirp-compensating AOTFs provided 11% feedback (Fig. 34). The reflectance of the feedback-coupling facet was 3×10^{-5}, leading to a ratio of diode cavity loss to external-cavity loss of 36 dB. The wavelength was measured versus drive frequency in 10-kHz steps across an 80-nm range. A theoretical tuning curve of the form $\lambda = (a/f_a) + b$ was fit to the data. The residual of the fit was 0.036 nm rms averaged across the 80-nm tuning range.

A ring configuration was also studied (Fig. 35). The ring cavity provided about 1% feedback but the ratio of diode cavity to external-cavity loss was increased to 46 dB because both facets of the gain medium were AR coated ($R_{\text{facet}} \approx 5 \times 10^{-4}$). In this case the rms tuning error decreased to 0.018 nm. This study demonstrates the utility of the cavity-loss ratio as a figure of merit for optimizing tuning fidelity.

9. MODE SELECTIVITY OF GRATING CAVITIES

Of the various types of filters used to tune ECLs, diffraction gratings provide the narrowest nonperiodic spectral bandwidth. As shown earlier, the grazing-incidence configuration has the narrowest bandwidth. Most of this advantage comes from the use of a steeper incidence angle (~85° for the grazing-incidence configuration versus ~50° for the Littrow configuration). In addition, double passing gives another factor of 2. Thus, *for identical beam diameters*, the grazing-incidence configuration has a resolution advantage of about $2 \times [\tan(85°) / \tan(50°)] \approx 20$ times over the Littrow configuration. However, this conclusion carries the important stipulation that the grating must capture the full width of the beam.

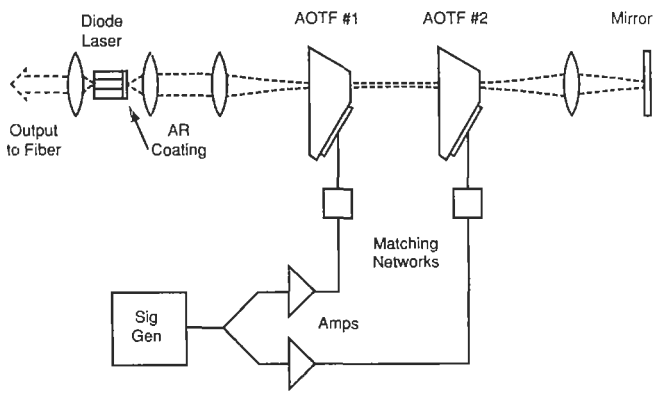

FIGURE 34 Extended cavity laser tuned with two chirp-compensating AOTFs. (Reproduced with permission from Zorabedian [46]. © 1995 IEEE.)

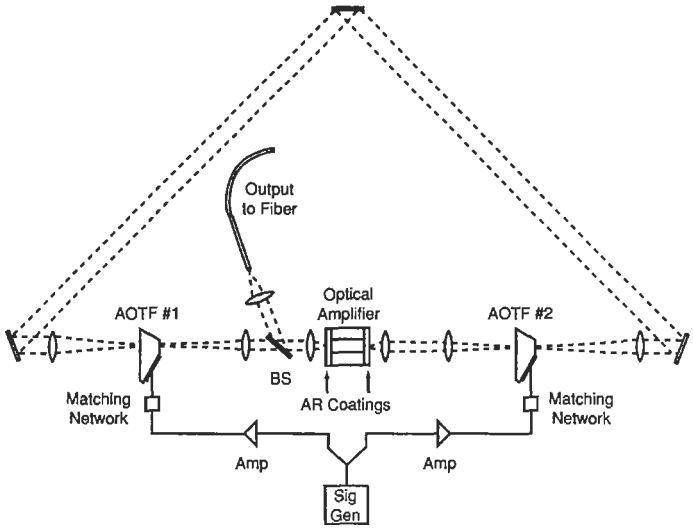

FIGURE 35 Ring ECL tuned with two chirp-compensating AOTFs. (Reproduced with permission from Zorabedian [46]. © 1995 IEEE.)

In practice, the grating resolution will ultimately be limited by the width of the ruled area. For example, assume both configurations use a 30-mm wide grating that is fully illuminated by the coupling optics. In this case, the grazing-incidence geometry will have a filled depth of 30 mm × sin(85°) = 29.9 mm, whereas in Littrow the filled depth will be 30 mm × sin(50°) = 23.0 mm. This reduces the spectral resolution advantage of the grazing-incidence configuration to a factor of about $2 \times (30/23) \approx 2.5$, that is, by almost an order of magnitude.

Furthermore, the figure of merit for determining how well a cavity maintains single-mode operation is not the filter bandwidth but rather the number of longitudinal modes within the passband. Cavity parameters that are representative of a typical grazing-incidence cavity are $\lambda = 670$ nm, beam diameter = 1 mm, grating angle = 85°, and cavity length = 7.5 to 15 cm [105]. Therefore, the number of modes in the grating passband is between one and three. For a Littrow cavity, the number of modes in the passband is given by

$$N_{modes} = \frac{2}{\pi} \frac{L_{cav}}{L_g} , \tag{69}$$

where L_{cav} is the total cavity length and L_g is the filled depth of the grating. By eliminating as much air space as possible within the cavity, a practical limit of about two modes can be reached. One way to minimize the cavity length for a given resolution is to butt the grating up against the coupling lens [83]. This tends

to result in a fairly short cavity. If a longer cavity is needed in order to obtain a narrower linewidth, the requisite path length can be filled with prisms to expand the filled depth in proportion to the total length. A 1300-nm external cavity containing a GRIN rod collimator followed by two silicon prisms resulted in a 7-cm-long cavity with about three modes in the grating passband [61]. Single-mode operation was achieved over a 50-nm tuning range with a linewidth of 100 kHz or less.

10. PHASE-CONTINUOUS TUNING

Phase-continuous tuning [106] means tuning without mode hopping or otherwise interrupting the phase of the oscillation. A prerequisite for phase-continuous tuning is that the mode number—the number of half-wavelengths between the laser mirrors—remains constant as the wavelength is varied. Phase-continuous tuning is required for locking the oscillation to a wavelength reference. It is also useful for interferometric measurements, optical frequency synthesis schemes, and in general whenever fine control of the laser wavelength is needed.

Two regimes of phase-continuous tuning can be distinguished: short range and long range. Short-range phase-continuous tuning over several external-cavity mode spacings (i.e., up to a few tens of gigahertz) can be accomplished by changing the cavity length while keeping the position of the filter peak fixed [84]. Eventually the lasing mode moves too far from the filter peak and a mode hop occurs to a new mode with lower loss. Long-range phase-continuous tuning over many nanometers requires precisely coordinated simultaneous slewing of the axial-mode frequencies in synchronism with the filter peak. The requirements for this type of tuning are considered next.

10.1 General Requirements for Long-Range Phase-Continuous Tuning

In phase-continuous tuning, the longitudinal modes must be shifted at exactly the same rate as the filter peak so that the same mode maintains its status as the lowest loss mode and thus continues to oscillate. Assume that the q'th longitudinal mode of the ECL starts out exactly at the peak of the filter passband. The frequency of the q'th mode is given by

$$\nu_q = \frac{qc}{2L_{\text{eff}}} \tag{70}$$

where q is an integer, c is the speed of light, and

$$L_{\text{eff}} \equiv \int_0^{L_{\text{ext}}} n(z)\, dz \tag{71}$$

is the effective optical path length of the laser. The wavelength of the q'th mode is given by $\lambda_q = 2L_{\text{eff}}/q$. The peak wavelength of the filter passband is represented by λ_{pk}.

For the q'th mode to remain oscillating as the filter is tuned, λ_q must track λ_{pk} exactly. One way to fulfill this requirement is to change the cavity length by ΔL_{eff} as the filter is tuned by $\Delta\lambda_{\text{pk}}$ so that

$$\Delta\lambda_q = \frac{d\lambda_q}{dL_{\text{eff}}}\Delta L_{\text{eff}} = \frac{2}{q}\Delta L_{\text{eff}} = \Delta\lambda_{\text{pk}} \ . \tag{72}$$

Dividing both sides of Eq. (72) by L_{eff} and rearranging factors gives the following condition for phase-continuous tuning:

$$\frac{\Delta L_{\text{eff}}}{L_{\text{eff}}} = \frac{\Delta\lambda_{\text{pk}}}{\lambda_{\text{pk}}} \ . \tag{73}$$

This equation can be integrated to give

$$\frac{\ln\left(L_{\text{eff1}}\right)}{\ln\left(L_{\text{eff2}}\right)} = \frac{\ln\left(\lambda_{\text{pk1}}\right)}{\ln\left(\lambda_{\text{pk2}}\right)} \ . \tag{74}$$

The required accuracy with which the cavity length must track the filter is very high. Assuming that the change in mode number must be $|\Delta q| < ½$ to avoid a mode hop, then it is easy to show that tracking precision is specified by

$$\left|\frac{\Delta L_{\text{eff}}}{L_{\text{eff}}} - \frac{\Delta\lambda_{\text{pk}}}{\lambda_{\text{pk}}}\right| < \frac{\lambda_{\text{pk}}}{2L_{\text{eff}}} \ . \tag{75}$$

The value of this quantity is 5×10^{-6} for a 1-μm wavelength and a 10-cm cavity.

The condition for phase-continuous tuning can also be expressed in terms of optical frequency. Assume that the laser starts out oscillating in one longitudinal mode that is coincident with the peak frequency of the filter: $\nu_q = \nu_{\text{pk}}$. Further assume that the filter frequency is swept at a constant rate $d\nu_{\text{pk}}/dt$. Tuning will be phase continuous if the modes of the cavity are somehow swept at a rate identical to that of the filter:

$$\frac{d\nu_q}{dt} = \frac{d\nu_{\text{pk}}}{dt} \ . \tag{76}$$

This relation suggests that it should be possible to implement phase-continuous tuning by applying a controlled chirp to the longitudinal modes without actually

changing the cavity length. As will be shown later, this can be accomplished by AOTFs without the use of moving parts in the cavity.

10.2 Embodiments of Phase-Continuous Tuning

Phase-continuous tuning over a 15-nm range was obtained without servocontrol from a 1.26-μm Littrow-grating-tuned extended-cavity laser using a rather complex mechanical arrangement in which the grating was mounted on a bar whose ends were pinned to a pair of orthogonal sliding stages [107]. It is also possible to achieve continuous tuning with a single mechanical degree of freedom. Phase-continuous tuning over a range of 1000 GHz was obtained by pushing with a PZT on a pivot arm that simultaneously rotates and translates the grating [108] (Fig. 36). Up to 82 nm (more than 10,000 GHz) of phase-continuous tuning has been reported [109]. The grating is mounted on a pivot arm, which is rotated about an axis lying near the intersection of the grating surface and the plane of the laser diode output facet. The mode-hop-free tuning range is quite sensitive to the precise location of the rotation axis (Fig. 37). There have been several studies of the optimum location of this "magic" pivot point, taking into account chromatic dispersion and phase shifts introduced by the gain medium and various intracavity optical elements [110–113].

Phase-continuous tuning can also be realized with an acousto-optically controlled ECL. Introducing a slight offset (e.g., ~1 Hz) between the drive frequencies of the two intracavity filters will generate a net chirp of the oscillating mode on each round-trip. If the passbands of the filters are simultaneously slewed so as to match the induced chirp, phase-continuous tuning will result [114]. The key to the success of this method is to obtain single-mode oscillation in the first place, which is difficult because of the broad bandwidth of AOTFs.

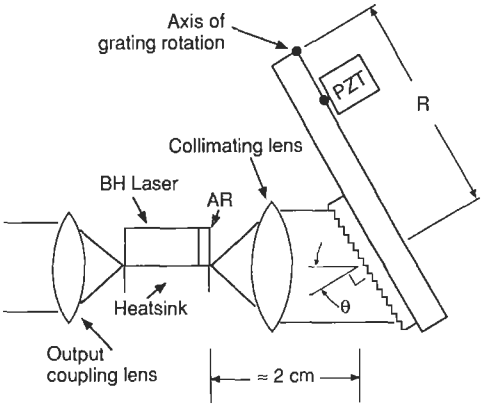

FIGURE 36 Phase-continuous tuned grating extended-cavity laser with PZT actuator. (Reproduced with permission from Schremer and Tang [108]. © 1990 IEEE.)

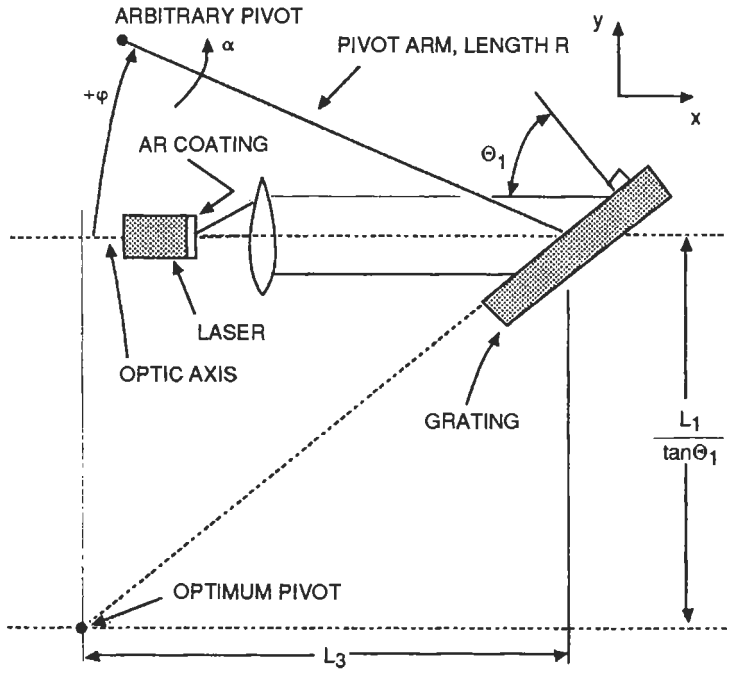

FIGURE 37 Location of optimum pivot point in phase-continuous tuned grating extended-cavity laser. (Reproduced with permission from Trutna and Stokes [112]. © 1993 IEEE.)

11. CHARACTERIZATION METHODS FOR EXTERNAL-CAVITY LASERS

To design and construct external lasers with well-characterized and reliable behavior, routine measurement of the laser's properties is essential. Table 7 indicates several commonly measured quantities and the measurement techniques for each.

12. MEASUREMENT OF FACET AND EXTERNAL-CAVITY REFLECTANCES

12.1 Determination of Gain and Loss Parameters for Solitary Diode Lasers

To determine the internal gain and loss parameters of the gain medium, the minimum information required is the threshold current I_o and the original lasing wavelength λ_o of the solitary diode laser prior to antireflection coating. The solitary threshold current is given by

TABLE 7 Quantities and Measurement Techniques for ECLs

Parameter	Instrument or method	Resolution/sensitivity
Wavelength	Optical spectrum analyzer	Resolution ~0.1 nm
	Michelson interferometer wavelength meter	resolution ~5 ppm
Power	Optical power meter	resolution ~0.01 dBm
Threshold current	Measurement of L-I curve under computer control [115]	0.05-mA resolution requires 2 to 3 sec per wavelength
Sidemode ratio	Scanning Fabry–Perot interferometer	Sensitivity ~-15 to -20 dB
	Lightwave signal analyzer [24]	Sensitivity ~-60 dB
Linewidth	Delayed-self-heterodyne method with Mach-Zender interferometer [116] (Fig. 38)	minimum resolvable linewidth ~½ τ_d, where τ_d is the differential delay of the interferometer

$$I_o = \frac{1}{\gamma}\left[\alpha_{int} + \frac{1}{L_{int}}\ln\left(\frac{1}{r_o^2}\right)\right] + I_{tr} \ . \tag{77}$$

One way to determine the internal parameters of the gain media is to sacrifice a sampling of them by coating them with a partially reflective coating r_1 on one facet. The reflectance of the test film is measured from a witness sample. The threshold current becomes

$$I_1 = \frac{1}{\gamma}\left[\alpha_{int} + \frac{1}{L_{int}}\ln\left(\frac{1}{r_o r_1}\right)\right] + I_{tr} \ . \tag{78}$$

Assuming the laser diode still lases at λ_o, the following relations for the internal gain and loss parameters are obtained

$$\gamma = \frac{1}{L_{int}}\frac{\ln(r_o/r_1)}{(I_1 - I_o)} \ . \tag{79}$$

and

$$\left[\gamma I_{tr}(\lambda_o) + \alpha\right] L_{int} = \frac{\ln(r_o/r_1) I_o}{I_1 - I_o} + \ln(r_o^2) \ . \tag{80}$$

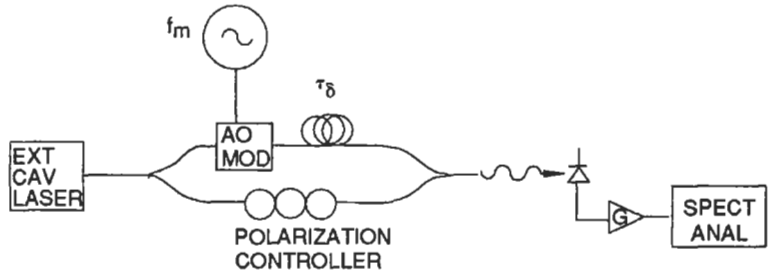

FIGURE 38 Delayed self-heterodyne interferometer for linewidth measurement.

Typical values for a GaInAsP buried crescent device with $L_{int} \approx 300$ μm at 1300 nm are $[\gamma I_{tr}(\lambda_o) + \alpha]L_{int} \approx 0.7$ and $\gamma L_{int} \approx 0.12$ mA^{-1}.

12.2 External-Cavity Reflectance

The following calculations pertain to the basic extended-cavity configuration. They can readily be modified for the double-ended ECL or ring ECL configurations. It is relatively straightforward to determine the transmission losses of the various intracavity elements separately. However, the mode-conversion loss due to the coupling lens is not easy to determine directly. Therefore, the external-cavity reflectance usually must be deduced from changes in the threshold current caused by modifications to the feedback. To determine the external feedback strength, place the laser diode in the external cavity, tune to the vicinity of the solitary lasing wavelength λ_o, and measure the external-cavity threshold current versus wavelength over one period of its ripple pattern. Compute the average external-cavity threshold current

$$\bar{I}_{ext} = \frac{1}{2}\left(I_{ext}^{max} + I_{ext}^{min}\right) , \tag{81}$$

which is related to the wavelength-averaged external-cavity reflectance $\overline{r_{ext}}$ by

$$\bar{I}_{ext} = \frac{1}{\gamma}\left[\alpha_{int} + \frac{1}{L_{int}} \ln\left(\frac{1}{r_o \overline{r_{ext}}}\right)\right] + I_{tr} . \tag{82}$$

At this point, assuming γL_{int} is independently known from test devices, the external-cavity reflectance can now be determined from

$$I_o - \bar{I}_{ext} = \frac{1}{\gamma L_{int}} \ln \frac{r_{ext}}{r_o} . \tag{83}$$

If γL_{int} is not independently known, then an alternative method must be used. This method involves inserting a filter of known amplitude transmittance x and negligible wavefront distortion into the external cavity so that its round-trip amplitude reflectance is reduced by a factor x^2. Then experimentally determine the new wavelength-averaged threshold current $\bar{I}_{ext*}$ for the modified external cavity. The value is related to the modified external feedback by

$$\bar{I}_{ext*} = \frac{1}{\gamma}\left(\alpha L_{int} - \ln r_0 x^2 r_{ext*}\right) + I_{tr} \ . \tag{84}$$

From the various threshold currents, the known additional filter loss, and the bare-fact Fresnel reflectance, the external-cavity reflectance is then given by

$$r_{ext} = r_0 x^2 \exp\left(\frac{\bar{I}_{ext*} - \bar{I}_{ext}}{\bar{I}_{ext} - I_0}\right) \ . \tag{85}$$

The preceding formulas are only valid at the original oscillation wavelength of the solitary diode laser prior to coating. To obtain a value of external-cavity reflectance at other wavelengths, one can factor in any known spectral variation in the losses of the individual intracavity optical components and the filter.

12.3 Facet Reflectance

There are basically three methods for measuring the reflectance of AR-coated facets. These are summarized as follows.

The first method is a simple approach, but it can be used only for devices with one coated facet and only when the beams from both facets are unobstructed. After coating, the laser is operated above its new, higher threshold current and the L-I curves from both facets are measured. The unknown reflectance of the coated facet is related to the assumed-known Fresnel reflectance of the uncoated facet ($R_u = 0.31$) by [117,118]

$$\frac{\eta_c}{\eta_u} = \sqrt{\left(\frac{R_u}{R_c}\right)\frac{(1-R_c)}{(1-R_u)}} \ , \tag{86}$$

where η_u and η_c are the slope efficiencies for the uncoated and coated facets, respectively (Fig. 39). Obviously, this method only determines the facet reflectance at the emission wavelength of the solitary diode laser.

The second method [119] can be applied to gain media with AR coatings on one or both facets, and it does not require an unobstructed beam from either facet. It relates a change in the round-trip amplification factor to a change in the

modulation index of the emission spectrum. The magnitude of the round-trip amplification factor is given by

$$|a| = \sqrt{R_{f1}R_{f2}}\,\exp\left[\left(g - \alpha_{\text{int}}\right)L_{\text{int}}\right] . \tag{87}$$

For an uncoated laser, $R_{f1}R_{f2} = R_u^2$ where $R_u = 0.31$ is the Fresnel reflectance of an uncoated facet. By definition, when the uncoated laser is driven at threshold, $|a| \equiv 1$. After coating, the value of $|a|$ at the same current and wavelength is reduced to

$$|a|^2 = \frac{R_{f1}R_{f2}}{R_u^2} . \tag{88}$$

The modulation index m of the subthreshold emission is given by

$$m = \frac{P_{\max} - P_{\min}}{P_{\max} + P_{\min}} , \tag{89}$$

where $P_{\max}$ and $P_{\min}$ are, respectively, the local maximum and minimum at the peak of the emission spectrum. When the coated device is driven at the original uncoated-laser threshold current, $|a|$ is related to m by

$$m = \frac{2|a|}{1 + |a|^2} . \tag{90}$$

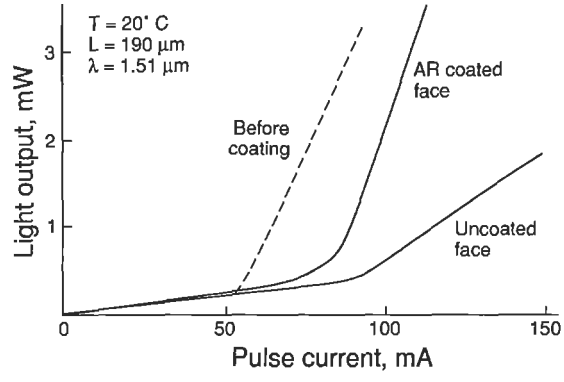

FIGURE 39 Light output versus current curves before and after AR coating. (Reproduced with permission from Wyatt and Devlin [118] and IEE Publishing.)

This method, like the previous one, is strictly accurate only at the original oscillation wavelength of the solitary laser diode. At other wavelengths the gain is lower, and this method tends to underestimate the reflectance. Furthermore, when both facets have been coated, it is often difficult to measure m, and the method only gives the product of the two coating reflectivities.

The third method determines the facet reflectance as a function of wavelength but requires operating the gain medium inside an ECL [115]. The ECL containing the gain medium under test is operated over wavelength and the threshold current is recorded as a function of wavelength. Let $I_{max}(\lambda)$ and $I_{min}(\lambda)$ be, respectively, the local maxima and minima. The facet reflectance is given by

$$r_{ar}(\lambda) \approx \gamma L_{int}\left[I_{max}(\lambda) - I_{min}(\lambda)\right]\frac{r_{ext}}{2\left(1 - r_{ext}^2\right)}, \tag{91}$$

where the methods for determining γL_{int} and r_{ext} were described in the previous two subsections. The use of this method for the measurement of the reflectances of single-layer facet coatings has given good agreement with theory (Fig. 40).

13. MULTIMODE SUPPRESSION

There are a number of ways to deal with the problem of multi-longitudinal-mode oscillation. The first line of defense is in the design of the cavity;

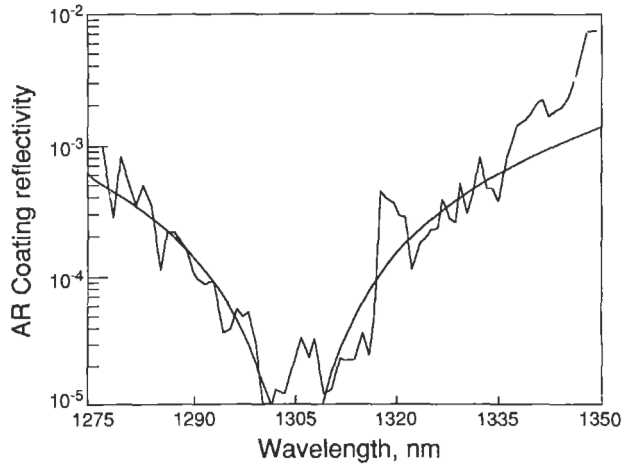

FIGURE 40 Reflectance versus wavelength measured with a diode in an extended-cavity laser and calculated for an ideal single-layer coating. (Reproduced with permission from Stokes [115]. © 1993 IEEE.)

maximization of the external feedback strength and axial mode selectivity along with minimization of the residual facet reflectance help to reduce multimoding. Limiting the drive current to within twice the threshold current also lessens the problem. These measures may not be wholly effective, owing to the properties of the cavity components and the facet coating, or to the required output power. In that case, it may be necessary to implement one of several reported methods for multimode detection and suppression. The methods can be divided into two categories, optical and electrical, according to whether the control signal is applied to the external cavity or the diode laser.

13.1 Optical Multimode Suppression Methods

Two elements are needed to implement an automatic control loop for multimode suppression: (1) a means for deriving an error signal and (2) an effective control variable.

The presence of multiple longitudinal modes in the output spectrum can be directly observed with a scanning Fabry–Perot interferometer. With this instrument, however, it is difficult to detect sidemode ratios less than ~−20 dB. In addition, some kind of software or firmware interpretation of the spectrum, either with a computer or a digital oscilloscope, is necessary to use this information as the error signal to drive a control loop. Alternatively, the microwave mode-beating signal from a wide-band detector is a much more sensitive indicator of multimoding and its output can be more easily used in a control loop. Heterodyne amplification gives this detection method a sidemode-ratio sensitivity ~−60 dB or better.

As for control variables, small changes in the cavity length have been observed to shift the laser's output spectrum from multimode to single mode. A possible explanation for this phenomenon is that when one mode is shifted to coincidence with the wavelength of minimum external-cavity loss, the differential loss for competing sidemodes is maximized, and they are suppressed. Another external-cavity control mechanism requires the use of an intracavity etalon to supplement the wavelength selectivity of a diffraction grating. Controlling the angle of the etalon so that its loss minimum corresponds with that of the grating is also effective for sidemode suppression.

A multimode suppression servo system for a Littrow-grating ECL was reported [120] that used the rf beat signal generated by multiple longitudinal modes as an error signal. The error signal was fed into an integrator whose output was used to drive the axial position of the grating using a PZT (Fig. 41). The published implementation used a Mach-Zender interferometer with unequal path lengths to create temporal overlap between modes. I have built similar systems using the mode-beating error signal to drive either the cavity length or the angle of an intracavity etalon and have found that sufficient error signal could be generated without the differential-delay interferometer.

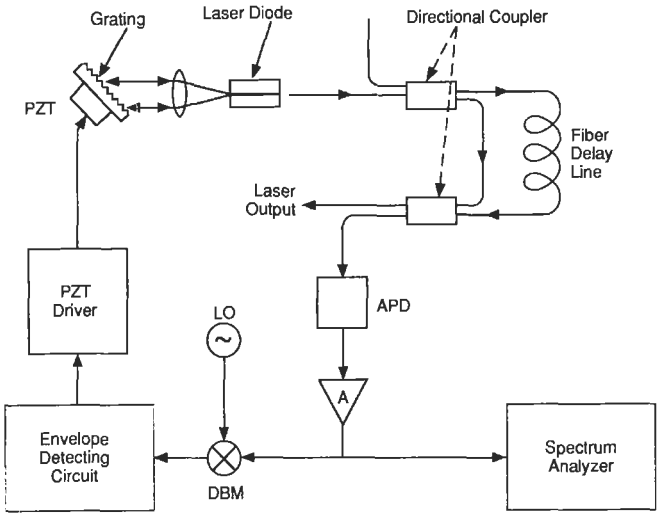

FIGURE 41 Interferometric apparatus for mode-hopping suppression in an extended-cavity laser. (Reproduced with permission from Ohtsu *et al.* [120]. © 1989 IEEE.)

Open-loop control is an alternative to a closed-loop servo system. Synchronism of the peak transmission wavelengths of an intracavity etalon and a grating can be maintained in open-loop fashion by means of careful calibration. This is the basis for maintaining single-mode oscillation in the Hewlett-Packard 8167A/8168A tunable laser source products [93].

13.2 Electrical Multimode Suppression Methods

As mentioned previously, multimoding is correlated with the wavelengths of the residual diode laser internal Fabry–Perot modes. Therefore, it should be possible to suppress multimoding by controlling the positions of the residual solitary cavity longitudinal modes. In a conventional diode laser, this is possible by changing the injection current or the temperature. Using these controls is undesirable because changing the injection current changes the output power, and changing the temperature is slow. Use of a two-section diode laser with separate gain and phase-control terminals solves this problem by providing a way to shift the internal modes with only minimal influence on the gain. Elimination of multimoding in a grating-tuned ECL with a two-section diode laser by varying the phase-control current has been demonstrated [121] (Fig. 42). Without using the phase-control current, the laser showed periodic regions of multimoding separated by the internal-mode spacing. By varying the phase-control current from 0 to 1 mA, single-mode operation could be obtained in any of the previously multimode regions. A

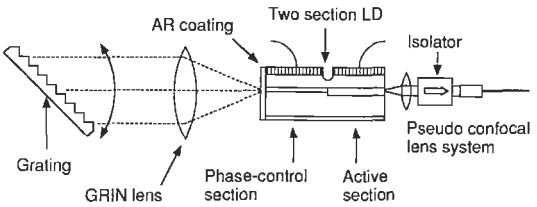

FIGURE 42 Extended-cavity laser with two-section gain medium for mode-hopping suppression. (Reproduced with permission from Notomi *et al.* [121]. © 1990 IEEE.)

completely nonoptical control loop based on the detection of terminal electrical noise in the gain medium has also been reported [122].

14. MULTIPLE-WAVELENGTH OPERATION

In some applications it is necessary to generate multiple wavelengths simultaneously from an ECL. This is a different situation from multimoding because the multiple wavelengths will in general have a separation greater than the bandwidth of the intracavity filter and will be either arbitrarily selected or chosen from a predetermined set. In this section various types of multiple-wavelength ECLs are reviewed.

14.1 Multiple-Wavelength AO ECLs

The AOTF will transmit multiple wavelengths when multiple electrical drive frequencies are simultaneously applied to the transducer. Dual- and triple-wavelength output from an AO ECL has been demonstrated [103]. Because the diode laser gain is usually strongly homogeneously broadened, the drive levels at the multiple frequencies must be carefully balanced. In addition, the total acoustic power must be limited, which leads to reduced feedback at each wavelength. As a result of these problems the number of simultaneous wavelengths that can be generated is limited and the power balance between the wavelengths might not be very stable.

14.2 Multiple-Wavelength Grating ECLs with Conventional Gain Media

Simultaneous feedback at two wavelengths can be obtained with an extended-cavity configured as a Michelson interferometer with a Littrow grating in each arm [123]. Dual-wavelength operation has also been obtained in a grazing-incidence cavity by placing a mask containing a v-shaped double slit in front of the end

mirror [124]. The average wavelength and the wavelength separation of the feedback are controlled, respectively, by tangential and sagittal translation of the mask. This scheme was actually implemented using a 10-stripe 0.8-μm laser diode array, but the array was phase locked and functionally it was essentially the same as a high-power single-stripe element. The minimum and maximum wavelength separations obtained were 3.52 and 11.29 nm, respectively. Because of the need to provide equal gain to each wavelength, operation was restricted to wavelengths symmetrically displaced with respect to the gain peak.

14.3 Multiple-Wavelength ECLs with Multi-stripe Gain Media

To avoid the problems associated with multiple wavelengths competing for gain in a single active stripe, a multistripe laser diode array can be coupled to a grating extended cavity to form a *multichannel grating cavity* [125]. The extended cavity can be configured so that each of a set of discrete wavelengths resonates between a different gain stripe and a common collection waveguide, which can either be itself a separate gain stripe in the array [126] or an optical fiber [127]. A monolithically integrated version, called a *multistripe array grating integrated cavity* (MAGIC) laser, has also been developed [128–130]. Another scheme in which a laser diode array is coupled to a grazing-incidence grating external cavity to generate multiple output wavelengths with nearly constant offsets and single-knob tuning has also been proposed [131].

15. WAVELENGTH STABILIZATION

Narrow intrinsic linewidths of <100 kHz have been demonstrated in ECLs at all the major wavelengths (0.67, 0.78, 0.85, 1.33, and 1.55 μm). Despite these narrow instantaneous linewidths, ECLs generally display much larger center-frequency jitter or drift (collectively known as *residual FM* noise) due to thermal, mechanical, and acoustic disturbances. For many applications, it is important that the residual FM be reduced by active stabilization.

There are two requirements for an ECL frequency stabilization system: (1) a fine-tuning mechanism by which the laser's frequency can be servoed and (2) a frequency reference is needed with respect to which frequency drift can be sensed. Current modulation or cavity-length variation can be used to fine-tune the frequency of an ECL. Laser diode temperature can also be used, but it has a slower response time. The transmission peaks of Fabry–Perot etalons and fiber resonators and the absorption lines of atomic or molecular vapors are commonly used frequency references. Frequency locking is typically implemented by applying a small frequency dither to the laser to generate the first derivative of the transmission or absorption peak. By applying negative feedback, the laser can then be locked to the zero of the derivative signal.

Fabry–Perot etalons can serve as frequency references in any wavelength region, but their resonance frequencies are susceptible to the same disturbances that cause residual FM noise in the laser. Absorption lines provide better stability. Atomic absorption lines originating from the ground state are available for stabilizing visible and near-infrared lasers. Due to the lack of atomic absorption lines originating from the ground state in the 1.3- and 1.5-μm wavelength regions, molecular transitions have been used for stabilization of long-wavelength communications lasers. Molecular spectra are generally more complex and weaker than atomic spectra. These complications have motivated some workers to use nonlinear crystals to generate the second harmonic of 1.3- and 1.5-μm laser output in order to make use of atomic lines at shorter wavelengths. An alternative for stabilizing 1.3- and 1.5-μm lasers is to use excited state transitions of noble gases such as neon, argon, krypton, or xenon inside a discharge lamp. Excited state absorption increases the population of the upper excited state of the transition. The upper state has a higher ionization probability because it requires less energy to be ionized. Thus, under resonant irradiation the lamp requires less discharge current to maintain the steady state so that its impedance is increased. This is called the optogalvanic effect [132]. A large number of optogalvanic transitions have been surveyed [133]. Table 8 lists a number of reports of solitary diode laser and ECL frequency stabilization.

16. ADVANCED MODELING TOPICS

16.1 Variation of Threshold Gain with Length

The oscillation threshold condition for an extended cavity laser is given by

$$r_{f1} r_{\mathrm{eff}}(\nu) \exp\left[\left(g_{\mathrm{th}} - \alpha_{\mathrm{int}}\right) L_{\mathrm{int}} + i 2\pi\nu\, \tau_{\mathrm{ext}}\right] = 1 \ , \tag{92}$$

where r_{f1} is the reflectance of the outer facet and $r_{\mathrm{eff}}(\nu)$ is the frequency-dependent effective reflectance of the external cavity defined by Eq. (32). In the following, the assumption is made that the oscillation frequency ν is an independent variable that is identical to the peak feedback wavelength of the external-cavity filter. The threshold gain as a function of frequency is then determined by simultaneous solution of the magnitude and phase parts of the threshold condition [23]:

$$g_{\mathrm{th}}(\nu) = \alpha_{\mathrm{int}} + \frac{1}{L_{\mathrm{int}}} \ln\left[\frac{1}{r_{f1}\left|r_{\mathrm{eff}}(\nu)\right|}\right] \tag{93}$$

and

TABLE 8 Frequency Stabilization Experiments

Type of Laser	Wavelength	Frequency standard	Reference
Extended-cavity laser	850 nm	Cs–D_2 line	[134]
Solitary laser diode	850 nm	Fabry–Perot etalon	[135]
DFB laser	1.3 μm	Ar (optogalvanic effect)	[136]
DFB laser	1.5 μm	Kr (optogalvanic effect)	[137]
Extended-cavity laser	1.5 μm	NH_3 absorption line	[138]
DFB laser	1.5 μm	Rb (second harmonic generation of laser output in organic fiber)	[139]
Ring external-cavity laser	1.3 μm	Fiber resonator	[140]
Extended-cavity laser	780 nm	^{85}Rb $5S_{1/2} \rightarrow 5D_{5/2}$	[141]
DFB laser	1.5 μm	C_2H_2 absorption line	[142]
DFB laser	1560 nm	^{87}Rb D_2 line at 780 nm (second harmonic generation in $KNbO_3$ crystal)	[143]
Extended-cavity laser	1.25–1.54 μm	Survey of 26 atomic transitions for frequency stabilization by optogalvanic effect	[133]

$$\nu - \nu_q = -\frac{c}{4\pi\, n\, L_{\text{int}}} \operatorname{Arg}\left[r_{\text{eff}}(\nu)\right] , \tag{94}$$

where n is the semiconductor index of refraction and ν_q is the q'th longitudinal mode of the solitary gain chip Fabry–Perot cavity. If n and ν_q are assumed to be constants, then we obtain an approximately sinusoidal variation of the threshold gain with respect to ν [44]. However, it is actually quite important to take into account the back reaction of the threshold gain on the index of refraction, which is given by

$$n = n_o + \alpha \frac{c}{2\omega}\left(g_{\text{th}} - g_o\right) , \tag{95}$$

where n and g_{th}, respectively. denote the index of refraction and threshold gain in the presence of external feedback at the frequency ν, and n_o and g_o are the corresponding quantities for the solitary laser diode in the absence of external feedback. Incorporation of the gain-dependent refractive index shift described by Eq. (95) into the phase part of the threshold condition described by Eq. (94) results in

$$\nu - \nu_q^o = \frac{c}{4\pi\, n_o L_{\text{int}}} \left\{ \alpha \ln \left[\frac{\left| r_{\text{eff}}(\nu) \right|}{r_{f2}} - \operatorname{Arg}\left[r_{\text{eff}}(\nu)\right] \right] \right\} , \tag{96}$$

where r_{f2} is the reflectance of the feedback-coupling facet, and now the ν_q^o are the longitudinal modes of the solitary gain-chip cavity in the absence of external feedback and thus serve as constant-frequency markers. The net effect of the gain-dependent refractive index shift is to change the dependence of the threshold gain on wavelength from a sinusoid to an asymmetric sawtooth pattern. Depending on the values of α, r_{f2}, and r_{ext}, the threshold versus wavelength can be either single-valued or *reentrant* (Fig. 43). The condition where the threshold versus wavelength curve is reentrant (or overhanging) corresponds to the condition of bistability [23]. In this case wavelength bands exist that occur with the periodicity of the solitary cavity longitudinal mode spacing in which the oscillation threshold is multivalued (actually triple valued). When the bias current is turned up from zero, the laser goes into the low-threshold state. However, if the cavity is momentarily blocked while the bias current remains on, the oscillation will switch to the high-threshold state when the obstruction is removed (Fig. 44).

16.2 Bistability and Axial Mode Instability

As mentioned earlier, the regions in which the threshold versus wavelength curve is multivalued actually contain three sets of threshold states. It turns out that the middle states are unstable and will not support steady-state oscillation. This can be shown by performing a classical stability analysis on the rate equations and determining the conditions under which the circulating field and carrier density return to their steady-state solutions following a small perturbation. The existence of such classically unstable states has been experimentally correlated with a transition from single-mode to multimode output [24]. Each intermediate-threshold unstable mode lies between a pair of high- and low-threshold modes along the frequency axis [144]. For a given external reflectance r_{ext} and linewidth broadening factor α, it can be shown that unstable states appear when the facet reflectance r_{f2} exceeds a critical value r_{f2}^*, which is given by

$$\frac{r_{f2}^*}{1+(r_{f2}^*)^2} = \frac{r_{ext}}{\sqrt{\alpha^2 \dfrac{1-r_{ext}^2}{1+r_{ext}^2} + 1}} \ . \tag{97}$$

This equation can be solved analytically and provides a boundary surface between sets of cavity parameters for which all steady-state solutions are stable and those for which some solutions are unstable (Fig. 45). An approximate expression for the critical facet reflectance is given by

$$r_{f2}^* \approx \frac{r_{ext}}{\alpha} \ . \tag{98}$$

The quantity r_{f2}^* represents the maximum feedback-coupling facet reflectance that can be tolerated while maintaining unconditional stability of the laser at all

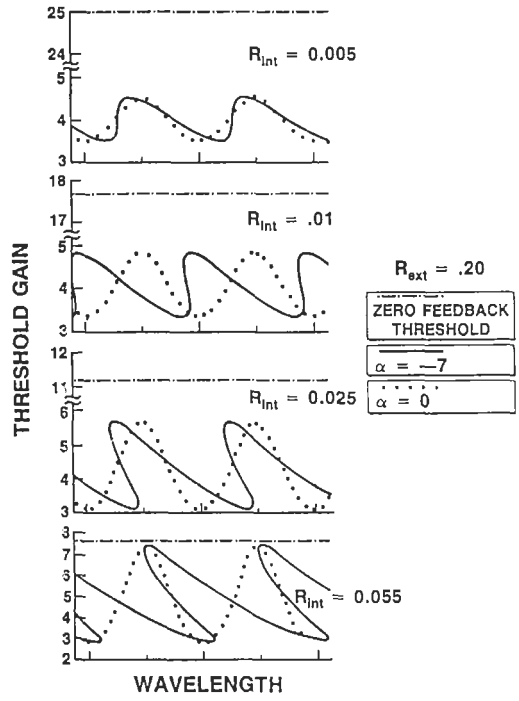

FIGURE 43 Threshold gain versus wavelength for various combinations of facet and external-cavity reflectances, demonstrating evolution of regions of bistability. (Reproduced with permission from Zorabedian *et al.* [23]. © 1987 IEEE.)

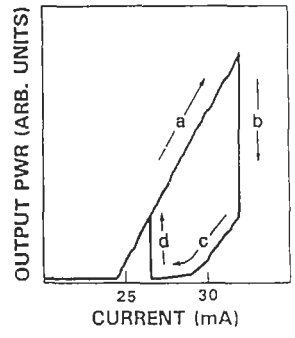

FIGURE 44 Light output versus current curve for a bistable ECL. (Reproduced with permission from Zorabedian *et al.* [23]. © 1987 IEEE.)

wavelengths. The stability analysis shows that the tolerance of the laser to residual facet reflectance is increased by increasing external feedback strength and reducing α. There are limits to the effectiveness of either approach. First, it is difficult to obtain external feedback in excess of the feedback of an uncoated

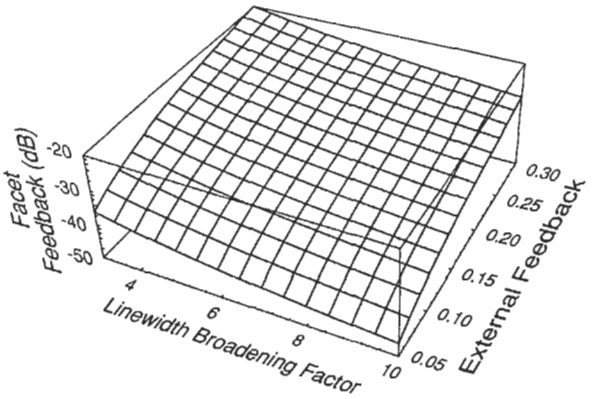

FIGURE 45 Facet reflectance at onset of axial mode instability versus external feedback and linewidth broadening factors. (Reproduced with permission from Zorabedian [24]. © 1994 IEEE.)

facet, that is, ~31%. Second, the linewidth broadening factor is usually not a parameter that is directly under the control of the cavity designer. For 1300- and 1550-nm Fabry–Perot diode lasers, α has a typical value of 4 to 7 near the gain peak and increases to >10 at the band edge [6], which implies that stability is more difficult to achieve at the long-wavelength edge of the tuning range. This has been experimentally confirmed.

Note that this analysis has its limitations. Although it is intuitively obvious that the resolution of the intracavity filter should have a strong influence on axial mode stability, this parameter is not taken into account. Therefore, the analysis should be interpreted in the following way: If unstable as well as stable modes lie within the filter bandwidth, the laser is likely to go into a multimode state. Narrowing the filter bandwidth increases the ability to reject the unstable modes and achieve steady-state single-mode operation.

16.3 Tuning Nonlinearity

Oscillation occurs at the cavity mode with the lowest threshold gain. Due to residual facet feedback, this mode may differ appreciably from the peak wavelength of the filter. For a given set of cavity parameters (filter bandwidth, facet reflectance, and external feedback) the lowest threshold mode can be found numerically for every position of the filter peak [145]. A plot of oscillation wavelength versus filter peak wavelength shows the tuning fidelity of the laser. A filter bandwidth that is narrow compared to the solitary mode spacing and a large ratio of external feedback to facet feedback results in a nearly linear tuning curve (Fig. 46). A broader filter bandwidth and a smaller feedback ratio gives a more nonlinear tuning curve that tends toward a staircase (Fig. 47). Overall tun-

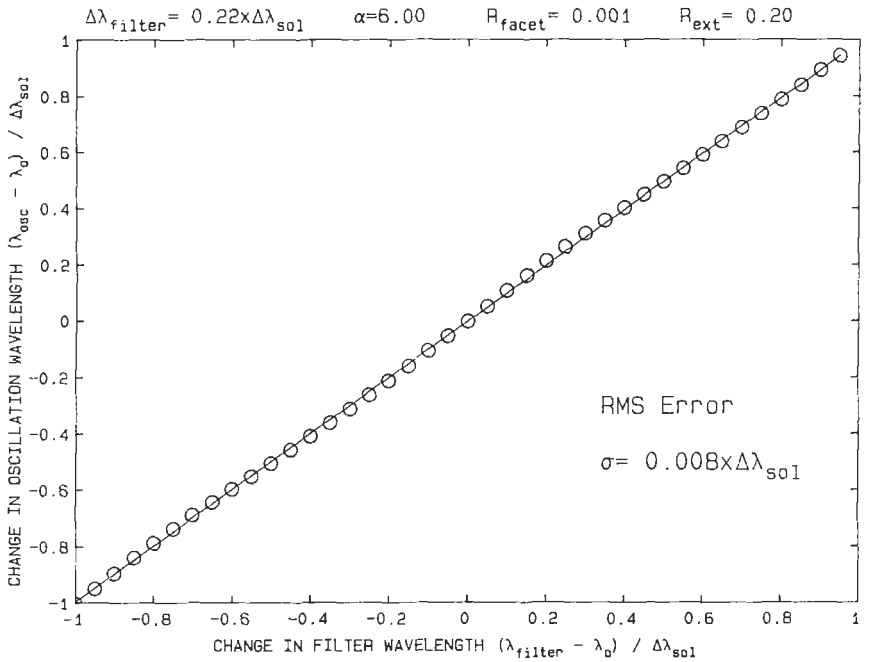

FIGURE 46 Calculated tuning curve for 20% external feedback, 0.1% coated-facet reflectance, linewidth broadening factor = 6, filter bandwidth = 0.22 times solitary mode spacing.

ing fidelity can be characterized by the rms residual of a linear fit to the calculated or measured tuning curve [46].

17. CONSTRUCTION AND PACKAGING

Packaging means taking construction of a laser beyond the optical breadboard stage. Packaged designs should be capable of operation in laboratory or production environments without the need for readjustment due to normally expected vibrations, microphonics or temperature fluctuations. Packaged lasers can be divided into two categories: laboratory modules and full instruments. Lab modules are suited for laboratory research work. They may require some manual adjustments and additional support apparatus such as current sources, motor drives, and wavelength meters. Instrument-grade ECLs are fully self-contained, programmable, do not require optical bench siting, and meet the requirements for automated test and measurement work.

An early (1975) packaging effort at Lincoln Laboratory [57] resulted in a laboratory module that featured a tuning knob with a mechanical readout gauge

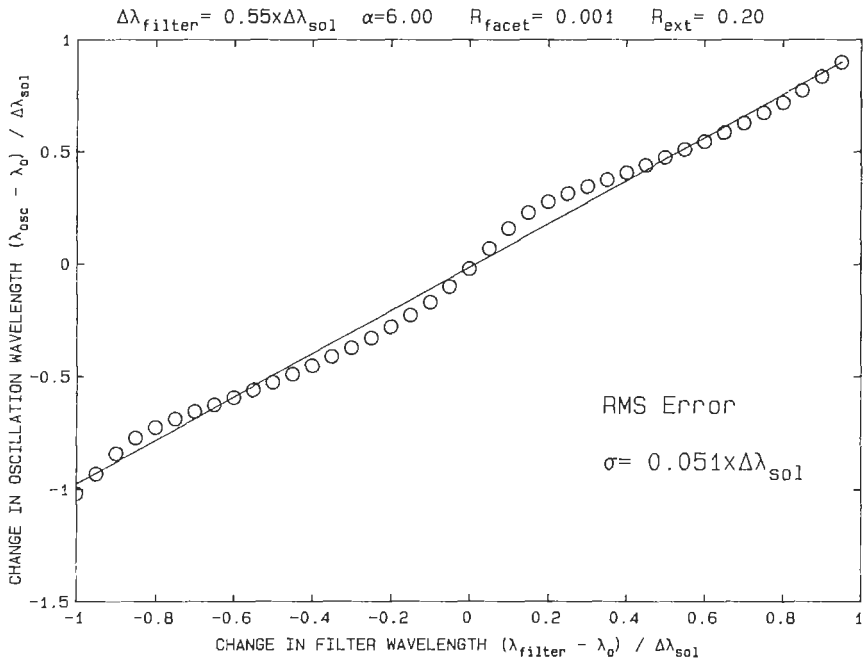

FIGURE 47 Calculated tuning curve for 20% external feedback, 0.1% coated-facet reflectance, linewidth broadening factor = 6, filter bandwidth = 0.55 times solitary mode spacing.

to indicate the wavelength. The cavity was based on an 880-nm pulsed GaAsP laser diode in a Littrow-grating configuration packaged in a 6-in.-long cylindrical body shaped like a flashlight. It incorporated TV camera lenses with adjustable focusing rings for the intracavity and output beams.

Work at British Telecom Research Labs in the 1980s resulted in two versions: Littrow-grating ECLs packaged in fiber-pigtailed lab modules. The first design [82] was basically a compact optical breadboard. Separate mounts were used for the grating, tuning plate, microscope-objective collimator, and the laser diode, which had an output fiber butt-coupled to the uncoated facet. Increased thermal, mechanical, and acoustic stability were achieved by minimizing the number of moving parts and attaching the individual components to a silica base plate placed in a thick-walled temperature-controlled aluminum box. The wavelength was preselected by choosing the grating angle prior to bonding it to the baseplate. Fine-tuning was accomplished by piezoelectric adjustment of the grating and tuning plate. The overall package dimensions were $14.5 \times 9 \times 6.5$ cm.

The second British Telecom package design [84] was a miniaturized cavity comprising a Littrow grating, GRIN lens collimator, and an AR-coated 1.53-μm laser diode with lensed fiber output coupling at the uncoated facet (Fig. 48). The

laser diode, output fiber, and collimating lens were combined in a single laser-welded, hermetic subpackage. The diode laser unit and the grating were mounted on opposing bulkheads of a small (palm-size) box. Coarse grating rotation up to ±2° was accomplished with manual adjusting screws. Fine-tuning up to 50 GHz was done piezoelectrically. The overall package dimensions were $30 \times 30 \times 50$ mm. This laser was marketed for a few years by BT&D (now Fiber Optic Components Operation of Hewlett-Packard).

Another compact ECL lab module was developed at the National Institute of Standards and Technology in Boulder, Colorado [37]. This compact module featured an inexpensive mechanical body using a homemade gimbal for tuning the grating and a flexure pivot for adjusting the distance between the laser and the collimating lens (Fig. 49). The module was designed to make use of commercial diode laser packages in which only one facet is accessible. The free-space output beam was taken either from the zeroth-order grating reflection or from an optional intracavity beamsplitter.

In a number of high-resolution laboratory applications, acoustic shielding is mandatory to reduce the residual FM of an ECL. For this purpose, layering is very effective. Enclosure in a Plexiglas box with tightly sealed joints followed by several layers of lead and rubber foam greatly increases the isolation from microphonic disturbances. Plywood is also a good sound and vibration absorbing material.

Several commercial ECLs are now on the market. Some of these are in the laboratory prototype category and require significant support equipment such as motors and wavelength-measuring instruments. A brief description of the packaging of Hewlett-Packard's instrument-grade 8167A and 8168A tunable laser source products (1300 and 1550 nm, respectively) is as follows [93]: The extended-cavity laser is tuned with a Littrow-grating in conjunction with an etalon and includes an extracavity optical isolator and a fiber-pigtailed output. The unit contains a dual-output hermetically sealed diode laser module. The diode laser module is incorporated into an optical block that is heated to 55°C. The optical block is an independent and pretested subassembly and is seated in

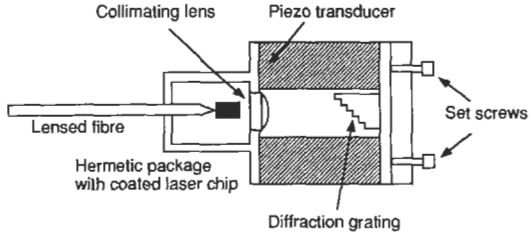

FIGURE 48 Compact module with fiber output. (Reproduced with permission from Mellis *et al.* [84] and IEE Publishing.)

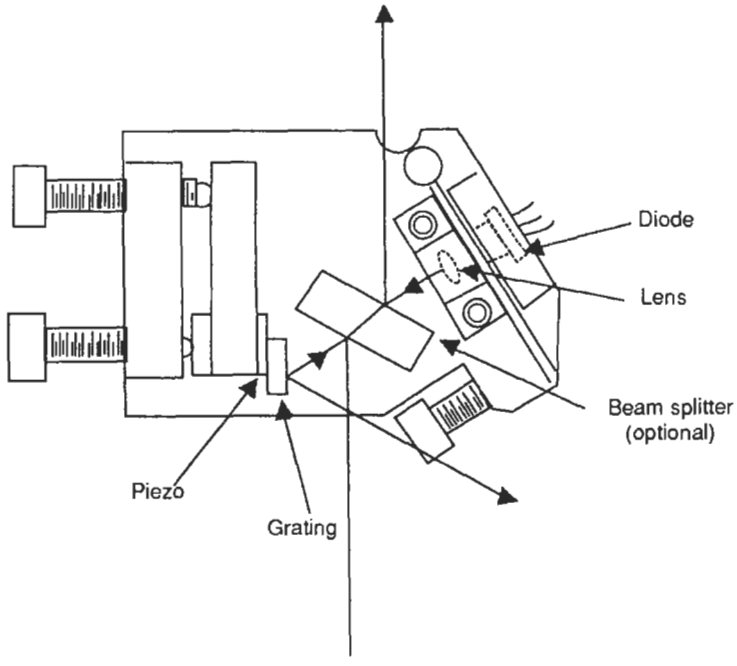

FIGURE 49 Extended-cavity laser module with free-space output based on commercial laser diode package without back-facet access. (Reproduced with permission from Wieman and Hollberg [37] and the American Institute of Physics.)

the instrument chassis using soft rubber spacers to reduce mechanical stress. Together with the mainframe, the design forms a two-stage shock absorbing system. As a result, the unit is able to withstand use in both laboratory and production environments without special handling. The overall dimensions are $425 \times 132 \times 497$ mm, of which the optical block takes one-third of the volume. The remainder contains printed circuit cards and the power supply.

18. APPLICATIONS

18.1 Lightwave Communications

18.1.1 Coherent (Optical Heterodyne) Systems

A number of different modulation schemes fall under the heading of "coherent," that is, optical heterodyne or homodyne transmission. Two of the most widely used coherent transmission methods are phase-shift keying (PSK) and frequency-shift keying (FSK). The spectral performance required of the optical

transmitter and local oscillator (LO) depends on the modulation scheme and on the bit rate. However, in general, coherent optical communications systems require optical sources that are single frequency (sidemode suppression ratio >30 dB) and narrow linewidth ($\delta\nu \sim 100$ kHz). In addition, the LO laser must be tunable.

In the early 1980s, workers at British Telecom Research Laboratories used ECLs to demonstrate the feasibility of coherent transmission over long-haul fiber optic links. A PSK heterodyne experiment was reported in which a grating-tuned ECL was used as the LO in a PSK heterodyne experiment, and a 1.52-μm HeNe laser was used as the transmitter [146]. A receiver sensitivity of −59 dBm was obtained over a transmission path consisting of 109 km of optical fiber. In another experiment, a pair of grating-tuned ECLs served as the transmitter and LO in an FSK heterodyne experiment at 1.54 μm [147]. A receiver sensitivity of −55 dBm was measured over 200 km of optical fiber. In both experiments, the intermediate frequency was stabilized by cavity-length tuning of the LO laser using an intracavity silica tuning plate mounted on a galvanometer.

No coherent systems have yet been commercially deployed. All fiber optic telecommunication systems in use today utilize on–off keying and direct detection. Compared to coherent technology, this is loosely analogous to the status of spark-gap radio transmission prior to the commercial introduction of superheterodyne receivers in 1924 [148]. As the demand for bandwidth increases and component technology improves, it is likely that coherent transmission will become commercially significant at some time in the future. Although it is likely that the transmitters and LOs in coherent fiber optic telecommunication links will be monolithically integrated tunable lasers such as DFB lasers, ECLs will undoubtedly be used in test instrumentation for the characterization of these monolithic sources and in the maintenance of the installed coherent transmission links.

18.1.2 Wavelength-Division-Multiplexed Systems

Wavelength division multiplexing (WDM) increases the capacity of fiber optic telecommunication links by transmitting at multiple-wavelength channels to utilize the broad spectral transmission window of optical fiber. A demonstration of 1.37 terabit km/sec transmission capacity over 68 km of fiber was made using 10 single-frequency DFB lasers [149]. To my knowledge, no WDM system demonstrations using ECLs have been published, but recently there has been activity to develop multiwavelength multistripe grating-cavity lasers specifically for WDM applications [126–128].

18.2 Lightwave Testing and Measurement

The most important commercial use of ECLs is in instrumentation for the testing and measurement of components for lightwave communications systems. This is an ideal application for ECLs because performance is at a premium, and the high value of the systems under test can support the relatively high cost of a

high-performance instrument-grade tunable source. A WDM link containing a fiber optic amplifier is a good example of a system that an ECL might be used to test. Such a system contains both passive and active components.

18.2.1 Testing of Passive Components

Passive components include such devices as filters, couplers, isolators, and wavelength multiplexers. It is often necessary to measure the wavelength dependence of the transmittance, splitting, and isolation of these devices [150]. Measurements of the fiber chromatic dispersion [151,152] and polarization-mode dispersion [153] in fiber and in optical components also require tunable ECLs.

18.2.2 Testing of Optical Amplifiers

ECLs are used to test the gain, polarization sensitivity, and saturation characteristics of traveling-wave semiconductor amplifiers [154] and rare-earth-doped optical fiber amplifiers [155]. At present, optical fiber amplifiers are commercially dominant over semiconductor amplifiers. Low noise, high output power, and wide tuning range are important requirements of the tunable laser used for amplifier testing.

18.2.3 Swept-Source Measurements

The ability to observe the transmission or reflection spectrum in real time would be of considerable value for making adjustments to optical components and systems. The wavelength agility of the acousto-optically tuned ECL makes it viable as a swept source for optical network analysis (Fig. 50). Swept-source measurements have been made on AO filters serving as devices under test [46]. The measured transmission characteristics were in good agreement with results obtained using a grating-tuned ECL (Fig. 51).

18.3 High-Resolution Atomic Spectroscopy

The ease of use and broad tunability of ECLs makes them attractive replacements for dye and Ti:sapphire lasers in a number of high-resolution atomic spectroscopy applications. Absorption lines of calcium cesium, iodine, oxygen, neon, and uranium vapors lie within the tuning ranges of 650-, 780-, and 850-nm ECLs [37,156,157].

18.4 Gas Monitoring

ECLs with InGaAsP/InP and InGaAs/InP gain media can tune to transitions in a number of molecular gas species, for example HF (1.31 μm), H_2O (1.39 μm), HO_2 (1.5 μm), H_2F (1.57 μm), and CH_4 (1.65 μm). Carbon monoxide can also be detected using its vibrational overtones at around 1.65 μm. Applications

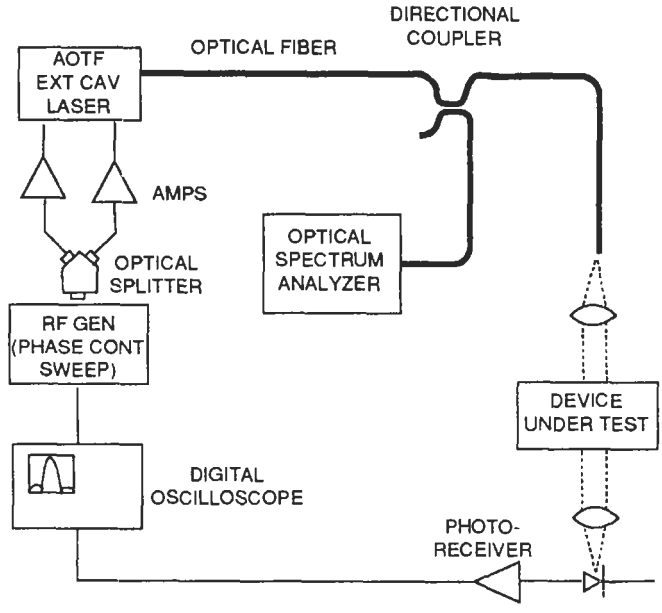

FIGURE 50 Setup for demonstration of optical network analysis with an acousto-optically tuned ECL.

include analysis of process gas purity, chemical refining, combustion diagnostics, and pollution monitoring.

18.5 Metrology

A grating tuned ECL has been used in an optically pumped cesium-beam frequency standard [158]. A pair of optically phase-locked ECLs was used in a laser-cooled cesium atomic-fountain clock [159,160].

18.6 Second Harmonic Generation

There is a great deal of interest in generating blue light for optical data storage. The cost and size constraints of this application dictate the use of diode lasers. While blue diode lasers based on II–VI semiconductors appear to be on the horizon, the technology for near-infrared III–V semiconductor lasers is mature and inexpensive. There have therefore been investigations into second harmonic generation of 850-nm laser diodes using nonlinear crystals. In second harmonic generation, $P_{2\omega} \propto P_{\omega}^2$. Therefore, high fundamental power is required for efficient harmonic generation. In addition, the phase-matching condition requires a fundamental bandwidth of a few tenths of a nanometer. The nonlinear

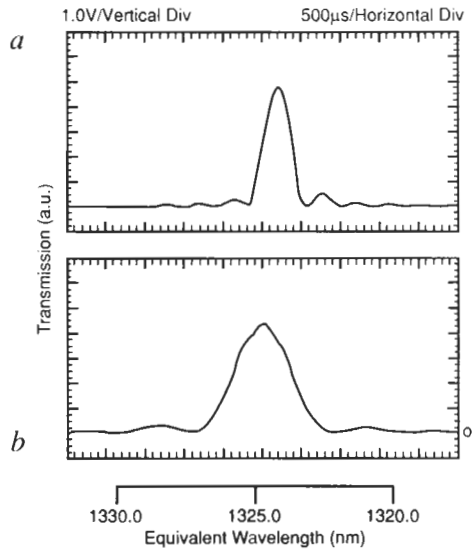

FIGURE 51 Swept-wavelength measurements of AOTF transmittance characteristics: (a) Crystal Technology filter driven at 88.5 MHz. (b) Matsushita filter driven at 68.54 MHz. (Reproduced with permission from Zorabedian [46]. © 1995 IEEE.)

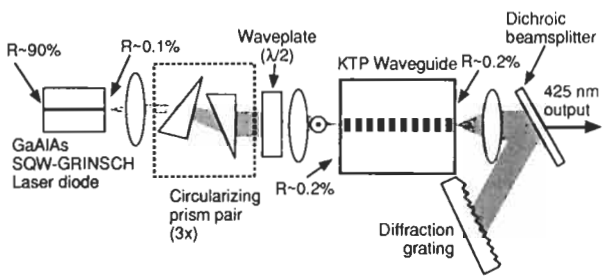

FIGURE 52 Grating-tuned extended-cavity laser containing a quasi-phase-matched KTP waveguide for intracavity frequency doubling. (Reproduced with permission from Risk *et al.* [162] and the American Institute of Physics.)

crystal can be placed inside an ECL to take advantage of the higher circulating intracavity power and the wavelength control provided by the tuning element. Intracavity second harmonic generation has been performed in grating ECLs using angle-phase-matched α-iodic acid (HIO_3) bulk crystals [161] and quasi-phase-matched, periodically poled waveguides in KTP substrates [162] (Fig. 52). Ten milliwatts of 532-nm light has been generated from a Nd:YVO_4 laser internally doubled with a KTP crystal and pumped with 55 mW from an interference-filter-controlled quasi-degenerate ECL at 809 nm [163] (Fig. 53).

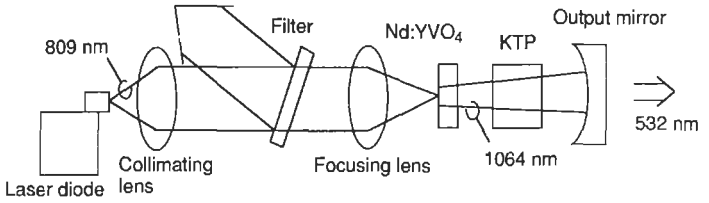

FIGURE 53 Interference-filter-tuned extended-cavity laser used to pump intracavity-doubled $Nd:YVO_4$. (Reproduced with permission from Kitaoka *et al.* [163].)

18.7 Injection Seeding

The optical parametric oscillator (OPO) is arguably the most widely tunable coherent optical source. However, it is difficult to obtain narrow-bandwidth output from an OPO. Use of dispersive elements in the OPO cavity complicates tuning. An alternative is to use a tunable ECL as an injection-seeding source. A 1.55-μm grating ECL with a 150-kHz linewidth has been used to seed a lithium niobate OPO [164]. The OPO was pumped at 1.064 μm with a Nd:YAG laser. Seeding reduced the bandwidth of the signal from 50 GHz without seeding to 0.18 GHz with seeding. Seeding was obtained for injected signal wavelengths from 1.526 to 1.578 μm, corresponding to an idler wavelength range of 3.26 to 3.51 μm. The authors noted that these limits could be extended with improved cavity optics and a different seeding source. The tunable idler radiation is useful for atmospheric spectroscopy because many species absorb in the 3- to 4-μm atmospheric transmission window.

REFERENCES

1. Y. Tohmori, F. Kano, H. Ishii, Y. Yoshikuni, and Y. Kondo, "Wide Tuning with Narrow Linewidth in DFB Lasers with Superstructure Grating (SSG)," *Electron. Lett.* **29,** 1350–1351 (July 1993).
2. Y. C. Chung and Y. H. Lee, "Spectral Characteristics of Vertical-Cavity Surface-Emitting Lasers with External Optical Feedback," *Photon. Technol. Lett.* **3,** 597–599 (July 1991).
3. S. Jiang, Z. Pan, M. Dagenais, R. A. Morgan, and K. Kojima, "Influence of External Optical Feedback on Threshold and Spectral Characteristics of Vertical-Cavity Surface-Emitting Lasers," *Photon. Technol. Lett.* **6,** 34–36 (Jan. 1994).
4. The internal quantum efficiency η_{int} is defined as the ratio of the total carrier lifetime τ_c to the radiative lifetime τ_r.
5. C. H. Henry, "Theory of the Linewidth of Semiconductor Lasers," *IEEE J. Quantum Electron.* **QE-18,** 259–264 (1982).
6. L. D. Westbrook, "Dispersion of Linewidth-Broadening Factor in 1.5 μm Laser Diodes," *Electron. Lett.* **21,** 1018–1019 (1985).
7. K. Naganuma and H. Yasaka, "Group Delay and α-Parameter Measurement of 1.3 μm Semiconductor Traveling-Wave Optical Amplifier Using the Interferometric Method," *IEEE J. Quantum Electron.* **27,** 1280–1287 (1991).

8. M. Osinski and J. Buus, "Linewidth Broadening Factor in Semiconductor Lasers—An Overview." *IEEE J. Quantum Electron.* **QE-23,** 9–28 (1987).
9. P. J. Anthony, "Fabrication and Characterization of Semiconductor Lasers" in *Optoelectronic Technology and Lightwave Communications Systems,* (C. Lin, Ed.), Van Nostrand Reinhold, New York (1989).
10. K. Kobayashi, "Transverse Mode Control in Semiconductor Lasers" in *Optoelectronic Technology and Lightwave Communications Systems* (C. Lin, Ed.), Van Nostrand Reinhold, New York (1989).
11. J. N. Walpole, E. S. Kintzer, S. R. Chinn, C. A. Wang, and L. J. Missaggia, "High-Power Strained-Layer InGaAs/AlGaAs Tapered Traveling Wave Amplifier." *Appl. Phys. Lett.* **61,** 740–742 (1992).
12. D. Waarts, "Semiconductor Lasers for Frequency Conversion," *Compact Blue-Green Lasers Topical Mtg.*, Salt Lake City, UT (1994).
13. Amnon Yariv, *Quantum Electronics*, 3rd ed., John Wiley & Sons, New York (1989).
14. P. Zorabedian and W. R. Trutna, Jr., "Interference-Filter-Tuned Alignment-Stabilized, Semiconductor External-Cavity Laser." *Opt. Lett.* **13,** 826–828 (1988).
15. New Focus product literature.
16. M. de Labachelerie and P. Cerez, "An 850 nm Semiconductor Laser Tunable Over a 300 Å Range." *Opt. Commun.* **55,** 174–178 (Sept. 1985).
17. Hewlett-Packard product literature.
18. D. Mehuys, L. Eng, M. Mittlestein, T. R. Chen, and A. Yariv, "Ultra-Broadband Tunable External Cavity Quantum Well Lasers." in *Laser-Diode Technology and Applications II. Proc. SPIE* **1219,** 358–365 (1990).
19. Peter S. Zory, Jr., *Quantum Well Lasers*, Academic Press, New York (1993).
20. D. Mehuys, M. Mittelstein, and A. Yariv, "Optimised Fabry–Perot (AlGa)As Quantum-Well Laser Tunable Over 105 nm." *Electron. Lett.* **25,** 143–145 (Jan. 1989).
21. L. E. Eng, D. G. Mehuys, M. Mittelstein, and A. Yariv, "Broadband Tuning (170 nm) of InGaAs Quantum Well Lasers," *Electron Lett.* **26,** 1675–1677 (1990).
22. A. Lidgard, T. Tanbun-Ek, R. A. Logan, H. Temkin, K. W. Wecht, and N. A. Olsson, "External-Cavity InGaAs/InP Graded Index Multiquantum Well Laser with a 200 nm Tuning Range," *Appl. Phys. Lett.* **56,** 816–817, (Feb. 1990).
23. P. Zorabedian, W. R. Trutna, Jr., and L. S. Cutler, "Bistability in Grating Tuned External-Cavity Semiconductor Lasers," *J. Quantum Electron.* **QE-23,** 1855–1860 (Nov. 1987).
24. P. Zorabedian, "Axial Mode Instability in Tunable External-Cavity Semiconductor Lasers," *IEEE J. Quantum Electron,* **30,** 1542–1552 (1994).
25. T. Saitoh, T. Mukai, and O. Mikami, "Theoretical Analysis and Fabrication of Antireflection Coatings on Laser-Diode Facets," *IEEE J. Lightwave Technol.* **LT-3**(2), 288–293 (1985).
26. J. Chen, D. Li, and Y. Lu, "Experimental and Theoretical Studies on Monitored Signals from Semiconductor Diodes Undergoing Antireflection Coatings," *Appl. Opt.* **30,** 4554–4559 (1991).
27. I.-F. Wu, I. Riant, J.-M. Verdiell, and M. Dagenais, "Real-Time in Situ Monitoring of Antireflection Coatings for Semiconductor Laser Amplifiers by Ellipsometry," *IEEE Photon. Technol. Lett.* **4,** 991–993 (1992).
28. I.-F. Wu, J. B. Dottellis, and M. Dagenais, "Real-Time in Situ Ellipsometric Control of Antireflection Coatings for Semiconductor Laser Amplifiers Using SiO_x," *J. Vac. Sci. Technol. A.* **11**(5), 2398–2406 (Sept./Oct. 1993).
29. M. J. O'Mahoney and W. J. Devlin, "Progress in Semiconductor Optical Amplifiers," in *Technical Digest on Optical Amplifiers and Their Applications,* paper MC1, pp. 26–29 (1990).
30. R. L. Jungerman, D. M. Braun, and K. K. Salomaa, "Dual-Output Laser Module for a Tunable Laser Source," *Hewlett-Packard* J. **44**(1), 32–34 (Feb. 1993).
31. G. Eisenstein, G. Raybon, and L. W. Stulz, "Deposition and Measurements of Electron-Beam Evaporated SiO_x Antireflection Coatings on InGaAsP Injection Laser Facets," *IEEE J. Lightwave Technol.* **6**(1), 12–16 (Jan. 1988).

32. G. Eisenstein and L. W. Stulz, "High Quality Antireflection Coatings on Laser Facets by Sputtered Silicon Nitride," *Appl. Opt.* **23**(1), 161–164 (1984).
33. D. R. Scifres, W. Streifer, and R. D. Burnham, "GaAs/AgAlAs Diode Lasers with Angled Pumping Stripes." *IEEE J. Quantum Electron.* **QE-14,** 223–227 (1978).
34. N. K. Dutta, "Optical Amplifiers," in *Progress in Optics,* Vol. 31, p. 202, North-Holland, Amsterdam (1993).
35. M. C. Robbins, J. Buus, and D. J. Robbins, "Analysis of Antireflection Coatings on Angled Facet Semiconductor Laser Amplifiers." *Electron. Lett.* **26,** 381–382 (1990).
36. N. K. Dutta, A. B. Piccirilli, M. S. Lin, R. L. Brown, J. Wynn, D. Coblentz, Y. Twu, and U. K. Chakrabarti, "Fabrication and Performance Characteristics of Buried-Facet Optical Amplifiers," *J. Appl. Phys.* **67,** 3943–3947 (1990).
37. C. E. Wieman and L. Hollberg, "Using Diode Lasers for Atomic Physics," *Rev. Sci. Instrum.* **62**(1), 1–20 (Jan. 1991).
38. M. W. Fleming and A. Mooradian, "Spectral Characteristics of External-Cavity Controlled Semiconductor Lasers," *IEEE J. Quantum Electron.* **QE-17**(1), 44–59 (Jan. 1981).
39. E. Patzak, A. Sugimura, S. Saito, T. Mukai, and H. Olesen, "Semiconductor Laser Linewidth in Optical Feedback Configurations," *Electron. Lett.* **19**(24), 1026–1027 (Nov. 1983).
40. R. Wyatt, K. H. Cameron, and M. R. Matthews, "Tunable Narrow Line External Cavity Lasers for Coherent Optical Systems," *Br. Telecom. Technol. J.* **3,** 5–12 (1985).
41. R. A. Linke and K. J. Pollock, "Linewidth vs. Length Dependence for an External Cavity Laser." in *Proc. 10th IEEE Int. Semiconductor Laser Conf.*, Kanazawa, Japan, p. 118 (1986).
42. M. Ohtsu, K.-Y. Liou, E. C. Burrows, C. A. Burrus, G. Eisenstein, "A Simple Interferometric Method for Monitoring Mode Hopping in Tunable External-Cavity Semiconductor Lasers." *J. Lightwave Technol.* **7,** 58–75 (1989).
43. D. Mehuys, D. Welch, and D. Scifres, "1W cw, Diffraction-Limited, Tunable External-Cavity Semiconductor Laser." *Electron. Lett.* **29**(14), 1254–1255 (July 1993).
44. A. Olsson and C. L. Tang, "Coherent Optical Interference Effects in External-Cavity Semiconductor Lasers," *IEEE J. Quantum Electron.* **QE-17,** 1320–1323 (1981).
45. P. Zorabedian, W. R. Trutna, Jr., and L. S. Cutler, "Bistability in Grating Tuned External-Cavity Semiconductor Lasers." *J. Quantum Electron.* **QE-23,** 1855–1860 (Nov. 1987).
46. P. Zorabedian, "Tuning Fidelity of Acousto-Optically Controlled External-Cavity Semiconductor Lasers," *IEEE J. Lightwave Technol.* 13, 62–66 (1995).
47. R. E. Wagner and W. J. Tomlinson, "Coupling Efficiency of Optics in Single-Mode Fiber Components." *Appl. Opt.* **21,** 2671–2688 (1982).
48. H. Kogelnik and T. Li, "Laser Beams and Resonators," *Appl. Opt.* **5,** 1550 (1966).
49. A. E. Siegman, *Lasers,* University Science Books, Mill Valley, CA (1986).
50. J. A. Arnaud, *Beam and Fiber Optics,* New York, Academic Press (1976).
51. A. Gerrard and J. M. Burch, *Matrix Methods in Optics*, John Wiley and Sons, New York (1975).
52. D. Kuntz, "Specifying Laser Diode Optics." *Laser Focus*, pp. 44–55 (Mar. 1984).
53. NSG SELFOC Handbook.
54. R. Kingslake, *Lens Design Fundamentals*, Academic Press, New York (1978).
55. M. A. Fitch, "Molded Optics: Mating Precision and Mass Production," *Photon. Spectra* **25,** 83–87 (Oct. 1991).
56. H. Asakura, K. Hagiwara, M. Iida, and K. Eda, "External Cavity Semiconductor Laser with a Fourier Grating and an Aspheric Lens, *Appl. Opt.* **32,** 2031–2038 (Apr. 1993).
57. H. Heckscher and J. A. Rossi, "Flashlight-Size External Cavity Semiconductor Laser with Narrow-Linewidth Tunable Output." *Appl. Opt.* **14,** 94–96 (1975).
58. H. S. Sommers, Jr., "Performance of Injection Lasers with External Gratings," *RCA Rev.* **38,** 33–59 (Mar. 1977).
59. H. Kuwahara, M. Sasaki, and N. Tokoyo, "Efficient Coupling from Semiconductor Lasers into Single-Mode Fibres with Tapered Hemispherical Ends," *Appl. Opt.* **19**, 2578–2583 (1980).

60. P. Zorabedian and W. R. Trutna, Jr., "Alignment-Stabilized Grating-Tuned External-Cavity Semiconductor Laser," *Opt. Lett.* **15,** 483–485 (1990).
61. P. Zorabedian, "Characteristics of a Grating-External-Cavity Semiconductor Laser Containing Intracavity Prism Beam Expanders," *IEEE J. Lightwave Technol.* **10,** 330–335 (1992).
62. *Diffraction Grating Handbook,* 2nd ed. (Christopher Palmer, Ed.), Milton Roy Co., Rochester, New York (1994).
63. N. D. Viera, Jr., and L. F. Mollenauer, "Single Frequency, Single Knob Tuning of a cw Color Center Laser," *IEEE J. Quantum Electron.* **QE-21,** 195–201 (Mar. 1985).
64. W. V. Sorin, P. Zorabedian, and S. A. Newton, "Tunable Single Mode Fiber Reflective Grating Filter," *IEEE J. Lightwave Technol.* **LT-5,** 1199–1202 (1987).
65. F. A. Jenkins and H. E. White, *Fundamentals of Optics,* 4th ed., 301–305, McGraw-Hill, New York (1976).
66. Melles Griot Optics Guide IV, 11–25.
67. J. W. Evans, "The Birefringent Filter," *J. Opt. Soc. Am.* **39,** 229–242 (1949).
68. J. W. Evans, "Solc Birefringent Filter, *J. Opt. Soc. Am.* **48,** 142–145 (1957).
69. J. Staromlynska, "A Double-Element Broad-Band Liquid Crystal Tunable Filter; Factors Affecting Contrast Ratio," *IEEE J. Quantum Electron.* **28,** 501–506 (1992).
70. R. S. Seymour, S. M. Rees, J. Staromlynska, J. Richards, and P. Wilson, "Design Considerations for a Liquid Crystal Tuned Lyot Filter for Laser Bathymetry," *Opt. Eng.* **33,** 915–923 (1994).
71. H. Walther and J. L. Hall, *Appl. Phys. Lett.* **17,** 239 (1970).
72. R. C. Alferness and L. L. Buhl, *Appl. Phys. Lett.* **47,** 1137–1139 (1985).
73. S. E. Harris and R. W. Wallace, "Acousto-Optic Tunable Filter," *J. Opt. Soc. Am.* **59,** 744–747 (June 1969).
74. S. E. Harris and S. T. K. Nieh, "$CaMoO_4$ Electronically Tunable Optical Filter," *Appl. Phys. Lett.* **17,** 223–225 (Sep. 1970).
75. T. Yano and A. Watanabe, "New Noncollinear Acousto-Optic Tunable Filter Using Birefringence in Paratellurite," *Appl. Phys. Lett.* **24,** 256–258 (Mar. 1974).
76. T. Yano and A. Watanabe, "Acoustooptic TeO_2 Tunable Filter Using Far-Off-Axis Anisotropic Bragg Diffraction," *Appl. Opt.* **15,** 2250–2258 (Sep. 1976).
77. I. Kurtz, R. Dwelle, and P. Katzka, "Rapid Scanning Fluorescence Spectroscopy Using an Acousto-Optic Tunable Filter," *Rev. Sci. Instr.* **58,** 1996–2003 (1987).
78. R. C. Booth and D. Findlay, "Tunable Large Angular Aperture TeO_2 Acousto-Optic Filters for Use in the 1.0–1.6 μm Region," *Opt. Quantum Electron.* **14,** 413–417 (1982).
79. N. K. Dutta and N. A. Olsson, "Effects of External Optical Feedback on Spectral Properties of External Cavity Semiconductor Lasers," *Electron. Lett.* **20**(4), 588–589 (1984).
80. D. K. Wilson, "Optical Isolators Cut Feedback in Visible and Near-IR Lasers," *Laser Focus World* **24,** 103–108 (Dec. 1988); "Optical Isolators Adapt to Communication Needs," *Laser Focus World,* 175–180 (Apr. 1991).
81. R. Ludeke and E. P. Harris, "Tunable GaAs Laser in an External Dispersive Cavity," *Appl. Phys. Lett.* **20,** 499–500 (1972).
82. M. R. Matthews, K. H. Cameron, R. Wyatt, and W. J. Devlin, "Packaged Frequency-Stable Tunable 20 kHz Linewidth 1.5 μm InGaAsP External Cavity Laser," *Electron. Lett.* **21,** 113–115 (1985).
83. J. Wittmann and G. Gaukel, "Narrow-Linewidth Laser with a Prism Grating/GRIN Rod Lens Combination Serving as External Cavity," *Electron. Lett.* **23,** 524–525 (May 1987).
84. J. Mellis, S. A. Al-Chalabi, R. Wyatt, J. C. Regnault, W. J. Devlin, and M. C. Brain, "Miniature Packaged External-Cavity Semiconductor Laser with 50 GHz Continuous Electrical Tuning Range," *Electron. Lett.* **24,** 988–989 (Aug. 1988).
85. K. C. Harvey and C. J. Myatt, "External-Cavity Diode Laser Using a Grazing-Incidence Diffraction Grating," *Opt. Lett.* **16,** 910–912 (June 1991).

86. A. P. Bogatov, P. G. Eliseev, O. G. Okhotnikov, G. T. Pak, M. P. Rakhval'skii, and K. A. Khairetdinov, "ew Operation of an Injection Ring Laser," *Sov. Tech. Phys. Lett.* **8,** 346–347 (July 1982).
87. S. Oshiba, K. Nagai, M. Kawahara, A. Watanabe, and Y. Kawai, "Widely Tunable Semiconductor Optical Fiber Ring Laser," *Appl. Phys. Lett.* **55,** 2383–2385 (1989).
88. E. T. Peng and C. B. Su, "Properties of an External-Cavity Traveling-Wave Semiconductor Ring Laser," *Opt. Lett.* **17,** 55–57 (1992).
89. J. M. Kahn, C. A. Burrus, and G. Raybon, "High-Stability 1.5 μm External-Cavity Semiconductor Lasers for Phase-Lock Applications," *IEEE Phot. Technol. Lett.* **1,** 159–161 (July 1989).
90. H. Tsuda, K. Hirabayashi, Y. Tohmori, and T. Kurokawa, "Tunable Light Source Using a Liquid Crystal Fabry–Perot Interferometer," *IEEE Photon. Technol. Lett.* **3,** 504–506 (June 1991).
91. M. J. Chawki, I. Valiente, R. Auffret, and V. Tholey, "All Fibre, 1.5 μm Widely Tunable Single Frequency and Narrow Linewidth Semiconductor Ring Laser with Fibre Fabry Perot Filter," *Electron. Lett.* **29,** 2034–2035 (Nov. 1993).
92. N. A. Olsson and J. P. Van der Ziel, "Performance Characteristics of 1.5 μm External Cavity Semiconductor Lasers for Coherent Optical Communication," *IEEE J. Lightwave Technol.* **LT-5,** 510–515 (1987).
93. E. Muller, W. Reichert, C. Ruck, and R. Steiner, "External-Cavity Laser Design and Wavelength Calibration," *Hewlett-Packard J.* **44**(1), 20–27 (Jan. 1993).
94. R. M. Jopson, G. Eisenstein, M. S. Whalen, K. L. Hall, U. Koren, and J. R. Simpson, "A 1.55 μm Semiconductor-Optical Fiber Ring Laser," *Appl. Phys. Lett.* **48,** 204–206 (Jan. 1986).
95. F. Heismann, R. C. Alferness, L. L. Buhl, G. Eisenstein, S. K. Korotsky, J. J. Veselka, L. W. Stulz, and C. A. Burrus, "Narrow-Linewidth, Electro-Optically Tunable InGaAsP-Ti:$LiNbO_3$ Extended Cavity Laser," *Appl. Phys. Lett.* **51**(3), 164–166 (1987).
96. T. Findakly, and C.-L. Chen, *Appl. Opt.* **17,** 469 (1978).
97. F. Heissmann, L.L. Buhl, and R. C. Alferness, *Electron. Lett.* **23,** 572 (1987).
98. A. Schremer and C. L. Tang, "Single-Frequency Tunable External-Cavity Semiconductor Laser Using an Electro-Optic Birefringent Modulator," *Appl. Phys. Lett.* **55**(1), 19–21 (1989).
99. J. R. Andrews, "Low Voltage Wavelength Tuning of an External Cavity Diode Laser Using a Nematic Liquid Crystal-Containing Birefringent Filter," *IEEE Photon. Technol. Lett.* **2**(5), 334–336 (May 1990).
100. W. Streifer and J. R. Whinnery, "Analysis of a Dye Laser Tuned by Acousto-Optic Filter," *Appl. Lett.* **17,** 335–337 (1970).
101. D. J. Taylor, S. E. Harris, S. T. K. Nieh, and T. W. Hansch, "Electronic Tuning of a Dye Laser Using the Acousto-Optic Filter," *Appl. Phys. Lett.* **19**(8), 269–271 (1971).
102. G. A. Coquin and K. W. Cheung, "Electronically Tunable External Cavity Semiconductor Laser," *Electron. Lett.* **24,** 599–600 (1988).
103. G. Coquin, K.-W. Cheung, and M. M. Choy, "Single- and Multiple Wavelength Operation of Acoustooptically Tuned Semiconductor Lasers at 1.3 μm," *IEEE J. Quantum Electron.* **25,** 1575–1579 (1989).
104. S. Oshiba, T. Kamijoh, and Y. Kawai, "Tunable Fiber Ring Lasers with an Electrically Accessible Acousto-Optic Filter," in *Photonic Switching II, Proc. Int. Topical Mtg.*, Kobe, Japan, 1990, 241–244.
105. T. Day, F. Luecke, and M. Brownell, "Continuously Tunable Diode Lasers," *Lasers Optron.* 15–17 (June 1993).
106. This terminology is used to avoid ambiguity, since many authors use the terminology "continuous tuning" to signify quasi-continuous tuning as defined earlier in this chapter, i.e., tuning by hopping to successive external-cavity modes.
107. F. Favre, D. Le Guen, J. C. Simon, B. Landousies, "External-Cavity Semiconductor Laser with 15 nm Continuous Tuning Range," *Electron. Lett.* **22,** 795–976 (1986).
108. A. T. Schremer and C. L. Tang, "External-Cavity Semiconductor Laser with 1000 GHz Continuous Piezoelectric Tuning Range," *IEEE Photon. Technol. Lett.* **2,** 3–5 (1990).

109. F. Favre and D. Le Guen, "82 nm of Continuous Tunability for an External Cavity Semiconductor Laser," *Electron. Lett.* **27,** 183–184 (1991).
110. P. McNicholl and H. J. Metcalf, "Synchronous Cavity Mode and Feedback Wavelength Scanning in Dye Laser Oscillators with Gratings," *Appl. Opt.* **24,** 2757–2761 (1985).
111. M. de Labachelerie and G. Passedat, "Mode-Hop Suppression of Littrow Grating-Tuned Lasers," *Appl. Opt.* **32,** 269–274 (1993).
112. W. R. Trutna, Jr. and L. F. Stokes, "Continuously Tuned External Cavity Semiconductor Laser," *IEEE J. Lightwave Technol.* **11,** 1279–1286 (1993).
113. H. Lotem, "Mode-Hop Suppression of Littrow Grating-Tuned Lasers: Comment," *Appl. Opt.* **33,** 1 (1994).
114. W. R. Trutna, Jr. and P. Zorabedian, "Optical Oscillator Sweeper," U.S. Patent Nos. 5, 140, 599 (Aug. 18, 1992) and 5, 263, 037 (Nov. 16, 1993).
115. L. F. Stokes, "Accurate Measurement of Reflectivity over Wavelength of a Laser Diode Antireflection Coating Using an External Cavity Laser," *IEEE J. Lightwave Technol.* **11,** 1162–1167 (1993).
116. K. Kikuchi and T. Okoshi, "High Resolution Measurement of the Spectrum of Semiconductor Lasers," *JARECT Series, Optical Devices and Fibers,* pp. 51–59, Ohm Publishing Co., Tokyo (1982).
117. H. Higuchi, H. Namizaki, E. Oomura, R. Hirano, Y. Sakibara, W. Susaski, and K. Fukijawa, "Internal Loss of InGaAsP/InP Buried Crescent (1.3 μm) Laser," *Appl. Phys. Lett.* **41,** 320–321 (1982).
118. R. Wyatt and W. R. Devlin, "10kHz Linewidth 1.5 μm InGaAsP External Cavity Laser with 55 nm Tuning Range," *Electron. Lett.* **19,** 110–112 (1983).
119. I. P. Kaminow, G. Eisenstein, and L. W. Stulz, "Measurement of the Modal Reflectivity of an Antireflection Coating on a Superluminescent Diode," *IEEE J. Quantum Electron.* **QE-19,** 493–495 (Apr. 1983).
120. M. Ohtsu, K.-Y. Liou, E. C. Burrows, C. A. Burrus, and G. Eisenstein, "A Simple Interferometric Method for Monitoring Mode-Hopping in Tunable External-Cavity Semiconductor Lasers," *IEEE J. Quantum Electron.* **7,** 68–75 (1989).
121. M. Notomi, O. Mitomi, Y. Yoshikuni, F. Kano, and Y. Tohmori, "Broad-Band Tunable Two-Section Laser Diode with External Grating Feedback," *IEEE Photon. Technol. Lett.* **2,** 85–87 (1990).
122. P. A. Andrekson, "Electrical Mode-Hopping Noise in External-Cavity Semiconductor Lasers and Mode-Hopping Elimination by a Nonoptical Control Loop," *IEEE J. Quantum Electron.* **QE-23,** 2078–2083 (1987).
123. H. Lotem, Z. Pan, and M. Dagenais, "Tunable Dual-Wavelength Continuous-Wave Diode Laser Operated at 830 nm," *Appl. Opt.* **32,** 5270–5273 (1993).
124. C.-L. Wang and C.-L. Pan, "Tunable Dual-Wavelength Operation of a Diode Array with an External Grating-Loaded Cavity," *Appl. Phys. Lett.* **64,** 3089–3091 (1994).
125. I. H. White, "A Multichannel Grating Cavity Laser for Wavelength Division Multiplexing Applications," *IEEE J. Lightwave Technol.* **9,** 893–899 (1991).
126. I. H. White and K. O. Nyairo, "Demonstration of a 1 × 2 Multichannel Grating Cavity Laser for Wavelength Division Multiplexing (WDM) Applications," *Electron. Lett.* **26,** 832–833 (1990).
127. G. M. Foster, R. Cush, T. J. Reid, and A. C. Carter, "Four Channel Multiwavelength Source with Individually Addressable Elements," *Electron. Lett.* **29,** 930–931 (1993).
128. J. B. D. Soole, K. Poguntke, A. Scherer, H. P. LeBlanc, C. Chang-Hasnain, J. R. Hayes, C. Caneau, R. Bhat, and M. A. Koza, "Multistripe Array Grating Integrated Cavity (MAGIC) Laser: A New Semiconductor Laser for WDM Applications," *Electron. Lett.* **28,** 1805–1806 (1992).
129. K. R. Poguntke, J. B. D. Soole, A. Scherer, H. P. LeBlanc, C. Caneau, R. Bhat, and M. A. Koza, "Simultaneous Multiple Wavelength Operation of a Multistripe Array Grating Integrated Cavity Laser," *Appl. Phys. Lett.* **62,** 2024–2026 (1993).

130. K. R. Poguntke and J. B. D. Soole, "Design of a Multistripe Array Grating Integrated Cavity (MAGIC) Laser," *IEEE J. Lightwave Technol.* **11,** 2191–2200 (1993).
131. G. C. Papen, G. M. Murphy, D. J. Brady, A. T. Howe, J. M. Dallesasse, R. Y. Dejule, and D. J. Holmgren, "Multiple-Wavelength Operation of a Laser-Diode Array Coupled to an External Cavity," *Opt. Lett.* **18,** 1441–1443 (1993).
132. Y. C. Chung, "Frequency-Locked 1.3- and 1.5 μm Semiconductor Lasers for Lightwave Systems Applications," *IEEE J. Lightwave Technol.* **8,** 869–876 (1990).
133. A. J. Lucero, Y. C. Chung, and R. W. Tkach, "Survey of Atomic Transitions for Absolute Frequency Locking of Lasers for Lightwave Systems," *IEEE Photon. Technol. Lett.* **5,** 484–486 (1991).
134. M. de Labachelerie and P. Cerez, "Frequency Locking of a 850 nm External-Cavity Semiconductor Laser on a Doppler-Free Cs-D_2 Line," *Proc. SPIE* **701,** 182–184 (1986).
135. Y. C. Chung and T. M. Shay, "Frequency Stabilization of a Laser Diode to a Fabry–Perot Interferometer," *Opt. Eng.* **27,** 424–427 (1988).
136. Y. C. Chung and R. W. Tkach, "Frequency Stabilization of a 1.3 μm DFB Laser to an Argon Line Using Optogalvanic Effect," *Electron. Lett.* **24,** 804–805 (1988).
137. Y. C. Chung and C. B. Roxlo, "Frequency-Locking of a 1.5 μm DFB Laser to an Atomic Krypton Line Using Optogalvanic Effect," *Electron. Lett.* **24,** 1048–1049 (1988).
138. M. de Labachelerie, C. Latrasse, K. Diomandé, P. Kemssu, and P. Cerez, "A 1.5 μm Absolutely Stabilized Extended-Cavity Semiconductor Laser," *IEEE Trans. Instr. Meas.* **40,** 185–190 (1991).
139. Y. Toda, T. Enami, and M. Ohtsu, "Frequency Stabilization of 1.5 μm Diode Laser Using Nonlinear Optical Frequency Conversion in Organic Fiber," *Jpn. J. Appl. Phys.* **32,** L1233–L1235 (1993).
140. E. T. Peng, S. F. Ahmed, and C. B. Su, "Frequency Stabilization of a Traveling-Wave Semiconductor Ring Laser Using a Fiber Resonator as a Frequency Reference," *IEEE Photon. Technol. Lett.* **6,** 334–337 (1994).
141. Y. Millerioux, D. Touahi, L. Hilico, A. Clairon, R. Felder, F. Biraben, and B. de Beauvoir, "Towards an Accurate Frequency Standard at λ=778 nm Using a Laser Diode Stabilized on a Hyperfine Component of the Doppler-Free Two-Photon Transitions in Rubidium," *Opt. Commun.* **108,** 91–96 (1994).
142. C. Latrasse and M. de Labachelerie, "Frequency Stabilization of a 1.5-μm Distributed Feedback Laser using a heterodyne spectroscopy method for a space application," *Opt. Engineering* **33** pp. 1638–1641 (1994).
143. M. Poulin, C. Latrasse, m. Têtu, and M. Breton, "Second-harmonic generation of a 1560-nm Distributed-Feedback Laser by use of a $KNbO_3$ Crystal for Frequency Locking to the ^{87}Rb D_2 Line at 780 nm," *Opt. Lett.* **19,** 1183–1185 (1994).
144. B. Tromborg, J. H. Osmundsen, and H. Olesen, "Stability Analysis for a Semiconductor Laser in an External Cavity," *IEEE J. Quantum Electron.* **QE-20,** 1023–1032 (1984).
145. J. O. Binder, G. D. Cormack, and A. Somani, "Intermodal Tuning Characteristics of an InGaAsP Laser with Optical Feedback from an External-Grating Reflector," *IEEE J. Quantum Electron.* **26,** 1191–1199 (1990).
146. R. Wyatt, T. G. Hodgkinson, and D. W. Smith, "1.52 μm PSK Heterodyne Experiment Featuring an External Cavity Diode Laser Local Oscillator," *Electron. Lett.* **19,** 550–551 (July 1983).
147. R. Wyatt, D. W. Smith, T. G. Hodgkinson, R. A. Harmon, W. J. Devlin, "140 Mbit/s Optical FSK Fibre Heterodyne Experiment at 1.54 μm," *Electron. Lett.* **20,** 912–913 (Oct. 1984).
148. T. L. Koch and U. Koren, "Semiconductor Lasers for Coherent Optical Fiber Communications," *IEEE J. Lightwave Technol.* **8,** 274–293 (1990).
149. N. A. Olsson, J. Hegarty, R. A. Logan, L. F. Johnson, K. L. Walker, and L. G. Cohen, "68.3 km Transmission with 1.37 Tbit km/s Capacity Using Wavelength Division Multiplexing of Ten Single-Frequency Lasers at 1.5 μm," *Electron. Lett.* **21,** 105–106 (1985).
150. C. Hentschel and E. Leckel, "Characterizing Fiber-Optic Components with a Tunable Laser," *Lightwave Seminar*, Hewlett-Packard Co. (1992).

151. F. Mengel and N. Gade, "Monomode Fiber Dispersion Measurement with a Tunable 1.3 μm External Cavity Laser," in *Proc. ECOC '84*, Stuttgart, paper 7A5, pp. 126–127 (1984).
152. Y. Horiuchi, Y. Namihira, and H. Wakabayashi, "Chromatic Dispersion Measurement in 1.55 μm Narrow-Band Region Using a Tunable External-Cavity Laser," *IEEE Photon. Technol. Lett.* **1,** 458–460 (1989).
153. B. L. Heffner, "Automated Measurement of Polarization Mode Dispersion Using Jones Matrix Eigenanalysis," *Photon. Technol. Lett.* **4,** 1066–1069 (1992).
154. J. C. Simon, B. Landousies, Y. Bossis, and p. Doussiere, "Gain, Polarization Sensitivity, and Saturation Power of 1.5 μm Near-Traveling-Wave Semiconductor Laser Amplifier," *Electron. Lett.* **23,** 332–334 (1987).
155. B. Maisenbacher, E. Leckel, R. Jahn, and M. Pott, "Tunable Laser Source for Optical Amplifier Testing," *Hewlett-Packard J.* **44,** 11–19 (Feb. 1993).
156. T. Day and K. D. Li Dessau, "New Kid on the Spectroscopic Block," *Photon. Spectra*, 99–103 (Mar. 1994).
157. A. Celikov, F. Riehle, V. L. Velichansky, and J. Helmcke, "Diode Laser Spectroscopy in a Ca Atomic Beam," *Opt. Commun.* **107,** 54–60 (1994).
158. E. de Clercq, G. D. Rovers, S. Bouzid, and A. Clairon, "The LPTF Optically Pumped Primary Frequency Standard," *IEEE Trans. Instr. Meas.* **42,** 457–461 (Apr. 1993).
159. A. Clairon, Ph. Laurent, A. Nadir, G. Santarelli, M. Drewsen, D. Grison, B. Lounis, and C. Salomon, "A Laser Cooled Cesium Fountain Clock: Design and Expected Performances," in *Frequency-Stabilized Lasers and Their Applications, Proc. SPIE* **1837,** 306–313 (1992).
160. G. Santarelli and A. Clairon, "Heterodyne Optical Phase-Locking of Extended-Cavity Semiconductor Lasers at 9 GHz," *Opt. Commun.* **104,** 339–344 (1994).
161. H. A. Edmonds and A. W. Smith, "Second-Harmonic Generation with the GaAs Laser," *IEEE J. Quantum Electron.* **QE-6,** 356–360 (1970).
162. W. P. Risk, W. J. Kozlovsky, S. D. Lau, G. L. Bona, H. Jaeckel, and D. J. Webb, "Generation of 425-nm Light by Waveguide Frequency Doubling of a GaAlAs Laser Diode in an Extended-Cavity Configuration," *Appl. Phys. Lett.* **63,** 3134–3136 (1993).
163. Y. Kitaoka, K. Yamamoto, and M. Kato, "Intracavity Frequency Doubling of a Nd:YV O_4 Laser Pumped by a Wavelength-Locked Laser Diode Using a Transmission-Type Optical Filter," *Opt. Lett.* **19,** 810–812 (1994).
164. M. J. T. Milton, T. D. Gardiner, G. Chourdakis, and P. T. Woods, "Injection Seeding of an Infrared Optical Parametric Oscillator with a Tunable Diode Laser," *Opt. Lett.* **19,** 281–283 (1994).

9 Tunable Free-Electron Lasers

Stephen Vincent Benson
Accelerator Division
Continuous Electron Beam Accelerator Facility
Newport News, Virginia

1. INTRODUCTION

1.1 Description of FEL Physics

The free-electron laser (FEL) uses a relativistic beam of electrons passing through an undulating magnetic field (a wiggler) to produce stimulated emission of electromagnetic radiation (Fig. 1). The quantum-mechanical description for this device is based on stimulated emission of Bremsstrahlung [1]. The initial and final states of the electron are continuum states so the emission wavelength is not fixed by a transition between bound states. Although the initial description by Madey was quantum mechanical, there was no dependence of the gain on Planck's constant. This is a necessary but not sufficient condition for the existence of a classical theory for the laser. In fact, it was found that the device was almost completely described by a classical theory [2].

The classical theory of FELs is an extension of the theory of the ubitron developed by Phillips [3,4]. The ubitron is a nonrelativistic version of the FEL. It was developed in a classified program between 1957 and 1964. It is a fast-wave variant of the traveling-wave tube (TWT) amplifier and uses a transverse motion of the electrons to couple a copropagating electromagnetic wave to the electron beam. The classical formulation is therefore similar to the formulation for a

Tunable Lasers Handbook
Copyright © 1995 by Academic Press, Inc. All rights of reproduction in any form reserved.

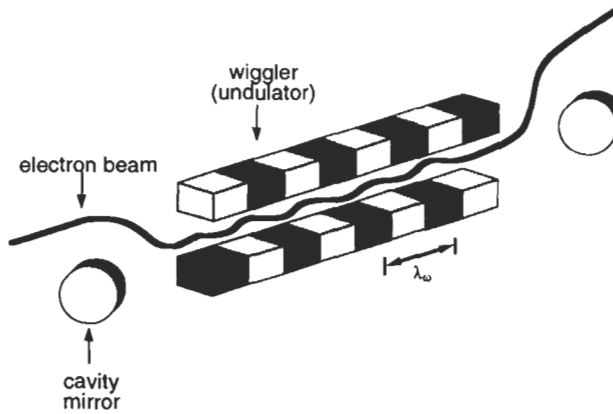

FIGURE 1 A schematic of a FEL oscillator is shown. The electron beam is bent into a wiggler using bending magnets (not shown). The electron beam wiggles along the optical axis of a cavity, which is collinear with the axis of the wiggler. The wiggler shown consists of alternating North (light gray) and South (dark gray) poles that alternately bend the beam left and right. The light is usually coupled out of one of the mirrors. In an actual device, the electron beam and usually the mirrors are in a vacuum chamber. The electron beam is shown as a continuous line, but in most devices it is a pulsed beam.

TWT amplifier. It describes the interaction as a bunching of the electrons at a wavelength near the resonant wavelength λ_0 defined by the relation

$$\lambda_0 = \frac{\lambda_w}{2h\beta^2\gamma^2}\left|1 + \left(\frac{eB\lambda_w}{2\pi mc^2}\right)^2\right|, \tag{1}$$

where h is the harmonic number for harmonic lasing, B is the rms magnetic field in the wiggler, β is the speed of the electrons divided by the speed of light, γ is the electron-beam relativistic energy divided by its rest mass mc^2, and λ_W is the wiggler wavelength. Equation (1) assumes that the electromagnetic wave is traveling at the speed of light in a vacuum. Doria *et al.* have described the resonance condition for a FEL in a waveguide for which the phase velocity is greater than c [5]. We will assume here that the electromagnetic wave is traveling in a vacuum.

Figure 2 graphically shows how the resonance works. At the resonant wavelength, one wavelength of the optical wave slips past the electron in the time that the electron travels one wiggler period. At wavelengths near λ_0 the vector product $\mathbf{E}\cdot\mathbf{v}$ is slowly varying so that there is a net exchange of energy between the optical and electron beams. At exactly the resonant wavelength when the beam current is low there is as much electron acceleration as deceleration so there is no net gain. For wavelengths longer than λ_0 the interaction provides net gain for

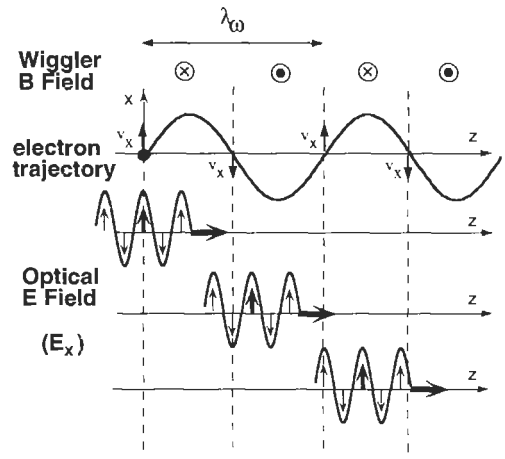

FIGURE 2 At resonance in a FEL the copropagating optical field slips past the electrons one optical period in the time it takes the electron to travel one wiggler period. The magnetic field is perpendicular to the page. The electron horizontal position oscillates as the electron travels down the wiggler. The optical field polarization is assumed to be horizontal. Note that, as the electron shown moves through the wiggler, it sees an electric field, which changes sign as it changes velocity. The electron therefore experiences a net deceleration as it goes through the wiggler. Other electrons may see acceleration or no effect depending on their initial phase with respect to the optical beam.

the optical wave and a net deceleration for the electrons, whereas for shorter wavelengths the interaction provides a net loss for the optical wave and net acceleration for the electrons. The functional form of the gain curve for a uniform wiggler is shown in Fig. 3. An interesting aspect about FELs is that gain and loss appear at different wavelengths so that, unlike conventional lasers, there is no threshold current for gain. The laser designer's task is therefore to provide gain that is sufficient to exceed resonator losses in the case of an oscillator or useful gain (usually an order of magnitude or larger) in the case of an amplifier.

The quantity in parentheses in Eq. (1), $eB\lambda_W/2\pi mc^2$, is referred to as the *wiggler parameter* (or sometimes the *deflection parameter*) and is typically represented by the symbol K. It is usually of order unity and can be calculated by the relation

$$K = 0.934B(T)\lambda_W\,(\mathrm{cm})\ . \tag{2}$$

At low electron-beam energies, the space charge in the electron beam complicates the analysis because space charge waves can be set up in the electron beam that couple to the density modulation caused by the FEL interaction. When this occurs, the FEL is said to be operating in the Raman regime. When space charge waves are a negligible part of the interaction, the device is said to be

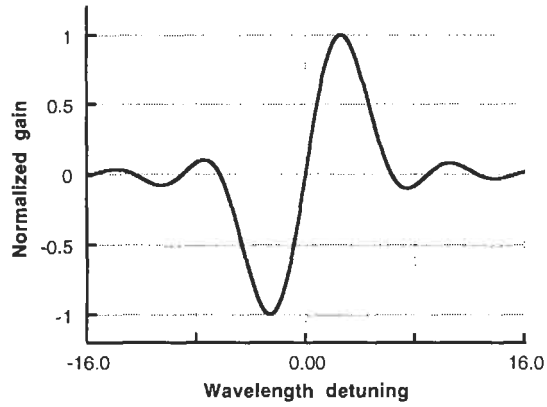

FIGURE 3 The normalized gain function versus the normalized wavelength detuning defined by $\nu = 2\pi h N_w \delta\lambda/\lambda$ is shown. The wavelength detuning is defined with respect to the resonant wavelength. At the resonant wavelength there is no gain. At longer wavelengths there is gain, and at shorter wavelengths there is loss. A uniform wiggler was assumed for this curve.

operating in the Compton regime. Because the space charge interaction varies in strength as γ^{-3}, lasers using highly relativistic electron beams are all Compton regime lasers. Note that the converse is not true; that is, a low-energy FEL is not necessarily a Raman device. In order for the gain to be enhanced by the space charge wave, the wiggler field must have a longitudinal component. This is not true in many low-energy Compton regime devices. Only Compton regime lasers are used in user facilities to date so I will confine my discussion to them.

Because the parameter γ is generally quite large compared to unity, the resonant wavelength can be much smaller than the wiggler wavelength. By varying the electron-beam energy, a single wiggler can support a very large range of wavelengths. As a result, FELs have operated in the Compton regime at wavelengths from 8 mm to 240 nm. An individual laser does not operate over such a large range, but FELs operating in three different wavelength ranges have demonstrated a tuning range greater than 8 to 1 in a single laser.

Other authors have given very complete descriptions of the theory of FELs. I will therefore not spend much space in this chapter on the details of free-electron theory. Interested readers are urged to consult Brau's excellent textbook [6] or Volume 4 of the *Laser Handbook* [7]. This chapter discusses the characteristics of FELs without going into much detail about how they arise and will study various means by which one may cover a broad wavelength range with a FEL. I then discuss some of the issues involved in achieving a large tuning range. FELs are large and expensive devices. They are therefore usually used in a user facility setting rather than an individual's lab. I will describe some of the broadly tunable lasers available at various user facilities around the world. Other free-electron

lasers exist that are not set up as user facilities but have many useful and interesting properties. These are not discussed here.

1.2 General Characteristics of FELSs

Although free-electron lasers have used many accelerator technologies, wiggler technologies, and optical resonator designs, they have several characteristics in common:

1. Because the electron beam is almost always smaller than the optical mode, the gain medium acts as a spatial filter and provides almost perfect mode quality. Efforts to disturb the optical mode by mis-steering or defocusing the electron beam reduce the power and gain with no apparent change in the optical mode structure. The laser beams out of the FEL can be focused to spot sizes limited only by the quality of the transport and focusing optics. There is no thermal distortion of the mode due to heating of the gain medium since the gain medium leaves the laser at the speed of light. The only refractive effects present in the gain medium have to do with the gain process and their only effect is to focus the beam slightly but not to change its beam quality. Because the saturated gain is independent of the small-signal gain (it is just a function of the total cavity losses), the output mode of the laser does not depend on the laser power.

2. FELs have high peak power. Electron-beam energies used to date range from a few megaelectron-volts up to 800 MeV. Peak currents are in the range of 2 to 500A. The peak electron-beam power in current experiments has therefore been between 4 MW and 36 GW. Power extraction is usually on the order of 1%, so the peak laser power is typically in the 0.1- to 10-MW range, though power in the gigawatt range has been demonstrated in lasers with better extraction efficiency. Although it has not been demonstrated to date, FELs are also capable of high average power. FELs to date have operated with up to 11 W of average power but the average laser power is limited only by the average power of the electron beam and the attainable efficiency (1% is typical but 45% has been demonstrated). Electron-beam powers as high as a megawatt have been demonstrated to date in electron accelerators, so kilowatt lasers are quite feasible.

3. FELs can have very short pulses. The bandwidth of a FEL can easily be as high as 10%. This leads to the possibility of very short optical pulses. Experiments have demonstrated subpicosecond pulses from FELs [8]. Note that no attempt to produce very short pulses was made in this case. Unlike many mode-locked lasers, the FEL has very little gain or power unless it has a very short pulse. When one optimizes the electron beam for maximum laser power, one automatically produces very short pulses. It has been suggested that chirping the energy of the electron pulses can produce chirped laser pulses that can be compressed in a prism pair [9]. Recently, researchers at Duke University have used this technique to produce optical pulses shorter than 250 fs in the 4-μm range.

4. FELs typically have low duty cycles. Because electron beams have such high peak powers, no continuous FEL has been demonstrated at this time. It should eventually be possible to construct a continuous FEL operating in the far-infrared region where an energy recovery electrostatic accelerator can be used, but a near-infrared or ultraviolet continuous wave (CW) laser would be exceedingly difficult to build. As noted, the electron-beam power required for lasing is many megawatts. Assuming even several percent efficiency, the exhaust beam from this laser would be a formidable problem. FELs therefore usually have a pulsed time structure, often with a micropulse/macropulse character as shown in Fig. 4. Compton regime lasers usually have very short pulses, ranging from 500 fs to 10 ps. The separation between these pulses ranges from a few hundred picoseconds to a few hundred nanoseconds. Researchers at CEBAF in Newport News, Virginia, are building a continuously pulsed FEL that will have 1-ps pulses separated by 40 ns. Just by eliminating the macropulse structure, the laser power in this design has been raised to the multikilowatt level despite a duty cycle of less than 10^{-4}. (The exhaust beam from this laser will be decelerated back down to low energy to reduce the problems of a megawatt beam dump and to increase the laser efficiency.) If one wants to increase the average power one usually does so by increasing the duty cycle, but even at the 100-kW power level the duty cycle will be less than 1%.

5. FELs are easy to tune. In fact, one design challenge in any FEL is to keep the wavelength under control so that it does not drift or jitter. When desired, tuning over a very large wavelength range is usually extremely easy. The optical cavity must be very broad band to take advantage of this tunability.

6. FELs exhibit harmonic lasing. This feature is described in more detail later. Lasing at a high harmonic can extend the operating range of a laser over a much larger wavelength range than is possible with only energy and field tuning.

7. FELs are large and expensive. This point has already been mentioned, but it alters the design of many lasers in ways that are not obvious. Efforts are under way around the world to make FELs more compact and inexpensive. The cost and size achieved to date however make it impractical for an individual investigator to purchase one. The best alternative is to use one at a user facility. The cost of using the laser at a user facility is not any more than using any smaller laser because many users do research at the FEL centers at the same time. The inconvenience of using a laser outside of one's own laboratory can be discouraging however. Most researchers who have the opportunity to use a conventional laser in their own laboratories to accomplish their research will do so if the wavelength and power are available. Due to this fact, most FEL centers do not plan for use of the laser where conventional sources are available (in the visible, near ultraviolet, and near infrared). Research requiring mid-infrared or deep-UV laser light at low average power can often use optical parametric generation or harmonic generation to produce light for their experiments. Researchers requiring light outside this wavelength range or requiring more average power (hun-

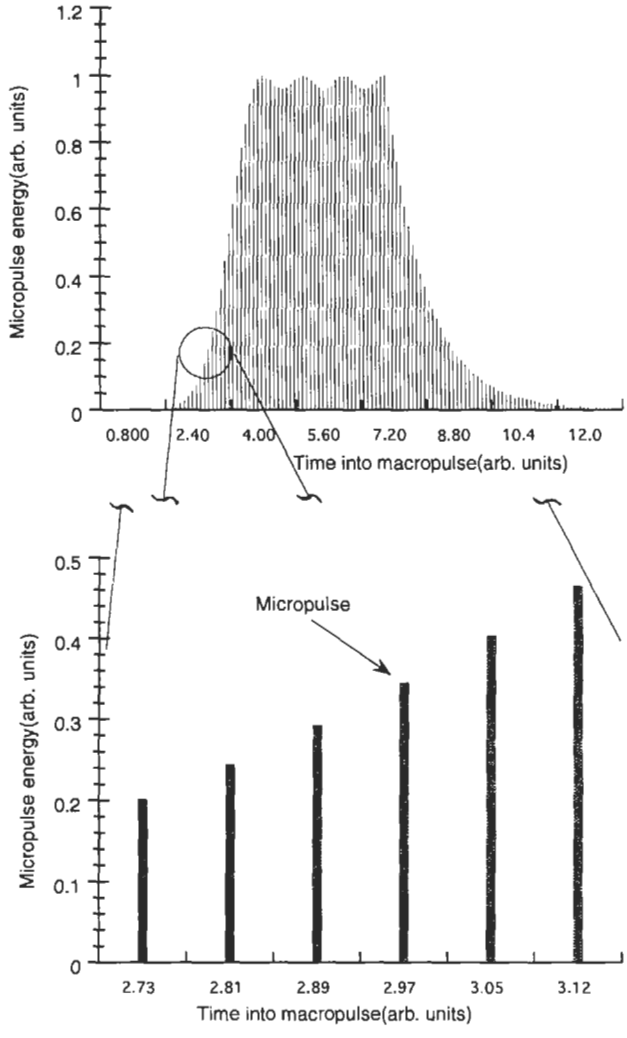

FIGURE 4 A typical time structure is shown for a laser pulse from a FEL based on a pulsed rf linear accelerator. The laser macropulse consists of hundreds of short micropulses. In most FELs operating to date, the micropulses are 1 to 10 ps in length and the macropulse is from 1 to 100 μs in length. The macropulses repeat at a repetition rate limited by the accelerator; usually in the range of several hertz up to 120 Hz. The micropulse repetition rate can be anywhere from several megahertz up to several gigahertz. The ripple on the pulse is due to modulations in the arrival time and energy of the electrons caused by effects in the microwave power source in the accelerator.

dreds of milliwatts or more) or a picosecond time structure may find that the FEL provides just the laser light source they need.

2. METHODS OF WAVELENGTH TUNING

Obviously one can vary the resonant wavelength defined in Eq. (1) by varying any of the four parameters on the right-hand side: the electron energy, the wiggler magnetic field, the harmonic number, or the wiggler wavelength. The last two of these are not continuously variable, so they are more useful for changing wavelength ranges rather than continuous wavelength tuning. There are good reasons for using these parameters to extend the wavelength tuning range, as will be shown later. I will discuss the advantages and disadvantages of each method of wavelength tuning. One should remember that the methods are not mutually exclusive but can all be used in one facility.

There are a few other means to tune the wavelength of the laser that I will not discuss in detail. One is changing the average angle of the beam. This method is usually not feasible because the gain degrades too strongly with the electron-beam angular spread. The second is gas-loaded operation [10]. This has been demonstrated on both the Mark III and SCAFEL lasers at Stanford University but is still very technically challenging to implement and has not yet achieved broadband tuning. Harmonic generation outside the laser has been demonstrated using conventional second harmonic generation techniques [11]. In principle, it is possible to drive an optical parametric oscillator or amplifier as well. These methods are quite useful when the wavelength range is limited by the design of the laser, but more power can usually be obtained by operating the laser at the desired wavelength.

2.1 Energy Tuning

The first demonstrated method of wavelength tuning was to change the electron-beam energy. This was done on the first FEL at Stanford [12] but the tuning range was limited to ±10% by the rather narrow reflectivity band of the resonator mirrors.

The group at Los Alamos National Laboratory (LANL) used copper mirrors with hole output coupling to change the laser wavelength from 9 to 35 μm by varying the electron-beam energy by a factor of approximately 2 [13]. The evidence for lasing at the longer wavelengths was indirect however (the output window was opaque to the laser radiation) so it was not known with certainty whether fundamental lasing was achieved over this range. In later work [14] the LANL team demonstrated lasing over a range of 9 to 45 μm with direct observation of the laser light.

The far-infrared laser at the University of California at Santa Barbara (UCSB) demonstrated operation at wavelengths covering the range of 200 to 800 μm [15]. Tuning via energy change was continuous only over a very small energy range due to the necessity of maintaining good energy recovery in the

electron beamline. This range has been extended to a 10% wavelength range (5% in energy) more recently by use of a computer control system [16].

The TRW/Stanford FEL collaboration was successful in achieving lasing between 4.0 and 0.5 μm by varying the electron-beam energy [17]. This laser uses the same superconducting accelerator used for the first Compton regime FEL.

Tuning the wavelength via energy change has several advantages and disadvantages. One major advantage is in the undulator design. A fixed undulator is simpler and less expensive to design and build than a tunable undulator. For an undulator with more than around 80 periods it becomes extremely difficult to built a wiggler whose field can be adjusted continuously. The wiggler parameter K can also be smaller. Most designs for compact wigglers result in values of K much less than unity [18–20]. These designs must therefore rely on energy tuning to achieve a broad tuning range.

Another advantage of energy tuning is that it can be exceedingly rapid. The laser should be able to tune at a rate of one gain bandwidth per turn-on time. This can lead to tuning across a range of 10% in tens of microseconds. The TRW/Stanford collaboration has demonstrated tuning of 2%/ms during a macropulse several milliseconds long. Researchers at LANL [21] and at the FELIX facility [22] have also demonstrated fast wavelength tuning via energy change. This feature might be quite useful in lidar applications.

The primary disadvantage to energy tuning is the need to readjust the entire electron-beam transport line leading to the laser. In some lasers this can be a very slow task. A good computer control system can, in principle, allow reasonably rapid scanning of the electron-beam energy over a factor of 2 range as is done in storage rings, but this has not been demonstrated in a FEL device to date.

The second disadvantage is that, if the beam current is fixed, the electron-beam power decreases as the electron energy decreases. Thus, the power out of the laser varies as the inverse square root of the wavelength. Because the gain often increases as the energy decreases, it is possible to change the undulator and increase the efficiency as the laser wavelength is increased. Just removing periods would present severe mechanical design challenges. It has been shown that introducing a taper to the wiggler field enhances the efficiency [23]. One can change the taper, and therefore the efficiency, as the wavelength is increased. In some accelerators, it is possible to reduce the energy by increasing the beam current while holding the beam power constant. This could also be used to tune the wavelength at constant laser power. A special case of energy tuning is that of a storage ring FEL, whose power is proportional to the third power of the electron-beam energy. The gain is not a steep function of electron-beam energy and tapering is not usually an option due to the energy aperture of the storage ring so energy tuning is not a good choice for storage-ring-based FELs.

Finally, in an energy recovery linac such as in the FEL planned for CEBAF, the efficiency for the overall system will decrease at lower electron-beam

energies. A taper in the undulator cannot be used to recover the power in this case since the deceleration leg has a limited energy aperture that would be exceeded for tapered operation.

2.2 Wiggler Tuning

The wiggler parameter can be varied by changing the magnetic field. If the wiggler parameter is approximately equal to or greater than unity, this can lead to large changes in the wavelength. In permanent magnet undulators one can vary the gap of the wiggler in order to vary the magnetic field strength. Electromagnetic wigglers can be varied by changing the energizing current. The group at Orsay pioneered gap tuning on the ACO storage-ring-based laser [24]. Continuous tuning was demonstrated over the bandwidth of the mirrors. The VEPP-3 project at Novosibirsk demonstrated continuous tunability over the range of several sets of mirrors by varying the current of their electromagnetic wiggler [25]. Both the Mark III FEL and the Rockwell FEL at Stanford used gap tuning to tune over a large wavelength range [23,26]. The Mark III could tune continuously over a 70% change in wavelength in a matter of seconds. This technique is also used at Vanderbilt [27], the CLIO project at Orsay [28] and the FELIX project at the FOM institute at Rinhuizen, The Netherlands [29]. The latter two systems have demonstrated two to one tuning range at a single electron-beam energy.

The advantages and disadvantages of this approach are opposite to those of the energy tuning approach. The power output is fairly independent of wavelength over a large range. Tuning the laser is quite simple. It is quite easy to design for single-knob tuning by a factor of 2 to 4. This can be quite convenient in a user facility, since no understanding of the computer control system is necessary for the user. The tuning control can even be isolated so that it does not interfere with the accelerator control system. The tuning cannot be carried out as quickly as energy tuning in a mechanically tuned wiggler but might be quite fast in a properly designed electromagnetic wiggler (especially a pulsed electromagnetic undulator).

The largest disadvantage is in the constraints placed on the wiggler construction. Wiggler tuning is only useful when one has a high K wiggler. Great care must be taken in the construction of the wiggler so that the input and output steering is independent of the magnetic field strength. The field quality of the wiggler must remain high as the wiggler is tuned. All these constraints are most easily satisfied for an electromagnet. There is more interest these days in using electromagnets in future user facilities. The proposed high-average-power facility at CEBAF uses an electromagnet to tune over a range of 4 to 1 [30]. A new facility at Princeton University will use a superconducting wiggler in a compact infrared FEL (CIRFEL) [31] built by Northrop–Grumman.

2.3 Harmonic Operation

Operation of a FEL at an odd harmonic of the fundamental wavelength was first proposed by Madey and Taber [32]. The full theory of harmonic lasing was given by Colson in 1981 [33]. The gain at the harmonic can actually be higher than that of the fundamental. If one is using this approach to lase at a short wavelength without raising the energy of the accelerator, the wiggler parameter K must be greater than unity for the harmonic gain to be higher than the gain at the fundamental. The gain at the harmonic is much more sensitive to degradation by the energy spread and emittance of the electron beam, as well as the wiggler field quality, so in practice the harmonic gain is rarely higher than the gain at the fundamental for most existing systems.

Experimental verification of third harmonic lasing was demonstrated in 1987 at Stanford [34], in 1988 at LANL [35], and in 1992 at Orsay [28]. Lasing at harmonics higher than the third has not yet been demonstrated. Warren has proposed that operation at very high harmonics may be a good way to operate a compact FEL [36]. The analysis below is a summary of his approach. An approximate gain formula for a FEL with a linearly polarized wiggler takes the form

$$g = 0.004 I\gamma Q N_\beta^2 \eta_\varepsilon \eta_\gamma \eta_f \eta_\mu \ , \tag{3}$$

where I is the peak current, $N_\beta = N_W K/\gamma$ is the number of betatron periods in the wiggler, Q is a factor that depends on the wiggler parameter and the harmonic number h:

$$Q = \frac{h^2}{1+K^2}\left[J_{(h-1)/2}(h\xi) - J_{(h-1)/2}(h\xi)\right]^2 \ , \tag{4}$$

where the variable ξ is given by

$$\xi = \frac{K^2}{2\left(1+K^2\right)} \ , \tag{5}$$

η_γ is the gain degradation due to the energy spread,

$$\eta_\gamma = \left[1 + \left(4\sqrt{2}hN\sigma_\gamma/\gamma\right)^2\right]^{-1} \ , \tag{6}$$

η_ε is the gain degradation due to the rms emittance ε (the emittance is a measure of the transverse phase space area occupied by the electron beam distribution)

$$\eta_\varepsilon = \left[1 + \eta_\gamma \left(4\pi^2 \varepsilon N_\beta / \lambda\right)^2\right]^{-1/2} , \tag{7}$$

η_f is the filling factor for the optical mode

$$\eta_f = \left(1 + 4\pi\, \varepsilon/\lambda\right)^{-1} , \tag{8}$$

and η_μ is the gain degradation due to slippage effects

$$\eta_\mu = \left[1 + \left(hN\lambda / 3\sigma_z\right)\right]^{-1} , \tag{9}$$

where σ_z is the rms electron pulse length. The gain degradation due to the energy spread and the emittance are similar to inhomogeneous broadening effects in conventional lasers and arise because some of the electrons have a resonant wavelength that differs from the resonant wavelength of an average electron by a large fraction of the gain bandwidth. The gain reduction due to the filling factor is simply the result of an overlap integral between the optical mode and the electron beam. Equation (8) assumes that the optical mode and the electron beam are focused optimally in the gain region. Because the gain medium can affect the actual optical mode waist, this equation is an approximation. Three-dimensional simulation codes can be used to get a better estimate of this term. The gain reduction due to slippage occurs when the Fourier transform of the electron bunch shape in time has a spectral bandwidth comparable to or larger than the gain bandwidth. This reduces the coupling of the electron beam to the optical pulse.

Given the electron-beam parameters such as emittance ε, energy spread σ_γ, the peak current I, and energy γ, it is possible to design an undulator that produces a gain reduction parameter η_ε or η_γ of 0.5. Warren showed that for large values of ε/λ the harmonic at which both gain degradation factors were equal to 0.5 can be quite high. Unfortunately, the gain is usually too small to be useful when this is the case. For small values of ε/λ it is still possible to design the wiggler that sets η_γ equal to 0.5, and one finds that the values of η_ε and η_f are always greater than 0.5. If one wants to work at a high harmonic, the number of wiggler periods is usually quite small. Because the gain reduction due to slippage is the same for all harmonics, the value of η_μ is usually close to unity.

The value of Q for a given harmonic number and optimum K varies very little. This is shown in Table 1, which lists the optimum value for Q and the K for which the maximum value occurs. Also listed are the values of K for which the value of Q falls by 10% and 50% from its peak value. As can be seen from Table 1, the optimum value for Q varies little from $h = 3$ to $h = 15$. This implies that,

if the inhomogeneous gain reduction factor, slippage factor, and filling factor do not degrade very fast with harmonic number, the gain will be fairly independent of harmonic. In addition, the values for $K_{90\%}$ are in the accessible range of 1 to 2. Warren *et al.* have pointed out that wiggler parameters around unity can be achieved for periods as short as 3 mm by using a pulsed electromagnetic wiggler [37]. Efforts to operate a FEL using such a wiggler have thus far failed [38].

As an example of a system that can achieve broadband tunability by harmonic lasing, I have calculated the gain versus wavelength for a laser operated in the infrared using an electron beam with parameters similar to those present in the LANL APEX photoelectron injector operated at 20 MeV [39] or the Princeton CIRFEL device [31]. Such a device would be quite compact and would be capable of lasing between 3 and 80 μm with gains in excess of 30%. At each harmonic the wavelength would be varied by tuning the electron-beam energy.

2.4 Wiggler Wavelength Tuning

No one has come up with a method by which the wiggler wavelength can be continuously tuned. The wavelength of any wiggler is essentially fixed. Nevertheless, one can choose wavelength bands by selection of the wiggler wavelength. A large part of the cost of a FEL is the electron source. Once this is available, one can produce several undulators and optical cavities, each of which covers a wavelength band for which it is optimized.

This concept is so appealing that several user facilities are adopting it. The FEL facility at UCSB is in the process of installing a set of three FELs on its accelerator which will cover these ranges: from 2 mm to 300 μm, from 300 to 63 μm, and, using third harmonic lasing, from 63 to 30 μm. The design tuning range is therefore extended from the 8 to 1 range available in an individual laser to 67 to

TABLE 1 Maximum Values for Q at Several Harmonic Numbers and the Wiggler Parameters for Which the Maximum, 90% of Maximum, and Half of Maximum Occur

h	Q_{max}	K_{max}	$K_{90\%}$	$K_{50\%}$
3	0.36064	1.064	0.832	0.566
5	0.30946	1.428	1.158	0.852
7	0.28843	1.684	1.383	1.048
9	0.27665	1.886	1.560	1.200
11	0.26901	2.057	1.709	1.327
15	0.259521	2.337	1.953	1.533

1 for the entire system. See Sec. 5.6 for a more complete description of this facility. The FELIX FEL (Sec. 5.3) user facility in the Netherlands also uses two undulators to cover the wavelength range of 6 to 110 μm, thus covering a wavelength range of 18 to 1. Finally the Stanford Picosecond FEL center (see Sec. 5.5) has three wigglers available covering a 21 to 1 wavelength range from 3 to 64 μm.

3. BROADLY TUNABLE OPTICAL CAVITIES

A broadly tunable FEL offers some unique design challenges for the optical cavity designer. Difficulties arise from three features of the laser—the need for broad tunability, the extremely high saturation intensity of the device, and the fact that the gain medium is almost always smaller than the optical mode.

3.1 Mirror Technologies

It is obvious that broadly tunable lasers in the infrared to millimeter range should be able to use metal mirrors to achieve high damage thresholds, broad tunability, and reasonable optical figure. Metal mirrors can withstand pulsed fluences in the infrared as large as 50 J/cm^2 for a microsecond. The damage threshold scales as the square root of the pulse length (e.g., the damage threshold is 5 J/cm^2 for a 10-ns pulse). For some lasers with long macropulses and a low micropulse repetition rate, the damage threshold must be calculated for both the macropulse fluence and the micropulse fluence. The smaller of the two should then be used. For very long macropulses the power density is limited by thermal distortion. Commercially available mirrors can easily tolerate 1 kW/cm^2. The metal can be deposited on a low expansion coefficient material such as SiC for cw operation in order to improve the figure. Pulsed operation generally requires a good match between the metal coating and the substrate to keep the coating from flaking off the substrate. Silver on copper has proven to be a good combination.

At shorter wavelengths, dielectric mirrors must be used. This limits the damage threshold and tunability. Removal of heat deposited in the mirrors also poses design challenges. There is usually a trade-off of damage threshold and bandwidth in dielectric mirrors, so the range of tunability of the mirrors is usually only around ±10%. At least a dozen sets of mirrors might be needed to cover the range of 1.5 to 0.2 μm. Fortunately, the fact that a mirror can be used at odd harmonics of the design wavelength can reduce the number somewhat. It is also possible, in lasers with low power loading in the mirrors, to use broadband coatings similar to those used in some dye lasers or Ti:sapphire lasers. These coatings can extend the wavelength tuning range to ±25%. Dielectric mirrors may also be used as output couplers in low-gain infrared lasers operating between 1 and 15 μm. At longer wavelengths, it is difficult to find a transparent substrate. Changing mirrors can be accomplished easily if the mirrors are not in the vacuum chamber. If they are

inside the vacuum chamber, the mirror change can take anywhere from a couple of hours to a couple of days depending on the quality of vacuum desired. Many user facilities are considering the use of *in vacuo* turntables so that the vacuum does not have to be broken to change a mirror.

3.2 Unstable Resonators

If one has an optical cavity with all metal optics the obvious question arises of how to couple the laser power out of the cavity. One common method to accomplish this is to use an unstable resonator [40]. Because the gain medium is unidirectional, an obvious design is the negative branch ring unstable resonator [41]. No FEL has been operated in an unstable mode in order to outcouple the laser light. A couple of lasers have been operated in an unstable configuration either by accident or with dielectric mirror output coupling [42,43]. Due to the small gain volume of FELs and their relatively small saturation gain, the only possible unstable resonator designs are negative branch nearly confocal cavities. This allows the mode to be quite small in the gain region while keeping the mode large on the output coupler. One can have a cylindrically symmetric cavity or have one axis of the cavity stable and one unstable as proposed by Siegman [44]. The stable/unstable cavity has the advantage of a slower change in the optical mode size as the wavelength is changed. Shih has studied how to configure the stable/unstable cavity in order to optimize the output mode quality [45].

3.3 Brewster Plate Output Coupling

Because the light from a FEL is usually strongly linearly polarized one can install a Brewster plate in the cavity without adding to the cavity losses (with the exception of scatter and absorption, which can be kept quite small). If one then rotates the plate by a few degrees, one can increase the losses by a calculated amount. The light can then be deflected out of the laser mode and through an output window. There will be four reflections from the plate, two in each direction. Because the Brewster angle is insensitive to wavelength, the cavity is quite broadband. The optical mode quality is quite good for each of the four reflections. One also has the interesting possibility of continuously variable output coupling. There are, however, many disadvantages of this method.

1. If one uses a parallel plate, one gets two almost overlapping spots in the output beam separated in time. This is bad for any applications that require individual pulses or diffraction-limited spots. If one wedges the plate, one can eliminate the extra spot with the penalty of decreased output coupling efficiency. One can use a separate mirror to recover at least one of the two backwards reflections, but this also reduces the mode quality.

2. The choice of materials is quite limited. The Brewster plate material must be a very high quality material with exceedingly high transparency over as large a wavelength range as possible, very high damage threshold, high radiation damage threshold, and good optical figure. In the visible and near infrared, fused quartz or silica are good choices. Sapphire can also be used but must be carefully oriented to preserve the polarization of the beam. In the infrared, zinc selenide and barium fluoride are the best choices. Barium fluoride has a higher damage threshold but smaller transparency range and lower radiation damage threshold. Zinc selenide is a semiconductor and is subject to a relatively low damage threshold and multiphoton absorption leading to nonlinear losses, though it is remarkably free of radiation damage due to its large band gap. Between approximately 15 and 100 μm there are no good materials available for use, though CVD diamond films show promise as pellicle Brewster plates. Salts are transparent in most of this range but are exceedingly sensitive to radiation.

3. The plate adds dispersion to the cavity and forces one to change the cavity length as the wavelength changes. This is not always a disadvantage. Brewster plate dispersion was used to separate the fundamental and harmonic lasing in the first third harmonic lasing experiments [34]. The cavity length change is well defined and can be programmed into a computer control system to change the cavity length as the wavelength is changed.

3.4 Hole Output Coupling

Several FELS have used a hole in the mirror to couple the power out of the laser. This was tried in conventional lasers but was found to be inefficient due to the tendency of the optical mode to avoid the hole [46,47]. In a FEL the gain medium interacts much more strongly with the lowest order Gaussian mode than with the higher order modes so that the mode with the highest net gain is not the same as the mode that has the lowest loss [48]. This leads to reasonably efficient output coupling via a hole in one end mirror. The scatter and diffraction off the hole edge limits the output coupling efficiency (defined here as the power transmitted through the hole over the total cavity losses) to no more than 50% for small output coupling. One potential problem is the change in the output coupling as the wavelength, and therefore the mode size, changes. Xie and Kim [48] have demonstrated using Fox and Li simulations that broad tunability can be achieved in a hole coupled resonator while keeping the output coupling efficiency higher than 40%. Hole output coupling has the additional advantage of allowing one to image the hole onto one's experiment and obtain a spot size that is independent of the wavelength. Typically, the damage threshold of the mirror is greatly reduced by the presence of a sharp edge near the center of the mirror. At this point hole output coupling has proved to be the best compromise among the available cavity designs for lasers in the mid-infrared to the far-infrared regions. It is not without disadvantages but it has the least problems of all available designs.

3.5 Focusing Effects

The optical cavity has a stronger effect on the gain of a FEL than in most conventional lasers and the gain can also affect the optical mode. The gain is maximized for an optimal overlap between the electron beam and the optical mode. As noted in Sec. 1.2 the electron beam acts as a spatial filter and typically produces a diffraction-limited beam in the absence of cavity figure errors. Note that the gain medium does focus the optical mode and therefore can change the waist size and location of the optical mode in the cavity from the cold cavity case (though the mode remains diffraction limited). This can be a problem in a system with an inflexible optical transport line. Some matching capability may be necessary to take advantage of the change in mode characteristics with the saturated laser gain (which is a function of the output coupling).

4. WIGGLER CONSIDERATIONS

Since wigglers are used on both FELS and storage ring synchrotron radiation sources, they have an extensive development history. The state of the art at this writing can produce wigglers with periods of a few millimeters up to tens of centimeters with fields of up to a tesla and precision approaching the measurement accuracy. Each type of wiggler is optimal for a given wavelength range. I will describe them in decreasing order of wavelength. A common denominator of widely tunable wigglers is the need for a gap that is sufficiently large for the longest optical wave to propagate with low losses. This implies that the wiggler will need a large field at a large gap. The vacuum chamber is usually inside the gap and reduces the available aperture for the optical mode. Typical period to gap ratios are as small as 2 to 1. Because the maximum field varies inversely as the exponent of this ratio, it makes little sense to make the ratio much smaller.

4.1 Room-Temperature Electromagnets

Devices with a large bore and a long wavelength benefit from the use of an electromagnetic wiggler. This design has the disadvantage of requiring a large power supply and cooling for the wiggler and cannot have a wiggler period shorter than around 5 cm due to the nature of the power density scaling [49], but it has several very advantageous features for a broadly tunable laser. The wiggler is rather inexpensive to build. It is usually less than one-half the cost per meter of any other design even when the cost of the power supply is included. The tuning is rapid and easy to interface to a computer control system. Because the field integral is usually independent of the excitation, the trajectory is usually nearly ideal at all field strengths. The laser behavior is therefore nearly optimized at all wavelengths if it is optimized for one wavelength. Shaw [50] has demonstrated

rapid single-knob tuning in the far infrared using an electromagnet, and the VEPP-3 laser at Novosibirsk has turned over the transparency range of several sets of mirrors with their electromagnetic optical klystron [25].

4.2 Permanent Magnets

One can also use arrays of permanent magnets, either by themselves or using flux concentrating iron poles, to make a high field wiggler. In applications where the ionizing radiation levels can be kept reasonably low, the material of choice is neodymium iron boron due to its high remanent field. When the radiation levels might be too high ($>10^7$ rad/year absorbed dose in the wiggler), the best material is samarium cobalt. A permanent magnet wiggler has the advantage of needing no power supply, except when the field is being changed. It also can be scaled down to wiggler wavelengths as short as 1 cm or less. The maximum field is dependent only on the type of material used and the gap to period ratio. Permanent magnet wigglers are relatively expensive to build. They become even more expensive if the field strength must be varied because they must be trimmed to keep a good field at many different gaps. The forces pulling the jaws together can be several tons so the mechanism used to support the jaws must be carefully designed. Fixed gap wigglers can be much simpler to build and tune. The group at UCSB has developed a robot adjuster that adjusts the pole positions in response to measurements of the field strength for each pole [16]. This had resulted in some extremely high-quality wigglers. Most user facilities use gap tunable permanent magnet wigglers at this point.

4.3 Superferric Magnets

Researchers at Brookhaven National Laboratory (BNL) have been developing a type of electromagnet wiggler that can be scaled down to wavelengths much shorter than 5 cm. By using superconducting wire they are able to have much higher current density and reduce the wiggler period to as little as 8 mm while maintaining fields close to 1 T (rms $K>0.5$). This design has not yet been used for an FEL but it is planned for use in a FEL at BNL and eventually at Princeton University. It has all the advantages of the normal conducting electromagnets plus the ability to get to a shorter wavelength. It has the disadvantages, however, of the cost and inconvenience of cryogenics. If one is using a superconducting accelerator this is not as much of a problem since the cryogenic support services are on site.

5. TUNABLE LASER FACILITIES AND THEIR CHARACTERISTICS

Many user facilities in the United States and Europe are now providing beam time to users. Most of them have made a large effort to provide as large a

range of wavelength coverage as possible. This section describes the major facilities available now and one facility that is scheduled to come on line shortly. More detailed information can be obtained from the individual institutions. Interested readers can contact the institution which seems to have the best match of capabilities and submit a proposal to use their facility. Each facility has strengths and weaknesses and is best matched to a given range of experiments. For each laboratory, I will describe the available wavelength range, the power available over the wavelength range, the temporal and spectral structure, and any unique features of the facility. Most of the facilities are driven by rf linacs and therefore have a micropulse/macropulse structure, so the power quoted in the literature may be peak power during the micropulse, average power during the macropulse, or, rarely, the long-term average power. One can also quote micropulse energy or macropulse energy. For most research applications average power is unimportant. The energy per macropulse and micropulse and the pulse lengths are usually the most important quantities. For all the facilities, the mode quality is nearly diffraction limited, so that feature will not be discussed here. Another common feature is that the lasers are generally locked to the a-c line frequency for stability purposes. Some of the properties of the facilities are listed in Table 2. Note that only ranges of power and pulse lengths can be given since they often vary by as much as a factor of 10 as the wavelength is changed. The power, microbunch length, and spectral bandwidth in rf linear accelerator-based devices can be strongly dependent on the cavity length, sometimes varying by as much as a factor of 10. It is therefore useful for the user to have control of the cavity length to optimize the power, bunch length, or spectral width. Note that

TABLE 2 Properties of User Facilities around the World[a]

Location of facility	Wavelength range (μm)	Micropulse frequency (MHz)	Macropulse frequency (Hz)	Micropulse power (MW)	Macropulse power (kW)
CLIO, Orsay, France	2–17.5	31–250	1–50	1–10	1–6
Mark III, Duke University	2–9	2857	1–30	0.5–3	2–30
FELIX, FOM, Netherlands	6–100	1000	5	0.1–3	1–10
CIRFEL, Princeton University[b]	5–15	142.8	10	1–5	1–7
SCAFEL, Stanford University	3–64	11.82	1–120	0.1–1	0.001–0.01
CFELS, UCSB	62–2500	[c]	0.25–4	[c]	1–27
Vanderbilt University	2–7.7	2857	1–30	1–10	2–30

[a]For more details, see the text descriptions. Third harmonic lasing is not included in the wavelength range when available.
[b]System being commissioned.
[c]This accelerator has no micropulse structure.

the pulses are usually transform limited so that the product of the spectral bandwidth and the pulse width is approximately constant.

There are several new user facilities either proposed or under construction in the world. I have included one of them to show that the trend is toward smaller devices with larger energy per micropulse and a lower energy electron beam.

5.1 CLIO, LURE

The *Collaboration pour un laser infra-rouge* or CLIO project has constructed a user facility using a FEL at the Laboratoire pour l'Utilisation de Radiation Electromagnetique (LURE) at la Université de Paris Sud in Orsay, France. It has been in operation since mid-1992 [28]. This laser has operated in the range of 2 to 17.5 μm using Brewster plate output coupling with a ZnSe Brewster plate and using hole coupling. The power is rather insensitive to wavelength over the range of 3 to 12 μm with peak powers in the range of 1 to 10 MW as measured at the experimental table. The power drops at the long-wavelength end of the range due to diffraction. In fact, the laser is lasing quite nicely at 17.5 μm but the output beam is poorly matched to the transport line [51]. The power drops rapidly at short wavelengths due to reduced gain. The wavelength can be tuned over a range of a factor of 2 at any given electron-beam energy using gap tuning of the permanent magnet wiggler. Different wavelength ranges can be reached by running the accelerator in one of four energy settings. The wavelength can be changed by wiggler tuning in seconds. The electron-beam energy can be changed in approximately 20 min. Although they have succeeded in operating the laser at 3.3 μm using third harmonic lasing, the power was lower than when the laser was operated at the fundamental at the same wavelength.

The wavelength spread is typically about 0.4% full width at half-maximum (FWHM) over most of the wavelength range, though it can vary from 0.2 to 3% depending on the wavelength and the cavity length. The center wavelength is stable to approximately 0.2% over a period of hours. The user has control over the cavity length in order to optimize the laser for his or her needs. The user can also scan the wavelength with a resolution of 0.2% (one usually quotes resolution in cm^{-1} but the resolution of this device is really a function of the wavelength so it is 1.1 cm^{-1} at 17.5 μm and 8 cm^{-1} at 2.5 μm).

A unique feature of this laser is the possibility of a variable micropulse time structure. The macropulses are up to 10 μs long at a repetition rate up to 50 Hz. The micropulse repetition rate can be varied from 31.25 MHz (32-ns separation) up to 250 MHz in steps of a factor of 2. In operation to date they have operated at up to 125 MHz. The micropulses are quite powerful with energies up to 40 μJ. With a micropulse time separation of up to 32 ns it is possible to carry out experiments that require only a single pulse hitting the sample or those requiring a sample to relax before the next pulse. The micropulses are typically 1 to 6 ps in

length. Recently they have succeeded in operating in a mode with very short pulses of only 500 fs [52].

There are four user rooms serviced by the purged optical beamlines. The users are supplied with basic optical equipment such as optical benches, detectors, and monochromators, and, because LURE is a synchrotron light user facility, there are many user services such as machine shops and electronics shops.

As with most facilities there is always interest in extending the wavelength range and improving the performance in other ways. There is only one laser on the accelerator and they have no room to add another. They therefore must modify the laser they have to improve the performance. One simple upgrade is to increase the repetition rate of the electron beam in order to increase the average power. They expect to be able to operate with up to 10 W of output power in the mid-infrared region. The second upgrade, already complete, is to replace the wiggler chamber bore to reduce diffraction and allow operation at longer wavelengths.

5.2 Duke University

Duke University runs a small user facility using an infrared FEL similar to the one used at Vanderbilt University (see Sec. 5.7). The so-called Mark III IRFEL [26] operates in the range of 2 to 9 μm on the fundamental and has operated at the third harmonic at wavelengths between 1.4 and 1.7 μm. As in the CLIO device, the long-wavelength end is determined by the diffraction in the wiggler bore, and power drops rapidly at wavelengths longer than 8 μm. The maximum power is available between 3 and 5 μm. The peak power is approximately 1 to 3 MW delivered to the optical bench. The average power during the macropulse varies from 2 to 30 kW depending on the wavelength and the output coupler used. The wavelength can be tuned over a factor of 1.7 by gap tuning the wiggler. Changing the energy can take several hours so user time is scheduled to make use of similar wavelengths on any given day.

The output coupling is via a Brewster plate output coupler. They have recently tried out hole coupling with mixed results [53]. The time structure has micropulses arriving at 2.857 GHz and 1- to 4-μs macropulses occurring at a repetition rate of up to 30 Hz. The spectral bandwidth is typically 0.5% FWHM in the 2- to 4-μm wavelength range, increasing to approximately 1% at the long-wavelength end of the range.

The user area is quite small with one user table available, and the user time available for outside use is less than at other infrared facilities in the United States but the lab has an active machine physics program, which results in a machine with great flexibility. Researchers at Duke have phase locked the microbunches in the laser, thus increasing the mode spacing in the frequency domain to 2.857 GHz [54]. One of the modes was then filtered out and high-resolution spectroscopy was carried out with it. The lab is also working on pulse

compression to achieve subpicosecond pulses tunable over the 2- to 4-μm range [9]. The beam is transported to the user room in a dry-air purged transport line. Various other lasers and a wet lab for biological or chemical preparations are available to users. Users have control over the wiggler gap, the cavity length, and the mirror steering. The macropulse length and the output coupler can easily be changed by the operator on request.

The lab is in the process of commissioning a storage ring-based FEL operating in the UV to VUV. This laser will be phase locked to the infrared laser but with a lower repetition rate of only 2.79 MHz. The present plan is to modify the accelerator for the infrared laser so that the repetition rate will be lowered to only 89.28 MHz. This modification would also allow greater micropulse energy and the ability to do pump probe experiments with a relatively long relaxation time. With the UV laser running, the facility will be capable of doing two-frequency pump probe experiments with one wavelength in the UV and one in the infrared. This upgraded facility may be available sometime in 1996. The lab has also proposed adding an addition to the lab that will provide approximately 13,000 ft^2 of additional lab space to the facility.

5.3 Institute for Plasma Physics, FOM

This well-run facility at the FOM Institute in Rinhuizen, the Netherlands, offers users a very large range of wavelengths in the infrared. The facility has two lasers, which, between them, cover the wavelength range between 6 and 100 μm. The first laser, called FEL-1, has a design wavelength range of 17 to 80 μm and has been operated betweeen 16 and 110 μm with usable power over the range of 16 to 100 μm. The average power during a 10-μs macropulse is greater than 1 kW (or micropulse energy of 1 μJ) over almost all of this range. The power versus wavelength curve has a broad peak of 10 kW between 25 and 50 μm. The second laser, FEL-2, has a design wavelength range of 8 to 30 μm and has been operated in the range of 6 to 20 μm to date. The power levels are again in the kilowatt range or larger over most of the available wavelength range. The first laser can tune over a wavelength range of a factor of 2 at a given energy. The second laser can tune over a factor of 3 due to its smaller vacuum chamber.

Because the mircopulse repetition rate is high (1 GHz) it makes sense to phase lock the micropulses as is done at Duke (in fact, they tend to phase lock without any effort due to the good coherence of the electron beam). Once the modes are locked, a single mode can be isolated from the frequency comb of the spectrum. Due to the long wavelength and short electron bunches, it is quite easy to trade off the spectral bandwidth and microbunch length [29].

There are six rooms available to users with all necessary utilities and signals provided. The optical beam is transported to the user area via an evacuated

beamline. The user facility is now an international user facility and will provide increased user time and more facilities for the users.

5.4 Princeton/Northrop–Grumman [31]

This compact facility, being constructed by Northrop–Grumman at Princeton University, is designed to provide operation in the wavelength range of 5 to 15 μm with high-energy micropulses produced at 142.8 MHz. Initial operation should be in the long-wavelength end of the design range since they are using a permanent magnet wiggler from LANL. Later operation will use an 8-mm period superferric undulator developed in collaboration with BNL. This will allow operation down to the shortest wavelengths in the range. The facility will be a university-based user facility rather than a national user facility.

5.5 Stanford University [55]

This user facility uses a superconducting accelerator to provide lasing in the infrared from 3 to 15 μm with very long macropulses of several milliseconds and a large separation between micropulses of 84.6 ns. The macropulses can occur at up to 120 Hz. The long separation between micropulses allows for samples to cool or relax between pulses and also allows the use of acousto-optic or electro-optic switches to pick out single pulses with good contrast. The microbunches have typically about 0.1 to 1 μJ of energy so the power in the laser beam delivered to the lab is on the order of 1 to 10 W during the macropulse. The micropulse length can be varied from one to several picoseconds in length so the peak power is from 0.1 to 1 MW during the micropulses. The facility has three operational lasers, with one operating in the near infrared from 3 to 8 μm, the second operating in the mid-infrared region from 5 to 15 μm, and the third operating in the far-infrared region from 18 to 64 μm.

The spectral bandwidths range from 0.1 to 1% FWHM. Due to a rather low gain, the laser must usually operate with dielectric optics so the user is generally limited to the wavelength range of the set of mirrors for the length of a shift. The mirrors can be changed in a couple of hours to change the wavelength range. The wavelength is changed by changing the electron beam energy.

The unique features of the Stanford facility include the following:

1. The wavelength is extremely stable. Using feedback techniques, it is possible to hold the wavelength stable to 0.01% over hours. The user can vary the wavelength over several percent using a single knob.
2. The wavelength can be slewed by several percent during the macropulse in any pattern the user desires. This may be useful in some vibrational studies.

3. The facility has tunable dye and Ti:sapphire lasers that are phase locked to the FEL so that two-frequency pump probe experiments can be carried out. The rms timing jitter between the two lasers is less than 5 ps.

There are eight experimental areas available for the users. Extensive diagnostics, an FTIR, and other non-mode-locked lasers are also available to users. This facility is quite well suited to chemical studies due to its good wavelength stability and slow micropulse repetition rate.

In the future the lab plans to upgrade the facility to include the use of a long-wavelength laser operating at wavelengths out to 100 μm. The laser has already been operated and is being commissioned. There are also plans to upgrade the electron-beam current to provide more energy per micropulse as well as more average power. In principle, one of the lasers at Stanford could provide hundreds of watts of average power in a mode-locked diffraction-limited beam.

5.6 University of California at Santa Barbara [16]

This facility is quite unique in that it uses an electrostatic accelerator instead of an rf linac to accelerate the beam. This results in quite a different temporal structure. There are no micropulses. The laser operates with pulses lasting up to 20 μs at a repetition rate of up to 4 Hz. The facility has two lasers operating, which provide wavelength coverage from 2.5 mm to 340 μm for the long-wavelength laser and 313 μm to 62 μm for the short-wavelength laser. The short-wavelength laser typically operates between 2 and 6.5 kW of output power. This can be enhanced somewhat by using a cavity dumper to produce tens of kilowatts of power for approximately 30 ns. The long-wavelength laser tends to operate for shorter macropulses but higher output powers with powers up to 27 kW available.

The laser usually operates with several longitudinal modes present in the cavity. With some care it is possible to injection lock the laser to an external laser, producing single-longitudinal-mode operation. The wavelength is tuned via changes in the electron-beam energy. This may be accomplished by computer tuning of the accelerator and electron-beam optics over a range of up to 10% in wavelength. Setting up a new wavelength may take anywhere from a few minutes to a few hours depending on whether the laser has operated at that wavelength in the past.

The laser output coupling is via hole coupling. The light is transported through an evacuated beamline to the four user areas.

The laser facility is used primarily to study heterostructures and other electronic materials although it is possible to use it to do any useful research in that wavelength range. Condenses matter interactions are the most obvious applications but some interesting biophysics experiments are also being carried out there.

There are plans to extend the wavelength range to shorter wavelengths by using a third wiggler operating at the third harmonic. This would provide light in the 30- to 90-μm range with kilowatts of power during the pulses.

5.7 Vanderbilt University [56]

This laser is very similar to the Mark III laser at Duke. In fact, the design of the Mark III was used to build the laser at Vanderbilt. The user demand at Vanderbilt has resulted in a slightly smaller tuning range of 7.7 to 2 μm, though the laser should be capable of going to longer wavelengths. The macropulses are approximately 5 μs in length and the energy per macropulse can be as high as 350 mJ. All these results were obtained using a Brewster plate output coupler. The laser has recently been modified to allow output coupling via a dielectric mirror. The peak power was improved greatly at the expense of some average power. The micropulse energy is as high as 10 μJ with macropulse energies as high as 200 mJ. The mirrors are mounted in a purged chamber so that mirrors can be changed in minutes.

The wavelength can be tuned via gap tuning over a range of ±25% by the user. Larger changes take less than an hour. A typical laser linewidth is 0.7% though it can be smaller at the smaller wavelengths and larger at the longer wavelengths. The wavelength is continuously monitored in the control room using a low power pickoff beam. This allows the operator to hold the wavelength steady over a shift to better than 0.2%.

The unique feature of the Vanderbilt facility is its excellent facilities available to the medical users. A fully equipped surgical suite is available for surgical studies on animals. This operating theater is equipped with a laser manipulator arm, and a computer-controlled mirror steering system allows the surgeon to make precision cuts in soft or hard tissue using acoustic sensors to monitor the cutting and control incision depth. The user can select the repetition rate of the laser from a local computer and can turn the laser on and off via the computer or a foot switch. There are presently five user rooms in addition to the surgical suite. The beam is delivered in an evacuated beamline to each of the rooms. Remote control of the beamline allows easy switching of the beam from room to room. Several other lasers, including a doubled mode-locked Nd:YAG laser, a tunable dye laser, an argon laser, and an excimer, are available to users.

In the future, the facility plans to install a Smith–Purcell device to provide coherent radiation in the range of 50 to 200 μm. They also have a program to backscatter the infrared laser off the electron beam to provide monochromatic X rays in the 10- to 18-keV range for use in medical imaging. Finally, they have recently obtained funding to add two more floors to their lab in order to provide more space for users and at least one surgical suite qualified for clinical surgery.

6. SUMMARY

I have tried to summarize some of the broad spectrum of science and technology in the field of tunable FELs. This is quite a difficult task. The capabilities of each laser tend to be varied and inconstant due to the constant drive to improve and upgrade the lasers. Although the first FEL operated almost 20 years ago, tunable sources of FELs that could be used by researchers in other fields besides laser physics only became available recently. The pace of development of tunable laser sources has been quite rapid since then. During the same period, FEL was "discovered" in Europe, Japan, China, and the former Soviet Union. Groups in all these countries have built several excellent user facilities and are in the process of bringing more of them on line each year. The present status is that there are six fully functional user facilities with seven more under construction and several more proposed. Federal research support in the United States has remained centered at the existing user facilities but, as the laser designs become smaller and less expensive, some private or state sources are funding efforts to provide users access to this useful research tool.

Although much progress has been made in the understanding and optimization of tunable FELs, much work still must be done in order to optimize the FEL versus cost and performance. I think that the Advanced Free-electron Laser (AFEL) at LANL [57] and the CIRFEL facility being commissioned at Princeton University are the future of low-average-power tunable FELs in the infrared and that this design of laser will allow better optimization of the design for users. For high average power, energy recovery linear accelerators and electrostatic accelerators will provide coverage with continuous electron beams such as those being developed at the University of Central Florida and UCSB or continuously pulsed beams such as in the CEBAF designs [30].

REFERENCES

1. J. M. J. Madey, *J. Appl. Phys.* **42** , 1906–1913 (1971).
2. W. B. Colson, Ph.D. Thesis, Stanford University (1977).
3. R. M. Phillips, *IRE Trans. Electron Dev.* **ED-7,** 231 (1960).
4. R. M. Phillips, *Nucl. Instrum. Meth.* **A272,** 1–9 (1988).
5. A. Doria, G. P. Gallerano, and A. Renieri, *Opt. Commun.* **80,** 417–424 (1991).
6. C. A. Brau, *Free-Electron Lasers*, Academic Press, San Diego (1990).
7. M. L. Stitch and M. S. Bass, Eds., *Laser Handbook*, Vol. 4, North Holland, Amsterdam (1985).
8. S. V. Benson, J. Schultz, B. A. Hooper, R. Crane, and J. M. J. Madey, *Nucl. Instrum. Meth.* **A272,** 22–28 (1988).
9. E. B. Szarmes, S. V. Benson, and J. M. J. Madey, *Nucl. Instrum. Meth.* **A296,** 755–761 (1990).
10. R. H. Pantell *et al.*, *J. Opt. Soc. Am. B* **6,** 1008–1014 (1989).
11. B. A. Hooper, S. V. Benson, R. C. Straight, and J. M. J. Madey, *Nucl. Instrum. Meth.* **A296,** 797–803 (1990).
12. J. N. Eckstein *et al.*, "Additional Experimental Results from the Stanford 3 Micron FEL," in *Free-electron Generators of Coherent Radiation* (G. T. Moore, S. F. Jacobs, H. S. Piloff, M.

Sargent, M. O. Scully, and R. Spitzers, Eds.). Vol. 8, pp. 49–75, Addison-Wesley, Reading, MA (1981).
13. B. E. Newnam *et al.*, *IEEE J. Quant. Elec.* **QE-21,** 867–881 (1985).
14. A. H. Lumpkin *et al.*, *Nucl. Instrum. Meth.* **A296,** 181–185 (1990).
15. L. Elias, *IEEE J. Quantum Electron.* **QE-23,** 1470–1475 (1987).
16. G. Ramian, *Nucl. Instrum. Meth.* **A318,** 225–229 (1992).
17. T. I. Smith, J. C. Frisch, R. Rohatgi, H. A. Schwettman, and R. L. Swent, *Nucl. Instrum. Meth.* **A296,** 33–36 (1990).
18. S. C. Chen, G. Bekefi, S. DiCecca, and R. Temkin, *Nucl. Instrum. Meth.* **A285,** 290–293 (1989).
19. J. C. Goldstein, R. L. Sheffield, B. E. Carlsten, and R. W. Warren, *Nucl. Instrum. Meth.* **A296,** 282–287 (1990).
20. K. P. Paulson, *Nucl. Instrum. Meth.* **A296,** 624–630 (1990).
21. R. W. Warren *et al.*, *Nucl. Instrum. Meth.* **A285,** 1–10 (1989).
22. A. F. G. Van der Meer *et al.*, *Nucl. Instrum. Meth.* **A341,** ABS 23 (1994).
23. M. Curtin *et al.*, *Nucl. Instrum. Meth.* **A296,** 69–74 (1990).
24. M. Billardon *et al.*, *IEEE J. Quantum. Electron.* **QE-21,** 805–823 (1985).
25. G. N. Kulipanov *et al.*, *Nucl. Instrum. Meth.* **A296,** 1–3 (1990).
26. S. V. Benson *et al.*, *Nucl. Instrum. Meth.* **A296,** 110–114 (1990).
27. C. A. Brau, *Nucl. Instrum. Meth.* **A318,** 38–41 (1992).
28. R. Prazeres, J. M. Berset, F. Glotin, D. Jaroszynski, and J. M. Ortega, *Nucl. Instrum. Meth.* **A331,** 15–19 (1993).
29. R. J. Bakker *et al.*, *Nucl. Instrum. Meth.* **A331,** 79–93 (1993).
30. G. Neil, S. V. Benson, "Issues in High Power FEL Design at the Continous Electron Beam Accelerator Facility," in *Laser Resonators and Coherent Optics: Modeling, Technology, and Applications, Proc. SPIE* **1868,** 41–55. SPIE, Bellingham, WA (1993).
31. J. Krishnaswamy *et al.*, "Design and Construction of a Compact Infra Red Free Electron Laser CIRFEL," in *IEEE 1993 Particle Accelerator Conf.*, Vol. 2, pp. 1527–1529. IEEE, Washington D.C. (1993).
32. J. M. J. Madey and R. C. Taber, "Equations of Motion for a Free-electron Laser with a Transverse Gradient," in *Free-electron Generators of Coherent Radiation* (S. F. Jacobs *et al.*, Eds.), Vol. 7, pp. 741–774, Addison-Wesley, Reading, MA (1979).
33. W. B. Colson, *IEEE J. Quantum Electron.* **QE-17,** 1417–1427 (1981).
34. S. V. Benson and J. M. J. Madey, *Phys. Rev.* **A39,** 1579–1581 (1989).
35. R. W. Warren, L. C. Haynes, D. W. Feldman, W. E. Stein, and S. J. Gitomer, *Nucl. Instrum. Meth.* **A296,** 84–88 (1990).
36. R. W. Warren, *Nucl. Instrum. Meth.* **A304,** 512–515 (1993).
37. R. W. Warren, D. W. Feldman, and D. Preston, *Nucl. Instrum. Meth.* **A296,** 558–562 (1990).
38. R. W. Warren *et al.*, *Nucl. Instrum. Meth.* **A331,** 48–51 (1993).
39. P. G. O'Shea *et al.*, *Nucl. Instrum. Meth.* **A331,** 62–68 (1993).
40. A. E. Siegman, *Proc. IEEE* **53,** 277–287 (1965).
41. Y. A. Anan'ev, N. A. Sventsitskaya, and V. E. Sherstobitov, *Sov. Phys. JETP* **28,** 69–74 (1969).
42. R. W. Warren, private communication.
43. G. N. Kulipanov *et al.*, *Nucl. Instrum. Meth.* **A331,** 98–102 (1993).
44. A. E. Siegman, *IEEE J. Quantum Electron.* **QE-28,** 1243 (1992).
45. C. C. Shih, "Analysis of Stable-Unstable Free-Electron Laser Resonators," in *Laser Resonators and Coherent Optics: Modeling, Technology, and Applications, Proc. SPIE* **1868,** 278–285. SPIE, Bellingham, WA (1993).
46. G. T. McNice and V. E. Derr, *IEEE J. Quant. Electron.* **QE-5,** 569–574 (1969).
47. D. E. McCumber, *Bell Syst. Tech. J.* **48,** 1919–1935 (1969).
48. M. Xie and K. J. Kim, *Nucl. Instrum. Meth.* **A318,** 877–884 (1992).
49. R. P. Walker, *Nucl. Instrum. Meth.* **A237,** 366–380 (1985).
50. E. D. Shaw and R. J. Chichester, *Nucl. Instrum Meth.* **A318,** 47–51 (1992).

51. J. Ortega, private communication.
52. F. Glotin *et al.*, *Nucl. Instrum. Meth.* **A341,** 49–53 (1994).
53. G. A. Barnett, S. V. Benson, and J. M. J. Madey, *IEEE J. Quantum Electron.* **29,** 479–486 (1993).
54. E. B. Szarmes, A. D. Madden, and J. M. J. Madey, Optical phase locking of a 2.856 GHz harmonically modelocked free-electron laser, *J. Opt. Soc. America B.*, in press.
55. T. I. Smith, H. A. Schwettman, K. W. Berryman, and R. L. Swent, "Facilities at the Stanford Picosecond FEL Center," in *Free-electron Laser Spectroscopy in Biology, Medicine and Material Science, Proc. SPIE* **1854,** 23–33, SPIE, Bellingham, WA (1993).
56. C. A. Brau and M. Mendenhall, "The Vanderbilt University Free-electron Laser Center," in *Free-electron Laser Spectroscopy in Biology, Medicine and Material Science, Proc. SPIE* **1854,** 2–10, SPIE, Bellingham, WA (1993).
57. D. C. Nguyen *et al.*, *Nucl. Instrum. Meth.* **A341,** 29–33 (1994).

Index

Achromatic
  multiple-prism beam expander, 181
Acousto-optic filter, 369, 380, 393–397, 405–407, 411, 420, 432
Amplified spontaneous emission (ASE), 12, 42, 177, 178, 181, 223, 299
Amplifier, 36, 48
  dye laser, 178–180
  excimer laser, 36, 42, 48
  master-oscillator power (MOPA), 178
  multistage, 180
Antireflection coatings, 365–367, 377, 415–417

Bandwidth, 34, 174, 283, 284
Beam divergence, 19, 44, 186, 360
  equation, 19
Birefringent filters, 285–286, 393, 392, 404, 405
Bistability, 365, 377, 424, 425
Boltzman distribution, 74
Broadening
  Doppler, 82
  homogeneous, 77
  inhomogeneous, 78

Cavity
  cw dye laser, 187–189
    linear, 189, 190
    ring, 189, 190
  dumping, 221
  femtosecond dye laser, 193, 196–197
    linear, 193, 194, 196–197
    ring, 193, 194, 196–197
  free electron laser, 456–459
  grazing-incidence grating, 10, 13, 14, 35, 36, 46–47, 284
  hybrid multiple-prism grazing incidence (HMPGI) grating, 10–14, 35, 178
  Littrow grating, 10, 284
  loss ratio, 378, 407
  Michelson interferometer, 47
  multipass grating interferometer, 35, 47
  multiple-etalon, 10, 35, 36
  multiple-prism Littrow (MPL) grating, 10–14, 35, 36, 178
  Q, 79
  semiconductor laser
    double ended, 368–369, 378
    extended, 368, 378

Cavity *(continued)*
external, 349–468
ring, 369, 378
telescopic, 13
Cesium atomic standard, 89–90
Complementarity
tunable laser, 4–5
Compton regime, 446, 448
Chromatic aberration, 382, 383
Confinement factor, 353

Degenerate resonator, 381, 402, 403, 434, 435
Density
Al_2O_3, 249
$BeAl_2O_4$, 254
GSGG, 272
$LiCaAlF_6$, 265
MgF_2, 277
YAG, 272
Diffraction, 16–18
equation, 16–17
Diffraction grating, 15, 17, 369, 380, 384, 385–390, 393, 396, 398–401, 404–409, 411, 418, 419–421, 428, 429, 431–434
efficiency, 26, 388–389
equation, 19, 21, 45, 283
grazing-incidence, 387–389, 399, 407, 408, 420, 421
Littrow, 369, 384, 387, 388, 389, 398, 407, 408, 411, 418, 420, 428, 429
Dirac formalism, 16–17
Dispersion
equations, 17
etalon, 28
generalized, 21–23
grating, 19, 21, 284
intracavity, 19, 21–24, 28
multiple-prism, 21–24, 43, 44
prism materials, 195
zero, 181
Dispersive
cavity (*see* Oscillators)
linewidth (*see* Linewidth)
Distributed
Bragg reflector, 351, 390
feedback laser, 351, 423, 431
Divergence (*see* Beam divergence)
Double heterostructure, 358

Electron beam, 446, 447, 451, 454
Electronic configuration, 226, 230
Energy, 3, 13–14, 35, 36, 175, 178, 179, 183, 186, 199
electronic, 37, 168–170
rotational, 69–70
vibrational, 65–69, 169, 171
Energy level diagram
CO_2 laser, 67, 70, 71, 94
dye laser, 173
excimer laser, 37
transition metal solid-state laser, 227, 231, 243, 247, 252
Etalon, 10, 13, 20, 28, 48, 186, 286, 372, 376, 380, 383, 391, 392, 399, 402–404, 418, 421–423, 429
dispersion, 28
finesse, 28
Excimer
laser transitions, 34
bandwidth, 34
rare gas, 41
rare gas halide, 37–41

Fabry-Perot (*see* Etalon)
Femtosecond
pulse free electron laser, 447
pulse dye lasers, 191–197
pulses, 194, 196–197
Forced oscillator (*see* Oscillator)
Fourier transform, 455
Frequency
absolute, 95
CO_2 laser, 99–136
stabilization, 79–95, 137–143, 189–192
Fresnel number, 16, 18

Gain, 352
bandwidth, 362–364
stripe, 360–362, 375
Gaussian (*see also* Transverse mode, single), 78, 296, 299, 300, 356, 458
Geometrics
cell, 176–177
excitation, 175–176
Grating (*see* Diffraction grating)
Group velocity dispersion (GVD), 23, 192, 194

Heat capacity
Al_2O_3, 249
$BeAl_2O_4$, 254
GSGG, 272

$LiCaAlF_6$, 265
MgF_2, 277
YAG, 272
Heterodyne
CO_2 laser system, 87–88, 137–143
Homogeneous broadening (*see* Broadening)
HMPGI grating oscillator (*see* Oscillators)

Inductive stabilization, 57
Inhomogeneous broadening (*see* Broadening)
Injection seeding, 435
Interference
equation, 16–17
filter, 392, 402, 434
one-dimensional, 16
two-dimensional, 17

Lamb dip, 83, 84, 86
Laser dye molecule, 168, 173, 175, 182–183, 196–198, 200–213
absorber, 191, 196–197
Lasers
argon ion, 187
CO_2, 6, 13, 35
CO_2 isotope, 63–161
absolute frequencies, 95–137
broadening, 76–79
design, 149–154
pressure shift, 137–143
regular band laser transitions, 71–76
reference, 88
small signal gain, 144–149
spectral purity, 79–82
spectroscopic applications, 159–160
stability, 79–95, 137–143
dye, 2, 3, 5, 13, 14
cw, 2, 3, 185–191
femtosecond, 191–197
flashlamp-pumped, 179–185
laser-pumped, 172–180, 184, 195, 198, 199
pulsed, 2, 3, 13, 14, 172–185, 195, 198, 199
solid-state, 14, 195, 198, 199
excimer, 33–59
Ar_2*, 41
ArCl, 40
ArF, 3, 6, 13, 34, 35, 37
discharge, 53–59
Kr_2*, 41
KrCl, 40
KrF, 3, 6, 13, 34, 35, 38, 174
Xe_2*, 41
XeBr, 40
XeCl, 6, 13, 34, 35, 40, 174, 175
XeF, 6, 34, 38, 35, 40, 174
free electron laser (FEL), 2, 3, 4, 443–468
cavities, 456–459
facilities, 460–468
general characteristics, 447–449
harmonic operation, 453–455
oscillator, 444
physics, 443–447
polarization, 445, 453
power, 461
tuning, 450–456
wavelength range, 461
wiggler, 444–446, 451–453, 455, 459–460
HgBr, 3, 174
krypton ion, 187
metal-vapor
cadmium, 174
calcium, 174
copper, 3, 174, 175, 178
gold, 174
strontium, 174
nitrogen, 3, 174
semiconductor, 1, 2, 5, 13, 349–435
AlGaAs/GaAs, 363
AlGaInP/GaAs, 363
alignment stability, 380
alignment tolerance, 381
astigmatism, 356, 359, 360
bulk active region, 358
chromatic aberration, 382, 383
GaAlAs, 2, 13, 358
GaAlAs/GaAs, 364
GaAs/AlGaAs, 365
internal loss, 353
InGaAlP/GaAs, 364
InGaAs/AlGaAs, 365
InGaAs/InGaAsP, 365
InGaAs/InP, 363
InGaAsP/GaAs, 363
InGaAsP/InP, 2, 13, 363, 364
lead-salt, 155–158
mirror loss, 353, 376, 377
mode hopping, 377
mode selectivity, 378, 407–409
multimode oscillation, 373
multimode suppression, 417–419, 424
quantum well, 358, 363–365, 403
reflectance facet, 361, 365–368, 374, 399, 415–418, 424–426
sidemode suppression, 401, 403, 404, 418, 431

Lasers *(continued)*
threshold current, 352–354, 356, 358–361, 363, 376, 405, 412–418, 422
vertical cavity, 351
wavelength stabilization, 421
transition metal solid-state, 219–288
Co:MgF_2, 275–281
Cr: Al_2O_3 (ruby), 174, 246–251
Cr:$BeAl_2O_3$ (alexandrite), 2, 3, 6, 13, 251–258
Cr:GSAG, 270–275
Cr:GSGG, 270–275
Cr:YAG, 270–275
Cr:$LiCaAlF_6$, 263–269
Cr:$LiSrAlF_6$, 263–269
Ni:MgF_2, 275–281
Nd:YAG, 174, 222, 262, 263
physics of, 232–246
Ti:Al_2O_3 (titanium sapphire), 2–4, 6, 13, 258–263
V:MgF_2, 275–281
Lattice constant
Al_2O_3, 249
$BeAl_2O_4$, 254
GSGG, 272
$LiCaAlF_6$, 265
MgF_2, 277
YAG, 272
Lens
aspheric, 383
ball, 382, 384, 399
camera, 384, 398, 428
cylinder, 382, 399
GRIN, 382, 383, 399, 409, 428
microscope objective, 382, 383, 429
silicon, 383
Linewidth, 13–14, 17–19, 22, 35, 36, 41, 44, 77–78, 178, 186, 190
broadening factor, 355, 424–426
dispersive, 17–19, 22, 44
Doppler, 78, 82
double-longitudinal-mode, 182
external cavity laser, 350, 355, 360, 373
multiple-pass, 22, 44
Schawlow–Townes, 80, 82, 155
single-longitudinal-mode, 190
solitary laser diode, 349, 355
Lineshape function, 76–79
Liquid-phase epitaxy, 358
Lorentzian profile, 76, 79

Magnetic pulse compression, 55, 56
Magnets, 459–460
Maxwelian distribution, 78
Melting point
Al_2O_3, 249
$BeAl_2O_4$, 254
GSGG, 272
$LiCaAlF_6$, 265
MgF_2, 277
YAG, 272
Metrology, 433
Modal instability, 365, 377, 424, 425
Mode locking
colliding pulse (CPM), 191, 192, 194
hybrid, 197
passive, 196
Molecular constants
CO_2 laser, 95–136
MPL grating oscillator (*see* Oscillators)
MPMMA (*see* Lasers, dye, solid-state)
Multiple-prism
beam expander, 11, 17, 20–22
generalized array, 22
pulse compression array, 24–25
transmission efficiency, 24–25

Optical fiber, 375, 390, 421, 431
lensed, 384, 429
Optical isolator, 369, 376, 397, 399, 401, 404, 429
Optical parametric oscillators (OPOs), 1–3, 5, 12, 293–345
acceptance angles, 306–314
ADP, 323, 325, 331, 332
$AgGaS_2$, 323, 325, 331
$AgGaSe_2$, 306, 307–308, 310, 323, 325, 331, 337, 338
average power limitations, 317–321
BBO, 2, 323, 325, 331, 335
CD*A, 323, 325, 331, 333
CdSe, 323, 325, 331, 339
KDP, 323, 324, 331, 332
KTP, 323, 325, 331
LBO, 323, 325, 331
$LiNbO_3$, 3, 323, 325, 331, 333, 334, 336
nonlinear crystals, 321–328
biaxial, 324
index, 323
nonlinear coefficients, 324–325
Sellmeier coefficients, 331
thermal conduction, 323
transmission, 323
uniaxial, 324
performance, 334–342

phase matching calculations, 328–334
spectral bandwidth, 306–314
Tl_3AsSe_3, 323, 325, 331, 341
tuning, 343–345
$ZnGeP_2$, 323, 325, 331, 340
Optical transparency
Al_2O_3, 249
$BeAl_2O_4$, 254
GSGG, 272
$LiCaAlF_6$, 265
MgF_2, 277
YAG, 272
Optogalvanic effect, 422
ORMOSIL (*see* Lasers, dye, solid-state)
Oscillator
CO_2 laser, 144–148
dispersive, 10–16, 35
dye laser, 13–14, 176–179, 182, 183, 185, 186
solid-state, 14
excimer laser, 42, 43, 48
free electron laser, 444
forced, 36, 183, 185, 186
grazing-incidence grating, 10, 13, 14, 27, 35, 36
HMPGI grating, 10–15, 26, 177, 178, 181, 184
Littrow grating, 10, 27
local, 141, 157, 351, 431
master, 36, 178, 181, 183, 185, 186
MPL grating, 10-14, 16, 26, 35, 36, 177, 178, 181, 182, 184–186
multiple-etalon, 35, 36, 48, 186
narrow-linewidth, 5, 6, 9–31
ruggedized, 182, 183, 184, 186
solid-state laser, 14
semiconductor laser, 14
tuning range, 13–14

Parametric
interactions, 297–301
oscillation, 301–306
PMMA (*see* Lasers, dye, solid-state)
Polarization, 12, 26, 248, 253, 255, 260, 266, 267, 278, 280, 282, 285, 297, 298, 302, 314, 317, 356, 388, 445, 453
Polarizer
output coupler, 12, 15, 182
Power
average, 3
cw, 3, 190
pulsed, 41, 461
Prepulse discharge, 57
Preionization
corona, 55
UV, 53
VUV, 55
X-ray, 54, 55
Prism (*see also* Multiple-prism), 24, 282, 349, 351, 384, 387, 399, 409
Probability, 16–17
amplitude, 16–17
Pulse compression, 23–24, 192–195
double-prism compressor, 23–24, 194
four-prism compressor, 23–24, 194
intracavity multiple-prism dispersion, 23–24, 192–195
six-prism compressor, 23–24

Q-switch, 220–221

Rate equations
dye laser, 168–172
Ray transfer matrix, 20, 29–30
distance, 20
etalon, 20
grating, 20
lens, 20
mirror, 20
multiple-prism, 20, 29–30
telescope, 20
Refractive index
Al_2O_3, 249
BK7, 195
$BeAl_2O_4$, 254
F2, 195
GSGG, 272
LaSF9, 195
$LiCaAlF_6$, 265
MgF_2, 277
quartz, 195
SF10, 195
YAG, 272
ZnSe, 195

Saturable absorber (*see* Laser dye, absorber)

Telescope
Galilean, 17, 20
multiple-prism, 11, 17
Newtonian, 20

Thermal
  conductivity
    Al_2O_3, 249
    $BeAl_2O_4$, 254
    GSGG, 272
    $LiCaAlF_6$, 265
    MgF_2, 277
    YAG, 272
  expansion
    Al_2O_3, 249
    $BeAl_2O_4$, 254
    GSGG, 272
    $LiCaAlF_6$, 265
    MgF_2, 277
    YAG, 272
Transition, 173, 174, 186
  cross sections, 173
  electronic, 168, 169
  rates, 173
  vibronic, 228
Transmission efficiency
  prismatic, 25
Transverse mode
  calculations, 16, 18
  single, 10, 15, 93, 153
Tuning
  CO_2 laser, 98
  energy, 450–451
  excimer laser, 13, 41–48
  dye laser, 13–14, 168, 190
  etalon, 28
  grating, 26
  lead-salt semiconductor laser, 155
  nonlinearity, 372, 377, 426
  optical parametric oscillators, 343–345
  phase continuous, 409–412
  prismatic, 27–28
  quasi continuous, 372
  range, 2, 3, 13–14, 98, 154, 168, 190, 362–364, 461
  semiconductor laser, 14, 362–364, 372, 377, 399–407, 409–412, 426
  solid state laser, 14, 281–288
  synchronous, 27
  wiggler, 452–455

Ultrashort pulses, 3, 4, 194, 196–197
Unidirectional device, 188
Unstable resonator
  dye laser, 185
  excimer laser, 50–53
  free electron laser, 457

Waveguide, 358–360
Wavelength
  division mulitplexing, 431, 432
  jitter, 186
  stabilization, 421–422
  tuning (*see* Tuning)

X-ray preionization (*see* Preionization)

ZnSe, 195, 458

Optics and Photonics

Edited by Paul F. Liao, *Bell Communications Research Inc., Red Bank, New Jersey*
Paul L. Kelley, *Electro-Optics Technology Center, Tufts University, Medford, Massachusetts*
Ivan P. Kaminow, *AT&T Bell Laboratories, Holmdel, New Jersey*

N.S. Kapany and J.J. Burke, *Optical Waveguides*
Dietrich Marcuse, *Theory of Dielectric Optical Waveguides*
Benjamin Chu, *Laser Light Scattering*
Bruno Crosignani, Paolo DiPorto and Mario Bertolotti, *Statistical Properties of Scattered Light*
John D. Anderson, Jr., *Gasdynamic Lasers, An Introduction*
W.W. Duley, *CO_2 Lasers: Effects and Applications*
Henry Kressel and J.K. Butler, *Semiconductor Lasers and Heterojunction LEDs*
H.C. Casey and M.B. Panish, *Heterostructure Lasers: Part A. Fundamental Principles, Part B. Materials and Operating Characteristics*
Robert K. Erf, editor, *Speckle Metrology*
Marc D. Levenson, *Introduction to Nonlinear Laser Spectroscopy*
David S. Kliger, editor, *Ultrasensitive Laser Spectroscopy*
Robert A. Fisher, editor, *Optical Phase Conjugation*
John F. Reintjes, *Nonlinear Optical Parametric Processes in Liquids and Gases*
S.H. Lin, Y. Fujimura, H.J. Neusser and E.W. Schlag, *Multiphoton Spectroscopy of Molecules*
Hyatt M. Gibbs, *Optical Bistability: Controlling Light with Light*
D.S. Chemla and J. Zyss, editors, *Nonlinear Optical Properties of Organic Molecules and Crystals, Volume 1, Volume 2*
Marc D. Levenson and Saturo Kano, *Introduction to Nonlinear Laser Spectroscopy, Revised Edition*
Govind P. Agrawal, *Nonlinear Fiber Optics*
F.J. Duarte and Lloyd W. Hillman, editors, *Dye Laser Principles: With Applications*
Dietrich Marcuse, *Theory of Dielectric Optical Waveguides, 2nd Edition*
Govind P. Agrawal and Robert W. Boyd, editors, *Contemporary Nonlinear Optics*
Peter S. Zory, Jr., editor, *Quantum Well Lasers*
Gary A. Evans and Jacob M. Hammer, editors, *Surface Emitting Semiconductor Lasers and Arrays*
John E. Midwinter, editor, *Photonics in Switching, Volume I, Background and Components*
John E. Midwinter, editor, *Photonics in Switching, Volume II, Systems*
Joseph Ziss, editor, *Molecular Nonlinear Optics*
William Burns, editor, *Optical Fiber Rotation Sensing*
Mario Dagenais, editor, *Integrated Optoelectronics*
Robert H. Kingston, *Optical Sources, Detectors, and Systems: Fundamentals and Applications*
F.J. Duarte, editor, *Tunable Lasers Handbook*

Yo-Han Pao, *Case Western Reserve University, Cleveland, Ohio*, Founding Editor 1972–1979

Tunable Lasers HANDBOOK

Edited by
F. J. Duarte
Eastman Kodak Company, Rochester, New York

A Volume in the OPTICS AND PHOTONICS Series
(formerly Quantum Electronics)

Tunable Lasers Handbook provides an up-to-date survey on the physics, technology, and performance of widely applicable sources of tunable coherent radiation. Topics include dispersive oscillators, excimer lasers, CO_2 lasers, dye lasers, tunable solid state lasers, optical parametric oscillators, tunable semiconductor lasers, and free electron lasers.

This book gives active researchers and engineers the practical information they need to choose an appropriate tunable laser for their particular applications.

Key Features

- Presents a unified and integrated perspective on tunable lasers
- Includes coverage of optical parametric oscillators and tunable gas, liquid, solid state, and semiconductor lasers
- Provides sources spanning the electromagnetic spectrum from the UV to the FIR
- Contains 182 figures and 68 tables

ISBN 0-12-222695-X
90018
9 780122 226953

Academic Press